Dissertation

submitted to the
Combined Faculties for the Natural Sciences and for Mathematics
of the Ruperto-Carola University of Heidelberg, Germany
for the degree of
Doctor of Natural Sciences

Put forward by

Simon Mayer

born in Mannheim

Oral examination: 18.01.2017

Dynamics of reactive and inert gases in soil air and groundwater in the context of noble gases as environmental tracers

Referees:

Prof. Dr. Werner Aeschbach
Prof. Dr. Ingeborg Levin

Abstract

Applications of inert gases in groundwater hydrology require a profound understanding of underlying biogeochemical processes. Some of these processes are, however, not well understood and therefore require further investigation. This is the first study simultaneously investigating soil air and groundwater in the context of noble gas tracer applications, accounting for seasonal effects in different climate regions. The sampled data confirm a general reliability of common assumptions proposed in the literature. In particular, a solubility-controlled description of excess air formation and of groundwater degassing can be confirmed. This study identifies certain effects which need to be taken into account to reliably evaluate noble gas patterns. First, long-term samplings suggest a permanent temperature-driven equilibration of shallow groundwater with entrapped air bubbles, even some years after recharge. Second, minor groundwater degassing is found to challenge existing excess air model approaches, depending on the amount and the fractionation of excess air. Third, soil air composition data of this study imply a potential bias of noble gas temperatures by up to about 2°C due to microbial oxygen depletion and a reduced sum value of O_2+CO_2. This effect causes systematically lower noble gas temperatures in tropical groundwater samples and in shallow mid-latitude groundwater samples after strong recharge during the warm season. However, a general bias of noble gas temperatures in mid-latitudes is probably prevented by a predominant recharge during the cold season, accompanied by nearly atmospheric noble gas mixing ratios in the soil air. Findings of this study provide a remarkable contribution to the reliability of noble gas tracer applications in hydrology, in particular with regard to paleoclimate reconstructions and an understanding of subsurface gas dynamics.

Zusammenfassung

Traceranwendungen inerter Gase in Grundwasserstudien erfordern ein tiefgründiges Verständnis zugrundeliegender biogeochemischer Prozesse. Diese sind bei weitem noch nicht vollständig verstanden und zeigen daher einen entsprechenden Forschungsbedarf auf. Dies ist die erste Studie, in der auf Basis von Edelgasen und unter Berücksichtigung saisonaler Effekte in verschiedenen Klimaregionen sowohl Bodenluft als auch Grundwasser simultan untersucht werden. Erhobene Messdaten bestätigen allgemein grundlegende Annahmen entsprechender Traceranwendungen. Insbesondere wird der Ansatz einer löslichkeitsbasierten Beschreibung von Luftüberschuss und Grundwasserentgasung motiviert. Daneben werden auch Aspekte aufgezeigt, deren Berücksichtigung essentiell für verlässliche Edelgasstudien ist. Erstens implizieren Langzeitbeobachtungen an flachem Grundwasser einen permanenten Gasaustausch mit in der Porenmatrix eingeschlossenen Luftblasen, selbst Jahre nach der eigentlichen Grundwasserneubildung. Zweitens kann mikrobielle Gasbildung im Grundwasser traditionelle Interpretationsansätze erschweren, in Abhängigkeit von der Menge des Luftüberschusses und dessen Fraktionierung. Drittens legen Bodenluftanalysen eine potenzielle Verfälschung von Edelgastemperaturen um bis zu 2°C nahe, hervorgerufen durch Sauerstoffzehrung und einen reduzierten Summenwert von O_2+CO_2. Die Relevanz dieses Effektes wird für tropische Regionen, als auch für flaches Grundwasser der mittleren Breiten nach ausgeprägten Niederschlagsperioden im Sommer bestätigt. Generell jedoch ist in mittleren Breiten eine entsprechende Verfälschung von Edelgastemperaturen durch atmosphärische Bodenluftzusammensetzungen und eine vorherrschende Grundwasserneubildung im Winter beschränkt. Die Erkenntnisse dieser Studie leisten einen wichtigen Beitrag zur Verlässlichkeit von hydrologischen Traceranwendung inerter Gase, insbesondere in Hinblick auf Paläoklimastudien sowie ein Verständnis der Gasdynamik im Untergrund.

Contents

1 Introduction 1

2 Theoretical basis 5
2.1 Soil compartments and their interaction . . . 5
2.1.1 Soil parameters (litosphere) . . . 5
2.1.2 Soil water and groundwater (hydrosphere) . . . 7
2.1.3 Microbiological activity (biosphere) . . . 12
2.1.4 Soil air (atmosphere) . . . 19
2.2 Subsurface transport processes . . . 21
2.2.1 Solute transport . . . 21
2.2.2 Heat transport . . . 26
2.2.3 Gas exchange . . . 28
2.3 Tracers in environmental physics . . . 31
2.3.1 Stable noble gas isotopes . . . 31
2.3.2 Radioactive noble gas isotopes . . . 37
2.3.3 Tritium . . . 38
2.3.4 Stable isotopes of water . . . 39

3 Measurement techniques and data evaluation 45
3.1 Mobile samplings and in-situ measurements . . . 45
3.1.1 Soil gas composition . . . 45
3.1.2 Volumetric soil moisture . . . 46
3.1.3 Radon . . . 49
3.1.4 Soil material analysis . . . 49
3.1.5 Soil temperature . . . 50
3.1.6 Groundwater sampling . . . 50
3.2 Laboratory analysis . . . 53
3.2.1 Analysis of gas sample composition by Omnistar . . . 53
3.2.2 Analysis of noble gases in soil air and groundwater . . . 61
3.2.3 Tritium: Low level counting . . . 70
3.2.4 Stable isotopes of water: Cavity Ring Down Spectroscopy . . . 70
3.3 Data evaluation and modeling . . . 70

3.3.1 Excess air models 70
3.3.2 Excess air model fits and NGT determination 76
3.3.3 ^{3}H–^{3}He dating of water samples 77
3.3.4 Modeling of subsurface gas dynamics and soil gas fractionation 78

4 Sampling sites 83
4.1 Long-term sampling site near Mannheim (Germany) 83
4.2 Sampling sites near Santarém (Brazil) 88

5 Long-term observations in mid-latitudes 93
5.1 Unsaturated zone 93
5.1.1 Soil air composition 93
5.1.2 Soil moisture and -temperature 97
5.2 Saturated zone 100
5.2.1 Physical groundwater parameters 100
5.2.2 Noble gases and stable isotopes of water 102
5.2.3 Excess air model fits and NGT determination 107
5.3 Discussion 116
5.3.1 Determining factors of soil air composition under mid-latitude climate conditions 116
5.3.2 Seasonal fluctuations of NG concentrations in shallow groundwater 123

6 Tracer applications in tropical latitudes 139
6.1 Unsaturated zone 139
6.1.1 Soil air composition 139
6.1.2 Physical parameters of the unsaturated zone 141
6.2 Saturated zone 142
6.2.1 Stable isotopes of water 142
6.2.2 Physical and chemical groundwater parameters 144
6.2.3 Dissolved NG contents in groundwater 146
6.2.4 Groundwater dating 147
6.2.5 Excess air model applications and determination of NGTs 148
6.3 Discussion 153
6.3.1 Determining factors of soil air composition under tropical climate conditions 153
6.3.2 Saturated zone: determinants of dissolved NG contents 157
6.3.3 Saturated zone: discussion of excess air model applications and of NGTs . . 159

7 General discussion and summary 165
7.1 Unsaturated zone: determinants of soil air composition 165
7.2 Saturated zone: determinants of dissolved gas contents 168
7.3 Subsurface gas dynamics in the context of gas tracer applications 172

8 Conclusion and Outlook **175**

A Calculations and annotations **177**

B Measurement results and further data **187**

List of tables **i**

List of figures **iii**

Bibliography **vii**

Glossary

AEW	Air equilibrated water
ATP	Adenosine triphosphate
CE	Closed system equilibration
CT	Charcoal trap
EM	Electromagnetic
FDR	Frequency domain reflectometry
GR	Gas diffusion relaxation
GMWL	Global meteoric water line
GWT	Groundwater temperature
LMWL	Local meteoric water line
MAAT	Mean annual atmospheric temperature
MAST	Mean annual soil temperature
NG	Noble gas
NGT	Noble gas temperature
OD	Oxygen depletion
ORP	Oxidation-reduction potential
PR	Partial re-equilibration
SEM	Secondary electron multiplier
SST	Stainless steel trap
TDR	Time domain reflectometry
UA	Unfractionated excess air
VSMOW	Vienna standard mean ocean water
WC	Water column
WTT	Water table temperature

Chapter 1

Introduction

Applications of environmental tracers provide an enormous potential to understand the Earth's climate system and its underlying physical processes. In this context noble gases (NGs) proved to be reliable tracers, favored by their chemical inertness and by well-known natural sinks and sources. Prominent research areas of NG studies are exchange processes between different geochemical reservoirs and paleoclimate reconstruction (Stute and Schlosser, 1993; Aeschbach-Hertig and Solomon, 2013), but also dating purposes (Cook and Solomon, 1997) and subsurface gas dynamics (Amos et al., 2005; Jones et al., 2014). All these applications take advantage of suitable archives such as groundwater, stalagmites, sea water or ice cores (Burnard, 2013).

This study treats NG tracer applications in hydrological studies, with a main focus on groundwater which proved to be a useful archive for climate conditions during recharge. Tracer applications require a profound understanding of underlying biogeochemical processes characterizing the investigated system. This especially concerns dissolved gas contents in groundwater, due to the co-existence and the interaction of a gaseous, a liquid and a solid phase in the subsurface, as shown in Fig. 1.1. The *unsaturated zone* is the link between atmosphere and groundwater, involving different gas dynamical processes which can be summarized to sinks or sources, gas/water partitioning and transport processes. Their interplay determines the dissolved gas contents in percolating water which finally reaches the *saturated zone* as groundwater. Here, the gas exchange with entrapped air bubbles plays a crucial role for the final gas concentrations in groundwater, potentially inducing an enhancement of dissolved gas contents (denoted as *excess air*) or a depletion (denoted as *degassing*), respectively. Figure 1.1 shall not provide a detailed description of these processes, but rather demonstrate their diversity.

A crucial role comes up to NG mixing ratios in soil air, which are commonly assumed to be approximately atmospheric (Aeschbach-Hertig and Solomon, 2013). This approach was justified by studies suggesting a usually negligible impact of subsurface transport mechanisms on NG mixing ratios in soil air, regarding typical measurement uncertainties (Stute and Schlosser, 1993; Severinghaus et al., 1996). However, non-satisfying descriptions of some published data sets, e.g. from Ma et al. (2004) or Hall et al. (2005), challenge the reliability of traditional approaches to describe dissolved NG contents in groundwater. Microbial activity was proposed by Stute and Schlosser (1993) and by Hall et

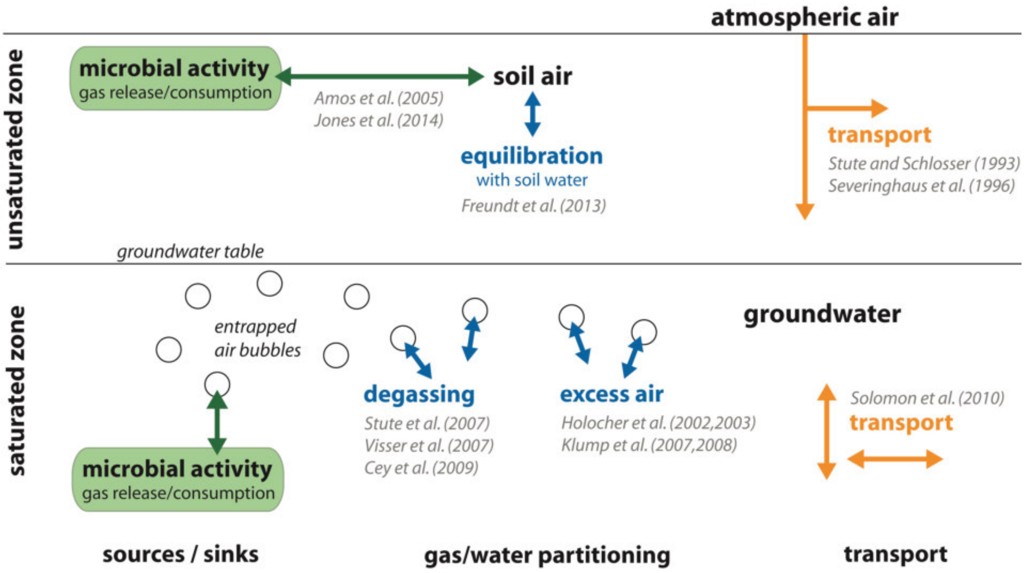

Figure 1.1: Summary of subsurface gas dynamics determining soil air composition and dissolved gas contents in groundwater. Processes are distinguished between sinks/sources (green), gas/water partitioning (blue) and transport (orange). Relevant publications are labeled in gray next to the corresponding process of interest.

al. (2005) to potentially bias NG mixing ratios in soil air: Oxygen depletion causes a deficit in O_2, which is usually compensated by CO_2. The preferential dissolution of CO_2 may induce a depletion of the sum value of O_2+CO_2 below its atmospheric value, accompanied by a likewise increase of the remaining gas mixing ratios with respect to their respective atmospheric values. This effect has been experimentally confirmed by now (Freundt et al., 2013; Jones et al., 2014). However, recent publications about NG mixing ratios in soil air do not allow for general conclusions, due to a lack of seasonal observations or as a consequence of very specified sampling conditions, e.g. at contaminated sites. In particular, an actual impact of varying NG mixing ratios in soil air on NG concentrations in recharging groundwater has not been confirmed so far.

Besides the potential impact of a varying soil air composition, the processes taking place in the transition zone between saturated and unsaturated zone are not entirely understood regarding their relevance for NG tracer applications in groundwater hydrology. This concerns, in particular, the existence of entrapped air bubbles within the shallow saturated zone. There exist different suggestions about the underlying physical processes determining the formation of excess air (Sun et al., 2010; Aeschbach-Hertig and Solomon, 2013). And even widely accepted explanation approaches are supposed to be challenged by groundwater degassing which may locally occur due to microbial gas release (Cey et al., 2009).

The preceding explanations point out that open questions still remain with regard to subsurface gas dynamics and its impact on dissolved NG contents in groundwater. In particular, existing publications (see references in Fig. 1.1) treat individual aspects, but they do not account for relations between them. This study is the first one treating these issues in a combined way. The chosen approaches are complementing findings of recent studies and allow to identify relevant processes. General conclusions are obtained by a joint evaluation of samplings from different climate regions and of modeling outcomes, both of them based on an analysis of inert gas tracers. The findings of this study demonstrate the potential of NGs as environmental tracers, but also difficulties and crucial aspects which have to be taken into account during their applications such as paleoclimate reconstruction. Even though this study was motivated so far with regard to the reliability of NG tracer applications in groundwater hydrology, the obtained conclusions are of an own interest by providing a deeper understanding of subsurface gas dynamics, e.g. concerning the treatment of soil contamination.

The theoretical introduction in chapter 2 gives an overview of the various biogeochemical processes taking place in the subsurface. Besides this, environmental tracer methods are described, accompanied by a motivation of their application in the context of this study. The investigation of subsurface gas dynamics requires sophisticated sampling procedures and analysis methods as well as appropriate evaluation approaches, which are presented in chapter 3. To confirm the reliability of the extensive set of obtained data, accuracy and precision of the applied mass spectrometric systems are investigated in detail. Chapter 4 motivates the selection of sampling sites for this study, covering different climate regions and allowing for investigations on a seasonal level.

After this introducing part, the subsequent chapters provide resulting data as well as their respective discussion. Chapter 5 starts with a presentation of the obtained results from continuous long-term observations at a mid-latitude sampling site in Germany. Associated findings are complemented by results from tracer applications in the tropics of Brazil, provided in chapter 6. Individual conclusions are transferred to a more general level in chapter 7, including a summary of main findings as well as an explanation of general implications concerning gas tracer applications in hydrology. Finally, this work closes with a short outlook in chapter 8.

Chapter 2

Theoretical basis

The study of subsurface gas dynamics requires a profound understanding of biogeochemical aspects which determine processes of interaction and of transport. The chapter begins with a presentation of different soil compartments, distinguished according to their phases occurring in the subsurface environment. After this, transport processes are explained in detail, meaning transport of solutes and of heat as well as the partitioning between gas and water phase. Since this study treats applications of environmental tracers, a detailed presentation of different tracer methods is finally given.

2.1 Soil compartments and their interaction

The so-called *pedosphere* can be regarded as a four phases system, where *biosphere* (living phase), *litosphere* (hard phase), *hydrosphere* (fluid phase) and *atmosphere* (gaseous phase) overlap each other. This region usually has a thickness in the range of millimeters up to several tens of meters. Typically, a fraction of almost 50 % of the total soil volume consists of the hard phase, while about 25 % are covered by fluid and gaseous phase, respectively. The living phase accounts only for about 0.5 % (Ottow, 2011). However, these quantities differ over a wide range, since there are multiple interaction processes between these four phases. Consequently, it is impossible to describe biogeochemical processes in one of these phases without any consideration of each other. To mention some aspects, microorganisms influence the amount of organic substance which in turn plays an important role for the soil matrix structure. The composition of the subsurface gas phase is determined by microbiological activity which depends on the fluid and the gaseous phase, respectively. Furthermore, transport processes in the gaseous and the water phase depend on the hard phase, meaning the soil matrix.
In this study, the subsurface dynamics of reactive and inert gases is investigated. For this purpose, a detailed understanding of the pedosphere and of locally occurring biogeochemical processes is necessary. The following contents are classified according to the just mentioned four phases, mainly based on Flühler and Roth (2004), Blume et al. (2009) and Ottow (2011).

2.1.1 Soil parameters (litosphere)

The Earth's crust as well as its outer mantle region are denoted as so-called *lithosphere*. For this study, the topmost lithosphere is of particular interest. This region, simply denoted as soil in the following,

is not a rigid continuum but rather an accumulation of grains consisting of inorganic as well as of organic compounds like stones, mineral particles or plant parts. Four basic processes of soil formation can be distinguished (Gisi, 1997): The degradation of bedrock is denoted as *weathering*, caused e.g. by dissolution or by microbiological activity. Weathering results in a regeneration of new minerals and in a provision of nutrients for plants. The second process is the so-called *humification* describing the decomposition of dead organic material by microorganisms and soil animals, resulting in a corresponding mineralization[1]. The third process is the so-called *translocation* of bedrock particles as well as of products from weathering and from humification, e.g. by dissolution or transport in water. Finally, the *creation and reduction of microstructures* results in the typical porous soil structure by consecutive processes of contraction and expansion, e.g. during freezing and thawing.
Soils cannot be seen as static structures. They are rather dynamically changed by microorganisms and plants as well as by climatic conditions such as temperature changes or precipitation. The previously mentioned processes lead all together to very complicated soil structures of a wide range of scales, with grain size magnitudes of some µm (clay or plant particles) up to several cm (gravel and stones) (Blume et al., 2009). The structure of a soil is usually described according to grain sizes or rather so-called *equivalent diameters* of its specific constituents. Grains larger than 2 mm are generally denoted as *soil skeleton*, smaller ones as *fine earth*. The latter is classified into three types: sand (50 – 2000 µm diameter), silt (2 – 50 µm) and clay (< 2 µm), each type with corresponding subtypes, respectively (Gisi, 1997). The relative shares of them determine the type of soil.

A treatment of soils on reasonably extended scales requires a description on an average level. The consideration of so-called *representative* soil volume fractions allows for a transition from the microscale to a continuous macroscale. Each soil consists of a pore matrix and a pore space, which can be mathematically expressed as the unitless so-called *porosity*

$$\phi = \frac{V_{\text{pore}}}{V_{\text{tot}}} \tag{2.1}$$

with the pore space V_{pore} within a certain considered soil volume V_{tot}. Natural porosity values typically fluctuate between 0.3 and 0.65 (Blume et al., 2009). The porosity is increasing with decreasing grain size and, thus, depends on the soil material. For transport processes it is common to regard the so-called *effective porosity* $\phi_{\text{eff}} \leq \phi$ which neglects the fraction of pore space which is not connected to the remaining pores and, consequently, not contributing to transport processes. Similar to the range of grain sizes, the pore sizes occurring in a soil exhibit a certain distribution, too. Typical pore sizes vary in a range between less than 0.2 µm and more than 50 µm (Blume et al., 2009). Coarse pores with diameters above 50 µm play a major role for transport processes such as soil ventilation which will be discussed in more detail in chapter 2.2. In sandy soils, such coarse pores make up a pore fraction of about 30 %, while they account typically for only about 8 % in clayey soils. A reverse pattern is typically found for fine pores of less than 2 µm diameter (Blume et al., 2009).
Soil type and pore space are related to the so-called *bulk density* ρ_{b} which is defined as the relation

---

[1] Mineralization describes the natural release of chemical elements from organic compounds which are used subsequently for the creation of new inorganic end products like H_2O, CO_2 or NH_4^+ (Gisi, 1997).

of dry mass and volume of a considered soil parcel. Typical values vary between 0.5 and 2.0 g/cm^3 (Gisi, 1997; Blume et al., 2009). The bulk density has to be distinguished from the so-called *particle density* ρ_p describing the density of the proper soil matrix material. Since quartz is typically the most abundant soil mineral in nature, the particle density is usually close to 2.65 g/cm^3. However, this value may differ for less sandy soils such as silty or clayey ones, since these soil types typically contain also so-called *secondary minerals* developed after soil formation (Gisi, 1997).

2.1.2 Soil water and groundwater (hydrosphere)

The so-called *hydrosphere* comprises the whole amount of water on Earth. It can be seen as a link between the biosphere, the lithosphere and the atmosphere. Water is transported within the so-called *hydrological cycle* by evaporation from the oceans to the continents, from where precipitating water finally returns to the oceans via continental runoff. The largest component of the hydrological cycle is the ocean, containing about 96 % of the total amount of water on Earth. Almost all freshwater is contained in ice (about 69 %) and groundwater (about 30 %). Thus, groundwater provides the largest reservoir of fluid freshwater on Earth. Lakes, atmospheric water and soil moisture account for only about 0.5 %, 0.18 % and 0.04 % of the global amount of freshwater, respectively (Mook, 2000). Even though these numbers should only be seen as a rough order of magnitude rather than as exact quantities, they give a good insight into the relations of the different components of the hydrological cycle.
In this study, water is considered according to three of the previously mentioned reservoirs: atmospheric water, soil moisture and groundwater. These reservoirs contain a comparatively small amount of the globally existing water. However, in all these compartments, water has an outstanding role for biological activity but also for the Earth's climate system, caused by its exceptional physical and chemical characteristics. Properties of water like its high heat capacity, its low viscosity or its strong solution capability result from the polar nature of water molecules and from their ability to form hydrogen bonds among themselves but also with other compounds (Paul and Clark, 1996). To mention some consequences, water enables energy transport and reduces environmental temperature fluctuations. The high dissolving power of water causes its important role for geochemical transport processes. Its high surface tension is crucial for the formation of cloud droplets, for solute transport within organisms as well as for the water balance of soils.

The mean residence times of water within its reservoirs reflect transport and exchange processes with other compartments of the hydrological cycle. It accounts for about 10 days in the atmosphere after which atmospheric water typically ends up in precipitation. A very simple model of water transport in the atmosphere is that from oceanic evaporation in equatorial regions towards polar regions, going along with a continuous rain out. The average global amount of precipitation accounts for 970 mm per year and is higher above the oceans than above the continents. The mean residence of soil water is half a year, after which it typically evaporates back into the atmosphere or ends up in the groundwater. The comparatively high mean residence time of 500 years in groundwater results from slow flow velocities and the small atmospheric impact on deeper soil regions (Mook, 2000).

Unsaturated zone

Every fluid fills up the pore space of the soil matrix, e.g. atmospheric precipitation as the main source of soil water. This is formally described by introducing the unitless volumetric fluid content

$$\theta_\mathrm{i} = \frac{V_\mathrm{i}}{V_\mathrm{tot}} \tag{2.2}$$

which can be directly applied to define the *volumetric soil moisture* θ_w. Obviously, any volumetric fluid content is limited to the available pore space, thus $\theta_\mathrm{i} \leq \phi$. Thus, the following relation follows for every soil consisting of matrix material and respective phases of gas and water:

$$\phi = \theta_\mathrm{w} + \theta_\mathrm{g} = 1 - \theta_\mathrm{m} \tag{2.3}$$

The flow of fluids is usually induced by differences in potential. The potential energy ψ_w [J/m^3] to move a water parcel from a reference state to a certain state in a porous medium depends of respective contributions of different components[2]:

$$\psi_\mathrm{w} = \psi_\mathrm{m} + \psi_\mathrm{g} + \psi_\mathrm{p} + \psi_\mathrm{o} \tag{2.4}$$

The so-called *matric potential* ψ_m results from adsorption of water molecules to soil particles and from mutual cohesive bindings. It is always zero or negative and, thus, lowers the potential energy of soil water with respect to free water. The *gravity potential* ψ_g is always positive and results from the fact that a water parcel has to be moved inside the Earth's gravity field. The *pressure potential* ψ_p describes the internal energy of a water parcel due to the pressure of overlying water and of atmospheric air. Thus, the pressure potential is always zero or positive. In a partially water saturated soil, the pressure potential reduces to the atmospheric air pressure which is usually chosen as reference state p_0. In a water saturated soil, it is determined by the height of the overlying water column. The *osmotic potential* ψ_o is neglected in this study, since all substances of interest can be assumed to be transported unhindered with the soil water flow (van Elsas et al., 2006). With regard to dissolved chemicals, the osmotic potential is always zero or negative. For soil water in the unsaturated zone, eq. (2.4) can be just expressed as

$$\psi_\mathrm{w} = \psi_\mathrm{m} + \psi_\mathrm{g} = [\mathrm{p}_\mathrm{w}(\mathbf{x}) - \mathrm{p}_0] + \int_{z_0}^{z_1} \rho_\mathrm{w}(z)\,\mathbf{g}\,\mathrm{d}z = \underbrace{[\mathrm{p}_\mathrm{w}(\mathbf{x}) - \mathrm{p}_0]}_{\text{matric potential}} + \underbrace{[z_1 - z_0]\,\rho_\mathrm{w}\mathbf{g}}_{\text{gravity potential}} \tag{2.5}$$

with the vertical component z of the position vector $\mathbf{x}$, the gravitational vector $\mathbf{g}$ and assuming water to be an incompressible medium, meaning that ρ_w does not depend on z. In this approach, the pressure potential is included into the term describing the matric potential. The matric potential in eq. (2.5) is associated with capillary forces and can be described by the *Young-Laplace equation* (Landau and

---

[2] The contribution of kinetic energy is negligible since typical subsurface flow velocities are very small (Roedel and Wagner, 2010).

Lifschitz, 1991)

$$\psi_{\mathrm{m}} = \mathrm{p_w} - \mathrm{p_0} = \sigma_{\mathrm{wa}} \cdot \left(\frac{1}{r_1} - \frac{1}{r_2}\right) \tag{2.6}$$

with the pressure $\mathrm{p_w}$ in the water phase. The radii of curvature r_1 and r_2 are, by definition, positive when they are located in the liquid phase. At 20°C, the interfacial tension σ_{wa} accounts for 0.0725 N/m (Flühler and Roth, 2004).
Capillary forces play an important role for drying and wetting of soils. When the matric potential in eq. (2.6) decreases below the so-called *air entry value*, the corresponding curvature radii may get smaller than the radius R of the corresponding soil pore. In this case, the water-air interface vanishes and the pore is drained. Thus, the water content θ_{w} (ψ_{m}) is a function of the matric potential, which is denoted as *soil water characteristic*. Typical trends are given in Fig. 2.1. The pore size distribution determines the soil water characteristic. Due to the larger range of different pore sizes in a loamy soil, there is not such a strong decrease of the soil water content during drying as observable for a sandy soil. Typically, the soil water content of a soil is higher during drying than during wetting. Such a hysteresis effect results from the difference between the diameters at the necks and at the widest point of a pore. A detailed description of hysteresis in this context is given in Flühler and Roth (2004). As shown in Fig. 2.1, a small water content remains in the soil even for very low matric potentials, which is called *residual water content*.

Any gradient of potential energy as defined in eq. (2.4) drives a subsurface water flow. Since typical soil water flow velocities are very small compared to the viscosity of water, the corresponding

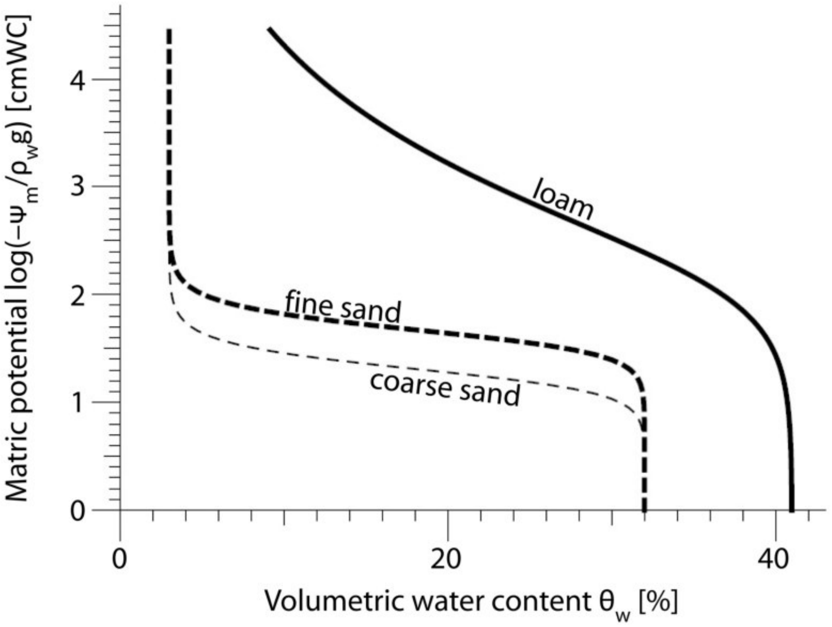

Figure 2.1: Typical soil water characteristics for a loamy soil (solid line) as well as for a fine sandy soil (thick dashed line) and for a coarse sandy soil (thin dashed line). The matric potential h_{w} is given in units of cmWC (cm water column). The higher saturation water content results from the higher porosity of the loamy soil. The air entry value for the sandy soil is about −30 cmWC which corresponds to a pore radius of about $R = 0.05$ mm, according to eq. (2.6). Adapted from Flühler and Roth (2004).

water flux is in general laminar. Thus, a linear relation between water flow j_w [m/s] and potential energy gradient can be assumed according to the *Buckingham Darcy law* (Darcy, 1856):

$$j_\mathrm{w} = -\mathbf{K}(\theta_\mathrm{w})\,\nabla\psi_\mathrm{w} = -\mathbf{K}(\theta_\mathrm{w})\,[\nabla\psi_\mathrm{m} - \rho_\mathrm{w}\mathbf{g}] \tag{2.7}$$

The hydraulic conductivity $\mathbf{K}(\theta_\mathrm{w})$ [m^5 J^{-1} s^{-1}] is a tensor which is usually non-isotropic, in particular for spatial arranged soil structures such as fissured rocks. The hydraulic conductivity is typically higher for horizontal flow directions compared to vertical ones. It describes the ability of the soil material to transmit water and depends on the soil water content θ_w.
Accounting for mass conservation ($\partial_\mathrm{t}\theta_\mathrm{w} + \nabla j_\mathrm{w} = 0$, indicating that there are no sources or sinks of water), eq. (2.7) leads to the so-called *Richard's equation*

$$\partial_\mathrm{t}\theta_\mathrm{w} - \nabla\left(\mathbf{K}(\theta_\mathrm{w})\,[\nabla\psi_\mathrm{m} - \rho_\mathrm{w}\mathbf{g}]\right) = 0 \tag{2.8}$$

which describes the flow of water in an unsaturated porous medium. Obviously, the water flux depends on soil material properties. Since the soil water content $\theta_\mathrm{w}(\psi_\mathrm{m})$ is usually a hysteresis function, it is very hard to handle the Richard's equation analytically but rather for purely evaporation or infiltration processes (Flühler and Roth, 2004).

The soil water content is usually applied to differentiate two characteristic soil regions as shown in Fig. 2.2: The topmost soil region with a non-vanishing gas content ($\theta_\mathrm{g} \neq 0$, $\theta_\mathrm{w} < \phi$) is referred to as *unsaturated zone* since the pore matrix is not totally filled by water. The soil water in the unsaturated zone is bound by interfacial forces, meaning $\psi_\mathrm{m} < 0$, $\psi_\mathrm{p} = 0$ and $p_w < p_0$.
In contrast, the soil region where the gas content is vanishing ($\theta_\mathrm{g} = 0$, $\theta_\mathrm{w} = \phi$) is denoted as *satu-*

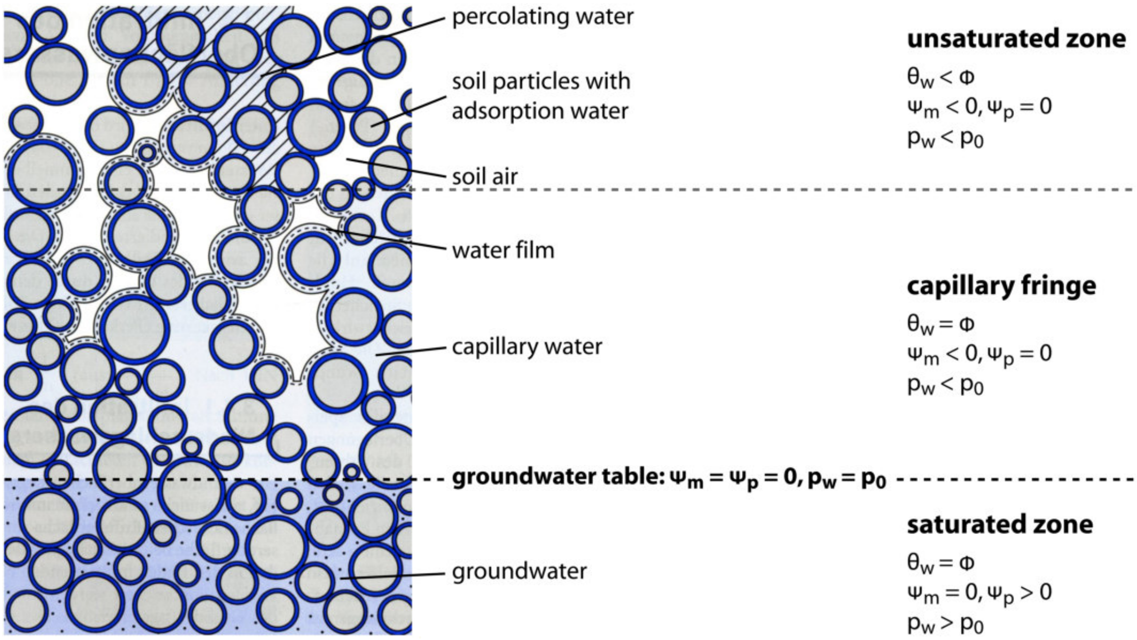

Figure 2.2: Overview of the different subsurface zones, defined according to their water content.

rated zone. However, there is usually an undissolved gas phase fraction in the topmost part of the saturated zone, motivating a denotation as *quasi-saturated zone* (Faybishenko, 1995; Holocher et al., 2002, 2003; Klump et al., 2008). This gas phase consists of unconnected small air bubbles entrapped in the pore matrix, resulting from water table fluctuations or microbial gas production. The saturated zone is the region of groundwater flow with $\psi_\mathrm{m} = 0$, $\psi_\mathrm{p} > 0$ and $p_w > p_0$, indicting a free water phase. Thus, it is $\psi_\mathrm{m} = \psi_\mathrm{p} = 0$ and $p_w = p_0$ directly at the groundwater table. The so-called *capillary fringe* is characterized by (nearly entire) saturation but at once by a bound fluid phase with $\psi_\mathrm{m} < 0$ and $p_w < p_0$, induced by capillary forces.

Saturated zone

Considering water flow inside the saturated zone, it is less intuitive to regard the potential energy, but rather the so-called *hydraulic head* or *piezometric head*

$$h_\mathrm{w}\,[\mathrm{m}] = \frac{\psi_\mathrm{w}}{\rho_\mathrm{w} g} = \frac{\psi_\mathrm{p} + \psi_\mathrm{g}}{\rho_\mathrm{w} g} = \frac{\mathrm{p_w}}{\rho_\mathrm{w} g} + z \tag{2.9}$$

which is defined as potential energy per unit weight. The contribution of the matric potential is zero in the saturated zone. Analogously to eq. (2.7), the groundwater flow q_w [m/s] is described by *Darcy's law*:

$$q_\mathrm{w} = -\mathbf{K}\,\nabla h_\mathrm{w} \tag{2.10}$$

Here, the hydraulic conductivity **K** [m/s] does not depend on the soil water content since there is only one fluid in the saturated zone. However, **K** is still non-isotropic indicating that it is a tensor. Under natural conditions, the order of magnitude of **K** varies over a wide range, depending on the considered sediment. Typical values are 10^{-8} m/s for clay, 10^{-3} m/s for very fine sand and 10 m/s for pure gravel (Mook, 2000). The parameter q_w is also called *Darcy velocity* and describes the infiltration velocity of water. Due to the pore space geometry, the Darcy velocity has rather a hypothetical character, since it has to be distinguished from the *actual flow velocity* v_w [m/s] describing the transport of substances:

$$v_\mathrm{w} = \frac{q_\mathrm{w}}{\phi} \tag{2.11}$$

For groundwater flow, the effective porosity $\phi_\mathrm{eff} < \phi$ is applied.

According to eq. (2.10), groundwater flows perpendicular to equipotential lines which are called *groundwater-surface contours*. They are usually induced by pressure gradients resulting from the height difference to the recharge area. Soil layers with a high water conductivity are usually referred to as *aquifers* while impermeable layers are denoted as *aquitards*. There are two types of aquifers. A so-called *unconfined* or *phreatic aquifer* has an open water surface, meaning the height of groundwater level corresponds to the hydraulic head. In contrast, a *confined aquifer* is characterized by a hydraulic head which is higher than the actual water level. Such a case is induced by an comparatively impermeable layer above the aquifer. The water level in a well at a confined aquifer may rise above the Earth's surface, leading to a so-called *artesian well*.

2.1.3 Microbiological activity (biosphere)

The fraction of total organic material in soils is quite small with only a few percent, from which only less than 4 % are living (Theng et al., 1989). However, the global carbon and nitrogen cycles as well as their underlying exchange processes are influenced considerably by organic soil material. In this section, the influence of living organics on gas transport and on the composition of the subsurface gas phase is explained in detail. To give some exemplary aspects, plants, fungi or bacteria play a major role during soil formation on different scales, e.g. due to root channels as a direct connection between the atmosphere and deeper soil regions. Furthermore, the surface of organic material is an important sorbent for biochemical reactions and microorganisms.

The sizes of organic substances cover a wide range of magnitudes, ranging from the order of less than 10 µm (e.g. bacteria, fungi) up to some mm (acarians, plant roots) (Ottow, 2011). Microorganisms make up the highest fraction (60 − 80 %) of living organic material in soils, followed by macrofauna (15 − 30 %) and roots (5 − 10 %) (Theng et al., 1989). Typically, microbial respiration accounts for about 90 % of the total respiration within an ecosystem (Blume et al., 2009) and is of major importance for the subsurface gas household. As a consequence of microbiological activity, the composition of soil air is different from the atmospheric one. The most obvious influence is usually observable on O_2, CO_2, N_2 and CH_4. However, gas species like NH_3, H_2, CO and SO_2 as well as forms of NO_x are affected, too (Paul and Clark, 1996).

Carbon based soil respiration

Since soil respiration as discussed in this study comprises in particular the release of CO_2, the main principles of the natural global carbon cycle shall be discussed, based on Le Quéré et al. (2015). Carbon is circulated between atmosphere, ocean and terrestrial biosphere. Compared to the global biosphere (2 500 Pg C, of which 500 Pg C is bound in above-ground vegetation) and the oceans (38 000 Pg C), the atmosphere containing about 800 Pg C is a comparatively small carbon reservoir. The given shares result mainly from CO_2 sinks as fixation by photosynthesis and dissolution in water. Soil respiration releases carbon into the atmosphere. The corresponding exchange fluxes between atmosphere and biomass account for about 120 Pg C per year, which is more than the exchange between atmosphere and oceans (about 79 Pg C per year). The biosphere also plays a major role as a sink for anthropogenic CO_2 emissions, increasing the corresponding carbon uptake by about 2.5 Pg C per year. Even though the just mentioned quantities are just rough estimates with a high uncertainty, they underline the role of the the terrestrial biosphere for the global carbon cycle.

Figure 2.3 illustrates the main carbon exchange processes between atmosphere and subsurface biosphere. Carbon from the atmosphere gets into the soil via plant photosynthesis and dead organisms. Microorganisms decompose such organic material. Soil respiration causes a release of CO_2, while O_2 is equivalently consumed. Soil water has a direct influence on such metabolism and affects subsurface concentrations of CO_2 due to its high solubility (see chapter 2.2.3). To complete the cycle, carbon is released into the atmosphere in form of CO_2. The amount of carbon turnover varies across different climate zones. In tropical latitudes, it accounts for about 1 kg carbon per m^2 and year, while values of only about 0.2 kg per m^2 and year are typical for mid-latitudes (Gisi, 1997).

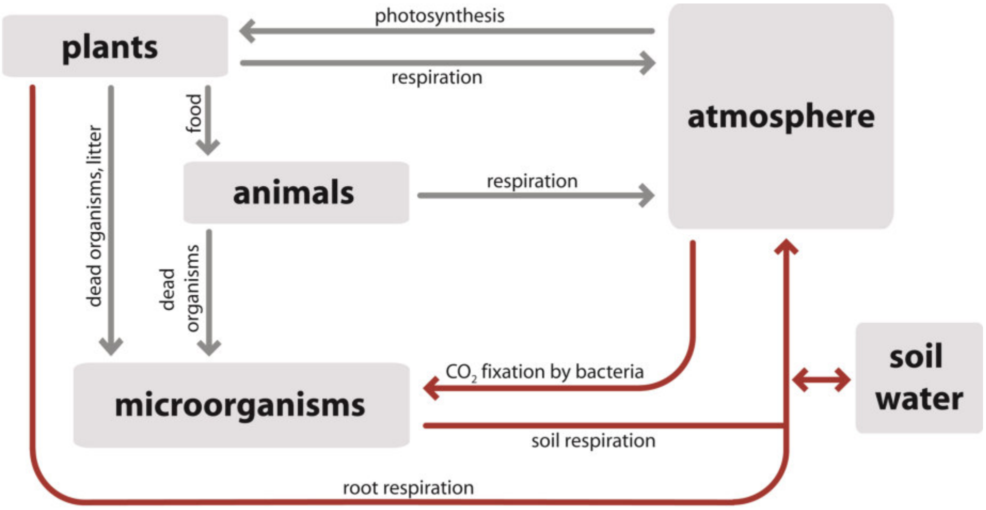

Figure 2.3: Schematic illustration of interactions between atmosphere and biosphere in the carbon cycle. Subsurface processes, which are of major interest in this study, are indicated as red lines. Based on Gisi (1997) and Blume et al. (2009). The sink-property of soil water on CO_2 in soil air is a result of chemical reactions between minerals and dissolved CO_2 in soil water (not depicted in the graph).

In the following, the underlying principles of aerobic as well as of anaerobic respiration shall be explained. Soil respiration is the result of energy consumption by microorganisms. The corresponding metabolism involves the release of electrons from (usually hydrogen) donors, which are transferred to acceptors (e.g. O_2) during an oxidation process. This procedure serves the production of so-called *adenosine triphosphate* (ATP) which is used later for constructive metabolism (Ottow, 2011). The most prominent example for an acceptor/product pair is O_2/H_2O. The oxidation process can be generally described as follows:

$$\underbrace{(CH_2O)_x}_{\text{organic matter}} + O_2 \rightarrow \underbrace{CO_2}_{60-80\,\%} + \underbrace{H_2O + IP + MB + E}_{40-20\,\%} \tag{2.12}$$

From the amount of decomposed organic matter, about 60 − 80 % is transformed into CO_2. The rest is transformed into water, intermediate products (IP), microbiological biomass (MB) or into energy (E) (Gisi, 1997). Such a process in presence of oxygen is called *aerobic*. The total number of gas molecules is conserved, meaning that the molar amount of consumed O_2 is equal to the amount of produced CO_2. A prominent example for such a process is the aerobic decomposition of glucose (Blume et al., 2009):

$$C_6H_{12}O_2 + 6\,O_2 \rightarrow 6\,CO_2 + 6\,H_2O + 2\,800\,\text{kJ/mol} \tag{2.13}$$

Metabolism also occurs in absence of oxygen, which is denoted as *anaerobic* process. In case of O_2 concentrations below about 1 vol% and a lack of nitrogen oxides such as nitrate or nitrite, metabolism only occurs in an anaerobic way (Paul and Clark, 1996). If high amounts of energy-rich carbon sources are available, anaerobic conditions are induced as soon as the required amount of electron acceptors is higher than provided by oxygen. One exemplary reaction is the anaerobic decomposition of glucose (Blume et al., 2009):

$$C_6H_{12}O_2 \rightarrow 3\,CO_2 + 3\,CH_4 + 188\,\text{kJ/mol} \tag{2.14}$$

The total number of gas molecules is not conserved in this case, which may lead to an enhanced pressure in the gas phase if a pressure balance is not possible. During strongly reducing conditions, SO_4^{2-} and CO_2 serve as electron acceptors, resulting in a release of H_2S and CH_4 (methanogenesis), respectively (Whiticar et al., 1986; Ottow, 2011).

Both aerobic as well as anaerobic conditions usually occur directly next to each other within distances of less than 1 mm. As shown in Fig. 2.4, microorganisms can be assumed to be distributed within a grained soil structure surrounded by gas and water films. Whether aerobic or anaerobic metabolism occurs, depends primarily on the amount of required electron acceptors. Assuming an availability of enough energy-rich substrates, the amount of available oxygen directly next to the microorganisms is crucial for the type of metabolism. Soil water constrains the transfer of gas or rather of oxygen, thus potentially inducing anaerobic regions due to a worse ventilation. The influence of water on subsurface gas transport is discussed in more detail in chapter 2.2.

Nitrogen based soil respiration

Besides their contribution to the carbon cycle, subsurface microorganisms also play an important role for the global nitrogen cycle. The largest reservoir of nitrogen is the atmosphere, containing more than 99 % of the global nitrogen budget. In contrast, less than 0.1 % of the global nitrogen is bound in organic compounds (Ottow, 2011). After elementary nitrogen – which is not directly usable for plants – gets into the soil, it is transformed into different organic and inorganic compounds. Examples are amino acids, proteins, vitamins and chlorophyll (Blume et al., 2009). Caused by the comparatively

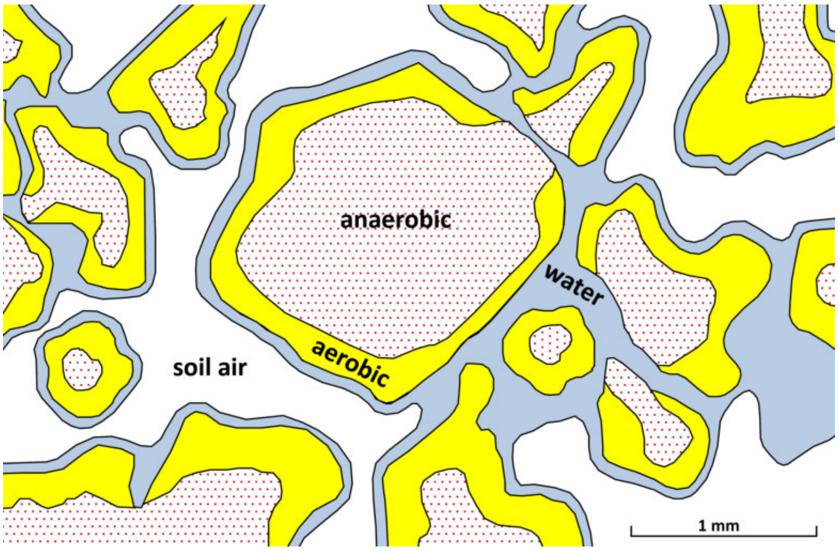

Figure 2.4: Illustration of aerobic (yellow areas) and anaerobic (gray shaded areas) regions in a small-scale soil structure. Soil water is illustrated as blue areas. The distribution is a consequence of the influence of water on the soil ventilation. Based on Gisi (1997).

high dissociation energy of the dinitrogen molecule, any corresponding reaction requires a high activation energy. Nitrogen is returned into the atmosphere in form of gas species like N_2 and N_2O, but also NO or NH_3. The main steps of the terrestrial nitrogen cycle are illustrated in Fig. 2.5. The depicted processes account for about 95 % of the total terrestrial nitrogen turnover, while the direct exchange of nitrogen between soils and atmosphere accounts only for about 5 % (Gisi, 1997).

During the so-called *ammonification* process, subsurface organic nitrogen compounds $R{-}NH_2$ are used by microorganisms to produce NH_4^+ for metabolism (Ottow, 2011):

$$R - NH_2 + H_2O \rightarrow NH_3 + R - OH \tag{2.15}$$

$$NH_3 + H^+ + OH^- \leftrightarrow NH_4^+ + OH^- \tag{2.16}$$

$R{-}OH$ denotes a chain of organic compounds for which an example is nitroxyl (N−OH) (Gisi, 1997). The unused excess of ammonium ions (NH_4^+) is used by further microorganisms during the so-called *nitrification* process. NH_4^+ and nitrite ions (NO_2^-) are then used as electron donors to generate ATP. Nitrification requires the availability of oxygen and is usually done by bacteria of the species *Nitrosomonas* and *Nitrobacter*. The overall nitrification process is generally described by the following transformation to nitrate (Paul and Clark, 1996):

$$NH_4^+ \rightarrow NO_2^- \rightarrow NO_3^- \tag{2.17}$$

Nitrification in soils occurs in particular for pH values between 5.5 and 8.0 and at temperatures between 20 and 25°C, while it occurs hardly at all for temperatures below 2°C (Gisi, 1997; Blume et al., 2009). Its reaction velocity depends in particular on the availability of oxygen and, thus, on the soil moisture content or rather on the soil aeration (as explained later in detail). In well-aerated mid-latitude soils, the nitrate from ammonification processes is consumed quite quickly during nitri-

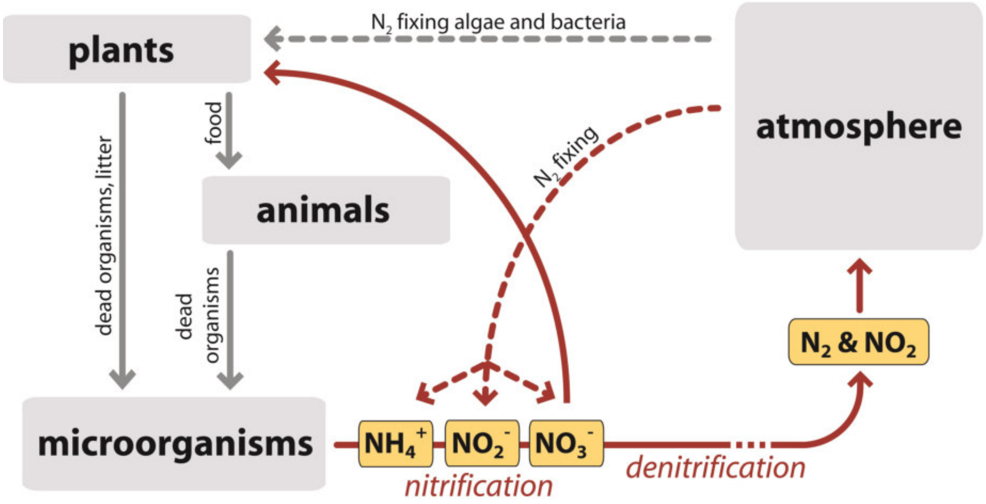

Figure 2.5: Schematic illustration of the nitrogen cycle interactions between atmosphere and biosphere. Subsurface processes, which are of major interest in this study, are indicated as red lines. Based on Gisi (1997) and Blume et al. (2009).

fication. In contrast, the ammonification usually dominates the nitrification process in tropics with soil temperatures above 30°C and high soil moisture contents (Blume et al., 2009).
While nitrification occurs in well aerated soils, some microorganisms can also generate ATP by using oxygenic nitrogen compounds like NO_3^- as alternative electron acceptors in case of a worse oxygen supply. This so-called *denitrification* process involves a variety of different bacteria and leads to a release of different gases (Wood, 1995; Ottow, 2011):

$$2\,NO_3^- \rightarrow 2\,NO_2^- \rightarrow 2\,NO \rightarrow N_2O \rightarrow N_2 \qquad (2.18)$$

During denitrification, organic substrates serve as electron donors. Due to the wide range of participating microorganisms, the corresponding partial reactions require different ambient conditions. If enough organic substances are available, the occurrence of denitrification is generally determined by the available amount of oxygen. A complete denitrification with a release of N_2 requires a minimum temperature of about 5°C, while an incomplete transformation, with more emission of N_2O, is typically observed in mid-latitude soils during winter time (Blume et al., 2009). Even though nitrate respiration is not as efficient as oxygen respiration, it can be seen as an alternative way for microorganisms to generate ATP under inhibited oxygen supply.

Parameters influencing microbial activity

So far microbial activity was discussed in the context of the global cycles of carbon and nitrogen. In the following, factors generally determining below-ground microbial activity rates shall be described. Any subsurface metabolism depends mainly on three parameters: the soil water content, the soil temperature and the depth below Earth surface.

Water plays a crucial role for microorganisms. It serves as building material, it reduces temperature variations and it keeps up the osmotic potential of cells. Furthermore, it determines the transport and the absorption of dissolved substances like salts (van Elsas et al., 2006; Ottow, 2011). Water has both, a direct as well as an indirect influence on microbial activity. Its direct influence follows from the just mentioned role of water for microorganisms: Whenever the soil moisture content is decreasing below a critical value, microbial activity decreases significantly. Organisms have to apply work against the combined matric and osmotic potential to obtain water. An indirect influence of soil water results from its influence on soil aeration or rather on subsurface transport processes and the availability of oxygen for aerobic metabolism which is, thus, limited by high soil moisture contents.
Both mentioned effects suggest the existence of an optimum soil moisture content with regard to microbial activity rates, which is typically about $-0.01\,\mathrm{MPa}$, corresponding to $-102\,\mathrm{cmWC}$. The threshold below which microbial activity decreases depends strongly on the type of microorganism and can be even in the range of $-65\,\mathrm{MPa}$ or less (Paul and Clark, 1996). Water potentials above the optimum, meaning of up to $0\,\mathrm{MPa}$, correspond to waterlogged soils while lower values reflect dried soils. Generally, fungi are less sensitive to water deficiency than bacteria which again exhibit strong differences among each other (Paul and Clark, 1996; Blume et al., 2009). Caused by differing pore space geometries and, thus, different water characteristics, the maximum microbial activity in sandy

soils occurs at lower water contents than in loamy soils.

The ambient temperature determines the activity of microorganisms as well as their spatial distribution. It directly affects the physiology of organisms, but it also indirectly determines the supply by nutrients due to the temperature dependence of physicochemical processes such as dissolution and diffusive transport (van Elsas et al., 2006). Microorganisms are usually active within a comparatively wide temperature range from about 1°C up to 55°C (Ottow, 2011). According to a formula stated by Arrhenius (1889), an enhanced temperature favors a higher reaction rate k [s^{-1}] of microbial processes as given by

$$k = A \cdot \exp\left(-\mathrm{E_a}/RT\right) \tag{2.19}$$

with the parameter A denoting the frequency of molecular collisions, the temperature T, the activation energy $\mathrm{E_a}$ and the universal gas constant R (Ratkowsky et al., 1982). Even though the application of eq. (2.19) requires a detailed knowledge about the type of microorganism, the reaction velocity of carbon mineralization can be supposed to increase typically by a factor of two during a temperature increase by 10°C within a temperature range between 0 and −30°C (van Elsas et al., 2006; Blume et al., 2009).

The number of microorganisms typically decreases with increasing soil depth. The depth-dependent amount of microorganisms is not caused by a smaller amount of available oxygen but by the depth profile of organic carbon. Thus, even the density of anaerobic microorganisms does not increase necessarily with increasing soil depth and lower oxygen contents. The topmost meter of a soil usually contains almost all organic carbon, of which only about $1-6\,\%$ is microbiologically bound carbon (Gisi, 1997; Ottow, 2011). Typically, the highest CO_2 production rate is found in a soil depth of $5-10\,\mathrm{cm}$ below Earth surface (Blume et al., 2009), resulting from dehydration above this layer and less organic carbon below it.

The influences of soil moisture, temperature and depth on subsurface microbial activity are not independent since they mutually affect each other. Thus, a reliable differentiation is hardly possible since the corresponding effects may be additive or even multiplicative (Paul and Clark, 1996). Numerical simulations as from Bunnell and Tait (1974) can help to get an insight into the different contributions. As shown in Fig. 2.6, both parameters soil moisture and temperature play a crucial role for microbial activity rates. There is no soil moisture content and no soil temperature for which soil respiration occurs even for non-beneficial values of the other parameter, respectively.

Altogether, the just mentioned factors influence temporal and spacial variations of subsurface microbial activity and their influence on soil air composition. Figure 2.7 illustrates the seasonality of soil respiration for different climatic conditions. In mid-latitudes, microbial activity is limited by low temperatures in winter and by low soil moisture contents in summer. In contrast, tropical regions are expected not to show such a limitation due to permanently high temperatures and high soil moisture contents. Figure 2.8 shows a typical mid-latitude seasonality of O_2 and CO_2 concentrations in soil air. Soil respiration increases during summer time, resulting in a higher CO_2 concentration in soil air. Microbial CO_2 production increases by a multiple after changes from dry to wet conditions (Ottow, 2011).

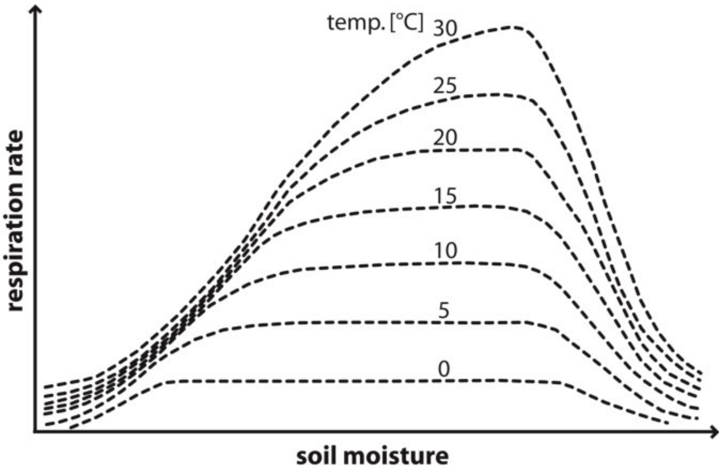

Figure 2.6: Simulated soil respiration rate in a certain soil depth for varying soil temperature and soil moisture contents. Adapted from Bunnell and Tait (1974).

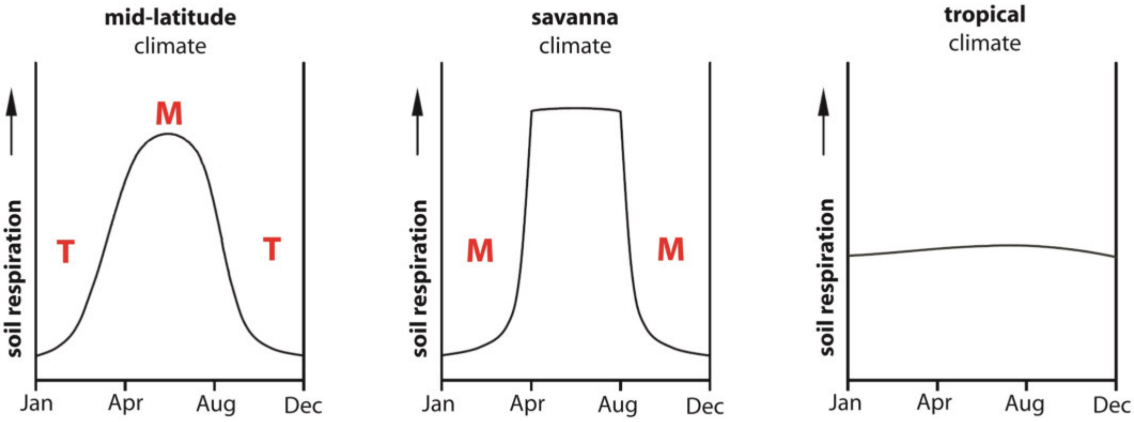

Figure 2.7: Seasonal variations of soil respiration for different climate conditions on the northern hemisphere. Red letters indicate the limiting factors of microbiological activity, which is soil moisture (M) or soil temperature (T). Adapted from Blume et al. (2009).

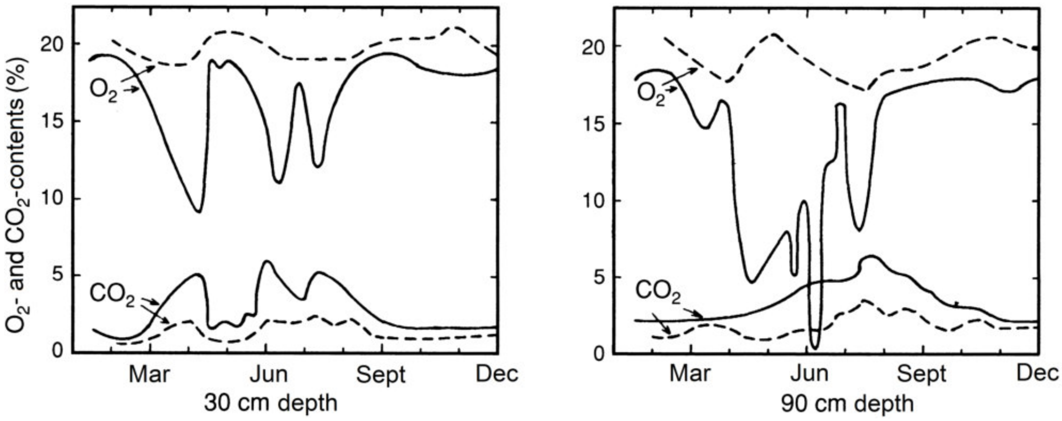

Figure 2.8: Contents of O_2 and CO_2 in a sandy clay (dashed line) and a silty clay soil (continuous line) at 30 cm and 90 cm depth, respectively. Adapted from Blume et al. (2009).

The above mentioned processes are only a short insight into the quite complex field of soil microbiology. However, an importance for subsurface gas tracer studies becomes clear. Microbial activity plays a major role in global cycles of carbon and nitrogen. By this way, it influences the composition of soil air as well as that of groundwater. Anaerobic processes such as denitrification lead to subsurface gas production which may cause degassing of groundwater due to an equilibration of emerging air bubbles with the surrounding water phase (Blicher-Mathiesen et al., 1998; Stute et al., 2007; Visser et al., 2007). A consideration of these processes will be essential during the evaluation of data presented in this study.

2.1.4 Soil air (atmosphere)

The gas phase within the unsaturated zone has a more or less similar composition as atmospheric air, caused by exchange processes at the soil surface. This analogy motivates to start the following explanations with a short view on the atmosphere itself.
Table 2.1 gives an overview about the mixing ratios of the most abundant gas species in dry atmospheric air, ordered according to their relative abundance. To determine the partial pressure p_i of a specific gas species in the atmosphere, the water vapor pressure as well as the height-dependent air pressure P_a have to be taken into account:

$$p_\mathrm{i}\,(z,T) = [P_\mathrm{a} - h \cdot e_\mathrm{s}\,(T)] \cdot x_\mathrm{i} \tag{2.20}$$

The volumetric fractions x_i are referred to dry atmospheric air, while the unitless parameter h denotes the relative humidity. The saturation water vapor pressure e_s depends on the ambient temperature T and can be described empirically by the so-called *Magnus formula* (Sonntag, 1990)

$$e_\mathrm{s} = 6.112\,\mathrm{hPa} \cdot \exp\left(\frac{17.62 \cdot (T\ [\mathrm{K}] - 273.15\,\mathrm{K})}{243.12\,\mathrm{K} + (T\ [\mathrm{K}] - 273.15\,\mathrm{K})}\right) \tag{2.21}$$

which provides a reliable description above liquid water and within a temperature range between about −45 and 60°C. For typical mid-latitude soil temperature regimes, the saturation water vapor pressure ranges from about 6 mbar (at 0°C) up to 32 mbar (at 25°C) and can be roughly assumed to double for a temperature increase of 10°C. In the unsaturated zone, the gas phase is usually assumed to be nearly water saturated, meaning $h \approx 1$ (Stute and Schlosser, 2000; Blume et al., 2009). Due to adsorbed water films and capillary water, this assumption is valid for regions of temperate and tropical climate. However, substantially lower soil air humidities may occur in arid areas. Altogether, the relative amount of water vapor is typically higher in soil air compared to atmospheric air.
The atmospheric pressure P_a depends on the corresponding height z above sea level and can be determined according to the so-called *Barometric formula*:

$$P_\mathrm{a}\,(z) = P_\mathrm{a}\,(0) \cdot \exp\left(-z/z_s\right) \text{ with } z_s = RT/\mathrm{Mg} \tag{2.22}$$

The *scale height* z_s depends on the molar mass of dry atmospheric air (M = 28.97 u), the universal gas constant R and the gravitational constant g. A value of about 8 000 m results assuming a mean

Table 2.1: Mixing ratios of the eight most abundant gases in dry atmospheric air, meaning under the assumption of no existing water vapor. Adapted from Roedel and Wagner (2010) and Tans and Keeling (2015).

gas	mass [u]	vol. mixing ratio [vol%]
N_2	28	78.09
O_2	32	20.95
Ar	40	0.93
CO_2	44	0.04
Ne	20	$18.21 \cdot 10^{-4}$
He	4	$5.24 \cdot 10^{-4}$
CH_4	16	$1.89 \cdot 10^{-4}$
Kr	84	$1.14 \cdot 10^{-4}$

atmospheric temperature of 15°C (Roedel and Wagner, 2010).

Referring back to the subsurface gas phase, its composition is of main interest during this study. It reflects biotic as well as abiotic processes, while deviations from atmospheric air are constrained by exchange processes at soil surface. A major impact is usually observed on gases affected directly by microbial activity. Due to oxygen depletion, subsurface metabolism typically causes a depletion of O_2 in the range of some vol%, accompanied by a corresponding enrichment of CO_2. Oxygen depletion for itself does not affect the sum value of O_2+CO_2. As will be described in chapter 2.2, the preferential dissolution of CO_2 in water, however, may lead to a reduction of O_2+CO_2 (Yamaguchi et al., 1967; Paul and Clark, 1996). Further gases may be directly affected by microbial activity, even though to quite strongly varying extents: Besides O_2 and CO_2, the gases N_2 and CH_4 are subject to potential variations in soil air. Recent soil air studies at contaminated sites stated an occurrence of strong variations from atmospheric mixing ratios with methane concentrations of up to 20 vol% and nitrogen concentrations of less than 55 vol%, depending on specific local conditions such as porosity and soil aeration (Amos et al., 2005; Jones et al., 2014).

It is important to keep in mind that soil air composition is not just a function of soil respiration. Subsurface gas dynamics such as advective or diffusive transport mechanisms have to be considered in this context. This already suggests that even inert gas mixing ratios in soil air may be exposed to variations with respect to the respective atmospheric values. One crucial aspect is the indirect influence of oxygen depletion. Reduced sum values of O_2+CO_2 are inducing an advective flow, compensating the arising pressure deficit and, thus, a likewise increase of the mixing ratios of all gas species. Such an effect on soil air composition was already proposed by Stute and Schlosser (1993) and experimentally confirmed by Freundt et al. (2013) for NG mixing ratios in soil air. Besides advective pressure balancing, some reasons for diffusion-based transport were proposed in the literature concerning their potential impact on soil air composition:

- In case of local subsurface temperature gradients, thermal diffusion induces a migration of heavier gas species towards the colder region (Chapman and Dootson, 1917; Ibbs et al., 1928).
- Gravitational fractionation according to the Barometric formula results in an enrichment of heavier gas species at the lower end of a soil column, coming along with a gas-specific scale

height, see eq. (2.22) (Dalton, 1826; Craig et al., 1988).

- Water vapor gradients may induce diffusive transport as proposed by Severinghaus et al. (1996): The mixing ratio of water vapor in soil air is usually different from that in atmospheric air (regarding typical relative humidities), while the total pressure inside these both gas phases is almost equal. This goes along with concentration gradients of all remaining gas species, thus inducing a diffusive flux.

- As a consequence of any advectively caused concentration gradient (e.g. caused by a reduced sum value of O_2+CO_2 as described above), a diffusive balancing is induced (Freundt et al., 2013; Jones et al., 2014).

A formal explanation of diffusive transport is given in chapter 2.2.1. An important consequence of any diffusion-based mechanism is a fractionating effect on gas phase composition, caused by the mass-dependence of its action. In this context, a strong impact is expected on helium which has by far the highest diffusivity of all gas species considered in this study.

To summarize, subsurface gas phase composition is in fact similar to the atmospheric composition. However, it is not at all uniform, neither on temporal nor on local scale. Arising gradients of mixing ratios are a consequence of microbial activity as well as of gas dynamical processes, even affecting inert gas species like NGs.

2.2 Subsurface transport processes

The subsurface distribution of certain substances or conditions is usually not uniform, due to specific locations of sinks and sources. For example, heat from incident solar radiation enters the soil from the above-ground atmosphere. Microbial gas production usually occurs in the topmost meter of a soil, while degassing of groundwater releases gas from the lower end of the unsaturated zone. Such processes result in subsurface transport mechanisms, tending to compensate imbalances.

The following descriptions will start with subsurface transport of solutes or rather of gases. A profound understanding of subsurface gas dynamics is essential for many gas tracer applications. For example, it allows to describe microbial activity, to quantify exchange processes between soil air and atmosphere, but also to investigate volatile organic gas compounds and their transport into the groundwater at contaminated sites.

2.2.1 Solute transport

In this study, the subsurface transport of solutes is of particular interest. The two fluids or rather solvents of interest are air and water. Two main transport mechanisms are distinguished: the movement of solutes with the carrier fluid (*advection*) and within it (*diffusion*). The corresponding underlying processes as well as their mathematical description are fundamentally different and will be discussed in the following.

Advective transport

Advective transport describes the transport of substances together with the carrier fluid. It depends mainly on the physical properties of the fluid as well as on the geometry of the pore space. The advective flux $\vec{j}_{\mathrm{adv}}$ [kg m^{-2} s^{-1}] is formally described by

$$\vec{j}_{\mathrm{adv}} = c \cdot \vec{v} \tag{2.23}$$

with the concentration c [kg/m^3] of the transported substance and the actual flow velocity $\vec{v}$ [m/s] of the transport medium (Roedel and Wagner, 2010). The mass within a system is assumed to be conserved, meaning

$$\frac{\partial c}{\partial t} = -\vec{\nabla}\vec{j} + S \tag{2.24}$$

with a parameter S [kg m^{-3} s^{-1}] denoting sinks or sources. Thus, eq. (2.24) can be formulated as

$$\frac{\partial c}{\partial t} = -\vec{\nabla}\,(c\vec{v}) + S \tag{2.25}$$

giving the temporal evolution of the local concentration due to advective flow. Obviously, the flow is directed into a preferential direction, given by the flow direction of the carrier fluid.

Advective groundwater flow is usually induced by gradients of the hydraulic head. Within the unsaturated zone, corresponding pressure gradients may result from barometric pressure variations, wind effects, penetrating water fronts after precipitation, temperature-induced volume changes, non-equimolar gas production due to microbial activity or from groundwater table fluctuations (Molins and Mayer, 2007). The occurrence of advective gas flow requires much smaller pressure gradients compared to water flow, since the dynamic viscosity of air is about 50 times lower than that of water (Meschede, 2015).

Molecular diffusive transport

Diffusive flux results from the stochastic movement or rather from the thermal motion of the particles. It results in a net flux along the concentration gradient of a substance, tending to balance it. According to the principle of equipartition of energy, the mean[3] kinetic energy $\langle E_{\mathrm{kin}} \rangle$ of a gas molecule with the mass m and the mean velocity v can be determined as

$$\langle E_{\mathrm{kin}} \rangle = \frac{3}{2}\,\mathrm{k_B}\,T \overset{!}{=} \frac{1}{2}\,m\,\langle v^2 \rangle \Leftrightarrow \sqrt{\langle v^2 \rangle} = \sqrt{\frac{3\mathrm{k_B}T}{m}} \tag{2.26}$$

with the Boltzmann constant $\mathrm{k_B} = 1.38 \cdot 10^{-23}$ J/K and the temperature T (Landau and Lifschitz, 1991). Inserting the average atomic mass of atmospheric air, a mean velocity of about 600 m/s is obtained for room temperature. After a mean free path length of about $\lambda_{\mathrm{G}} = 0.06\,\mu\mathrm{m}$ (Roedel and Wagner, 2010), a particle hits another one and changes its flight direction which is not correlated with the previous direction.

A single particle moves by Δx before it collides again after the time span $\Delta\tau$. According to the *central*

---

[3] The notation $\langle\,\rangle$ indicates the mean of all considered particles.

limit theorem, the expectation value of its position vanishes due to the statistical independence of such irregular movements: $\langle \Delta x \rangle = 0$ (Landau and Lifschitz, 1991). After n collisions, the time

$$t_n = n \cdot \langle \Delta \tau \rangle \tag{2.27}$$

can be used to describe the variance σ_n of its position as follows (Flühler and Roth, 2004):

$$\sigma_n^2 = n \cdot \langle \Delta x^2 \rangle = t_n \cdot \frac{\langle \Delta x^2 \rangle}{\langle \Delta \tau \rangle} =: 2Dt_n \tag{2.28}$$

The so-called *diffusion coefficient* D [m^2/s] does not depend on time but rather on properties of the particle and carrier fluid. It can be used to describe diffusive flux $\vec{j}_{\text{diff}}$ [kg m^{-2} s^{-1}] by means of the empirical *Fick's first law* (Fick, 1855)

$$\vec{j}_{\text{diff}} = -D\vec{\nabla}c \tag{2.29}$$

where the spacial extent σ [m] is proportional to the square root of the time span t [s]:

$$\sigma = \sqrt{2Dt} \propto \sqrt{t} \tag{2.30}$$

Applying for mass conservation, see eq. (2.24), the temporal evolution of the concentration is obtained as

$$\frac{\partial c}{\partial t} = \vec{\nabla}\left(D\vec{\nabla}c\right) + S \tag{2.31}$$

which is also known as *Fick's second law*.

Dispersive transport

As already described, solutes can be regarded to be transported within fluid parcels. Dispersion is the result of diffusive movements of solutes between fluid parcels of different flow velocities. Such velocity gradients occur due to the flow within a pore matrix. This can easily be seen for the simple case of a perfectly cylindrical capillary, in which a parabolic velocity distribution appears due to molecular friction at the outer capillary walls, also referred as *Hagen-Poiseuille flow* (Prandtl et al., 2013). Additionally, flow velocities and flow directions may differ across different pores due to their specific shape, leading also to dispersion effects. In the saturated zone, the so-called *macro dispersion* is induced by varying hydraulic conductivities or different flow paths.

Dispersion leads to a stronger and faster broadening of a certain substance distribution than just expected by molecular diffusion. It is thus comparable to turbulent mixing which occurs in above-ground waters and causes a net transport balancing concentration gradients. Dispersive flux $\vec{j}_{\text{disp}}$ [kg m^{-2} s^{-1}] is described analogously to molecular diffusion:

$$\vec{j}_{\text{disp}} = -\mathbf{D}_{\text{disp}}\vec{\nabla}c \tag{2.32}$$

The so-called *dispersivity* $\mathbf{D}_{\text{disp}}$ [m^2/s] is a tensor due to the spacial inhomogeneity of the fluid velocity field. It depends only on the velocity field of the carrier fluid and not on the solute. The overall impact of dispersion on transport depends on the time-scale of interest. Usually, for very short time limits, the impact of diffusion between fluid parcels of different velocities can be neglected. A detailed description of dispersion on different time-scales is given in Flühler and Roth (2004).

Summary and discussion of subsurface solute transport

The formal descriptions of advection, diffusion and dispersion as explained so far are generally valid for free fluids without any spatial restriction. A first constraint to mention in this context is that of adsorption. Subsurface transported substances adsorb to a specific extent on the surface of the soil matrix. Adsorption leads to a retardation of transport, depending on the rock type, the regarded substance, the transport medium as well as on the ambient temperature. A linear relationship can be generally assumed between the substance concentration c within the carrier medium and the total concentration c_{tot} of the regarded substance (Brusseau, 1994):

$$c_{\text{tot}} = \phi R c \tag{2.33}$$

For adsorbing substances, the so-called *retardation parameter* is $R \geq 1$, implying a slowing down of solute transport by a factor of $1/R$. The soil porosity ϕ is taken into account since the total concentration is usually referred on the total soil volume of interest (including the pore matrix), while the concentration c is referred on the carrier medium which can just fill up the pore space.

Irrespective of adsorption, the porosity has to be considered during a formal description of any respective transport mechanism, since subsurface transport – with and within both the water as well as the gas phase – occurs inside the pore space of a soil matrix. For the simple case of a porous medium completely saturated by either gas or water, subsurface transport fluxes can be expressed within a single transport equation:

$$\frac{\partial \phi R c}{\partial t} = \underbrace{-\phi_{\text{eff}} \vec{\nabla} \left(c \vec{v} \right)}_{\text{advective}} + \underbrace{\vec{\nabla} \left(\phi / \tau \cdot D_{\text{soil}} \vec{\nabla} c \right)}_{\text{diffusive}} + \underbrace{\phi_{\text{eff}} \mathbf{D}_{\text{disp}} \vec{\nabla} c}_{\text{dispersive}} + S \tag{2.34}$$

The effective porosity ϕ_{eff} has to be considered for advective and dispersive transport since they are restricted on the flux-participating pore space of the soil matrix (Blume et al., 2009). In contrast, diffusion also concerns even very small pores which do not participate in advective flow, which is why the porosity ϕ is considered for diffusive flux instead of the effective porosity. The center of the solute pattern is transported advectively, while diffusion and dispersion cause a relative spreading. The subsurface diffusion coefficient D_{soil} [m^2/s] in eq. (2.34) is defined as

$$D_{\text{soil}} = -\frac{1}{\tau} \cdot \phi \cdot D \tag{2.35}$$

with the free air diffusion coefficient D. The unitless *tortuosity* parameter τ accounts for the influence of the pore geometry restricting the transport on the available bent flow paths. Different models are proposed in the literature stating a formal description of the tortuosity. The most frequently consulted formulation is from Millington and Quirk (1961) describing the tortuosity for transport within the fluid i:

$$\tau = \frac{\phi^2}{\theta_\mathrm{i}^{7/3}} \tag{2.36}$$

A water content of $\theta_\mathrm{w} = \phi$ is usually found in the saturated zone, which is why eq. (2.34) can be seen as a reliable description of solute transport in groundwater. In contrast, inside the unsaturated zone, an entire fill-up of the pore space by soil air is usually not observed, due to the non-negligible residual water content $(\theta_\mathrm{a} \neq \phi)$. Transport thus occurs within both the gaseous and the water phase. The volumetric contents of air θ_a and of water θ_w have to be taken into account in eq. (2.34), respectively – instead of the (effective) porosity. Considering diffusive transport, it is appropriate to neglect the contribution of the water phase compared to that of the gaseous phase, since the diffusion coefficient of gaseous substances in air is about four orders of magnitude higher than in water (Blume et al., 2009). Thus, in eq. (2.35) the porosity ϕ is usually replaced by θ_a. Subsurface advective flow is typically induced by barometric pressure gradients, migrating down to several meters depth during a time scale of days and, thus, usually by far more effective than diffusive flux (Thorstenson and Pollock, 1989; Massmann and Farrier, 1992). However, the permeability of a soil matrix structure determines the respective impact of transport processes. For example, advection is dominant in high permeable materials, while diffusion is more effective in low permeable materials (Nazaroff and Sextro, 1989).

A formal description of transport mechanisms in the unsaturated zone is more sophisticated than in the saturated zone. Within the saturated zone, dispersive flux plays a crucial role and typically dominates molecular diffusive flux. In contrast to a pure water phase, a zero velocity condition at the walls cannot be assumed for gas flowing through a capillary (Klinkenberg, 1941; Tanikawa and Shimamoto, 2006). Even though a contribution of dispersion to transport within the subsurface gaseous phase is observed to some extent (Auer et al., 1996), the relative contribution of dispersion within the unsaturated zone can usually be neglected with respect to diffusion, due to comparatively small gas flow velocities (Popovičová and Brusseau, 1997; Scanlon et al., 2002).

The above given formal description of molecular diffusion implies isothermal and isobaric conditions, as well as a mean free path length of the considered particles, which is much smaller than the pore size. However, in case of a mean free path length greater than the pore radius, particle collisions with the pore walls dominate over intermolecular collisions. This effect is formally analogously described by the so-called *Knudsen diffusive flux*, where the Knudsen diffusion coefficient depends on the pore geometry (Cunningham and Williams, 1980). While Knudsen diffusion plays a role for transport within the subsurface gaseous phase, it can usually be neglected in the saturated zone due to the comparatively small mean free path length of particles in water (Scanlon et al., 2002).

Molecular diffusion as described above has to be complemented by an additional transport process for pairs of gases with an unequal molar weight. In such a case of non-equimolar diffusion, lighter molecules move faster than heavier ones according to the kinetic gas theory. The arising pressure buildup results in an advective kind of non-separative transport which is called *bulk diffusive flux* and has to be distinguished from the above discussed advective flow (Scanlon et al., 2002).

Obviously, the complex nature of transport processes within the unsaturated zone is caused by the coexistence of water and gas phase. A reliable description of subsurface gas dynamics thus requires an application of numerical simulations and, in particular, an incorporation of Knudsen as well as of bulk diffusion into the corresponding transport equation (Massmann and Farrier, 1992). The so-called *Dusty gas model* has proven as a reliable tool, for which a detailed explanation is given in Cunningham and Williams (1980). A description of subsurface transport mechanisms requires, furthermore, a simplification by introducing so-called *effective material properties*, to handle multiphase flow fields within a complex heterogeneous medium. To give some examples, dispersive transport is determined from the mutual influence of the flow velocity distributions of gas and water. Mass transfer has to be considered as a result from gas exchange between gas and water phase. Furthermore, gas cannot be seen as incompressible (which is approximately the case for water) since its density depends on the ambient pressure, going along with a non-linearity of the corresponding flow equation (Scanlon et al., 2002). All mentioned aspects motivate a description of unsaturated zone transport by means of effective properties and an application of numerical inversion (Flühler and Roth, 2004).

2.2.2 Heat transport

The main heat source of soils is the incident solar radiation which accounts in the mean for 342 W/m^2 related to the whole Earth surface (Roedel and Wagner, 2010). About 30 % of the incident solar radiation is directly reflected by soils, with strong variations according to the soil-specific albedo[4]. Only the non-reflected fraction has a relevance for the subsurface heat budget. About 80 % of the non-reflected share leads to water evaporation, while about 5 % is used for photosynthesis. Thus, a fraction of just about 15 % ends up in subsurface sensible heat (van Elsas et al., 2006). Regarding the topmost meters of a soil, solar radiation usually plays a by far larger role than the geothermal heat flux of about 0.05 W/m^2 on global average (Sclater et al., 1980). Besides the just mentioned sources, the subsurface heat balance also requires a sink which is the disposal of latent and sensible heat as well as thermal radiation into the atmosphere according to *Wien's Displacement Law*[5] (Blume et al., 2009; Roedel and Wagner, 2010).

Subsurface heat transport is driven by *advection*, *radiation* and *conduction*. Advection is of relevance in particular within the topmost cm of a soil (Gisi, 1997). Heat requires a transport medium which is, caused by its high heat capacity, usually water. However, within the unsaturated zone, the contribution of (water saturated) gas flow is not negligible due to the release of latent heat. Heat radiation occurs by means of electromagnetic waves and plays a major role for the heat exchange between soil and atmosphere according to the *Stefan Boltzmann Law*[6].

While advective transport requires the presence of a carrier fluid, heat conduction – as the most relevant subsurface heat transport mechanism – occurs permanently and anywhere. According to the

---

[4] Typical soil albedo values range from 5 % up to 60 %, e.g. 5 – 10 % for farmland, 15 – 40 % for sandy soils and 10 – 20 % for grass land. It is strongly influenced by the soil constituents such as organic matter and their colors (Blume et al., 2009).

[5] Wien's Displacement Law gives the temperature T [K] dependent wave length $\lambda_{\max}$ [µm] at which a black body emits the strongest radiation power: $\lambda_{\max} = T^{-1} \cdot 2\,897.8$ µm K (Meschede, 2015).

[6] According to the Stefan Boltzmann Law, the intensity of the radiation power of a black body is proportional to T^4. The proportionality constant depends on the so-called *Stefan Boltzmann constant* $\sigma = 5.67 \cdot 10^{-8}$ Wm^{-2}K^{-4} and the emissivity of the considered emitter, which is usually $\epsilon = 0.4 - 0.5$ for soils (Gisi, 1997; Meschede, 2015).

Fourier law, the heat flux j_th [W/m^2] is described as follows:

$$\vec{j_\mathrm{th}} = -\lambda \vec{\nabla} T \text{ with } \lambda = \chi \cdot \rho \cdot \mathrm{c_P} \tag{2.37}$$

The thermal conductivity λ [W m^{-1} K^{-1}] is a material property depending on the temperature conductivity χ [m^2/s], the density of the material ρ and its specific heat capacity $\mathrm{c_P}$ [J kg^{-1} K^{-1}] (Meschede, 2015). The heat capacity of a soil depends on the relative contributions of its three constituents soil matrix (m), air (a) and water (w):

$$\mathrm{c} = \theta_\mathrm{m}\mathrm{c_m} + \theta_\mathrm{a}\mathrm{c_a} + \theta_\mathrm{w}\mathrm{c_w} \tag{2.38}$$

For a given temperature gradient, the thermal conductivity describes the amount of heat flowing through a cross sectional area within a time span of 1 s. Typical values are 0.025 W m^{-1} K^{-1} for air, 0.6 W m^{-1} K^{-1} for water and 2.9 W m^{-1} K^{-1} for clay, which can be seen as temperature independent within typical natural temperature ranges (Flühler and Roth, 2004; Blume et al., 2009). Obviously, the thermal conductivity of a soil typically depends on its bulk density and its volumetric water content, both determining the heat conduction between individual grains.
Based on the analogy of eq. (2.37) to Fick's first law, it can be applied to obtain the temporal evolution of the soil temperature

$$\frac{\partial T}{\partial t} = \chi \Delta T + S \tag{2.39}$$

with a thermal heat source term denoted as S resulting usually from subsurface phase transitions, where heat is released (condensation/freezing) or consumed (evaporation/melting). The partial differential equation (2.39) is solved by the following approach (Kirkham and Powers, 1972):

$$T(z,t) = \tilde{T} + A(z) \cdot \sin(\omega t + kz) = \tilde{T} + A(z_0) \cdot \exp(-z \cdot k) \cdot \sin(\omega t + kz) \tag{2.40}$$

Eq. (2.40) already indicates that the subsurface temperature oscillates with a wave number k and an amplitude $A(z)$ around a certain temperature denoted as $\tilde{T}$. The amplitude is exponentially attenuated with increasing soil depth according to $k = \sqrt{\omega/2\chi}$ [m^{-1}]. The angular velocity $\omega = 2\pi/\hat{t}$ [s^{-1}] depends on the time scale $\hat{t}$ of the considered fluctuations, which is one year if $\tilde{T}$ reflects the mean annual atmospheric temperature (MAAT). For the limiting case at the soil surface ($z = 0$), eq. (2.40) results in the non-attenuated atmospheric temperature cycle. For very large soil depths ($z \to \infty$), the temperature converges to $\tilde{T}$, corresponding to a vanishing temperature gradient. Amplitudes of temperature fluctuations with higher frequency are damped stronger with increasing soil depth. The so-called *attenuation length* $z_\mathrm{a} = 1/k = \sqrt{2\chi/\omega}$ [m] is the depth where the local temperature amplitude A is attenuated by a factor of e^{-1} relative to the atmospheric temperature amplitude.

The periodic fluctuation of incident and emitted heat leads to typical subsurface temperature fluctuations on daily as well as on annual time scales. Both processes, advection and heat conduction, determine the resulting subsurface thermal regime. Figure 2.9 shows typical diurnal and annual temperature variations as well as their attenuation with increasing soil depth, calculated according to eq. (2.40). Since source and sink of heat are both located at the soil surface, the temperature amplitude

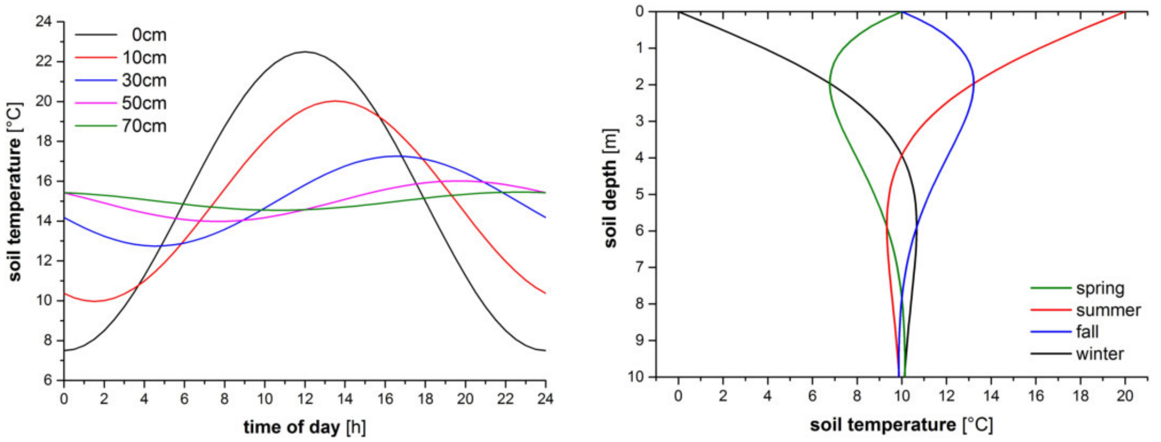

(a) Diurnal time-dependent temperature fluctuations at different depths, calculated for $z_\mathrm{a} = 0.25\,\mathrm{m}$, $\tilde{T} = 15°\mathrm{C}$ and $A(z_0) = 7.5°\mathrm{C}$.

(b) Annual depth-dependent temperature fluctuations in different seasons, calculated for $z_\mathrm{a} = 2.5\,\mathrm{m}$, $\tilde{T} = 10°\mathrm{C}$ (corresponds to MAAT) and $A(z_0) = 10°\mathrm{C}$.

Figure 2.9: Diurnal and annual fluctuations of soil temperature, calculated according to eq. (2.40) by means of typical values given by Stute and Schlosser (1993) and Blume et al. (2009).

reaches its maximum there. The exact oscillation pattern is determined by local soil type and climate conditions. Soils with a higher thermal conductivity – e.g. due to a high soil water content or a high bulk density – typically show a stronger temperature attenuation at the soil surface, while corresponding temperature waves are conducted deeper into the soil. Local plant populations may also attenuate the amplitude of temperature oscillations in the topmost soil region. In contrast, very dry or loose soils exhibit stronger temperature fluctuations within the topmost soil layer, favoring e.g. the occurrence of soil freezing.

A crucial aspect for data evaluation in this study is the relationship between MAAT and mean annual soil temperature (MAST) at a certain soil depth. The previous explanations suggest that annual temperature cycles within the topmost meters of a soil fluctuate around the MAAT, see Fig. 2.9(b). However, several studies give evidence for deviations from such an idealized case. MASTs may potentially deviate from the local MAAT by some °C, depending on site-specific factors such as vegetative cover, snow cover, insolation, evaporation, soil moisture and soil material (Powell et al., 1988; Stute and Sonntag, 1992; Beyerle et al., 2003; Zhang, 2005; Cey, 2009). To give an example, loamy soils usually exhibit a stronger cooling by evaporation compared to sandy ones (Cey, 2009), while vegetative cover may induce a subsurface cooling (Stute and Sonntag, 1992). Furthermore, a significant discrepancy of MAAT and MAST is usually observed at deeper soil layers below about 20 m, as a consequence of geothermal heat flow accounting for a global average of about 3°C/100 m (Bischof, 1837; Chow et al., 2011). A detailed overview of recent findings about subsurface temperatures and their relation to MAAT is given in Cey (2009) and in Aeschbach-Hertig and Solomon (2013).

2.2.3 Gas exchange

The subsurface pore space consists of either gas or water. Thus, exchange processes between these two phases play an important role in the context of subsurface gas dynamics. In this section, the gas transport across the boundary between gaseous and water phase is discussed, mainly based on Brutsaert and Jirka (1984).

If a soluble substance is brought into a system consisting of a gaseous and a water phase, a *solution equilibrium* will arise. According to the so-called *Henry law*, the respective concentrations of a substance i within the gas phase C_i^g and the water phase C_i^w are proportional to each other:

$$C_\mathrm{i}^\mathrm{g}(T, P_\mathrm{a}) = H_\mathrm{i}'(T, S) \cdot C_\mathrm{i}^\mathrm{w}(T, S, P_\mathrm{a}) \tag{2.41}$$

The *Henry coefficient* H_i' depends on the temperature T and on the salinity S and is unitless, presuming that the concentrations are given in the same units (usually in the volumetric unit mol/l). As already described in eq. (2.20), the partial pressure $p_\mathrm{i} = [P_\mathrm{a} - h \cdot e_\mathrm{s}(T)] \cdot x_\mathrm{i}$ of a specific gas species within the gaseous phase depends on the atmospheric pressure P_a, the saturation water vapor pressure e_s, the relative humidity h and the specific volumetric mixing ratio x_i in dry air.

Since air can be considered as an ideal gas[7], the concentration within the gas phase is related to a corresponding partial pressure p_i by

$$C_\mathrm{i}^\mathrm{g}(T, P_\mathrm{a}) = \frac{p_\mathrm{i}(z, h, x_\mathrm{i}, T)}{RT} \tag{2.42}$$

with the universal gas constant R and the temperature T. Thus, an alternative formulation of the Henry law is achieved:

$$p_\mathrm{i}(z, h, x_\mathrm{i}, T) = RTH_\mathrm{i}'(T, S) \cdot C_\mathrm{i}^\mathrm{w}(T, S, P_\mathrm{a}) = H_\mathrm{i}(T, S) \cdot C_\mathrm{i}^\mathrm{w}(T, S, P_\mathrm{a}) \tag{2.43}$$

Here, the *Henry coefficient* H_i has a dimension of the form $\mathrm{l\,atm\,mol^{-1}}$. The reciprocal of the Henry constant is also denoted as *Ostwald solubility*:

$$L_\mathrm{i}(T, S) = \frac{1}{H_\mathrm{i}'(T, S)} \quad \text{and} \quad \lambda_\mathrm{i}(T, S) = \frac{1}{H_\mathrm{i}(T, S)} \tag{2.44}$$

The dependence of the solubility on the salinity can be neglected in this study, since young groundwater of vanishing salinity is investigated. The temperature dependence of the Henry coefficient was formulated empirically by Benson and Krause Jr (1976), see appendix A.1. Figure 2.10 gives an overview of the temperature dependence of the empirical Ostwald solubilities of several gas species, respectively.

The solubility of gases in water depends on temperature and salinity, but also on chemical reactions within the water phase, which is of particular relevance for CO_2 but not for inert gases like noble gases. Besides the atmosphere, the subsurface water phase is the main sink for CO_2 released from

---

[7] The ideal gas law $pV = nRT$ depends on the gas pressure p, its occupied volume V, the amount of substance n, the universal gas constant $R = 8.3144\,\mathrm{J\,mol^{-1}\,K^{-1}}$ and the temperature T (Meschede, 2015).

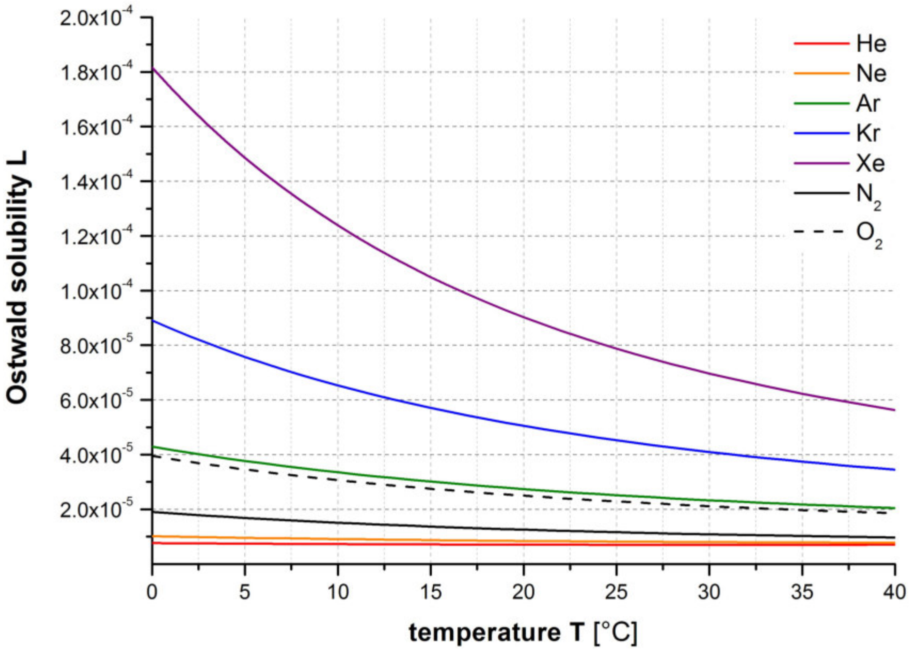

Figure 2.10: Empirical Ostwald solubilities (unitless) for noble gases (He, Ne, Ar, Kr and Xe) as well as for O_2 and N_2, determined according to Benson and Krause Jr (1976).

microbial activity. Reactions of the carbonate chemistry can be summarized as

$$\underbrace{\mathrm{CO_2\,(g)}}_{\text{gas phase}} \rightleftharpoons \underbrace{\mathrm{CO_2\,(aq) + H_2O \rightleftharpoons H_2CO_3 \rightleftharpoons HCO_3^- + H^+ \rightleftharpoons CO_3^{2-} + 2\,H^+}}_{\text{gas phase / soil water}} \rightleftharpoons \underbrace{\mathrm{CaCO_3\,(s)}}_{\text{calcite}} \tag{2.45}$$

and determine the pH value of the soil water due to the influence on the concentration of positively charged hydrogen ions. Analogous reactions within the water phase also explain the high solubility of ammonia (NH_3) and sulfide (H_2S). Compared to the solubility of oxygen, the solubility of CO_2, NH_3 and H_2S in water is about 40 times, 90 times and 12 500 times higher, respectively (Lange and Dean, 1979).

Henry's law describes the gas amount dissolved in water at equilibrium conditions, which means usually at atmospheric air pressure. However, distinct higher gas amounts may be dissolved as a consequence of increasing ambient pressure as it is the case in the saturated zone due to the hydrostatic pressure. Gas bubble formation in a certain depth $z*$ below the groundwater table occurs if the sum of all partial pressures of dissolved gases exceeds the ambient pressure $p\,(z*)$:

$$\sum_{\mathrm{i}} p_{\mathrm{i}} > p\,(z*) = P_{\mathrm{a}} + \rho \cdot \mathrm{g} \cdot z* \tag{2.46}$$

A subsequent enhancement of the dissolved gas pressure in groundwater (above the equilibrium amount dissolved originally at atmospheric pressure) can result from the dissolution of entrapped air bubbles during a rising groundwater table (Holocher et al., 2002, 2003), from subsurface gas production due to microbial activity (Klump et al., 2006; Stute et al., 2007; Visser et al., 2007), but also from magmatic processes in volcanic areas (Aeschbach-Hertig et al., 1996, 1999a).

A common way to describe gas exchange in surface waters was developed by Whitman (1923) and considers two boundary layers of thickness δ_x at the transition of media, respectively. A simplification of this approach is to regard only one single boundary layer, either on the gas side (for gases with high solubility) or on the water side (volatile gases with low solubility). The one dimensional so-called *stagnant film model* results in an exchange flux j_i^ex

$$j_\mathrm{i}^\mathrm{ex} = -D_\mathrm{i}^\mathrm{w} \cdot \frac{\partial C_\mathrm{i}}{\partial z} = \frac{D_\mathrm{i}^\mathrm{w}}{\delta_\mathrm{w}} \cdot \left(C_\mathrm{i} - C_\mathrm{i}^\mathrm{eq}\right) = v_\mathrm{w} \cdot \left(C_\mathrm{i} - C_\mathrm{i}^\mathrm{eq}\right) \tag{2.47}$$

with the molecular diffusion coefficient D_i^w of the gas i in water, the concentration C_i in the interior water phase and the equilibrium concentration C_i^eq at the gas/water transition. According to mass conservation

$$\frac{\partial C_\mathrm{i}}{\partial t} = -\frac{\partial j_\mathrm{i}^\mathrm{ex}}{\partial z} \tag{2.48}$$

the concentration C_i approaches exponentially towards the equilibrium concentration, described by a time constant:

$$\tau = \frac{\delta_\mathrm{w}}{v_\mathrm{w}} \tag{2.49}$$

For subsurface conditions, the stagnant film model does not directly apply, since it actually presumes an efficient mixing of interior fluid phases by turbulence. However, usual pore matrix diameters of several µm constrain the subsurface water film thickness δ_w. Considering a typical exchange velocity v_w in the range of meters per day (Brutsaert and Jirka, 1984), the resulting time constant τ is of the order of seconds. This rough estimation shows that soil water usually stays in equilibrium with the surrounding soil gas phase.

2.3 Tracers in environmental physics

Environmental tracers are natural or anthropogenic emitted substances used to investigate natural processes as well as their timescales and pathways. Variations of their usually very small abundances are used in corresponding studies. Environmental tracers are distinguished into so-called *transient* and *geochemical* tracers (Elderfield et al., 2006). Transient tracers exhibit a time dependent input function and usually have an anthropogenic origin (e.g. CFCs and ^{3}H from nuclear weapon tests). In contrast, geochemical tracers have a natural origin and are characterized by a constant input function (e.g. stable isotopes of water and, in general, noble gases). In the following, tracer methods are presented, which are applied in this study to investigate subsurface gas dynamics.

2.3.1 Stable noble gas isotopes

Noble gases (NGs) have proved as reliable tool in environmental tracer studies, mainly to investigate geological processes (Kipfer et al., 2002; Aeschbach-Hertig and Solomon, 2013). The largest NG reservoir on Earth is the atmosphere, containing by far higher amounts of NGs than the Earth's crust and mantle or the oceans. Furthermore, the atmosphere is assumed to contain most of its gases since the early history of Earth. These two facts explain the stability of atmospheric NG mixing ratios within the atmosphere during the past (Ozima and Podosek, 2002; Burnard, 2013). Table 2.2 gives an overview of the relative abundances of NGs in atmospheric air.

The application of NGs in tracer studies is motivated at the one hand by their chemical inertness. Their abundances in natural waters and in soil air are, thus, only determined by geophysical processes. On the other hand, NGs are characterized by low natural background concentrations as well as by well-known and quantifiable sources and sinks in the subsurface, which are radioactive decay and exchange with atmospheric air.

Due to sophisticated analysis methods, NGs are rather specialized tracers, in contrast to the widely used stable isotopes of water (Aeschbach-Hertig and Solomon, 2013). In groundwater hydrology, dissolved NG contents are particularly used to study climatic conditions during recharge − which is also a major focus of this study. Any tracer application of NGs requires a reliable understanding of subsurface gas dynamics as well as of the origins of different dissolved gas components in groundwater, which is explained in the following, based mainly on Kipfer et al. (2002) and Aeschbach-Hertig and Solomon (2013).

Equilibrium component

During groundwater recharge, an equilibrium state establishes between respective NG concentrations in the subsurface gas and water phase, as described by Henry's law. This results in an *equilibrium component* of dissolved NGs in groundwater:

$$c_{\mathrm{i}}^{\mathrm{w,eq}}(T,S,P_a) = \frac{p_{\mathrm{i}}(z,h,x_{\mathrm{i}},T)}{H_{\mathrm{i}}(T,S)} = \frac{[P_{\mathrm{a}} - h\cdot e_{\mathrm{s}}(T)]\cdot x_{\mathrm{i}}}{H_{\mathrm{i}}(T,S)} \tag{2.50}$$

In analogy to eq. (2.43), the key parameters are the temperature T, the salinity S (which can usually be neglected for groundwater) and the NG partial pressure p_{i} within the gas phase. An exact knowledge of NG partial pressures is essential for any conclusions about dissolved NG contents. In this context,

Table 2.2: Fractions of isotopes of different NG species in homogeneously mixed dry atmospheric air, adapted from Berglund and Wieser (2011) and Porcelli et al. (2002). This survey reflects those isotopes which are typically of main interest in NG tracer studies.

noble gas	vol. mixing ratio	isotope	mole fraction
He	$5.24\cdot10^{-6}$	^{3}He	0.00000134
		^{4}He	0.99999866
Ne	$1.818\cdot10^{-5}$	^{20}Ne	0.9048
		^{22}Ne	0.0925
Ar	$9.34\cdot10^{-3}$	^{36}Ar	0.003336
		^{40}Ar	0.996035
Kr	$1.14\cdot10^{-6}$	^{84}Kr	0.56987
Xe	$8.7\cdot10^{-8}$	^{132}Xe	0.269086

most studies suppose NG mixing ratios in soil air and atmosphere to be equal, apart from a small deviation due to different water vapor contents (Stute and Schlosser, 1993; Aeschbach-Hertig and Solomon, 2013).

Even in water equilibrating directly with atmospheric air, a bias of the equilibrium component is observed, even though it provides a rather small change: The relative abundances of dissolved NG isotopes are not exactly equal to the respective atmospheric values, which is a consequence of isotope mass differences and, thus, slightly varying solubilities. This fractionation effect is more relevant for lighter NG species such as helium or neon, due to stronger relative mass differences between certain isotopes of these gas species. The resulting change of the equilibrium component was found to be in the range of several per mill for isotopes of neon and argon (Beyerle et al., 2000). In this study, a corresponding effect will be considered during the evaluation of ^{3}He/^{4}He ratios in the context of groundwater dating (see chapter 3.3.3).

Figure 2.11 gives an overview of different components of dissolved NGs in groundwater, normalized to the equilibrium component, respectively. Each of these components is discussed in the following.

Excess Air component

Groundwater usually shows a significantly larger dissolved gas content than expected as equilibrium component. Such a gas surplus exhibits similar relative NG abundances as atmospheric air and is usually not found in surface waters. Heaton and Vogel (1981) denoted this phenomenon as so-called *excess air*. Even though the occurrence of excess air is already known for some decades, it was studied in more detail quite recently. Experimental investigations show that excess air originates

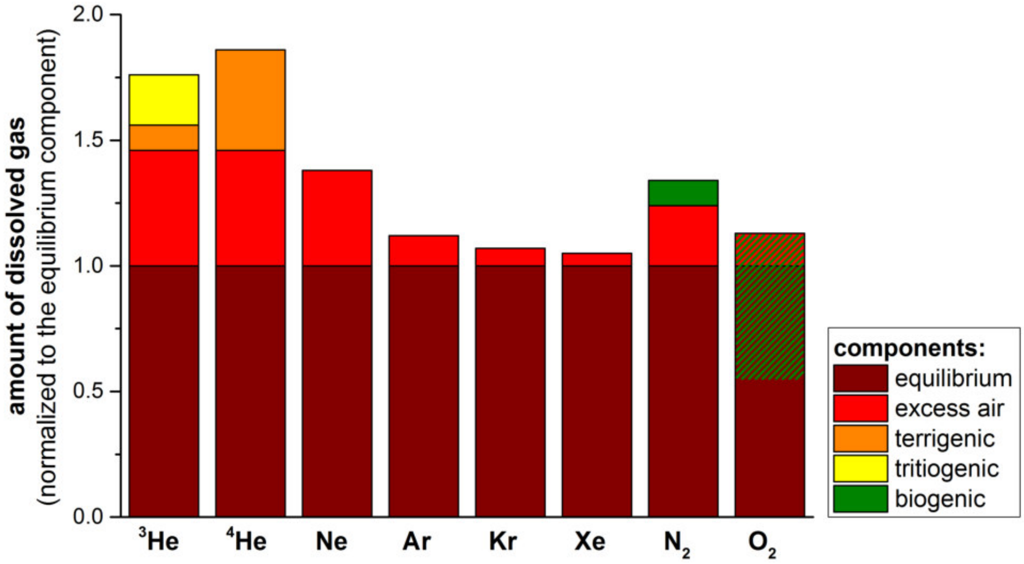

Figure 2.11: Different components of dissolved NGs in groundwater. Dissolved contents of N_2 and O_2 are also illustrated for comparison, to point out their additional dependence on subsurface microbial activity. This may result in gas release (exemplarily shown as green column for N_2) or gas consumption (exemplarily shown as green shaded area for O_2). Excess air components are calculated (according to an UA model approach as described in chapter 3.3.1, for $T = 11°C$ and an excess air amount of $A = 4$ cc/kg). Remaining components are estimated based on typical values given in Kipfer et al. (2002).

from entrapped air bubbles within the pore matrix, which are dissolved partially or completely during an increase of hydrostatic pressure (Holocher et al., 2002, 2003; Klump et al., 2007, 2008). Such pressure variations are typically induced by fluctuations of the groundwater table. Its physical origin allows to use the excess air component as a proxy for groundwater table fluctuations and, thus, to constrain amounts of precipitation during recharge (Aeschbach-Hertig et al., 2002a; Kulongoski et al., 2009). It is convenient to describe the amount of excess air as the so-called *relative neon excess*

$$\Delta\mathrm{Ne}\ [\%] = \left(\frac{c_{\mathrm{Ne}}^{\mathrm{w,tot}} - c_{\mathrm{Ne}}^{\mathrm{w,eq}}}{c_{\mathrm{Ne}}^{\mathrm{w,eq}}} \right) \cdot 100\,\% \tag{2.51}$$

with the total measured concentration $c_{\mathrm{Ne}}^{\mathrm{w,tot}}$ and the equilibrium concentration $c_{\mathrm{Ne}}^{\mathrm{w,eq}}$. On the one hand, the good applicability of neon in this context is a consequence of the marginal temperature dependence of its solubility, allowing for reliable conclusions even for not exactly known recharge temperatures. On the other hand, neon has an almost purely atmospheric origin, with hardly any subsurface sources as explained later (Kipfer et al., 2002; Aeschbach-Hertig et al., 2002a). Entrapped air bubbles usually occur in the topmost meters of the saturated zone (Faybishenko, 1995), which is thus also referred in the literature as quasi-saturated zone as mentioned before. The relative fraction of entrapped air accounts typically for 2 – 15 % of the available pore space (Fayer and Hillel, 1986). As shown in Fig. 2.11, the relative influence of excess air differs across the different gas species. Lighter gas species, such as helium and neon, show a stronger relative impact by excess air. This is a direct consequence of the mass dependence of solubility: The smaller the solubility of a certain gas species, the stronger is the difference between its concentrations within the gaseous and the water phase, respectively. Thus, for lighter gas species the potential relative impact of air bubble dissolution is stronger than for heavier ones.

So far, the relative shares of excess air component and equilibrium component were considered. Regarding just the excess air component for itself, its composition would be actually expected to be atmospheric, based on the assumption of a full dissolution of entrapped air bubbles. However, NG mixing ratios of excess air patterns were found to differ from atmospheric air. Such a fractionation effect appears as an enrichment of concentrations of heavier NGs with respect to concentrations of lighter NGs (Stute et al., 1995; Aeschbach-Hertig et al., 1999b; Ballentine and Hall, 1999). Different models were proposed to describe the formation of excess air, taking a fractionation effect into consideration. The approach of these models to explain fractionation is the mass dependence of diffusion or of solubility, respectively. Corresponding models are applied for data evaluation in this study and are, therefore, explained in detail in chapter 3.3.1.

Radiogenic, terrigenic and tritiogenic component

Subsurface NG production occurs directly by radioactive decays as well as indirectly by nuclear reactions. For a correct interpretation of dissolved NG contents in groundwater, such processes have to be taken into account as a so-called *radiogenic component*. This concerns in particular ^{4}He produced by the U-Th decay series and other α emitting particles as well as, although to a lesser extent, ^{40}Ar originating from the decay of ^{40}K. Further amounts of NGs originate from so-called secondary nuclear reactions induced by α decays, even though corresponding impacts are usually hardly detectable against the atmospheric background, except for ^{3}He and ^{21}Ne in very old groundwater (Ballentine and Burnard, 2002; Meibom et al., 2005).

Dissolved NG contents originating from different geochemical reservoirs of the solid Earth are denoted as *terrigenic component*. A significantly higher intrinsic ^{3}He/^{4}He ratio[8] is found in the Earth's mantle ($7-9\,R_\mathrm{a}$ in mid-ocean ridge basalts, see Graham (2002)) compared to the Earth's crust ($\approx 0.015\,R_\mathrm{a}$, see Mamyrin and Tolstikhin (1984)), resulting from local radiogenic helium production. Corresponding amounts of NGs may be trapped by deep circulating groundwater.

In general, subsurface produced helium isotopes tend to accumulate in groundwater as long as it is not in contact with a gaseous phase. This results from the physical properties of helium – meaning its low solubility and its high diffusivity – and allows for a qualitative interpretation of dissolved ^{4}He contents in terms of a residence time (Aeschbach-Hertig et al., 1999a; Castro et al., 2000).

The so-called *tritiogenic component* affects only the isotope ^{3}He which is produced during the β^- decay of the heavy hydrogen isotope ^{3}H (tritium) with a half-life of 12.32 a (Radiochemical Institute Karlsruhe, 1996; Lucas and Unterweger, 2000):

$$^3\mathrm{H} \longrightarrow {}^3\mathrm{He} + \mathrm{e}^- + \bar{\nu}_\mathrm{e} \tag{2.52}$$

The tritiogenic component is used for dating young groundwater as described in more detail in chapter 2.3.3.

Figure 2.12 summarizes the influence of the above described helium sources on dissolved NG contents in groundwater, by means of a so-called *three isotope plot* illustrating the corresponding ^{3}He/^{4}He ratios of different reservoirs. Tritium decay leads to an additional amount of ^{3}He and, thus, to an upward shift in Fig. 2.12.

Biogenic component

The *biogenic component* of dissolved gases in groundwater is not of direct relevance with regard to NGs. However, further gases are directly affected by microbial gas production and consumption, as exemplary shown in Fig. 2.11 for O_2 and N_2. Corresponding processes were already explained in detail in chapter 2.1.3.

The biogenic component shall not be discussed here in detail. However, a potential indirect influence on dissolved NG contents has to be kept in mind, known as the phenomenon of *groundwater degassing*. A biogenic release of gases like N_2 provides an additional gas phase within the saturated zone, containing originally no NGs. According to Henry's law, a net transfer of previously dissolved NGs is induced into that gaseous phase (not depicted in Fig. 2.11). Groundwater degassing is rather a local phenomenon which may result in dissolved NG contents which are even smaller than expected as equilibrium component (Klump et al., 2006; Stute et al., 2007; Visser et al., 2007).

---

[8] In groundwater hydrology studies, ^{3}He/^{4}He ratios are usually normalized to the atmospheric value $R_\mathrm{a} = 1.384 \cdot 10^{-6}$ (Ma et al., 2005).

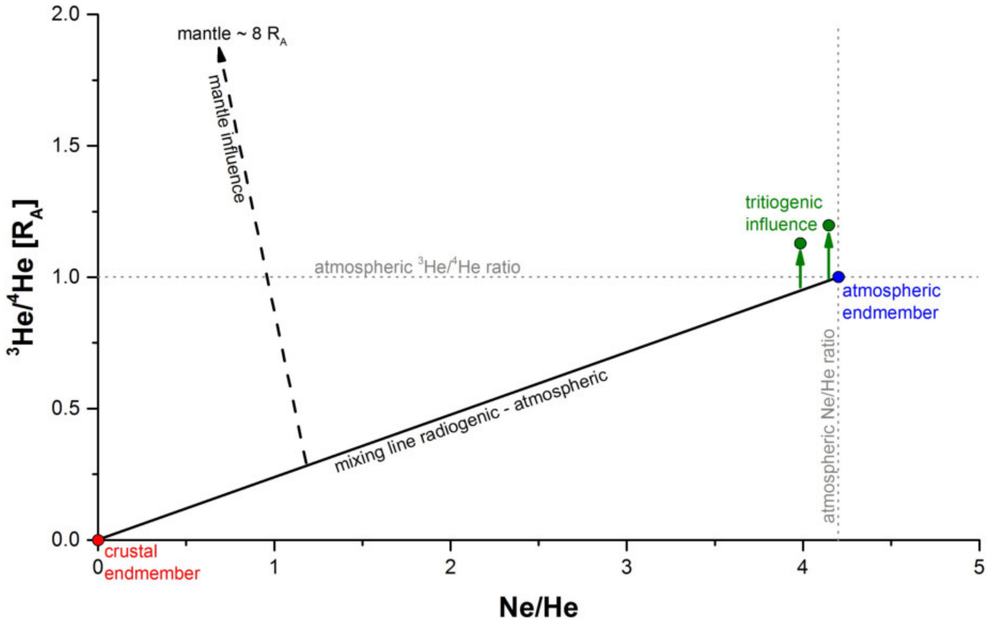

Figure 2.12: Three isotope plot indicating the influence of different geochemical reservoirs on dissolved helium contents in groundwater. ^{3}He/^{4}He ratios are normalized to the atmospheric value R_a (blue point). Due to radiogenic helium, older groundwater accumulates ^{4}He, leading to a decreased value of Ne/He, tending towards the crustal endmember (red point) with a ^{3}He/^{4}He ratio of $0.015\,R_\mathrm{a}$ (Mamyrin and Tolstikhin, 1984). Tritium decay results in an upward shift (green arrows/points). The mantle endmember reflects a wide range of ^{3}He/^{4}He ratios, ranging from $7-9\,R_\mathrm{a}$ in mid-ocean ridge basalts (assumed as reference value in this plot) up to $50\,R_\mathrm{a}$ in volcanic areas (Graham, 2002).

Summation of all components

Altogether, the total measured concentration $c_\mathrm{i}^\mathrm{tot}$ of a certain NG species consists of the above introduced components which can be summed up as follows:

$$c_\mathrm{i}^\mathrm{tot} = \underbrace{c_\mathrm{i}^\mathrm{eq} + c_\mathrm{i}^\mathrm{ex}}_{\text{atmospheric}} + \underbrace{c_\mathrm{i}^\mathrm{rad} + c_\mathrm{i}^\mathrm{ter} + c_\mathrm{i}^\mathrm{tri}}_{\text{non-atmospheric}} \tag{2.53}$$

The quantification of these components requires a measurement of different NG species. Depending on the exact circumstances of a NG tracer study, some terms in eq. (2.53) may be neglected. In general, all non-atmospheric components are only of relevance for some certain NG isotopes. In particular the tritiogenic component $c_\mathrm{i}^\mathrm{tri}$ plays only a role for ^{3}He. For all NG species (apart from helium) at least one isotope exists, which can be assumed to have a pure atmospheric origin, respectively. These are ^{20}Ne, ^{36}Ar and virtually all isotopes of Kr and Xe (Kipfer et al., 2002). This fact favors a quantification of equilibrium and excess air components, as described in chapter 3.3.1.

An important application of dissolved NGs in groundwater is the determination of so-called noble gas temperatures (NGTs). The underlying idea was already developed several decades ago (Oana, 1957; Mazor, 1972; Andrews and Lee, 1979). The determination of NGTs is based on a quantification of the equilibrium component which depends on local conditions during the last gas/water partitioning, meaning in particular the ambient temperature. The NGT reflects the water table temperature (WTT) during recharge. The WTT in turn typically reflects the local MAST, while deviations may be found in very shallow unsaturated zones, when the WTT is fluctuating on seasonal or daily scale (Stute and Schlosser, 1993; Cey, 2009; Aeschbach-Hertig and Solomon, 2013). A by far more critical relationship is that between MAST and MAAT, which was described in chapter 2.2.2.

2.3.2 Radioactive noble gas isotopes

Besides stable NG isotopes, there exist also unstable or rather radioactive NG isotopes which are used as tracers, mainly to investigate time-dependent properties such as residence times, flow velocities or mixing and exchange processes. Most prominent examples are ^{85}Kr ($T_{1/2} = 10.776\,\mathrm{a}$), ^{39}Ar ($T_{1/2} = 269\,\mathrm{a}$) and ^{81}Kr ($T_{1/2} = 229\,\mathrm{ka}$) (Audi et al., 2003), allowing to investigate processes occurring on time-scales comparable to their respective half-lives, even though very low abundances hamper a corresponding analysis (Lu et al., 2014; Ritterbusch et al., 2014).

Besides the NG species introduced up to now, radon is another one comprising just radioactive isotopes (see Tab. 2.3). In the environment, radon mainly occurs as ^{220}Rn and ^{222}Rn. Due to their short lifetimes and low abundances, ^{218}Rn and ^{219}Rn are usually not of relevance for environmental tracer studies. In contrast to other NG species, radon originates solely from radioactive reactions within the Earth's crust. ^{220}Rn (also denoted as *Thoron*) is produced from the decay of ^{224}Ra as a progeny of ^{232}Th, while ^{222}Rn originates from the decay of ^{226}Ra as a progeny of ^{238}U (Audi et al., 2003; Radiochemical Institute Karlsruhe, 1996). All corresponding daughter nuclides from ^{232}Th to ^{224}Ra and from ^{238}U to ^{226}Ra can be assumed to be in equilibrium, respectively, since for these decay chains, ^{220}Rn and ^{222}Rn are the first gaseous elements which are able to escape from soils (Karstens et al., 2015).

After their production, radon isotopes may escape the rock material and reach the subsurface air or water phase, where they take part in transport processes such as advection, dispersion or diffusion. Within the unsaturated zone, diffusion can lead to transport distances of ^{222}Rn from several centimeters up to some meters, depending on the soil water content (Nazaroff, 1992). Typical subsurface radon activities are in the range of several thousand Bq/m^3 (Blume et al., 2009), while above-ground activities account for only 10 to 100 Bq/m^3 (Nazaroff, 1992). Thus, the overall radon transport can be regarded as directed from the soil into the atmosphere which acts as sink due to its negligible radon content.

Its radioactive property, together with the relative locations of sink and source, determine an exponential decreasing concentration of radon from deeper soil layers towards the atmosphere (Dörr and Münnich, 1990). However, a depth dependent radon profile depends strongly on local conditions such

Table 2.3: Half-lives of natural Rn isotopes (Audi et al., 2003; Radiochemical Institute Karlsruhe, 1996).

noble gas	isotope	half-life
Rn	^{218}Rn	0.35 ms
	^{219}Rn	3.96 s
	^{220}Rn	55.6 s
	^{222}Rn	3.8235 d

as on subsurface transport (determined by soil porosity and soil moisture) and on subsurface radon production (determined by the rock material). Since these parameters vary horizontally as well as vertically, subsurface radon fluxes cannot be assumed to be uniform on large scale (Nazaroff, 1992; Karstens et al., 2015). Local radon profiles may thus differ significantly from the "ideal" exponential behavior (Dörr and Münnich, 1990).

Radon provides a powerful tool for the investigation of environmental processes occurring on time scales which are comparable to the half-lives of the corresponding isotopes. Radon is a geochemical tracer, since it exhibits a continuous natural input. Prominent applications are the mixing of lakes (Maiss et al., 1994) or subsurface exchange processes such as between lakes and groundwater (Kluge et al., 2007; Schmidt et al., 2009). Furthermore, radon enables to investigate exchange processes between the subsurface gas phase and atmosphere (Karstens et al., 2015). In this study, radon isotopes are used as indicators for both soil aeration and contamination of the sampled soil air.

2.3.3 Tritium

The hydrogen isotope tritium (^{3}H) is naturally produced by cosmic rays in the upper atmosphere (Libby, 1946):

$$^{14}\mathrm{N} + \mathrm{n} \longrightarrow {}^{12}\mathrm{C} + {}^{3}\mathrm{H} \tag{2.54}$$

Tritium enters the hydrological cycle as precipitation and, thus, reaches the soil region. A further contribution comes from geogenic production, accounting for about one order of magnitude less than cosmogenic production. By this way, tritium is produced by lithium and neutrons originating from U-Th series or even from cosmic rays (Clark and Fritz, 1997):

$$^{6}\mathrm{Li} + \mathrm{n} \longrightarrow \alpha + {}^{3}\mathrm{H} \tag{2.55}$$

The global natural inventory of tritium amounts to about 4 kg (Rozanski et al., 1991). Apart from natural sources, a considerable reservoir of tritium exists in the stratosphere, where it was inserted in enormous amounts by nuclear bomb tests since the middle of the fifties. This tritium has, consequently, an anthropogenic origin and enters the hydrological cycle during the annual exchange between tropospheric and stratospheric air. Bomb tests resulted in an enhancement of the atmospheric tritium concentration by a factor of about 1 000, which is decreasing since 1963 (Mook, 2000) (see Fig. 2.13). Tritium concentrations are usually given as a multiple of the ratio $^3\mathrm{H}/^1\mathrm{H} = 10^{-18}$ which is defined as 1 TU (tritium unit)[9]. Tritium can thus be seen as a transient tracer of anthropogenic and temporarily varying input, but also as a geochemical tracer of a rather constant natural input function. Regarding its half-life of 12.32 a (Radiochemical Institute Karlsruhe, 1996; Lucas and Unterweger, 2000), tritium provides a tool to determine groundwater residence times in the range of up to about 50 years (Cook and Solomon, 1997). However, the amount of tritium in atmospheric precipitation is not a monotonously decreasing function of time − due to the strong bomb peak, but also as a result of the seasonal exchange between troposphere and stratosphere (see annual fluctuations in Fig. 2.13). A certain measured tritium content in groundwater may thus indicate various residence times. It is

---

[9] 1 TU corresponds to an activity concentration of 0.118 Bq per liter of water (Mook, 2000).

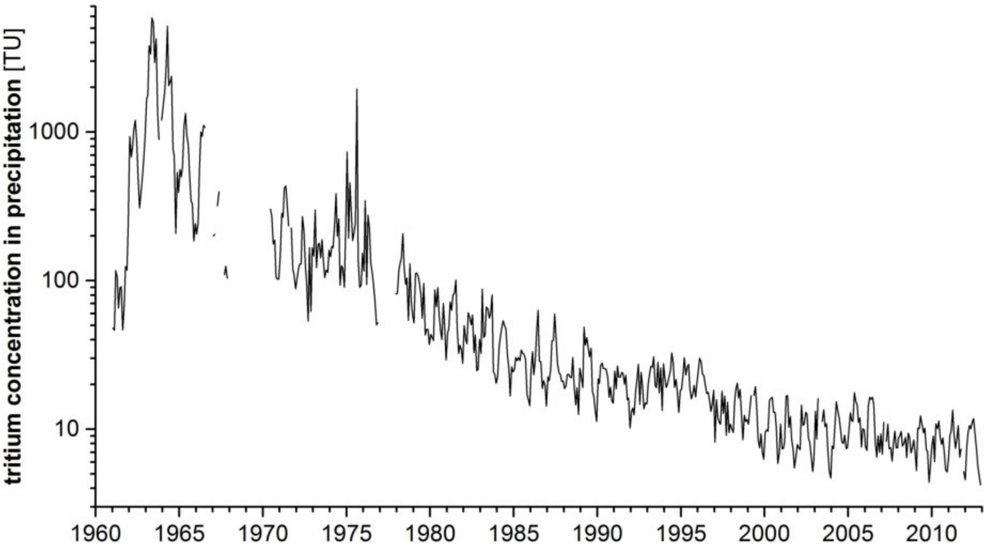

Figure 2.13: Tritium concentrations in precipitation in Stuttgart (Bad Cannstatt) from 1961 to 2012. Data from GNIP (2016) of IAEA/WMO.

therefore more common to apply tritium as well as its decay product ^{3}He which is accumulated in the water phase once it does not stand in contact to the unsaturated zone anymore. The corresponding time span τ since the last equilibration can be determined by means of the law of radioactive decay as

$$\tau = \frac{1}{\lambda} \cdot \ln\left(1 + \frac{^3\mathrm{He}^{\mathrm{tri}}}{^3\mathrm{H}}\right) \tag{2.56}$$

with the decay constant $\lambda = \ln(2)/T_{1/2} = 0.05626\,\mathrm{a}^{-1}$ and the half-life $T_{1/2}$ of tritium (Clark and Fritz, 1997). Due to the non linearity of eq. (2.56), the resulting *apparent water age* may differ from the true mixing age if the sampled water is a mixture of water parcels of various ages (Kipfer et al., 2002). A mixture may lead to a bias towards the age of the mixing component containing the higher amount of ^{3}H and becomes, in general, smaller for younger groundwater (Schlosser and Winckler, 2002).

It has to be kept in mind that the ^{3}H$-^3$He age reflects the time span since a water parcel was isolated from soil air (when ^{3}He started to accumulate). In contrast, the mere ^{3}H age for itself gives the time span since a water parcel reached the soil region as precipitation. The determination of $^3\mathrm{He}^{\mathrm{tri}}$ requires a quantification of further ^{3}He components in groundwater (meaning in particular the excess air component) since only the amount of total dissolved $^3\mathrm{He}^{\mathrm{tot}}$ is directly measured. A formal description of ^{3}H$-^3$He dating is given in chapter 3.3.3.

2.3.4 Stable isotopes of water

The two elementary constituents of a water molecule, oxygen and hydrogen, occur as different stable isotopes in nature. Table 2.4 gives an overview about their relative abundances, respectively. The by far most abundant water molecule consists of $^1\mathrm{H}_2{}^{16}\mathrm{O}$, followed by $^1\mathrm{H}^2\mathrm{H}^{16}\mathrm{O}$ and $^1\mathrm{H}_2{}^{18}\mathrm{O}$. As markers of water molecules, stable isotopes can be used as geochemical tracers for physicochemical processes within the hydrological cycle. The underlying processes are explained in the following, mainly based

Table 2.4: Stable isotopes and molar fractions of oxygen and hydrogen, adapted from Berglund and Wieser (2011).

element	isotope	mole fraction
O	^{16}O	0.99757
	^{17}O	0.00038
	^{18}O	0.00205
H	^{1}H	0.999885
	^{2}H	0.000115

on Mook (2000) and Clark and Fritz (1997). Any chemical compound containing heavy and light isotopes of a certain element species can be described by the ratio

$$R = \frac{\text{abundance of rare (heavy) isotope}}{\text{abundance of abundant (light) isotope}} \tag{2.57}$$

which is usually a quite small number. Since measurements of absolute abundances are usually more uncertain and since variations of isotopic compositions are of main interest, it is common to regard relative deviations. For different compounds A and B, the relative deviation of their respective ratios R can be defined as follows:

$$\delta_x = \left(\frac{R_A - R_B}{R_B}\right) \cdot 1000\,‰ = \left(\frac{R_A}{R_B} - 1\right) \cdot 1000\,‰ \tag{2.58}$$

It is common to determine the relative deviation from a certain reference value or rather from a standard value R_{std}, where positive values of δ indicate a higher abundance of the rare (heavy) isotope with respect to the standard and negative values a corresponding lower abundance.
In this study, the fractionation of stable isotopes of hydrogen and oxygen is investigated. Usually, the so-called *Vienna Standard Mean Ocean Water* (VSMOW)[10] is used as standard for the ratios of $^2H/^1H$ and $^{18}O/^{16}O$. All isotope fractionation values given in this study are reported relative to the VSMOW standard.

The δ value of a certain compound in nature cannot be seen as permanently constant since the behavior of heavier and lighter isotopes is slightly different during physicochemical processes such as phase transitions. This results in a partitioning or rather in an *isotope fractionation*, which is a consequence of the different masses of the atomic nuclei. A higher atomic mass goes along with a lower mobility, implying a lower diffusivity or rather a lower collision frequency. Additionally, heavier molecules exhibit higher binding energies as a result of their partition function[11] (Urey, 1947). The fractionation process between two compounds is formally described by a *fractionation factor*

$$\alpha_{B/A} = \frac{R_B}{R_A} \tag{2.59}$$

---

[10] The VSMOW standard is defined according to measurements on water samples from all oceans (IAEA, 1977), with a $^2H/^1H$ ratio of $(155.75 \pm 0.08) \cdot 10^{-6}$ (de Wit et al., 1980) and a $^{18}O/^{16}O$ ratio of $(2005.20 \pm 0.45) \cdot 10^{-6}$ (Baertschi, 1976).

[11] The partition function of a molecule is based on the three molecular movements (vibration, translation, rotation) and determines the difference in dissociation energy of certain molecules (Clark and Fritz, 1997).

or, in a more evident way, by the so-called *fractionation*

$$\epsilon_{\mathrm{B/A}} = (\alpha_{\mathrm{B/A}} - 1) \cdot 1000\,‰ \tag{2.60}$$

since natural fractionation effects are small and, thus, $\alpha \approx 1$. For $\epsilon_{\mathrm{B/A}} > 0$, the rare (heavy) isotope gets enriched within phase B, while it gets correspondingly depleted for $\epsilon_{\mathrm{B/A}} < 0$. Since these values are very small, it can be assumed that $\epsilon_{\mathrm{B/A}} \approx -\epsilon_{\mathrm{A/B}}$ (Mook, 2000). During any fractionation process, heavier isotopes tend to be enriched in the denser compound or in the compound with the larger molecular weight, respectively. To give an example, the heavy oxygen isotope ^{18}O tends to be enriched in the liquid water phase compared to the instantaneously formed water vapor during evaporation.

Two fundamental types of isotopic fractionation are generally distinguished: *equilibrium fractionation* and *kinetic fractionation*. The first one occurs at equilibrium conditions between two compounds and can be seen as a reversible process. A prominent example is the evaporation of water vapor within a closed system. In contrast, kinetic fractionation occurs as an irreversible or rather as an one-way process. A prominent example is the withdrawal of just evaporated water vapor, preventing an equilibration. A further example is diffusive transport. Usually, kinetic fractionation occurs additionally to equilibrium fractionation, which complicates an exact quantitative description. A detailed discussion of the underlying thermodynamical principles of isotope fractionation is given in Mook (2000).

The different compartments of the hydrological cycle exhibit typical isotopic compositions, resulting from above described fractionation processes. Ocean water has (by definition of the VSMOW standard) an isotopic composition between δ^{18}O ≈ -0.5 ‰ and $+0.5$ ‰. Even tough higher values of up to 2 ‰ are locally observed in tropical latitudes due to evaporation, the overall isotopic composition of ocean water can be seen as nearly unaffected due to the large size of this reservoir. At equilibrium conditions, evaporating water vapor is depleted by $\epsilon \approx 8 - 10$ ‰, depending on the ambient temperature[12]. Due to kinetic fractionation, a stronger depletion is typically observed in regions characterized by a low relative humidity of atmospheric air (Craig and Gordon, 1965).

The global distribution of δ^{18}O in precipitation shows strong variations, resulting from different climatic conditions on local scales. Due to the temperature dependence of the saturation water vapor pressure, air masses continuously rain out during their movement from equatorial regions towards polar regions. The equatorial origin of water vapor masses results from the local maximum of incident solar radiation (Peixóto and Oort, 1983). During every rain out process, lighter isotopes tend to remain within the gaseous phase, while the formed precipitation is enriched in heavy isotopes. During the progressive rain out, the remaining water vapor as well as the instantaneously formed precipitation become more and more depleted[13], respectively. It is important to note that this depletion is primarily a consequence of the temperature dependence of the saturation water vapor pressure rather than of the

---

[12] The fractionation ϵ between liquid water and instantaneously formed water vapor is decreasing for an increasing temperature. A summary of corresponding experimental works and empirical formulations is given in Clark and Fritz (1997).

[13] The progressive rain out and its effect on the isotopic composition of precipitation is described formally by the so-called *Rayleigh depletion process*. A detailed formal description is given in Mook (2000) and Clark and Fritz (1997).

temperature dependence of the fractionation $\epsilon_{\mathrm{w/v}}$ between liquid water and water vapor. Precipitation can thus be generally assumed to be more depleted in higher latitudes, which is also referred to as *latitudinal effect*. A likewise consequence of progressive (temperature induced) rain out is a stronger depletion of precipitation at higher altitudes (*altitude effect*), during winter time (*seasonal effect*) and in regions located more inland (*continental effect*), respectively. During heavy storms, δ^{18}O values are usually more negative compared to slight rainfalls, caused by less re-evaporation during heavy rainfalls (*amount effect*) as described in Dansgaard (1964).

Comparable effects as for δ^{18}O are also observable for δ^{2}H values in freshwater on the global scale. Craig (1961) and Dansgaard (1964) stated the relation

$$\delta^{2}\mathrm{H} \approx 8 \cdot \delta^{18}\mathrm{O} + 10\,‰ \tag{2.61}$$

which is denoted as *global meteoric water line* (GMWL). The stable isotope composition of precipitation is, thus, generally predictable on a global scale. Waters strongly depleted in ^{18}O and ^{2}H are associated with colder regions, while less depleted waters are found in warmer regions.

The slope of the GMWL (which is ≈ 8) results from the ratio of equilibrium fractionation factors of hydrogen and oxygen[14]. The intercept of the GMWL (which is ≈ 10 ‰) is denoted as *deuterium excess* and is usually non-zero as a consequence of kinetic fractionation during evaporation. It depends in particular on the relative air humidity in the region of evaporation, which was investigated in detail by Craig and Gordon (1965). A thin layer above the water surface can be assumed to be determined by equilibrium fractionation due to a relative humidity of 100 %, while diffusive transport towards the overlying free atmosphere (with a typical relative humidity of less than 100 %) goes along with a subsequent kinetic fractionation process. However, the deuterium excess also depends on further factors favoring kinetic fractionation such as wind speed and salinity (Clark and Fritz, 1997). Figure 2.14 gives a schematic illustration of the processes which determine the isotopic composition of water vapor originating from ocean water as well as of instantaneously formed precipitation, respectively. The GMWL is illustrated as red line, constraining the isotopic composition of water vapor and precipitation.

The GMWL should be treated as an average of many local meteoric water lines (LMWLs), characterized by individual values of both, the slope and the deuterium excess. A knowledge of the LMWL is essential for studies investigating isotopic compositions of local surface waters or of groundwater.

---

[14] The exact value of the slope of the GMWL may be affected by evaporation on rain drops after the condensation process, leading to a kinetic fractionation (Dansgaard, 1964).

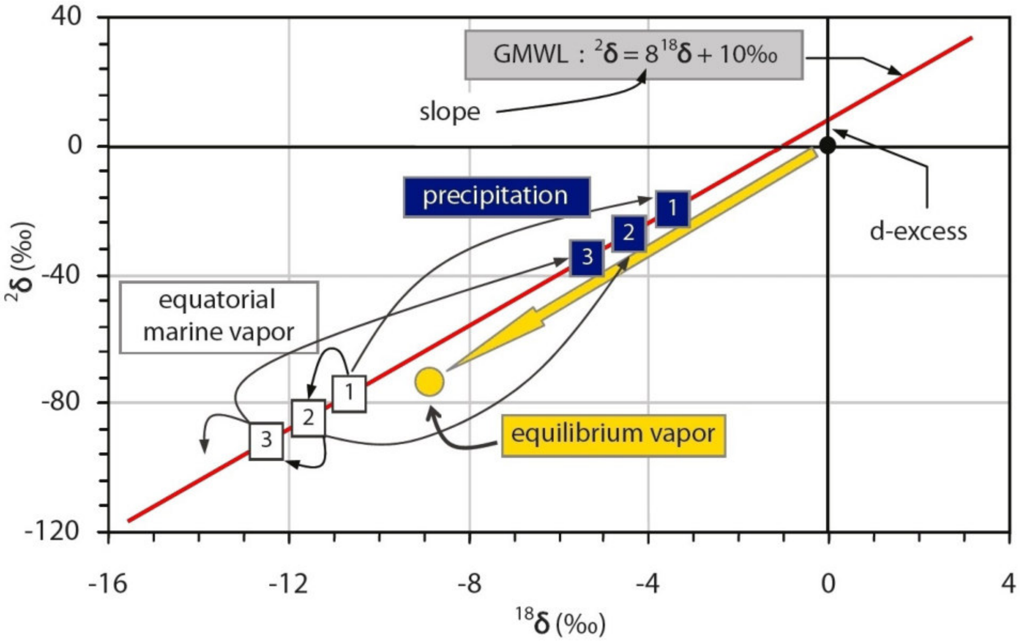

Figure 2.14: Schematic illustration of isotope fractionation during the formation of precipitation, adapted from Mook (2000). Due to kinetic fractionation (relative atmospheric humidity below 100 %), water vapor from ocean water ends up on the GMWL (white square labeled by number 1), thus differing from equilibrium vapor (yellow symbol). Precipitation is illustrated as blue squares, that one originating from the first formed water vapor is labeled by number 1. After the first rain out, the remaining water vapor is more depleted in heavier isotopes as depicted by number 2, resulting in the second formed precipitation and so on. All data are given relative to the VSMOW standard.

Chapter 3

Measurement techniques and data evaluation

This chapter starts with a presentation of the sampling procedures and of in-situ measurement techniques, followed by a description of the laboratory analysis of samples. Soil air and groundwater was analyzed in particular by means of two mass-spectrometric methods, for which the precision and the accuracy were investigated in the scope of this study based on a long-term series of analyzed reference samples. The evaluation of measured data is described in the third part of this chapter, comprising an explanation of applied models and of the underlying formal descriptions, respectively.

3.1 Mobile samplings and in-situ measurements

3.1.1 Soil gas composition

Soil air sampling was performed by a *Geotech BM2000* biogas monitor pumping with a flow rate of 500 ml/min. The gas was pumped from different soil depths through thin copper tubes of about 20 cm length and 0.4 mm inner diameter. After flushing it, a copper tube was closed airtight by a pneumatic plier, as shown in Fig. 3.1(a). Each sample has a length of about 6 cm and contains $0.8 - 1.0\,\mathrm{cm}^3$ of soil air at atmospheric pressure. The applied sampling procedure already proved to be reliable in past studies and allows to store closed samples for a long time, meaning even several years (Wieser, 2006; Schneider, 2009; Mayer, 2012; Freundt et al., 2013). The gas composition was analyzed in the laboratory by mass spectrometry as described in chapter 3.2.1 and 3.2.2.

Additionally, about $30 - 50$ ml of soil air was stored into a glass syringe at every sampled soil depth (see Fig. 3.1(b)). Glass syringes were applied for a direct analysis of the sampled soil air still on the same day, performed by a quadrupole mass spectrometer as described in chapter 3.2.1. The used glass syringes were tested before by Jenner (2014) to be tight for at least one week, if the piston is moistened.

Even though the *BM2000* device allows to detect O_2, CO_2 and CH_4, its measured data[1] were only

---

[1] According to manufacturer's data, O_2 is measured electrochemically with an uncertainty of ±1 vol%, CO_2 and CH_4 are measured independently from oxygen by infrared spectroscopy with an uncertainty of ±0.5 vol% (±1 vol% for absolute values higher than 5 vol%) for CO_2 and ±0.5 vol% (±1 vol% for absolute values higher than 5 vol%) for CH_4.

(a) Squeezing of a copper tube by a pneumatic plier. Picture taken during field campaign in Brazil.

(b) Sampling into glass syringes. Picture taken during sampling near Mannheim.

Figure 3.1: Sampling procedure for soil air and storage of the sampling gas in copper tubes and glass syringes, respectively.

used for a qualitative detection of CH_4 and to ensure a sufficient long flushing time during sampling. The obtained values were otherwise dropped since their reliability is questionable: Data given by the *BM2000* device show a strong temperature dependence, leading to a significant underestimation of oxygen concentrations for ambient temperatures above 20°C and to a corresponding overestimation below 5°C. The temperature dependence of data measured by the *BM2000* device was already described in detail by Mayer (2012).

To sample soil air from a certain depth, two different methods were applied. A silicone tube was perforated at its lower end and installed in the soil to allow for continuous long-term sampling. This procedure is described in the context of the presentation of the sampling sites in chapter 4.1. A second "mobile" sampling technique was applied, using hollow stainless steel tubes of 50 cm length, respectively, which are connected to each other. The geometry of the applied connection adapters is chosen in a way to prevent any contamination by soil air flowing along the outer side of the tubes. The lowermost tube has a sharp end and is perforated on a length of about 10 cm. The tubes were drilled into the soil by a rubber mallet and removed after sampling by a lever pulling device. Detailed information about this sampling system is given in Beck (2014). Leakage tests were carried out in the laboratory by means of flowing water as well as under vacuum conditions. Furthermore, the composition of soil air sampled by the mobile method showed no significant difference compared to soil air samples taken from a permanently installed silicone tube at the same depth. This mobile sampling method can thus be assumed to be suitable for soil air sampling. It allows for soil air sampling from depths of several meters.

3.1.2 Volumetric soil moisture

To determine the volumetric soil moisture content, the so-called *time domain reflectometry* (TDR) method was applied. A detailed description of the TDR method is given in Roth et al. (1990), Robinson et al. (2003) and Klenk and Jaumann (2015), which are also the main references of the following explanations.

The TDR method is based on the subsurface propagation of electromagnetic (EM) waves. A pulsed EM waveform is applied by a generator[2] on metal rods of a sampling probe which is installed in the soil. Since the soil water content determines the dielectric properties of a certain soil volume, it constrains the propagation velocity v_{prop} of an EM wave. Thus, the travel time of the EM wave along the probe rods can be interpreted in terms of a volumetric soil moisture content. Due to a change in the wave impedance, any EM wave is partially reflected at transitions between media of different permittivity. Such differences originate from subsurface geometric or material changes and result in a reflected signal of the previously emitted EM wave. Figure 3.2 shows a typical TDR trace with the two characteristic reflections which are recorded by the software *PCTDR* and subsequently used for a soil moisture determination.

The relative dielectric permittivity ϵ_c is determined by means of the travel time t_{prop} of an EM wave along the probe rods of a known length L and the speed of light c in vacuum:

$$v_{\text{prop}} = \frac{c}{\sqrt{\epsilon_c}} = \frac{2L}{t_{\text{prop}}} \Leftrightarrow \sqrt{\epsilon_c} = \frac{c \cdot t_{\text{prop}}}{2L} \tag{3.1}$$

The volumetric soil water content follows by the assumption that the relative permittivity can be seen as a composition of the relative permittivities of the soil matrix ($\epsilon_{\text{matrix}} \approx 4-5$), of water ($\epsilon_{\text{water}} \approx 80$) and of air ($\epsilon_{\text{air}} \approx 1$). Their relative contributions can be described by a simple mixing formula (Roth

---

[2] For this study, a *Campbell TDR100* generator was used to apply pulsed EM waveforms on sampling probes, with a frequency between 20 kHz and 1.5 GHz.

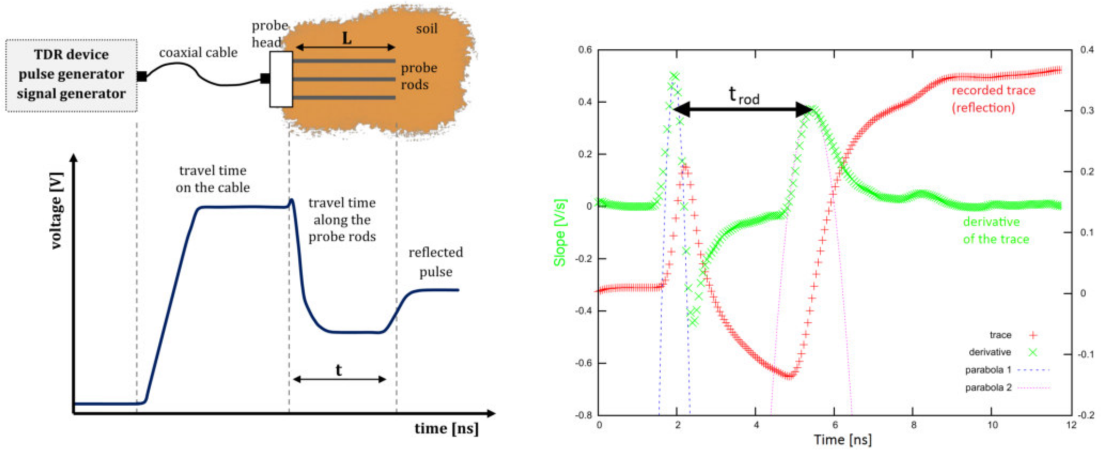

(a) Typical TDR trace showing the reflection of the EM wave at the top of the sampling probe as well as at its lower end. Adapted from Klenk and Jaumann (2015).

(b) Determination of the EM wave travel time along the sampling probe, based on the derivative of the recorded TDR trace (Mayer, 2012). The maximum values of the derivative were determined by two second order polynomial fits (see blue dashed curves).

Figure 3.2: Principle of the TDR method and exemplary data evaluation.

et al., 1990):

$$\sqrt{\epsilon_c} = \underbrace{\theta_w \cdot \sqrt{\epsilon_{water}}}_{\substack{\text{soil water}\\ \text{contribution}}} + \underbrace{(\phi - \theta_w) \cdot \sqrt{\epsilon_{air}}}_{\substack{\text{soil air}\\ \text{contribution}}} + \underbrace{(1 - \phi)\ \sqrt{\epsilon_{matrix}}}_{\substack{\text{soil matrix}\\ \text{contribution}}} \tag{3.2}$$

To calibrate a sampling probe, measurements are performed in deionized water as well as in air – providing a two-point calibration with (rather unrealistic) extreme values of the relative permittivity of a certain soil sample. For this study, sampling probes with rod lengths of about 20 cm were used. The resulting soil moisture contents thus reflect an average value across the entire rod length.
The TDR method proved to be a very accurate method for soil moisture analysis (Roth et al., 1990), typically achieving absolute precisions in the range of a few vol%. However, the TDR method is quite sensitive for systematical errors. In particular, any air gaps around the inserted metal rods have to be avoided. Furthermore, high soil conductivities may reduce the signal of the second reflection peak, leading to a higher uncertainty of the obtained travel time (Mayer, 2012). Reliable results require a good knowledge about the relative permittivity of air, water and the soil matrix, respectively. The relative permittivity of water depends on the ambient temperature and on the ion concentration, which can be estimated with a sufficient accuracy[3]. However, the relative permittivity of the solid matrix is rather difficult to estimate, since it depends on the soil material (Daniels, 2004). For this study, a value of $\epsilon_{matrix} = 5$ was chosen, which can be seen as typical for most natural soils, while being constant in the TDR frequency range (Klenk and Jaumann, 2015). A further required parameter is the porosity ϕ which was measured at the long-term sampling site of this study as described in chapter 3.1.4. Further sampling sites were evaluated in this study by assuming a value of $\phi = 0.38$, which is a good approximation for natural soils if no further information is available (Klenk and Jaumann, 2015). Figure 3.3 shows the procedure of TDR measurements.

Additionally to TDR samplings, the volumetric soil moisture was recorded continuously every 15 min by a *Driesen+Kern DK650* data logger with *ECH2O* soil moisture probes. Data are measured according to the *frequency domain reflectometry* (FDR) principle. As it is the approach of the TDR method, the volumetric water content is determined based on relative permittivity measurements. In this case the relative permittivity is deduced from the impedance instead of the travel time of an EM wave. An advantage of FDR measurements is their fast response time, going along with the possibility of higher time resolutions and an independence of soil conductivity. However, a soil specific calibration is needed to obtain a comparable precision as achieved by TDR measurements (Muñoz-Carpena et al., 2004). For this purpose, some 100 cm^3 of the topmost soil layer at the sampling site were taken into the laboratory for a subsequent calibration, resulting in an absolute measurement precision of 1 vol% for all calibrated sensors. The calibration procedure is described in appendix A.2.

---

[3] The relative permittivity consists of a real part and an imaginary part: $\epsilon(\nu, T) = \epsilon'(\nu, T) - i \cdot \epsilon''(\nu, T)$. For water, the imaginary part can be neglected for frequencies higher than 1 GHz (Gerhards, 2008). The relative permittivity of water can be determined according to a polynomial given by Kaatze (1989): $\log_{10}\epsilon_{water}(T) = 1.94404 - 1.991 \cdot 10^{-3}\,\mathrm{K}^{-1} \cdot (T\,[\mathrm{K}] - 273.15\,\mathrm{K})$.

(a) Installation of sampling probes at the sampling site near Mannheim: FDR (left) and TDR (right).

(b) Record of a TDR trace at the sampling site by means of a laptop and a high frequency generator.

Figure 3.3: In-situ measurement of volumetric soil moisture.

3.1.3 Radon

Measurements of the two radon isotopes ^{222}Rn and ^{220}Rn were performed by a *DURRIDGE RAD7* device. It pumps gas with a flow rate of 500 ml/min and detects the radon decay products ^{218}Po (half-life 3.05 min) and ^{216}Po (half-life 0.15 s) (Radiochemical Institute Karlsruhe, 1996). According to manufacturer's data, an equilibrium between the parent isotope ^{222}Rn and its daughter isotope ^{218}Po is reached after about 20 min, while this is already the case after a few seconds for ^{220}Rn and ^{216}Po. For this reason, soil air from a certain depth was sampled during three consecutive cycles of 10 min, respectively – allowing for a reliable detection of both radon isotopes. After flushing the device by atmospheric air, soil air was sampled in-situ for in total 30 min. The corresponding measurement uncertainties are based on statistical 2σ errors of the counting records.

The efficiency of α particle detection by the *RAD7* device is reduced for an increasing humidity of the sampled gas, which is problematic for soil air exhibiting a relative humidity of about 100 %. Thus, soil air was transferred through a drying pillar, trapping water vapor and leading to a relative humidity below 10 % which should, according to manufacturer's data, not affect the resulting data anymore.

A nearly constant activity of the short-lived isotope ^{220}Rn is expected during every of the three recorded 10 min cycles, thus suggesting that the soil air was continuously pumped from the same depth. The sampling of ^{220}Rn allows to detect any contamination on short time scales, arising after pumping durations of only a few minutes. In contrast, the relevant activity of the long-lived isotope ^{222}Rn is obtained from the third and last measurement cycle of each sampling procedure. For every sampled soil depth, the temporal trend of ^{222}Rn data was analyzed across the entire study, first, to investigate the seasonality of soil aeration and, second, to identify any contamination or leakage on long-term scale.

3.1.4 Soil material analysis

A knowledge of soil parameters is essential for any reliable interpretation of subsurface dynamics of gas and water. This is why a study was carried out by Engelhardt (2015) within a distance of about 50 m from the long-term measurement site of this study (see chapter 4.1). A set of soil material samples was taken from the topmost 1.6 m of the soil and subsequently analyzed in the laboratory for Geomorphology and Geoecology at Heidelberg University.

Samples were taken at different soil depths to obtain a vertical profile of the analyzed parameters. Sampling depths were chosen according to the vertical soil material profile, ranging from a loamy topmost layer to more sandy and gravelly layers below. The exact sampling procedure depends on the parameters of interest: So-called *undisturbed samples* were taken for an analysis of the pore size distribution, of the porosity and of the hydraulic conductivity. For this purpose, soil samplers of a well-defined volume (about 250 cm^3) were used. In contrast, it was sufficient to take some cm^3 of so-called *disturbed samples* for an analysis of the organic carbon content, of the grain size distribution and of the soil material density. A detailed description of the sampling procedure and the laboratory analysis is given in Engelhardt (2015). The obtained parameter values, meaning in particular the porosity values, were used for the data evaluation in this study.

3.1.5 Soil temperature

At the long-term sampling site, the soil temperature was measured continuously every two hours by *CiK LogTag®* *TREX-8 / TRIX-8* loggers with an uncertainty of ±0.5°C. The temperature sensors were installed into different soil depths and subsequently connected with a data logger at their topmost ends. At other sampling sites, the soil temperature was measured only within the topmost 10 cm of soil by means of a *Greisinger GMH3710* thermometer exhibiting an uncertainty of ±0.03°C.

3.1.6 Groundwater sampling

In this study, groundwater was generally sampled by submersible pumps. Suction pumps were not applied to avoid any degassing of the water during sampling. Usually, a mobile pump operating at 12 V voltage was used, generating a flow rate of about 5 l/min for pumping depths of up to 10 m. At some wells sampled in Santarém (Brazil), a submersible pump was already installed, providing flow rates of several 10 l/min. Before the actual sampling procedure started, the contained water volume within a well was exchanged three times – to ensure that no water is sampled which was previously in contact with atmospheric air.

The applied sampling procedure is described in Beyerle et al. (2000) and Aeschbach-Hertig and Solomon (2013): Groundwater is conducted through copper tubes of 8 mm inner diameter, which are flushed and slightly drummed to avoid an inclusion of air bubbles. The copper tubes are sealed airtight by closing stainless steel clamps at both ends of an aluminum rack, to prevent any contamination by atmospheric air after sampling. To suppress degassing, the system is permanently kept at pressure by closing first the upper end of the sample. The obtained water samples were subsequently used for a NG analysis in the laboratory, as described in chapter 3.2.2. Furthermore, two bottles were filled with 50 ml of groundwater, respectively, for a laboratory analysis of tritium (see chapter 2.3.3) and of stable isotopes of water (see chapter 3.2.4).

During each sampling procedure, physical as well as chemical parameters were recorded. For this

purpose, a *WTW Multi 340i* device was used, measuring the dissolved oxygen content in units of mg/l or as percentage saturation anomaly (relative uncertainty ±0.5 %), the pH value (uncertainty ±0.01), the conductivity κ_{25} in units of µS/cm (relative uncertainty ±0.5 %), the oxidation-reduction potential (ORP) in units of mV (uncertainty ±1 mV) and the water temperature (uncertainty ±0.1°C). The temperature was additionally recorded by a *Greisinger GMH3710* thermometer exhibiting an uncertainty of ±0.1°C.
In-situ measurements of physical and chemical parameters were performed inside a bucket through which water was continuously flowing. For all mentioned parameters, their respective uncertainties were estimated during the measurement procedure, based on the observed fluctuations of the displayed data, while the uncertainty given by the manufacturer was taken as a minimum value. All above described equipment for groundwater sampling is depicted in Fig. 3.4.

For long-term observations of this study near Mannheim (Germany), three data loggers were permanently installed in one of the wells. The *STS® DL/N 70* sensor records the water temperature (uncertainty ±0.25°C), the conductivity κ_{25} (relative uncertainty ±2 %) and the groundwater table level (measured as water pressure with an uncertainty of ±2 mbar, corresponding to about ±2 cm), in time intervals of 10 min. An *AquiStar® TempHion™ Smart Sensor* was used to record the water temperature (uncertainty ±0.2°C), the pH value (uncertainty ±0.2) and the ORP value (uncertainty ±0.1 mV) in time intervals of 10 min, respectively. A *Driesen+Kern O2-Log3050-INT* sensor was used to measure the water temperature (uncertainty ±0.2°C) and the dissolved oxygen content (relative uncertainty ±2 %), also in time intervals of 10 min, respectively.

Figure 3.4: Groundwater sampling during the field campaign in Brazil. From right to left: copper tubes on aluminum racks for NG analysis; *Greisinger GMH3710* thermometer (yellow device); *WTW Multi 340i* (blue device) with sensors for pH value, ORP value and dissolved oxygen content; the conductivity sensor is inserted into the bucket. Bottles for tritium and stable isotope analysis are situated above the sensors.

The usage of different sensors for an analysis of the same physical parameters allows for a comparison to check the reliability of the obtained values. Even if continuous data logging had the advantage to provide information about short-term fluctuations, it is more sensitive to a bias of the internal calibration or to defects of the power supply. Such circumstances occurred during this study and resulted in a loss of data during certain periods. The calibration procedure is of particular importance for the values of pH, ORP and dissolved oxygen content. Since all sensors can only be calibrated outside of the well, a trade-off is necessary between a frequent calibration and interventions into the sampled system, the latter possibly affecting the temporal comparability of data. Thus it was decided to re-calibrate the continuously recording sensors every 3 – 4 months, while the *WTW Multi 340i* sensors were calibrated before each sampling procedure. Time dependent trends and offsets of the sensitivity of continuously logging sensors were, however, observed for some periods, resulting from different temperatures during calibration (at atmospheric temperature) and measurement (at groundwater temperature). Altogether, data of the logging sensors allow for an analysis of short-term fluctuations, even though data measured by the *WTW Multi 340i* are expected to be more reliable with regard to absolute values.

The groundwater temperature (GWT) shall be considered in more detail, since it is of major relevance in this study as a reference value for estimated recharge temperatures. Temperature data from above-ground (*WTW Multi 340i* and *Greisinger GMH3710*) as well as from below-ground sensors (data loggers) agree well among themselves, respectively. However, at the long-term sampling site of this study, above-ground measured data are systematically higher, on average by (0.5 ± 0.2)°C. Such an offset may result from heat released by the submersible pump which is cooled by the passing water. Such a potential effect is also indicated by the GWT time series of data loggers, showing temporary temperature shifts by 0.1 – 0.5°C during each sampling procedure. A heat turnover of about 67 W was measured, which corresponds – after subtracting the required power for pumping up the water – to an efficiency of 8 % which is probably thus small due to the pumping height of several meters, going along with a considerable friction along the walls of the used silicone tube. For a pumping rate of 4.4 l/min, a temperature enhancement of 0.2°C can be calculated for the pumped water[4]. This rough estimation confirms the assumption that above-ground water temperature measurements may be biased due to pumping heat. If below-ground recorded data were available, these water temperatures were considered, even though corresponding data loggers exhibit a mean uncertainty of ±0.2°C which is twice as much as that achieved by the *WTW Multi 340i* device. An extensive data set allowing to handle such a bias of water temperatures was unfortunately only available at the long-term sampling site of this study, while remaining GWTs were recorded above-ground by the *WTW Multi 340i* and the *Greisinger GMH3710* devices. Thus, a corresponding bias of measured GWTs has to be taken into account during the discussion of obtained GWT data.

---

[4] According to the definition of the specific heat capacity c, the temperature increase is determined as $\Delta T = \Delta Q / (\rho \cdot V \cdot c)$. The volume V results from the assumed pump rate and ρ denotes the density of water. The specific heat capacity of water is $c_\mathrm{w} = 4.182\,\mathrm{kJ/kg\,K}$ at 20°C (Meschede, 2015). Regarding the uncertainties of all parameters used for this calculation, c_w can be assumed as constant in naturally occurring temperature regimes. The amount of heat ΔQ follows from the assumed power input by the pump into the water.

3.2 Laboratory analysis

3.2.1 Analysis of gas sample composition by Omnistar

The analysis of soil air composition was performed using a *Pfeiffer Vacuum Omnistar™ GSD320* device. This gas analysis system allows to separate and to detect isotopes with atomic masses between 1 and 100 amu by means of a quadrupole mass spectrometer. Figure 3.5 shows the set-up of the system. The sample gas is inserted through a capillary of about 1 m length towards a heated electromagnetic inlet valve. The usage of a capillary and an adjacent orifice is necessary to reduce the sample pressure below 10^{-4} mbar. The inner diameter of the capillary has thus to be chosen according to specific sample conditions as described later. With appropriate capillaries, it is possible to analyze sample gases in the range between atmospheric pressure and about $5 \cdot 10^{-3}$ mbar (Pfeiffer Vacuum, 2010). The capillary and the inlet valve are heated up to 150°C, to prevent a condensation of water within the system. The heating is of importance for the analysis of soil air which typically exhibits a relative humidity of almost 100 %.

After passing the inlet valve, the sample gas reaches the analysis chamber which is evacuated by a turbo molecular pump to an ambient pressure in the lower 10^{-7} mbar range. A diaphragm pump is used as backing pump and for a first pump-down during the start up of the device. The actual gas analysis is performed by means of a *PrismaPlus™ QMG220* quadrupole mass spectrometer consisting of a tungsten cathode as ion source, a mass filter and two detectors.

Uncharged particles entering the analysis chamber are ionized by accelerated electrons emitted by the ion source. The separation of charged ions according to their mass/charge (m/q) ratio is done by means of a high-frequency electric quadrupole field which is generated between four stick electrodes separated by a field radius r_0 (see Fig. 3.6). The voltage between these electrodes consists of a high-frequency voltage $V \cdot \cos(\omega t)$ and a direct voltage U. Ions are inserted parallel to the field axis and are moving, as a consequence of the high-frequency field, on oscillatory trajectories vertically to the field axis. The specific value setup of U, V, ω and r_0 determines the ratio m/q of those ions which move

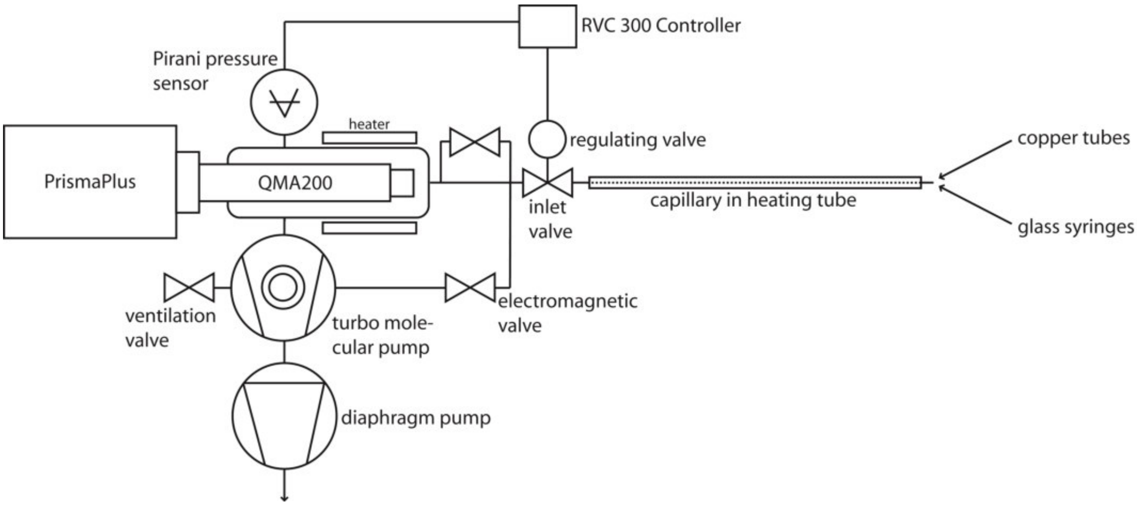

Figure 3.5: Setup of the *Omnistar* device, based on Pfeiffer Vacuum (2010).

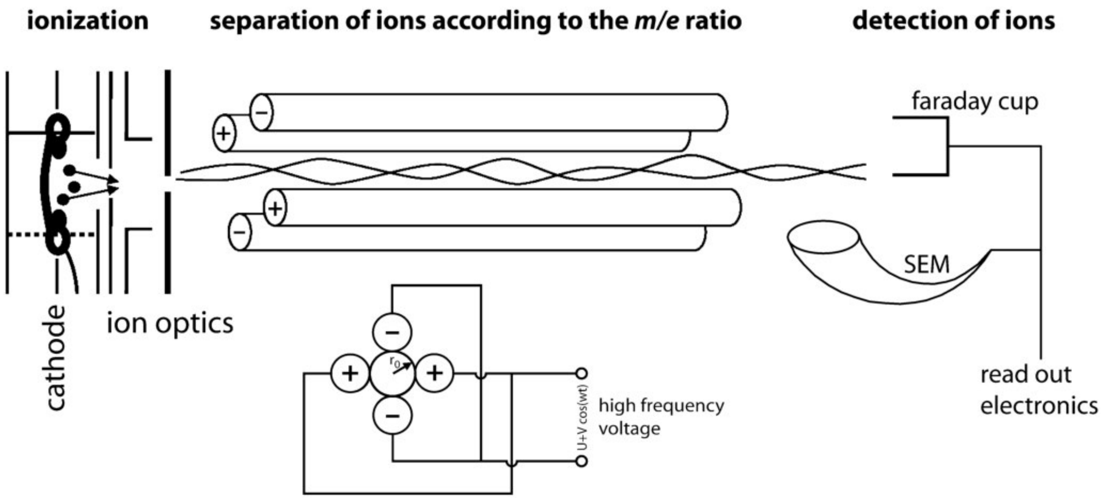

Figure 3.6: Operating principle of ion separation by quadrupole mass spectrometry. The stick electrodes used in the *Omnistar* device consist of stainless steel and have a length of 10 cm and a diameter of 6 mm. Adapted from Pfeiffer Vacuum (2010).

on a finite amplitude track, thus passing the separating field. Ions of another m/q ratio cannot pass the system as a consequence of exponentially increasing movement amplitudes[5]. The measurement setup allows to detect signals over a certain range of masses by varying the voltage $V \propto m/q$.

Two detectors are used for the charged ion detection: a *Faraday Cup* detector and a *Secondary Electron Multiplier* (SEM), which mainly differ in their sensitivity and detection rate. An explanation of these types of detectors is given in chapter 3.2.2 in the context of the sector field mass spectrometer *MM5400*. A detailed explanation of the hardware setup of the *Omnistar* device as well as of its adjustments is given in Horstmann (2016).

Sample preparation and gas inlet

For this study, two different capillaries were used to insert gas samples, depending on the amount of sampled gas or rather on the pressure within the gas reservoir. A capillary of 0.13 mm inner diameter was used for samples at atmospheric pressure, which were stored in glass syringes in the field. The advantage of glass syringes is that the piston allows to keep the pressure within a syringe at atmospheric level even during suction by the *Omnistar* device.

If sampling by glass syringes was not possible, e.g. due to long unavoidable storage times, copper tubes were used as reservoirs for soil air samples. In the laboratory, the copper tube was installed inside an inlet volume measuring approximately 30 cm^3. After the inlet volume was evacuated, the copper tube was opened by squeezing it with a cracker valve, resulting in an ambient pressure of about 20 – 30 mbar inside the inlet volume. A capillary of 0.5 mm inner diameter was used to transfer the sample gas into the analysis chamber of the *Omnistar* device. Due to the gas suction, the pressure within the inlet volume decreased by about 20 – 30 % during an analysis time of 3 – 4 min, resulting in a time-dependent trend of the recorded detector signals. To compensate this trend, the corresponding

---

[5] For the given quadrupole potential, the equation of movement of a specific ion results in the so-called *Mathieu's differential equations* which have two types of solutions, depending on the ion charge q and its mass m: a stable movement with finite amplitude and an unstable movement with an exponentially increasing amplitude (Demtröder, 2008).

signal at the moment of the gas injection was extrapolated as the intercept of a quadratic fit. The fitting procedure is demonstrated in appendix A.3. Since the available amount of the sample gas within a copper tube is less than inside a glass syringe, the signal to background ratio is lower by a factor of two for samples from copper tubes. This is why the measurement duration was extended to 3 – 4 min, while a further enhancement did not improve the fit uncertainty.

Measurement procedure

The measurement practice presented so far does not directly account for the amount of analyzed sample gas, due to varying sample gas amounts and measurement times. Such a procedure is suitable for a determination of isotope ratios, but it does not allow for any direct conclusion about the partial pressure of a certain gas species. To obtain absolute values and concentration data, respectively, detector signals have to be compared to signals from calibration measurements of a well-known reference gas. The *Omnistar* setup allows for two fundamentally different analysis methods: On the one hand, *absolute* amounts can be determined by directly comparing the obtained detector signals of a certain gas species in the sample gas and in the reference gas, respectively. This procedure requires identical total pressures within the reservoirs containing sample gas and reference gas. The most simple way to realize this is the usage of glass syringes at atmospheric pressure.

On the other hand, detector signals can be interpreted in a *relative* way, meaning that obtained detector signals are related to the sum of signals of all gas species. Measured mixing ratios of all gas species are, thus, summed up to 100 vol%. This approach is based on the possibility to simultaneously analyze all relevant gas species contained in a sample gas. Since the detector sensitivity cannot be assumed to be equal for all gas species, the relative measurement procedure also requires the usage of a well-known reference gas.

In this study the relative analysis method was applied, avoiding the difficulty to ensure sufficiently equal inlet pressures. The relative analysis method is of advantage in particular for samples from copper tubes, for which the analyzed gas amount is very difficult to regulate. However, this is also a critical aspect for samples from glass syringes, since the atmospheric pressure has to be stable during the entire measurement run, lasting typically several hours. Besides this restriction, a relative gas analysis goes along with the remarkable advantage not to require any knowledge about the exact amount of water vapor within the sampled gas. Water vapor is simply omitted during the analysis, resulting in mixing ratios directly comparable to literature values of dry atmospheric air. In case of an absolute gas analysis, a determination of the amount of water vapor would require a sophisticated approach and a detailed knowledge about sampling conditions (see the discussion in chapter 3.2.2 about the water vapor correction for measurements at the *MM5400* mass spectrometer). However, a relative analysis procedure goes along with some disadvantages which have to be kept in mind during data interpretation: First, it is necessary to include all most abundant gases like N_2, O_2 and ^{40}Ar in the measurement routine, since the contributions of all analyzed gases are summed up to 100 vol%. Depending on the gas species, a simultaneous analysis of different gas species may go along with mass interferences. For this study, the just mentioned three gas species are of main interest anyway, while their most relevant mass peaks do not interfere. Second, biased signals of one single gas species may affect signals obtained for another gas species. During this study, such outcomes were rarely identified and corresponding results were omitted. And third, even the relative analysis method requires preferably similar inlet pressures of all (reference) gas samples, since the calibrated detector sensitivity may otherwise vary. However, initial inlet pressures during all runs of this study did not differ relatively by more than 0.5 %, for which an impact of varying detector sensitivities turned out to be negligible.

Applied reference gases

To calibrate the detector signals, a set of in total three different calibration standards is available. One of them was chosen to have a similar composition as it is typically observed in soil air, to avoid a data bias by the expected non-linearity of the detector signals. Compared to atmospheric air, this means an increased mixing ratio[6] of CO_2 and a decreased mixing ratio of O_2. This reference gas was mainly applied in this study and is denoted in the following as “Air Liquide standard”. Only the most abundant gas species detectable by the Faraday detector were included into the Air Liquide standard mixture, first, to simplify the gas mixing procedure and, second, to avoid mass interferences like that of doubly ionized ^{40}Ar and ^{20}Ne.

Two additionally available reference gases shall be mentioned in this context, even though they were rarely used in this study, but rather by Horstmann (2016) and Jenner (2016). One of them is just atmospheric air (denoted as “ATM standard”) which has well-known contents of the most gas species. It is quite uncomplicated to use atmospheric air for calibration, notably during in-situ measurements in the field. A disadvantage of a calibration with atmospheric air comes from its composition, providing the potential of mass interferences. Furthermore, the exact CO_2 content of atmospheric air is usually unknown, in particular in urban areas. This is why a further reference gas was introduced, denoted as “GC standard”[7] which has a well-known and nearly atmospheric content of CO_2.

Table 3.1 gives an overview of the compositions of the three available calibration gases. Together, these three reference gases provide a calibration set which allows for an analysis of typical soil gas compositions, but also of nearly atmospheric gases. For most samples analyzed in this study, the Air Liquide standard was used for calibration. Atmospheric air samples were used to check the reliability of the resulting data as described below. Mixing ratios of helium, neon and krypton in soil air were not analyzed by the *Omnistar* system, since these gas species were measured independently with a higher precision by the *MM5400* mass spectrometer as described in chapter 3.2.2.

Data evaluation

The manufacturer’s evaluation software *Quadera®* was used for operating the *Omnistar* device and to record detector signal data. It allows for a background signal subtraction as well as for a gas

---

[6] The mixing ratio of ^{40}Ar in the Air Liquide standard was determined by a series of 9 measurements at the *MM5400* mass spectrometer. The remaining gas compounds were specified by the manufacturer (Air Liquide).

[7] The reference gas “GC standard” is usually applied at the Institute of Environmental Physics for calibration of gas chromatographic measurements of SF_6 and CFCs. Its composition was determined by a repeated set of measurements as follows: CO_2 by a gas-chromatographic system (Carbon Cycle Group Heidelberg, 2014), noble gas contents at the *MM5400* mass spectrometer and N_2/O_2 by *Omnistar* device itself (calibrated with the Air Liquide standard). Apart from CO_2, gas contents of the GC standard differ slightly from that of atmospheric air.

Table 3.1: Composition of reference gases available for the calibration of measured signals by the *Omnistar* system. Atmospheric air composition is taken from Roedel and Wagner (2010) and Tans and Keeling (2015).

	Air Liquide standard	**GC standard**	**ATM standard**
N_2	(78.051 ± 0.183) vol%	(78.25 ± 0.23) vol%	78.084 vol%
O_2	(17.970 ± 0.180) vol%	(20.88 ± 0.23) vol%	20.946 vol%
CO_2	(3.013 ± 0.030) vol%	(420.1 ± 0.1) ppm	≈ 400 ppm
^{40}Ar	(0.966 ± 0.009) vol%	(0.877 ± 0.009) vol%	0.934 vol%
^{4}He	-	(4.92 ± 0.04) ppm	5.24 ppm
^{20}Ne	-	(15.45 ± 0.11) ppm	16.45 ppm
^{84}Kr	-	(0.712 ± 0.006) ppm	0.65 ppm

specific calibration to convert the measured detector signals into mixing ratios. For this purpose, a calibration matrix is created, assigning a sensitivity factor to every evaluated mass contribution of a specific gas. The reliability of resulting data is enhanced by considering not just the main mass of a gas species (e.g. 28 amu for N_2), but also less contributing mass peaks (e.g. 14 amu for N_2), induced by the ionization process. A calibration of pure detector signals would also be possible independently of the *Quadera* software, preventing the character of a “black box” type evaluation. However, the software-internal way simplifies the measurement routine and allows for a fast identification of arising technical problems, for example due to a contamination with atmospheric air.

Several tens of samples were analyzed in a common measurement run, alternating with the reference gas. Evaluated data from reference gas measurements showed slight but significant systematic biases during most of the measurement runs, probably due to the one-point calibration and because only one single calibration procedure was performed to determine the calibration matrix. This is why it was decided to re-calibrate all resulting data obtained from the *Quadera* software by means of the series of continuously performed reference gas measurements during the run. By this way, the occurrence of the just mentioned bias was avoided.

The evaluation procedure is illustrated in Fig. 3.7. A gas specific calibration factor results from the average deviation of measured reference gas composition from its known composition. The calibration factor is used to correct the results of all analyzed gas samples. The uncertainty of a calibration factor was determined by Gaussian error propagation based on the uncertainty of both, the known reference gas composition (see Tab. 3.1) as well as of the actually measured reference gas composition (determined as standard deviation of all reference gas measurements). Short-term fluctuations of the detector signals as well as errors of the fit functions were not considered separately, assuming that their influence is already represented by the standard deviation of reference gas measurements. A discussion of short-term fluctuations is given later in this chapter.

Accuracy and reproducibility of obtained data

Figure 3.8 illustrates the time series of reference gas measurements from the Air Liquide standard, recorded during a time span of more than one year. Gas specific data are depicted as deviation from the expected reference gas value, respectively. Since just these reference gas measurements were used for a calibration of their own detector signals, it is clear that the depicted data fluctuate around a value

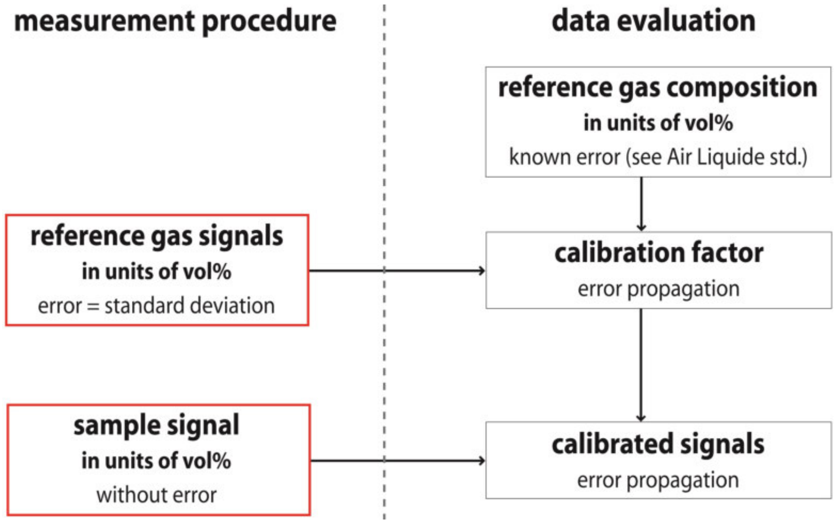

Figure 3.7: Illustration of the evaluation procedure of measurements with the *Omnistar* quadrupole spectrometer. A gas specific calibration factor is determined by means of continuous reference gas measurements, whose uncertainty is calculated by means of Gaussian error propagation. The uncertainty of the average reference gas signals is determined as standard deviation of the corresponding signals. The uncertainty of a single sample signal is neglected.

of 1.0. Reference gas samples, thus, do not allow for any conclusions about the accuracy of the whole evaluation procedure. However, the analysis of atmospheric air samples from copper tubes (see blue crosses in Fig. 3.8) indicates that the applied evaluation method results in reliable outcomes. Atmospheric samples from copper tubes give unfortunately no evidence about the accuracy of CO_2 data since, first, the exact mixing ratio of CO_2 in urban atmospheric air is not constant in time (Vardag et al., 2015) and, second, a systematic bias is expected due to the large difference between the respective CO_2 mixing ratios of the Air Liquide standard (3.013 vol%) and of atmospheric air (about 400 ppm). The time series of measured reference gas data provide the possibility to determine the reproducibility of *Omnistar* measurements. The gas specific standard deviations of reference gas measurements were determined for all runs depicted in Fig. 3.8. Their average values are summarized in Tab. 3.2. Regarding the detection limit given by the manufacturer ($<$ 20 ppm for the Faraday detector and $<$ 1 ppm for the SEM detector), the obtained standard deviations are of the same order of magnitude. The uncertainty of the Air Liquide standard composition is, however, about one order of magnitude higher than all gas specific reproducibilities. The overall uncertainty of samples analyzed by the *Omnistar* system is thus mainly constrained by the uncertainty of the Air Liquide standard composition. This is easily seen by comparing the fluctuation range of reference gas data (black symbols) and the uncertainties of atmospheric samples (blue symbols) in Fig. 3.8.

For analyzing short-term variations of the detector sensitivity during a single measurement run, some test measurements were carried out by Jenner (2016). Short-term fluctuations of detected signals are mainly caused by ambient air pressure variations, determining the inlet pressure of the measured gas. Since all measurement runs of this study were carried out within some hours and under nearly constant pressure conditions, respectively, it is not necessary to account for possible short-term sensitivity fluctuations. Furthermore, even if the ambient air pressure varies by some millibar during a single measurement run, the obtained reproducibility is slightly worse, but still negligible regarding

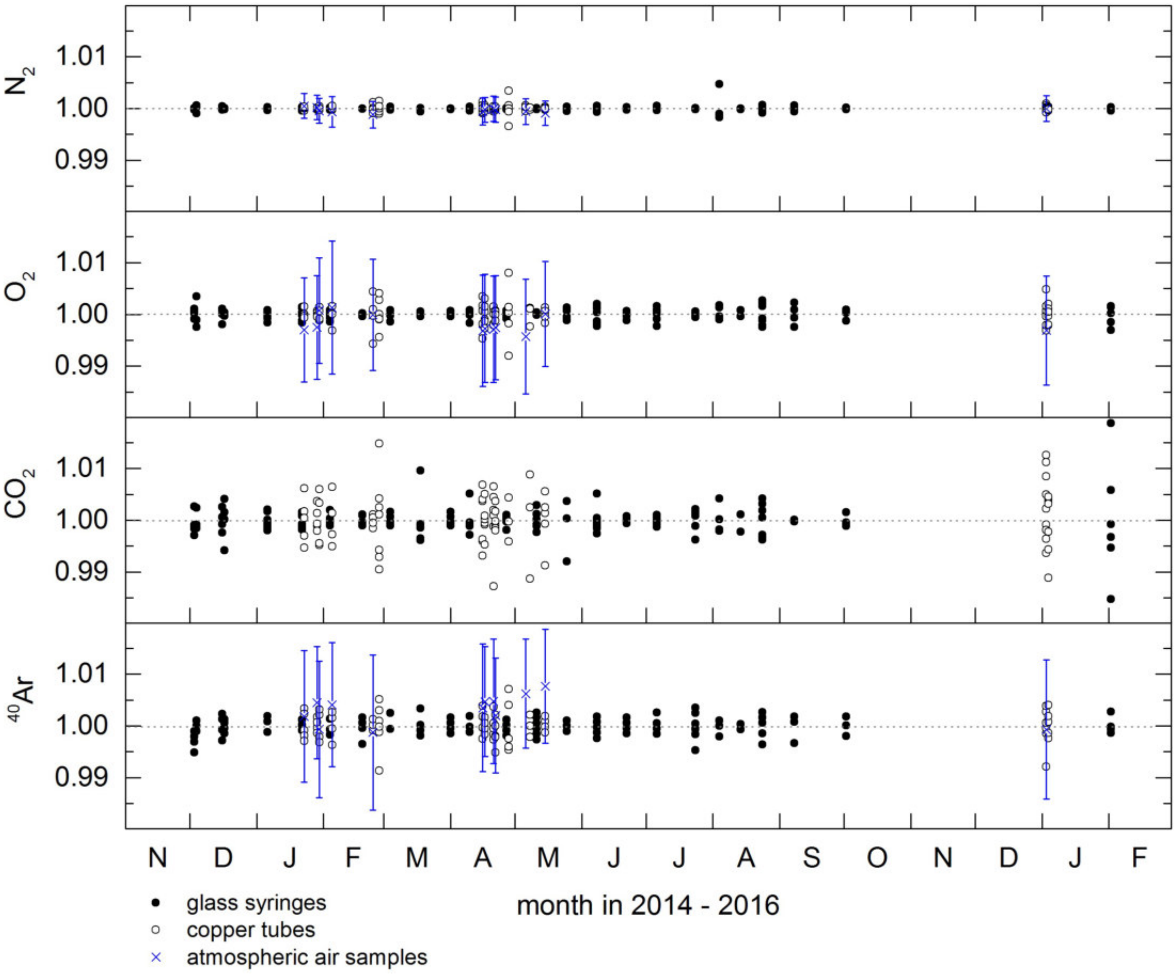

Figure 3.8: Reproducibility of *Omnistar* measurements: Time series of N_2, O_2, CO_2 and ^{40}Ar from measurements of the Air Liquide standard between November 2014 and February 2016. Every vertically arranged group of symbols represents one single measurement run – usually performed every two weeks directly after sampling in the field. Measurements from glass syringes are depicted as filled symbols, measurements from copper tubes as open symbols. All values are normalized to their expected values, respectively. Atmospheric air measurements from copper tubes are shown as blue crosses. Obtained data from copper tube analysis typically fluctuate stronger, due to the lower ratio of signal to background.

the uncertainty of the Air Liquide standard composition. Thus, so-called fast calibration measurements were not carried out for all *Omnistar* analysis of this study. Of course, such a simplification of the measurement procedure is just appropriate for measurements under laboratory conditions, meaning in particular at a rather constant temperature.

A comparison with precisions given for similar gas analysis systems suggests a satisfying precision of the applied evaluation principle for *Omnistar* data. Lippmann et al. (2005) used an identical device and give an absolute analytical precision of 1 vol% for N_2 and a relative precision of 5 % for ^{40}Ar and CO_2, respectively. For a similar but self-made system, Mächler et al. (2012) achieved a reproducibility of 1 % for N_2, O_2 and ^{40}Ar, respectively. Obtained reproducibilities during this study are similar or even better, which may result from the fact that the corresponding data in the literature originate from water sample extractions favoring the occurrence of further systematical uncertainties.

Table 3.2: Average of standard deviations of *Omnistar* measurements from about 20 measurement runs, normalized to the corresponding calibration standard concentrations, respectively.

	N_2	O_2	CO_2	^{40}Ar
glass syringes	0.03 %	0.11 %	0.25 %	0.15 %
copper tubes	0.04 %	0.19 %	0.54 %	0.24 %
uncertainty of Air Liquide std.	0.2 %	1.0 %	1.0 %	0.9 %

Regarding the reproducibility of NG measurements at the *MM5400* mass spectrometer (see chapter 3.2.2), the just presented reproducibilities for *Omnistar* measurements are of a similar order of magnitude and, thus, sufficiently good for the purpose of this study. However, the previous discussion suggests that a remarkably higher precision may be achieved by using a reference gas with a more precisely known composition. Yet, mass interferences and the lack of a gas species separation before the actual analysis challenge the applicability for atmospheric air. Another critical subject is the analysis of ^{20}Ne, which is complicated due to its interference with ^{40}Ar. Such a restriction may be handled by varying the ionization energy as it is investigated in more detail by Horstmann (2016).

Influence of sample storage time

A final note shall be given to the dependence of measured sample gas composition on the duration of the storage time between sampling and laboratory analysis. A storage within copper tubes may go along with a subsequent bias of the sample gas composition. Such an impact was already described by Hofer and Imboden (1998), who found a full oxygen degradation in water filled copper tubes after about one month, caused by copper oxidation. Even though the amount of available water in soil air samples is by far less than in water filled copper tubes, the effect of oxygen degradation has to be discussed in the context of this study.

Atmospheric air samples were taken in the tropics, to obtain samples of a high water vapor content. Air samples from the same sampling day were analyzed after 2 months of storage as well as after 8 months. All samples were stored in the laboratory, meaning at rather constant ambient temperature. The results of oxygen measurements are shown in Fig. 3.9(a). Measured oxygen concentrations after different storage times agree well within their uncertainties. It should be noted that atmospheric air samples from the tropics provide an upper limit of water vapor content, typically higher than in mid-latitude soil air. Thus, even very high water vapor contents do not go along with a significant reduction of oxygen contents in the sample gas after a storage time of some months.

Besides this, the effect of very long storage times was investigated. For this purpose, some samples of atmospheric air from Germany were available, sampled some years ago by Mayer (2012). Figure 3.9(b) illustrates the measured oxygen contents in dependence of the storage time of these atmospheric air samples. Obviously, a long storage time does only go along with a significant reduction of oxygen mixing ratios, if the corresponding sample contains a high amount of water vapor. The two samples showing a significant oxygen depletion indicate an average decrease of oxygen concentration by about 0.15 vol% per year. Typical storage duration of samples from the sampling site of this study near Mannheim were in a range of 100 – 650 days, while samples from Brazil were typi-

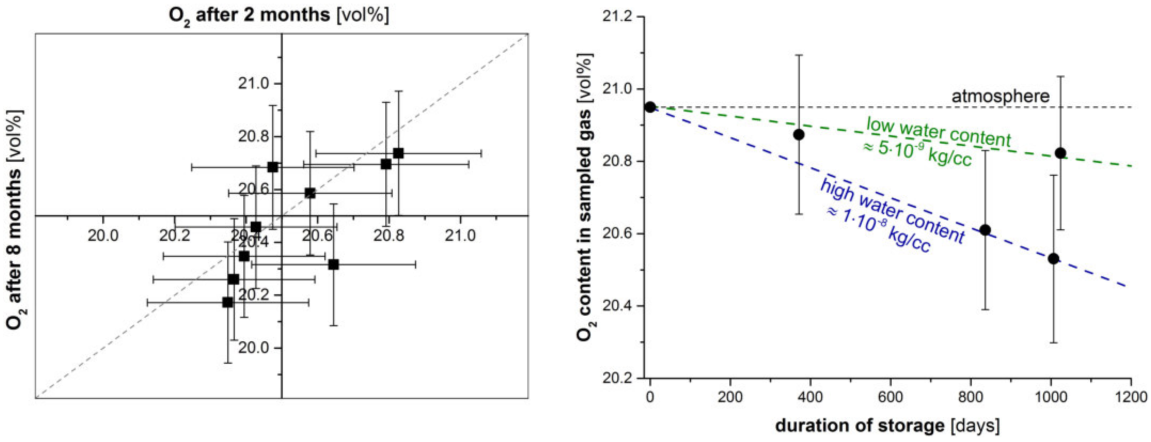

(a) Effect of high water vapor contents: Atmospheric air samples from tropical regions, stored for several months. The contained amount of water vapor inside the samples is about $2 \cdot 10^{-8}$ kg/cc.

(b) Effect of long storage times: Atmospheric air samples with varying contents of water vapor, stored for up to 3 years. Oxygen concentrations are lower in stored samples containing a higher amount of water vapor (see blue dashed line) compared to samples containing less water vapor (green dashed line).

Figure 3.9: Influence of copper oxidation on the mixing ratios of oxygen in stored gas samples. To give a better classification of corresponding water vapor contents: Soil air at 5.5 m depth near Mannheim (Germany) contains about $8 \cdot 10^{-9}$ kg of water per cm^3 of air.

cally measured 50 – 250 days after sampling. Regarding the uncertainty of *Omnistar* measurements, a corresponding impact of copper oxidation can thus be neglected. Even for storing times of a few years, the available set of samples does not allow to determine the extent of oxygen degradation with a sufficient accuracy, considering that data of long stored samples would be particularly biased by a wrongly estimated degradation rate.

3.2.2 Analysis of noble gases in soil air and groundwater

Groundwater and soil air samples were analyzed for their concentrations of ^{3}He, ^{4}He, ^{20}Ne, ^{22}Ne, ^{36}Ar, ^{40}Ar, ^{84}Kr and ^{132}Xe using a *GV Instruments MM5400* sector field mass spectrometer. The main difference to the measurement principle of the *Omnistar* quadrupole spectrometer is a separation of gas species before the analysis, followed by a determination of their absolute amounts, respectively. The *MM5400* spectrometer setup for extraction, preparation and ion detection was implemented by Friedrich (2007) and is described in the following.

Sample preparation and measurement principle

Before the actual NG analysis starts, (dissolved) gases need to be extracted from samples. For this purpose, water samples are degassed by stirring within a previously evacuated round-bottom flask, while gas samples already exist in gaseous form. After water vapor is removed by means of a zeolithe trap, the gas is subsequently collected on a cryogenic trap system. It consists of a stainless steel trap (SST) at a temperature of 25 K, collecting all NGs except for He and Ne which are collected on a charcoal trap (CT) at about 10 K. The entire adsorption process takes about 50 min.

The separation of individual NG species from each other is done by their temperature dependent release from the cryogenic trap system. First, He and Ne are released at 42 K and at 90 K, respectively, and transmitted consecutively into the mass spectrometer for the analysis. A quadrupole gas analyzer is used prior to check whether the amount of gas requires a splitting[8]. This procedure avoids overrange signals at the detector. After the measurements of He and Ne are finished, the CT is cleaned by pumping with a turbo molecular pump at a temperature of 180 K. The analysis of He and Ne is performed separately since a higher electron energy is used for He ionization to improve the resolution of the ^{3}He peak. A separation of the Ne detection from the Ar analysis is reasonable because of the nearly identical m/q ratio of doubly ionized ^{40}Ar and ^{20}Ne.

The amount of Ar in typical water or gas samples is about three orders of magnitude higher than that of the remaining NGs (see composition of the atmosphere in chapter 2.1.4). Thus, a splitting is also necessary for the gas trapped on the SST. Such a splitting is realized by a volume of 2 000 ml, into which the gas is expanded by heating the SST to 290 K. After this, one single pipette of 0.5 ml (dilution of 1/4000) is extracted from the splitting volume. After reactive gases were adsorbed by a sorption pump, the remaining gas is frozen back on the SST at 56 K, whereas Ar is still gaseous at this temperature and pumped away[9]. Such a sophisticated procedure avoids an otherwise observed bias of the Kr/Xe data by the contained Ar fraction as described in Wieser (2010). A dilution of Kr and Xe by a factor of 4000 is reasonable since the separation from Ar is only effective for small amounts of reactive gases which otherwise block the SST for NGs. Furthermore, corresponding desorption curves are pressure dependent and, finally, the splitting procedure reduces the background signal in the mass spectrometer. After the release of Ar, the fraction of Kr/Xe is transferred into the mass spectrometer and analyzed consecutively. Finally, Ar is measured by taking another pipette from the 2 000 ml splitting volume, which is freed from reactive gases and directly transferred into the mass spectrometer.

Particles entering the mass spectrometer are ionized by collisions with electrons originating from an ion source. The resulting charged ions are accelerated by a voltage of 4.5 kV. Their separation results from the *Lorentz force*[10] according to their m/q ratio and is done by means of an adjustable magnetic field.

Signals of ^{4}He, ^{20}Ne, ^{22}Ne, ^{36}Ar and ^{40}Ar are detected by a Faraday cup detector, consisting of a metal cup on a constant potential. Incident ions generate a potential drop on a resistance due to an electron flow compensating their positive charge, thus the signal is recorded in units of voltage. Measured samples usually contain quite small amounts of ^{3}He, ^{84}Kr and ^{132}Xe, which are thus measured by an electron multiplier detector: Ions reaching a dynode cause a release of electrons which are accelerated to another dynode, releasing electrons there − causing a subsequently detected electron avalanche after passing a series of such dynodes. Data are recorded in units of counts per second (cps).

---

[8] If necessary, the amount of gas is reduced one or more times by a factor of about 8.4. For this purpose, the gas is expanded into a splitting volume of 350 ml.

[9] To get rid of Ar unintentionally trapped, the SST is heated up to 75 K, refrozen to 57 K and pumped again, resulting in a fraction of Kr/Xe which is free of Ar (Stanley et al., 2009). According to measurements from Wieser (2010), the remaining Ar content after the temperature cycling is of an order of magnitude comparable to background measurements.

[10] The Lorentz force acts on charged particles moving perpendicular to the force lines of a homogeneous magnetic field and results in a particle movement along a circular trajectory (Meschede, 2015).

To obtain corresponding NG amounts, the detector signals from analyzed samples are compared to results from calibration measurements. The latter originate from a well-known air standard[11] and are measured exactly the same way as previously described for samples. The amount of calibration gas can be chosen between 0.2 ml and 5.0 ml by means of two pipettes[12] to account for any non-linearity during ionization or detection, which would bias the results in case of an one-point calibration. To compensate short-term sensitivity fluctuations of the detectors, so-called *fast calibration measurements* of pure He, Ne, Kr and Xe are performed directly before every "main measurement", respectively. For argon, such a fast calibration measurement is not done since the sensitivity of the Faraday detector is usually sufficiently constant in time.

Data evaluation

The evaluation of detector signal data is done by the software *WuCEM*, for which a detailed description is given in Wieser (2010). Usually, a decreasing trend of the detected signal is observed during every measurement due to diminishing gas amounts within the ion source. By suitable (and mostly linear) fitting curves, the initial signal at the inlet time is extrapolated for every analyzed isotope, respectively. Clearly outlying signal points are skipped to reduce the fit uncertainty. Resulting extrapolated data are corrected by fast calibration measurements to compensate short-term fluctuations of the detector sensitivity. A subsequent blank correction accounts for the background signal of each isotope, respectively.

The whole procedure results in modified data which are used to convert the sample data given in units of voltage (Faraday detector) or cps (Multiplier detector) into absolute gas amounts. This is done by a calibration curve describing the relationship between detector sensitivity and calibration signal. The resulting absolute NG amount is obtained in units of ccSTP (cubic centimeters at standard conditions: $T_0 = 273.15\,\text{K}, p_0 = 1013.25\,\text{mbar}$). Its uncertainty is mainly determined by the scattering of modified calibration measurements constraining the just mentioned calibration curve.

To convert the absolute amounts of NGs into concentrations, the amount of sampled water is determined by weighing. The uncertainty of this procedure is smaller than 1 ‰ and, thus, negligible compared to the uncertainty resulting from NG data evaluation.

For gas samples, the determination of the exact gas amount is more sophisticated and requires a determination of several parameters as depicted in Fig. 3.10. Copper tubes containing sample gas are cracked within an evacuated volume V_{inlet}. Its exact volume is well-known, based on a series of volumetric measurements (see appendix A.4). The arising pressure p_{inlet} allows to determine the exact gas amount ν [mol] according to the equation of state for ideal gases, since air can be regarded in good

---

[11] The calibration standard is usually taken at conditions with preferably low air humidity, such as cold and clear weather in winter. The crucial parameters for an exact determination of the contained NG contents within the calibration standard are, thus, the ambient air temperature and pressure as well as the relative air humidity.

[12] The applied pipettes have an exactly known size: The small pipette has a volume of (0.1974 ± 0.0004) ml, the big pipette of (0.9813 ± 0.0010) ml (both installed in February 2016).

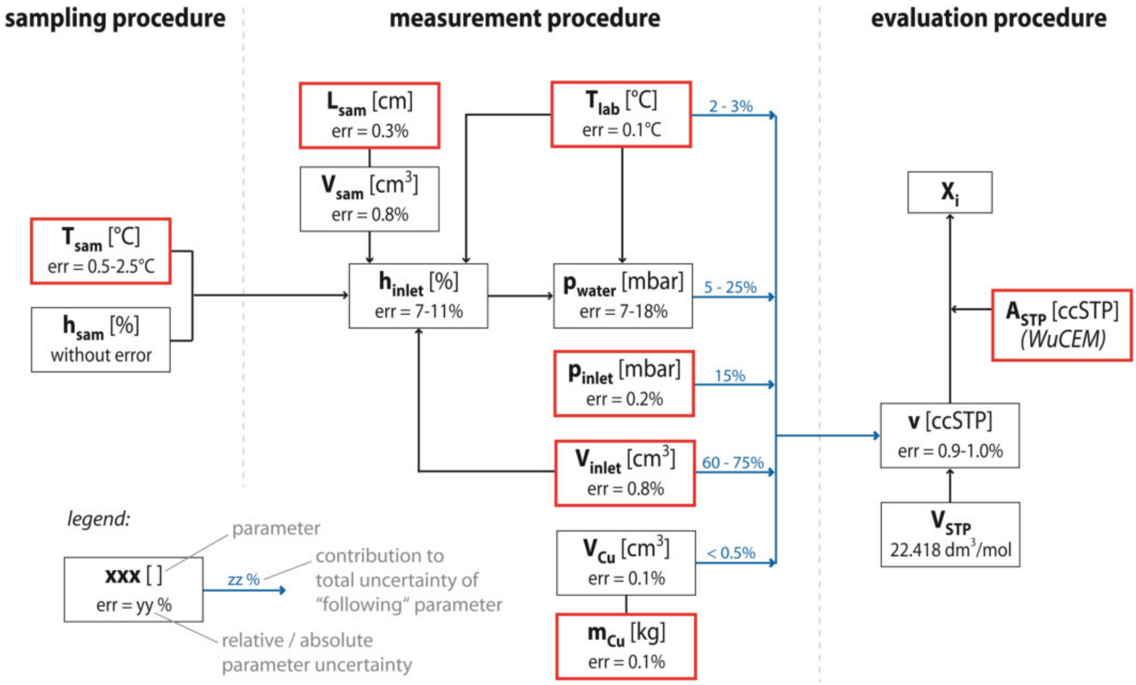

Figure 3.10: Determination of NG mixing ratios X_i in gas samples analyzed at the *MM5400* mass spectrometer. Red boxes indicate measured parameters: sampling temperature T_sam, laboratory temperature T_lab, length L_sam and mass m_Cu of copper tubes, inlet pressure p_inlet and inlet volume V_inlet. Remaining boxes indicate calculated or theoretically estimated parameters. Uncertainties are estimated or rather calculated by Gaussian error propagation. For calculated errors, a typical range is given, respectively. Blue arrows illustrate the calculation from eq. (3.3).

approximation as an ideal gas (Roedel and Wagner, 2010):

$$v = \frac{(p_\mathrm{inlet} - p_\mathrm{water}) \cdot (V_\mathrm{inlet} - V_\mathrm{Cu})}{R \cdot T_\mathrm{lab}} \tag{3.3}$$

The ambient temperature T_lab within the laboratory is measured simultaneously to the inlet pressure. The inlet volume has to be corrected by the volume $V_\mathrm{Cu} = m_\mathrm{Cu}/\rho_\mathrm{Cu}$ occupied by the copper material[13] itself. Since NG concentrations in gas samples are compared to the literature values of dry air, the inlet pressure has to be corrected by the arising partial pressure of water vapor

$$p_\mathrm{water} = \frac{h_\mathrm{inlet}\ [\%]}{100\,\%} \cdot e_\mathrm{s}\,(T_\mathrm{lab}) \tag{3.4}$$

which depends on the saturation water vapor pressure $e_\mathrm{s}\,(T_\mathrm{lab})$ at laboratory temperature (see eq. (2.21)) and on the relative humidity h_inlet within the inlet volume after opening the gas sample. Its value can be determined according to

$$h_\mathrm{inlet} = \frac{h_\mathrm{sam} \cdot e_\mathrm{s}\,(T_\mathrm{sam}) \cdot V_\mathrm{sam} \cdot T_\mathrm{lab}}{T_\mathrm{sam} \cdot V_\mathrm{inlet} \cdot e_\mathrm{s}\,(T_\mathrm{lab})} \tag{3.5}$$

---

[13] The mass m_Cu is determined by weighing a sample before or after a measurement. For copper, a density of $\rho_\mathrm{Cu} = 8.92\,\mathrm{g/cm^3}$ is assumed (Greenwood et al., 1988).

with the assumption of a relative humidity $h_{\mathrm{sam}} = 100\,\%$ of soil air and the volume V_{sam} inside the closed copper tube. The temperature T_{sam} determines the saturation water vapor pressure during field conditions and, thus, the amount of water within the gas sample. This is why the soil gas temperature during sampling has to be estimated or rather taken from a data logger at the respective soil depth. However, if the soil air temperature was higher than the ambient atmospheric temperature during sampling, water condensed within the above-surface silicone tube during sampling, which was observed on some cold winter days. In this case, the atmospheric temperature has to be assumed instead of the corresponding soil temperature. A detailed derivation of eq. (3.5) is given in appendix A.5.

The obtained amount of sampling gas in eq. (3.3) allows to determine the mixing ratio X_{i} of a certain NG isotope within dry soil air:

$$X_{\mathrm{i}} = \frac{A_{\mathrm{STP}}\ [\mathrm{ccSTP}]}{V_{\mathrm{STP}}\ [\mathrm{ccSTP/mol}] \cdot \nu\ [\mathrm{mol}]} \tag{3.6}$$

The parameter A_{STP} [ccSTP] denotes the measured NG amount at standard conditions and follows from the *WuCEM* evaluation as described above. The denominator corresponds to the volume occupied by the whole dry sample gas at standard conditions. The molar volume[14] V_{STP} of an ideal gas at standard conditions accounts for 22.418 $\mathrm{dm^3/mol}$. In this study, resulting mixing ratios X_{i} are usually compared to the respective values X_{atm} in dry atmospheric air, thus the ratio $X_{\mathrm{i}}/X_{\mathrm{atm}}$ is determined.

The uncertainty of a NG mixing ratio ΔX_{i} depends, on the one hand, on the uncertainty of the absolute NG amount ΔA_{STP} as obtained from the *WuCEM* evaluation. On the other hand, it depends on the uncertainty of the sample gas amount $\Delta\nu$ which is determined by the uncertainties of the inlet pressure $\Delta p_{\mathrm{inlet}}$, the inlet volume $\Delta V_{\mathrm{inlet}}$ and the water vapor pressure $\Delta p_{\mathrm{water}}$ (see Fig. 3.10). The first two are limited by the used laboratory equipment such as the pressure sensor and the procedure of volumetric measurements. The low precision of the water vapor pressure p_{water} is mainly caused by the two parameters T_{sam} and h_{sam} determining the amount of water vapor within the sampled gas. While an assumption of 100 % relative humidity seems to be appropriate for soil air, the estimation of T_{sam} goes along with a non-avoidable and sometimes high uncertainty, depending on the sampled soil depth (see appendix A.5 for a detailed discussion). Even though p_{water} exhibits a high uncertainty, its overall influence depends on the actual amount of water within a gas sample, which in turn depends on the climatic conditions during sampling. While the amount of water vapor is rather small for soil temperatures of 5 – 15°C (samples taken during winter time or from deeper soil layers in mid-latitudes), its influence increases strongly for temperatures higher than 20°C (samples taken from shallow soil depths during summer or in tropical regions) due to the exponential dependence of the water saturation pressure on the ambient temperature. The finally achieved precision of the sample gas amount $\Delta\nu$ can be seen as acceptable for the data evaluation of ^{132}Xe, ^{84}Kr and ^{3}He, since their uncertainties ΔA_{STP} resulting from the evaluation in *WuCEM* account for about 1 – 2 %. However, for the remaining isotopes of He, Ne and Ar, the uncertainty $\Delta\nu$ dominates the corresponding values of ΔA_{STP} which are in a range of only 0.3 – 0.5 %.

Figure 3.10 gives an overview of the relative contributions of individual parameter uncertainties to

---

[14] The molar volume V_{STP} follows from the equation of state for ideal gases: $V_{\mathrm{STP}} = \frac{V}{\nu}\Big|_{\mathrm{STP}} = \frac{R \cdot T_0}{p_0} = 22.418\,\mathrm{dm^3/mol}$.

the total resulting uncertainty Δv. The dominating parameter uncertainty is that of the inlet volume $\Delta V_{\mathrm{inlet}}$, followed by that of $\Delta p_{\mathrm{inlet}}$ or $\Delta p_{\mathrm{water}}$ – depending on the water vapor content of the sampled gas. The relative influence of the copper mass uncertainty Δm_{Cu} as well as of the laboratory temperature ΔT_{lab} is rather negligible.

The previous explanations show that for gas sample analysis at the *MM5400* mass spectrometer, the two critical parameters are the sampling temperature T_{sam} as well as the size of the inlet volume V_{inlet}. The inlet volume size provides the highest potential for improvements, for example by using a more precisely known reference volume for the volumetric determination. A detailed description of the associated error calculation of the ratio $X_{\mathrm{i}}/X_{\mathrm{atm}}$ and the corresponding estimations going along with it is given in appendix A.5.

Systematical biases and reproducibility

The single sample uncertainties obtained from the evaluation of NG data as described above do not contain some systematical biases which may play a role in NG studies while being difficult to quantify (Visser et al., 2014). Even though water sampling is done carefully to avoid any contamination, systematical biases may arise during the sampling procedure, when air bubbles are enclosed inside the copper tube or sampled groundwater originates from different subsurface depths. Another non-avoidable systematical bias may arise from the calibration of water sample data by means of a gas standard, going along with a larger required range of necessary calibration gas amounts and, thus, with a stronger influence of possible non-linearities of the calibration curves. Besides this, the extent of evacuation of the sample inlet region, the capability of water vapor extraction by the zeolite trap as well as the gas extraction efficiency may differ across water samples – even though these effects should be negligible due to long enough time spans for pumping and adsorption. For gas samples, the main reason for systematical biases is a wrong determination of the exact amount of dry sample gas. In this context, a crucial parameter is the amount of water vapor contained in a gas sample, which is mainly determined by a (sometimes error-prone) estimation of climatic conditions during sampling. The real data reproducibility should thus be taken into account during the NG analysis, in particular for water samples, to avoid NGT estimations with an unrealistic outcome which otherwise may result from an underestimation of NG data uncertainties.

To determine the reproducibility of NG data obtained in this study, a long-term record of reference samples was analyzed. Reference water samples were taken as deep lake water of the Willersinnweiher in Ludwigshafen a. R. (Germany). To ensure an equal composition of all reference samples, sampling was done during a summer stratification some meters below the thermocline, since NG concentrations of shallow lake water may fluctuate during sampling as a consequence of turbulent water mixing and short-term variations of temperature and barometric pressure. This way, about 30 samples were taken within some hours. Even though the exact equilibration temperature or rather the NG content of deep lake water can only be estimated (assuming an equilibration temperature of about 4 – 6°C), all samples can be assumed to exhibit the same dissolved NG content. An alternative type of reference samples would be so-called *air equilibrated water* (AEW), reflecting well-known climate conditions. However, a reliable generation is rather difficult due to a required stability of equilibration conditions during some days. This is why it was preferred to obtain reference samples from lake water instead of AEW. Atmospheric air was used as reference for gas samples. For given climate conditions, the NG mixing ratios of moist atmospheric air are known, even though with a certain uncertainty, depending on ambient temperature and relative humidity. For this reason, atmospheric samples were usually taken during dry and cold weather conditions, to achieve a small amount of water vapor inside the samples.

Both gas and water reference samples were analyzed at the *MM5400* spectrometer continuously about every week to obtain a long-term record and, thus, an information about the data reproducibility. In case of an influence of the above mentioned systematical biases, it is expected that typical analytical uncertainties (in the following denoted as “single sample uncertainties”) of individual reference samples are smaller than the standard deviation obtained from the entire set of reference samples.
The resulting time series of NG concentrations in reference samples are depicted in Fig. 3.11. There is no long-term trend observable for any NG species, neither for water samples nor for gas samples. The analysis of atmospheric air samples with known NG mixing ratios confirms a satisfying data accuracy for almost all analyzed NG species. However, atmospheric air samples on average show a systematic underestimation of about 1.3 % for both ^{20}Ne and ^{22}Ne. Such a deviation was not found in AEW samples generated at the Institute of Environmental Physics in Bremen and analyzed at the *MM5400* mass spectrometer (not shown in Fig. 3.11). Comparing measured isotope ratios of calibration measurements, water samples and gas samples, a systematic underestimation of neon contents is only observed for gas samples. The reason for this bias was found out to be a too short adsorption duration on the charcoal trap. The zeolite trap between the sample inlet and the cryogenic trap system retards the gas flow. This is not a problem for water samples, since the permanently outgassing water vapor acts as a transport medium inducing a permanent advective flow. However, during the analysis of gas samples, the currently remaining amount of gas in the inlet region constrains the overall pressure gradient between sample and cryogenic trap, leading to a less effective advective transport of sample gas towards the cryogenic trap system. Calibration measurements are not biased, since their gas amounts are not running through the zeolite trap. From August 2016 on, the freezing time on the charcoal trap was thus increased by 5 min for gas samples. Even though the underestimation of neon contents concerns all gas samples analyzed in this study, it shows a rather uniform data bias. This is why all neon contents of gas samples were corrected by a corresponding multiplicative factor.
The average single sample uncertainties as well as the standard deviations of the entire set of reference samples are summarized in Tab. 3.3. The obtained standard deviations are quite similar for gas and water samples. However, there are differences regarding the single sample uncertainties. Regarding water samples, single sample uncertainties are equal or smaller than the obtained standard deviations for most of the analyzed NG isotopes, with the largest relative difference for ^{4}He, ^{20}Ne, ^{22}Ne and ^{40}Ar. Their abundance allows to detect these isotopes by a faraday cup detector, resulting in a more precise signal analysis. Since most systematical biases besides statistical noise typically affect all analyzed NG isotopes in a similar way, the obtained reproducibility of more abundant isotopes is expected to be relatively worse compared to the respective single sample uncertainties. For gas samples, single sample uncertainties are equal or higher than the obtained standard deviations. This finding indicates

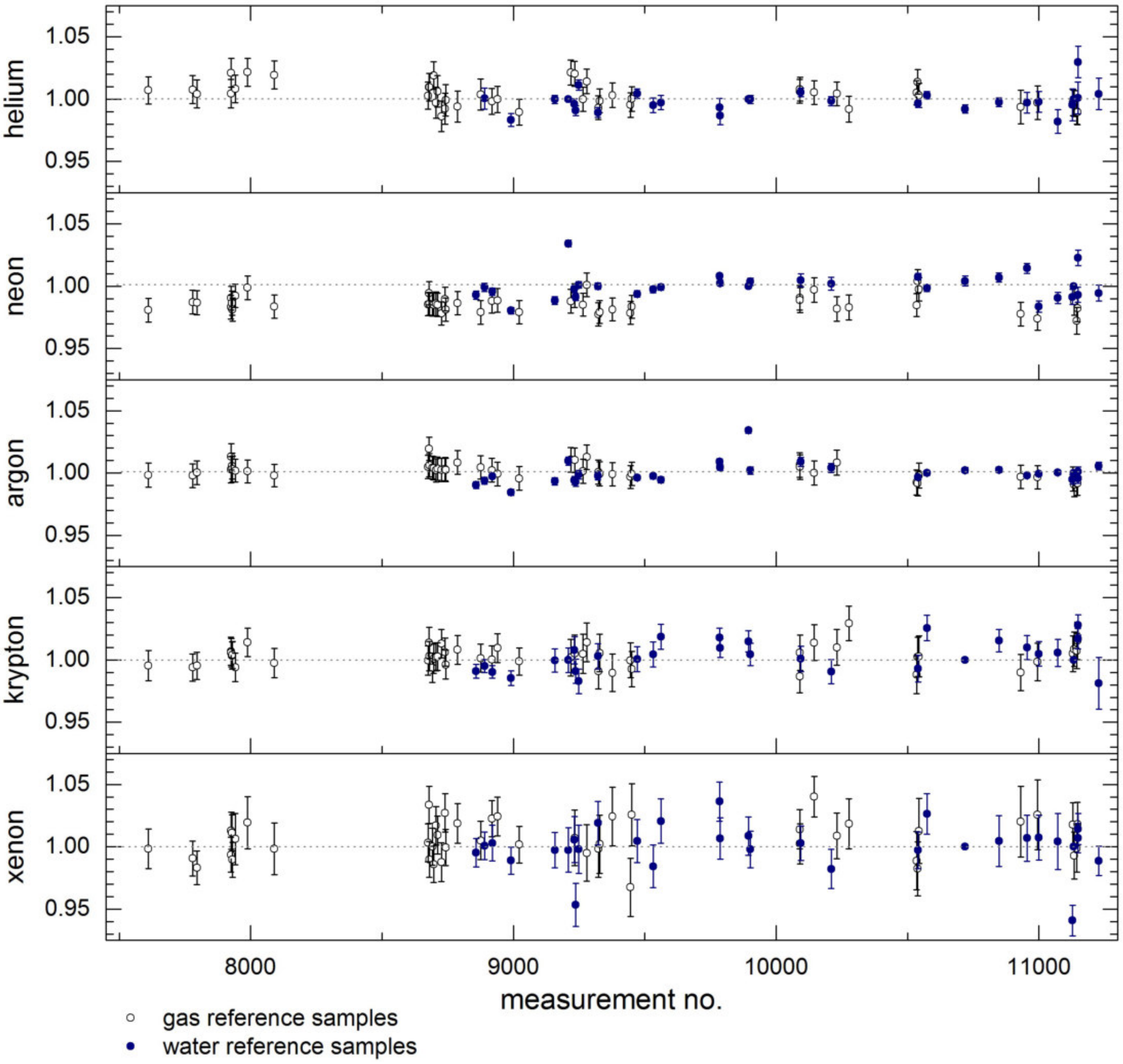

Figure 3.11: Time series of measured reference samples: Lake water samples between September 2014 and February 2016, normalized to their mean value (blue filled symbols) and gas samples between November 2013 and January 2016, normalized to the literature value for dry atmospheric air (black open symbols).

an influence of systematical errors which are included into the individual error calculation, while not affecting the obtained reproducibility. As already discussed above, the inlet volume V_{inlet} can be seen as crucial parameter determining the single sample uncertainties of gas samples.

The achieved reproducibilities were considered during the data evaluation of both water and gas samples. Any single sample uncertainty smaller than the corresponding isotope-specific standard deviation was replaced by the latter, respectively. The standard deviations in Tab. 3.3 reflect, thus, a minimum uncertainty of NG data analyzed in this study.

Wieser (2010) found similar but slightly lower standard deviations for a set of 18 reference water samples analyzed at the same mass spectrometer, accounting for 0.2 %, 0.6 %, 0.3 %, 0.7 % and 1.2 % for He, Ne, Ar, Kr and Xe, respectively. In particular the standard deviations for helium and argon data are smaller than those found in this study. For a similar mass spectrometric system, Beyerle et al.

Table 3.3: Mean single sample uncertainties as well as standard deviations of all measured reference samples at the *GV Instruments MM5400* mass spectrometer. For water samples, ^{3}He data showed an increasing trend as a result of ^{3}H decay during the time span between sampling and measurement. This is why ^{3}He data were detrended by means of a linear fit before determining the standard deviation.

NG isotope	^{3}He	^{4}He	^{20}Ne	^{22}Ne	^{36}Ar	^{40}Ar	^{84}Kr	^{132}Xe
water samples:								
single sample uncertainty	1.8 %	0.5 %	0.3 %	0.3 %	1.1 %	0.3 %	0.9 %	1.6 %
standard deviation	2.4 %	0.7 %	0.7 %	0.7 %	1.0 %	0.7 %	1.0 %	1.7 %
gas samples:								
single sample uncertainty	1.8 %	1.1 %	0.9 %	1.0 %	1.7 %	1.0 %	1.1 %	1.6 %
standard deviation	1.4 %	0.9 %	0.7 %	0.7 %	0.9 %	0.5 %	0.8 %	1.6 %

(2000) give values of 0.3 %, 0.9 %, 0.3 %, 0.8 % and 1.0 % for He, Ne, Ar, Kr and Xe, respectively.

The current measurement performance at the *MM5400* mass spectrometer still has a potential for improvements. Regarding ^{3}He data, a much better reproducibility would be desirable for a reliable determination of ^{3}H–^{3}He ages. Even though Beyerle et al. (2000) give a similar ^{3}He precision of 2.7 %, they achieved a precision of 0.7 % by determining the ratio ^{3}He/^{4}He – which may be a better option for future ^{3}He measurements at the *MM5400* mass spectrometer. The operating voltage of the electron multiplier detector provides only a small potential for improvements of obtained counting rates for ^{3}He, ^{84}Kr and ^{132}Xe, since it is restricted by an arising instability of detected signals at too high operating voltages. The setup of ion source parameters turned out to be crucial for the obtained uncertainties and for long-term trends of recorded signals at both detectors. In this context, the so-called *ion repeller* voltage shall be mentioned, inducing an electric field as homogeneous as possible during ionization (Friedrich, 2007). Its setup was found to have a strong impact on data uncertainties. A further but limited improvement of the measurement precision may be obtained by enlarged sample volumes and longer signal integration times. The first approach is of interest rather for studies interested mainly on ^{3}He data, since 20 ml of groundwater typically contains high enough amounts of dissolved gases for an usual NG analysis. The durations of integration times were investigated in recent studies (Friedrich, 2007; Wieser, 2010; Kaudse, 2014), but might provide a further potential for future improvements.

Nevertheless, the advantage of an improved data reproducibility is questionable in the context of a more reliable data interpretation. Dissolved NG contents of groundwater samples analyzed in this study are interpreted on the base of widely accepted solubility data from Weiss (1970, 1971) and Clever (1979), as suggested by Aeschbach-Hertig et al. (1999b). However, comparisons with further publications indicate deviations in the percentage range (Kipfer et al., 2002), which is usually not taken into account in NG studies such as NGT determinations. Regarding these discrepancies, it seems to be appropriate to assume reproducibilities around 1 % as obtained for most NG isotopes in this study.

3.2.3 Tritium: Low level counting

An analysis of the tritium contents in groundwater samples was done by means of low level counting at the Institute of Environmental Physics in Heidelberg, as described in detail by Grothe (1992) and Schneider (2014). For one measurement, an amount of 18 ml water is reduced together with magnesium to gaseous hydrogen inside an oven at 580°C. Tritium measurements were carried out subsequently by a low level proportional counting chamber during a time span of 48 hours.

Resulting data have a precision of about 1 TU. The detection limit accounts for 2 TU which is not problematic for young groundwater samples from mid-latitude areas as in Germany. However, young tropical groundwater usually exhibits tritium concentrations in the range of 2 – 3 TU, which is why only rough estimations of recharge times are possible for such groundwater samples.

3.2.4 Stable isotopes of water: Cavity Ring Down Spectroscopy

Stable isotopes of water were measured by a *Picarro Cavity Ring Down L-2130i Spectrometer* (CRDS) at the Institute of Environmental Physics in Heidelberg. The measurement principle is based on the absorption of laser light by a certain substance. The system consists of three high-reflective mirrors. After laser light is coupled into the cavity through a semi-reflective mirror, its overall pathlength within the cavity is expanded by the mirrors, allowing for a detection of very small abundances of a substance (Leinfelder, 2014). The actual measurement is done by transmitting the laser light through one of the mirrors with small transmissivity to reach a detector. After turning off the laser, the so-called *ring down time* is measured, indicating how long it takes until the detected light intensity decreases down to a certain value. This time span depends on the system setup but also on the absorption by the medium in between the mirrors, meaning the sampling gas (Paldus and Kachanov, 2005). For this study, corresponding data were measured relative to VSMOW standard with a mean uncertainty of 0.05 ‰.

3.3 Data evaluation and modeling

In the following, the methods for evaluating measured NG data are described. This includes, in particular, a presentation of excess air model approaches and fitting procedures. The chapter closes with a description of the applied model routine to simulate gas dynamics within the unsaturated zone.

3.3.1 Excess air models

A reliable estimation of noble gas temperatures (NGTs) requires a good knowledge about subsurface processes determining the amount of excess air in groundwater. Several approaches were developed to describe the origin or rather the formation of the excess air component. All of them can be applied to fit modeled NG concentrations on measured data by varying specific model parameters, going along with a NGT estimate.

Prior to a description of the fit procedure in chapter 3.3.2, the most common models as well as their underlying physical principles are presented, mainly based on Aeschbach-Hertig et al. (2008) and Aeschbach-Hertig and Solomon (2013). Figure 3.12 gives an overview of the presented excess air models, which are formally described in the following by using molar units.

The most simple approach is to assume an equilibrium between the NG concentration $c_{\mathrm{i,a}}$ in the gas phase and $c_{\mathrm{i,w}}^{\mathrm{EQ}}$ in the water phase, this means neglecting the excess air component. This approach is referred as *equilibrium* (EQ) model which is directly described by Henry's law:

$$c_{\mathrm{i,w}}^{\mathrm{EQ}}(T,S,P) = \frac{c_{\mathrm{i,a}}}{H_{\mathrm{i}}'(T,S)} = \frac{[P_{\mathrm{a}} - p_{\mathrm{w}}] \cdot x_{\mathrm{i}}}{RT \cdot H_{\mathrm{i}}'(T,S)} \tag{3.7}$$

Equation (3.7) simply describes the equilibrium component for the gas species i as introduced in chapter 2.3.1, depending on three unknown parameters: the equilibration temperature T (also denoted as recharge temperature), the salinity S and the total gas phase pressure P_{a}. A common assumption is to state atmospheric NG concentrations $c_{\mathrm{i,a}}$ in the subsurface gas phase, where equilibration takes place. For vanishing amounts of excess air, the EQ model can be used to obtain reasonable good results. However, the amount of excess air in groundwater can usually not be neglected with regard to the equilibrium component, thus demanding for more sophisticated model approaches.

The so-called *unfractionated air* (UA) model states a full dissolution of entrapped air bubbles due to fluctuations of the groundwater table and, thus, of the hydrostatic pressure (Andrews and Lee, 1979; Stute and Schlosser, 1993). The concentration of a dissolved gas species in the water phase is described as

$$c_{\mathrm{i,w}}^{\mathrm{UA}}(T,S,P,A) = c_{\mathrm{i,w}}^{\mathrm{EQ}}(T,S,P) + A \cdot c_{\mathrm{i,a}} = c_{\mathrm{i,w}}^{\mathrm{EQ}}(T,S,P) \cdot \left(1 + AH_{\mathrm{i}}'\right) \tag{3.8}$$

and depends on the equilibrium component and on the amount of excess air expressed by the scaling parameter $A = V_{\mathrm{a}}/V_{\mathrm{w}}$ which describes the relative fraction of entrapped air V_{a} within a certain water volume V_{w}. A common alternative formulation contains the NG mixing ratio x_{i} as well as a dimensional parameter A' [air per unit mass of water] describing the amount of dissolved air: $c_{\mathrm{i,w}}^{\mathrm{EQ}} \cdot AH_{\mathrm{i}}' = A \cdot c_{\mathrm{i,a}} = A' \cdot x_{\mathrm{i}}$ (Aeschbach-Hertig and Solomon, 2013). However, as a consequence of its simplicity, the UA model cannot explain observed mass-dependent fractionation effects of the excess air component (Aeschbach-Hertig et al., 2000; Stute et al., 1995).

A further approach was proposed by Stute et al. (1995) as the so-called *partial re-equilibration* (PR) model. Coming from a complete dissolution of entrapped air bubbles as assumed in the UA model, the PR model assumes a subsequent partial loss by a diffusion-controlled gas exchange at the groundwater table. The formal description is given by

$$c_{\mathrm{i,w}}^{\mathrm{PR}}(T,S,P,A,F_{\mathrm{PR}},\beta) = c_{\mathrm{i,w}}^{\mathrm{EQ}}(T,S,P) \cdot \left(1 + AH_{\mathrm{i}}' \cdot \exp\left[-F_{\mathrm{PR}}\left(\frac{D_{\mathrm{i}}}{D_{\mathrm{Ne}}}\right)^{\beta}\right]\right) \tag{3.9}$$

and depends on the diffusion coefficient D_{i} in water, normalized to the corresponding value of neon which has an almost pure atmospheric origin. The fractionation parameter F_{PR} depends on the degree of re-equilibration, leading to an approximation to the UA model for $F_{\mathrm{PR}} \to 0$ and to the EQ model for

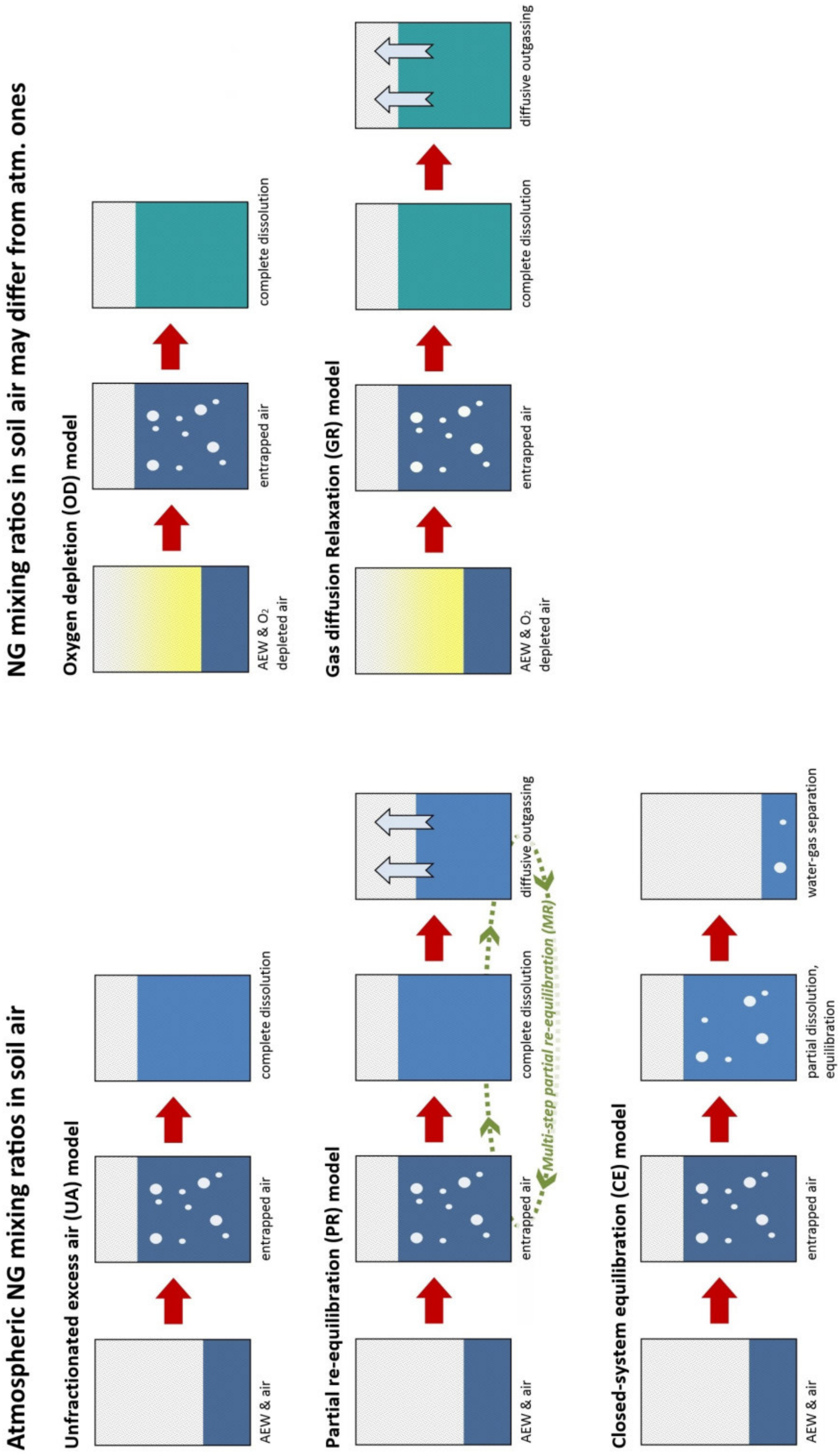

Figure 3.12: Overview of excess air models applied in this study, based on Aeschbach-Hertig and Solomon (2013). AEW denotes *air equilibrated water* and, thus, the equilibrium component.

$F_{\mathrm{PR}} \rightarrow \infty$. The parameter β originates from gas exchange theory and can assume values between 0.5 and 1 (Aeschbach-Hertig et al., 2008). Due to the mass dependence of molecular diffusion, heavier NGs are enriched within the remaining gas excess, while lighter NGs tend to escape preferentially into the gas phase. However, there exist NG patterns which cannot be explained by the PR model (Ballentine and Hall, 1999) or lead to unphysical outcomes (Kipfer et al., 2002). Such difficulties motivated a modification into the *multi-step partial re-equilibration* (MR) model introduced by Kipfer et al. (2002), assuming a series of n air bubble intrusions with subsequent diffusion processes:

$$c_{\mathrm{i,w}}^{\mathrm{MR}}\left(T,S,P,A,F_{\mathrm{MR}},\beta,n\right) = c_{\mathrm{i,w}}^{\mathrm{EQ}}\left(T,S,P\right) \cdot \left(1 + AH_{\mathrm{i}}' \cdot \sum_{k=1}^{n} \exp\left[-k \cdot F_{\mathrm{MR}}\left(\frac{D_{\mathrm{i}}}{D_{\mathrm{Ne}}}\right)^{\beta}\right]\right) \tag{3.10}$$

Comparing this approach to that of the PR model, the estimated model parameters are supplemented by n. Obviously, MR and PR model equal each other for $n = 1$ as well as for strong degassing, meaning the simultaneous occurrence of $n \rightarrow \infty$ and $F_{\mathrm{MR}} \gg 1$. Since both of these cases are rarely observed, the MR model can be seen as an improved PR model (Kipfer et al., 2002), even though in practice it exhibits similar limitations as the PR model (Aeschbach-Hertig and Solomon, 2013).

The lack of a satisfying description of a Brazilian NG record from Stute et al. (1995) led to the proposal of another model, breaking with the assumption of a complete dissolution of entrapped air bubbles and suggesting that entrapped gas amounts are usually too large to be completely dissolved by typical occurring water table increases. The so-called *closed system equilibration* (CE) model proposed by Aeschbach-Hertig et al. (2000) assumes a partial dissolution of entrapped air bubbles, followed by a subsequent equilibration with the surrounding water phase. This approach goes along with the assumption that diffusion is usually too slow to induce a significant diffusive gas exchange across the water table (Peeters et al., 2003), while there is sufficient time for an equilibration between remaining air bubbles and the surrounding water phase. The CE model is formally described by

$$c_{\mathrm{i,w}}^{\mathrm{CE}}\left(T,S,P,A,F_{\mathrm{CE}}\right) = c_{\mathrm{i,w}}^{\mathrm{EQ}}\left(T,S,P\right) \cdot \frac{1 + AH_{\mathrm{i}}'}{1 + BH_{\mathrm{i}}'} = c_{\mathrm{i,w}}^{\mathrm{EQ}}\left(T,S,P\right) \cdot \left(1 + \frac{\left(1 - F_{\mathrm{CE}}\right)AH_{\mathrm{i}}'}{1 + F_{\mathrm{CE}}AH_{\mathrm{i}}'}\right) \tag{3.11}$$

with the air/water ratio $A = V_{\mathrm{a}}^{\mathrm{A}}/V_{\mathrm{w}}$ during the initial state and $B = V_{\mathrm{a}}^{\mathrm{B}}/V_{\mathrm{w}}$ during the final state, meaning after the partial bubble dissolution (Aeschbach-Hertig et al., 2008). The introduced fractionation factor is defined as the following ratio:

$$F_{\mathrm{CE}} = \frac{B}{A} = \frac{V_{\mathrm{a}}^{\mathrm{B}}}{V_{\mathrm{a}}^{\mathrm{A}}} \tag{3.12}$$

This factor describes the reduction of the entrapped air volume due to partial dissolution and compression: A typical excess air behavior is obtained for $F_{\mathrm{CE}} < 1$, while $F_{\mathrm{CE}} > 1$ indicates an occurrence of degassing and $F_{\mathrm{CE}} = 0$ leads to an approximation on the UA model, going along with a complete dissolution of the air bubbles. While the before mentioned PR and MR models propose diffusion as the reason for a mass-dependent fractionation of the excess air component, the CE model states the mass-dependence of solubility as the reason for this phenomenon.

Equation (3.11) is also given in the literature as an alternative formulation – similar as mentioned before for the UA model – by introducing a dimensional excess air parameter A' [air per unit mass of water], together with the NG mixing ratio x_i (Aeschbach-Hertig et al., 2000). However, it is important to note that, in this case, A' describes the amount of entrapped air and not of dissolved air. A parameter interpretation in full analogy to the UA model is, thus, only appropriate in case of a complete dissolution of entrapped air.

Further excess air models were developed in the recent past, although the development of the CE model resolved current difficulties concerning the interpretation of published NG patterns (Aeschbach-Hertig and Solomon, 2013). These recently proposed models break with some basic assumptions of the "traditional" models described up to now.
A new approach was proposed by Mercury et al. (2004) as so-called *negative pressure* (NP) model, based on pressure dependent thermodynamic properties of water. As a consequence of negative ambient pressures as it is observed due to capillary forces in the capillary fringe, gas solubilities are increasing. This effect may result in higher NG concentrations in capillary water than expected as equilibrium component, potentially affecting dissolved gas contents in groundwater if capillary water reaches the saturated zone during water table fluctuations. The NP model thus affects the equilibrium component instead of the excess air component and can be formally described as

$$c_{\mathrm{i,w}}^{\mathrm{NP}}(T,S,P,A,P_c) = c_{\mathrm{i,w}}^{\mathrm{NP}}(T,S,P,P_c) + A \cdot c_{\mathrm{i,a}} \tag{3.13}$$

with a new equilibrium component depending also on the ambient capillary pressure P_c. Even though the NP model is usually not applied for NGT determinations, the capillary pressure might be a parameter of own interest containing paleoclimate information (Aeschbach-Hertig and Solomon, 2013).

A further excess air model was proposed by Hall et al. (2005) as an explanation for systematically too low NGTs from modern groundwater samples (Ma et al., 2004). The so-called *oxygen depletion* (OD) model breaks with the assumption that recharging groundwater equilibrates with a subsurface gas phase exhibiting atmospheric NG concentrations. As described in chapter 2.1.4, subsurface oxygen depletion without an equivalent balance by CO_2 – caused by a preferential dissolution in soil water (Yamaguchi et al., 1967; Paul and Clark, 1996) – may result in a depleted sum value of O_2+CO_2 compared to its atmospheric value of 20.99 vol%. Due to a balancing of the arising pressure deficit, the mixing ratios of the remaining gas species may get enhanced relative to their atmospheric values, which would also be of relevance for NGs. Such an unconsidered enhancement of NG mixing ratios in soil air would provide an explanation for systematically lower NGTs. The OD model comes up with the formula

$$c_{\mathrm{i,w}}^{\mathrm{OD}}(T,S,P,A,P_{\mathrm{OD}}) = c_{\mathrm{i,w}}^{\mathrm{EQ}}(T,S,P) \cdot P_{\mathrm{OD}} + A \cdot c_{\mathrm{i,a}} = c_{\mathrm{i,w}}^{\mathrm{EQ}}(T,S,P) \cdot \left(P_{\mathrm{OD}} + AH_{\mathrm{i}}'\right) \tag{3.14}$$

introducing a new parameter $P_{\mathrm{OD}} = X_{\mathrm{i}}^{\mathrm{soil}}/X_{\mathrm{i}}^{\mathrm{atm}}$ describing a uniform enhancement of all NG mixing ratios in soil air relative to those in dry atmospheric air. Theoretically, a full consumption of O_2 in soil air with no corresponding CO_2 increase would, thus, cause an increase of NG mixing ratios by 26.6 % with respect to atmospheric values (see Fig. 3.13). From mass conservation, one obtains

$$\alpha \cdot X^{\mathrm{atm}}_{\mathrm{O_2+CO_2}} + \mathrm{P_{OD}} \cdot \sum_{\mathrm{i \neq O_2, CO_2}} X^{\mathrm{atm}}_{\mathrm{i}} = 1 \tag{3.15}$$

with $\alpha = X^{\mathrm{soil}}_{\mathrm{O_2+CO_2}} / X^{\mathrm{atm}}_{\mathrm{O_2+CO_2}}$ and $X^{\mathrm{atm}}_{\mathrm{O_2+CO_2}} = 0.2099$ (Roedel and Wagner, 2010). For $\sum_{\mathrm{i \neq O_2, CO_2}} X^{\mathrm{atm}}_{\mathrm{i}} = 0.7901$ this results in the following range of values:

$$\mathrm{P_{OD}} = (1 - \alpha \cdot 0.2099)/0.7901 \Leftrightarrow 1 \leq \mathrm{P_{OD}} \leq 1.266 \text{ for } 0 \leq \alpha \leq 1 \tag{3.16}$$

Recent studies showed that the usual assumption of equal NG mixing ratios in soil air and atmosphere does indeed not always apply (Amos et al., 2005; Freundt et al., 2013; Jones et al., 2014). The P_{OD} parameter is determined by an ensemble fit for all samples and, thus, not individually for each groundwater sample. Such an ensemble fit is necessary because a simultaneous treatment of excess air, temperature and pressure is hardly possible due to parameter correlations (Aeschbach-Hertig and Solomon, 2013). For $P_{\mathrm{OD}} = 1$ the OD model approximates to the UA model, while a value of $P_{\mathrm{OD}} > 1$ can be seen as equivalent to a higher atmospheric pressure value P in the UA model.

Due to its analogy, the OD model goes along with the same restrictions as described above for the UA model. To overcome mass-dependent fractionation effects, the so-called *gas diffusion relaxation* (GR) model was proposed by Sun et al. (2008). The GR model can be seen as a combination of OD and PR model, containing a final step of diffusive outgassing which allows for mass-dependent fractionation. The formal description

$$c^{\mathrm{GR}}_{\mathrm{i,w}}(T, S, P, A, P_{\mathrm{GR}}, F_{\mathrm{GR}}) = c^{\mathrm{EQ}}_{\mathrm{i,w}}(T, S, P) \cdot \left(P_{\mathrm{GR}} + AH'_{\mathrm{i}} \cdot \exp\left[-F_{\mathrm{GR}} D^{\beta}_{\mathrm{i}}\right]\right) \tag{3.17}$$

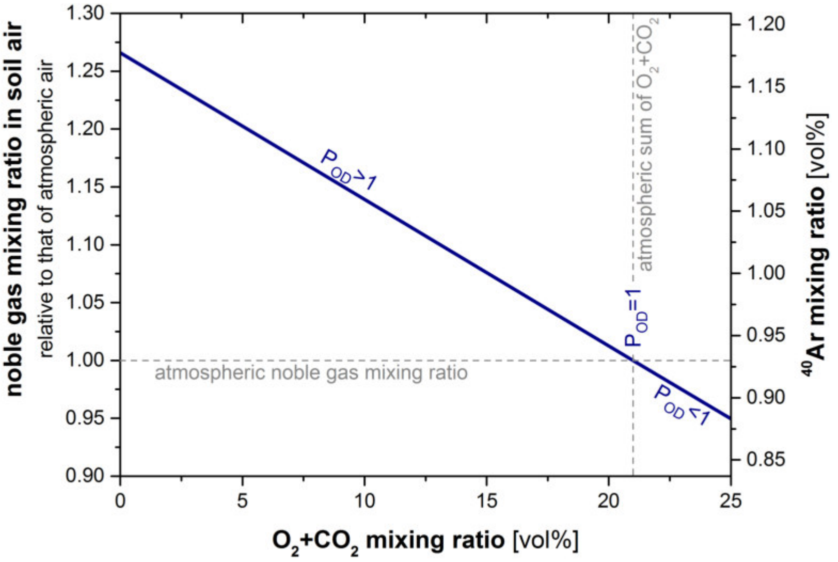

Figure 3.13: Theoretically expected correlation between the sum value of O_2+CO_2 [vol%] and NG mixing ratios, as a consequence of subsurface oxygen depletion and CO_2 dissolution.

introduces again an enhancement parameter P_{GR} as well as a relaxation parameter F_{GR} describing the amount of gas diffusing out of the water phase. By means of an ensemble fit, the values of the parameters P_{GR} and F_{GR} are determined as uniform values for all samples, respectively. The limiting case $F_{\mathrm{GR}} = 0$ leads to an approximation to the OD model. In contrast to the PR model, the diffusion process is expected to occur within the gas phase, because of the importance of the zone directly above the groundwater table for the formation of disconnected gas pores and of excess air. Thus, the values of D_{i} are taken for a diffusion process within a gas phase, which damps the resulting isotope fractionation effect. Accounting for gas exchange conditions near the water table, a parameter value of $\beta = 2/3$ is assumed (Sun et al., 2008).

3.3.2 Excess air model fits and NGT determination

The application of excess air models allows to quantify the equilibrium component as well as to separate it from the excess air component, which is necessary for a determination of NGTs. However, further model specific parameters are often of interest, for example if groundwater degassing is supposed (F_{CE}, F_{PR}, F_{GR}), for a quantification of the amount of entrapped or dissolved air (A) or for a conclusion about gas phase composition during recharge (P_{OD}, P_{GR}).

From the five measured NG species, the concentrations of Ne, Ar, Kr and Xe are typically used for a fit procedure. Measured He data are, in general, omitted, since non-atmospheric sources as radiogenic or terrigenic ^{4}He are usually not negligible. Thus, four model equations of the type

$$c_{\mathrm{i}}^{\mathrm{tot}} = c_{\mathrm{i}}^{\mathrm{eq}} + c_{\mathrm{i}}^{\mathrm{ex}} \tag{3.18}$$

are obtained, meeting a set of up to three model parameters, depending on the considered excess air model. The salinity S and atmospheric pressure P can be estimated with a sufficient accuracy. The salinity of groundwater during recharge is usually negligible ($S \approx 0$) and the gas phase pressure follows from the height of the recharge region with respect to the sea level by applying the barometric formula.

Equation (3.18) thus results in an overdetermined system. Inverse modeling technique allows for an error-weighted least squares fit of modeled NG concentrations $c_{\mathrm{i,w}}^{\mathrm{mod}}$ on measured ones $c_{\mathrm{i,w}}^{\mathrm{tot}}$, while the corresponding set of model parameters is estimated (Aeschbach-Hertig et al., 1999a; Ballentine and Hall, 1999). The best set of parameters is found by minimizing the so-called χ^2 value, indicating the goodness of the fit. It is expressed as the sum of squared deviations of modeled from measured NG concentrations, weighted by the experimental 1σ uncertainties (Kipfer et al., 2002):

$$\chi^2 = \sum_i \frac{\left(c_{\mathrm{i,w}}^{\mathrm{tot}} - c_{\mathrm{i,w}}^{\mathrm{mod}}\right)^2}{\sigma_i^2} \tag{3.19}$$

If the applied model provides a good description of measured data, any deviations should result from analytical uncertainties – giving a χ^2 value comparable to the number of degrees of freedom of the fit (Aeschbach-Hertig and Solomon, 2013). This number of degrees of freedom is obtained by subtracting the number of determined model parameters (up to 3) from the number of measured NG species (usually 4). By this way, the χ^2 value can be seen as an objective measure of the probability that the model describes the reality in a reliable way. It turned out to be reasonable to reject fit results with a probability below 1 % (Aeschbach-Hertig and Solomon, 2013).

The corresponding fits for this study were carried out by the software *program for the analysis of noble gas data* (PANGA). A detailed explanation of the software and the underlying inverse modeling approach is given in Jung and Aeschbach (2016). To obtain more accurate estimates and to handle samples resulting in physically unrealistic outcomes, *PANGA* allows to perform a freely selectable number of Monte Carlo simulations which are evaluated in one or two dimensional histograms of the determined parameters. An application of Monte Carlo simulations allows to identify and to skip problematic clusters of obtained parameter values.

3.3.3 ^{3}H–^{3}He dating of water samples

The quantification of different NG components in a water sample allows to determine the tritiogenic helium component $^3\mathrm{He}^{\mathrm{tri}}$ which is required to determine a ^{3}H–^{3}He age as mentioned in chapter 2.3.3. The following explanations are referred to groundwater samples, by accounting for excess air. However, analogous considerations follow for surface waters such as lake water. Detailed explanations about ^{3}H–^{3}He dating are given in Schlosser et al. (1989) and Aeschbach-Hertig (1994).

The actually measured amount of $^3\mathrm{He}^{\mathrm{tot}}$ is subdivided into different components, allowing to determine the tritiogenic component:

$$^3\mathrm{He}^{\mathrm{tri}} = {}^3\mathrm{He}^{\mathrm{tot}} - {}^3\mathrm{He}^{\mathrm{eq}} - {}^3\mathrm{He}^{\mathrm{ex}} - {}^3\mathrm{He}^{\mathrm{rad}} \tag{3.20}$$

The equilibrium component

$$^3\mathrm{He}^{\mathrm{eq}} = {}^4\mathrm{He}^{\mathrm{eq}} \cdot R_{\mathrm{eq}} \tag{3.21}$$

is determined by means of the equilibrium component $^4\mathrm{He}^{\mathrm{eq}}$ and the ratio $R_{\mathrm{eq}} = \left({}^3\mathrm{He}/{}^4\mathrm{He}\right)_{\mathrm{eq}}$ in air equilibrated water, which slightly differs from the atmospheric ratio $R_{\mathrm{a}} \approx R_{\mathrm{eq}}/0.983$ due to isotope fractionation during gas/water partitioning (Benson and Krause Jr, 1980). The equilibrium component is directly calculated based on the known equilibration conditions such as temperature, pressure and salinity. The latter both are usually known for the sampling area, while the equilibration temperature can either be derived from an excess air model fit (as NGT) or even be estimated in case of well-known recharge conditions.

An estimation of the excess air component based on measured neon data is motivated by the almost purely atmospheric origin of neon in groundwater:

$$^3\mathrm{He}^{\mathrm{ex}} = {}^4\mathrm{He}^{\mathrm{ex}} \cdot R_{\mathrm{ex}} = \mathrm{Ne}^{\mathrm{ex}}\mathrm{L}_{\mathrm{ex}} \cdot R_{\mathrm{ex}} = \left(\mathrm{Ne}^{\mathrm{tot}} - \mathrm{Ne}^{\mathrm{eq}}\right)\mathrm{L}_{\mathrm{ex}} \cdot R_{\mathrm{ex}} \tag{3.22}$$

where $R_{\mathrm{ex}} = \left({}^3\mathrm{He}/{}^4\mathrm{He}\right)_{\mathrm{ex}} \approx R_{\mathrm{a}}$ denotes the isotope ratio in the excess air component, which is usually approximated as atmospheric ratio. The directly measured amount of neon in a water sample is denoted as $\mathrm{Ne}^{\mathrm{tot}}$, while the equilibrium component $\mathrm{Ne}^{\mathrm{eq}}$ is again determined based on estimates about recharge conditions as mentioned above. A simple approximation for the element ratio $\mathrm{L}_{\mathrm{ex}} = (\mathrm{He}/\mathrm{Ne})_{\mathrm{ex}}$ of helium and neon in the excess air component is the atmospheric ratio of 0.288 (Schlosser et al., 1989). However, a more general estimation should be favored as

$$\mathrm{L}_{\mathrm{ex}} = \frac{\mathrm{He}^{\mathrm{mod}} - \mathrm{He}^{\mathrm{eq}}}{\mathrm{Ne}^{\mathrm{mod}} - \mathrm{Ne}^{\mathrm{eq}}} \tag{3.23}$$

where $\mathrm{He}^{\mathrm{mod}}$ and $\mathrm{Ne}^{\mathrm{mod}}$ denote the respective sums of equilibrium and excess air components estimated by an excess air model fit. This approach is motivated by the finding that excess air patterns are usually fractionated, going along with a smaller value of $\mathrm{L}_{\mathrm{ex}} \leq 0.288$ (Peeters et al., 2003). In eq. (3.23), modeled components from excess air model fits are considered instead of the directly measured data of $\mathrm{He}^{\mathrm{tot}}$ and $\mathrm{Ne}^{\mathrm{tot}}$, since possibly existing radiogenic helium may otherwise cause a biased ratio of $L_{\mathrm{ex}} > 0.288$.
Finally, the radiogenic component $^3\mathrm{He}^{\mathrm{rad}}$ is determined:

$$^3\mathrm{He}^{\mathrm{rad}} = {}^4\mathrm{He}^{\mathrm{rad}} \cdot R_{\mathrm{rad}} = \left({}^4\mathrm{He}^{\mathrm{tot}} - {}^4\mathrm{He}^{\mathrm{eq}} - {}^4\mathrm{He}^{\mathrm{ex}}\right) \cdot R_{\mathrm{rad}} = \left({}^4\mathrm{He}^{\mathrm{tot}} - {}^4\mathrm{He}^{\mathrm{eq}} - \mathrm{Ne}^{\mathrm{ex}}\mathrm{L}_{\mathrm{ex}}\right) \cdot R_{\mathrm{rad}} \tag{3.24}$$

The radiogenic component brings a difficulty when it is not exactly known. Its impact may bias $^3\mathrm{H}$–$^3\mathrm{He}$ ages in areas with an influence of geochemical reservoirs (Earth's mantle and crust) and requires a determination of the radiogenic ratio $R_{\mathrm{rad}} = \left({}^3\mathrm{He}/{}^4\mathrm{He}\right)_{\mathrm{rad}}$ in the sampling area. However, such a complication is not expected in areas showing hardly any radiogenic influence (nearby the atmospheric endmember in Fig. 2.12) as it is the case in this study. If necessary, a radiogenic ratio of $\mathrm{R}_{\mathrm{rad}} \approx 2 \cdot 10^{-8}$ is usually assumed for crustal helium (Aeschbach-Hertig, 1994). Besides the above mentioned parameter L_{ex}, the relative contribution of radiogenic helium as well as an appropriate estimation of R_{rad} can thus in general be seen as crucial factors determining the reliability of $^3\mathrm{H}$–$^3\mathrm{He}$ dating.

3.3.4 Modeling of subsurface gas dynamics and soil gas fractionation

To identify relevant subsurface transport mechanisms, a numerical modeling routine was implemented for this study by means of the software *MathWorks® MATLAB*. The model setup considers diffusive and (at least indirectly) advective transport. A similar diffusion-based model was proposed by Severinghaus et al. (1996) to describe soil gas fractionation in a sand dune, neglecting any impact of oxygen depletion. Sampled data of this study suggest that a pure diffusion-based approach may be appropriate in dry coarse-grained soil structures, but not in typical mid-latitude soils or in tropical regions. This is why the modeling approach presented in the following accounts for an indirect impact of oxygen depletion on inert gas mixing ratios. It was furthermore decided to apply a time-dependent modeling routine, since seasonal effects within the topmost meters of a soil may challenge any approach based on steady state considerations.

The applied model is based on a one-dimensional column of in total 31 boxes of $\Delta z = 25\,\mathrm{cm}$ length, respectively. This corresponds to a soil column of 7.5 m height with one overlying box reflecting the atmospheric boundary condition. Calculations are performed in time intervals of $\Delta t = 600\,\mathrm{s}$. Any influence of the chosen initial conditions on the model outcome was prevented by running the model through a total time span of several years. At the lowermost end of the soil column, the concentration within the last box is assigned to be equal to its overlying box, corresponding to a vanishing flux. Diffusion-based transport is described by Fick's second law (see chapter 2.2.1), stating the temporal evolution of the concentration of a gas species:

$$\frac{\Delta c}{\Delta t} = -D\frac{\Delta c}{\Delta z^2} \tag{3.25}$$

Even though formal descriptions are based on concentration values c, mixing ratios X are referred to in the following. The initial value of mixing ratios in all modeled boxes is stated as atmospheric mixing ratio X_{atm} of the considered gas species. Every box is assumed to be homogeneously mixed. Both parameters the box length Δz and the time interval Δt are chosen in a way to ensure that arising gradients are in good approximation invariant during each calculation step, even for strongly diffusing gas species such as helium.

Different drivers of diffusion-based transport are treated separately and formally described in the following. It has to be kept in mind that no index is used for the type of gas species, since transport was simulated independently for all gas species, which is an appropriate approach for inert gases.

- *Water vapor gradients*: The water vapor content within a box determines the mixing ratio of the considered gas species $X_{z,t} = X_{\mathrm{atm}} \cdot (1 - E_{z,t})$ (Severinghaus et al., 1996), which is assumed to change instantaneously by advective transport. Locally varying water vapor contents thus cause mixing ratio gradients between a certain box z, its overlying box $z-1$ and the subjacent box $z+1$. Thus, diffusive balancing affects the gas species mixing ratio $X_{z,t}$ in the considered box:

$$X_{z,t} = X_{z,t-1} + \left[-D\left(\frac{X_{z,t-1} - X_{z-1,t-1}}{\Delta z^2}\right) - D\left(\frac{X_{z+1,t-1} - X_{z,t-1}}{\Delta z^2}\right)\right] \cdot \Delta t \tag{3.26}$$

- *Thermal gradients*: Thermal diffusion is caused by temperature gradients across different boxes, resulting in a change of local mixing ratios (Platten, 2006; De Groot and Mazur, 2013):

$$X_{z,t} = X_{z,t-1} + X_{z,t} \cdot (1 - X_{z,t}) \cdot \left[-D_T\left(\frac{T_{z,t-1} - T_{z-1,t-1}}{\Delta z^2}\right) - D_T\left(\frac{T_{z+1,t-1} - T_{z,t-1}}{\Delta z^2}\right)\right] \cdot \Delta t \tag{3.27}$$

  The thermal diffusion coefficient is defined as $D_T = D \cdot \alpha/T$ and depends on the gas-specific diffusivity D and on the gas-specific thermal diffusion factor α as defined in Grew and Ibbs (1952). Such temperature-induced gradients of mixing ratios cause a subsequent diffusive balancing, described analogously to eq. (3.26).

- The *gravitational separation* of soil gas species is formally described as (Craig et al., 1988)

$$X_{z,t} = X_{\mathrm{atm}} \cdot \exp\left(mgz/RT_{z,t}\right) \tag{3.28}$$

  with the molar mass m of the considered gas species, the soil depth z, the universal gas constant R and the temperature T.

- *Oxygen depletion*: An advective balancing of varying O_2+CO_2 values determines the mixing ratio $X_{z,t} = X_{\mathrm{atm}} \cdot P_{\mathrm{OD},z,t}$. It results in a diffusive balancing of arising gradients, described analogously to eq. (3.26).

The parameter $P_{\mathrm{OD},z,t}$ is defined as follows (see chapter 3.3.1):

$$P_{\mathrm{OD},z,t} = \frac{1 - (\mathrm{O_2} + \mathrm{CO_2})_{z,t}}{0.7901} \tag{3.29}$$

In this simulation, its depth dependence is neglected ($P_{\mathrm{OD},z,t} \rightarrow P_{\mathrm{OD},t}$), assuming that values of $\mathrm{O_2}$+$\mathrm{CO_2}$ at a certain time t are in good approximation similar at all considered depths. This approach is justified by long-term records of this study, providing data of $\mathrm{O_2}$ and $\mathrm{CO_2}$ used for the simulation. Diffusive transport is thus induced by the gradient of mixing ratios in soil air and in atmospheric air.
The water vapor mixing ratio of soil air is calculated according to

$$E_{z,t} = h_{z,t} \cdot e_{\mathrm{s},z,t}/P \tag{3.30}$$

with the temperature dependent saturation water vapor pressure e_s (see chapter 2.1.4), normalized to the ambient air pressure P. The air humidity is usually $h_{z\neq1,t} = 1$ in soil air, meaning for all $z > 1$. At the soil surface, $h_{z=1,t}$ is assumed to fluctuate seasonally, based on local measurements, being thus permanently smaller than 1. A fluctuating relative humidity of atmospheric air goes along with a stronger impact of diffusion due to water vapor gradients (Severinghaus et al., 1996). The temperature dependence of e_s requires a knowledge of the subsurface temperature distribution which is described by the local MAAT and a sine function with an amplitude which is attenuated with increasing soil depth (see chapter 2.2.2). Figure 3.14 illustrates the model architecture.
The diffusivity D is approximated as binary diffusion coefficient of the considered gas species in atmospheric air, according to the method of Fuller and Giddings (1965). Since these coefficients are determined for a temperature of 298 K, their temperature dependence is considered as follows (Poling et al., 2000):

$$D_{z,t} = D_{298\,\mathrm{K},1\,\mathrm{atm}} \cdot \left(\frac{T_{z,t}}{298.15\,\mathrm{K}}\right)^{1.75} \cdot 1/P \tag{3.31}$$

Furthermore, the diffusivity is corrected by a factor of $\tau \cdot \theta_\mathrm{g}$ (see chapter 2.2.1), with an tortuosity of $\tau = \phi^2/\theta_\mathrm{g}^{7/3}$ (Millington and Quirk, 1961), while the gas phase content $\theta_\mathrm{g} = \phi - \theta_\mathrm{w}$ is determined based on measurements of the porosity ϕ and the soil moisture θ_w at the sampling sites of this study. An overview of the chosen gas-specific parameters is given in appendix A.8.

A final remark shall be given to the evaluation of model outcomes. For every diffusion-based transport mechanism, a δ [%] value is calculated, defined as

$$\delta = \left(\frac{R_{z,t}\big|_{\mathrm{diff}} - R_{z,t}\big|_{\mathrm{atm}}}{R_{z,t}\big|_{\mathrm{atm}}}\right) \cdot 100\,\% \tag{3.32}$$

with $R_{z,t}$ denoting a ratio of different gas species. By replacing it with $X_{z,t}$, this ratio is determined as that of the considered gas species and atmospheric air. Thus, $R_{z,t}\big|_{\mathrm{diff}}$ follows directly from the above described modeling routine for every diffusion-based mechanism, respectively. In contrast, $R_{z,t}\big|_{\mathrm{atm}}$ is determined by an analogous model simulation assuming specific transport parameters of atmospheric air, meaning an isotope mass of 29 u and corresponding values for the diffusivity and the thermal dif-

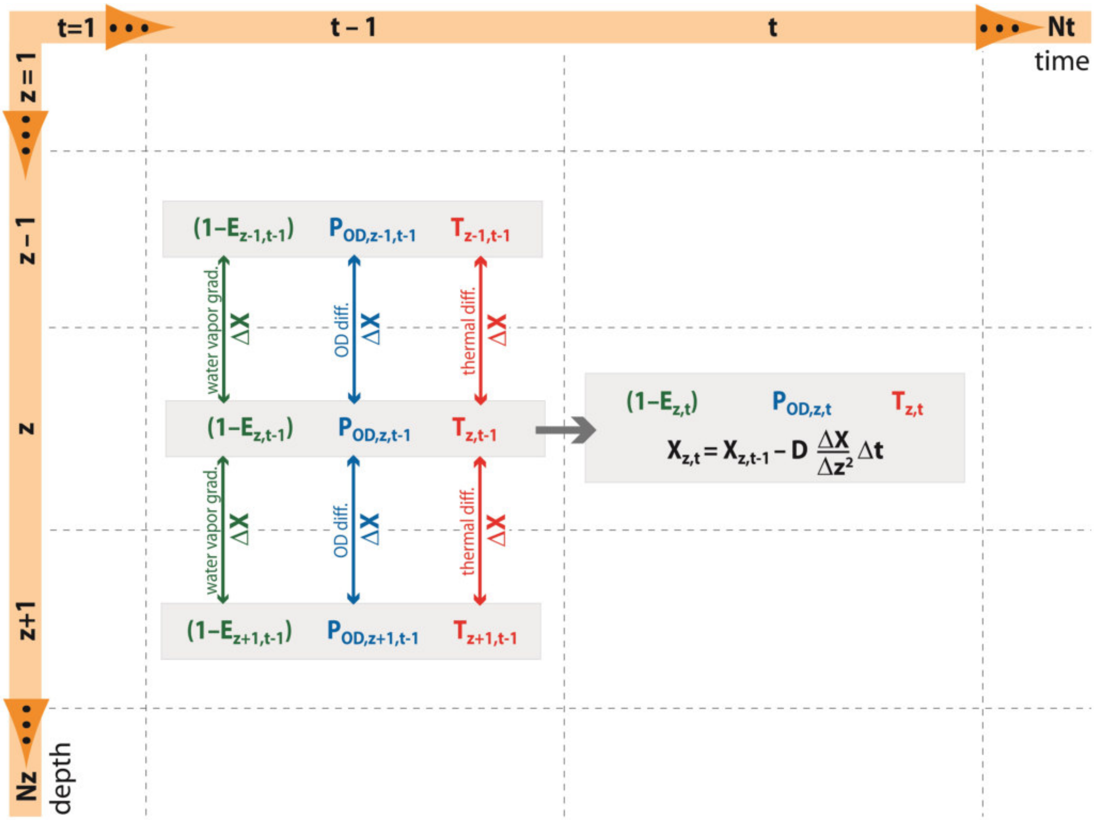

Figure 3.14: Architecture of the implemented soil gas transport model, consisting of in total Nz depth steps and Nt time intervals. The mixing ratio of the considered gas species is labeled as X, the water vapor mixing ratio as E, the ambient temperature as T and the advective contribution due to oxygen depletion as P_{OD}. The impact of depth-dependent gravitational separation is not depicted. The topmost box ($z = 1$) reflects the atmospheric boundary condition (porosity $\phi = 1$, tortuosity $\tau = 1$ and O_2+CO_2 = 20.99 vol%, temperature and relative air humidity are described by sine functions based on measured meteorological data).

fusion factor. The δ value thus describes the diffusion-caused fractionation, relative to an advectively mixed gas phase. The obtained δ values for all above described transport mechanisms are summarized to quantify the overall soil gas fractionation or rather the percentage deviation of a certain gas species mixing ratio in soil air from that in atmospheric air.

It has to be kept in mind that the impact of advective flow is not directly simulated according to its actual formal description (see chapter 2.2.1). It is just indirectly included into the model by assuming an instantaneous balancing of arising total pressure gradients. This procedure simplifies the model architecture, while it is motivated by measured data of this study, suggesting an efficient soil ventilation. However, such an approach – disregarding any direct impact of advective flow, e.g. due to barometric pressure fluctuations or penetrating water fronts – may induce biased outcomes. Furthermore, the simplified formal description does not account for the complexity of a system consisting of a water and a gas phase (see explanations in chapter 2.2.1). By this way, any exchange between these two phases is neglected as well as the transport within the water phase. However, the chosen model architecture allows for a simple identification of dominating transport mechanisms and their respective origins – as it was already justified by Severinghaus et al. (1996). Besides this, the generally reliable description of measured data in this study confirms the reliability of this approach. An inclusion of further impacts – e.g. that of soil water movement, Knudsen diffusion, precipitation, reactive gas behavior or of gas/water partitioning – requires by far more complex modeling approaches such as the model routine *Min3P* developed by Mayer et al. (2002). Of course, such a rather sophisticated model allows for more extensive conclusions due to a more comprehensive description of conditions which determine subsurface gas dynamics.

Chapter 4

Sampling sites

The selection of appropriate sampling sites for this study is essential to obtain a preferably general understanding of subsurface gas-dynamical processes and their implications for inert gas tracer applications. A first requirement was the availability of local climate records, concerning in particular atmospheric temperature and precipitation. Second, a knowledge of the local soil profile was required, since soil parameters such as porosity and hydraulic conductivity constrain subsurface gas dynamics. Third, sites were preferred offering the possibility to sample in groundwater recharge areas with a shallow water table depth, which allows for sampling through the entire vertical profile of the unsaturated zone.

A site in the community of Heddesheim near Mannheim was chosen for a long-term study of 2.5 years. Short-term variations of local subsurface gas dynamics are typically determined by mid-latitude climate conditions, implying the occurrence of a pronounced seasonality. The dominant impact of both soil temperature and soil moisture in this context motivates to realize analogous investigations under comparatively extreme climate conditions. For this purpose, samplings were performed in the tropical latitudes which are typically characterized by permanently high temperatures, strong amounts of precipitation as well as by high microbial activity rates (Raich and Schlesinger, 1992; Stute and Schlosser, 1993). Two field campaigns to the Brazilian tropics were carried out to complement the mid-latitude data set of this study.

4.1 Long-term sampling site near Mannheim (Germany)

A first analysis of the SF_6 concentration in groundwater of an already existing well in spring 2013 resulted in a groundwater age of (14.0 ± 1.0) years which is sufficiently young to allow for reliable assumptions about the climate conditions during recharge. However, since the existing well (in the following denoted as “deep well”) has a filter depth between 12.4 and 17.4 m, it was decided to install an additional well (denoted as “shallow well”) to sample groundwater directly below the water table which was at a depth of about 7 m during the installation of this sampling site. The shallow well was installed in May 2013 and has a total depth of 8.7 m, of which the lowermost 5 m are screened.

For sampling soil air, silicone tubes were perforated on their lowermost 10 cm and installed into boreholes of different depths and of 6 cm diameter, respectively. To ensure that only soil air from a certain

depth is sampled, a sophisticated tightening procedure was applied. First, the borehole was filled by about 1 liter of fine grained sand to create a well permeable filter around the perforated part of a tube, as shown in Fig. 4.1(a). Above this sand layer, the borehole was filled by pellets of swelling clay[1] which were irrigated. This procedure prevents a leakage between different soil layers, which could otherwise occur in vertical direction along the silicone tubes. Furthermore, every tube was installed into an individual borehole, to avoid any leakage resulting from an interspace between tubes. Sampling was not started before June 2013, to exclude any influence of remaining water from the irrigation of the clay pellets as well as to give some time for the borehole filling to settle.
Figure 4.2 gives an overview about the sampling site as well as of all measured parameters. The installations allow to sample soil air at depths of 1 m, 3 m, 4.4 m, 5.5 m and 6.5 m, respectively. The position of the groundwater level in May 2013 (7.1 m below terrain) motivated the choice of the deepest depth for soil air sampling. It was decided to install tubes also at 4.4 m and 5.5 m depth to allow for soil air sampling near the groundwater table even after a possible water level increase which occurred indeed already in June 2013. Figure 4.1(b) shows the sampling site during summer 2014.

The sampling procedure of soil air and groundwater as described in chapter 3.1 took place every two weeks between June 2013 and October 2015, thus for more than two years. Until December 2013, groundwater was sampled by a mobile pump which was installed from new for every sampling. From there on, a new pump was permanently installed at the shallow well, since the data loggers had otherwise to be moved out of the well during pumping, which led to temperature induced biases of the recorded data. By this way, the loggers had to be removed only every four months for changing batteries and recalibrating. In contrast, the deep well was always sampled by a temporarily installed mobile pump, since no data logger was installed at the deep well.

The sampling region is situated in the Rhine-Neckar region, where the topmost and unconfined aquifer

(a) Installation of silicone tubes for soil air sampling.

(b) Sampling site near Mannheim in August 2014. The picture shows the shallow groundwater well (left) as well as the soil air sampling site (middle).

Figure 4.1: Installation of the long-term sampling site near Mannheim.

---

[1] According to manufacturer's data, the used *Bentonit 10/200* clay pellets exhibit a hydraulic conductivity of $K_s = 2 \cdot 10^{-11}$ m/s after irrigation.

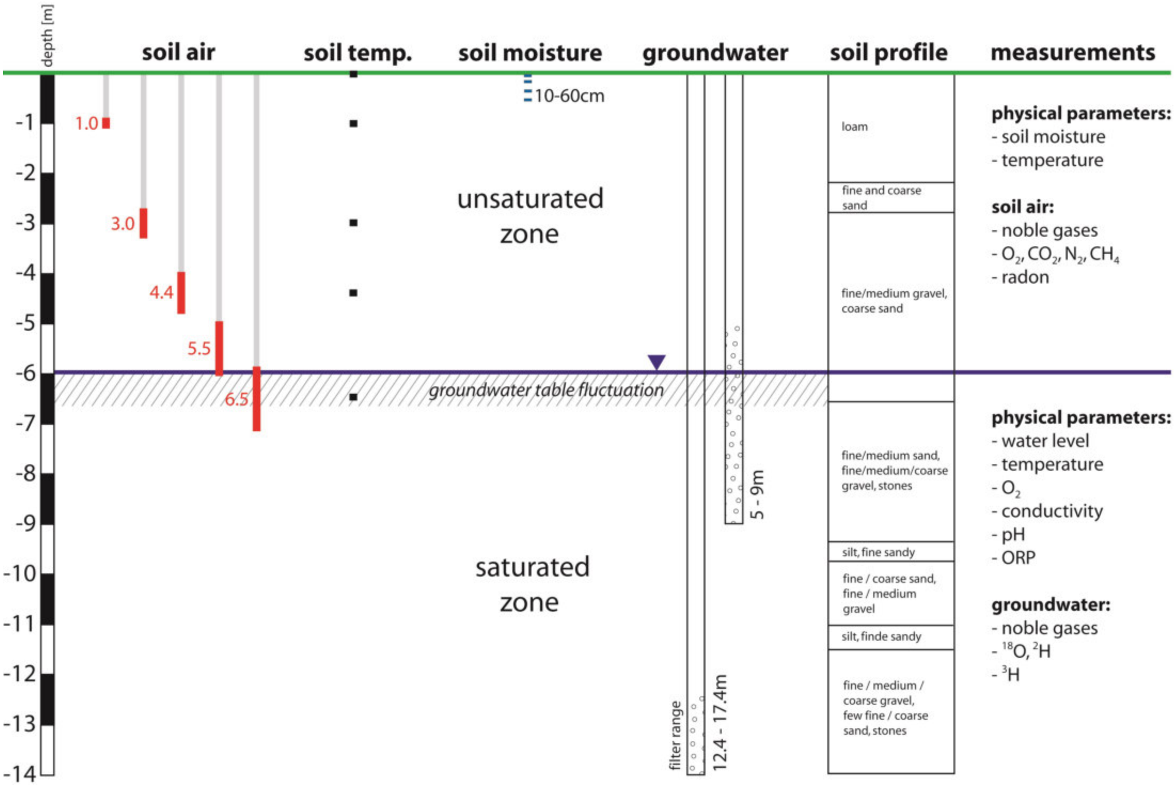

Figure 4.2: Setup of the long-term sampling site near Mannheim and continuously measured parameters. Red bars indicate the uncertainty range of the sampling depth which is assumed as ±5 % of the depth, estimated based on the stretchability of the used silicone tubes. The shaded area denotes the range of groundwater fluctuation during the sampling period (June 2013 until October 2015).

has a vertical extent of 25 – 30 m and consists mainly of sandy gravel and gritty sand, going along with a typical hydraulic conductivity in the range of about $K_s = 0.5 \cdot 10^{-3}$ m/s (LUBW, 1999). There exist two further subjacent groundwater aquifers: The middle aquifer consists of sandy gravel and is usually classified into an upper and a lower part, both exhibiting hydraulic conductivities slightly lower than that of the topmost aquifer, even though of the same order of magnitude. The underlying lowermost aquifer consists of sandy as well as of silty layers. In the following, only the topmost aquifer is regarded since the deeper aquifers are not of interest in the context of this study.

For the topmost aquifer, Fig. 4.3 gives an overview of the contour lines of local groundwater, characterizing the flow pattern. According to flow simulations by Bender (2003), the groundwater at the sampling site can be assumed to be unaffected by water from the Neckar river, meaning that local groundwater contains no fraction of river water. In the sampling area, groundwater recharge amounts for about 250 mm per year (LUBW, 1999).

Climate parameters (mainly air temperature, pressure and precipitation) are available from a station in Mannheim Vogelstang within a distance of about 2 km from the sampling site (see Fig. 4.3), operated by Germany's National Meteorological Service (DWD, 2016). Figure 4.4(a) illustrates the monthly average climate conditions which can be seen as typical for the mid-latitudes. The long-term average amount of precipitation is 669 mm per year. The local mean annual atmospheric temperature (MAAT) increased continuously, on average by about 0.04°C per year during the last three decades (see Fig.

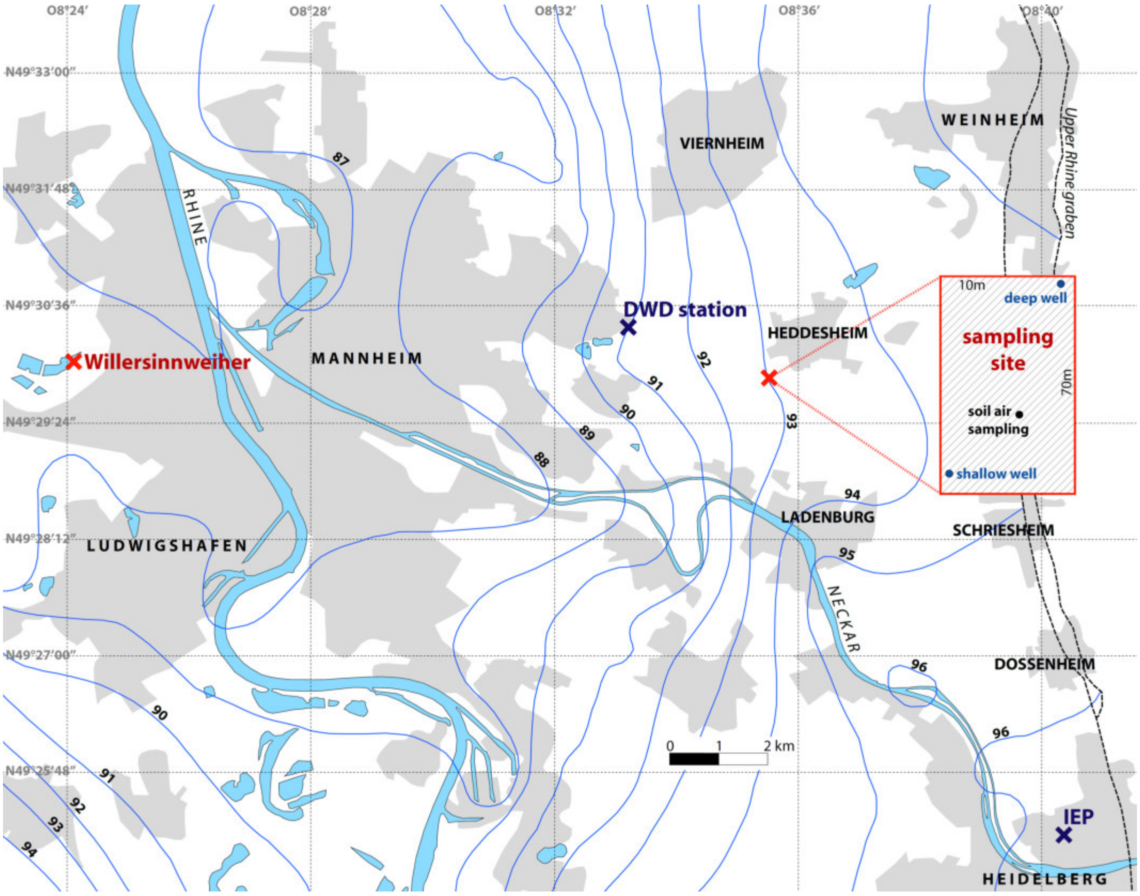

Figure 4.3: Contour lines of the topmost groundwater aquifer in the Rhine-Neckar region and positions of the long-term sampling site near Mannheim (49° 29.959' N, 8° 35.576' E) and the Institute of Environmental Physics (IEP). Populated areas are sketched in gray. Map adapted from Verwaltungsverlag (2012).

4.4(b)). Thus, the MAAT cannot be seen as constant on the time scales of interest for this study. The trend in Fig. 4.4(b) indicates a MAAT of 11.6°C in 2014.

Figure 4.5 shows time series of meteorological parameters as well as of groundwater table data. These records provide the possibility to classify climatic conditions during the sampling period of this study. Obviously, meteorological conditions during the sampling period of 2.5 years can be seen as representative for the last decades, meaning that there are no extreme weather events observable like remarkable strong precipitation periods, cold snaps or drought periods. This finding allows for a more general interpretation of obtained data.

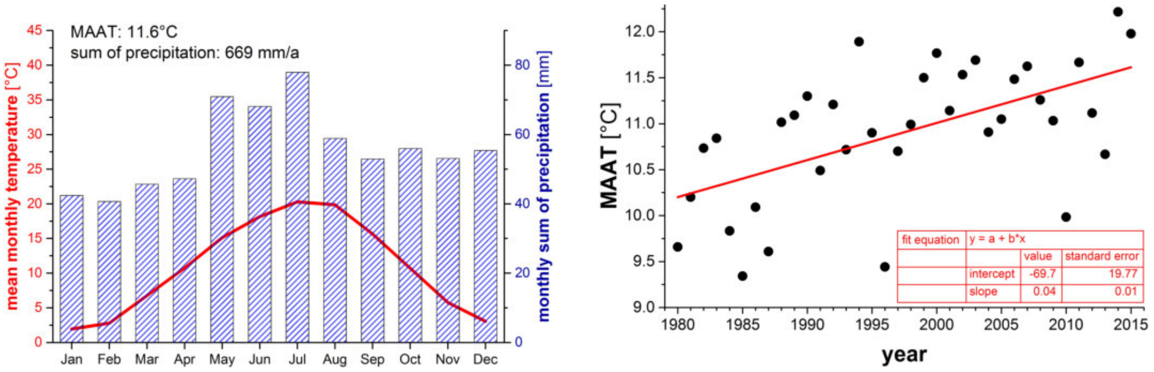

(a) Mean monthly temperatures and precipitation (data from 1980 – 2015).

(b) MAATs between 1980 and 2015 as well as a linear fit.

Figure 4.4: Climate data from a measurement site in Mannheim Vogelstang, which is in about 2 km distance from the sampling site of this study. Data adapted from DWD (2016).

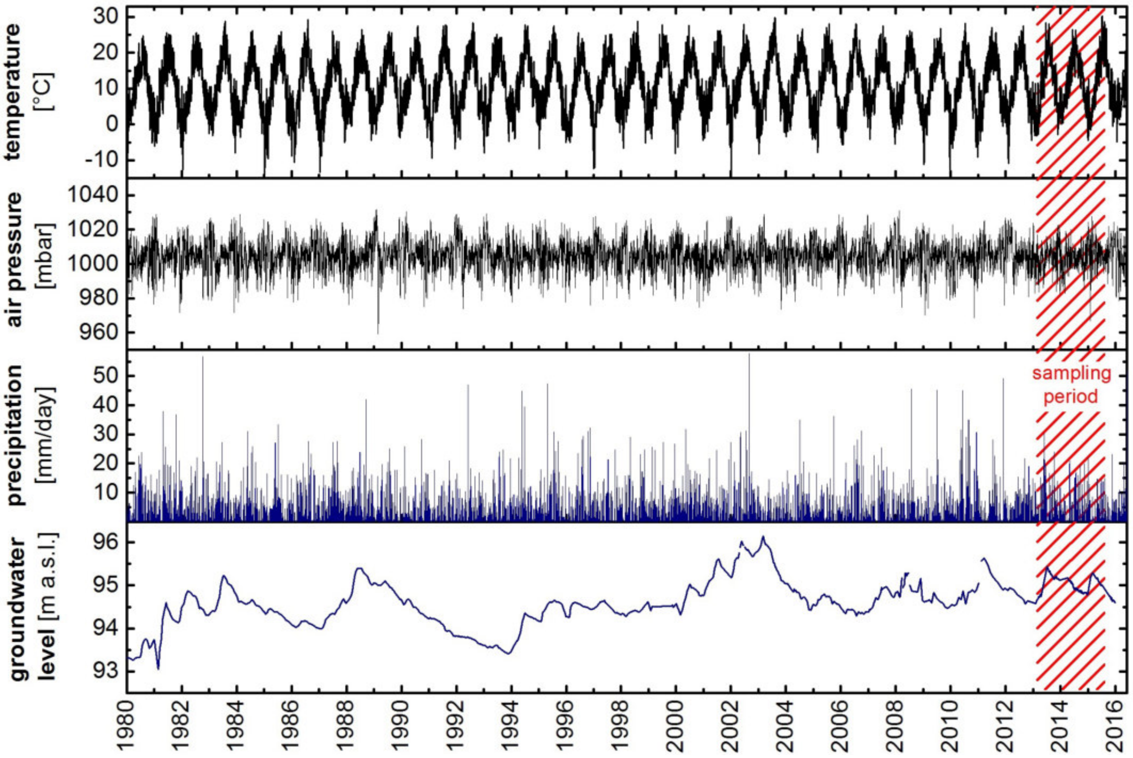

Figure 4.5: Long-term records of meteorological parameters (DWD, 2016) and of groundwater table fluctuations (LUBW, 2016) in the sampling region near Mannheim. The red shaded area indicates the sampling period of this study.

4.2 Sampling sites near Santarém (Brazil)

The sampling area around Santarém is located near the equator at the southern latitude 2°25' and, thus, characterized by the highest annual precipitation amounts as well as by the highest mean annual temperatures observed on the continent (see Fig. 4.6). Santarém is situated in the center of the lower Amazon region in Northern Brazil, where the Rio Tapajós flows into the Amazon river. The study area is characterized by a humid equatorial climate with a MAAT of 25 – 28°C, depending on local conditions such as vegetation (see Fig. 4.7). The amount of local precipitation accounts for about 2 300 mm per year. The mean monthly atmospheric temperatures fluctuate by about 2°C during the year. In contrast, the monthly sums of precipitation vary strongly with a rainy season in the first half of the year and a dry season in the second half. The water levels of the Amazon river and the Rio Tapajós typically fluctuate by about 6 – 7 m on seasonal scale (Tapajós et al., 2016), see Fig. 4.8.
The region around Santarém offers outstanding climate conditions for this study, due to yearlong high temperatures and the high amount of precipitation. Regarding the trend of monthly temperatures, possible seasonal variations are only expected between rainy and dry season. This fact determined the chosen times of the two sampling campaigns. The first one took place in June/July 2014, when the river water level reached its maximum at the end of the rainy season. The second campaign was carried out in November 2015 after the river water level reached its minimum at the end of the dry season. Figure 4.9 illustrates long-term trends of temperature, relative humidity, precipitation and river water level, measured during the last decades. Obviously, both sampling campaigns cover the corresponding seasonal conditions quite well. The first campaign took place directly after the strongest precipitation events ended, the second campaign was performed at the end of an unusual long dry

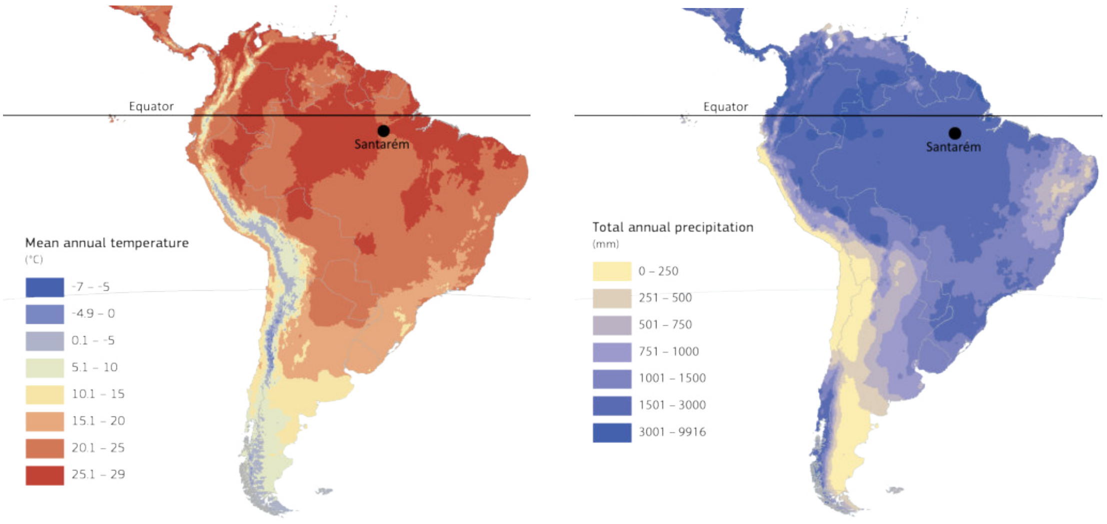

(a) Mean annual atmospheric temperature.

(b) Annual amount of precipitation.

Figure 4.6: Climate conditions in South America, adapted from Gardi et al. (2015). The sampling area of Santarém is characterized by the highest temperature reading of the continent, although local temperature fluctuations are damped by cloud cover and by heavy rainfall. High annual precipitation records of more than 2 000 mm as observed in Santarém are typical for the Amazon Basin.

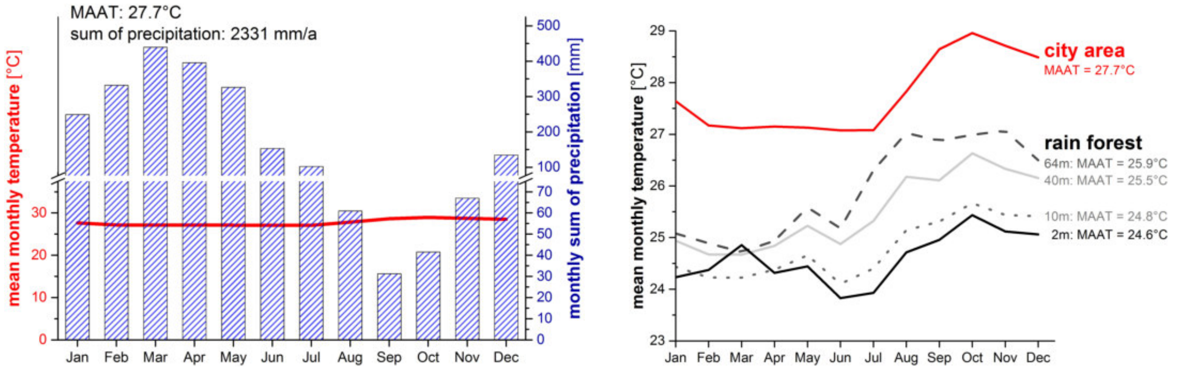

(a) Mean monthly values of temperature and precipitation in the city of Santarém. Precipitation data from ANA (2016) (station 00254000, 1968-2015), temperature data from INMET (2016) (station A250, 1997-2016).

(b) Comparison of temperature patterns: Mean monthly air temperature in the city of Santarém (ANA, 2016) (1968-2015) and at different heights inside the rain forest (Miller et al., 2009) (2000-2004).

Figure 4.7: Climatic conditions in the study area near Santarém (Pará).

(a) Amazon river at high water level at the end of the rainy season in 2014.

(b) Amazon river at low water level at the end of the dry season in 2015.

Figure 4.8: Water level fluctuations of the Amazon river in the sampling area near Santarém.

period. While typically the first heavy rains in Santarém occur in the beginning of November, this was not the case in 2015 when sampling took place. By this way, soil air and groundwater could be sampled at perfectly dry conditions and without any bias due to the otherwise beginning rainy season. The reason for such an extreme dry period can be seen in the strong El Niño occurrence in 2015/16 (Wolter, 2016; Jacox et al., 2016). Interestingly, the comparable strong El Niño phenomenon in 1997/98 can also be identified in the long-term record of Fig. 4.9 as an unusual temperature increase during the respective dry season.

During the campaign in 2014, groundwater sampling was done at 15 sites which were also sampled in 2015, together with 10 additional wells (see Fig. 4.10). Groundwater was sampled from already existing wells which are used for private or public water supply. Soil air sampling took place at 13 sites in 2014 and at 17 sites in 2015 – all of them situated directly next to sampled groundwater wells. Sampling of soil air was performed by means of a mobile sampling system.
From every sampled well, two samples were analyzed for their NG concentrations, respectively. Such a double measurement is reasonable since tropical groundwater is expected to exhibit high amounts

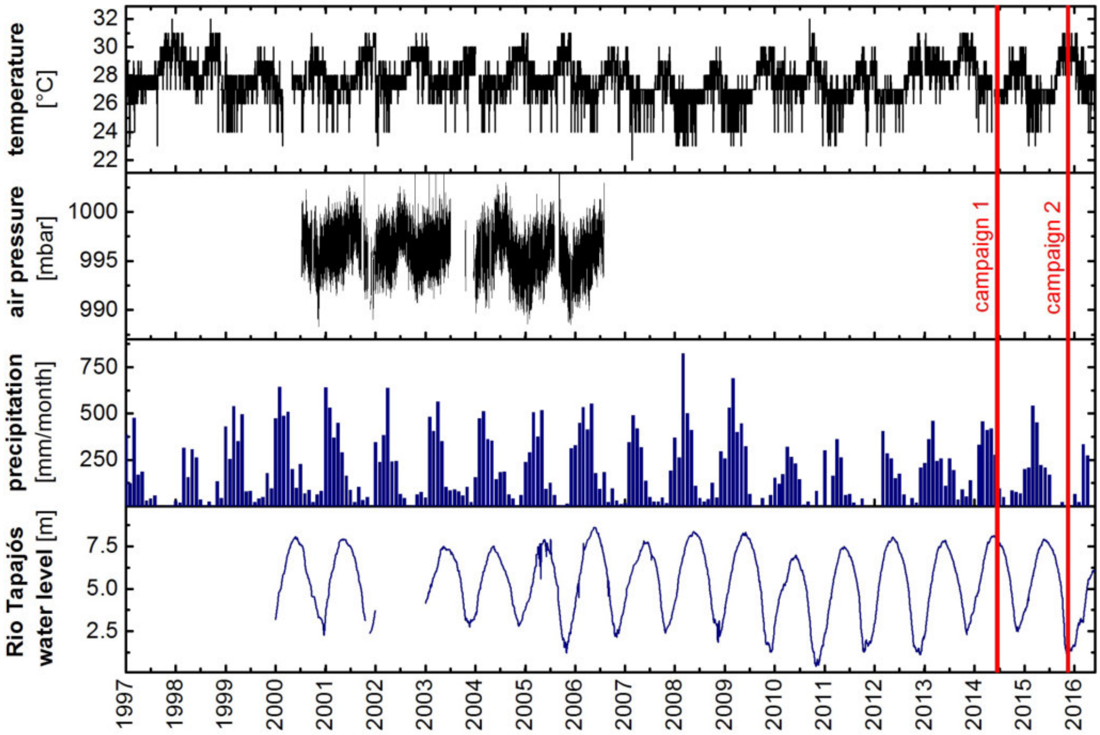

Figure 4.9: Long-term records of meteorological conditions (ANA, 2016) and river water table fluctuations of Rio Tapajós (Marinha do Brasil, 2016) in the sampling area near Santarém. Red lines indicate the times of the two sampling campaigns in June/July 2014 as well as in November 2015.

of excess air which cannot always be distinguished from a contamination by an inclusion of air bubbles during sampling. In case of a significant difference of the two analyzed samples, a third one was additionally analyzed. All data presented in the following are averages from multiple samples, while obvious outliers were rejected.

The topography of the sampling area can be divided into two regions: a higher area on a plateau (mean height of all local sampling sites: 120 m a.s.l.) and a lower area (mean height: 30 m a.s.l.) near the two rivers. As depicted in Fig. 4.11, the overall groundwater flow is assumed to be directed downwards from the plateau region towards the rivers (Tancredi, 1996). The local groundwater is part of the so-called *Alter do Chão aquifer* which is expected to store the largest groundwater volume on Earth (ABAS, 2010). For the topmost aquifer, Tapajós et al. (2016) assume a mean hydraulic conductivity of $K_s = 1.3 \cdot 10^{-4}$ m/s. Local soil constituents are strongly determined by alluvial deposits, with very sandy soils directly inside the flood plains (Oliveira, 1996). Above these plains, soils near the rivers are characterized by a mainly loamy fraction of about 3 to 50 m depth (Tancredi, 1996). With increasing height or rather on the plateau region, this pattern changes into dedritic-lateritic soils with a clay layer ranging down to about 3 – 30 m depth, followed by an underlying layer of sandstones (Oliveira, 1996).

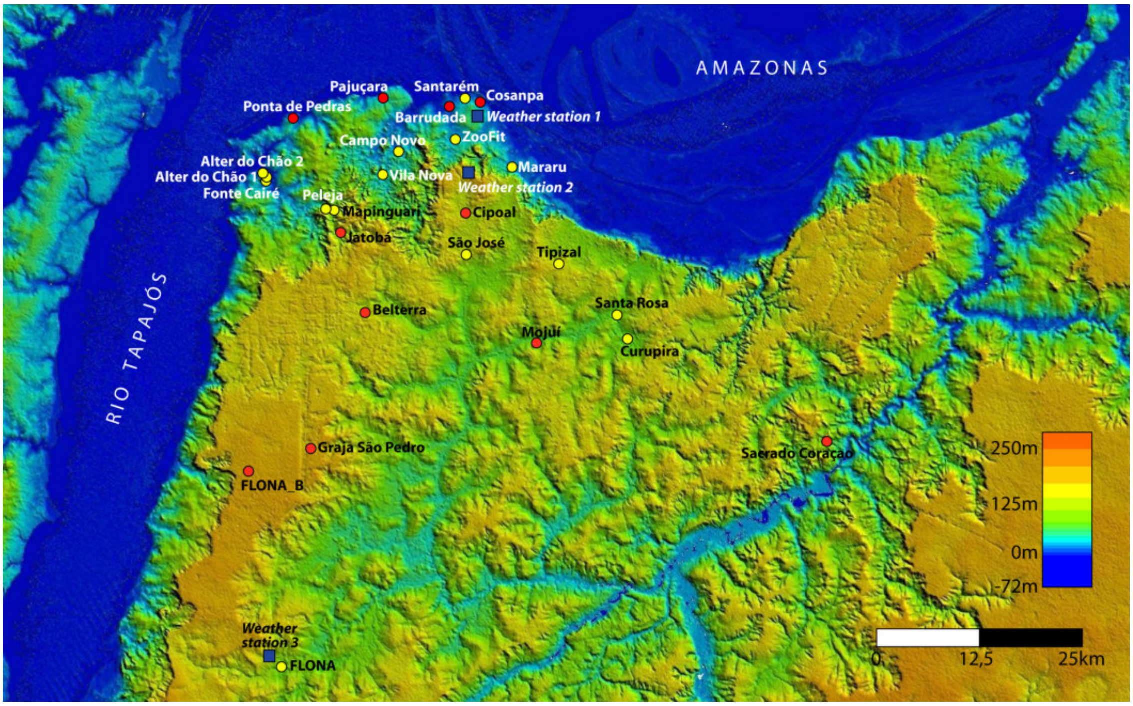

Figure 4.10: Topography of the sampling area around the city of Santarém, with a dimension of about 70 × 50 km^2. Sites sampled in 2014 as well as in 2015 are labeled as yellow points, the additional ones sampled only in 2015 are labeled as red points. Map adapted from Google Earth (2016).

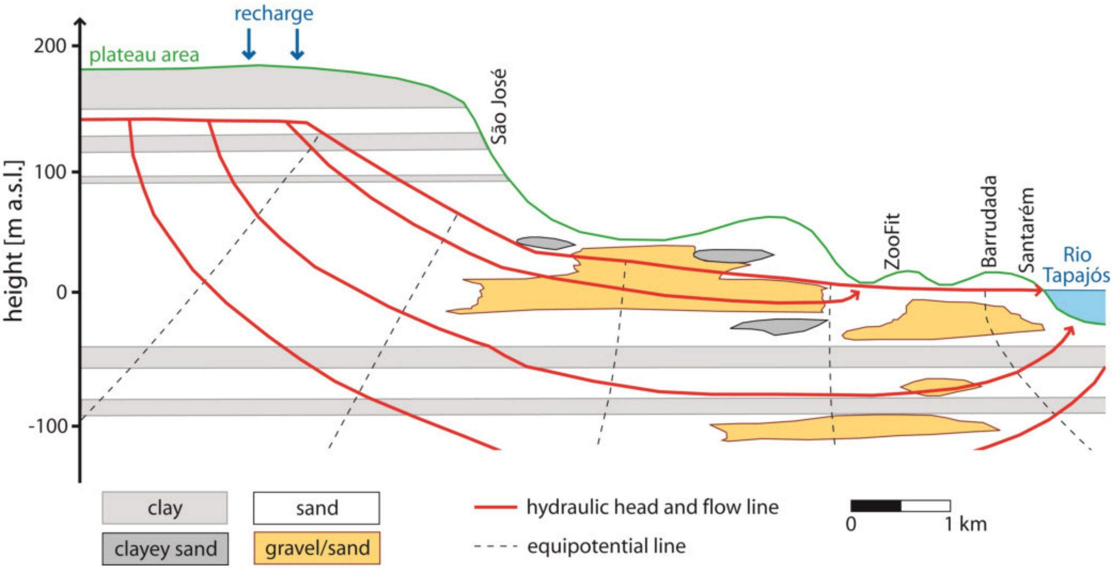

Figure 4.11: Schematic cross section of groundwater flow conditions near Santarém, based on Tancredi (1996). Lines of equal hydraulic potential and of groundwater flow are depicted.

Chapter 5

Long-term observations in mid-latitudes

This chapter presents results of the 2.5 year long-term study near Mannheim (Germany), for the unsaturated and saturated zone. Measured data are complemented by numerical simulation results. Based on measured noble gas (NG) contents of local groundwater, noble gas temperatures (NGTs) are determined by least squares fits applying different excess air models. The obtained data are discussed in the context of subsurface gas dynamics and its underlying physical processes causing the observed NG patterns in soil air and in sampled groundwater.

5.1 Unsaturated zone

The following data presentation starts with short-term fluctuations of soil air composition at different sampled depths, including a critical evaluation of the measurement uncertainty and possible systematic errors. After this, continuous records of soil moisture and soil temperature are presented.

5.1.1 Soil air composition

Local soil air was analyzed for its contents of N_2, O_2, CO_2 and NGs. In the following, values of O_2+CO_2 are regarded instead of separate data of O_2 and CO_2. This is motivated by the main focus of this study, which is on subsurface gas dynamics rather than just on microbial activity. Figure 5.1 gives a first overview of the measured O_2+CO_2 content in soil air and its temporal development at different depths. The data vary between about 19 and 22 vol%, while showing a clear seasonality and developing in a nearly uniform way at all sampled depths. To investigate this behavior in more detail, measured time series of certain gas species are depicted in Fig. 5.2 for soil depths of 1.0 m and 5.5 m. Recorded mixing ratios are normalized to their atmospheric values, respectively. The topmost soil layer at 1.0 m depth is expected to be most affected by exchange with atmospheric air, while the depth of 5.5 m allows to sample soil air directly above the groundwater table[1]. All measured soil air composition data are given in appendix B.3 and B.7.

The measured sum value of O_2+CO_2 deviates significantly from its atmospheric value during the most of the time of the study (see Fig. 5.1 and Fig. 5.2(b)/(d)). The strongest decrease of O_2+CO_2

---

[1] This depth was preferred to the also sampled depth of 6.5 m since the groundwater table increased several times above 6.5 m, hindering sampling during the major part of the study.

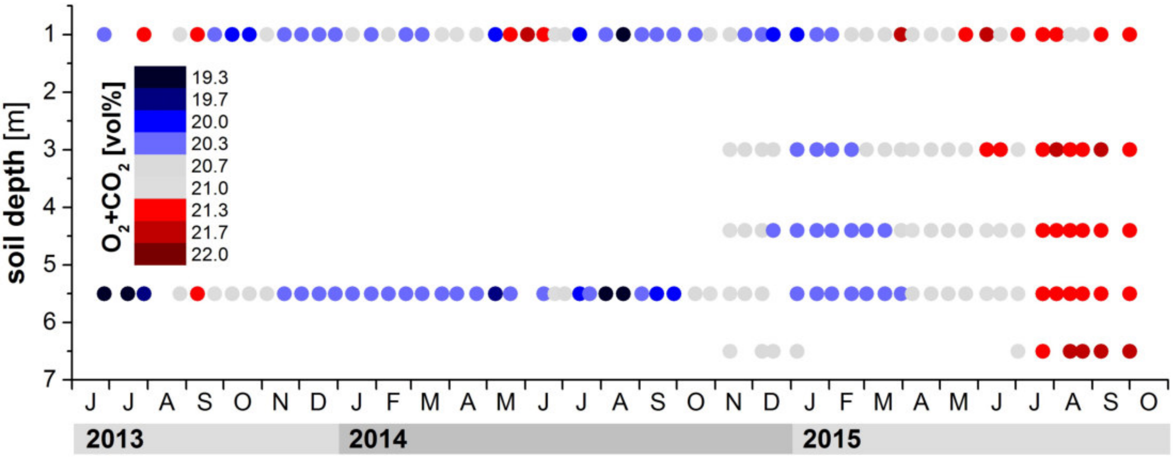

Figure 5.1: Mannheim: O_2+CO_2 time series in soil air at different depths. All data are given in units of vol%.

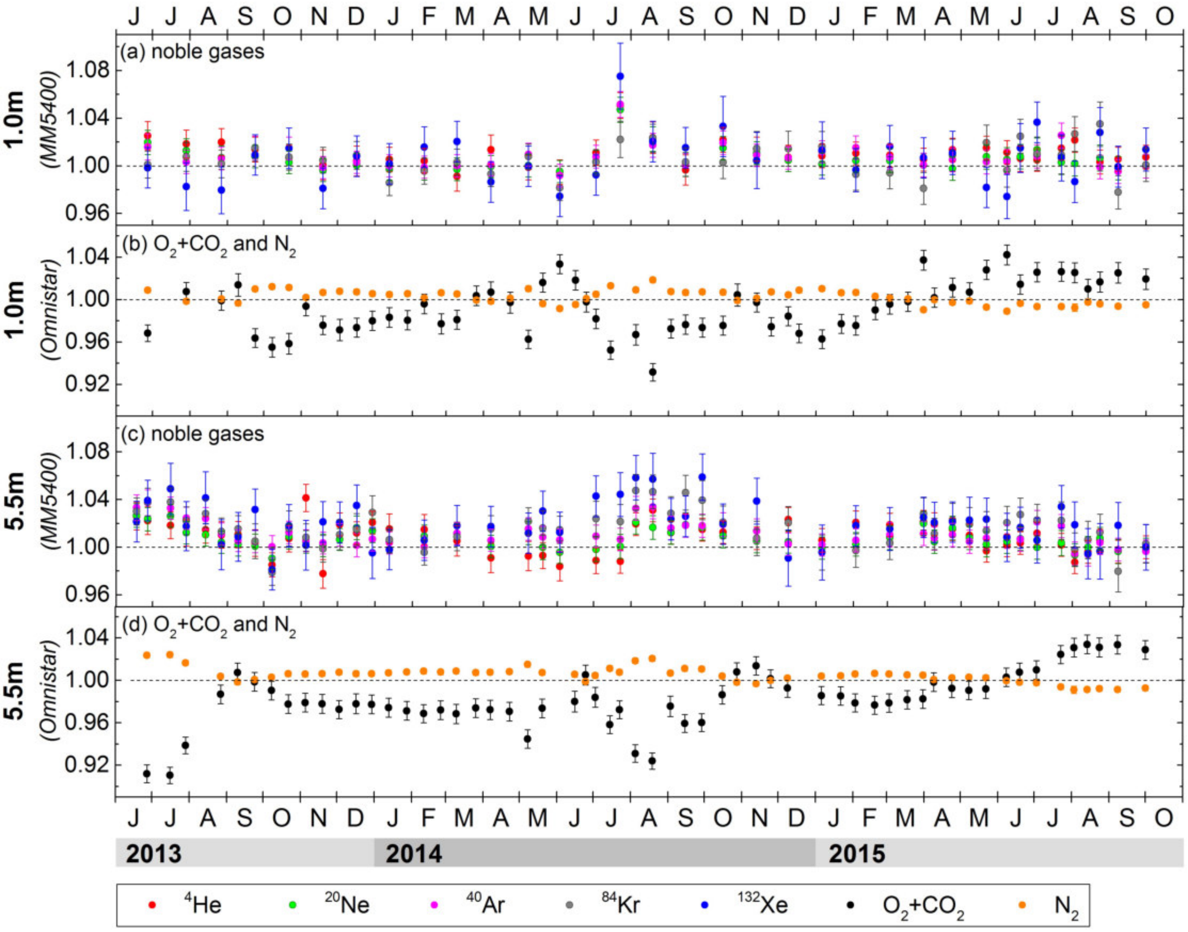

Figure 5.2: Mannheim: Time series of soil air composition near Mannheim at 1.0 m (panel (a) and (b)) and 5.5 m depth (panel (c) and (d)), respectively. Soil air mixing ratios of O_2+CO_2, N_2 and NGs are normalized to their values in dry atmospheric air, respectively. Thus, the black dashed lines indicate atmospheric composition.

with respect to its atmospheric value is observed during the summers of 2013 and 2014, while a slight decrease occurs generally during winter season. An opposite behavior – meaning a higher value of O_2+CO_2 than in atmospheric air – is observed during the entire summer 2015 as well as for very short periods during the preceding summers. Recorded trends of O_2+CO_2 are constrained by soil moisture and temperature as discussed later in this chapter. This explains stronger short-term fluctuations of O_2+CO_2 at shallow soil depths compared to deeper depths.

As a consequence of advective balancing, a decrease of O_2+CO_2 is expected to go along with an increase of the mixing ratios of the remaining gases. In the following, deviations are usually referenced to respective gas-specific mixing ratios in dry atmospheric air. Mixing ratios of N_2 show a significant increase whenever O_2+CO_2 falls below the atmospheric value and vice versa (see Fig. 5.2(b)/(d)). At the sampling site near Mannheim, N_2 may be treated as an inert gas, since any possible release or consumption by microbial activity is obviously negligible regarding the correlation with O_2+CO_2. A similar response effect on O_2+CO_2 is observed for NG mixing ratios (see Fig. 5.2(a)/(c)). Data indicate significant enhancements by up to several percent, especially during the summers of 2013 and 2014. A slight but non-significant increase of NG mixing ratios is observed during winter seasons, when O_2+CO_2 is slightly below the atmospheric value. During summer 2015, a decrease of the inert gas mixing ratios below their respective atmospheric values would be expected, regarding the observed enhancement of O_2+CO_2 in soil air. Such a decrease is only observed for N_2, but not significantly for NGs. During the most of the time of the study, enhanced NG mixing ratios in soil air go along with a permanent mass-dependent fractionation, meaning a stronger enhancement of heavier NGs like xenon, compared to lighter NGs like neon. Interestingly, such a pattern is observed even during periods of nearly atmospheric sum values of O_2+CO_2, which is discussed later in the context of modeling results. Table 5.1 summarizes average soil air composition data for summer and winter seasons, respectively.

The influence of O_2+CO_2 on mixing ratios of inert gases in soil air is shown in detail in Fig. 5.3. Measured mixing ratios of N_2 and NGs in soil air temporarily deviate significantly from the respective atmospheric values, while correlating with O_2+CO_2. Such a relationship was also found during recent studies by Mayer (2012) and Freundt et al. (2013). However, the above mentioned permanent fractionation – mainly visible as an offset of xenon data in Fig. 5.3(b) – cannot be explained by considering just O_2+CO_2 data. This gives a first hint on further subsurface transport processes affecting soil gas composition, as will be discussed later.

A further note shall be given to the reliability of the presented data. ^{40}Ar data measured by the

Table 5.1: Mannheim: Sum values of O_2+CO_2 [vol%] and mixing ratios of N_2/NGs (normalized to respective atmospheric values) in soil air at 5.5 m depth. Data are given as an average for summer (S) seasons 2013/14 and 2015, respectively (May–Oct) as well as for all winter (W) seasons (Nov–Apr). The unusually dry summer in 2015 is given separately. With respect to atmospheric air, mixing ratios of NGs are enhanced on average by (1.8 ± 1.2) % during the summers 2013/14, by (0.6 ± 1.3) % during summer 2015 and by (1.0 ± 1.2) % during winter.

	O_2+CO_2	ΔO_2+CO_2	**N_2**	ΔN_2	**He**	ΔHe	**Ne**	ΔNe	**Ar**	ΔAr	**Kr**	ΔKr	**Xe**	ΔXe
	[vol%]	[vol%]	deviations from mixing ratios in dry atm. air [%]											
S 2013/14	**20.3**	0.2	**0.9**	0.2	**0.8**	1.1	**1.0**	1.0	**1.8**	1.0	**2.4**	1.3	**2.8**	1.9
S 2015	**21.3**	0.2	**-0.4**	0.2	**0.1**	0.9	**0.2**	1.0	**0.5**	1.0	**1.1**	1.5	**1.3**	1.9
W 2013-15	**20.6**	0.2	**0.5**	0.2	**1.3**	1.1	**0.8**	1.0	**0.7**	1.0	**1.0**	1.3	**1.4**	1.8

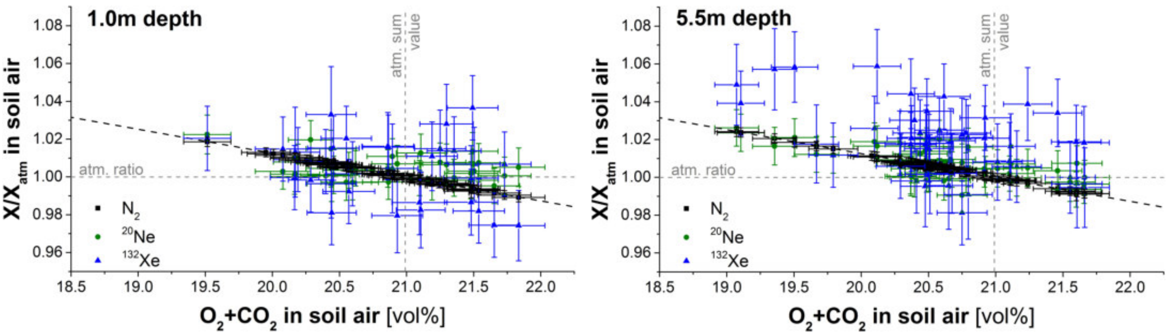

(a) Soil air samples from 1.0 m depth.

(b) Soil air samples from 5.5 m depth.

Figure 5.3: Mannheim: Correlation of O_2+CO_2 concentrations (in units of vol%) with mixing ratios of N_2, ^{20}Ne and ^{132}Xe in soil air. The black dashed line indicates the theoretically expected relationship as described in chapter 3.3.1.

MM5400 mass spectrometer and by the *Omnistar* device were compared to each other, resulting in a very good agreement of both analysis methods with a non-significant deviation of on average 0.25 % (see appendix B.1). This offset may be of purely statistical nature, considering the reproducibility of both methods, which is 0.5 % (*MM5400*) and 0.9 % (*Omnistar*), respectively. Even though such a comparison is only possible for ^{40}Ar data (since no further gas species was analyzed by both of these devices), the obtained agreement at least suggests a general reliability of measured NG data. In particular, the found data offset of heavier gas species in Fig. 5.3 seems to be not caused by a systematical bias of the estimated sample gas amount during the *MM5400* data evaluation.

The above shown seasonality of O_2+CO_2 was found to occur simultaneously at all sampled depths, indicating an effective soil aeration. Radon data were additionally used to investigate this phenomenon as well as to check the sampled soil air for a possible contamination. Figure 5.4 illustrates time series of the detected ^{222}Rn activities in soil air at all sampled depths. Data show a clear seasonality, going along with enhanced activities during winter time. Such a behavior was already observed by Mayer (2012) during a study in the same sampling region and originates from a varying soil ventilation due to higher soil moisture contents during winter time. The impact of soil moisture is also visible in absolute values of measured activities which are generally higher in loamy soil layers (see 1.0 m depth) compared to sandy layers (see remaining depths). This effect is also visible at 6.5 m depth in June 2014: Directly after the groundwater table decreased below this depth, the ambient soil layer contained still a higher soil water content. The measured local ^{222}Rn activity was, thus, significantly higher than in the subsequent weeks.

For all sampled depths, the consistent seasonality of ^{222}Rn data gives no evidence for any contamination on long-term scale, neither by atmospheric air, nor by air from another than the actually sampled soil depth. This conclusion is based on the assumption that another one than the actually sampled soil depth exhibits generally a (at least slightly) different radon activity, while atmospheric air is anyway characterized by a negligible radon activity.

The rather short time scales of subsurface ^{222}Rn fluctuations (in the order of days to weeks), without any appreciable time shift across the soil profile, point out the crucial role of advective flow for sub-

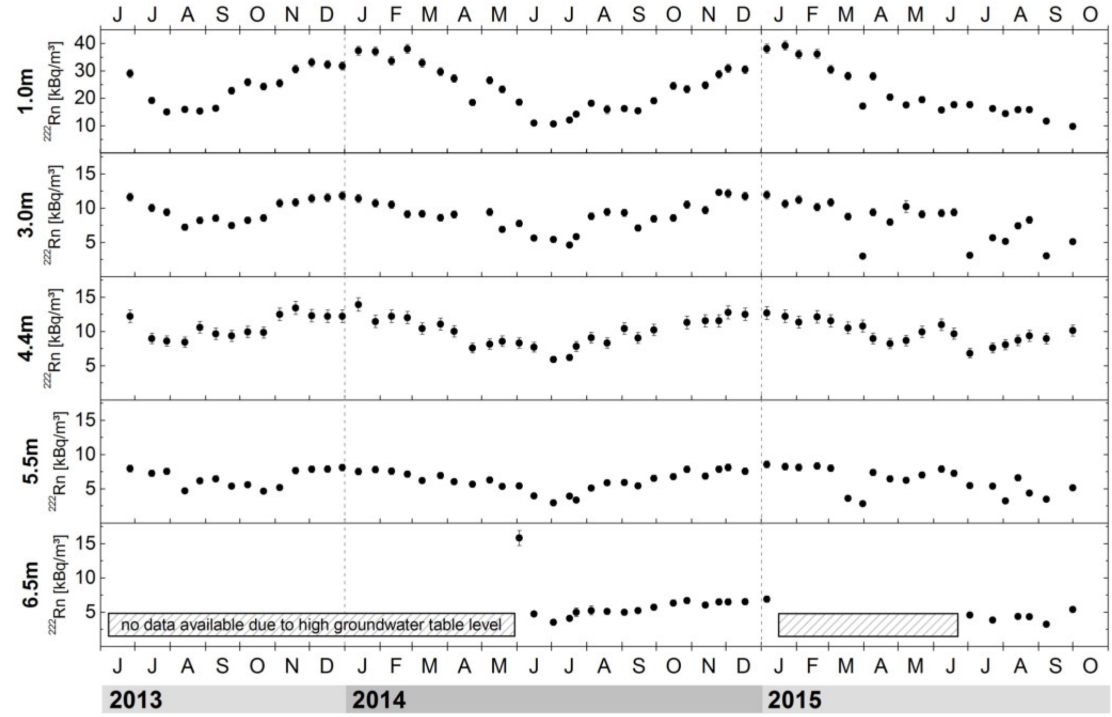

Figure 5.4: Mannheim: Measured activities of ^{222}Rn [kBq/m^3] in soil air at all sampled depths. Note that a more extended scale is depicted for 1.0 m depth, where higher activities are observed compared to the remaining sampled depths.

surface gas transport. This kind of transport is typically induced by barometric pressure fluctuations or penetrating water fronts (Nazaroff, 1992) and may go along with gas migration velocities of several meters per day (Clements and Wilkening, 1974; Elberling et al., 1998).
Measured activities of the short-lived ^{220}Rn give no evidence for short-term leakages or a change of soil air origin during a 30 min pumping procedure. Corresponding data are given in appendix B.4.

5.1.2 Soil moisture and -temperature

Soil moisture and soil temperature are of particular interest for this study, due to their influence on microbial activity, but also on subsurface gas dynamics. Figure 5.5 shows recorded time series of volumetric soil moisture contents at the sampling site. The two applied measurement methods (individual TDR measurements and continuous FDR records) result in strong deviations at 20 cm and 40 cm depth during winter time and, in contrast, in a generally good agreement at 60 cm depth. The most obvious reason for this difference is the calibration procedure of the FDR sensors. For calibration, a mixture of soil material from the topmost meter at the sampling site was used. This soil material might be not representative for the topmost two sampling depths, thus causing the obtained data bias observed in particular for soil moisture contents near saturation conditions. However, both measurement methods agree very well regarding their relative trends in time. Continuously recorded FDR data allow to identify only a few sharp variations of soil moisture on short time scales – occurring after strong precipitation events. Interestingly, such short-term fluctuations are reasonably well detected even by weekly TDR measurements. In the following, only TDR measurements are consid-

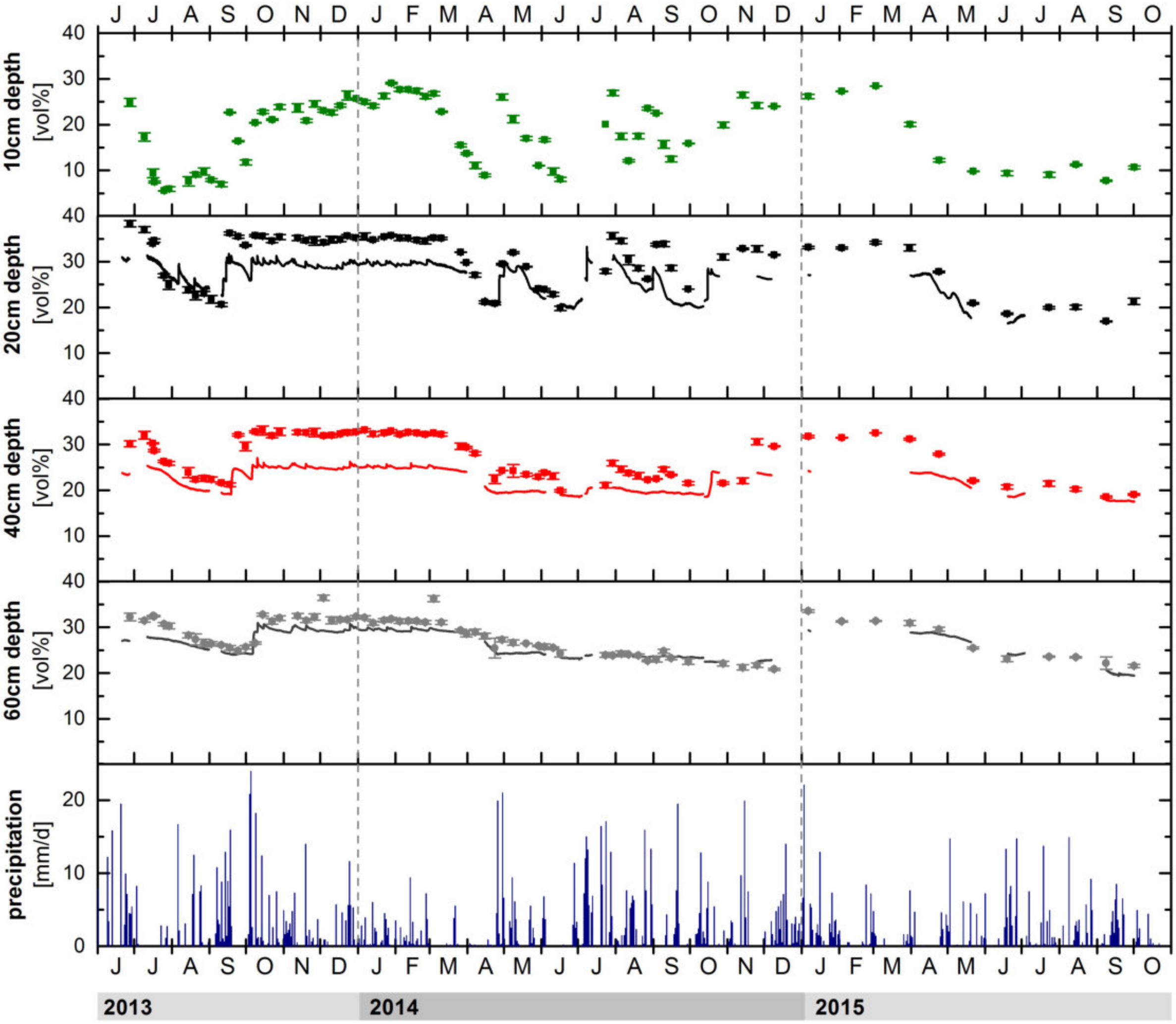

Figure 5.5: Mannheim: Time series of volumetric soil moisture contents at 10 cm, 20 cm, 40 cm and 60 cm depth, respectively. Continuous data logger measurements (FDR) are indicated as lines, while points illustrate TDR measurements. For FDR data, a measurement uncertainty of 1 vol% is assumed, based on calibration measurements. The uncertainty of TDR data results from the standard deviation of three independent measurements, respectively, and is depicted in the graph. Daily sums of precipitation are obtained from DWD (2016).

ered, since these data are available for nearly every sampling day, while some time periods of FDR data are missing due to technical problems.

Volumetric soil moisture contents show more pronounced fluctuations at shallow soil depths, as it is expected due to a stronger influence of evaporation at the soil surface. During winter time, the soil at the sampling site seems to be nearly water saturated for several months at all sampled depths. From spring on, soil moisture is decreasing down to about 10 vol% at 10 cm depth and 20 vol% at deeper layers, respectively. Soil moisture contents at shallower soil depths are influenced by stronger precipitation events, leading to variations by more than 10 vol% within a few days. Such variations continue to deeper layers time shifted and damped, while precipitation induced short-term variations are not observable at 60 cm depth. The trend of soil moisture data in summer 2015 differs from that observed in the two previous years, caused by unusually dry conditions. Obviously, there was no precipitation event strong enough to initiate an increase in soil moisture.

Figure 5.6 shows the time series of recorded soil temperatures at different soil depths. Fluctuations occur due to atmospheric temperature changes on seasonal as well as on daily time scales and are damped with increasing soil depth. While the seasonal temperature amplitude accounts for about 8.8°C directly below the soil surface, it is damped to about 0.5°C at 6.5 m depth, where the soil temperature fluctuates around a mean value of 11.8°C. This is in good agreement with the local mean annual atmospheric temperature (MAAT) of 11.6°C determined from long-term data of DWD (2016). A clear depth dependent time shift is observable.

A final remark shall be given to the depth-dependent annual means of subsurface temperature regimes. A crucial aspect of NGT studies is the relationship between MAAT, mean annual soil temperature (MAST) and water table temperature (WTT). In this study, corresponding WTT data are available, which is why no further assumptions are necessary concerning its relationship to the local MAAT. However, such a rather comfortable situation is usually not achieved in NGT studies (Aeschbach-Hertig and Solomon, 2013). As shown in Fig. 5.6, recorded MASTs[2] depend indeed on soil depth, while approaching the MAAT of 11.6°C with increasing depth. These warmer MASTs in the topmost soil may be a consequence of generally higher atmospheric temperatures in 2014 and 2015, compared to 2013 (DWD, 2016). This confirms a stronger variability of topmost MASTs and a corresponding damping with increasing depth. Another origin of depth-dependent MASTs might be less vegetative cover and, thus, a higher insolation (Powell et al., 1988; Beyerle et al., 2003). Here, the mentioned finding of MASTs approaching the MAAT with increasing soil depth would imply a rather local phenomenon, which is challenged since the sampling site can be seen as representative for the surrounding region.

---

[2] Given MASTs are determined for the sampling period between June 2013 and June 2015.

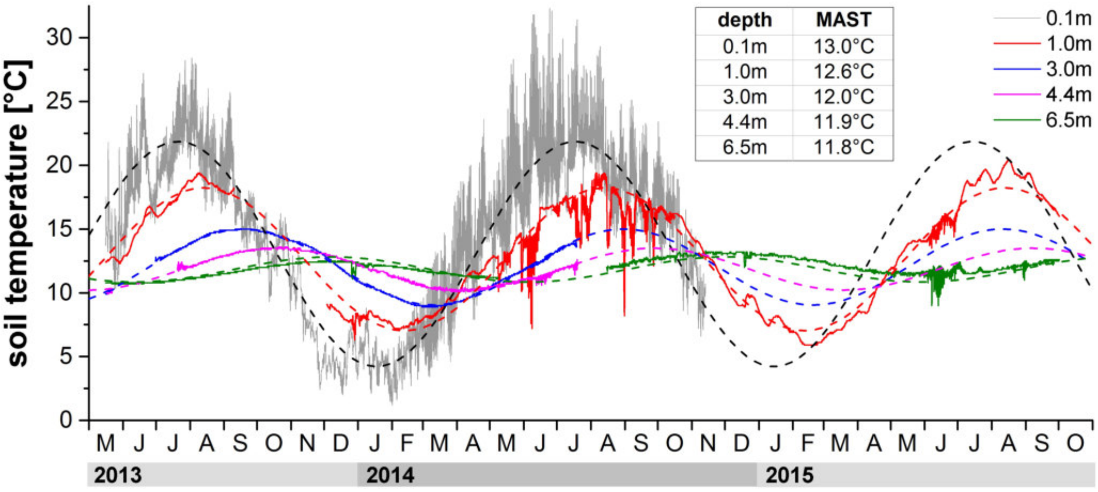

Figure 5.6: Mannheim: Time series of soil temperature at 0.1 m, 1.0 m, 3.0 m, 4.4 m and 6.5 m depth, respectively. Due to technical defects, data are missing for several time spans. Mean annual soil temperatures (MASTs) are determined from sine fits (see dashed lines).

5.2 Saturated zone

In the following, measured data from groundwater samplings at the shallow and deep well are presented, respectively. First, physical groundwater parameters are shown, followed by dissolved gas contents and stable isotopes of water. After this, excess air models are applied to describe the measured NG data.

5.2.1 Physical groundwater parameters

Figure 5.7 summarizes time series of physical groundwater parameters at the shallow well, beginning with the groundwater table level. Two characteristic trends can be distinguished: Strong water table level increases were observed in June 2013 and again in January 2015, accounting for more than 0.7 m and 0.5 m during one month, respectively. This is a result of high amounts of precipitation during these times (see chapter 5.1.2). A continuous decrease of the water table level is found between June 2013 and January 2015 as well as from March 2015 on, with a rate of about 0.5 m during half a year. After each sampling procedure, a return to original conditions was observed immediately after the pump was turned off, indicating only a short temporal impact on the local groundwater level inside the well.

Figure 5.7(b) illustrates the measured water table temperature (WTT). As discussed in chapter 3.1.6, data from above-ground measurements by the *WTW Multi 340i* device are probably biased due to heat released by the submersible pump. This is also indicated by continuously logged data as a small WTT increase during each pumping procedure, yet vanishing directly after pumping was finished. Thus, all WTT data referred to in the following of in this study originate from data loggers. The recorded WTT shows a clear seasonality with an average value of (11.6 ± 0.2)°C, an amplitude of 0.7 – 1.1°C and a maximum in late fall, which is in good agreement with previously presented soil temperature records. This is an important finding concerning the following data evaluation, indicating that there is no systematic bias between WTT and MAAT at the sampling site of this study. A decoupling by up to several °C may be a consequence of vegetation and forest cover (Stute and Sonntag, 1992) as well as of snow cover (Bartlett et al., 2004). The data thus confirm that such a temperature bias does not have to be considered in this study. A possible decoupling of local WTT and MAAT during the past decades – induced by slightly different climatic conditions – is also neglected in the following, based on numerical modeling experiments of Cey (2009) showing possible decoupling effects to be insignificant given the usual precision of NGTs.

Measured oxygen contents are depicted in Fig. 5.7(c). The data show a relative saturation between 60 % and 70 %. The observed correlation with water table fluctuations results from an input of oxygen into the groundwater by excess air during water table rises, as described later in the context of dissolved NG contents. A slight increase of dissolved oxygen by a few percent was observed during the most of the sampling procedures, which declined directly after pumping finished.

Figure 5.7(d) shows the time series of electrical conductivity. Enhanced values during winter time may result from road salt since there is a paved road within a small distance from the sampling site. Such an effect was already supposed by Hall et al. (2012). A direct influence of the pumping proce-

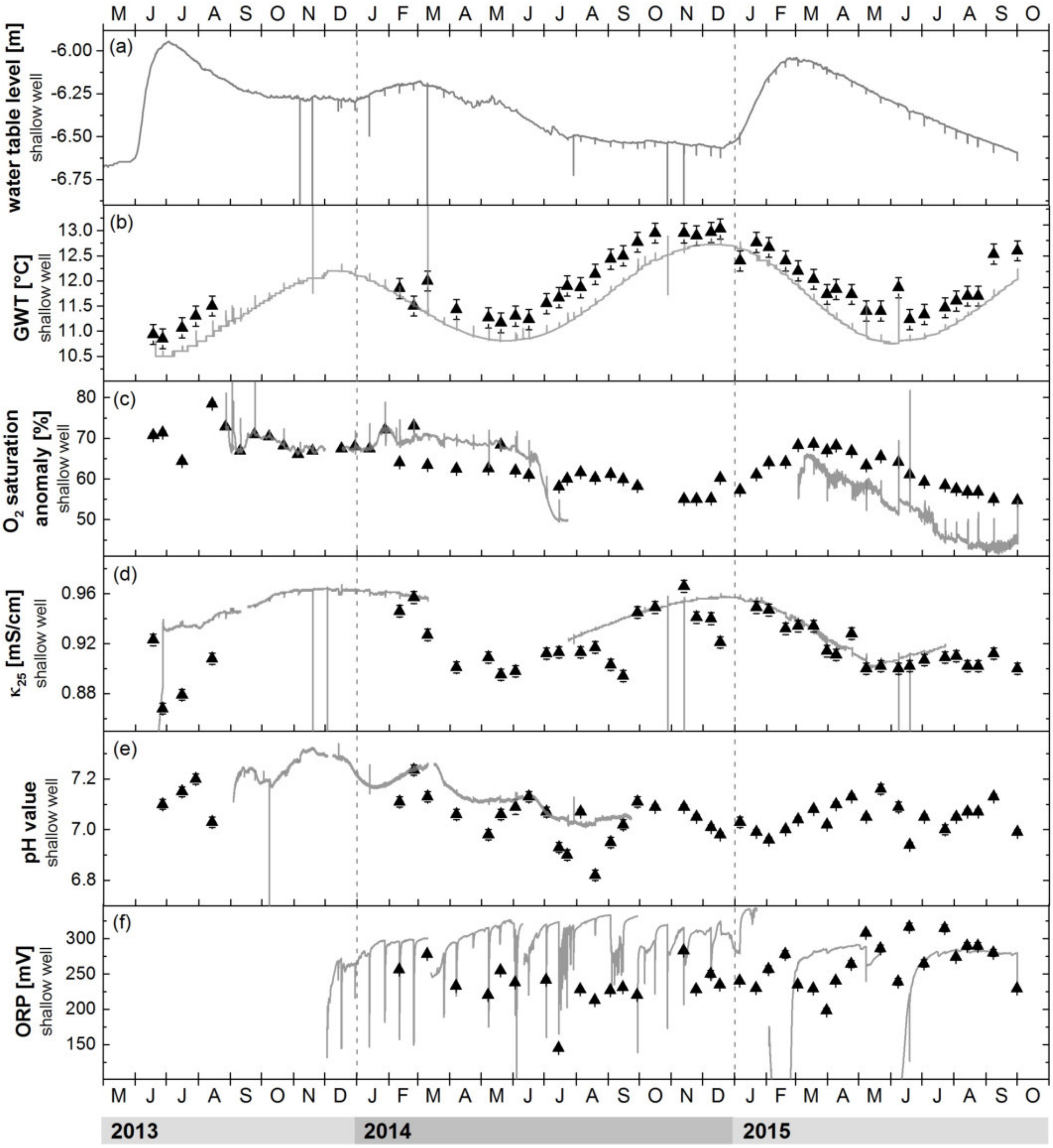

Figure 5.7: Mannheim: Measured time series of physical parameters at the shallow well. Data from continuously logging sensors are depicted as gray lines (uncertainties given in brackets), data measured by the *WTW Multi 340i* device as black triangles (uncertainties depicted in the figure). (a) Groundwater table level (uncertainty ±2 cm); (b) Water table temperature (WTT) [°C] (uncertainty ±0.2°C); (c) Oxygen saturation [%] (rel. uncertainty ±2 %); (d) Conductivity κ_{25} [mS/cm] (rel. uncertainty ±2 %); (e) pH value (uncertainty ±0.2); (f) ORP [mV] (uncertainty ±1 mV).

dure is not observable.

Figure 5.7(e) gives an overview of measured pH values which indicate neutral conditions during nearly the entire study, while slightly alkaline levels are observed during the first year. There is no seasonality observable, as well as no influence of the pumping procedure on pH values.

The oxidation-reduction potential (ORP)[3] shows positive values in a range between 200 mV and

---

[3] The ORP is measured in units of mV as voltage difference between an Ag and a Pt electrode, while positive values indicate oxidizing conditions and negative values indicate reducing conditions.

300 mV during the entire study (see Fig. 5.7(f)). This indicates oxidizing conditions which fits the observation of oxygen saturations above 60 %. This range of values excludes local methanogenesis which typically occurs for very low ORP values between −175 mV and −400 mV (Gerardi, 2007). ORP data are affected strongest by the pumping procedure, resulting in a temporal decrease by 100 − 150 mV, persisting for several days before returning to previous undisturbed values. From 2015 on, a non-return valve was installed above the submersible pump, preventing a back-flow of the water standing within the tube after sampling. Obviously, ORP values show no declines during and after samplings from this time on, aside from battery changes and recalibrations of the loggers.

All just presented parameter records indicate that there is no significant short-term influence of strong precipitation events on local groundwater. As discussed in chapter 3.1.6, only data measured by the *WTW Multi 340i* device will be considered in the following for any discussion concerning physical groundwater parameters (except for temperature) at the shallow well.

5.2.2 Noble gases and stable isotopes of water

Time trends of dissolved NGs and stable isotopes of water are shown in Fig. 5.8. The groundwater table trend as well as ^{3}H−^{3}He ages[4] of sampled water are illustrated in Fig. 5.8(a). Obtained ^{3}H−^{3}He ages fluctuate between 2.6 and 15.4 years, while increasing when the water table level is falling. Groundwater ages are significantly lower in June 2013 than in January 2015, indicating a stronger input of new recharged water in June 2013, even though unfortunately no age data are available before this study started.

Absolute concentrations of neon and xenon are depicted in Fig. 5.8(c). Caused by its low and hardly temperature dependent solubility, neon is a suitable indicator for groundwater table fluctuations and the amount of excess air, while the dissolved xenon content is strongly determined by the temperature during gas/water partitioning, due to the strong temperature dependence of its comparatively high solubility (Aeschbach-Hertig and Solomon, 2013). An increasing water table leads, due to an increasing hydrostatic pressure, to a higher amount of excess air as can be seen in summer 2013 as well as during spring 2015. In contrast, excess air is declining when the water level is falling. As a consequence, absolute neon contents correlate with groundwater table level, resulting in a correlation coefficient of 0.79 (see appendix B.2). Dissolved xenon contents show a negative correlation with the local WTT, going along with a correlation coefficient of −0.45. This correlation is not as clear as that observed for neon data, caused by the higher uncertainty of xenon measurements. Regarding the time trend of the WTT with a higher maximum in 2014 than in 2013, absolute xenon concentrations are expected to decrease more in 2014 than actually observed. This may result from an impact of deeper groundwater, exhibiting higher NG concentrations (as shown later). The continuous increase of the shallow groundwater age during the entire year 2014 indicates an input of older or rather deeper groundwater. This may compensate at least partially a temperature induced decrease of dissolved xenon contents.

Time series of NG concentrations are complemented by a relative analysis. For this purpose, NG data in Fig. 5.8(d) are normalized to the equilibrium component which is reflecting a gas exchange with atmospheric air, also denoted as *air equilibrated water* (AEW). Depicted data thus reflect a saturation

---

[4] Since no tritium data were available for all analyzed NG samples from the second half of this study, the resulting ages were estimated applying an average value of the available and hardly fluctuating tritium values.

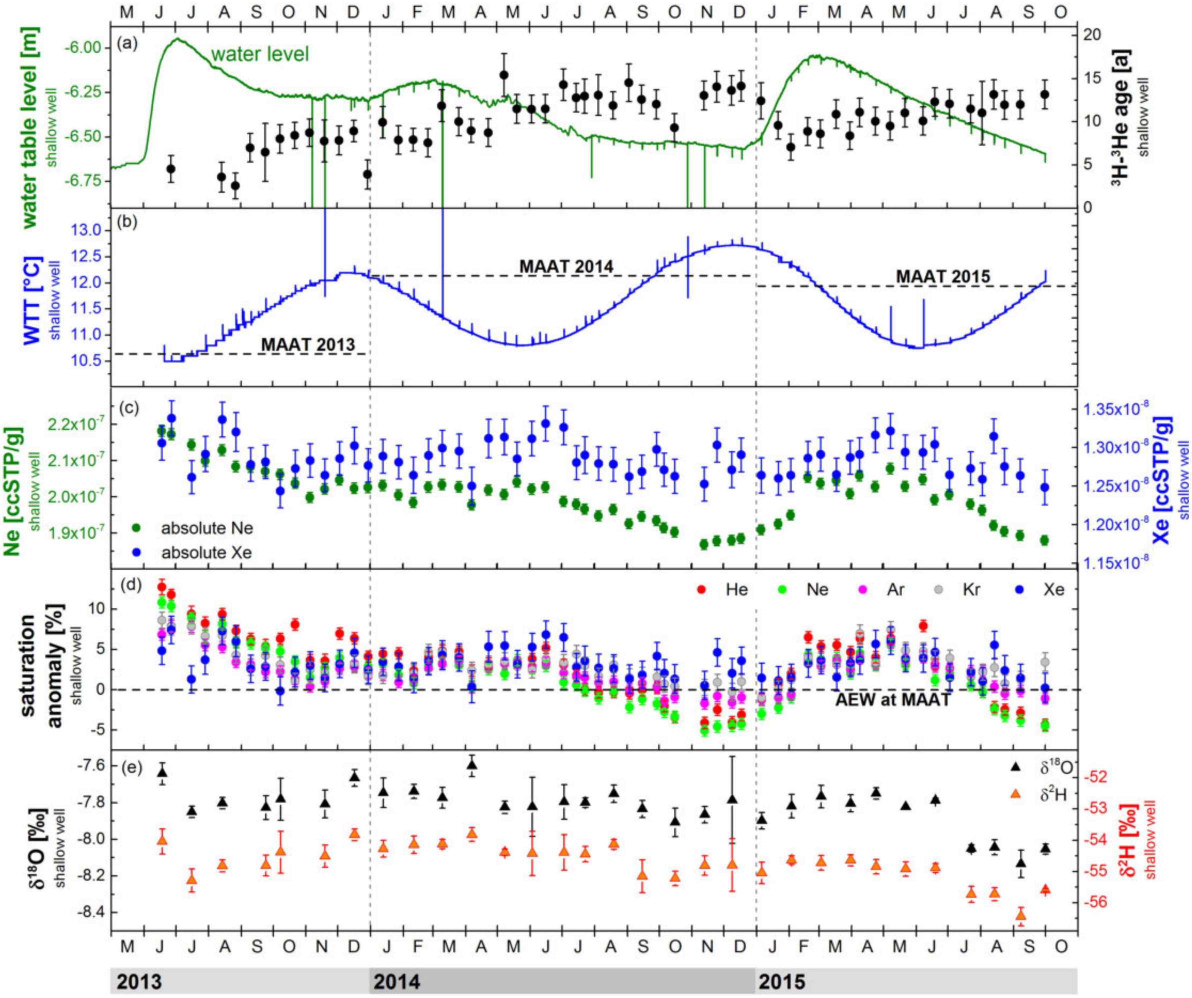

Figure 5.8: Mannheim: Measured time series of NGs and stable isotopes at the shallow well. (a) Groundwater table level (uncertainty ±2 cm) and ^{3}H–^{3}He ages (black symbols); (b) Water table temperature (WTT); (c) Concentrations of Ne and Xe, given in units of cm^3 at standard conditions per g of water (ccSTP/g); (d) NG data normalized to air equilibrated water (AEW) at 11.2°C ("average MAAT" in the expected mean recharge year 2004); (e) Stable isotopes of water: δ^{18}O and δ^{2}H, both relative to the VSMOW standard.

anomaly with respect to the supposed equilibrium component. A quantification of AEW requires an estimation of the equilibration temperature, for which the MAAT of the expected recharge year provides an appropriate estimation. The average of all ^{3}H–^{3}He ages accounts for (10.2 ± 1.8) years, indicating 2004 as average recharge year[5] for shallow well groundwater, going along with an "average MAAT" of 11.2°C.

Supersaturations of neon account for up to ΔNe = 6 – 11 %, as a consequence of an increasing water table or rather of the excess air phenomenon – going along with the typical stronger enrichment of lighter NGs with respect to heavier NGs. However, heavier NGs as krypton and xenon seem to be more enhanced as it is expected for such small values of ΔNe. During periods of falling water table,

---

[5] It has to be considered that ^{3}H–^{3}He ages typically reflect a mixture of diverse water parcels recharged at different times in the past. This motivates the use of an "average MAAT" resulting from a linear fit based on measured MAATs between 1980 and 2015 (see chapter 4.1). Thus, the "average MAAT" does not necessarily reflect the actually measured MAAT of a specific year.

ΔNe decreases down to −5 %. Such negative saturation anomalies are a clear indicator for groundwater degassing which typically occurs due to microbial gas production within the saturated zone, e.g. due to denitrification (Blicher-Mathiesen et al., 1998) or methanogenesis (Fortuin and Willemsen, 2005). The observed NG pattern during the degassing periods is explained by lighter NGs entering the arising gas phase rather than heavier NGs, caused by the mass-dependence of solubility. Degassing seems to be favored by a decreasing water table or rather by a lower hydrostatic pressure. The availability of oxygen as well as high ORP values and the absence of CH_4 in deep soil air give a first hint on denitrification to cause the degassing phenomenon. The data in Fig. 5.8(d) show a stronger decrease of neon with respect to helium during degassing periods. Such a pattern cannot be explained by the mass-dependence of solubility and may be caused by diffusion from the unsaturated zone, leading to a faster balancing of helium degassing compared to that of neon. A final remark shall be given to the reliability of preceding explanations. It is very unlikely that the obtained negative saturation anomalies originate just from a wrong estimation of the AEW component. This follows from a very unrealistic equilibration temperature of more than about 17°C which would be necessary to obtain positive values of ΔNe during the entire study.
A time series of stable isotopes of water is given in Fig. 5.8(e), showing values of $\delta^{18}O$ and $\delta^{2}H$ relative to the VSMOW standard. There is no seasonality observable, even though a significant step-like decrease occurs during the last 4 months of the study. A detailed description of stable isotope data is given later together with the deep well results.

Figure 5.9 summarizes measured parameters from deep well groundwater, depicted analogously to the just described shallow well records. The determined $^3H-^3He$ ages in Fig. 5.9(a) are significantly higher than the ages obtained at the shallow well. While the average age accounts for (23.0 ± 2.0) years in 2013, it shows a stepwise increase to (30.7 ± 2.2) years from 2014 on. Younger ages in 2013 result probably from the unusually strong recharge in spring 2013, since a preceding measurement at this deep well in March 2013 (not depicted here), thus before the period of strong precipitation, resulted in a $^3H-^3He$ age of (30.6 ± 2.1) years.
The recorded water temperature is denoted as groundwater temperature (GWT) instead of WTT since it is not measured directly below the water table. Corresponding data were measured by the *WTW Multi 340i* device and are, thus, adjusted by the above mentioned temperature bias due to heat released by the pump. This procedure is appropriate since sampling at the two wells was done by an identical submersible pump. Corresponding data are depicted in Fig. 5.9(b) and show seasonal fluctuations with a maximum during summer time. There is a temporal shift of about 5 months between temperature trends of the two sampled wells. The amplitude of temperature fluctuations is smaller in the deep well, caused by the damping of atmospheric temperature variations with increasing soil depth. The average deep well GWT in 2014 is (11.6 ± 0.2)°C and, thus, in a very good agreement with the average WTT of shallow well water as well as the MAAT, respectively.
Concentrations of neon and xenon in deep well groundwater do not show any systematic short-term variations such as seasonal fluctuations (see Fig. 5.9(c)). The concentrations are higher compared to those observed in shallow well water, resulting from a higher amount of excess air. To determine saturation anomalies of NGs, the AEW composition in Fig. 5.9(d) is determined based on a

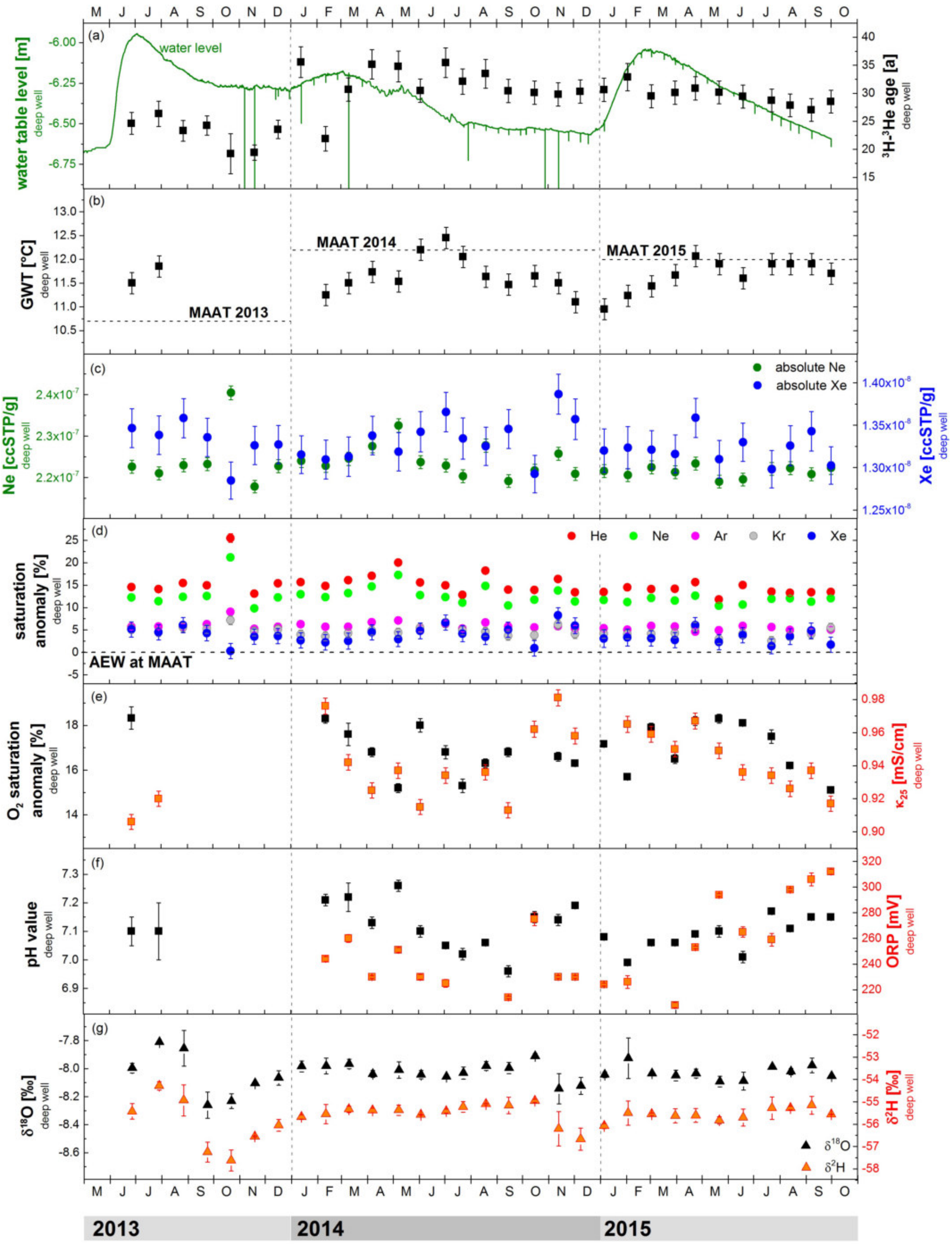

Figure 5.9: Mannheim: Measured time series at the deep well. (a) Groundwater table level and ^{3}H−^{3}He ages (black symbols); (b) Groundwater temperature (GWT); (c) Concentrations of Ne and Xe, given in units of ccSTP/g; (d) NG data normalized to air equilibrated water (AEW) at 10.4°C ("average MAAT" in the expected mean recharge year 1985); (e) Oxygen saturation anomaly [%] and conductivity κ_{25} [mS/cm]; (f) pH value and ORP [mV]; (g) Stable isotopes of water: δ^{18}O and δ^2H, both relative to the VSMOW standard.

average groundwater age of all deep well samples, which is (28.9 ± 2.2) years and gives 1985 as recharge year with an "average MAAT" of 10.4°C. Resulting saturation anomalies are rather uniform at $\Delta Ne = 12.8\,\%$ and $\Delta Xe = 3.8\,\%$. Xenon data reflect an unusual relative enhancement of heavier NGs compared to lighter NGs, as above mentioned for shallow well samples. Obviously, fluctuations of dissolved NG contents on time scales of months – as observed in shallow well groundwater – are not found any more in deeper groundwater, indicating a corresponding smoothing through a vertical distance of about several meters. This is likely a consequence of dispersion processes during the additional water residence time within the aquifer.

Measured oxygen contents in Fig. 5.9(e) show hardly fluctuations. The deep well samplings result in oxygen contents below 20 % saturation – thus indicating significantly less oxygen than found in shallow well water. Conductivity data show an enhancement during winter time as well as generally similar values at both wells.

Recorded pH values in Fig. 5.9(f) indicate permanently neutral conditions with slightly alkaline levels during the first year of the study. As already observed at the shallow well, ORP values vary within a range between 200 mV and 300 mV, indicating oxidizing conditions which does not fit to the observed low oxygen saturation.

Values of $\delta^{18}O$ and $\delta^{2}H$ in Fig. 5.9(g) do not show any seasonality. Deep well samples show a stronger depletion compared to samples from the shallow well, shifted by on average about 0.2 ‰ for $\delta^{18}O$ and 0.9 ‰ for $\delta^{2}H$. As Fig. 5.10 shows, measured stable isotope data of both wells are in good agreement with the local meteoric water line (LMWL). The isotopic composition of sampled groundwater from both wells thus indicates no significant isotopic fractionation due to evaporation.

All measured concentrations of NGs and tritium in groundwater as well as stable isotope data are listed in appendix B.8, B.13 and B.12, respectively.

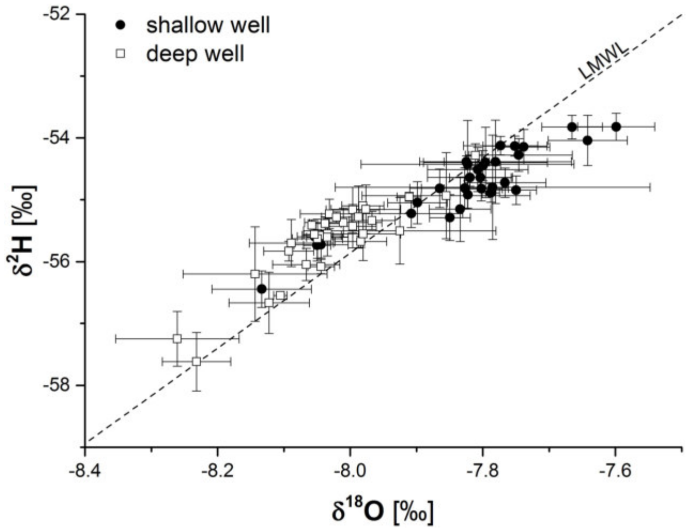

Figure 5.10: Mannheim: Stable isotopes of water: $\delta^{18}O$ and $\delta^{2}H$, both relative to the VSMOW standard. The local meteoric water line (LMWL) is determined by a linear fit as $\delta^2H\,[‰] = 7.7 \cdot \delta^{18}O\,[‰] + 5.74\,‰$, based on measurements of GNIP (2016) in Karlsruhe (Germany).

5.2.3 Excess air model fits and NGT determination

Measured NG concentrations of groundwater samples are applied to estimate NGTs. The evaluation of obtained NGTs is based on certain reference temperatures: The measured water table temperature (WTT) at the shallow well is assumed to reflect the equilibration temperature for water sampled at this well. In contrast, for deep well groundwater, the "average MAAT" of the expected recharge year is assumed to reflect the equilibration temperature, motivated by an increasing trend of the "average MAAT" during the last decades. These assumptions will be motivated later in this chapter.

A so-called Xe-Ne plot as depicted in Fig. 5.11 allows for a very simple graphical analysis of NG concentrations in groundwater. Referring to the small amount of excess air in shallow well samples, a NGT estimate already results from regarding just Xe data or rather their position with respect to the equilibration line. Such an approach results in a systematic underestimation of the recorded WTT as shown in Fig. 5.11(a). Regarding deep well samples, a small but not negligible amount of excess air is found. Deep well NGTs are graphically estimated by assuming an atmospheric Xe/Ne ratio and, thus, no fractionation of the excess air component. This procedure is indicated as black arrows in Fig. 5.11(b), resulting again in an underestimation of the expected equilibration temperature.

Obviously, this first rough estimation suggests a discrepancy between estimated NGTs and expected equilibration temperatures. However, this approach involves only two of in total five measured NG species. Furthermore, it does imply a full dissolution of entrapped air bubbles, neglecting any fractionation of the excess air component, due to a partial air bubble dissolution or diffusive outgassing. This motivates an application of both an inverse modeling technique and sophisticated excess air model setups.

NG data from both sampled wells were used to perform least squares fits by applying different excess

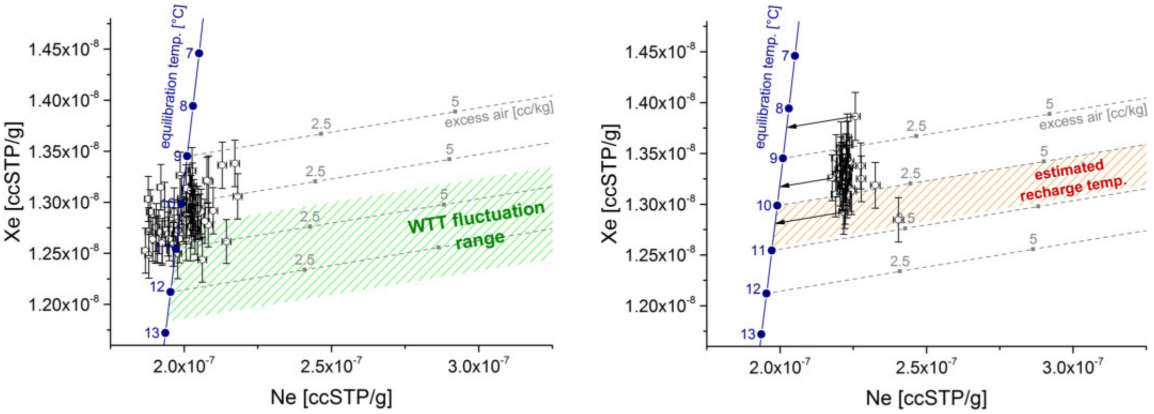

(a) Samples from the shallow well and range of WTT fluctuations (green dashed area).

(b) Samples from the deep well and estimated MAAT during recharge (red dashed area).

Figure 5.11: Mannheim: Xe-Ne plots illustrating dissolved NG contents of samples from both investigated wells. Blue lines illustrate the equilibrium component for a given equilibration temperature. Excess air lines are determined based on the assumption of an unfractionated excess air pattern (UA model approach). The amount of dissolved air (see gray numbers) is given in units of cc per kg of water. Estimated NGTs systematically underestimate the expected equilibration temperatures.

air models. For this study, two parameters are of main importance to discuss the reliability of fit results: the NG mixing ratio within the equilibrating gas phase and the resulting NGT. Fit outcomes going along with probabilities below 1 % are called into doubt and thus flagged in all figures. However, it has to be kept in mind that an adequate fit probability does not necessarily indicate that the applied model describes underlying physical processes in a reliable way. Results are first presented for the shallow well, followed by the deep well.

During the following analysis, the gas phase with which groundwater is equilibrating is referred to as “equilibrating gas phase” rather than just as “soil air”. This will be motivated later in detail, since it will turn out that entrapped air bubbles provide a gas phase for continuous equilibration. Consequently, the notation of an “equilibration temperature” is used rather than that of a “recharge temperature”, since this gas/water partitioning takes place independently of the actual recharge process. This notation shall just clarify the underlying physical processes, while the physical meaning of these expressions in terms of excess air model parameters is exactly the same.

To reduce the number of free parameters, salinity and ambient air pressure were estimated based on recorded site-specific data. A constant ambient air pressure at groundwater table level was assumed as 0.991 atm, based on data from DWD (2016) (see appendix B.6). Based on recorded conductivity data, an average salinity[6] of $S = 0.72$ g/kg was chosen. A detailed overview of the chosen start parameters as well as of all fit outcomes is given in appendix B.9 and B.10.

A further remark concerns the NG species included into the fit procedures. An usual approach is to omit helium due to non-atmospheric subsurface helium sources, meaning in particular the radiogenic component. For this specific sampling site, helium data were included, since both wells do not exhibit any radiogenic helium as can be concluded by atmospheric Ne/He ratios of all samples (see three isotope plot in appendix B.5).

Shallow well: evaluation for atmospheric NG mixing ratios in the equilibrating gas phase

Fits were performed assuming atmospheric NG mixing ratios in the equilibrating gas phase, as it is typically done in the literature (Aeschbach-Hertig and Solomon, 2013). Figure 5.12 gives an overview of the resulting NGT time series for the UA, CE and PR model, respectively. All fit outcomes are summarized in Tab. 5.2.

Obtained NGTs from all applied models show seasonal fluctuations as it was already described above for heavier NG concentrations in shallow well groundwater. The sampled groundwater seems to be permanently in equilibrium with a gaseous phase, which again motivates a comparison of NGTs with recorded WTTs.

The UA model provides a very simple description of excess air formation. Assuming atmospheric mixing ratios of NGs in the equilibrating gas phase, resulting NGTs underestimate the measured WTT, on average by (1.1 ± 0.2)°C, as shown in Fig. 5.12(a). During two periods, the resulting values of the parameter A (indicating the amount of dissolved excess air) are negative. Even though a

---

[6] For shallow well groundwater, a mean conductivity of $\kappa_{25} = 0.921$ mS/cm was obtained during the entire study. According to the formula $\kappa_{20} = \kappa_T \cdot (1.72118 - 0.0541369\,T + 1.14842 \cdot 10^{-3}\,T^2 - 1.222651 \cdot 10^{-5}\,T^3)$ (Bührer and Ambühl, 1975) with temperature T [°C] as well as the formula for the salinity $S = 0.87 \cdot 10^{-3}$ cm/µS $\cdot\, \kappa_{20}$ [µS/cm] (assuming calcium hydrogen carbonate dominates dissolved ions) (Täsch, 1987), a mean salinity of 0.72 g/kg results, which is assumed for both sampled wells.

negative value of A has no direct physical meaning, it gives a clear hint for groundwater degassing. Such a behavior is obtained for samples taken during the time spans between July 2014 and February 2015 as well as from August 2015 on. These time spans are in the following denoted as "degassing periods" and marked as shaded areas in Fig. 5.12.

The CE model proved to provide a reliable description of fractionated excess air components, but also in case of groundwater degassing (Aeschbach-Hertig et al., 2008). Obtained NGTs are depicted in Fig. 5.12(b). Besides T and A, the fractionation parameter F_{CE} is determined[7]. A start value of $F_{\mathrm{CE}} < 1$ is chosen for CE model fits of most samples, corresponding to a decrease of relative air bubble volume. In contrast, a start value of $F_{\mathrm{CE}} > 1$ is chosen for the degassing periods to ensure fits ending up in values of $F_{\mathrm{CE}} > 1$ – describing a relative increase of entrapped air bubble volumes as it is expected during degassing. Corresponding start values were selected based on the previously described A_{UA}[8] values from the UA model fit, with $F_{\mathrm{CE}} = 0$ for positive A_{UA} (no degassing) and

---

[7] The fractionation parameter $F_{\mathrm{CE}} = B/A$ reflects the quotient of respective air/water ratios in the initial state (A) and in the final state (B) of air bubble dissolution. Values of $0 < F_{\mathrm{CE}} < 1$ describe to a partial dissolution of entrapped air bubbles, while $F_{\mathrm{CE}} > 1$ is related to degassing or, in other words, to an increase of entrapped air bubbles. A full dissolution ($F_{\mathrm{CE}} \rightarrow 0$) represents an approach to the UA model case (see chapter 3.3.1).

[8] The index "UA" is labeled only in this phrase, to emphasize whether the excess air parameter is related to a CE model fit (denoted as A) or to an UA model fit (denoted as A_{UA}).

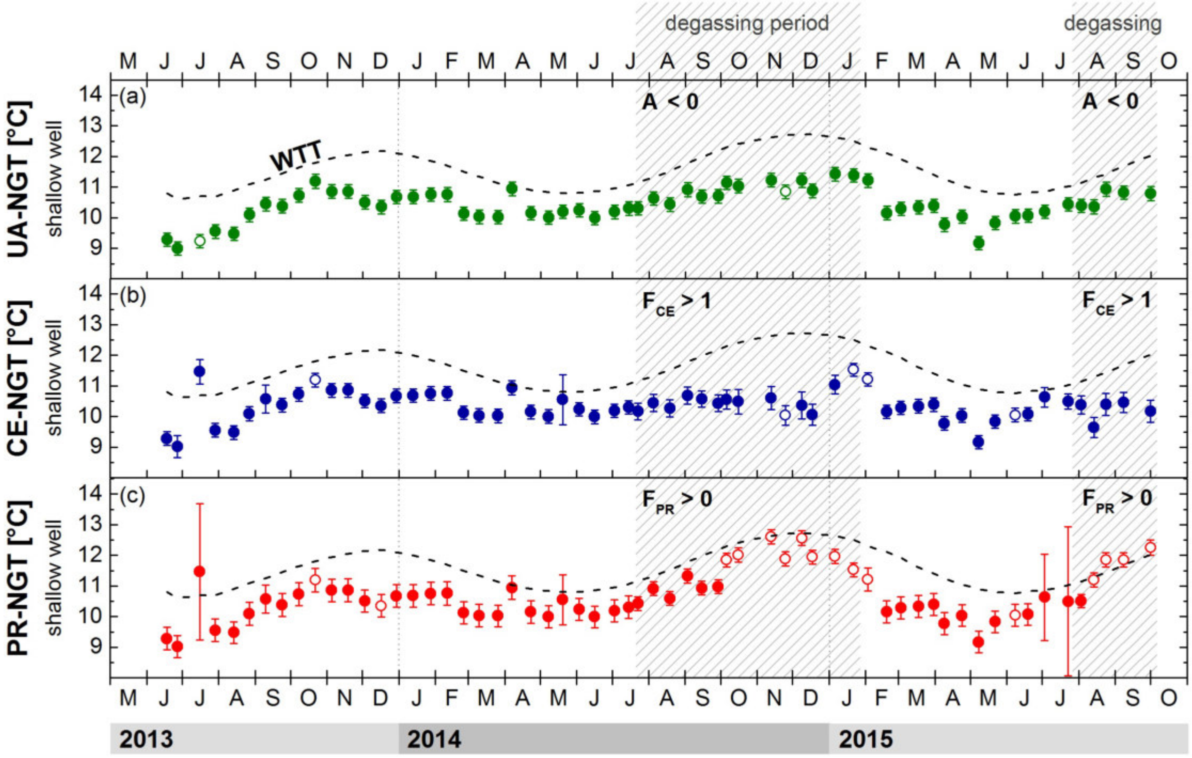

Figure 5.12: Mannheim: NGTs determined by excess air model fits as well as the recorded WTT (uncertainty 0.2°C) for shallow well samples. Fits were performed assuming atmospheric NG mixing ratios in the equilibrating gas phase. Fits with a probability above 1 % are illustrated as filled symbols, while open symbols indicate lower fit probabilities. All fits include data of He, Ne, Ar, Kr and Xe. (a) UA model fit; (b) CE model fit; (c) PR model fit.

$F_{\mathrm{CE}} = 3$ for negative A_{UA} (degassing phases).

For several samples, the CE model fit resulted in large negative F_{CE} values in combination with small positive values of A. Such a behavior was already investigated in detail by Jung and Aeschbach (2016) and described as *UA limit case*: Even though it seems physically not feasible, this outcome should be interpreted as a reasonable NG data description, implying an approximation of unfractionated excess air and a complete bubble dissolution as proposed by the UA model. The fit software offers the possibility of a *constrained* CE model fit which prevents from falling into large negative F_{CE} values. Based on an extended set of evaluated samples, Jung and Aeschbach (2016) propose to estimate parameter uncertainties of such a constrained fit by means of Monte Carlo simulations, which reproduce fit results very well while giving a more reliable estimate of uncertainties. Thus, for constrained fits, the obtained values of T, A and F_{CE} were taken as direct fit outcomes, while their respective uncertainties were estimated by Monte Carlo simulations. Such Monte Carlo simulations sometimes end up in different clusters, some of which are physically not reasonable. Thus, corresponding clusters of fit results were omitted to obtain a reliable uncertainty estimation as described in appendix B.9 and B.11.

Resulting NGTs from CE model fits underestimate the recorded WTT significantly by (1.2 ± 0.3)°C, as shown in Fig. 5.12(b). Apart from this offset, the WTT trend is not satisfactorily reproduced during the degassing periods, even though acceptable fit probabilities are obtained. Values of $F_{\mathrm{CE}} > 1$ are absolutely expected for degassed samples, but the CE model fits result in comparatively high and strongly uncertain values, accounting on average for $A = (0.05 \pm 0.05)$ cc/g during the degassing periods. Except of the two degassing periods, Monte Carlo simulations of most samples group into two clusters, one of which corresponds to a parameter of $F_{\mathrm{CE}} = 0$, while the other cluster belongs to values of $F_{\mathrm{CE}} \approx 0.8 - 1.0$. Such a phenomenon was already described by Jung et al. (2013) and seems to be a consequence of a small amount of excess air[9]. In this case, the parameter F_{CE} does not allow for reliable conclusions about the extent of change in entrapped gas amount. However, both mentioned clusters end up in the same equilibration temperature which can still be seen as a reliable estimate.

Given the recorded trend of the WTT, the CE model was also applied to estimate the ambient air pressure during equilibration, which reflects NG mixing ratios[10] in the equilibrating gas phase. Thus, a value of $p^* = 1$ indicates atmospheric mixing ratios, while higher values reflect correspondingly enhanced NG mixing ratios. Neglecting degassing periods, this fit scenario results in an average value of $p^* = 1.022 \pm 0.011$ which implies a NG enhancement by (3.1 ± 1.1) % in the equilibrating gas phase. This is in good agreement with the value derived from soil air composition in May/June 2013. Samples from the degassing periods were excluded for this fit procedure due to the above mentioned difficulties of the CE model to describe dissolved NG contents during these time spans.

---

[9] Higher amounts of excess air go along with smaller relative uncertainties and more significant deviations of fitted NG concentrations from measured ones. This allows for a more reliable exclusion of certain ranges of parameter values, based on the obtained fit probability. This is not possible in case of small amounts of excess air.

[10] The obtained value has still to be normalized to the ambient barometric air pressure of 0.991 atm, resulting in a mixing ratio of NGs in soil air.

The PR model includes a diffusion process resulting in a mass-dependent fractionation[11], which is explaining fractionation by the mass dependence of diffusivity. As Fig. 5.12(c) shows, NGTs determined by the PR model exhibit higher uncertainties than obtained by UA and CE model fits, while underestimating the WTT, on average by (0.8 ± 0.4)°C. During the degassing periods, NGTs reflect the WTT quite well, even though this outcome has to be rather seen as arbitrary since fit probabilities are near 0 %.

An absence of radiogenic helium allows to test the reliability of a diffusion-based approach as pursued by the PR model. The diffusivity of helium is much higher than that of heavier NG species, while the difference of gas-specific solubilities is less pronounced. If data were reliable described by a diffusion-based approach (instead of a solubility-controlled one), the PR model should be able to reproduce measured helium data when they are not included into the fit procedure. Neglecting those samples showing a very small fit probability, values of F_{PR} near zero are obtained for a PR model fit including helium data[12]. A model outcome of $F_{\mathrm{PR}} \rightarrow 0$ suggests a vanishing fractionation of the excess air component, thus excluding any diffusive degassing as it is actually stated by the PR model approach. This finding is confirmed by a PR model fit which does not comprise helium data, resulting in totally different and highly uncertain values of F_{PR}, ranging from -7 to $+18$. In this case, modeled helium amounts differ from measured ones by some percent. If measured helium data are not included into the fit, the PR model overestimates dissolved helium contents during the degassing periods, while it underestimates dissolved helium contents during the remaining time of this study. Thus, the model setup does not allow to describe measured helium data in shallow well groundwater by accounting for diffusion as underlying physical process. This is even the case during degassing periods, suggesting a solubility-controlled degassing process rather than a diffusive one.

Shallow well: evaluation for NG mixing ratios in the equilibrating gas phase differing from atmospheric values

The approaches of previously discussed excess air models presume a knowledge or at least a reliable assumption of NG mixing ratios in the equilibrating gas phase. The obtained underestimation of WTTs throughout all applied models may result from a wrong assumption of the gas phase composition concerning its NG mixing ratios. This motivates to redo analogous fit procedures, now assuming enhanced NG mixing ratios in the equilibrating gas phase with respect to atmospheric air. The extent of enhancement was estimated based on measured NG mixing ratios in soil air. Since $^{3}\mathrm{H}-^{3}\mathrm{He}$ ages indicate strong recharge at the beginning of this study in June/July 2013, the soil air composition during this time span at 5.5 m depth was considered[13] – giving a mean NG enhancement by 3.2 % with respect to atmospheric air. It has to be kept in mind that such a uniform enhancement does not include any mass-dependent fractionation effect which was actually observed in soil air. The modification of

---

[11] The fractionation parameter F_{PR} reflects the degree of diffusion-based re-equilibration. A value of $F_{\mathrm{CE}} \rightarrow 0$ represents an approach to the UA model setup, while $F_{\mathrm{CE}} \rightarrow \infty$ indicates a vanishing amount of excess air (see chapter 3.3.1).

[12] Average values of the fit parameters given in Tab. 5.2 are based on the outcomes obtained for all evaluated samples, thus disregarding respective fit probabilities. Regarding sample-specific outcomes in appendix B.9, nearly all samples resulting in satisfying fit probabilities go along with a value of $F_{\mathrm{PR}} \rightarrow 0$.

[13] The assumed recharge period is reflected by sampling numbers F1-F3, giving a mean NG enhancement by (3.2 ± 1.2) % with respect to atmospheric air at 5.5 m depth.

excess air model fits was realized by means of a simple enhancement of the ambient air pressure with respect to the assumed local barometric pressure of 0.991 atm. Yet the uncertainty of this pressure value was not included in the NGT fit.

Figure 5.13 gives an overview of the obtained NGTs. Obtained underestimations are (0.1 ± 0.2)°C (UA model), (0.3 ± 0.3)°C (CE model) and (0.8 ± 0.5)°C (PR model). By accounting for enhanced NG mixing ratios in the equilibrating gas phase, resulting NGTs of the UA and the CE model become higher and, with that, are in very good agreement with the WTT, as shown in Fig. 5.13(a)/(b). The PR model still exhibits strong uncertainties, mainly for samples outside the degassing periods, see Fig. 5.13(c). However, the PR model shall not be discussed here in more detail since previous explanations already challenged the underlying diffusion-based approach in the context of a reliable description of the present NG data set.

While all just considered models require an assumption about the equilibrating gas phase composi-

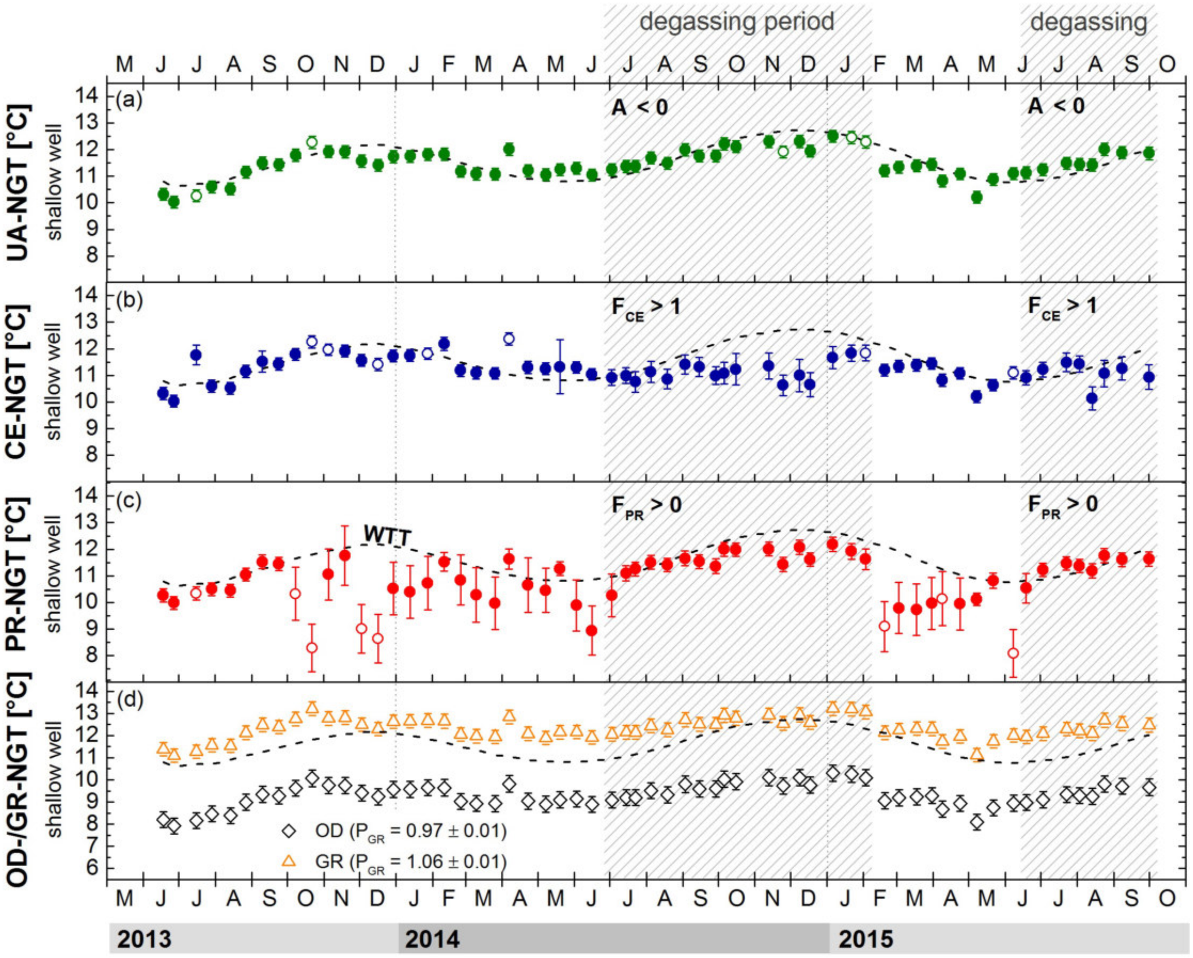

Figure 5.13: Mannheim: NGTs determined by excess air model fits as well as the recorded WTT (uncertainty 0.2°C) for shallow well samples. Fits were performed allowing for variations of atmospheric NG mixing ratios in the equilibrating gas phase from atmospheric values. Fits with a probability above 1 % are illustrated as filled symbols, while open symbols indicate lower fit probabilities. All fits include data of He, Ne, Ar, Kr and Xe. (a) UA model fit; (b) CE model fit; (c) PR model fit; (d) Fits of the OD model (black diamonds) and the GR model (orange triangles).

tion, dissolved NG contents in groundwater may alternatively provide information about gas phase compositions during equilibration. This became already evident before, by applying the CE model for a given equilibration temperature to determine the pressure parameter p^*. Such a possibility motivates the application of two further models, namely the OD and GR model. Both of them comprise a fit parameter which allows for a uniform deviation of NG mixing ratios in the equilibrating gas phase from atmospheric values. This "enhancement parameter" is assumed to be equal for all samples considered in a so-called *ensemble fit*. While the OD model has an analogous setup as the UA model, the GR model additionally complements the OD model by a diffusive transport step, which is equivalent to the PR model.

As shown in Fig. 5.13(d), applying the OD model results in NGTs that significantly underestimate respective WTTs, on average by (2.2 ± 0.4)°C. An ensemble parameter of $P_{\mathrm{OD}} = 0.97 \pm 0.01$ implies lower NG mixing ratios in the equilibrating gas phase as in the atmosphere. This rather unrealistic outcome is caused by sampled data during the degassing period, affecting the fit of all samples due to the application of an ensemble fit. A further scenario is not depicted but shall be mentioned here: Omitting degassed samples, the OD model results in $P_{\mathrm{OD}} = 0.99 \pm 0.01$ and NGTs that are still underestimating the WTT significantly by more than 1°C. Thus, the OD model suggests clearly no enhancement of NG mixing ratios in the equilibrating gas phase, even when dropping degassed samples.

Applying the GR model, an overestimation of the WTT is obtained, on average by (0.8 ± 0.3)°C and going along with $P_{\mathrm{GR}} = 1.06 \pm 0.01$. Due to the similar diffusion-based structure of the GR and PR model, a fit which not comprises helium data was carried out by the GR model, too. As already observed for the PR model, physically unrealistic values of $P_{\mathrm{GR}} = 1.46 \pm 0.16$ and $F_{\mathrm{GR}} = 6.1 \pm 0.4$ are obtained in this case, going along with a strong overestimation of the WTT by (7.5 ± 2.8)°C. Obviously, if the amount of helium is left free to the model fit, the GR model results in a strong outgassing of groundwater, which is compensated by very high NG mixing ratios in the gas phase to describe the measured NG data. In contrast, an inclusion of helium data into the fit results in rather small values of F_{GR} and, thus, in an approach to the OD model case. This again underlines that diffusive outgassing cannot provide a reliable description of the existing data set. Both the OD and GR model fits result in small fit probabilities near zero percent.

As can be seen in Tab. 5.2, the obtained probabilities of UA and CE model fits are rather unaffected by varying the assumptions about the gas phase composition. The comparatively high fit probabilities of PR and GR model fits (without an inclusion of helium data) clearly demonstrate that a high fit probability for itself does not yet indicate a physically reliable description of measured data.

Excess air model fits for samples from the deep well

Analogous fit procedures as described above were also performed for groundwater samples taken at the deep well. Outcomes are summarized in Fig. 5.14 and Tab. 5.3. Since there is no seasonality of NG concentrations, resulting NGTs are not compared to recorded groundwater temperatures but rather to the "average MAAT" of the expected recharge year, which is 10.4°C. This is why the nota-

Table 5.2: Mannheim: Overview of applied excess air model fits and obtained parameter values for shallow well samples. Outcomes as well as their uncertainties are averaged across all samples. For the fit probability *pr*, the standard deviation is given as uncertainty to give an impression of its typical fluctuation across the samples. For CE model fits, outcomes are distinguished according to the degassing phases (start value F_{CE} = 3, marked by an asterisk) and remaining periods (start value F_{CE} = 0).

equilibrating gas phase with atmospheric NG mixing ratios

model	NGs	***pr*** **[%]**	Δ*pr* [%]	***A*** [cc/g]	Δ*A* [cc/g]	$\mathbf{F_x}$	ΔF_x	$\mathbf{P_x}$	ΔP_x	***T*** **[°C]**	Δ*T* [°C]	**WTT-*T*** **[°C]**	ΔWTT-*T* [°C]
UA	He−Xe	**35**	29	**0.0002**	0.0001	-	-	-	-	**10.4**	0.2	**1.1**	0.2
CE	He−Xe	**27** **30***	26 24*	**0.017** **0.053***	0.008 0.045*	**0.10** **1.04***	0.08 0.06*	-	-	**10.3**	0.3	**1.2**	0.3
PR	He−Xe	**20**	25	**-0.012**	0.007	**1.62**	0.66	-	-	**9.7**	0.5	**1.8**	0.3
	Ne−Xe	**52**	31	**0.004**	0.018	**1.45**	261.03	-	-	**10.6**	1.2	**0.9**	1.2

equilibrating gas phase with enhanced NG mixing ratios (enhanced by 3.2 % with respect to the respective atmospheric values)

model	NGs	***pr*** **[%]**	Δ*pr* [%]	***A*** [cc/g]	Δ*A* [cc/g]	$\mathbf{F_x}$	ΔF_x	$\mathbf{P_x}$	ΔP_x	***T*** **[°C]**	Δ*T* [°C]	**WTT-*T*** **[°C]**	ΔWTT-*T* [°C]
UA	He−Xe	**31**	29	**-0.0001**	0.0001	-	-	-	-	**11.5**	0.2	**0.1**	0.2
CE	He−Xe	**22** **40***	25 27*	**0.007** **0.049***	0.030 0.048*	**0.12** **1.06***	0.09 0.04*	-	-	**11.2**	0.3	**0.3**	0.3
PR	He−Xe	**37**	31	**-0.011**	0.009	**2.11**	1.12	-	-	**10.8**	0.5	**0.8**	0.5
OD	He−Xe	**0**	0	**0.0004**	0.0001	-	-	**0.97**	0.01	**9.3**	0.4	**2.2**	0.4
GR	He−Xe	**0**	0	**-0.0006**	0.0001	**0.93**	0.11	**1.06**	0.01	**12.3**	0.3	**-0.8**	0.3
	Ne−Xe	**100**	0	**-0.066**	0.016	**6.10**	0.35	**1.46**	0.16	**19.0**	2.8	**-7.5**	2.8

tion of “recharge temperatures” is appropriate for NGTs from deep well samples.

The UA model fit results in NGTs significantly underestimating the expected recharge temperature, on average by (1.0 ± 0.2)°C, see Fig. 5.14(a). An analogous underestimation by (0.8 ± 0.4)°C follows from the CE model fit, as shown in Fig. 5.14(b). It is typical that the UA model results in systematically colder NGT outcomes compared to that obtained by the CE model fit, which is a result of the non-consideration of fractionation in the UA model approach[14].

CE model outcomes do not allow for a reliable interpretation of the resulting F_{CE} parameter values, even though the amount of excess air is higher in deep well groundwater compared to the shallow well. Two clusters of values arise in Monte Carlo simulations, leading to values of F_{CE} near 1 as well as near 0. Some samples evaluated by the CE model result in NGTs which agree apparently quite well with the MAAT. However, this agreement should be rather seen as arbitrary, going along with a high *A* value and a worse fit probability. The CE model was again applied to determine the ambient air pressure for a given recharge temperature of 10.4°C. This approach results in an average value of $p^* = 1.017 \pm 0.015$, implying a NG enhancement in the equilibrating gas phase by (2.6 ± 1.5) % with

---

[14] Analogous fit procedures for shallow well samples do not show this effect, since a nearly vanishing amount of excess air prevents such a temperature bias of NGTs due to a non-consideration of fractionation effects.

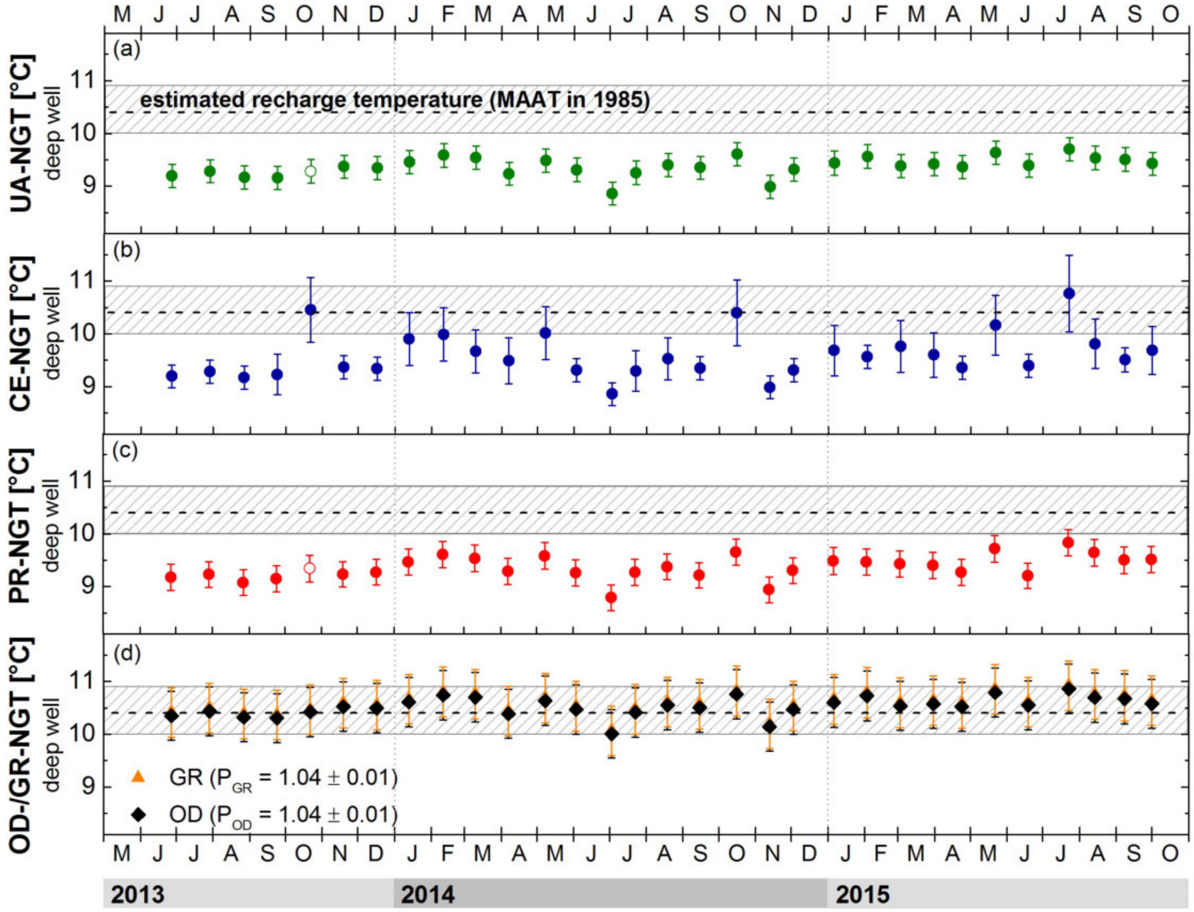

Figure 5.14: Mannheim: NGTs determined by excess air model fits for deep well samples, involving NG concentrations of He, Ne, Ar, Kr and Xe. Fits were performed assuming atmospheric NG mixing ratios in the equilibrating gas phase. Fits with a probability above 1 % are illustrated as filled symbols, while open symbols indicate lower probabilities. The "average MAAT" of the expected recharge year is depicted as black dashed line. Its uncertainty ranges from 10.0°C (MAAT in 1976) to 10.9°C (MAAT in 1997). (a) UA model fit; (b) CE model fit; (c) PR model fit; (d) Fit results from OD model (black diamonds) and GR model (orange triangles).

respect to atmospheric air. Since no local soil air observations are available from the last decades, this result cannot be directly verified as it was possible for samples from the shallow well. However, its order of magnitude seems to reflect a plausible NG enhancement in soil air, regarding soil air data of this study recorded during summer time.

As shown in Fig. 5.14(c), the PR model results in a significant underestimation of the expected recharge temperature by (1.0 ± 0.2)°C. Comprising helium data, the PR model outcome clearly approaches to that of the UA model ($F_{\mathrm{PR}} \rightarrow 0$), thus excluding any diffusive degassing. A PR model fit without helium data results in strong variations of F_{PR} values and higher uncertainties of all parameters.

Resulting NGTs from OD and GR model fits are in a good agreement with the expected recharge temperature, showing a non-significant overestimation, on average by (0.1 ± 0.5)°C and (0.2 ± 0.5)°C, respectively, see Fig. 5.14(d). NGT estimates of these models go along with values of $P_{\mathrm{OD}} = P_{\mathrm{GR}} = 1.04 \pm 0.01$, indicating an enhancement of NG mixing ratios in the equilibrating gas phase by (4.7 ± 1.3) % with respect to atmospheric air. As it is the case for the PR model, parameter estimates

Table 5.3: Mannheim: Overview of applied excess air model fits and obtained parameter values for deep well samples. Outcomes as well as their uncertainties are averaged across all samples. For the fit probability *pr*, the standard deviation is given as uncertainty to give an impression of its typical fluctuation across the samples. The last two columns give the deviation of obtained NGTs from the “average MAAT” in the expected recharge year 1985.

model	NGs	***pr*** **[%]**	Δpr [%]	***A*** [cc/g]	ΔA [cc/g]	$\boldsymbol{F_x}$	ΔF_x	$\boldsymbol{P_x}$	ΔP_x	***T*** [°C]	ΔT [°C]	**MAAT-*T*** **[°C]**	ΔMAAT-*T* [°C]
UA	He−Xe	**65**	28	**0.0010**	0.0001	-	-	-	-	**9.4**	0.2	**1.0**	0.2
CE	He−Xe	**61**	29	**0.005**	0.005	**0.37**	0.19	-	-	**9.6**	0.4	**0.8**	0.4
PR	He−Xe	**59**	28	**0.0010**	0.0002	**-0.01**	0.10	-	-	**9.4**	0.2	**1.0**	0.2
	Ne−Xe	**69**	24	**0.005**	0.005	**0.45**	1.78	-	-	**9.9**	0.9	**0.5**	0.9
OD	He−Xe	**100**	0	**0.0010**	0.0001	-	-	1.04	0.01	**10.5**	0.5	**-0.1**	0.5
GR	He−Xe	**100**	0	**0.0009**	0.0001	**-0.07**	0.07	**1.04**	0.01	**10.6**	0.5	**-0.2**	0.5
	Ne−Xe	**99**	0	**0.0060**	0.0070	**2.98**	1.70	**0.97**	0.08	**8.9**	1.9	**1.5**	1.9

by the GR model with and without an inclusion of helium data differ strongly. In particular, an inclusion of helium data results in values of $F_{GR} \rightarrow 0$ and, thus, in a clear approach to the OD model case. An overview of all fit outcomes for deep well samples is given in appendix B.10.

5.3 Discussion

Sampling results presented so far are discussed in the context of subsurface gas dynamics and their implications for NG tracer applications, starting with the unsaturated zone. Short-term fluctuations of O_2+CO_2 in soil air cannot entirely explain observed mixing ratios of inert gases. Data also indicate an influence of different transport mechanisms. This motivates to discuss local factors determining soil air composition, which includes the application of a modeling routine to identify relevant gas transport processes.

Regarding groundwater samples from the shallow well, three findings require a detailed discussion: first, the observation of seasonally fluctuating NG concentrations in groundwater, which seems to be in contradiction to a water age of several years. Second, excess air model outcomes indicate a possible impact of varying soil air composition during recharge – which was not confirmed so far in the literature. Third, the temporal degassing phenomenon requires a detailed analysis, since NG data from corresponding periods seem to be not reliably treated by excess air models.

5.3.1 Determining factors of soil air composition under mid-latitude climate conditions

The present data set provides the possibility to discuss the impact of both, soil temperature and soil moisture, on soil air composition. Figure 5.15 illustrates the correlation between recorded O_2+CO_2 mixing ratios in soil air and soil moisture contents. Due to the high solubility of CO_2 in water, the sum value of O_2+CO_2 is decreasing with increasing soil moisture contents. In contrast, O_2+CO_2 increases even above the atmospheric value of 20.99 vol% under very dry conditions, as will be explained later by modeling. It is worth mentioning that even the soil air composition at 5.5 m depth correlates with soil moisture contents measured near the soil surface – underlining the impact of topmost soil moisture contents on the ventilation of the entire soil profile. Data from winter time (see blue framed samples) are characterized by high soil moisture contents and seems to deviate from this trend. This is a consequence of low temperatures constraining subsurface microbial CO_2 production, going along with nearly atmospheric sum values of O_2+CO_2.

In contrast to soil moisture contents, the correlation between soil temperature and O_2+CO_2 in soil air is less pronounced, see Fig. 5.16. This behavior results from the just mentioned effect of soil moisture: While O_2+CO_2 is decreasing during the summers 2013/14, it shows an enhancement in 2015 – as a consequence of particularly dry conditions (see green framed area in Fig. 5.16). No correlation is found between deep soil temperature and soil air composition. This finding is indeed expected, first, due to the time shift of temperature with increasing depth and, second, since microbial activity takes place within the topmost soil layer, while gas dynamics in deeper soil layers is in fact constrained by ambient soil moisture contents rather than by ambient temperatures.

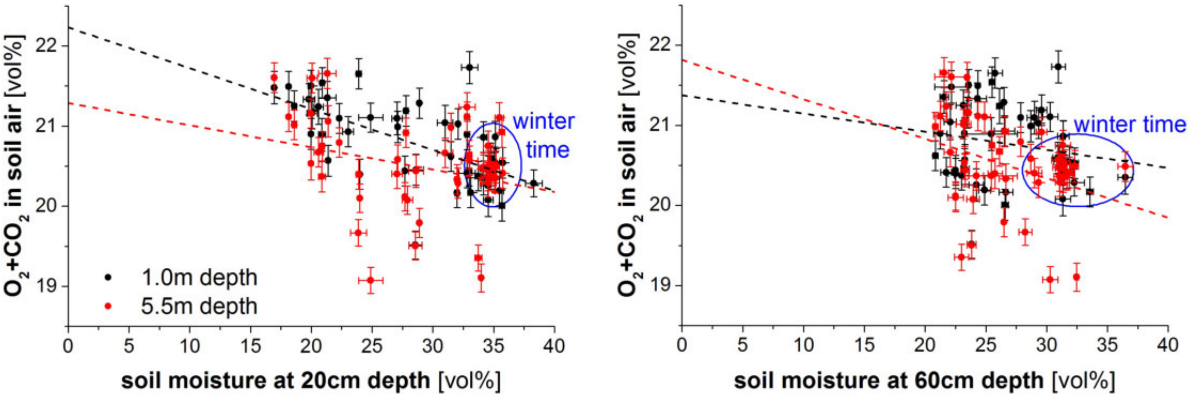

Figure 5.15: Mannheim: Correlation between soil air mixing ratios of O_2+CO_2 [vol%] and volumetric soil moisture contents at 20 cm and 60 cm depth, respectively. Mixing ratios of O_2+CO_2 as well as corresponding linear fits are given for 1.0 m (black points/line) and 5.5 m depth (red points/line).

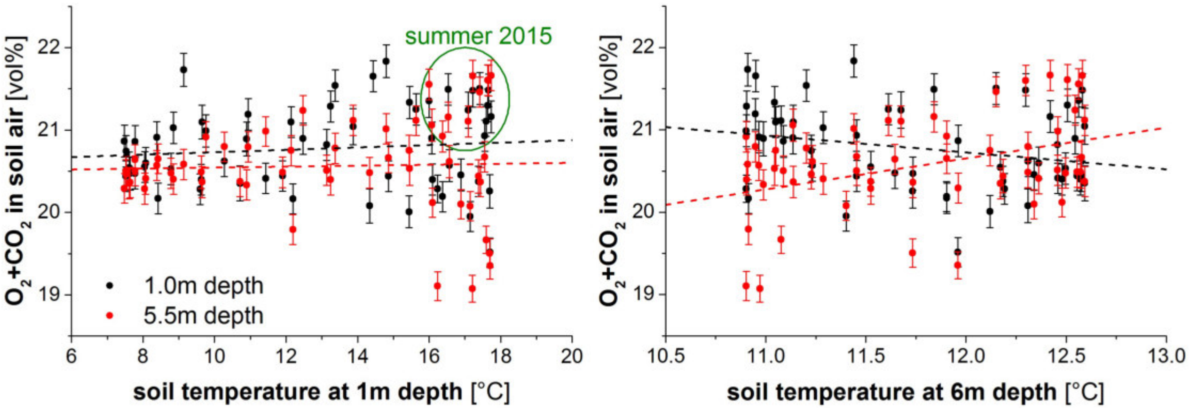

Figure 5.16: Mannheim: Correlation between soil air mixing ratios of O_2+CO_2 and soil temperatures at 1 m and 6 m depth, respectively. Mixing ratios of O_2+CO_2 as well as corresponding linear fits are given for 1.0 m (black points/line) and 5.5 m depth (red points/line). The uncertainties of soil temperature data (accounting for 0.5°C) are correlated and, thus, omitted for a better visibility.

Numerical simulation of subsurface gas transport

A model routine was applied to simulate subsurface gas transport at the sampling site near Mannheim, with the aim to identify dominating processes. The model approach is formally described in chapter 3.3.4. Meteorological input data (atmospheric temperature and relative humidity) are taken from DWD (2016), while the local porosity for the entire soil profile is assumed as $\phi = 0.39$ based on a study by Engelhardt (2015). Soil temperature fluctuations are assumed to be damped with an attenuation length of 3.9 m, which was estimated based on measured long-term trends of soil temperature. Since no records of soil moisture are available for soil depths below 0.6 m (see chapter 5.1.2), a constant soil moisture content of $\theta_\mathrm{w} = 0.2$ is assumed for the entire soil column. The model describes four different types of diffusive transport, which are treated separately:

- concentration gradients due to oxygen depletion (concerning O_2 and CO_2) and varying sum values of O_2+CO_2 (concerning inert gases) (denoted as “OD diffusion”)
- temperature gradients (“thermal diffusion”)
- varying water vapor contents (“water vapor gradients”)
- gravitational separation (“gravitation”)

First of all, the observation of O_2+CO_2 values increasing above the atmospheric value of 20.99 vol% shall be investigated. Since this phenomenon occurs mainly during very dry periods – associated with a distinct soil ventilation and an efficient subsurface oxygen supply – it is very unlikely to be caused by anaerobic soil respiration releasing CO_2 without any consumption of O_2. The occurrence of high soil air contents θ_g rather motivates to consider diffusion-based transport in this context. For this purpose, the described model routine was applied. Certain initial mixing ratios of O_2 (15 vol%) and CO_2 (5.99 vol%) were stated through the entire soil profile, reflecting an initial impact of oxygen depletion. Atmospheric mixing ratios provide the topmost boundary condition. Modeling is done for a soil depth of 5.5 m. Gravitational separation is neglected in this approach, due to its uniform nature which cannot account for a seasonal variation of O_2+CO_2 in soil air.

Starting from initial conditions, diffusive transport (described above as “OD diffusion”) balances the existing gradient of mixing ratios. Assuming an equal diffusivity of O_2 and CO_2, the model yields a uniform atmospheric sum value of O_2+CO_2 in soil air (see green dashed line/scenario 1 in Fig. 5.17(a)). In contrast, an enhanced sum value of O_2+CO_2 is obtained by accounting for the real values of gas-specific diffusivities[15] (see black line/scenario 2), gradually approaching the atmospheric value of 20.99 vol%. Even though initial subsurface mixing ratios of both O_2 and CO_2 deviate likewise by about 6 vol% from the respective atmospheric values – implying nearly equal concentration gradients between atmosphere and soil air – the deviation of O_2 is balanced faster than that of CO_2. In other words, a diffusive flux of O_2 into the soil is faster than that of CO_2 out of the soil.

This finding confirms that diffusive balancing of oxygen depletion-caused gradients may indeed cause an increase of O_2+CO_2 above the atmospheric value. The model outcome suggests an increase by

---

[15] The diffusivity of O_2 ($D_{\mathrm{O}_2} = 0.19962\,\mathrm{cm^2/s}$) is about 20 % higher than that of CO_2 ($D_{\mathrm{CO}_2} = 0.15733\,\mathrm{cm^2/s}$) at room temperature (Paul and Clark, 1996).

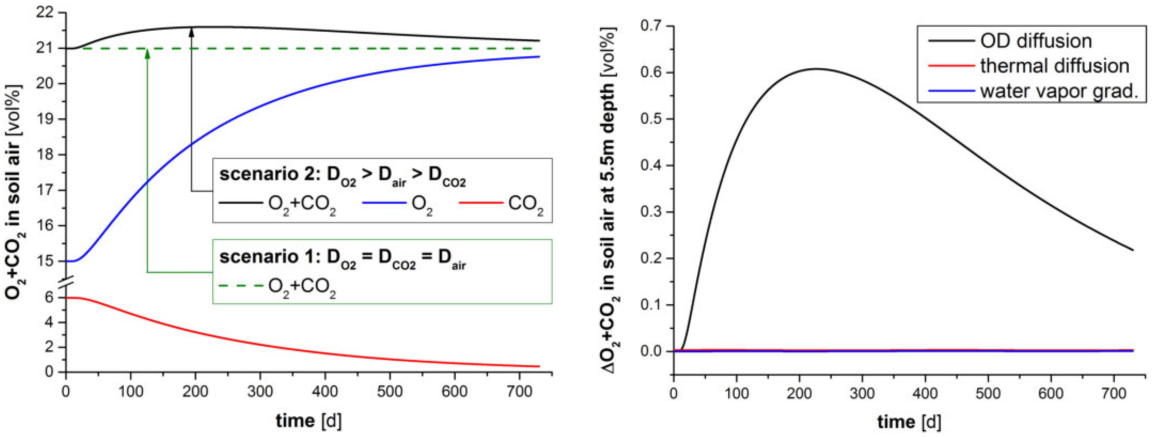

(a) Comparison of model outputs for equal (scenario 1) and gas-specific diffusivities (scenario 2) of O_2 and CO_2, respectively.

(b) Contribution of different diffusion-based mechanisms to the modeled change in O_2+CO_2, for gas-specific diffusivities of O_2 and CO_2.

Figure 5.17: Mannheim: Modeled soil air content of O_2+CO_2 at 5.5 m depth. The simulation was done for initial mixing ratios of 15 vol% for O_2 and 5.99 vol% for CO_2 (reflecting an impact of oxygen depletion).

about 0.6 vol% which is similar to that typically observed in measured data. As shown in Fig. 5.17(b), thermal diffusion and water vapor gradients do not contribute to this effect.

Now, mixing ratios of NGs and N_2 in soil air shall be discussed. Besides the above specified mechanisms of diffusion-based transport, advective balancing of varying O_2+CO_2 values by remaining gases is included into the model approach. For this purpose, real measured data of O_2 and CO_2 are consulted[16].

Figure 5.18 depicts percentage deviations of modeled gas mixing ratios in soil air from the respective atmospheric values. Contributions of separately treated transport mechanisms are distinguished (as colored areas) and also summed up (as lines) for helium and xenon – representing an inert gas species with high and low diffusivity, respectively.

The overall trend is determined by different mutually balancing effects. Diffusive transport, as a consequence of thermal gradients and varying water vapor contents, shows a clear seasonality which is induced by fluctuations of temperature and air humidity as well as by their depth-dependent variations across the considered soil profile. The typical temperature profile during winter (cold atmosphere and warmer soil air) causes a subsurface enrichment of lighter gas species due to thermal diffusion, while a converse behavior is obtained during summer. The typical temperature distribution during winter causes a water vapor flux out of the soil, i.e. a relative enrichment of lighter gas species in soil air. Drier atmospheric air during summer results in a reduction or even an inversion of this effect – leading to a similar seasonality as observed for thermal diffusion.

Advective pressure balancing as response to varying O_2+CO_2 values occurs likewise for all inert gas species (see dark green area “OD adv.”), since advective transport is not mass-dependent by itself. It induces a subsequent diffusive balancing (see light green area “OD diff.”). Due to the mass-

---

[16] Values of O_2+CO_2 are assumed to be depth-invariant. Furthermore, any balancing of a deficit or increase in O_2+CO_2 is stated to take place instantaneously.

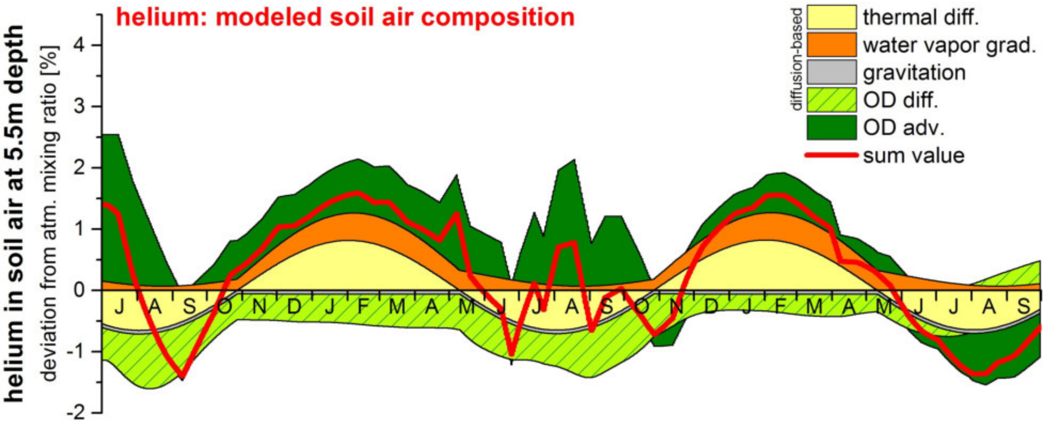

(a) Modeled helium contents in fractionated soil air. All effects are summed up as red line.

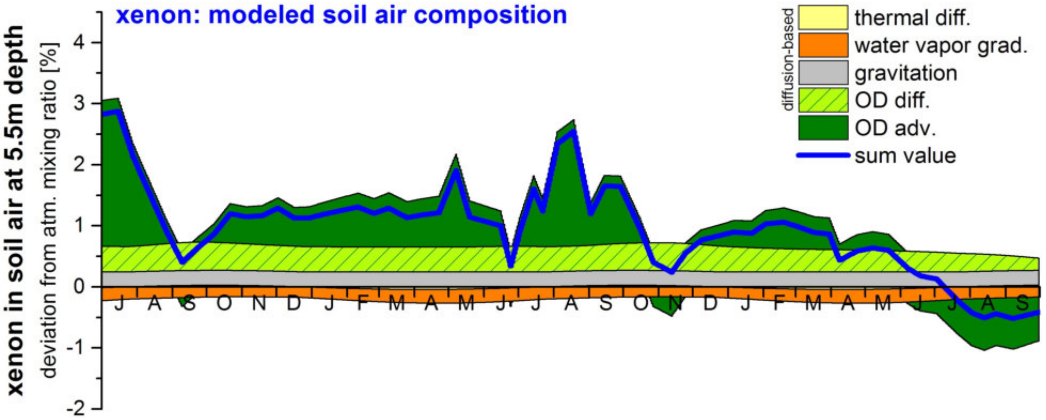

(b) Modeled xenon contents in fractionated soil air. All effects are summed up as blue line.

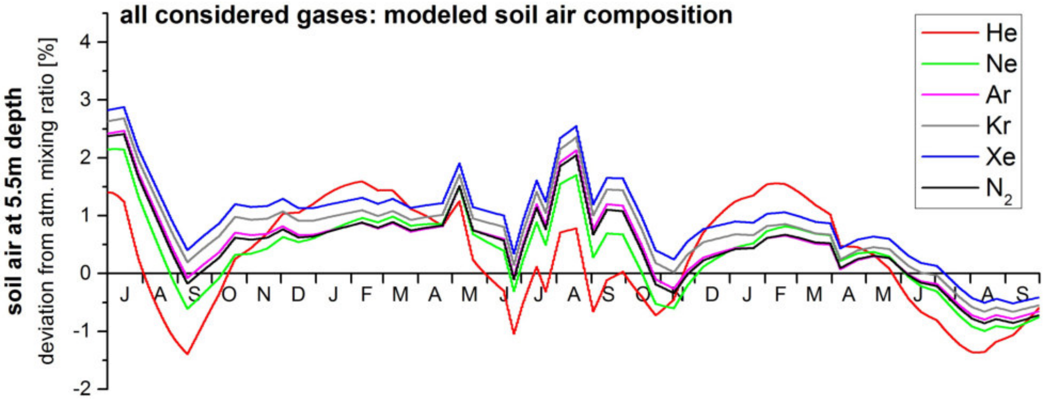

(c) Summed up trends of NGs and N_2 in fractionated soil air, respectively.

Figure 5.18: Mannheim: Modeled soil air composition at 5.5 m depth. Advective balancing of O_2+CO_2 is labeled in dark green (see “OD adv.”). Reasons for diffusion-based fractionation are distinguished according to water vapor gradients (orange areas, see “water vapor grad.”), gravitational settling (gray areas, see “gravitation”), thermal diffusion (yellow areas, see “thermal diff.”) and a diffusive balancing (light green areas, see “OD diff.”). Depicted data reflect the most abundant isotopes, respectively – meaning ^{4}He, ^{20}Ne, ^{40}Ar, ^{84}Kr, ^{132}Xe and ^{14}N.

dependence of diffusivity, the advective OD effect is typically reinforced for heavier gas species and counteracted for lighter ones compared to the average molecular mass of air. Such a diffusive transport follows its cause in a retarded and a smoothed way, since it operates on a different time scale than advective transport. This means, if the advective OD contribution changes the sign of its impact, diffusive balancing will follow delayed – see model outcomes during summer 2015. Figure 5.18(c) summarizes overall deviations from the respective atmospheric values for all modeled gas species. It is obvious that helium is most strongly influenced by diffusion-based mechanisms, resulting in a generally different temporal trend.

Preceding explanations already suggest that the type of overall dominating transport process depends on the mass of the considered gas species. Relative contributions of all treated mechanisms are summarized in Fig. 5.19. It becomes clear that diffusion-based mechanisms generally gain relevance for gas species of a stronger mass difference to that of atmospheric air. Thermal diffusion shows a negligible impact on most inert gas species besides the lightest ones as helium and neon. This is caused by the gas-specific thermal diffusion coefficients (see appendix A.8). Even though the model was applied for a rather shallow soil depth of 5.5 m, gravitational separation shows a noteworthy impact for krypton and xenon. Advective and thus induced diffusive impacts of oxygen depletion result together in a significantly stronger impact on gas mixing ratios compared to the other mechanisms discussed here. Regarding typical measurement uncertainties, it seems to be appropriate to omit effects of gravitational separation, water vapor gradients and thermal diffusion. For the latter two, this may be not correct in case of helium – showing corresponding contributions of quite similar magnitudes.

The reliability of previous conclusions shall be motivated by a comparison of model outcomes with measured data. Figure 5.20 indicates a good agreement for both helium and xenon, regarding respective measurement uncertainties. A significant and apparently systematic deviation is visible during the summers 2013/14, when modeled mixing ratios do not increase as strongly as observed for measured mixing ratios. This discrepancy may be caused by biased input parameter assumptions – possibly due to a temporal underestimation of soil moisture, which is favoring a too strong impact of diffusion-based mechanisms on model outcomes. Temporal enhancements of measured NG mixing ratios during summer are in fact expected to go along with a remarkable increase of soil moisture.

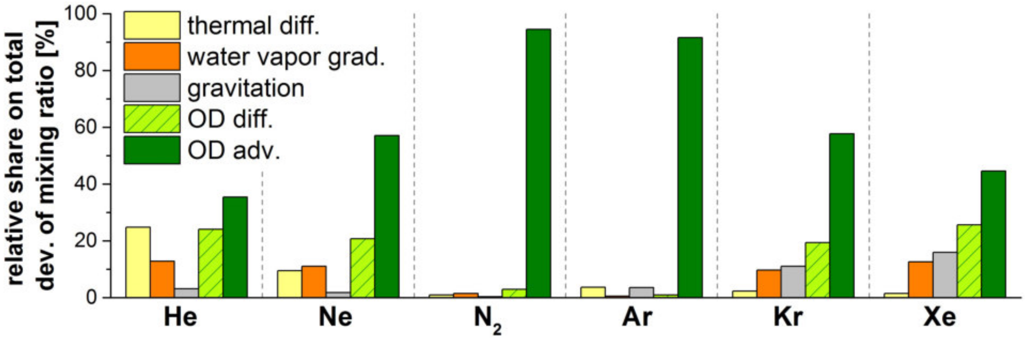

Figure 5.19: Mannheim: Modeled data, showing relative contributions of different transport processes. The algebraic sign is omitted, to clarify relative contributions instead of specific impacts. Depicted data reflect the most abundant isotopes, respectively – meaning ^{4}He, ^{20}Ne, ^{40}Ar, ^{84}Kr, ^{132}Xe and ^{14}N.

In general, it has to be kept in mind that the applied model approach does not account for advective flow in a formally correct way. Any deficit of O_2+CO_2 is assumed to be instantaneously balanced by atmospheric air, while it is in fact done by ambient soil air which potentially exhibits enhanced NG mixing ratios. Furthermore, gas/water partitioning and gas transport within the water phase is neglected. This approach may induce a bias, even though the relative fraction of dissolved gases is small as long as air-filled pore space becomes not very small. The overall contribution of such unconsidered processes seems to be rather small during the most of the time of this study, regarding the generally good agreement with measured data trends in Fig. 5.20. While this chapter treats rather specific conditions at the sampling site of this study, the general validity of conclusions derived from the presented modeling approach will be discussed later in chapter 7.

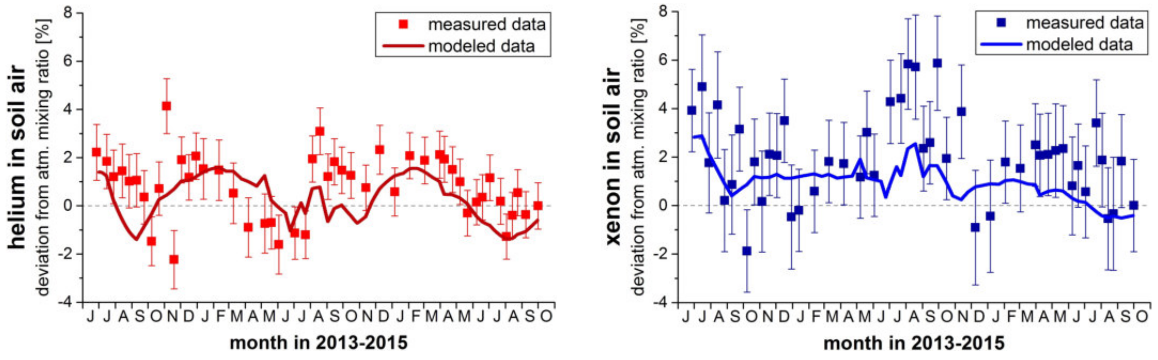

(a) Measured helium data (red symbols) and modeled data from Fig. 5.18(a) (solid red line).

(b) Measured xenon data (blue symbols) and modeled data from Fig. 5.18(a) (solid blue line).

Figure 5.20: Mannheim: Comparison of modeled and measured soil air composition at 5.5 m depth. Depicted model data reflect the sum of all above described mechanisms. Depicted data reflect the most abundant isotope, respectively – meaning ^{4}He and ^{132}Xe.

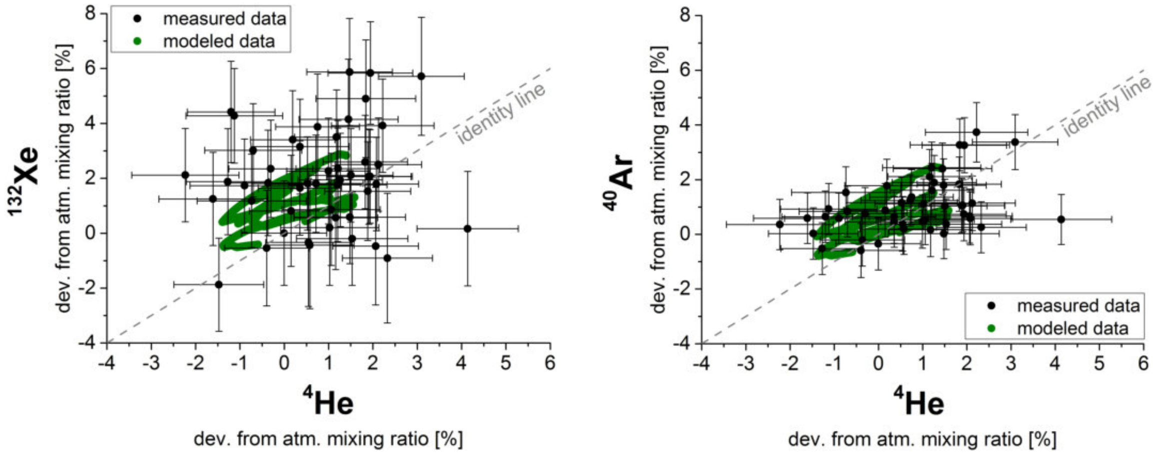

(a) Xe-He plot

(b) Ar-He plot

Figure 5.21: Mannheim: Fractionation plots showing modeled (green symbols) and measured (black symbols) NG mixing ratios in soil air at 5.5 m depth. Depicted data are given as percentage deviation from the atmospheric value, respectively.

Above presented model outcomes clearly indicate a mass-dependent fractionation due to diffusion-based mechanisms. Figure 5.21 gives a more evident overview of correlations between different NG species in soil air. Disregarding the measured high xenon mixing ratios during summer time, plots show a good agreement of measured (black symbols) and modeled data (green symbols).

Model outcomes in Fig. 5.21 follow a line which is rather parallel to the identity line. This means that enhanced NG mixing ratios in soil air do not necessarily go along with a stronger relative enhancement of heavier gas species compared to lighter ones, which would be actually expected by considering permanent steady state conditions. The latter was observed by Freundt et al. (2013) and Jones et al. (2014), even though samplings during those studies did not cover seasonal cycles. Preceding explanations rather suggest that the retarding nature of diffusive transport affects the occurrence of mass-dependent fractionation. Thus, advective balancing of varying O_2+CO_2 may cause remaining gas mixing ratios to fluctuate temporarily in a nearly uniform way, even in case of a non-negligible impact of diffusive transport.

5.3.2 Seasonal fluctuations of NG concentrations in shallow groundwater

Dissolved NG contents in shallow groundwater are observed to fluctuate seasonally in correlation with the local WTT. Obviously, measured NG data seem to reflect a temperature signal, the origin of which is still unclear. The following explanation will point out a permanent equilibration of groundwater with local entrapped air bubbles − driven by WTT fluctuations − as most probable approach to explain the observed seasonality of dissolved NG contents. Besides soil air of the unsaturated zone, there is a further subsurface gas phase consisting of entrapped air bubbles within the saturated zone, previously entrapped during recharge events. Such microscale air bubbles are assumed to be isolated from the unsaturated zone and, therefore, in permanent equilibrium with the surrounding groundwater, which was already proposed by Aeschbach-Hertig et al. (2000) as main principle of the CE model formulation. The assumption of a permanent equilibration with this gas phase is supported by obtained ^{3}H−^{3}He ages of shallow well samples, which are significantly higher than 0 years. This indicates that there is no loss of the total tritiogenic ^{3}He, which would be otherwise the case if groundwater stood in direct contact to the unsaturated zone. The aquifer region containing entrapped air is also referred to in the literature as *quasi-saturated zone* (Faybishenko, 1995; Holocher et al., 2002, 2003; Klump et al., 2008). It is thus the question whether shallow well samples of this study originated indeed from the quasi-saturated zone. Groundwater was pumped from a depth of 7.8 m below the earth surface. This region was indeed not permanently saturated during the last decades, since the local water table level lastly fell below 8 m depth in 1994 (see Fig. 5.22). Entrapped air bubbles should thus exist at the sampling depth of this study. In a laboratory experiment, Holocher et al. (2002) investigated the formation of excess air and the time dependent dissolution of air bubbles during a unidirectional vertical water flow. For flow velocities between 10 and 110 cm per hour, they found a timescale of about 6 days until complete bubble dissolution. These conditions cannot be directly compared to those at the sampling site of this study. Assuming a local groundwater recharge rate of 250 mm per year (LUBW, 2016) and a porosity of $\phi = 0.33$, a flow velocity of only about 80 cm per year is obtained. A simple linearized estimation results in a time scale of at least about

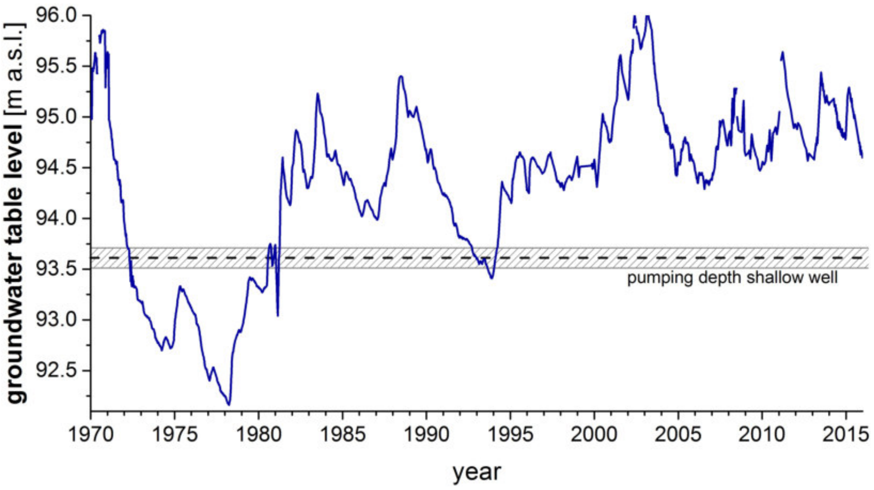

Figure 5.22: Mannheim: Groundwater table level measured by LUBW (2016) (well no. 0113/304-5 in Heddesheim, in about 3 km distance to the sampling site of this study). The pumping region at the shallow well sampled for this study is depicted as black dashed line with a dashed uncertainty range. The latter is just based on the depth uncertainty and might be even larger due to mixing within the well tube during pumping.

20 years until air bubbles are completely dissolved. It is thus appropriate to assume entrapped air bubbles as still existent at the sampling depth of the shallow well, providing a gas phase for equilibration. Besides this, even though a comparatively small amount of water was pumped during each sampling procedure, sampled groundwater likely originated not exactly from the pump depth but also from a certain vertical spread region below and above the pump, the latter containing most likely entrapped air bubbles. Altogether, sampled groundwater likely originates from the quasi-saturated zone.

Two further approaches to explain the observed seasonality of dissolved NG data were dropped, but shall be mentioned in this context. First, a simple explanation for observed NG content fluctuations in groundwater may be a reflection of seasonal atmospheric temperature fluctuations in the recharge area, assuming groundwater is formed continuously during the entire year and transported subsequently to the sampling site of this study. This approach also explains the obtained permanent non-zero groundwater ages. However, it is challenged on the one hand by the seasonality of local groundwater recharge which mainly takes place between January and May rather than during the entire year (see Fig. 5.23(a) and later discussion about annual recharge). Furthermore, it is in conflict with stable isotope data: Values of δ^{18}O and δ^{2}H show no seasonality, which is why it can be excluded that the observed seasonality of NG data is originating from seasonal temperature fluctuations of the precipitation in the recharge area. Otherwise, the stable isotope composition in groundwater should also reflect seasonal atmospheric temperature fluctuations[17]. Besides this, fluctuating NG concentrations and local WTT at the sampling site would have to be in perfect correlation by hazard, while a certain time shift between them would be expected due to transport within the aquifer.
A second approach is a permanent equilibration with soil air of the unsaturated zone. However, a per-

---

[17] In fact, a fluctuating WTT is actually expected to induce a seasonality of stable isotope data – even if all groundwater samples recharged under comparable climatic conditions. Given the uncertainty of stable isotope analysis, such a behavior is not observed due to the small extent of WTT variations and the comparatively weak temperature dependence of equilibrium fractionation (Mook, 2000).

manent local equilibration with soil air can be excluded for two reasons: On the one hand, obtained ^{3}H−^{3}He ages are always significantly higher than 0 years, indicating no loss of the total tritiogenic ^{3}He as already described above. On the other hand, except for some few months during summer time, measurements of soil air composition resulted in nearly atmospheric NG mixing ratios − while NG concentrations in groundwater indicate a permanent enhancement of NG mixing ratios in the equilibrating gas phase. A permanent equilibration with soil air of the unsaturated zone is thus excluded.

Previous explanations indicate that NG concentrations in groundwater, determined originally by climate conditions during recharge, may be affected subsequently by a temperature dependent equilibration, even some years after recharge. This process occurs independently from any exchange with the unsaturated zone, which explains why data show no loss of tritiogenic ^{3}He. Thus, the ^{3}H−^{3}He age of a groundwater sample does not necessarily reflect the time of the last temperature driven equilibration with a gas phase. However, it is important to note that this effect is only relevant for rather young groundwater since entrapped air bubbles as well as seasonal temperature fluctuations are usually not observed in deeper soil layers. Deep well groundwater was sampled just about 5 m deeper compared to the shallow well − resulting in dissolved NG contents showing no seasonal fluctuations, even though the local groundwater temperature is still slightly varying.

Due to climate change, a temperature increase of about 1°C is clearly observable during time periods of a few decades (see e.g. data of DWD (2016) used for this study), during which groundwater has not yet necessarily reached permanently saturated soil depths. By this way, a subsequent equilibration with entrapped air bubbles at a higher temperature may result in NGTs systematically overestimating the real recharge temperature.

Even though the general origin of fluctuating NG concentrations in groundwater is explained by an equilibration with entrapped air bubbles of the quasi-saturated zone, the origin of some further observations of the present data set still remains unclear. This concerns, on the one hand, the absolute amount of dissolved NGs in sampled groundwater. In this context, an influence of oxygen depletion and of fluctuating NG mixing ratios in soil air was suggested in the preceding explanations but not confirmed so far. On the other hand, the temporarily observed degassing phenomenon is of particular interest regarding the potential impact of subsurface gas dynamics on dissolved NG contents in groundwater.

Gas dynamics during recharge: impact of oxygen depletion

The estimation of NGTs based on measured NG concentrations in shallow groundwater resulted in a systematical underestimation of the WTT which is actually expected to provide a reliable estimate of the equilibration temperature. In the context of excess air model fits presented in chapter 5.2.3, this disagreement was met by assuming NG mixing ratios in the equilibrating gas phase to be enhanced with respect to atmospheric air. For this purpose, the beginning of this study in June/July 2013 was simply assumed as predominant recharge time of sampled groundwater, motivated by a strong increase of the water table level during this period. However, ^{3}H−^{3}He ages of shallow well groundwater are in a range of several years, indicating that a certain fraction of sampled water recharged further in the past, meaning not necessarily in June/July 2013 and possibly even not during summer time. This finding motivates a more general discussion of typical recharge periods in the sampling area.

While a general impact of oxygen depletion on NG mixing ratios in soil air is already confirmed by Freundt et al. (2013) as well as by previous explanations of this study, an influence on dissolved NG contents of recharging groundwater was just supposed in the literature (Stute and Schlosser, 1993; Hall et al., 2005; Sun et al., 2010). The previous presentation of soil air composition data show a significant seasonal enhancement of NG mixing ratios by several percent with respect to atmospheric air. Since this effect occurs seasonally, dissolved gas contents in recharging groundwater are generally expected to depend on the time of groundwater recharge and air bubble entrapment within the quasi-saturated zone.

A long-term record of groundwater table data from a well nearby the sampling site of this study – thus from the same aquifer – was analyzed to identify usual periods of local recharge. As Fig. 5.23(a) shows, the local water table level usually increases between January and May, with a maximum in March. This may be seen as typical time of local recharge. Regarding the annual distribution of groundwater level increases in Fig. 5.23(b), recharge also occurs during summer, even though the long-term net trend during summer and fall is a decrease of the groundwater table level.

Measured data of stable isotopes of water give further evidence about usual periods of groundwater recharge. Figure 5.24 illustrates the typical seasonal isotopic composition of local precipitation during the last decades (see red symbols). Obviously, measured data from this study are situated near the annual average (see red cross), indicating no predominant groundwater recharge neither during summer nor during winter time. Assuming that some recharge takes place during winter, there must be also a significant contribution of summer recharge to explain the measured isotopic composition of sampled groundwater, in particular at the shallow well. The stronger depletion of deep well sam-

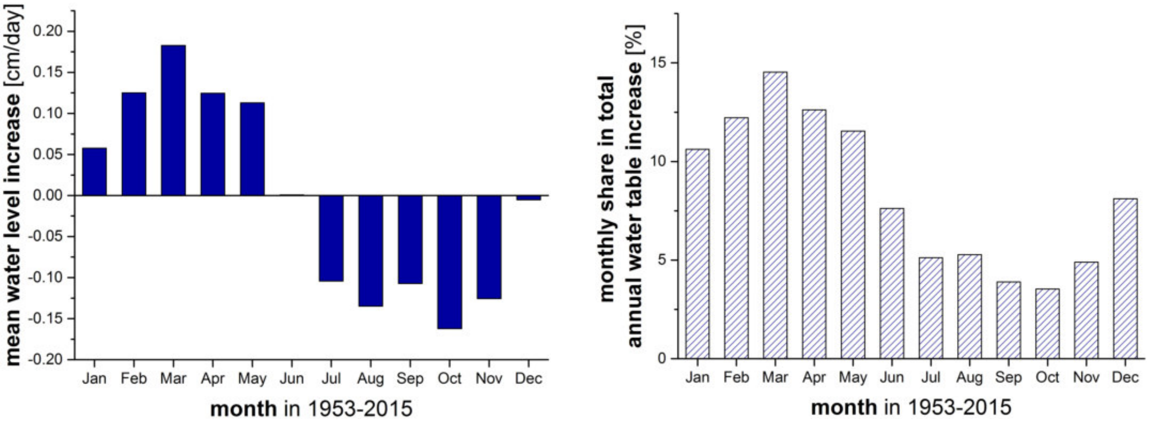

(a) Monthly net changes in groundwater table level.

(b) Monthly share in total annual groundwater table level increase. About one third of the annual water table increase occurs in the summer half year between May and October.

Figure 5.23: Mannheim: Monthly groundwater level changes and annual distribution of monthly water table increases. Data are determined based on a long-term water level record from LUBW (2016) (well no. 0113/304-5 in Heddesheim, in about 3 km distance to the sampling site of this study) and can thus be seen as average values for the time period between 1953 and 2015.

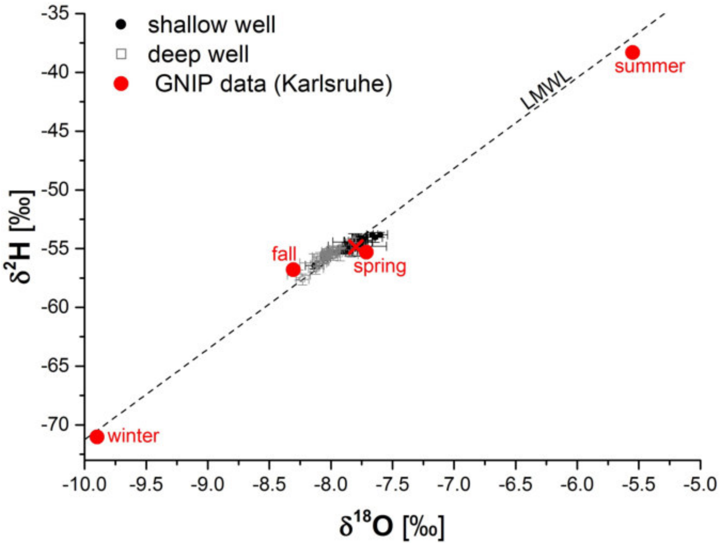

Figure 5.24: Mannheim: Stable isotopes of water: δ^{18}O and δ^{2}H, both relative to the VSMOW standard. The LMWL as well as seasonal data (average monthly values between 1977 and 2013, weighted by the mean monthly amount of precipitation) are based on records in Karlsruhe (Germany) taken from GNIP (2016) of IAEA/WMO.

ples can be partly explained by lower atmospheric temperatures during recharge some decades ago. However, a long-term record in Karlsruhe (Germany) taken from GNIP (2016) suggests that δ^{18}O in local precipitation varied by just 0.1 ‰ between the expected recharge years of both wells, which is why changes in the MAAT cannot account for the entire observed isotopic difference between the two sampled wells. Deep well data in Fig. 5.24 thus indicate a higher share of water recharged during the cold season, compared to the shallow well.

Groundwater table data describe a long-term behavior during the last decades, while stable isotope data reflect rather recharge during the last years. Obviously, sampled groundwater of both wells is more strongly affected by summer recharge events than expected from the long-term groundwater table record. This finding may result from a strong locality of summer recharge events. Based on an investigation of groundwater recharge in the Franconian mountains (Germany), Rau (1999) deduced that a yearlong recharge consists also of strong summer precipitations which are expected to contribute temporarily to local groundwater recharge, by infiltrating quite fast through highly permeable soil macro structures. In contrast, remaining (mainly winter) precipitation usually infiltrates continuously on a large scale area rather than locally. This explains why isotopic data may generally not indicate a clear winter recharge, even though the available water table record rather does so.

To summarize, local recharge events occur indeed also during summer time, even though the main share of annual recharge takes place usually during the cold season of the year. Regarding these findings as well as the determined ^{3}H–^{3}He ages of almost 0 years at the beginning of this study, it is very likely that at least some fraction of sampled groundwater at the shallow well recharged indeed in May/June 2013. This assumption is in line with the suggestion of Rau (1999) that strong recharge events during summer percolate the entire unsaturated zone through highly permeable structures. Groundwater recharged during this time was in equilibrium with local soil air, the composition of which is well-known from measurements of this study. As pointed out already, the measured relative enhancement of NG mixing ratios in soil air with respect to atmospheric air accounts for 3.2 % in Mai/June 2013, which was found to fit very well to that expected based on groundwater data, assuming that groundwater equilibrated at the recorded WTT.

Some further remarks shall be devolved to deep well groundwater. As shown above, obtained NGTs from deep well samples underestimate the expected recharge temperature (see Fig. 5.11(b)). Even though no observations of soil air composition are available for the estimated recharge time some decades ago, the previous discussion suggests recharge events during summer time as probable reason for this discrepancy. Water age as well as the location of the well motivate a further reason for this finding, seeming plausible on first view: If groundwater recharged in the Odenwald region at a higher altitude, a lower equilibration temperature than estimated for the Upper Rhine Graben would be expected. Assuming a hydraulic conductivity of $0.5 \cdot 10^{-3}$ m/s (LUBW, 2016), a distance of 6.5 km between sampling site and margin of the Upper Rhine Graben and a typical height difference of 200 m to the valley, a flow rate of 485 m/a is obtained by Darcy's law. This would indicate a time span of 13.5 a to overcome a distance of 6.5 km. Obviously, it may be imaginable that groundwater sampled at the deep well recharged in the Odenwald region. However, this approach cannot explain the observed discrepancy between NGTs and expected MAAT of deep well water. The recharge temperature at a higher altitude is described by the wet adiabatic temperature gradient of 0.5 K/100 m (Roedel and Wagner, 2010). However, the ambient air pressure is also decreasing with increasing height (according to the barometric formula), resulting again in a difference of NGT and expected recharge temperature. To overcome this discrepancy, recharge would have to take place at a height of at least about 600 m a.s.l., which is rather unrealistic regarding typical elevations of the Odenwald region. Furthermore, recharge is known to occur also inside the Rhine valley (LUBW, 1999) and should, thus, contribute significantly to local groundwater composition, which is why it is unlikely that the entire amount of deep well groundwater recharged at a higher elevation.

Altogether, the combined set of data from saturated and unsaturated zone indicates an influence of oxygen depletion and varying values of O_2+CO_2 on dissolved NG contents in local groundwater – mainly in samples from the shallow well but also in samples from the deep well. In this context, summer recharge seems to go usually along with enhanced NG mixing ratios in soil air. The unusually dry summer 2015 might appear as a counterexample, since NG mixing ratios in soil air were nearly atmospheric during this time. But it has to be noted that strong groundwater recharge during summer time goes necessarily along with high soil moisture contents and, thus, enhanced NG mixing ratios in soil air.

The impact of oxygen depletion on dissolved NG contents in groundwater shall still be discussed from a more general point of view. Oxygen depletion occurs everywhere in natural soils, even though its intensity depends on local conditions such as available organic material and soil structure. A potential impact of oxygen depletion or rather of varying values of O_2+CO_2 in soil air on NG concentrations in recharging groundwater is, thus, generally imaginable. However, published NGTs from modern groundwater samples are usually in good agreement with expected recharge temperatures, underlining the reliability of NGTs as a temperature proxy (Klump et al., 2007; Cey et al., 2009;

Aeschbach-Hertig and Solomon, 2013). This may appear as a contradiction to the findings of this study, stating a potential impact of oxygen depletion on dissolved NG contents in groundwater. A closer look at local recharge characteristics in the sampling region of this study clarifies this issue. As a consequence of mixing within the aquifer, it is expected that the influence of strong local recharge events during summer time on overall NG concentrations in deeper groundwater diminishes with increasing depth and water age, caused by an overall dominance of recharge during the cold season. In this study, a coincidence of strong water table rise and significant increase of NG mixing ratios in soil air occurred only once in more than 2.5 years (in June/July 2013), underlining the anomaly of this phenomenon.

To confirm this suggestion, further samplings were carried out in the region around the sampling site of this study. These additional wells allow to sample groundwater from the same aquifer but 3 – 57 m deeper compared to the deep well presented in this study. Figure 5.25(a) shows that dissolved NG contents show comparable excess air patterns, except for one well showing degassing (WK202_1). Roughly estimated equilibration temperatures seem already to be higher compared to the deep well. This assumption is confirmed by Fig. 5.25(b): For most wells, the assumption of atmospheric NG mixing ratios in soil air results in NGTs which are in good agreement with expected recharge temperatures. There is mostly no systematical underestimation as observed for sampled groundwater from both wells investigated in detail in this study. Thus, the evaluation of NG concentrations from additional deeper wells of the same aquifer confirms the assumption that dissolved NG contents in shallow groundwater may be affected by summer recharge and oxygen depletion within the unsaturated zone. An overall impact of such recharge events on dissolved NG contents of groundwater is damped and smoothed due to mixing with water recharged during the cold season under atmospheric NG mixing ratios in soil air. The time scale and soil depth for which summer recharge events still

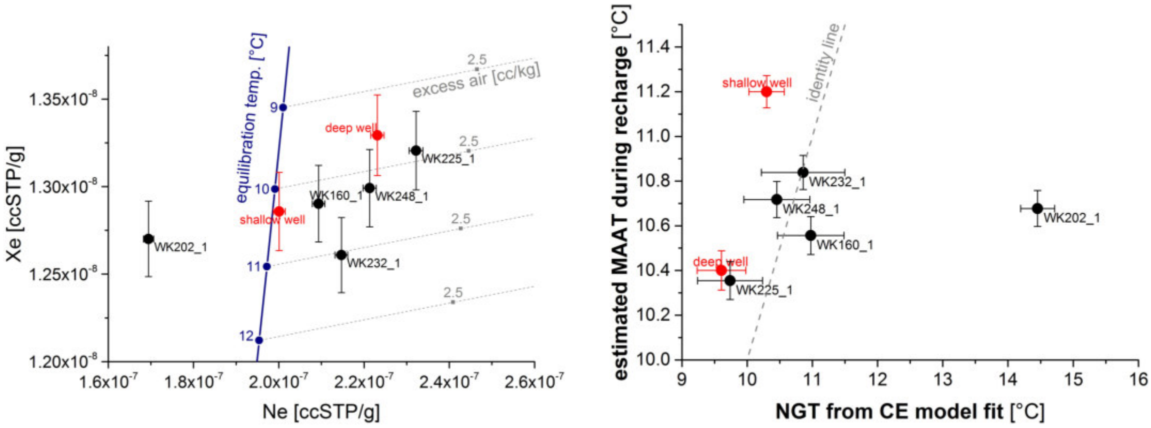

(a) Xe-Ne plot for additionally sampled wells. Excess air lines are determined based on the assumption of an unfractionated excess air pattern. The amount of dissolved air (see gray numbers) is given in units of cc per kg of water.

(b) Estimated recharge temperature (recharge year derived from ^{3}H–^{3}He age) and determined NGT from a CE model fit.

Figure 5.25: Mannheim: Evaluation of dissolved NG contents in groundwater from different wells in the Rhine-Neckar region around the sampling site near Mannheim. All wells are situated within some km distance. Deep and shallow well are labeled in red, respectively.

significantly affects dissolved NG contents in groundwater cannot be reliably determined. Samples from the deep well of this study indicate an age of up to 30 years, while still indicating an influence of summer recharge. In contrast, samples from other wells indicate less recharge during summer time while resulting in ages of about 20 years. This finding confirms the distinct locality of strong recharge events during summer time.

Gas dynamics after recharge: groundwater degassing

Shallow well samples give a clear evidence for temporal degassing. Its general occurrence was already described in several studies, showing depleted NG concentrations with respect to the equilibrium component (Lippmann et al., 2003; Klump et al., 2006; Stute et al., 2007; Visser et al., 2007). In the context of this study, groundwater degassing is of special interest, since it was proposed by Cey et al. (2009) as possible reason for biased excess air model outcomes, based on synthetic samples showing an underestimation of the expected recharge temperature for minor degassed fractionated excess air patterns.

To identify underlying physical processes determining NG concentrations of shallow well groundwater, a forward modeling approach was applied. Based on the CE model formulation, dissolved NG contents are calculated for a given set of model parameters. The formal description was introduced in chapter 3.3.1 as

$$c_{\mathrm{i,w}}^{\mathrm{CE}} = c_{\mathrm{i,w}}^{\mathrm{EQ}} \cdot \frac{1 + AH_{\mathrm{i}}'}{1 + BH_{\mathrm{i}}'} = c_{\mathrm{i,w}}^{\mathrm{EQ}} \cdot \left(1 + \frac{(1 - F_{\mathrm{CE}})AH_{\mathrm{i}}'}{1 + F_{\mathrm{CE}}AH_{\mathrm{i}}'}\right) \tag{5.1}$$

and depends on the equilibrium component $c_{\mathrm{i,w}}^{\mathrm{EQ}}$ as well as on the fractionation parameter

$$F_{\mathrm{CE}} = \frac{B}{A} \tag{5.2}$$

representing the quotient of the initial gas/water ratio A and the final gas/water ratio B after (partial) dissolution of entrapped air bubbles. A comparison to the UA model shows that excess air formation according to the CE model can be separated into a full dissolution of entrapped air, expressed by the term $1 + AH_{\mathrm{i}}'$, followed by a subsequent degassing step, expressed by the term $1/(1 + BH_{\mathrm{i}}')$. Thus, the CE model setup may be interpreted as describing the degassing of an originally unfractionated excess air pattern − which will allow for important conclusions during the following discussion.

The formulation in eq. (5.2) is very evident by just regarding gas/water ratios, aside from changes of the ambient pressure. However, it does not allow to distinguish the different physical causes of changing air bubble volumes, while the intended forward modeling approach should account even for distinct physical processes. This is why a modified CE model formulation is used during the following discussion, originally introduced by Aeschbach-Hertig et al. (2000):

$$F_{\mathrm{CE}} = \frac{v}{q} = \frac{\sum_i n_{i,B} / \sum_i n_{i,A}}{(P_B - e) \,/\, (P_A - e)} \tag{5.3}$$

In this formulation, $v = \sum_i n_{i,B} / \sum_i n_{i,A}$ represents the gas amount ratio in the entrapped air bubbles of final and initial state. The parameter $q = (P_B - e) \,/\, (P_A - e)$ denotes the change in ambient pressure

of final and initial state. Taking into account the correction by saturation water vapor pressure e, the parameter q reflects the ratio of dry gas pressure in the trapped gas phase relative to that in the free atmosphere. Even though the CE model formulation in eq. (5.3) is not that evident as regarding just gas/water ratios, it clearly reflects the two underlying physical processes determining the formation of excess air: a change in hydrostatic pressure (shrinkage/extension of bubbles, described by the parameter q) and a dissolution/exsolution of gases into/from the water phase (change of gas amount in bubbles, described by the parameter v). It has to be noted that both presented model formulations correspond to each other, thus resulting in the same parameter values of F_{CE}[18].
To allow for an independently occurring degassing process, the CE model setup has to be modified, which is done by complementing eq. (5.1) by an additional degassing term:

$$c_{\mathrm{i,w}}^{\mathrm{CE,d}} = c_{\mathrm{i,w}}^{\mathrm{CE}} \cdot \frac{1}{1 + B^d H_{\mathrm{i}}'} \tag{5.4}$$

This solubility-controlled degassing term was originally proposed by Brennwald et al. (2003) for a description of sedimentary pore water. An alternative formulation is to state a diffusion-controlled degassing term (Stute, 1989), which is not further pursued here since a permanent existence of entrapped air bubbles within the quasi-saturated zone clearly motivates a solubility-controlled form of degassing. It is important to note that the parameter B^d is independent (and usually different) from the parameter B describing the formation of original NG concentrations in groundwater according the "traditional" CE model setup. Even though eq. (5.4) describes dissolved NG contents in groundwater in a more general and appropriate way, it is not applied for inverse modeling in NG studies since it contains too many free parameters to achieve reliable estimates of further unknown parameters such as the recharge temperature (Aeschbach-Hertig et al., 2008). However, it allows to reproduce measured NG data in a more realistic way by forward modeling.

Four different scenarios were applied to reproduce the measured time series of dissolved NG contents in shallow well groundwater, gradually including more complex processes:

- **Scenario 1:** constant WTT and water level (expressed as pressure parameter q)
- **Scenario 2:** varying WTT and water level
- **Scenario 3:** varying WTT and water level, adding a degassing term (parameter B^d)
- **Scenario 4:** varying WTT and water level, adding a degassing term, assuming enhanced NG mixing ratios in the gas phase (described by enhanced and fractionated NG mixing ratios in the equilibrating gas phase)

All input parameters of the forward modeling approach as well as the measured data based on which their estimation was realized are described in appendix A.6. Given these parameter values, a time

---

[18] The relation between eq. (5.2) and (5.3) follows from the ideal gas law, stating that the ratio of gas amount n and pressure p is proportional to the volume V assuming equal temperatures in both states ($n/p \propto V$): $F_{\mathrm{CE}} = v/q = \frac{\sum_i n_{i,B} / \sum_i n_{i,A}}{(P_B-e)/(P_A-e)} = \frac{\sum_i n_{i,B}/(P_B-e)}{\sum_i n_{i,A}/(P_A-e)} = B/A$

series of NG concentrations in groundwater was modeled. To quantify the goodness of a specific scenario approach, modeled and measured data are compared by means of the least squares method as already described in chapter 3.3.2 for excess air models. For all 61 time steps, the error weighted deviations for all five NGs are summed up to obtain a χ^2 value for each scenario approach, respectively. Corresponding uncertainty values are assumed according to the reproducibility of NG measurements achieved in this study. In contrast to all remaining parameters, the parameter value of A – which is assumed as uniform for all 61 time steps – was manually modified in a way to minimize this obtained χ^2 value. The parameter A was selected for this purpose since all remaining parameters could be estimated at least roughly based on data records, while the amount of initially entrapped air is rather unknown.

This leads to a final note about the reliability of parameter estimations. Apart from the equilibrium component, components of excess air and degassing are based on parameter values which are just roughly estimated, referring in particular to the parameters v and B^d which are not directly based on recorded data. Furthermore, the determination of q is based on water table data and the assumption that only water from 7.8 m depth was pumped, which is probably not the case due to the vertical extent of the well perforation. These circumstances may result in a systematical bias of the obtained model outcomes, which appears in the resulting χ^2 values corresponding to vanishing fit probabilities – considering the degrees of freedom of the fits. However, the present modeling approach is not aimed at a perfect reproduction of measured data but rather on an identification of underlying physical processes which need to be incorporated to explain the measured NG patterns. Besides this, the achieved χ^2 values shall not be used to obtain a sufficiently high fit probability but rather to compare qualitatively the goodness of different scenario approaches.

Figure 5.26 depicts the time series of measured saturation anomalies (relative to AEW) in shallow well groundwater, as well as forward modeled saturation anomalies for the four presented scenarios. A consideration of a constant WTT and water level results in a worse fit, accompanied by the highest χ^2 value in scenario 1. An improvement is achieved by incorporating temporal variations of these two parameters as it is done in scenario 2. However, it is only possible to reproduce the observed temporary degassing pattern by including a separate degassing term in scenario 3, accompanied by a strong reduction of the obtained χ^2 value. Scenario 4 also includes a separate degassing term, but it accounts in addition for enhanced NG mixing ratios in the equilibrating gas phase, while mixing ratios of heavier NG species are stronger enhanced than those of lighter ones, as described before. Obtained χ^2 values of scenario 3 and 4 are in a comparable range. Resulting χ^2 values of the different scenarios may also be evaluated separately for each NG species (see Tab. 5.4). For reasons of simplicity, only the last two and most realistic scenarios shall be discussed in detail. Achieved χ^2 values for Kr and Xe are half as large in scenario 4, while scenario 3 seems to describe data of He and Ar in a better way. Similar χ^2 values are obtained for Ne. Summed up χ^2 values do not allow to reject one of these two scenarios. However, scenario 4 – accounting for mass-dependent fractionation in soil air – seems to improve the reproduction of heavier NG species which are crucial for NGT estimates.

Altogether, the forward modeling approach clearly indicates an influence of degassing on dissolved NG contents in shallow well groundwater at the sampling site of this study. Furthermore, this de-

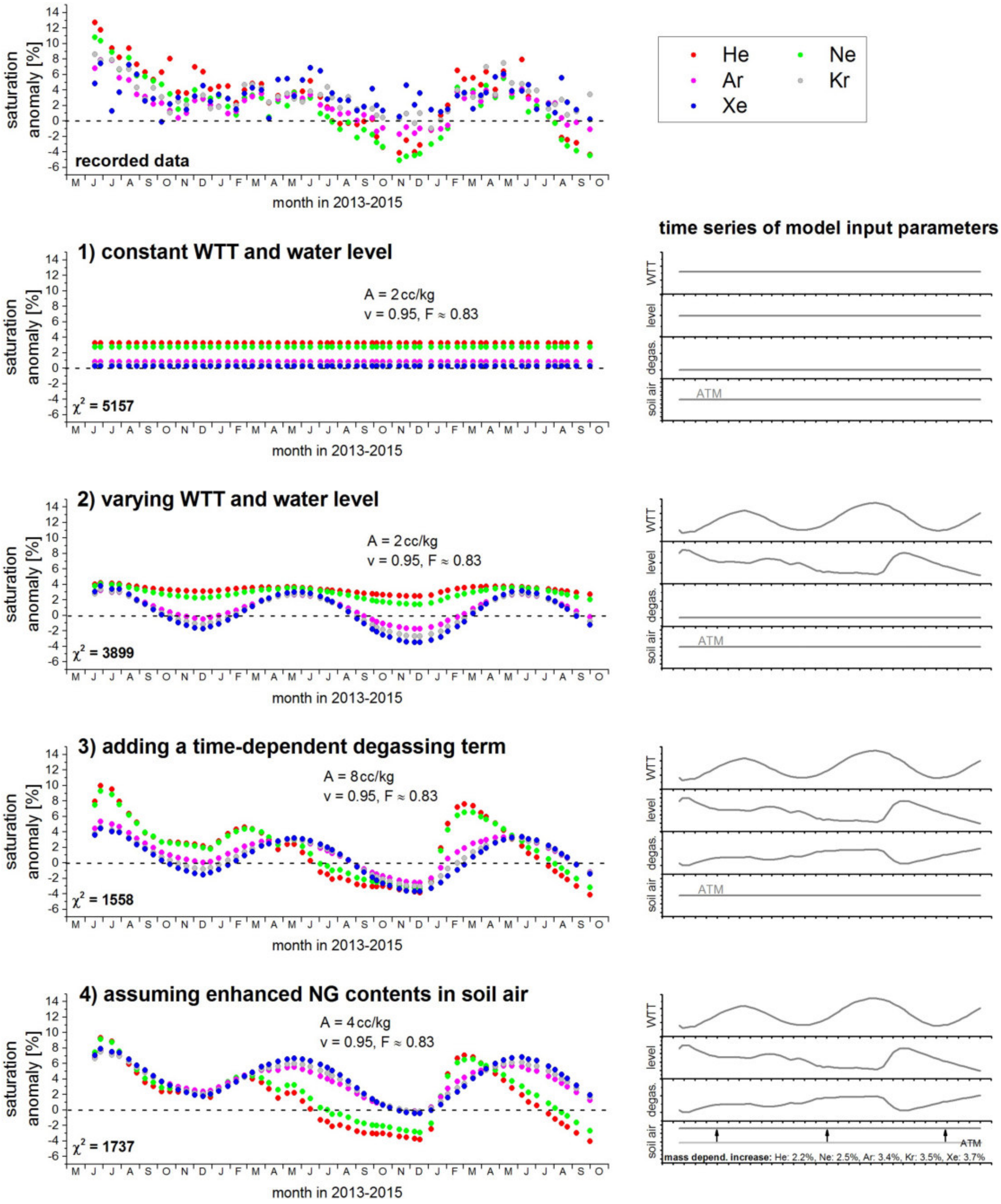

Figure 5.26: Mannheim: Measured saturation anomalies in shallow well groundwater (relative to AEW) and forward modeled saturation anomalies for the four different scenarios. The parameter *A* was modified to minimize the obtained χ^2 value which has to be compared to 304 degrees of freedom in each scenario. On the right side, time series of the input parameters are schematically illustrated.

Table 5.4: Mannheim: Obtained χ^2 values of different forward modeling scenarios, given separately for all considered NG species.

	He	Ne	Ar	Kr	Xe	$\sum\chi^2$
scenario 1	1755	1772	770	628	231	**5157**
scenario 2	1472	1382	379	447	218	**3899**
scenario 3	461	463	130	310	194	**1558**
scenario 4	643	384	478	132	100	**1737**

gassing phenomenon subsequently affects NG concentrations in groundwater developed before by usual excess air formation. This explains the difficulties that the CE model had to describe NG concentrations in groundwater during the degassing period, accompanied by high parameter uncertainties (see results of excess air model fits in chapter 5.2.3). In August 2016, enhanced nitrogen contents were found by an analysis of dissolved gas contents[19] in groundwater at the shallow and the deep well. This confirms nitrogen production as origin of the observed degassing phenomenon. A detailed quantification of dissolved gas contents at these two wells is given in Horstmann (2016).
Furthermore, forward modeling confirms that degassing correlates with the groundwater table level, since the parameter trend of B^d was chosen in correlation with available water level data. This behavior is a consequence of changes in hydrostatic pressure: A falling water table goes along with a lower hydrostatic pressure in the quasi-saturated zone. Consequently, the volume of entrapped air bubbles increases, since a certain amount of previously dissolved gases passes into the gaseous phase. A sinking water table for itself would usually just reduce the saturation anomaly of local groundwater, but not lead to the observed degassing phenomenon. However, an additional gas source as microbial nitrogen production within the saturated zone causes the occurrence of an additional gaseous fraction which initially contains just nitrogen and no NGs. By a subsequent gas/water partitioning, originally dissolved NGs end up in this gas fraction, thus causing the observed degassing phenomenon.

A closer look on the consequences of degassing for dissolved NG contents in groundwater will confirm in the following that just degassing and atmospheric soil air composition, as assumed in scenario 3, is rather unlikely to produce the measured NG pattern in shallow well groundwater. In contrast, scenario 4 will turn out to provide the most reliable description of the measured data.
Forward modeling outcomes of scenario 3 and 4 were used to determine NGTs by a CE model fit in *PANGA*, respectively. The corresponding NG patterns are in fact influenced by an additional degassing term, while a “traditional” CE model setup (without such a degassing term) is applied for their description. Figure 5.27 depicts obtained NGTs. Since forward modeling of both scenarios was based on the WTT as equilibration temperature, determined NGTs should reflect the WTT trend (see black dashed line). For scenario 4 (see red symbols in Fig. 5.27(a)), NGTs underestimate the WTT in a uniform way by about 1°C. This result is in very good agreement with the previously found underestimation obtained for a CE model fit of real measured data (see chapter 5.2.3). In contrast, no

---

[19] The analysis was done by means of a so-called *diffusion sampler*, consisting of a copper tube containing air which is in equilibrium with the surrounding groundwater by diffusion through a silicone membrane. The copper tube was analyzed by the *Omnistar* mass spectrometer.

underestimation is obtained for a fit based on data from scenario 3 (see blue filled symbols in Fig. 5.27(a)).

Investigating the influence of degassing on NGTs, Cey et al. (2009) found systematically too low NGTs from CE model fits of degassed groundwater samples. The extent of excess air fractionation turned out to be critical to the obtained temperature bias. The origin of this finding was not investigated so far in the literature. It shall thus be explained here: The CE model describes only degassing of originally unfractionated excess air patterns. Regarding the strong fractionation of shallow well data, the good agreement of WTT and NGTs from scenario 3 seems to be in contradiction to the finding by Cey et al. (2009). However, this is not the case, but rather a consequence of the comparatively small amount of excess air in shallow well samples. To demonstrate this, scenario 3 was modified by just increasing the amount of excess air (expressed by the parameter A) by a factor of 10, while keeping all remaining parameters unchanged. The obtained NGTs of this so-called scenario 3b are depicted in Fig. 5.27(b) as blue open symbols. Obviously, an underestimation of the WTT is now indeed obtained during the degassing phases. This demonstrates that a rather high amount of excess air is required to induce a comparable underestimation of the WTT as obtained by NGTs from scenario 4 data.

The occurrence of a degassing induced NGT bias shall still be discussed from a more general point of view: For this purpose, two synthetic water samples were created according to the “traditional” CE model setup, for a given fractionation parameter $F_{\mathrm{CE}} = 0.83$, an equilibration temperature of

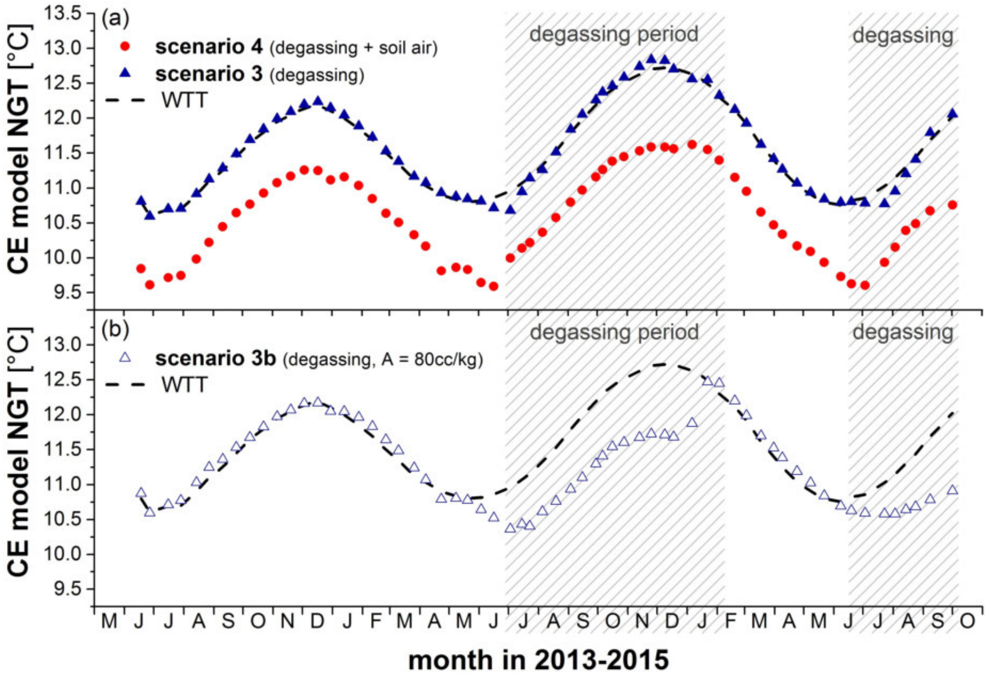

Figure 5.27: Mannheim: NGT determination by CE model fits with *PANGA*. Since all synthetic samples are generated with values of $F_{\mathrm{CE}} < 1$, the fits were carried out with a start value of $F_{\mathrm{CE}} = 0$, even during degassing periods. Chosen uncertainties for the fitting procedure are based on measurement reproducibilities given for this study. Obtained uncertainties of NGTs are not scenario specific and are, thus, not depicted for reasons of a better clarity.

$T = 11.6°C$ but different values of the parameter A (8 cc/kg and 80 cc/kg) indicating the amount of excess air. These two samples were subsequently gradually degassed in steps of $\Delta Ne = 1\,\%$, respectively. The red filled symbol in Fig. 5.28 illustrates the resulting NG concentration of the original (non-degassed) sample which is characterized by saturation anomalies of $\Delta Ne = 8\,\%$ and $\Delta Ne = 18\,\%$, respectively. These original samples were stepwise degassed, as can be seen as sequence of gray symbols. By means of Xe-Ne plots, three fit procedures are exemplarily explained. Filled squares indicate fitted NG data from *PANGA*, which may deviate from actual input data. Colored arrows indicate the NGT obtained by the corresponding fit procedure. The synthetic sample in Fig. 5.28(b) originally contains $\Delta Ne = 18\,\%$. For a gradually stronger degassing, the obtained NG pattern cannot be described any more by the "traditional" CE model setup, resulting in an underestimation of the original recharge temperature (which was 11.6°C). The output of CE model fits from *PANGA* (depicted below the Xe-Ne plot) confirms this finding in a more quantitative way. Fitting of gradually degassed samples results in an increase of the parameter value of A and F_{CE}, going along with a decreasing NGT and fit probability.

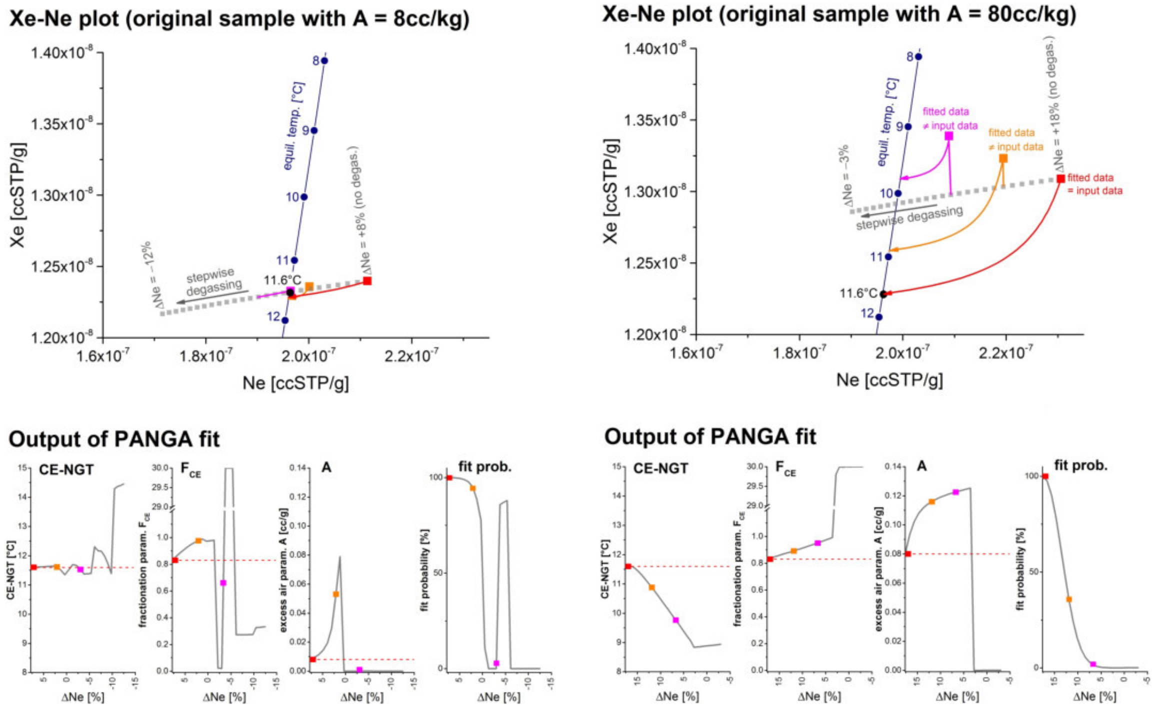

(a) Small amount of excess air: synthetic samples created at $T = 11.6°C$, $F = 0.83$ and $A = 8$ cc/kg.

(b) Large amount of excess air: synthetic samples created at $T = 11.6°C$, $F = 0.83$ and $A = 80$ cc/kg.

Figure 5.28: Mannheim: Illustration of dissolved NG contents in synthetic groundwater samples for varying degrees of degassing in steps of $\Delta Ne = 1\,\%$, respectively (see sequence of gray symbols). Blue lines indicate equilibrium conditions. Exemplary *PANGA* fit outcomes are marked for no degassing (red), degassing by $\Delta Ne = 6\,\%$ (orange) and degassing by $\Delta Ne = 12\,\%$ (purple). Large colored squares mark the determined sample composition of a corresponding *PANGA* fit, which may differ from respective input data (gray symbols). Estimated NGTs from *PANGA* fits are associated by colored arrows. Note that the exact path of such an arrow depends on the specific combination of estimated parameters. The same NGT is associated with a multitude of parameter combinations or rather with different paths. All depicted paths in this figure reflect a uniform value of $F_{CE} = 0.83$.

A totally different outcome is obtained for the synthetic sample in Fig. 5.28(a), originally characterized by ΔNe = 8 %. No significant underestimation of the real equilibration temperature is observed. Even though the “traditional” CE model setup does not provide the appropriate explanation for this degassed data set, it does not fail to end up at the correct NGT. However, a closer look to *PANGA* results below the Xe-Ne plot shows that parameter estimates of A and F_{CE} deviate from the expected values. The outcome of a correct NGT, going along with a sufficiently high fit probability, is favored by the small amount of excess air – preventing an appreciable impact of excess air-related parameters A and F_{CE} on NGT estimates.

A further note shall be given to undersaturated samples, meaning those of $\Delta\mathrm{Ne} < 0\,\%$. Fits for such strongly degassed samples result in high positive values of F_{CE} and vanishing A. This trend is expected, since degassing removed the entire excess air component. The physical meaning of a parameter value $F_{\mathrm{CE}} > 1$ is degassing. It seems thus to be more appropriate to start these fits with a start value of $F_{\mathrm{CE}} > 1$. Corresponding fit outcomes result in similar parameter estimates for these synthetic samples (not shown here). The outcome of unphysical high F_{CE} values is probably also a result of subsequent degassing – since original excess air formation (before degassing started) took place under conditions of $F_{\mathrm{CE}} < 1$. This again justifies to chose a start parameter of $F_{\mathrm{CE}} < 1$ for the fit procedure.

Referring to the different model scenarios 3 and 4, the previous discussion suggests that just degassing is rather unlikely to cause the measured NG patterns in shallow well groundwater, even though an analysis of synthetic samples confirmed the suggestion of Cey et al. (2009) that degassing may bias excess air model outcomes. The potential influence of degassing depends not only on the degree of fractionation but also on the amount of excess air. Theoretically, it might be possible to reproduce measured data indeed by a very high amount of excess air in combination with permanent strong degassing. By this way, measured NG concentrations of shallow well samples may be explained by assuming atmospheric NG mixing ratios in the equilibrating gas phase. However, it is appropriate to reject this approach for three reasons: First, the fraction of pore space filled by entrapped air is usually below 10 % during recharge (Fayer and Hillel, 1986), but even higher entrapped air volumes would be necessary for this approach. Groundwater table fluctuations at the sampling site of this study let not expect such large amounts of excess air. Second, the intensity of degassing obviously varies over time, as a consequence of water table fluctuations. Yet the resulting difference between WTT and NGTs from real measured data remains nearly uniform during the entire study. Third, the “traditional” CE model setup should provide a reliable data description at least during periods of strong water table increase. As described above, its approach can be physically interpreted as a full dissolution of entrapped air bubbles, followed by a degassing step. The only process which is not included in the CE model setup is a subsequent and independent occurring degassing step. Thus, if the initial formation of excess air and degassing occur both at the same time (which is at least partly expected in June 2013 and January 2015), the CE model should be able to describe these two processes in total, even though it cannot differentiate them. However, the CE model fit of real measured data does not provide a better agreement of WTT and NGTs during recharge periods.

Altogether, forward modeling confirms that degassing of an originally fractionated excess air pattern has to be incorporated to reproduce real measured data of shallow well samples. Even though such a degassing process is shown to occur, it cannot explain all characteristics of the measured data set – meaning in particular systematically lower NGTs. The forward modeling approach for shallow well samples suggests that NG mixing ratios in the equilibrating gas phase are enhanced with respect to atmospheric values, respectively, while showing a mass-dependent fractionation. This is in good agreement with the previous discussion about summer recharge and its implication concerning the potential impact of oxygen depletion on NG concentrations of groundwater.

Chapter 6

Tracer applications in tropical latitudes

Results of the two measurement campaigns to the Brazilian tropics are presented and discussed in this chapter, separately for the unsaturated and the saturated zone. Dissolved NG contents in local groundwater are applied to determine NGTs by least squares fits with different excess air models. In this chapter, obtained results are usually displayed according to the respective distance of the sampling site to the next river (Rio Tapajós or Amazon river), ranging from 80 m in Pajuçara up to 25 km in SacradoCoraçao. The height above sea level is generally increasing with river distance, leading to a plateau region as described in chapter 4.2.

6.1 Unsaturated zone

6.1.1 Soil air composition

Soil air composition data in Fig. 6.1 are given for rainy season (filled symbols) and for dry season (open symbols), respectively – indicating a clear seasonality of measured mixing ratios of O_2+CO_2, N_2 and NGs. During the rainy season, O_2+CO_2 is strongly depleted compared to its atmospheric value, while only a slight (but mostly still significant) depletion is observed during the dry season.
The majority of measured mixing ratios of inert gases in soil air is significantly higher compared to atmospheric values, while correlating with O_2+CO_2. With respect to atmospheric air, mixing ratios of NGs are, on average, enhanced by (4.5 ± 1.3) % during the rainy season and by (2.0 ± 1.4) % during the dry season. The distribution of NG data in Fig. 6.1 suggests a stronger enhancement of heavier NG species with respect to lighter ones. Such a fractionation effect was already observed during samplings in Germany and will be discussed later in the context of modeling results. Table 6.1 gives an overview of measured soil air composition for all inert gas species, given as average values of all samplings around Santarém. In the following, N_2 is treated as an inert gas inside the unsaturated zone, since there is no evidence for microbial release or consumption of it.

NG mixing ratios shown in Fig. 6.1 are based on absolute gas amounts measured by the *MM5400* mass spectrometer. Their evaluation requires a knowledge of the exact amount of water vapor contained within gas samples, which depends on both, the soil temperature and the relative humidity of

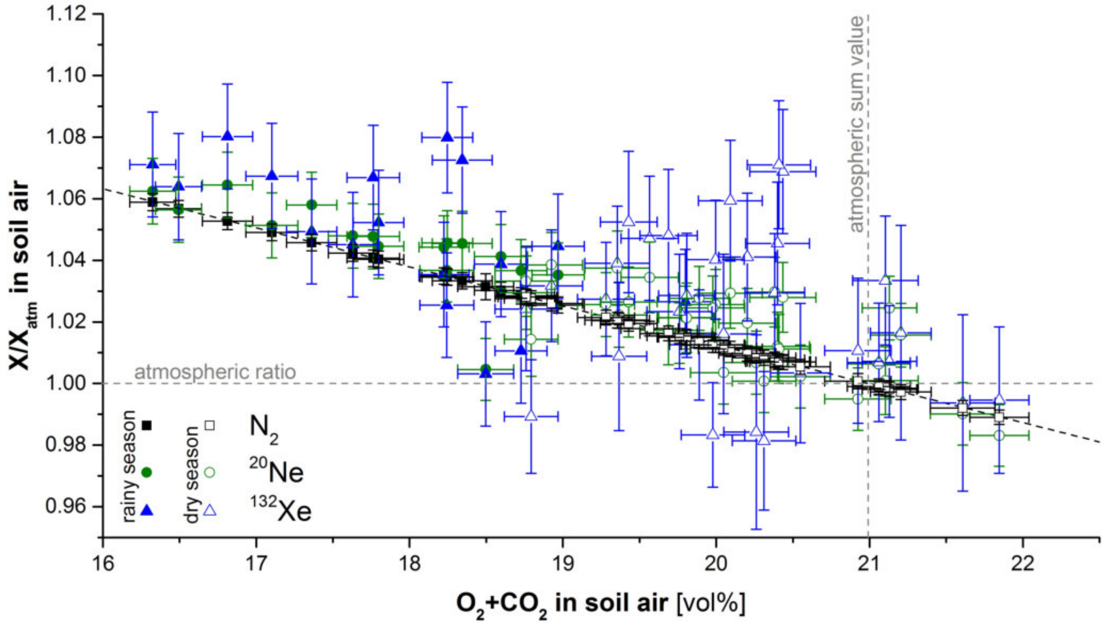

Figure 6.1: Santarém: Correlation between O_2+CO_2 contents in soil air and mixing ratios of N_2, ^{20}Ne and ^{132}Xe (normalized to their contents in dry atmospheric air, respectively). The black dashed line indicates the theoretically expected relationship as described in chapter 3.3.1.

Table 6.1: Santarém: Sum values of O_2+CO_2 [vol%] and mixing ratios of N_2/NGs (normalized to respective atmospheric values) in soil air during the rainy season and the dry season, respectively. Mixing ratios of NGs are enhanced with respect to atmospheric values, on average by (4.5 ± 1.3) % during the rainy season and by (2.0 ± 1.4) % during the dry season.

	O_2+CO_2 [vol%]	ΔO_2+CO_2 [vol%]	**N_2**	ΔN_2	**He**	ΔHe	**Ne**	ΔNe	**Ar**	ΔAr	**Kr**	ΔKr	**Xe**	ΔXe
			deviations from mixing ratios in dry atm. air [%]											
rainy season	**17.9**	0.2	**3.9**	0.3	**4.0**	1.3	**4.5**	1.0	**4.8**	1.0	**4.5**	1.2	**4.8**	1.7
dry season	**20.1**	0.2	**1.1**	0.2	**2.3**	1.2	**1.7**	1.1	**1.3**	1.0	**2.2**	1.7	**2.3**	2.2

the sampled soil air (see chapter 3.2.2). Based on available meteorological data from Fitzjarrald et al. (2009), a soil temperature of 25°C is assumed during the rainy season and 27°C during the dry season. These values are in good agreement with published data of topmost soil temperatures in the Amazon region (see appendix B.15).

The assumption of a relative soil air humidity of 100 % resulted in reliable outcomes for samples of this study taken in Germany. However, a first evaluation of soil air samples from Santarém (presuming water saturated soil air) resulted in unexpected high NG mixing ratios in samples from the dry season, but not in samples from the rainy season. This discrepancy motivated an analysis of the water vapor content of sampled soil air, which was performed by the *Omnistar* mass spectrometer[1] for in total 16 soil air samples from the dry season. Resulting water vapor mixing ratios amount on average to (1.8 ± 0.1) %, which is in conflict to an expected water vapor mixing ratio of about 3.5 % in water saturated soil air at 27°C. Such a deviation may be explained either by an unrealistically low

---

[1] To obtain an appropriate reference gas with a known mixing ratio of water vapor, *diffusion samplers* were used. Air-filled copper tubes were equilibrated with AEW at a constant temperature of 25°C for five days through a silicone membrane.

soil temperature[2] of 16°C or by a relative soil air humidity of only 52 %. The lack of appropriate soil temperature records does not allow for an exact conclusion concerning this issue. Soil material observations of the topmost meter during the dry-season campaign of this study confirm the assumption of a significant reduction of the relative air humidity in soil air, probably caused by the preceding dry period of several months. The evaluation of samples from the dry season was done by accounting for the above mentioned measured water vapor mixing ratio, while soil air samples from the rainy season were evaluated assuming water saturated soil air. By this way, the obtained ^{40}Ar data from both analysis methods – meaning *Omnistar* and *MM5400* – agree well within their uncertainties, as it was also observed for samplings in Germany (see appendix B.1). The evaluation method of the *Omnistar* analysis does not require a knowledge of the water vapor content of the sampled gas. Thus, the agreement of both measurement methods confirms the reliability of the chosen approach to evaluate soil air samples during the dry season. All soil air composition data from samplings near Santarém, including separate data of O_2 and CO_2, are summarized in appendix B.20.

6.1.2 Physical parameters of the unsaturated zone

Physical parameters determining subsurface gas dynamics were analyzed at most of the sampling sites. Figure 6.2(a) illustrates estimated grain size diameters which were determined based on observed soil constituents of the topmost meter and their typical grain sizes (see chapter 2.1.1). Smaller grain size diameters are generally found in the plateau region. Estimated data will be used later to discuss the influence of the topmost soil layer on soil aeration. It has to be kept in mind that obtained values reflect just a very rough quantification of the local soil structure, furthermore omitting any conditions below one meter depth.

Figure 6.2(b) shows measured soil temperatures[3] inside the topmost 10 cm of soil. A clear difference is observable between rainy and dry season, amounting on average to (4.4 ± 0.1)°C. This difference originates from the seasonality of cloudiness and of insolation as well as from varying soil moisture contents influencing the heat capacity of soils.

Measured volumetric soil moisture contents of the topmost 10 cm are shown in Fig. 6.2(c). For data evaluation, a mean porosity of $\phi = 0.38$ was assumed. Again, a clear seasonal difference is obtained, going along with nearly vanishing soil moisture contents inside the topmost 10 cm during the dry season. Three sampling sites were artificially irrigated during the dry season, thus showing unusually high soil moisture contents (see blue shaded ranges).

---

[2] Evaporative cooling may cause a significant soil temperature decrease during the dry season (Bertolo et al., 2006). However, its impact is expected to be rather small, since measured groundwater temperatures of this study (presented later) are in good agreement with local MAATs (Fitzjarrald et al., 2009).

[3] For some sites, no data of soil temperature and soil moisture are available. These parameters were only recorded in combination with soil air samplings, thus not at sites were only groundwater was sampled. Furthermore, some sites were only sampled during the dry season.

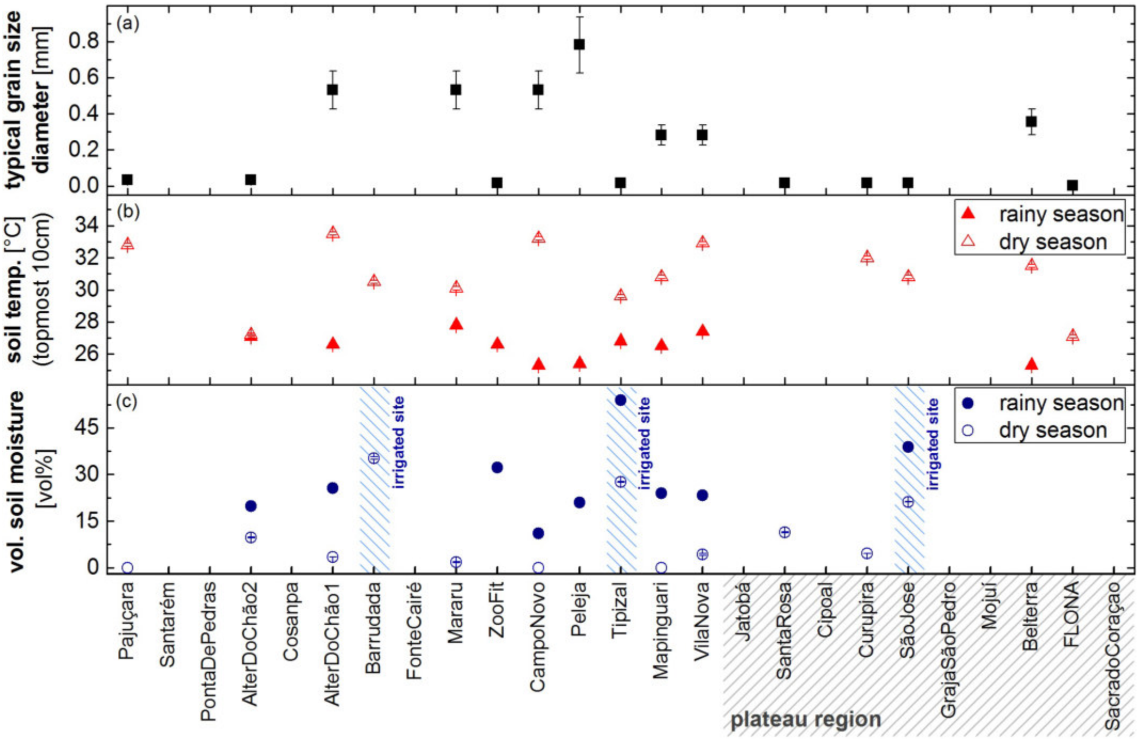

Figure 6.2: Santarém: Physical parameter analysis for the unsaturated zone: (a) estimated grain size diameters; (b) soil temperatures during rainy and dry season, respectively (topmost 10 cm); (c) volumetric soil moisture contents during rainy and dry season, respectively (topmost 10 cm). Irrigated sampling sites are shaded in blue.

6.2 Saturated zone

The evaluation of groundwater samples comprises an analysis of stable isotopes of water as well as of dissolved NG contents. Besides this, physical groundwater parameters are presented. Data are applied for groundwater dating as well as for excess air model applications.

6.2.1 Stable isotopes of water

The local meteoric water line (LMWL) for Santarém was constructed based on available data from GNIP (2016)[4], recorded mainly in Manaus (located about 600 km west of Santarém) and in Belém (located about 700 km east), see Fig. 6.3(a).

Stable isotopes of water were analyzed for all sampled wells. Data from groundwater sampled during the rainy season are in good agreement with the LMWL, as shown in Fig. 6.3(b). Dry-season data from several wells deviate significantly from the LMWL (see labeled symbols), which is probably a consequence of local evaporation: The isotopic composition of recharging groundwater was determined originally by precipitation according to the LMWL. A subsequent fractionation process due to evaporation causes a shift along a line of a lower slope compared to the LMWL (Ramanathan, 1977). This effect is caused by a relative atmospheric air humidity below 100 %, which is particularly

---

[4] The data network GNIP (2016) of IAEA/WMO provides some data directly from Santarém, even though not enough for a reliable determination of the LMWL.

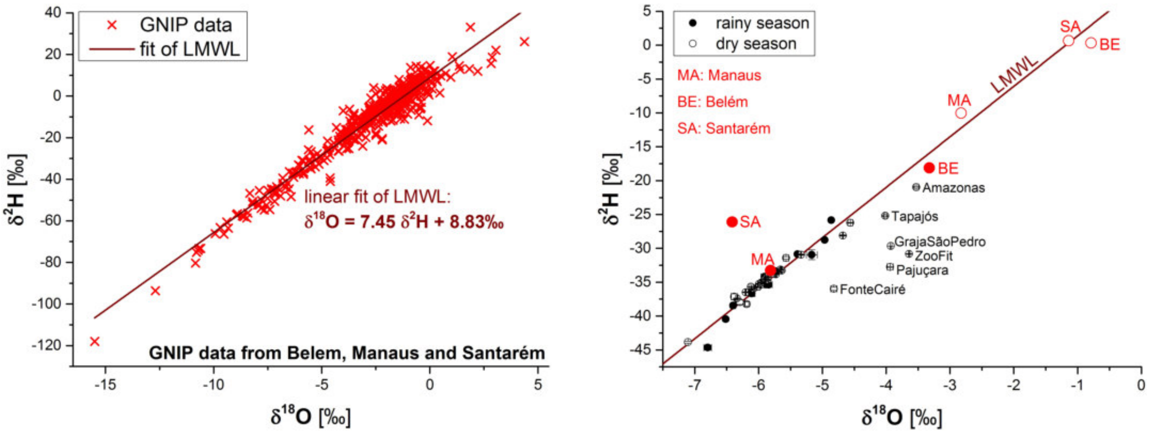

(a) Data from GNIP (2016) of IAEA/WMO (red crosses) and fit of the LMWL (dark red line).

(b) Stable isotope data from groundwater samples (black symbols) and LMWL.

Figure 6.3: Santarém: The typical isotopic composition of precipitation during the rainy (filled red symbols) and the dry season (open red symbols) is depicted, respectively. Samples indicating an impact of evaporation are labeled. Seasonal compositions of precipitation are based on data from GNIP (2016) of IAEA/WMO. All data are given relative to the VSMOW standard.

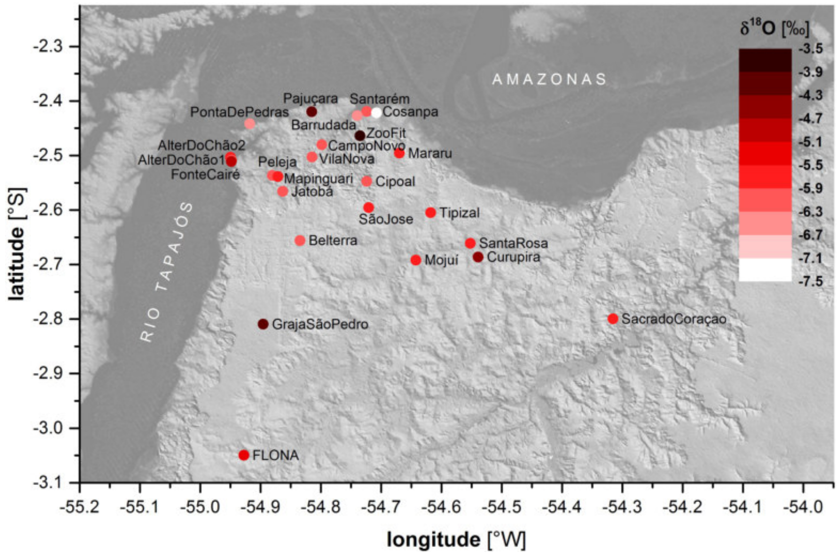

Figure 6.4: Santarém: Map of the sampling region, illustrating the spatial distribution of δ^{18}O data during the dry season.

found during the dry season[5]. Stable isotope data show a clear signature of rainy-season precipitation (see red filled symbols in Fig. 6.3(b)). This finding suggests a predominant recharge during the rainy season, which is expected regarding the annual distribution of precipitation.

Figure 6.4 illustrates the spatial distribution of δ^{18}O data in the sampling region during the dry season. Groundwater near the rivers seems to be more affected by evaporation. Such a dependence on the river distance is probably caused by the local distribution of insolation which tends to be higher near the rivers (see chapter 6.3.3).

---

[5] According to INMET (2016), the typical relative humidity in atmospheric air is more than 90 % during the rainy season, but only 60 – 70 % during the dry season.

6.2.2 Physical and chemical groundwater parameters

Local groundwater temperatures (GWTs) are depicted in Fig. 6.5 and range from 25.8°C to 31.9°C, which is in good agreement with a study from Tancredi (1996) carried out in the same region. As shown in Fig. 6.5(a), the data show a clear dependence of GWTs on the river distance. Even though local surface heights are varying, the maximum height difference between river and plateau region is about 160 m, which is why observed GWT differences of up to 5°C cannot be explained by an adiabatic lapse rate of about 0.5°C/100 m (Roedel and Wagner, 2010). Local GWTs are expected to reflect local MAATs which are higher at near-river sites compared to the plateau region, as will be discussed later in chapter 6.3.3. Besides this, warm river water may lead to an additional heating of riverside areas, regarding measured river water temperatures of 28.8°C during the rainy season and 30.2°C during the dry season.

As can be seen in Fig. 6.5(b), measured GWTs reflect the seasonality of atmospheric temperature fluctuations. GWTs measured during the dry season are on average (0.5 ± 0.1)°C warmer compared to those measured during the rainy season. There is no depth-dependent time shift in temperature, which is a clear hint that recorded GWTs are biased, probably those measured in the dry season, due to a subsequent heating of sampled water during the above-surface measurement. Dry seasonal weather conditions with air temperatures of about 35°C favor a heating of analyzed groundwater. No such bias is expected during the rainy season, which is why all GWTs referred to in the following reflect rainy-season data. For wells only sampled during the dry season, measured GWTs were reduced by the above mentioned average bias, respectively.

Physical and chemical parameters measured in local groundwater are listed in appendix B.25 and depicted in Fig. 6.6. Dissolved oxygen contents do hardly correlate with river distance as shown in Fig. 6.6(a). A slightly decreasing trend is observed at wells within a 12 km distance from rivers. Remaining wells in the plateau region do not show such a trend, which may be favored by high amounts

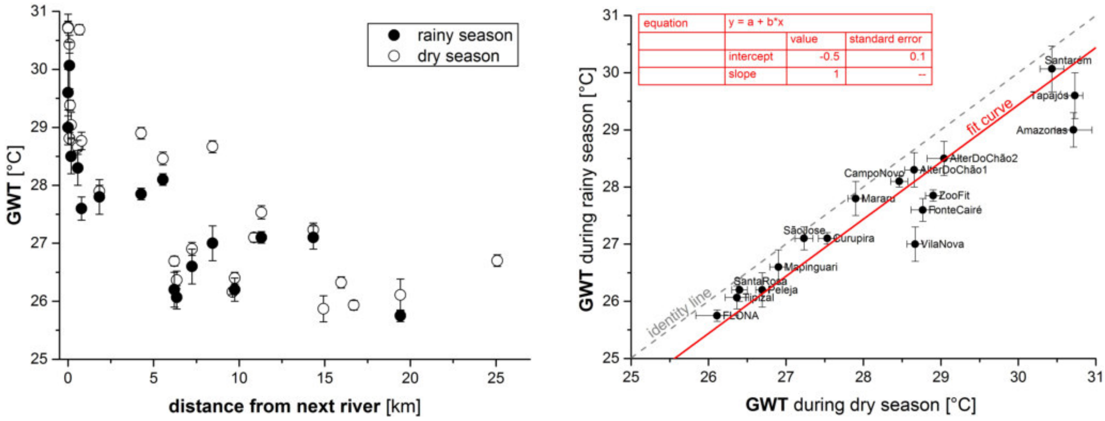

(a) Correlation of GWT and river distance.

(b) Measured GWTs during rainy/dry season.

Figure 6.5: Santarém: Measured groundwater temperature (GWT) data show a dependence on river distance. A linear fit indicates that GWTs measured during the dry season are on average warmer by (0.5 ± 0.1)°C compared to those measured during the rainy season.

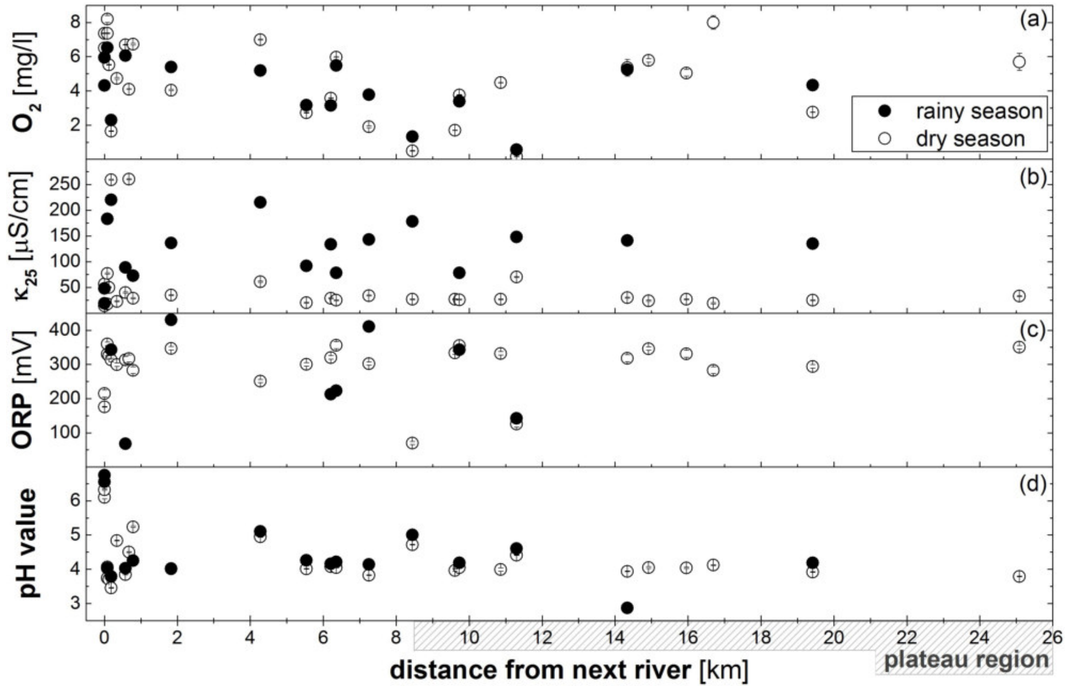

Figure 6.6: Santarém: Measured physicochemical parameters in groundwater, given for rainy (filled symbols) and dry season (open symbols), respectively.

of excess air in local groundwater (as described later in Fig. 6.7). A clear seasonality is not observed for dissolved oxygen contents, with a mean value of (4.1 ± 0.1) mg/l during the rainy season and (4.7 ± 0.1) mg/l during the dry season[6].

Measured conductivities shown in Fig. 6.6(b) are significantly higher during the rainy season with (124 ± 1) μS/cm compared to the dry season with (51 ± 1) μS/cm, apart from the two wells Barrudada and AlterDoChão2 showing unexpected high conductivities of more than 250 μS/cm during the dry season. Data indicate no correlation with river distance. Measurements of Tancredi (1996) in Santarém during the dry season resulted in values of 11 − 37 μS/cm, thus confirming the dry-season records of this study. The obtained seasonality is probably caused by a systematical measurement error: On the one hand, higher conductivities are actually expected during the dry season due to evaporation and an absence of recharge. On the other hand, a calibration of the measurement device was not possible during the field campaign in the rainy season 2014, even though a sensitivity check was performed before each measurement. Local groundwater in the sampling area of this study is thus rather assumed to exhibit a negligible salinity.

Recorded ORP values in Fig. 6.6(c) indicate oxidizing conditions at all sampled wells, while showing neither a seasonality nor a dependence on the river distance. During the rainy season, an average value of (272 ± 130) mV is obtained, during the dry season an average value of (302 ± 67) mV.

Figure 6.6(d) depicts recorded pH values. Data show no seasonality, with a mean pH value of 4.2 ± 0.5 during the rainy season and of 4.1 ± 0.4 during the dry season. Tancredi (1996) gives a similar mean value of 4.4 ± 0.3 for the sampling region around Santarém. Such low pH values may be explained

---

[6] Even though the given average values suggest a significant seasonal difference, it has to be kept in mind that some wells were sampled only during the dry season. Omitting these wells, a dry-season average of (4.2 ± 0.1) mg/l is obtained.

by dissolution of CO_2 from soil air and an equilibrium dominated by H_2CO_3, accompanied by pH values below 5 (Tancredi, 1996). Observed pH values in river water are higher than those measured in groundwater.

6.2.3 Dissolved NG contents in groundwater

Figure 6.7 gives an overview of measured NG concentrations in sampled groundwater, depicted as saturation anomaly with respect to the equilibrium component, respectively. The latter was determined for a temperature of $T = 26.0°C$, for a negligible salinity and an air pressure[7] of 0.991 atm – reflecting conditions recorded by several meteorological stations in the sampling region (Fitzjarrald et al., 2009).

Neon excesses in sampled groundwater are found in a range of up to 200 %. Such rather high values are typical for tropical regions and caused by strong fluctuations of groundwater tables due to pronounced rainy seasons and, thus, episodic recharge (Aeschbach-Hertig et al., 2002a). Comparing obtained saturation anomalies of dry and rainy season, no significant difference is observed at most of the sampled wells. The sampled groundwater from all wells shows a typical excess air pattern characterized by a stronger supersaturation of lighter NG species compared to heavier ones. However, some obtained excess air patterns indicate a mass-dependent fractionation, correlating with the amount of excess air. The relative difference between supersaturations of lighter and heavier NGs is smaller at wells exhibiting small amounts of excess air (see AlterDoChão1, CampoNovo, SantaRosa

---

[7] Local wells are usually constructed in a way to reach just the water table depth, which is why the heights of Earth surface and water table depth are in good approximation assumed to be equal. The pressure of 0.991 atm was determined for the main recharge period, meaning the first half of a year (see appendix B.17 for a more detailed description).

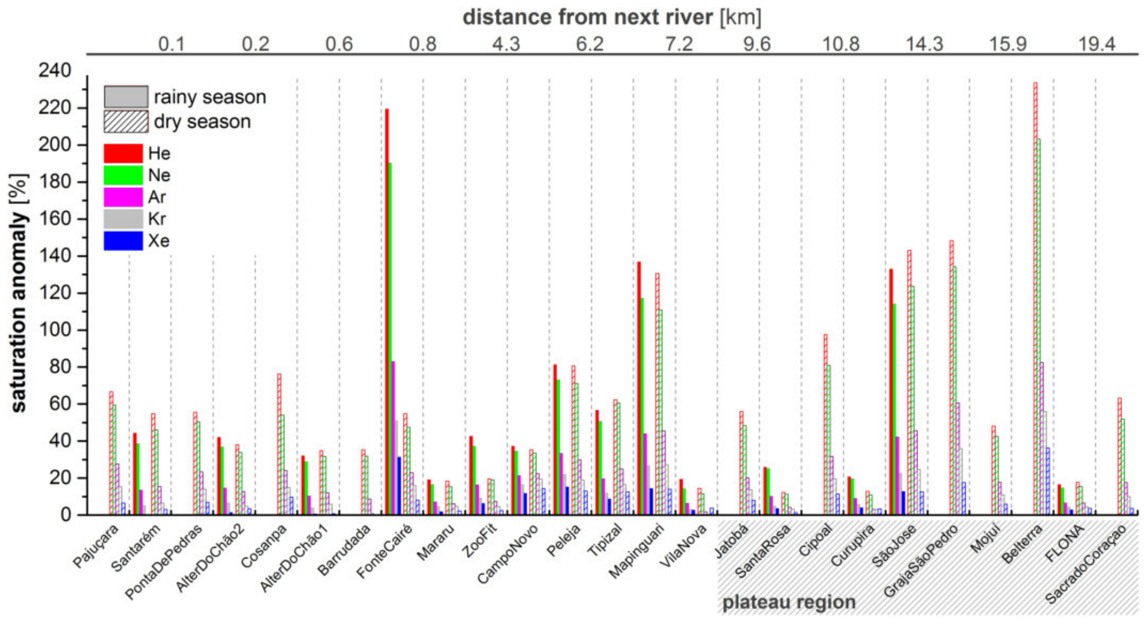

Figure 6.7: Santarém: Dissolved NG contents in sampled groundwater during the rainy season (filled columns) and dry season (shaded columns), respectively. Data are normalized to NG concentrations in AEW for given equilibration conditions of $T = 26.0°C$, $p = 0.991$ atm and $S = 0$ g/kg. All wells are arranged according to their distance to the next river (Rio Tapajós or Amazon river).

or Curupira), thus reflecting a stronger fractionated excess air pattern. In contrast, high amounts of excess air go along with a stronger relative difference in supersaturations (see Pajuçara, Cosanpa, Mapinguari or Cipoal), indicating a less fractionated excess air pattern. A more detailed discussion of excess air and fractionation effects will be given in chapter 6.3. All measured concentrations of NGs in groundwater are listed in appendix B.22.

6.2.4 Groundwater dating

The selection of sampling wells providing rather young groundwater motivates the application of tritium for dating. Resulting data are summarized in Fig. 6.8(a) and listed in appendix B.23. Most samples exhibit only small concentrations of tritium, meaning less than about 3 TU. Low tritium contents in local groundwater originate from the global latitudinal distribution of tritium in precipitation. The stratosphere acts as a reservoir for tritium originating from nuclear bomb tests. It reaches the troposphere during a mixing phase referred to as *spring leak*, occurring in particular in higher latitudes due to the warming of landmasses during spring at the Northern hemisphere (Schell et al., 1970; Michel et al., 2015). Besides atmospheric mixing patterns, the location of bomb tests generally caused a lesser extent of tritium in current precipitation on the Southern Hemisphere (Gat, 1980). Thus, tritium contents of a few TU in today's precipitation in Santarém are usual.

Considering such low tritium contents in precipitation and the achieved analysis precision of about 1 TU, a reliable dating procedure is rather difficult. Besides this, the amount of produced ^{3}He from tritium decay accounts only for a few percent of the ^{3}He amount dissolved by gas/water partitioning during recharge. The component of interest is thus hardly detectable regarding the ^{3}He reproducibil-

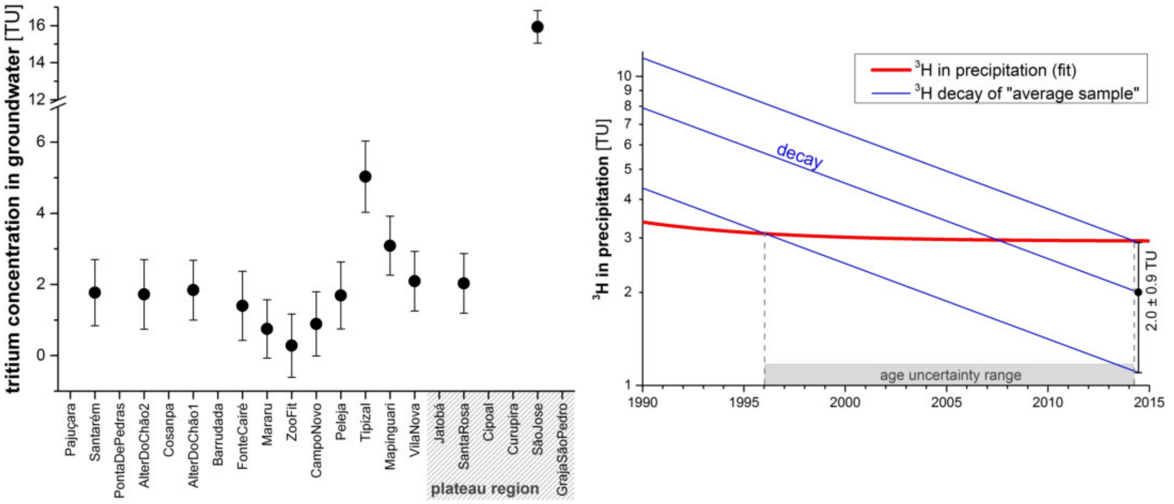

(a) Tritium contents in groundwater samples during the rainy season.

(b) Fit of tritium input and estimation of recharge time (see intersections of blue and red lines).

Figure 6.8: Santarém: The recharge time of sampled groundwater is estimated based on a fit on available data from a measurement site in Manaus (about 600 km west of Santarém), see appendix B.14.

ity of 2.4 % for samples evaluated in this study[8] (see chapter 3.2.2). Thus, the amount of tritium in current tropical precipitation is too small to allow for a sufficiently high dating precision by means of the applied measurement techniques[9] of this study.

However, tritium data allow for an estimation of the time of recharge, as illustrated in Fig. 6.8(b). Measured tritium concentrations in precipitation are available from a continuous record in Manaus, ranging from 1965 to 1990 (GNIP, 2016). This data set allows to determine a fit function in order to estimate the current tritium concentration in local precipitation by means of an extrapolation. Presuming that tritium concentrations in local precipitation of Santarém and Manaus are equal, a tritium concentration of about 3 TU is obtained for modern precipitation in the sampling area of this study, see red curve in Fig. 6.8(b). The tritium analysis of samples from Santarém results in an average tritium concentration of (2.0 ± 0.9) TU in local groundwater. This value allows to determine the time span between precipitating and sampling of the groundwater, ranging from 1996 to today. Even though the low amount of tritium in sampled groundwater does not allow for dating with a precision comparable to that usually achieved by ^{3}H$-^{3}$He dating, the preceding explanations indicate that sampled groundwater from nearly all sampled wells of this study recharged during the last two decades. This finding is of main importance for this study, since local climatic conditions can be assumed to be uniform during the last few decades.

6.2.5 Excess air model applications and determination of NGTs

Dissolved contents of xenon and neon in sampled groundwater allow for a first simple estimation of recharge temperatures. All obtained NGTs are compared to measured GWTs which are assumed to provide an appropriate estimate of the equilibration temperature during recharge. The reliability of this approach is discussed in detail in chapter 6.3.

Assuming an atmospheric Xe/Ne ratio and, thus, no fractionation of the excess air component, a graphical estimation results in NGTs between about 23°C and 29°C (see Fig. 6.9). Such a temperature range is in good agreement with the average of recorded GWTs, amounting to (27.2 ± 0.2) °C. Furthermore, data in Fig. 6.9 give no evidence for a seasonality, confirming the assumption that recharge varies on seasonal scale. However, the graphical evaluation includes only two NG species and presumes an unfractionated excess air pattern, while no information about the underlying physical processes of excess air formation is provided. An application of excess air models is thus motivated. Obtained outcomes of the applied least squares fit procedures are summarized in appendix B.24.

Excess air model applications for atmospheric NG mixing ratios in soil air

Recharge conditions are well described by a negligible salinity and an ambient air pressure given by the site-specific surface height. A height-dependent trend of mean annual air pressures from different

---

[8] The concentration of ^{3}He in AEW (for $T = 26.0$°C, $p = 0.991$ atm and $S = 0$ g/kg) accounts for an equivalent of about 23.9 TU. With a precision of 2.4 % for the ^{3}He analysis, an uncertainty of 0.6 TU results for this ^{3}He content. Assuming a tritium input of 3 TU in local precipitation, an equivalent ^{3}He production of only 1.5 TU is expected during one half-life period of tritium (12.32 a) – which is also a typical groundwater age for sampled wells Santarém as described below.

[9] A more precise ^{3}He/^{4}He analysis with a typical uncertainty of less than 0.4 % may be achieved by applying an appropriate mass spectrometric setup. The ^{3}He in-growth method provides the potential to measure tritium contents of water samples with a relative uncertainty of less than a few percent (Mook, 2000; Sültenfuß et al., 2009).

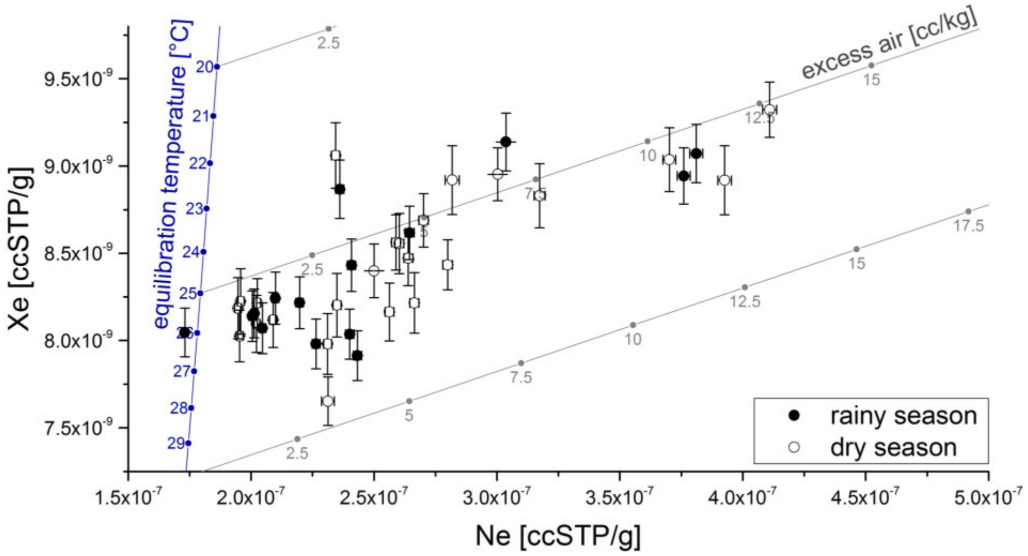

Figure 6.9: Santarém: Xe-Ne plot containing NG data from all sampled wells during rainy (filled symbols) and dry season (open symbols), respectively. Excess air lines are determined based on the assumption of an unfractionated excess air pattern. The amount of dissolved air (see gray numbers) is given in units of cc per kg of water.

meteorological stations was applied to estimate a site-specific air pressure during recharge (see appendix B.17). For all wells, assumed equilibration conditions are summarized in appendix B.19. Regarding the dependence of ^{3}He/^{4}He ratios on Ne/He contents in sampled groundwater, a small but not negligible component of radiogenic helium is expected in sampled groundwater (see appendix B.18). Based on this finding, He data are not included into the fit procedures.

Outcomes of excess air model fits are only presented for samples taken during the second campaign in the dry season 2015 – first, because not all presented wells were sampled in 2014 and, second, since dissolved NG contents show no seasonality at most of the sampled wells. Dissolved NG contents in samples from the wells Belterra and GrajaSãoPedro seem to be rather unrealistic and possibly biased due to an inclusion of air bubbles during sampling. Data of these two wells were used for fitting (apart from ensemble fits), but they are not further regarded during the discussion of NGTs.

Figure 6.10 illustrates the outcomes of excess air model fits, presuming atmospheric NG mixing ratios in soil air during recharge. Site-specific GWTs are depicted as black dashed line, reflecting the reference value for determined NGTs. GWTs measured at the rather deep wells Santarém, Cosanpa and Barrudada are probably biased by geothermal heat flow as discussed later in chapter 6.3. For these three wells, an “unbiased” GWT was estimated as an average of the GWTs measured at the two surrounding wells, respectively.

The specific parameters of all applied excess air models were introduced in chapter 3.3.1. UA model NGTs significantly underestimate the GWT, on average by (2.6 ± 0.4)°C. A smaller underestimation of (0.9 ± 0.9)°C is achieved by CE model fits and a non-significant underestimation by (0.2 ± 1.5)°C by PR model fits. Average fit outcomes of the different models are summarized in Tab. 6.2. The deviations between UA model NGTs and GWT tend to be higher for samples with a stronger fractionated

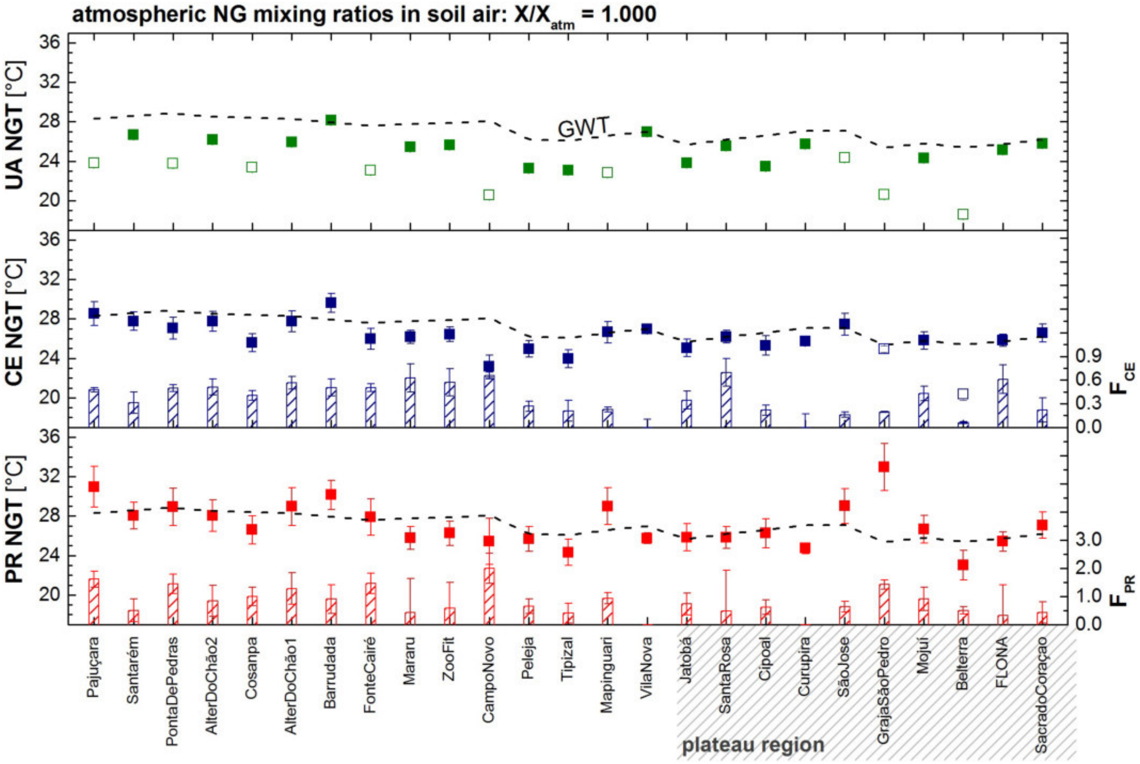

Figure 6.10: Santarém: Estimated NGTs from excess air model fits, assuming atmospheric NG mixing ratios in soil air during recharge and involving data of Ne, Ar, Kr and Xe. Fits with a probability above 1 % (resulting from χ^2 value and the degrees of freedom of the fit) are illustrated as filled symbols, while open symbols indicate lower probabilities. The uncertainty of GWTs (black dashed line) accounts on average for 0.2°C.

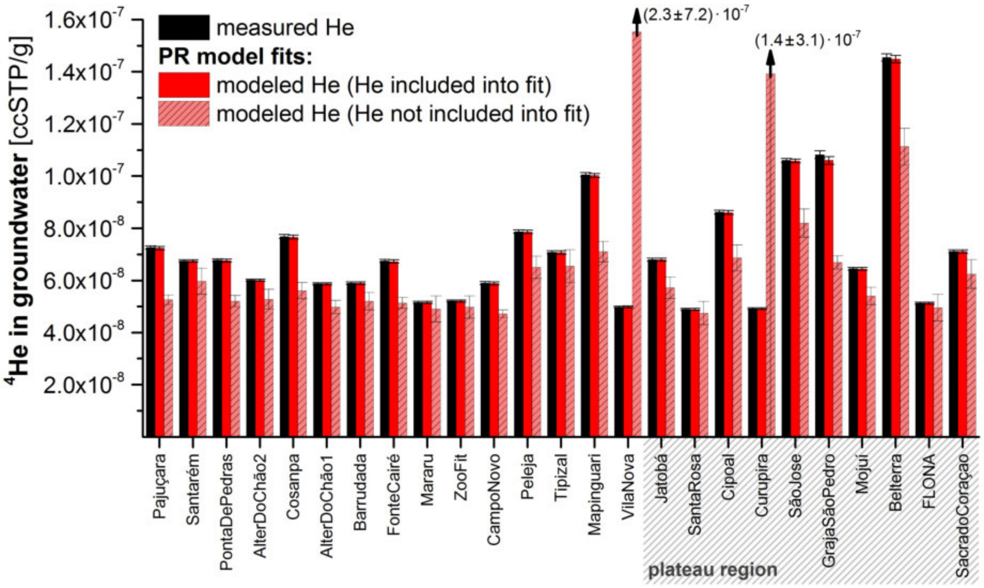

Figure 6.11: Santarém: Measured concentrations of helium as well as modeled helium concentrations by PR model fits with and without an inclusion of helium data, respectively. Fit outcomes show a significant deviation of modeled and measured helium concentrations if helium data have to be determined by the PR model.

Table 6.2: Santarém: Overview of the applied excess air model fits and obtained parameter values. Outcomes as well as their uncertainties are averaged for all samples included into the fits (except for Belterra and GrajaSãoPedro). For the fit probability *pr*, the standard deviation is given as uncertainty to give an impression of its typical fluctuation across the different samples.

atmospheric NG mixing ratios in soil air: X/X_{atm} = 1.000

model	pr [%]	Δpr [%]	A [cc/g]	ΔA [cc/g]	F_x	ΔF_x	P_x	ΔP_x	T [°C]	ΔT [°C]	GWT-T [°C]	ΔGWT-T [°C]
UA	25	31	0.0044	0.0001	-	-	-	-	24.6	0.3	2.6	0.4
CE	60	28	0.0122	0.0048	0.39	0.10	-	-	26.3	0.9	0.9	0.9
PR	61	28	0.0117	0.0045	0.44	0.86	-	-	27.1	1.5	0.2	1.5

enhanced NG mixing ratios in soil air (with respect to atmosphere): X/X_{atm} = 1.045

model	pr [%]	Δpr [%]	A [cc/g]	ΔA [cc/g]	F_x	ΔF_x	P_x	ΔP_x	T [°C]	ΔT [°C]	GWT-T [°C]	ΔGWT-T [°C]
UA	32	34	0.0041	0.0001	-	-	-	-	26.4	0.4	0.9	0.4
CE	59	28	0.0101	0.0104	0.31	0.14	-	-	27.8	0.9	−0.5	0.9
PR	61	27	0.0099	0.0041	−1.08	64.11	-	-	28.3	1.4	−1.1	1.4
OD	0	0	0.0031	0.0002	-	-	1.19	0.02	31.5	0.9	−4.2	0.9
GR	33	0	0.0116	0.0024	1.92	0.28	0.99	0.05	26.1	1.6	1.1	1.6

excess air component. This can be seen by regarding the obtained fractionation parameters, depicted as columns in the respective panels of Fig. 6.10. Obtained NGTs from CE model fits underestimate GWTs mainly at wells near the rivers, while a good agreement is found at wells in the plateau region. The origin of this finding is discussed later in chapter 6.3.

PR model NGTs do not show a temperature bias on average, but they go along with high uncertainties and fluctuations around the trend of GWT. Even though the obtained fit probabilities are higher than those obtained from other models, the PR model does not describe the measured NG data in a reliable way. The PR model is not able to reproduce measured helium contents in sampled groundwater, if helium data are not included into the fit procedure (see Fig. 6.11). As a consequence, modeled helium concentrations (red shaded columns) are significantly lower than actually measured helium concentrations (black columns). This is a consequence of the diffusion-based model approach, resulting in a strong depletion of helium compared to remaining NGs, caused by its high diffusivity. The obtained discrepancy indicates that diffusive transport cannot provide a reliable description of the data sampled in this study.

Excess air model applications for NG mixing ratios in soil air differing from atmospheric values

Measured data of soil air composition during the rainy season, which is the predominant recharge period, show an average enhancement of NG mixing ratios by 4.5 % with respect to the atmospheric values. To account for measured NG mixing ratios in soil air, fits were again performed for air pressures which were simply enhanced by a factor of 1.045, respectively. Outcomes are depicted in Fig. 6.12. Two further excess air models were applied, namely the OD and GR model – both allowing for an ensemble fit of the ambient air pressure parameter.

UA model outcomes still show a significant underestimation of the GWT, on average by (0.9 ± 0.4)°C, while a non-significant overestimation by (0.5 ± 0.9)°C is obtained for NGTs estimated by the CE model. A likewise non-significant overestimation by (1.1 ± 1.4)°C results from PR model fits – which is not discussed here in more detail due to the already described difficulty to describe the sampled data by a diffusion-based approach.

The still remaining bias of UA model NGTs can be regarded as a consequence of an unconsidered fractionation. By accounting for soil air composition data measured during the rainy season, a better agreement is obtained between CE model NGTs and GWT. As mentioned above, the corresponding deviations seem to depend on the river distance. This behavior becomes more clear by a separate consideration of CE model NGTs from the wells in the plateau region (average underestimation of GWT by (1.1 ± 0.8)°C) and the remaining wells near the rivers (average underestimation of GWT by (0.1 ± 1.0)°C).

An ensemble fit applying the OD model results in a significant overestimation of the GWT, on average by (4.2 ± 0.9)°C, going along with negligible fit probabilities and an unrealistic pressure parameter of

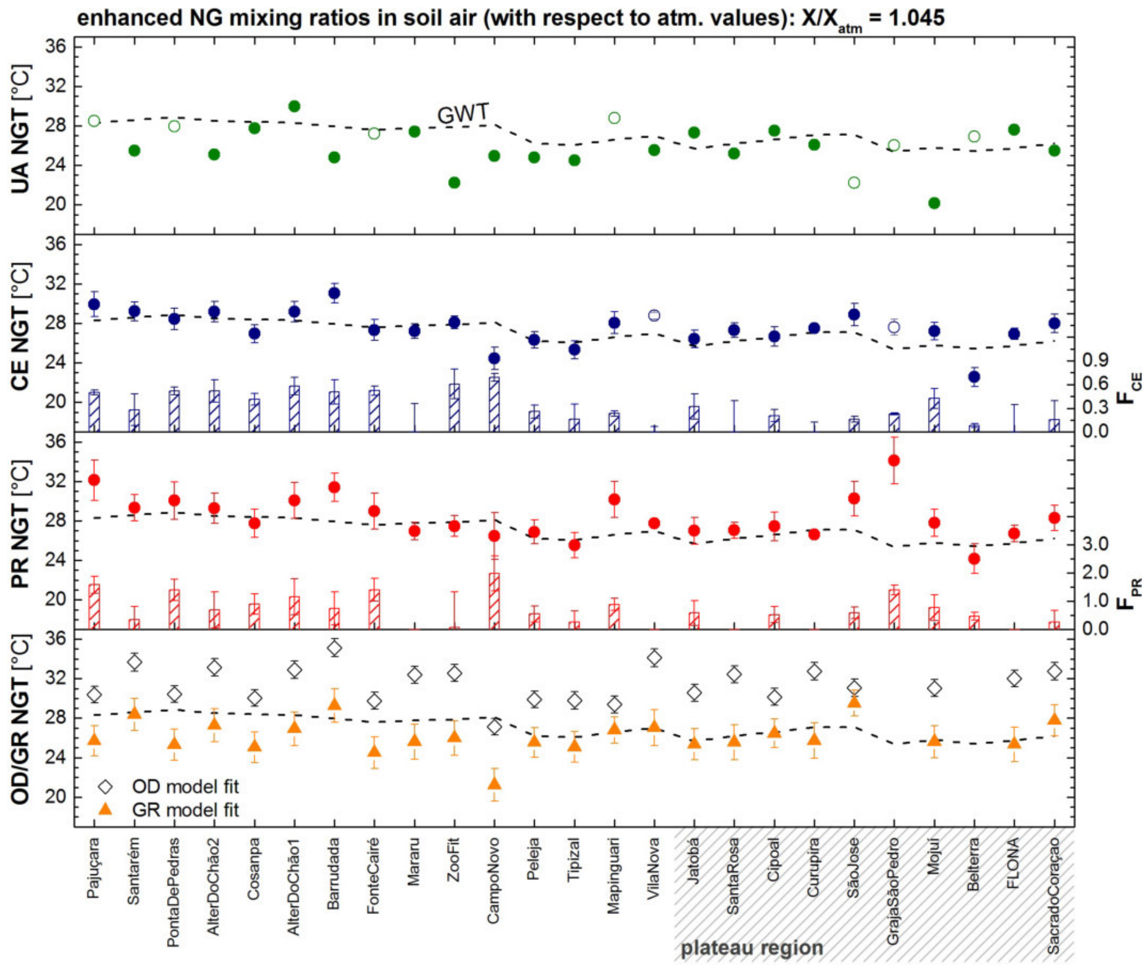

Figure 6.12: Santarém: Estimated NGTs from different excess air model fits assuming enhanced NG mixing ratios in soil air with respect to dry atmospheric air and involving data of Ne, Ar, Kr and Xe. Fits with a probability above 1 % (resulting from χ^2 value and the degrees of freedom of the fit) are illustrated as filled symbols, while open symbols indicate lower probabilities. The uncertainty of GWTs (black dashed line) accounts on average for 0.2°C.

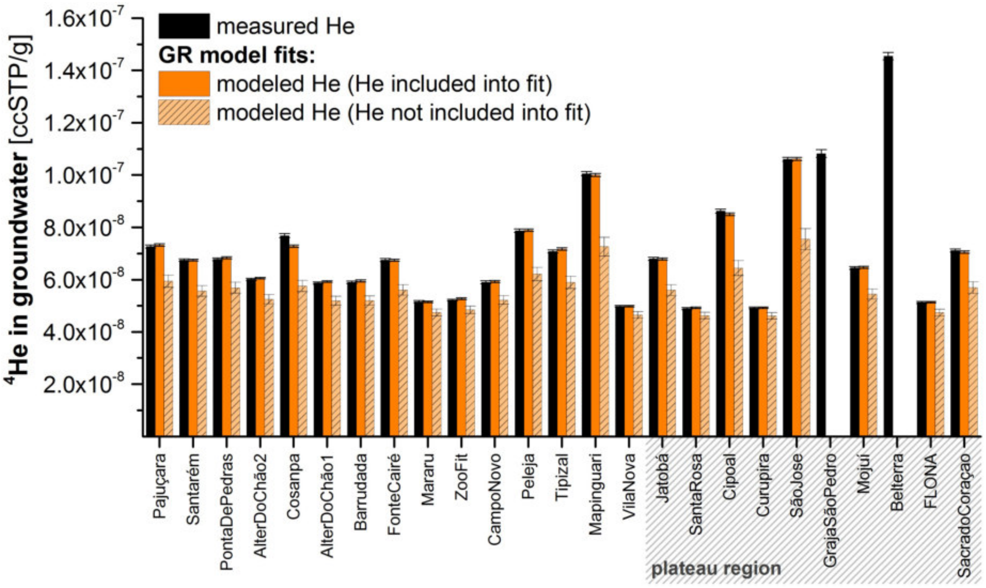

Figure 6.13: Santarém: Measured concentrations of helium as well as modeled helium concentrations by GR model fits with and without an inclusion of helium data, respectively. Fit outcomes show a significant deviation of modeled and measured helium concentrations if helium data have to be determined by the GR model.

$P_{\mathrm{OD}} = 1.19 \pm 0.02$. The GR model ensemble fit results in an underestimation of GWTs, on average by (1.1 ± 1.6)°C and accompanied by a pressure parameter of $P_{\mathrm{GR}} = 0.99 \pm 0.05$. As shown in Fig. 6.13, the diffusion-based approach of the GR model shows the same difficulty to describe helium data as already observed before for the PR model. Thus, the acceptable fit probability does not indicate a reliable data description.

6.3 Discussion

Unsaturated zone data are discussed with regard to parameters determining the soil air composition. For this purpose, a modeling routine is applied to identify underlying transport mechanisms. Above shown saturated zone data motivate a detailed discussion of two aspects: First, the origin of high excess air contents in sampled groundwater is investigated. In this context, tropical conditions as they are found in Santarém provide the potential to demonstrate the applicability of excess air as a climate proxy. Second, excess air model fits suggest systematical deviations of determined NGTs from expected recharge temperatures at near-river sites, while a good agreement is obtained in the plateau region. This temperature discrepancy shall be investigated, also in view of a potential impact of varying soil air compositions on dissolved NG contents in recharging groundwater.

6.3.1 Determining factors of soil air composition under tropical climate conditions

Soil air composition data show a seasonality as well as significant deviations across the sampling sites, motivating an investigation of the determining parameters. The sampling area was chosen in a way to ensure uniformly high temperatures[10], which is why variations of soil moisture get into the focus. As shown in Fig. 6.14(a), a correlation is observed between O_2+CO_2 contents of soil air and volumetric soil moisture contents. Obviously, an increasing soil water content leads to a stronger depletion of O_2+CO_2, as it is expected due to the preferential dissolution of CO_2 in soil water. Such a correlation is obtained although soil moisture contents were measured in the topmost 10 cm of soil, while soil air was pumped from depths of several meters. This finding confirms the significance of topmost soil layer conditions for the ventilation of the entire soil profile. An anomaly occurs at artificially irrigated sampling sites (see red symbols in Fig. 6.14), indicating that irrigation disturbs such a correlation. Argon data in Fig. 6.14(b) show a similar but inverse correlation with volumetric soil moisture. This behavior is mainly a response to respective values of O_2+CO_2, as will be discussed below in the context of modeling results.

Besides soil moisture contents, further parameters are expected to affect the soil air composition, meaning in particular the soil depth, temperature, soil structure and vegetation. As shown in appendix B.21, none of these parameters is found to correlate with recorded soil air data on significant scale, which justifies a common evaluation of tropical soil air data within the scope of this study, regardless of site-specific conditions.

Numerical simulation of subsurface gas transport

A simulation of subsurface gas transport was applied to reproduce measured soil air data. The model setup is the same as described before in chapter 3.3.4. Diffusive transport is assumed to be indirectly caused by oxygen depletion (denoted as “OD diffusion”), by temperature gradients (“thermal diffusion”), by varying water vapor contents (“water vapor gradients”) and by gravitational separation (“gravitation”).

---

[10] The yearlong temperature fluctuations in Santarém account for about 2°C and are, thus, negligible compared to mid-latitude conditions.

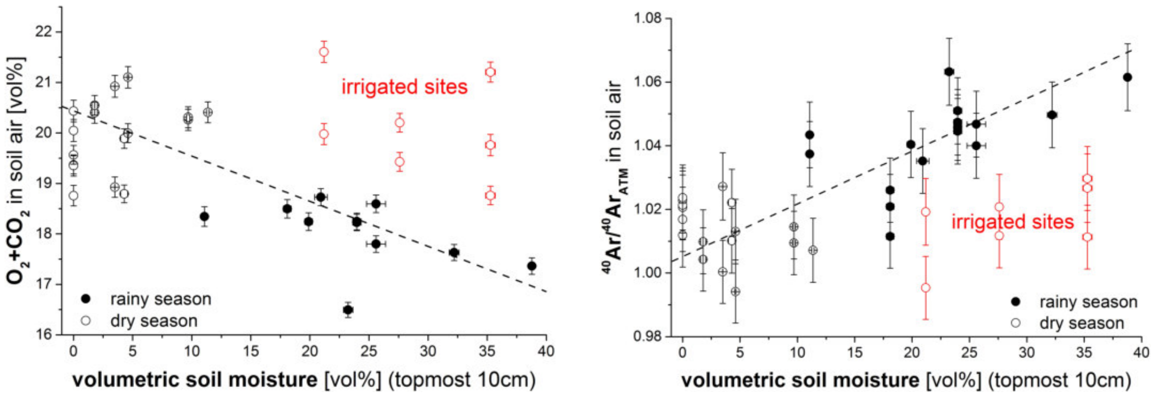

(a) Volumetric soil moisture and O_2+CO_2 mixing ratios in soil air.

(b) Volumetric soil moisture and ^{40}Ar mixing ratios in soil air.

Figure 6.14: Santarém: Correlation of soil air composition and volumetric soil moisture contents. Artificially irrigated sampling sites are illustrated as red symbols and not included into the black dashed trend line. Soil moisture was measured within the topmost 10 cm of soil, while soil air data originate from sampling at several meters depth, explaining the deviation of red symbols from the general relationship.

Meteorological input parameters (temperature and air humidity) are taken from Fitzjarrald et al. (2009). Data of input parameters sampled in the scope of this study (soil moisture and O_2+CO_2) are only available for the rainy and dry season, respectively, but not as a continuous yearlong record. This is why all input parameters are described by means of a sine type function, based on available maximum/minimum data. While seasonal temperature fluctuations are negligible in the tropics, this is not the case on daily scale. A sine function was applied to describe atmospheric temperature variations on daily scale, fluctuating between 31°C (by day) and 21°C (at night). Such fluctuations are assumed to be damped inside the soil with an attenuation length of 0.5 m. For atmospheric air humidity, a similar sine function was chosen, fluctuating between 56 % (by day) and 100 % (at night). Previously presented findings suggest that volumetric soil moisture contents vary on seasonal scale even at soil depths of several meters. In the entire soil profile, the volumetric soil moisture is thus described by a sine function fluctuating between saturation (rainy season) and $\theta = 12$ vol% (dry season). The soil porosity is estimated as $\phi = 0.38$.

While it is appropriate to assume equal meteorological conditions at all sites in the sampling area of this study, this is not the case for values of O_2+CO_2 which were observed to vary significantly across different sampling sites. It was thus decided to perform individual model runs for a certain range of O_2+CO_2 input data. Soil air measurements resulted in a data range of O_2+CO_2 between 16.3 vol% (deepest value during the rainy season) and 21.9 vol% (highest value during the dry season), with an average seasonal amplitude of 1.1 vol%. The model routine was thus performed for different sine type input functions which all have in common an amplitude of 1.1 vol%, while fluctuating around individual mean values chosen from the just mentioned range (in steps of 0.25 vol%). Apart from individual O_2+CO_2 inputs, all model runs have equal meteorological conditions and soil moisture contents in common.

Figure 6.15 illustrates the distributions of measured data (left columns) and of model outcomes (right columns) for all analyzed gas species, respectively. All data are given as deviations from the respective atmospheric mixing ratios. The shown distributions are complemented by a black shaded box reflecting their respective standard deviations. An evaluation of model outcomes based on standard deviations is motivated by a sampling procedure covering multiple sites, the data of which are assumed to be in good approximation normally distributed. The average value of each distribution is depicted as black vertical line.

During both seasons, measured and modeled data are in good agreement. Model outcomes of the rainy season suggest a slight mass-dependent fractionation (see black dashed line in Fig. 6.15(a)) which is hardly visible in measured data. The absence of a fractionation effect in measured data suggests an overestimated impact of diffusion-based mechanisms in the model, possibly due to an underestimation of soil moisture during the rainy season. During the dry season, model outcomes tend to be systematically lower than measured data. Even though this finding is not significant, it may also be caused by a wrong estimation of soil moisture contents.

A further remark shall be given to the spread of model outcomes, which generally diminishes for lighter gas species, most obviously for helium data. This behavior is probably caused by diffusive balancing. As a response to (usually depleted) O_2+CO_2 values, mixing ratios of all gas species are

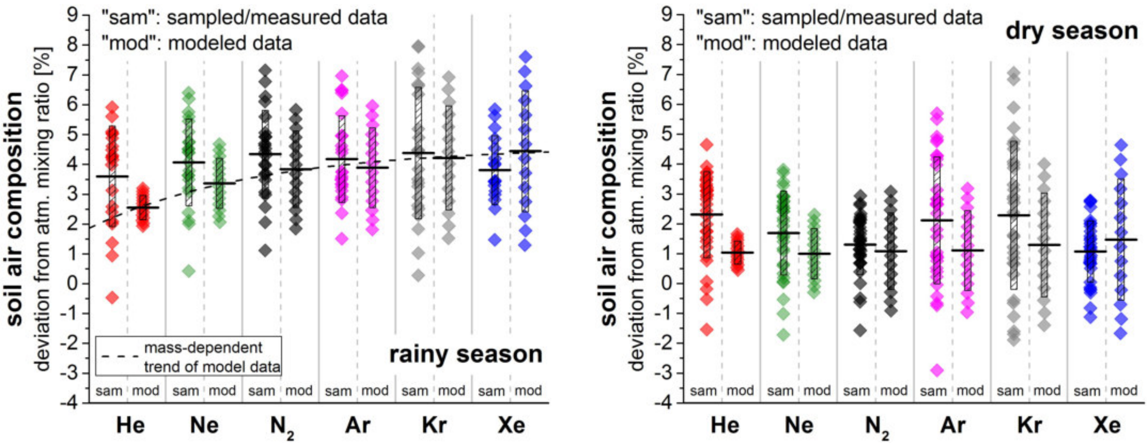

(a) Rainy season.

(b) Dry season.

Figure 6.15: Santarém: Comparison of measured data (left columns) and model outcomes (right columns). Modeled data are determined for a soil depth of 2 m. Black shaded boxes reflect the standard deviation of respective data distributions, black horizontal lines their average values. The black dashed line in Fig. 6.15(a) indicates a mass-dependent fractionation observed in model outcomes, visualized as exponential fit. Depicted data reflect the most abundant isotopes, respectively – meaning ^{4}He, ^{20}Ne, ^{40}Ar, ^{84}Kr, ^{132}Xe and ^{14}N.

advectively changed (usually enhanced) to the same extent. The consequently arising diffusive balancing flux results in a “counteracting” effect on lighter gas species, whereby a stronger advectively caused deviation goes along with a stronger subsequent diffusive balancing. By this way, the original spread of a distribution of mixing ratios is reduced due to diffusive balancing. For heavier gas species, a converse effect is supposed. In contrast to model outcomes, the spread of the respective distributions of measured data does not depend on the mass of the considered gas species. This discrepancy confirms an overestimated impact of diffusion-based mechanisms.

Mixing ratios of inert gases in soil air seem to be strongly affected by an advective balancing of O_2+CO_2 values. A subsequently occurring diffusive balancing of arising concentration gradients is expected to have a minor but not negligible impact. Thermal diffusion as well as water vapor flux may be generally omitted, which is a consequence of vanishing gradients of temperature and water vapor contents.

The absence of mass-dependent fractionation in measured data shall still be discussed in a more evident way. Figure 6.16 shows correlation plots for several NG species, containing model outcomes (blue/red lines) and measured data (filled/open symbols). It has to be kept in mind that modeled helium data are systematically lower than measured values (see explanations above). Imagining a rightward shift of the shown model data in Fig. 6.16(a) and Fig. 6.16(b), correlations of model data would be in a very good agreement with measured values. Depicted model outcomes are only given for the rainy and the dry season, respectively, but not for intermediate periods. Annual trends can be assumed to proceed on a path which connects certain points of the blue and the red line, respectively (exemplary shown as green lines). Thus, model data indicate that the yearlong trend of soil air fractionation does hardly vary on seasonal scale, by following a line which is nearly parallel to the shown identity line. Such a rather uniform yearlong fractionation of soil air was also observed during samplings in Germany.

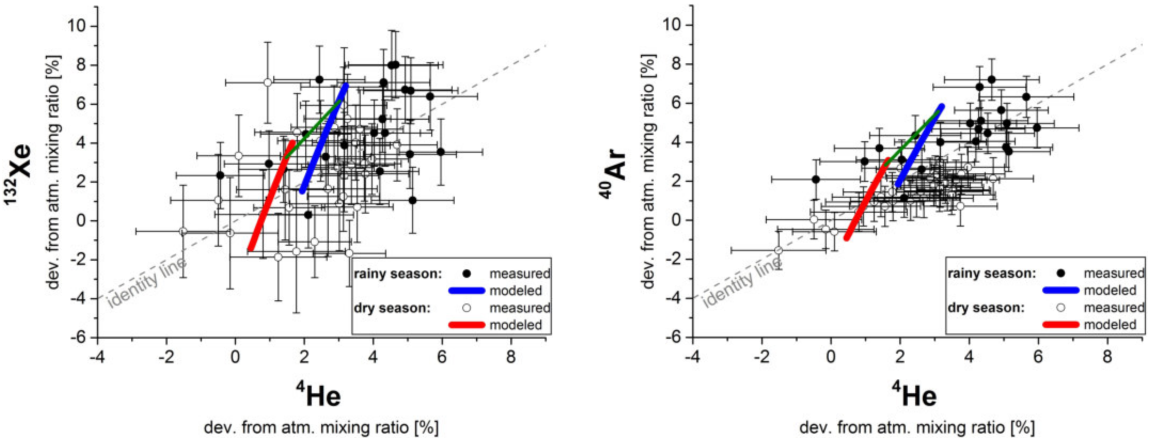

(a) Xe-He plot.

(b) Ar-He plot.

Figure 6.16: Santarém: Fractionation plots: Modeled data (blue/red lines) and measured data (filled/open symbols) during rainy and dry season, respectively. Depicted data are given as percentage deviation from the atmospheric values, respectively. Green lines exemplarily indicate yearlong trends of modeled data.

6.3.2 Saturated zone: determinants of dissolved NG contents

Dissolved NG contents in sampled groundwater imply neon excesses of more than 100 %, which is typical for tropical regions due to pronounced seasonal recharge. There exist only a few NG studies from the tropics allowing for a direct comparison with data of this study. Stute et al. (1995) found neon excesses of up to ΔNe = 105 % in Holocene groundwater of the Piauí Province in the northeast of Brazil. In old groundwaters, Stute and Talma (1998) found ΔNe values of more than 200 % in Namibia, while Beyerle et al. (2003) give values of up to ΔNe = 124 % in the Sahel. All these studies were performed by sampling old groundwater of semi-arid and tropical regions, which challenges a direct comparability with the mostly young and shallow groundwater sampled in Santarém. However, the previous explanations suggest that the dimensions of the observed saturation anomalies in this study are reasonable.

Obtained excess air contents at most of the sampled wells near Santarém do not vary significantly on seasonal scale. Only four wells show significantly lower amounts of excess air during the dry season compared to the rainy season: ZooFit, SantaRosa, Curupira and FonteCairé. The obtained variations of ΔNe at the first three of these wells may indeed be caused by seasonal water table fluctuations, which is confirmed by an analysis of backup samples. However, the high amount of excess air at the well FonteCairé in the rainy season has to be put into question because no backup sample was available from that well to verify the obtained data. The sampled water at this well originates from more than 110 m below ground. It is thus rather likely that measured NG concentrations during the rainy season are biased due to an inclusion of air bubbles during sampling.

The highest neon excesses are observed in particular in the plateau region, as previously shown in Fig. 6.7. Here, local unsaturated zones are expected to be potentially deeper, allowing for stronger water table fluctuations and, thus, for higher supersaturations compared to regions of a smaller extent of the unsaturated zone. Wells situated directly next to the rivers also show slightly enhanced neon excesses. Such a behavior may be caused by strong seasonal river water table fluctuations. Further strong neon excesses at the wells Peleja and Mapinguari may be induced in a similar way, since both of these wells are situated within a distance of only about 1 km from a small local stream.

Even though no records of local groundwater tables are available, measured NG data allow for some conclusions concerning water table fluctuations. Applying the CE model description introduced in chapter 5.3, the degree of partial dissolution of entrapped air bubbles is described by the fractionation parameter $F_{\mathrm{CE}} = v/q$. Its value depends on underlying physical processes causing a saturation anomaly of dissolved gases with respect to the equilibrium component: first, a change in the amount of gas within the air bubbles (expressed as parameter v) and, second, a change in ambient pressure due to water table fluctuations (expressed as parameter q). The pressure parameter

$$q = \sum_i x_i \cdot \frac{1 + A \cdot H_i'}{1 + B \cdot H_i'} \tag{6.1}$$

is defined as the sum of the pressure contributions of all dissolved gases i, with the gas phase mixing ratio x_i, the Henry coefficient H_i' and the excess air parameter A as well as the parameter $B = F_{\mathrm{CE}} \cdot A$ (Aeschbach-Hertig et al., 2002a). The formulation in eq. (6.1) goes along with a constraint which is important to keep in mind: It applies only for gas species satisfying the requirement of a closed system, meaning that they behave conservatively without any sources or sinks such as microbial release or consumption. Measured NG concentrations of all sampled wells in Santarém give no hint for degassing, which at least suggests an absence of non-equimolar microbial gas production. A further remark concerns the equilibrating gas phase composition. Here, atmospheric mixing ratios x_i are assumed in eq. (6.1) for all considered gas species, which may deviate from those in soil air. The main difference between atmospheric and subsurface gas phase composition is expected for O_2 and CO_2 due to oxygen depletion. Soil air mixing ratios of remaining gas species like N_2 and NGs are nearly atmospheric or their relative abundances are too small to cause a noteworthy change in q. Even though the solubility of CO_2 is about two orders of magnitude higher than that of O_2, resulting q values decrease on average by less than 1 % if typical CO_2 concentrations of soil air are taken into account. The uncertainty of an estimated CO_2 value for soil air is higher than that obtained by neglecting the impact of oxygen depletion.

Equation (6.1) was applied for all sampled wells, taking into account individual parameter outcomes for A and F_{CE} from CE model fits[11] presented previously in this chapter. The calculation of q was done by accounting for the contributions of the most abundant gases, meaning N_2, O_2 and Ar. Figure 6.17(a) shows the obtained correlation between q and ΔNe, describing a clear linear relationship. A good agreement is observed with data sets evaluated by Aeschbach-Hertig et al. (2002a), who already described this linear correlation in detail. Considering the physical meaning of q, previous explanations confirm the applicability of ΔNe as an indicator for water table fluctuations.

Referring to the sampling region around Santarém, the obtained q values indicate seasonal water table fluctuations by $4 - 8$ m ($q \approx 1.4 - 1.8$) in the plateau region and by $2 - 3.5$ m ($q \approx 1.2 - 1.35$) near

---

[11] Parameters were taken from that CE model approach presuming an atmospheric soil air composition during recharge (see chapter 6.2.5). This shall ensure a consistence with the assumption of atmospheric mixing ratios of all gas species in soil air.

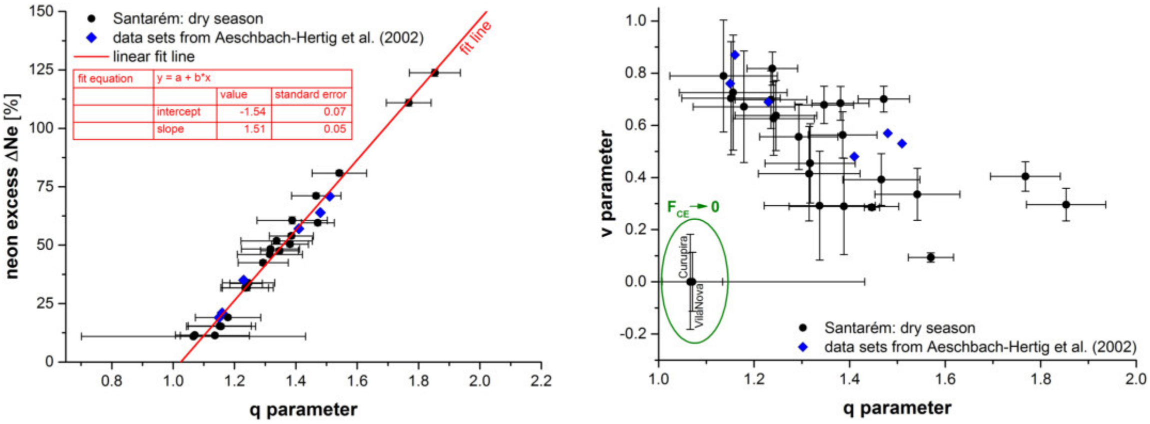

(a) Correlation of q and ΔNe.

(b) Correlation of q and v.

Figure 6.17: Santarém: CE model parameters describing the formation of excess air. Obtained data from the two wells GrajaSãoPedro and Belterra are not depicted. Green framed data reflect values of $F_{\text{CE}} \approx 0$. For comparison, parameters of different data sets evaluated by Aeschbach-Hertig et al. (2002a) are depicted as blue symbols.

the two rivers Rio Tapajós and Amazon. Seasonal river water table fluctuations seem to determine dissolved gas contents at wells near the rivers, even though local groundwater tables fluctuate to a lesser extent compared to the two large rivers showing seasonal water table fluctuations of up to 7 m (Tapajós et al., 2016).

The gas amount in entrapped air bubbles is described by the parameter v which is determined based on the F_{CE} values from the respective CE model fits. Data in Fig. 6.17(b) generally show a decreasing trend of v (expressing the gas amount in the bubbles) with increasing q (expressing the hydrostatic pressure). Even seasonal water table fluctuations of several meters seem not to be strong enough to induce a full dissolution of entrapped air bubbles. Two samples deviate from the overall trend in Fig. 6.17(b) (see green framed data): Respective CE model fits result in two clusters of F_{CE} values, one of which tends towards $F_{\text{CE}} = 0$. Such fit outcomes are favored by the small amounts of excess air at these two wells, thus challenging a reliable parameter estimation.

The previous discussion confirms that the degree of fractionation of the excess air component is related to the amount of excess air. This is a consequence of the varying extent of dissolution of entrapped air bubbles. Such a dependence of the fractionation on ΔNe was also found by Aeschbach-Hertig et al. (2002a) for samples from tropical and semi-arid regions, showing high amounts of excess air which were hardly fractionated.

6.3.3 Saturated zone: discussion of excess air model applications and of NGTs

The final part of this discussion shall investigate outcomes of excess air model applications. The assumption of atmospheric NG mixing ratios in soil air resulted in a systematic underestimation of the expected recharge temperatures in most UA and several CE model fits. In contrast, a better agreement was achieved by accounting for rainy-season soil air data, giving an average enhancement of NG mixing ratios in soil air by 4.5 % with respect to the atmospheric values.

Validation of the assumed recharge temperatures

Any test of the noble gas thermometer depends strongly on the reliability of the assumed recharge temperatures. Measured GWTs are applied for this purpose as described before. Thus, it is of main importance to verify whether the measured GWTs reflect indeed the respective temperatures during the last equilibration between soil air and recharging groundwater. The following discussion shall motivate their application as reference values for estimated NGTs. A potential bias of obtained GWTs during the measurement procedure – e.g. due to heat released by the submersible pumps – is rejected as described in detail in appendix A.7. The focus of the following discussion is thus on the plausibility of GWTs, regarding MAATs in the sampling region and a potential impact of geothermal heat flux.

Local MAATs from different weather stations in the sampling area around Santarém as well as measured GWTs are shown in Fig. 6.18. On a first view, MAATs (see black symbols) tend to be higher near the rivers compared to the plateau region. Data are reasonably well described by an exponential fit (see red curve). The local distribution of MAATs cannot be completely explained by the lapse rate, regarding a height difference of about 160 m within the sampling region. This motivates to consider further meteorological parameters as shown in Fig. 6.18(b). Near-river sites are characterized by a higher insolation and by higher wind velocities. Possibly, the local insolation is enforced due to reflection by river water, while less plant-covered areas near the rivers may favor higher amounts of dispersed dust enforcing light scattering.

Even though GWTs do not necessarily reflect local MAATs in general (Beyerle et al., 2003; Cey, 2009), a corresponding agreement is obtained in this study, which supports an application of measured GWTs as expected recharge temperatures. Measured GWTs at three wells (Cosanpa, Barrudada and Santarém) deviate considerably from the fitted trend of MAATs. Since these are deep wells, the deviation of measured GWTs may be a consequence of the local geothermal heat flux, accounting typically for about 3°C/100 m (Bischof, 1837). Such an influence is usually observed at depths below about 20 m (Chow et al., 2011). High annual recharge rates and the soil water turnover in the tropics

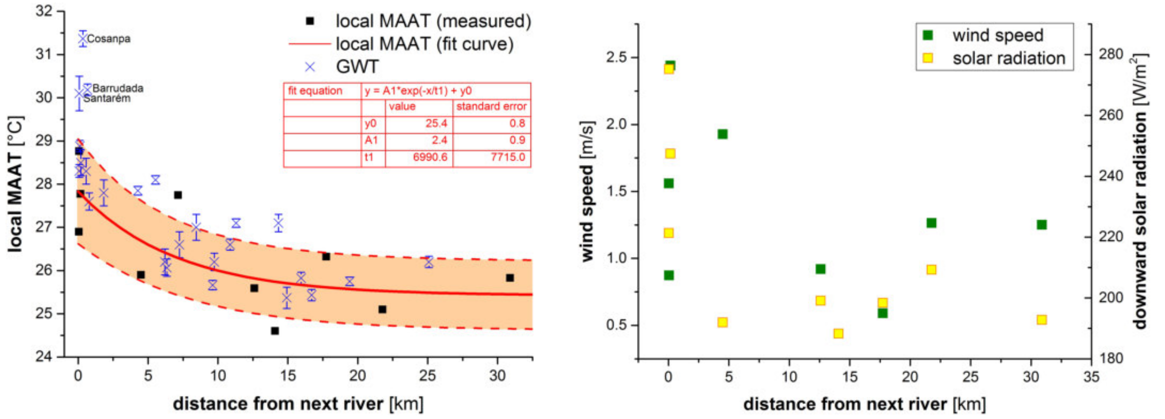

(a) Local MAATs (black symbols) with an exponential fit (red line with transparent uncertainty range) and measured GWTs during the rainy season (blue crosses).

(b) Wind speed (green symbols) and insolation (280 – 2 800 nm wavelength, yellow symbols).

Figure 6.18: Santarém: mean annual values of meteorological parameters in dependence of the river distance. The meteorological measurement stations are described in appendix B.16.

are expected to reduce the warming by geothermal heat flux within the topmost several tens of meters[12].

Based on the preceding explanations, measured GWTs are assumed to be reliable estimates of local recharge temperatures. In case of a supposed geothermal impact, GWTs of the nearby surrounding wells were applied for an appropriate estimate, respectively. It has to be emphasized that available MAAT data were just used to confirm the plausibility of measured GWTs. For this study, it is generally more appropriate to refer to recorded GWTs as recharge temperatures instead of MAATs, since the MAAT fit curve would go along with a further uncertainty of meteorological data.

Discussion of excess air model outcomes

A crucial aspect of this study is the ability of the applied excess air models to describe dissolved NG contents in sampled groundwater. It has to be kept in mind that even an agreement of assumed recharge temperature and NGT does not yet prove a reliable data description. As motivated before, diffusion-based models (PR and GR) are omitted, while UA and OD model fail to describe the observed fractionation of excess air patterns. In the following, CE model outcomes are discussed in detail, since its approach turned out to describe measured data in a reliable way, confirmed by satisfying fit probabilities.

Dissolved NG contents in groundwater provide information about the prevailing conditions during recharge, including the soil air composition. Given the assumed well-specific recharge temperatures, a CE model fit was applied to estimate the ambient air pressure during equilibration, which reflects NG mixing ratios in soil air[13]. A value of $p^* = 1$ indicates atmospheric mixing ratios, while higher values reflect correspondingly enhanced NG mixing ratios.

At near-river sites, obtained p^* values confirm the measured enhancement of NG mixing ratios in soil air during the rainy season (see Fig. 6.19). In contrast, a discrepancy is obtained for most of the samples from the plateau region, giving a p^* value which does not differ significantly from 1. This outcome is surprising, since the soil air analysis during the rainy season resulted in enhanced NG mixing ratios at almost all sampled sites, depending only on local soil moisture rather than on the exact location with respect to the rivers. Such a behavior was already suggested by excess air model outcomes presented in chapter 6.2.5, showing NGTs which underestimate local GWTs in particular at near-river sites. The following discussion will point out a plausible explanation for this obtained trend of p^* values: Gas/water partitioning in the plateau region may take place in presence of nearly atmospheric NG mixing ratios in local soil air, caused by an efficient ventilation of deep coarse-grained unsaturated zones.

There is no significant correlation between obtained p^* values and measured ^{40}Ar mixing ratios in soil air, as shown in Fig. 6.20. Thus, the obtained distribution of p^* values cannot be explained by

---

[12] Geothermal heat is not of relevance if sampled groundwater is pumped from a depth nearby the groundwater table, since in this case an influence of geothermal heat would affect both the GWT and the recharge temperature or rather the NGT. However, the pumping depths of the three wells Cosanpa, Barrudada and Santarém are expected to be deeper than the local water table levels, respectively.

[13] The obtained pressure values have to be divided by the site-specific atmospheric air pressure, respectively. Thus, the parameter values of p^* given in this chapter already reflect NG mixing ratios in soil air, normalized to atmospheric values.

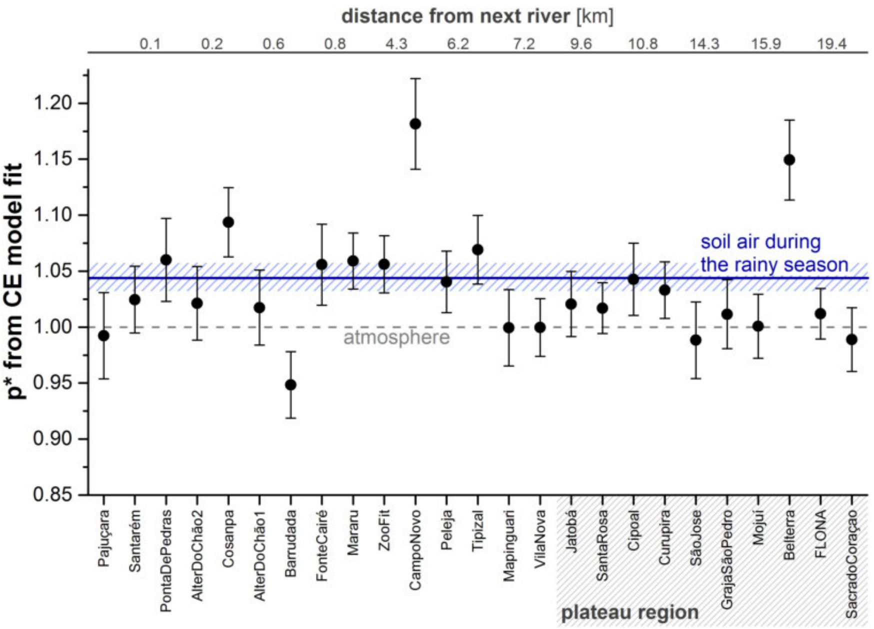

Figure 6.19: Santarém: NG mixing ratios in soil air, estimated for given recharge temperatures by a CE model fit and normalized to the site-specific barometric air pressure, respectively. The measured average enhancement of NG mixing ratios in soil air by (4.5 ± 1.3) % during the rainy season is illustrated as blue line with shaded uncertainty range. The gray dashed line indicates atmospheric conditions, meaning $p^* = 1$. Obtained data from the two wells GrajaSãoPedro and Belterra are possibly biased due to an inclusion of air bubbles during sampling.

locally varying NG mixing ratios in the sampled topmost soil air.

The last equilibration of recharging groundwater takes place at the groundwater table level at the ambient air pressure. However, the air pressure values considered for the calculation of p^* were determined for the respective heights of Earth surface, because the water table depths are not exactly known at the most of the wells. This approach is certainly suitable at near-river sites due to shallow unsaturated zone extents, going along with a depth uncertainty of only a few meters. In contrast, the extent of unsaturated zones in the plateau region is quite unknown. Tancredi (1996) measured water table depths of up to 45 m in the same sampling area, but not at the same wells as sampled for this study. Even though the deepest pumping depth of 115 m (at the well SãoJose) would reflect an equally extended unsaturated zone, a difference of only 1.4 % would result between the respective ambient air pressures at Earth surface and at the groundwater table. Such a pressure effect cannot balance an enhancement of NG mixing ratios by 4.5 %. Furthermore, an extent of unsaturated zones by more than 100 m has to be seen as a rather unrealistic upper limit.

However, the existence of deep unsaturated zones provides another potential impact on soil air composition near the groundwater table. The soil layer around the groundwater table is of main interest considering the equilibration process of recharging groundwater. Yet soil air sampling took place within the topmost meters, because sampling was not possible at depths of several tens of meters. The soil air composition at deeper soil layers may indeed significantly deviate from that of the topmost soil. This approach is motivated by local soil structures in the sampling area, where deeper soil layers in the plateau region are known to consist mainly of sand and gravel, while topmost layers contain a high fraction of clay (Tancredi, 1996; Oliveira, 1996). Sandy soils are usually characterized

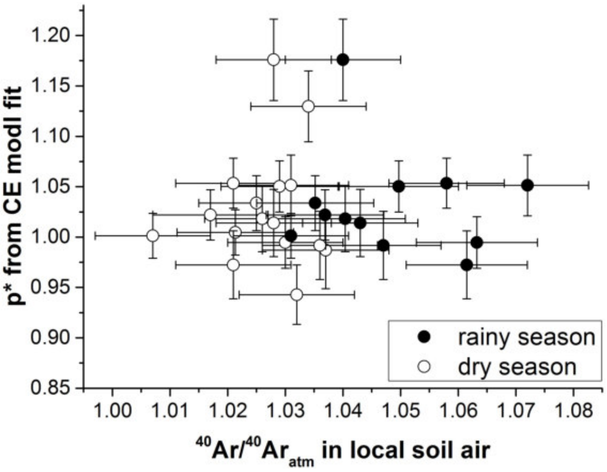

Figure 6.20: Santarém: Correlation of p^* with ^{40}Ar mixing ratios in soil air (normalized to the atmospheric value, respectively).

by lower soil moisture contents and by a better aeration, which typically occurs horizontally through well-permeable layers connecting deeper soil layers with atmospheric air (Massmann and Farrier, 1992). Thus, deep soil air may exhibit a yearlong atmospheric composition, even though NG mixing ratios in the topmost soil are enhanced with respect to atmospheric values.

The assumption of an atmospheric composition of deep soil air in the plateau region is confirmed by two additional soil air samplings which were carried out in the scope of this study. First, soil air was sampled in an artificial tropical house of the *Wilhelma Zoo* in Stuttgart (Germany). Climatic conditions in that tropical house are reproduced according to those in the *Floresta Nacional do Tapajós* which is located in the sampling area near Santarém (see sampling site “FLONA”). Soil air in the tropical house was sampled at soil depths of up to 2 meters, resulting in no significant deviation from the atmospheric composition – meaning that the sum value of O_2+CO_2 was not depleted by more than 1 vol% compared to its atmospheric value. Such soil air compositions might seem to be in contradiction to the expectations based on local climatic conditions. However, it is plausible by regarding the local soil structure. The very coarse-grained structure (with a mean grain diameter of about 4 mm) in the tropical house allows for a very good soil ventilation, while soil water contents tend to be rather low. The same observation resulted from samplings in a very sandy soil near Sandhausen (Germany) during summer 2015, after some weeks without any rain. The recorded soil air composition at soil depths of up to 2 m was nearly atmospheric at this sampling site. To summarize, preceding explanations suggest that NG mixing ratios in deep soil air may indeed be nearly atmospheric in the sampling region around Santarém.

Another possible approach to explain the trend of p^* values shall be mentioned here, even though it is rejected as explained in the following. Obtained p^* values may also be interpreted as reflecting an overall groundwater recharge in the plateau region, where local GWTs are known to be colder compared to near-river sites. Thus, dissolved NG contents of sampled groundwater near the rivers would reflect recharge conditions in the plateau region and, thus, colder equilibration temperatures – resulting in the observed deviation of NGTs from local GWTs or rather in enhanced values of p^*. However, this approach is rejected for two reasons: First, the distribution of neon excesses in the sampling area indicates that recharge also takes place at near-river sites. Second, the time span for groundwater flow from the plateau region towards the rivers would be too long regarding the estimated groundwater age. Considering a hydraulic conductivity of $K_s = 1.3 \cdot 10^{-4}$ m/s for the local topmost aquifer (Tapajós et al., 2016) and a height gradient of 100 m/10 km between the plateau region and near-river sites, a Darcy velocity of about 40 m/a results. Tritium data indicate a mean groundwater age of less than 18 years, providing thus a maximum flow distance of about 720 m which is by far too small to cover the actual distance between the plateau and the river region.

Referring to the above presented trend of p^* values, dissolved NG contents in local groundwater at near-river sites show a clear signal of enhanced NG mixing ratios in soil air. By accounting for soil air observations, a more reliable estimate of NGTs is achieved at near-river sites. In the plateau region, a corresponding adaption of the assumed soil air composition during recharge is not necessary.

Chapter 7

General discussion and summary

The preceding two chapters provide a detailed discussion of subsurface gas dynamics, based on field studies in the mid-latitudes (Germany) and in the tropics (Brazil). A long-term record in Germany offers insights into seasonal aspects, while data from Brazil complement these findings by accounting for totally different climatic conditions.

This chapter starts, first, with a combined discussion of general determinants of soil air composition, based on the individually gained insights of the preceding chapters. This is followed by a summary of main findings about gas dynamics within the unsaturated zone. Second, the findings about subsurface gas dynamics motivate a critical discussion of the different approaches of excess air models proposed in the literature. This concerns, in particular, the reliability of excess air models to describe NG contents in groundwater affected by degassing. A summary of the main conclusions of this study is also given for the saturated zone. Finally, general implications for NG tracer studies in hydrology are demonstrated.

7.1 Unsaturated zone: determinants of soil air composition

Soil air data from Germany and Brazil are depicted in Fig. 7.1. Measured sum values of O_2+CO_2 show a clear dependence on both soil moisture and soil temperature, see Fig. 7.1(a). The strongest depletion of O_2+CO_2 with respect to the atmospheric value is observed for high soil temperatures in combination with high soil moisture contents. Mid-latitude soil moisture contents during summer are usually not high enough to cause a comparable depletion of O_2+CO_2 as observed in the tropics.

Regarding the mixing ratios of NGs in soil air, a stronger enhancement with respect to the respective atmospheric values is observed for high temperatures in combination with high soil moisture contents. Such a behavior is likewise found for all analyzed inert gas species, and exemplarily shown for helium in Fig. 7.1(b), for argon in Fig. 7.1(c) and for xenon in Fig. 7.1(d). Measured data thus confirm the dominating impact of varying O_2+CO_2 values on inert gas mixing ratios in soil air, which is observed in both sampled climate regions.

The correlation between O_2+CO_2 and inert gas mixing ratios is more obvious in Fig. 7.2, showing soil air data from Germany (open symbols) and from Brazil (filled symbols). It is clearly visible that soil air contents of O_2+CO_2 tend to be stronger depleted in the tropics compared to mid-latitudes. A

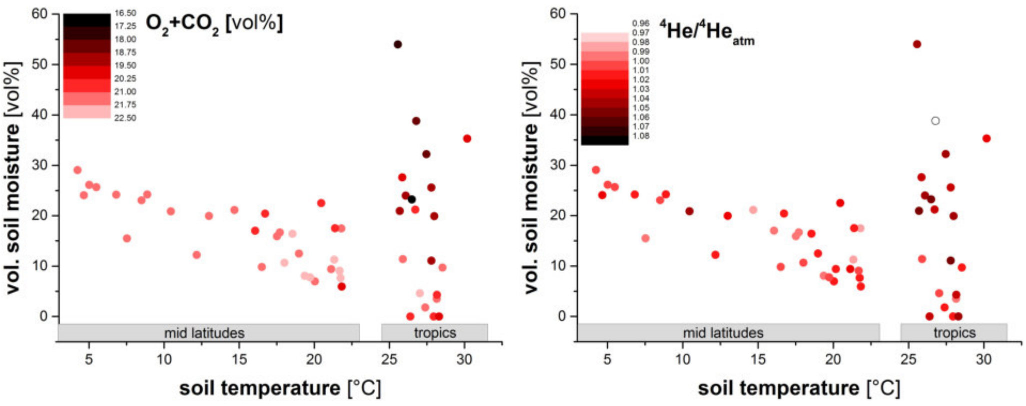

(a) O_2+CO_2 in soil air.

(b) ^{4}He/^{4}He$_{atm}$ in soil air.

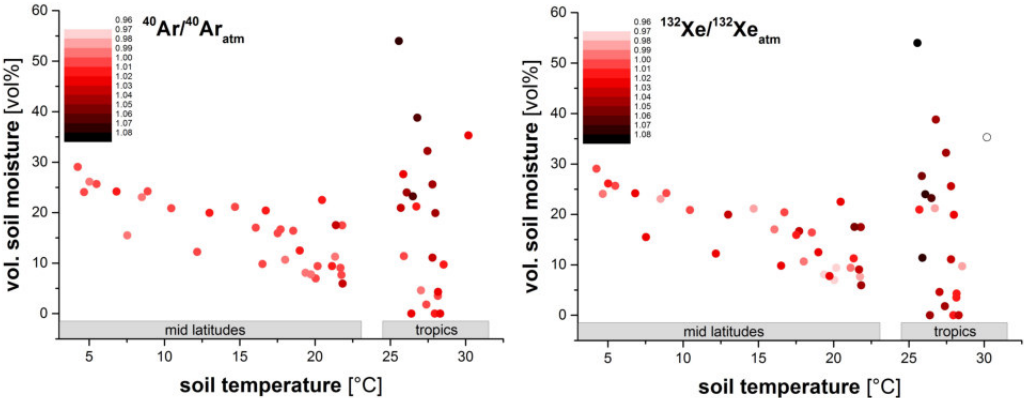

(c) ^{40}Ar/^{40}Ar$_{atm}$ in soil air.

(d) ^{132}Xe/^{132}Xe$_{atm}$ in soil air.

Figure 7.1: Dependence of soil air composition on soil temperature and volumetric soil moisture (measured both within the topmost 10 cm of soil). Presented data comprise soil air samplings from Mannheim (at 1.0 m and at 5.5 m depth) as well as data from Santarém, respectively.

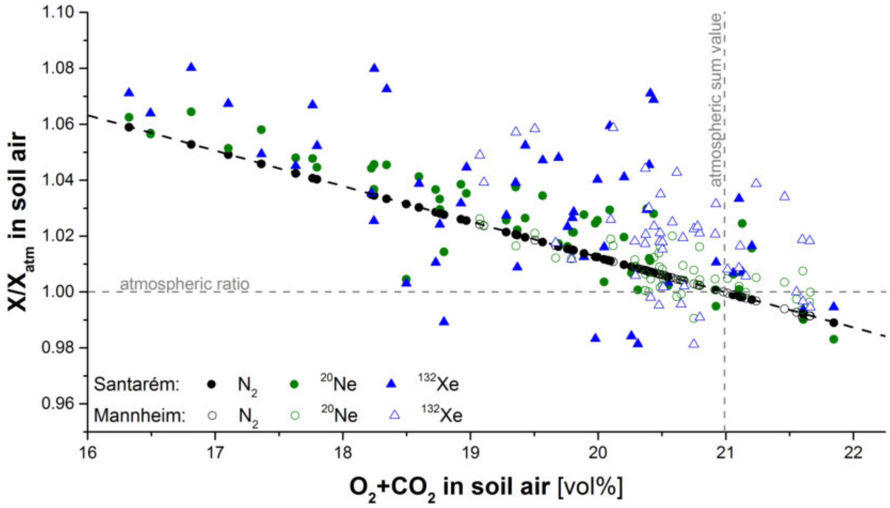

Figure 7.2: Measured soil air composition in Santarém/tropics and Mannheim/mid-latitudes: Correlation of O_2+CO_2 and mixing ratios of N_2 (black symbols), ^{20}Ne (green symbols) and ^{132}Xe (blue symbols). The black dashed line indicates the theoretically expected relationship as described in chapter 3.3.1.

yearlong fractionation effect is observed in both climate regions, going along with stronger enhanced mixing ratios of heavier gas species like xenon. Model outcomes presented before suggest diffusive transport to cause such a permanent fractionation.

Unsaturated zone: summary of main findings

Even though measured soil air data depend on local climate and on site-specific conditions, outcomes of this study allow for some general conclusions. Samplings in Germany were carried out at a meadow site which is situated in a region characterized by urbanization and agriculture, with a loamy-sandy soil profile. Such conditions can be regarded as representative for populated mid-latitude areas (Akça et al., 2005). The high-resolution long-term record allows to describe relative variations instead of just absolute values. Any conclusions are, thus, more independent from uniform impacts of site-specific parameters such as soil type. In Brazil, no long-term record is available, but sampling sites were chosen in a way to represent different local conditions such as varying degrees of deforestation, soil moisture and soil type. Such a multitude of different sites allows for general conclusions based on an evaluation of data distributions. Besides this, climate conditions during the respective sampling periods of this study were shown to be representative in the long-run, based on meteorological data records (see chapter 4).

Subsurface biogeochemical processes provide the potential to cause significant deviations of soil air composition from the atmospheric one. This also concerns mixing ratios of inert gases. Based on the previous discussions about soil air samplings in Germany and Brazil, respectively, general conclusions of this study shall be summarized here:

- **Variations of soil air composition:** Data of this study confirm the finding of Freundt et al. (2013), stating that oxygen depletion in combination with a preferential dissolution of CO_2 changes the sum value of O_2+CO_2 and, thus, the mixing ratios of NGs in soil air. The long-term record in Germany indicates a temporal enhancement of mixing ratios of inert gases by up to 3 % with respect to atmospheric values. Samplings in the Brazilian tropics show stronger enhancements of NG mixing ratios by up to 8 %. Observed effects in Brazil are mostly significant and reach a maximum during the rainy season. In Germany, significant effects are observed temporarily in summer time, but not during the cold season.

- **Seasonality:** Mixing ratios of inert gases in soil air are found to be generally affected by microbial release or consumption of gases, by gas/water partitioning and by subsurface transport mechanisms − meaning both advection and diffusion. The impact of all of these processes is defined by ambient temperature and soil moisture, resulting in seasonal variations of the soil air composition in mid-latitudes (summer/winter) as well as in the tropics (rainy/dry season).

- **Relevant processes:** Modeling results of this study indicate that varying sum values of O_2+CO_2 are the predominant origin of varying mixing ratios of inert gases in soil air. Any change of O_2+CO_2 induces, first, an advective flow compensating pressure gradients and, second, a diffusive balancing of the arising concentration gradients of inert gases. Further diffusion-based mechanisms, meaning thermal diffusion and water vapor flux as proposed by Severinghaus et al. (1996), are usually of minor importance. This may not generally hold for helium due to its high diffusivity. Gravitational separation as proposed by Stute and Schlosser (1993) is only of relevance for heavier gas species in deep unsaturated zones.

- **O_2+CO_2 in soil air:** Extended soil air samplings for this study show that, under natural conditions, the sum value of O_2+CO_2 is typically depleted with respect to its atmospheric value. However, the different diffusivities of O_2 and CO_2 may cause an increase of O_2+CO_2 above its atmospheric value under very dry conditions.

- **Mass-dependent fractionation:** Samplings of this study show a mass-dependent fractionation of soil air, meaning a relative enhancement of heavier gas species with respect to lighter ones. In this context, model outcomes of this study confirm the finding of Jones et al. (2014), stating that such a fractionation effect is caused by diffusive transport. Concentration gradients between soil air and atmosphere are faster balanced by lighter gas species compared to heavier ones. The data of this study additionally indicate a yearlong relative enhancement of heavier gas species with respect to lighter ones, showing no clear seasonality. This is a consequence of the time scale of diffusive transport, causing a rather uniform fractionation which is decoupled from the typically stronger fluctuating advective impact.

7.2 Saturated zone: determinants of dissolved gas contents

This study presents sampled data from the quasi-saturated zone which is just the region of interest regarding excess air formation. Obtained findings thus provide a good basis to evaluate the respective approaches of different excess air models concerning prevailing conditions during recharge – meaning during gas/water partitioning and excess air formation.

The evidence for a permanent equilibration of entrapped air bubbles with groundwater in the quasi-saturated zone clearly implies that the CE model provides a reliable description of dissolved NG contents in groundwater. Two further models are traditionally referred to in the literature: The UA model approach is based on a full dissolution of entrapped air bubbles, thus neglecting any fractionation of the excess air component. The approach of an unfractionated excess air component is challenged by the found permanent existence of entrapped air near the groundwater table, even in the tropics where strong groundwater table fluctuations favor a full dissolution of entrapped air bubbles. A typical consequence concerning UA model outcomes is an underestimation of the amount of excess air, accompanied by systematically lower NGT estimates. The PR model accounts for a fractionation effect, even though its diffusion-based approach is not able to reproduce measured helium data of this study. A data description by means of the PR model does not yet end up in strongly biased NGTs, since corresponding estimates are mainly based on the stronger temperature dependent Henry coefficients of heavier (less diffusive) NG species like krypton and xenon. However, even though diffusively influenced NG patterns were observed so far (Cey et al., 2009), findings of this study clearly support a solubility-controlled approach as it is provided by the CE model. Data from long-term samplings indicate that mass-dependent solubilities determine both, excess air formation as well as groundwater degassing.

Observed temporal variations of NG mixing ratios in soil air actually motivate an application of non-traditional approaches, meaning that of the OD and the GR model, respectively. Both of them allow for a uniform deviation of NG mixing ratios in the equilibrating gas phase from atmospheric values, which is described based on dissolved NG contents in sampled groundwater. However, in this study, most obtained outcomes of these two models are not satisfactory, going along with a systematical bias of resulting NGTs. The determination of an additional parameter (P_{OD} or P_{GR}) requires the application of an ensemble fit to match the set of available NG species for fitting. This procedure goes along with the disadvantage that the selected set of samples may affect the fit outcome which cannot be seen anymore as specific for each individual sample. In other words, only one single problematic sample may challenge the reliability of the obtained fit outcomes of all remaining samples. The applicability of ensemble fits seems to be questionable regarding the observed seasonality of NG mixing ratios in soil air, the temporal and local nature of degassing as well as possibly differing recharge times of groundwater sampled at different but collectively evaluated wells. These issues are of particular relevance concerning young shallow groundwater. The previous analysis suggests that an impact of oxygen depletion may be reliably treated by including estimates about the gas phase composition during recharge into fits of the CE or even of the UA model.

Regarding deeper groundwater, varying recharge conditions are rather smoothed due to mixing within the aquifer. For groundwater sampled at the deep well near Mannheim, outcomes of the OD and GR model fits are in good agreement with expected recharge conditions. However, in mid-latitudes, it is precisely this mixing which is assumed to go along with an overall dominance of recharge during the cold season. This puts the need of a setup like that of OD and GR model into question. A different situation may be found under tropical climate conditions, where a set of groundwater samples may indeed be described in a reliable way by an OD or a GR model approach, if all samples are characterized by similar recharge conditions. However, outcomes for tropical groundwater samples evaluated in this study again point out the difficulty concerning ensemble fits in case of individual problematic samples.

Altogether, dissolved NG contents in groundwater may allow for conclusions about the composition of the equilibrating gas phase during recharge. If the selected set of samples is not appropriate to be evaluated by ensemble fitting, an independent estimation or a measurement of soil air composition may allow for a reliable data evaluation. Nevertheless, it has to be considered that such a procedure requires an extensive effort while providing a strong potential for systematical errors, due to the heterogeneity of subsurface gas composition and varying recharge times.

A further note shall be given to the impact of degassing on the interpretation of dissolved NG contents. In general, the CE model was found to provide reliable descriptions of degassed NG patterns (Aeschbach-Hertig et al., 2008). However, its formal setup describes degassing of originally unfractionated excess air patterns which are formed by a full dissolution of entrapped air bubbles according to the UA model approach. For strongly fractionated excess air patterns which were presumably degassed, Cey et al. (2009) found systematically too low NGTs from CE model fits. Such problematic fit outcomes go typically along with a strong increase of the excess air parameter A and an increasing

F_{CE} parameter approaching to 1. It is important to note that minor groundwater degassing is absolutely compatible with values of $F_{\mathrm{CE}} < 1$. Even though the obtained fit probability is decreasing for more strongly degassed samples, the fit probability may not necessarily be small enough to give a clear hint for a non-satisfying data description. Minor degassing may remain unnoticed in such cases, providing the potential for biased excess air model outcomes.

The difficulty of the CE model to describe the subsequent degassing of an originally fractionated excess air pattern can unfortunately not be resolved by including an additional degassing term into the formal model setup, due to the limit of available measured NG data. The reason for problematic fit outcomes becomes evident by considering the degassing of a fractionated excess air pattern in terms of the CE model formulation:

$$c_{\mathrm{i,w}}^{\mathrm{CE},d} = \underbrace{c_{\mathrm{i,w}}^{\mathrm{EQ}} \cdot \frac{1 + AH'_{\mathrm{i}}}{1 + BH'_{\mathrm{i}}}}_{\text{original CE setup}} \cdot \underbrace{\frac{1}{1 + B^{d} H'_{\mathrm{i}}}}_{\text{degassing}} = c_{\mathrm{i,w}}^{\mathrm{EQ}} \cdot \frac{1 + AH'_{\mathrm{i}}}{1 + (B + B^{d}) \cdot H'_{\mathrm{i}} + B \cdot B^{d} \cdot H'^{2}_{\mathrm{i}}} \tag{7.1}$$

The applied parameters are the same as introduced before in chapter 5.3, with an equilibrium component denoted as $c_{\mathrm{i,w}}^{\mathrm{EQ}}$ and the excess air parameter A as well as $B = A \cdot F_{\mathrm{CE}}$. Regarding the denominator of the last term in eq. (7.1), a subsequent degassing process is partly included into a term which is linear in H'_{i}, while an additional term arises, which is quadratic in H'_{i}. The original CE model approach does not account for this quadratic term, meaning that the relative influence of this quadratic term determines the ability of the model to describe a subsequently degassed NG pattern in a reliable way. The quadratic term becomes more relevant for gas species with a low solubility (high Henry coefficient H'_{i}), for strong degassing (high B^{d}) as well as for an originally strongly fractionated excess air pattern (high B). Equation (7.1) thus provides an insight into parameter ranges which may challenge the reliability of NG data evaluations by the CE model in case of degassed groundwater.

While natural groundwater degassing is usually a consequence of microbial gas production, a somewhat contrary effect is potentially induced by microbial gas consumption. This is more obvious by replacing the degassing term in eq. (7.1) by a term of the form $1 + A^{*}H'_{\mathrm{i}}$, where A^{*} describes an additional enhancement of dissolved NG contents in groundwater. The parameter A^{*} typically differs from A since the considered microbial effect occurs independently from the original excess air formation. The formal description results again in a term which is quadratic in H'_{i}, accompanied by a potential difficulty of the CE model to describe this NG pattern. The potential bias of CE model outcomes is shown in appendix B.26 for synthetic data. Even though oxygen consumption is observed rather often in natural aquifers, its effect on NG concentrations was hardly described in the literature so far. Its impact is very difficult to distinguish from the common excess air component, in contrast to the above described degassing phenomenon which may induce a more obvious depletion of lighter NG species in groundwater. However, an influence of microbial gas consumption on dissolved NG contents is probably negligible in most cases: Aerobic microbial processes like oxygen depletion go usually along with the production of another gas species, thus preventing an increase of NG mixing ratios in entrapped air bubbles.

It clearly has to be pointed out that the CE model approach still provides the most appropriate and reliable description of degassed groundwater samples, in particular with regard to diffusion-based approaches. Furthermore, CE model outcomes should not generally be questioned, even not in regions of potential microbial gas production. This follows, on the one hand, from the strong locality of microbial activity which is not observed or even negligible in most gas tracer studies. On the other hand, this study gives a good example for degassed groundwater whose composition is indeed described at least temporarily in a reliable way by the UA and CE model, even though data clearly indicate an impact of degassing. As described above, small amounts of excess air reduce a potential bias of NGT estimates due to subsequent degassing. In such cases, the CE model setup provides indeed no absolutely correct description of measured data. This goes along with possibly unrealistic estimates of further parameters such as of A and F_{CE}, the values of which should be interpreted with caution in this case. However, the overall impact of minor degassing on the estimated equilibrium component may be that small to achieve still reliable NGT estimates. More problematic outcomes are expected for subsequently degassed groundwater containing high amounts excess air, e.g. in the tropics with pronounced seasonal recharge. Even though tropical groundwater samples evaluated in this study give no hint for minor degassing, such samples should be handled with particular caution to avoid any bias of derived parameters.

Saturated zone: summary of main findings

Preceding explanations allow for some general conclusions which shall be summarized here, all concerning dissolved gas contents in recharging groundwater:

- **Impact of varying soil air composition:** The annual recharge distribution seems to determine the actual impact of varying soil air composition on the equilibrium component of dissolved gases in groundwater. Samplings in Germany suggest that predominant recharge during the cold season prevents any corresponding bias. However, individual strong recharge events during the warm season may impose a certain signature on young shallow groundwater – which is smoothed out with increasing soil depth due to an overall dominance of usual recharge periods. In the tropics, a bias of the equilibrium component is expected due to a coincidence of the predominant recharge period and a soil air composition significantly deviating from the atmospheric one. This is indeed confirmed by samplings at several wells in Brazil.

- **Excess air formation:** Long-term records of this study indicate that entrapped air bubbles provide a gas phase for a permanent temperature-driven equilibration within the quasi-saturated zone. This process may affect dissolved gas contents even some years after recharge and without any influence on the ^{3}H–^{3}He age. Such an effect is not found in deeper groundwater, since there are neither entrapped air bubbles nor ambient temperature fluctuations. The continuous equilibration of shallow groundwater with entrapped air bubbles clearly confirms the physical idea of the CE model approach proposed by Aeschbach-Hertig et al. (2000). Data of this study suggest a general fractionation of the excess air component, even in the tropics under strong groundwater table fluctuations. In this context, samplings confirm that excess air is a reliable indicator for climatic conditions during recharge as it was already shown by Aeschbach-Hertig et al. (2002a).

- **Impact of oxygen depletion:** Even though new alternative models like the OD or GR model were introduced to account for a potential impact of oxygen depletion (Hall et al., 2005; Sun et al., 2008), they do not provide a satisfying description of the measured data in this study. The main reason for this finding seems to be the application of an ensemble fit setup. This motivates to treat an impact of oxygen depletion by including estimated (or better measured) soil air data into traditional excess air model approaches.

- **Groundwater degassing:** The finding of Cey et al. (2009) is confirmed, stating that even minor degassing may challenge the interpretation of dissolved gas contents, if it takes place independently from the original excess air formation. The forward modeling approach presented in this study allows to concretize this finding: Whether traditional excess air models describe yet dissolved gas contents in a reliable way, depends on specific circumstances such as the gas species of interest, the amount of excess air and the degree of degassing. In general, the CE model is able to handle even subsequently degassed groundwater samples in case of small amounts of excess air or for less fractionated excess air patterns. In this context, it is beneficial that high amounts of excess air usually tend to go along with a smaller degree of fractionation.

7.3 Subsurface gas dynamics in the context of gas tracer applications

A reliable description of gas concentrations in groundwater requires a profound understanding of the respective components of dissolved gases. Previous explanations suggest that a simple sum-up of excess air and an atmospheric equilibrium component provides not always an appropriate description. In fact, biogeochemical processes within both the unsaturated as well as the saturated zone determine dissolved gas contents during the actual recharge, but also subsequently.

Figure 7.3 refers to the graphic shown in the introduction chapter of this thesis, which is complemented here. The illustration allows to get an overview of the subsurface gas-dynamical processes which turn out to be relevant with regard to gas tracer studies. Microbial sinks and sources of gases (marked in green) directly affect gases like O_2, CO_2 and possibly N_2. Gas/water partitioning (marked in blue) affects the composition of soil air, mainly due to a preferential dissolution of CO_2. Besides this, a temperature driven equilibration occurs during the actual recharge process, but also permanently within the quasi-saturated zone, caused by entrapped air bubbles. Even though nitrogen production is labeled in Fig. 7.3 as the origin of local degassing, it has to be kept in mind that a release of other gases like CO_2 or CH_4 may also cause groundwater degassing. Transport processes (marked in orange) comprise advective and diffusive mechanisms. In the unsaturated zone, this concerns in particular the variation of O_2+CO_2 and its compensation by remaining gas species. Further diffusion-based mechanisms such as thermal diffusion, water vapor flux and gravitational separation (see waved gray lines) turned out to be usually of minor relevance.

General implications for NG tracer studies in groundwater hydrology

Implications of subsurface gas dynamics in the context of NG studies were recently subject of controversial explanation approaches. This mainly concerns published data from groundwater in Michigan

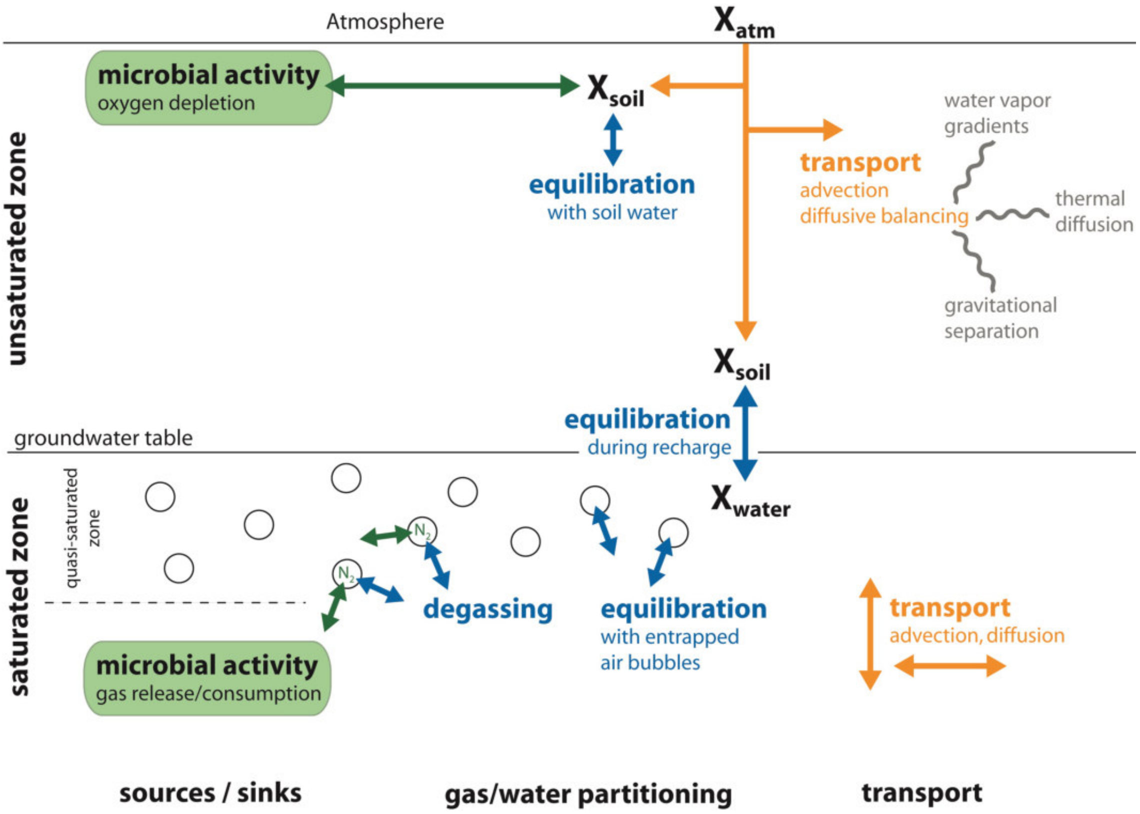

Figure 7.3: Summary of subsurface gas dynamics determining short-term fluctuations of NG concentrations in soil air and groundwater.

(USA), resulting in NGTs which systematically underestimated the expected recharge temperatures by about 2.5°C (Hall et al., 2005). But further studies exist, resulting in NGTs which systematically underestimate expected recharge temperatures by up to 4°C (Ma et al., 2004; Friedrich, 2007; Cey et al., 2009). Even though such strong temperature discrepancies are rarely referred to in the literature, their occurrence motivates a more precise consideration of specific gas-dynamical processes potentially inducing such biases.

Hall et al. (2005) provide enhanced mixing ratios of NGs in soil air as a possible explanation for systematically too low NGTs, caused by depleted sum values of O_2+CO_2. In mid-latitudes, such an approach would be confirmed by findings of this study in case of a tendency of local recharge to occur during the warm season, as it is indeed observed by Hall et al. (2006). However, it has to be emphasized that oxygen depletion for itself is rather unlikely to cause strong NGTs biases. Extensive samplings of this study indicate that oxygen depletion causes a potential bias of NGT estimates by not more than about 2°C. In this context it shall be mentioned that OD model outcomes proposed in the literature provide rather unrealistic estimates of NG mixing ratios in soil air. Hall et al. (2006) suppose NG enhancements in soil air by more than 10 % above atmospheric values to explain NG data from an aquifer in Maryland (USA) published by Aeschbach-Hertig et al. (2002b). In the same way, Castro et al. (2007) propose NG enhancements in soil air by 14 % to describe a NG data set from Texas (USA). Soil air samplings of this study give no evidence for such strong enhancements, neither in mid-latitudes nor in the tropics.

It is generally imaginable that degassing provides at least in part an explanation for temperature discrepancies described in the literature (Cey et al., 2009). This approach is confirmed by the fact that systematical NGT biases were observed so far just in a few studies. Microbial gas production within the saturated zone is expected to be a local phenomenon, while oxygen depletion in combination with a certain seasonal recharge distribution occurs rather on a regional scale. However, it has to be considered that a certain combination of different circumstances – concerning the amount/fractionation of excess air and the extent of degassing – is necessary to induce a strongly biased description of a degassed groundwater pattern by the CE model approach.

It is difficult to state the exact origin of NGTs differing from expected recharge temperatures. Obtained NG patterns influenced by oxygen depletion and minor degassing resemble each other, respectively. Both of these effects come along with a relative enhancement of heavier NGs, since variations of soil air composition as well as groundwater degassing involve a mass-dependent fractionation effect. It is thus necessary to handle corresponding NG patterns with caution and to involve further information about local conditions for a reliable data interpretation.

Chapter 8

Conclusion and Outlook

Concentrations of inert gases in soil air and groundwater depend on various biogeochemical processes taking place in the subsurface. A reliable application of gas tracers in hydrological studies requires an identification of relevant processes as well as a quantification of their respective impacts. This study, on the one hand, clearly points out the enormous potential of NGs as environmental tracers. In this context, findings confirm the general reliability of assumptions proposed in the literature, concerning the soil air composition during groundwater recharge and the formation of excess air. On the other hand, this study identifies circumstances under which NG data should be evaluated with particular caution. According to that, conclusions about NG patterns may be potentially biased as a consequence of entrapped air bubbles in shallow quasi-saturated zones, in case of depleted values of O_2+CO_2 in soil air during pronounced recharge periods as well as due to groundwater degassing in case of large and fractionated excess air components.

Explanations of this study motivate aspects which are worth to be investigated in more detail. The presented gas phase modeling approach allows to identify subsurface transport mechanisms, but a quantitative evaluation is not possible so far. Besides this, the non-consideration of gas/water partitioning and the non-satisfying description of molecular diffusive transport motivate an application of more sophisticated modeling approaches, as it is the subject of a current study by Jenner (2016). Further insights may be obtained from laboratory experiments which may allow to describe underlying processes at the transition between unsaturated and saturated zone under well-defined conditions. This study clearly points out the significance of groundwater degassing for gas tracer applications. Degassing was considered in the context of saturated zone data while soil air data did not indicate a corresponding impact. However, it is generally imaginable that microbial gas release in the saturated zone may affect the composition of soil air. A more detailed study of this issue is in particular motivated with regard to groundwater contamination and reorganization measures.

A deep understanding of subsurface gas dynamics contributes in a remarkable way to the reliability of NG studies. Applications of NGs in groundwater hydrology provide a potential concerning the issue of soil contamination, but also regarding the scarcity of fresh water in numerous regions of the world. In particular, findings of this study improve a well-established method of paleoclimate reconstruction which shows its potential with regard to a more profound understanding of the global climate system.

Appendix A

Calculations and annotations

A.1 Empirical formulation of the Ostwald solubility

An empirical formulation of the temperature dependent Ostwald solubility is given by Benson and Krause Jr (1976) as

$$\ln\left(H_\mathrm{i}\left(T, S = 0\right)^{-1}\right) = \ln\left(L_\mathrm{i}\left(T, S = 0\right)\right) = a_0 + a_1 \cdot \frac{1}{T} + a_2 \cdot \frac{1}{T^2} \qquad \text{(A.1)}$$

with the following parameter values:

Table A.1: Parameter values for the temperature dependency of the solubility L_i of non-polar gases under the assumption of a negligible salinity S, adapted from Benson and Krause Jr (1976). The atomic masses are given in atomic mass units of $\mathrm{u} = 1.661 \cdot 10^{-27}$ kg.

gas species	mass [u]	a_0 [−]	a_1 [K]	a_2 $\left[\mathrm{K}^2\right]$
He	4	−5.0746	−4127.8	627250
Ne	20	−4.2988	−4871.1	793580
Ar	40	−4.2123	−5239.6	995240
Kr	84	−3.6326	−5664.0	1122400
Xe	131	−2.0917	−6693.5	1341700
N_2	28	−4.3338	−5485.7	1010800
O_2	32	−4.0605	−5416.7	1026100

A.2 Calibration of Decagon soil moisture sensors

Soil moisture sensors working according to the FDR principle require a soil specific calibration to ensure a measurement uncertainty comparable to that of TDR measurements. For this reason, soil samples were taken at the sampling site near Mannheim. These samples were stored within steel cylinders of a known volume, so that the volumetric water content could be determined by weighting the sample before and after drying it. By this way, 3 cylinders were measured by the FDR probes and subsequently evaluated. To obtain a higher calibration range, these soil samples from Mannheim were afterward irrigated to different extents and analyzed by the same way, leading to in total 9 calibration

points per sensor.
The calibration was done according to the formula (Sakaki et al., 2008)

$$\theta_{\mathrm{w}} = \phi \cdot \frac{A^{\alpha} - A^{\alpha}_{\mathrm{dry}}}{A^{\alpha}_{\mathrm{sat}} - A^{\alpha}_{\mathrm{dry}}} \tag{A.2}$$

with the porosity ϕ and the measured sensor signals A_x [mV] for the sample, completely dry soil and water saturated soil, respectively. The resulting calibration curves are depicted in Fig. A.1 for all three sensors, respectively. The parameter α was determined by means of a fit. The values of $A^{\alpha}_{\mathrm{dry}}$ and $A^{\alpha}_{\mathrm{sat}}$ were determined by means of artificially created samples. Based on the standard deviation of α resulting from the fit, an relative uncertainty of $1-2$ vol% is achieved, depending on the exact signal data. This is in well agreement to the precision achievable according to manufacturer's data.

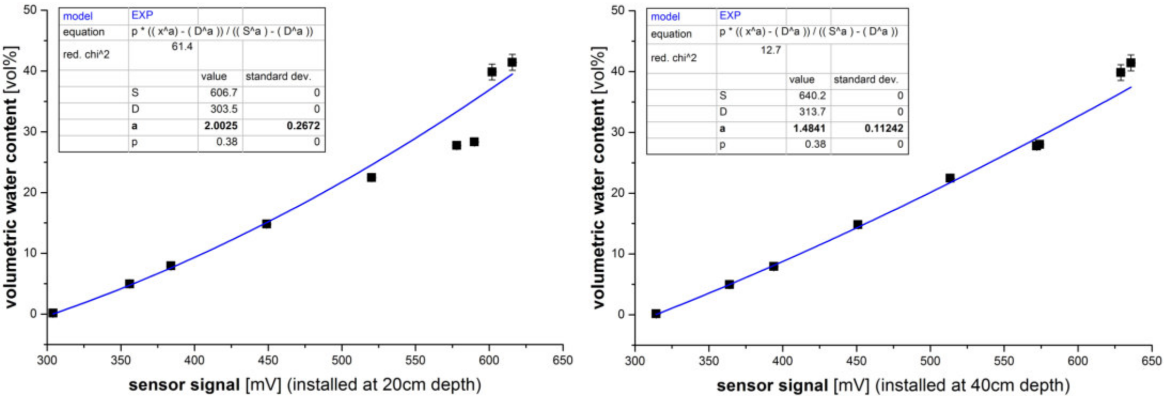

(a) Sensor at 20 cm depth

(b) Sensor at 40 cm depth

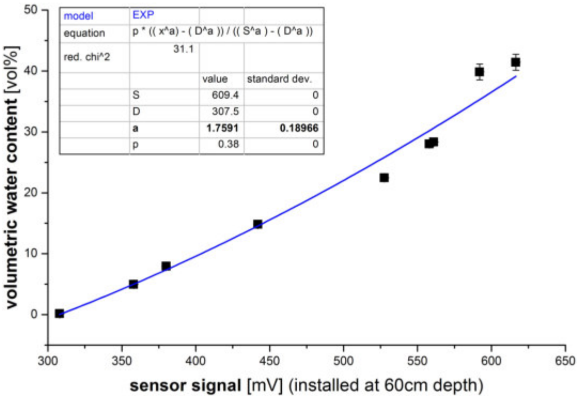

(c) Sensor at 60 cm depth

Figure A.1: Calibration curves for the three used *ECH2O* FDR sensors. The fit parameter "a" reflects α in eq. A.2, while $A^{\alpha}_{\mathrm{dry}}$ is denoted in the fit as D and $A^{\alpha}_{\mathrm{sat}}$ as S. A porosity of $\phi = 0.38$ was assumed for the fit of calibration curves.

A.3 Evaluation of Omnistar data for gas samples stored in copper tubes

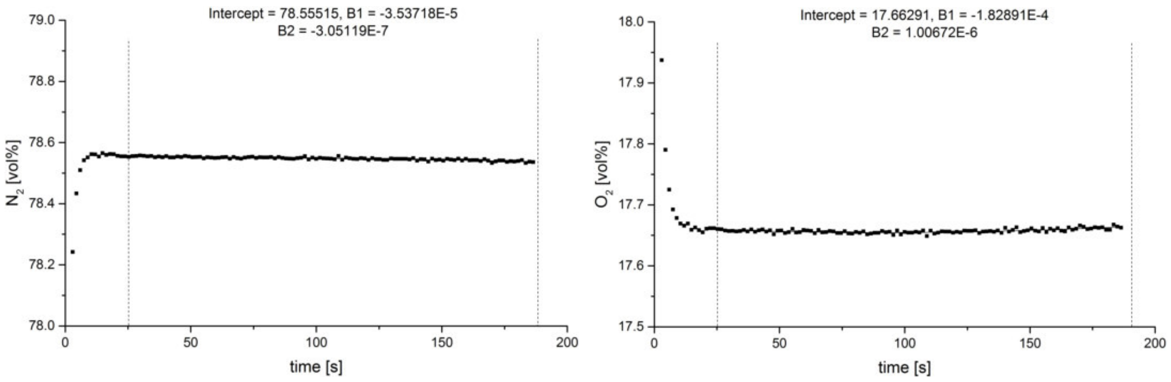

(a) N_2 analysis (b) O_2 analysis

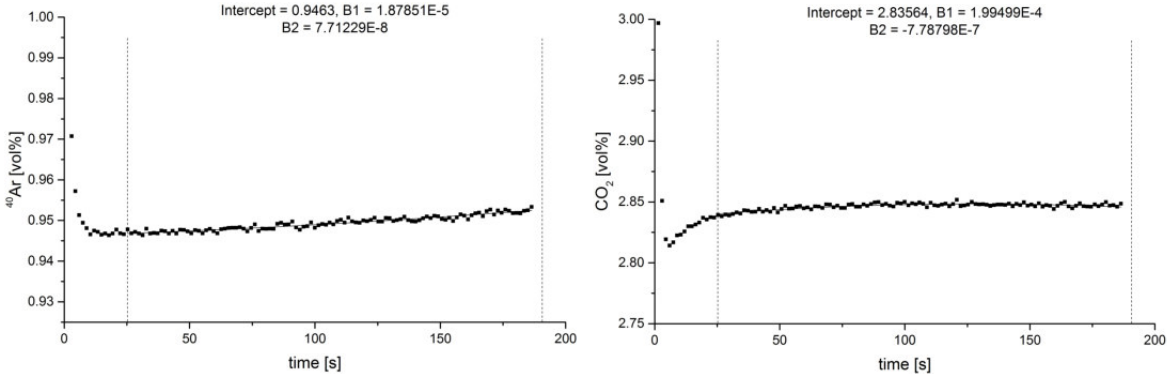

(c) ^{40}Ar analysis (d) CO_2 analysis

Figure A.2: Exemplary determination of gas mixing ratios (see intercept values) for samples from copper tubes analyzed by the *Omnistar* device. Signals at the inlet time were determined by means of a quadratic fit. The total measurement duration accounts for more than 180 s. Data from the first 25 s settling time were omitted.

A.4 Determination of the inlet volume for gas sample analysis

An exact knowledge of the volume V_{inlet} is essential for the determination of the amount of sampled gas. Starting from another well-known volume, gas was expanded into the volume V_{inlet}, while the variation of the gas pressure was used to calculate the exact volume content of V_{inlet}. The system consisted of a known part of the two volumes $V_1 = (38.876 \pm 0.470)$ cm^3 and $V_s = (77.338 \pm 0.040)$ cm^3, which are both connected to an unknown transfer volume V_2 leading to the volume of interest V_{inlet}. After $V_1 + V_s$ were flushed by atmospheric air up to a pressure p_1 between 1 and 11 mbar, the occupied volume is enlarged to $V_1 + V_s + V_2$ leading to a pressure p_2. Finally, the gas es expanded into $V_1 + V_s + V_2 + V_{\text{inlet}}$, resulting in the pressure value p_3. Every pressure value is measured after the volume expansion by a *Ceramic Capacitance Gauge* pressure sensor with an uncertainty of 0.1 %, respectively. This procedure allows to determine the content of the volume V_2

$$p_1 \cdot (V_1 + V_{\text{s}}) = p_2 \cdot (V_1 + V_{\text{s}} + V_2) \iff V_2 = (V_1 + V_{\text{s}}) \cdot \left(\frac{p_1}{p_2} - 1\right) . \tag{A.3}$$

which is used to calculate the content of the volume V_{inlet}:

$$p_1 \cdot (V_1 + V_\text{s}) = p_3 \cdot (V_1 + V_\text{s} + V_2 + V_{\text{inlet}}) \Longleftrightarrow V_{\text{inlet}} = (V_1 + V_\text{s}) \cdot \left(\frac{p_1}{p_3} - \frac{p_1}{p_2}\right) \tag{A.4}$$

The corresponding systematical error results from the uncertainty of the pressure sensor and of the well-known volumes, respectively. It is determined by Gaussian error propagation:

$$\begin{aligned} \Delta V_2 \ =& \left[\left(\left(\frac{p_1}{p_2} - 1\right) \cdot \Delta V_1\right)^2 + \left(\left(\frac{p_1}{p_2} - 1\right) \cdot \Delta V_\text{s}\right)^2 + \right. \\ & \left. \left(\frac{(V_1 + V_\text{s}) \cdot \Delta p_1}{p_2}\right)^2 + \left(\frac{(V_1 + V_\text{s}) \cdot p_1 \cdot \Delta p_2}{p_2^2}\right)^2\right]^{1/2} \end{aligned} \tag{A.5}$$

$$\begin{aligned} \Delta V_{\text{inlet}} \ =& \left[\left(\left(\frac{p_1}{p_3} - \frac{p_1}{p_2}\right) \cdot \Delta V_1\right)^2 + \left(\left(\frac{p_1}{p_3} - \frac{p_1}{p_2}\right) \cdot \Delta V_\text{s}\right)^2 + \left(\frac{(V_1 + V_\text{s}) \cdot p_1 \cdot \Delta p_2}{p_2^2}\right)^2 + \right. \\ & \left. \left(\frac{(V_1 + V_\text{s}) \cdot p_1 \cdot \Delta p_3}{p_3^2}\right)^2 + \left((V_1 + V_\text{s}) \cdot \left(\frac{1}{p_3} - \frac{1}{p_2}\right) \cdot \Delta p_1\right)^2\right]^{1/2} \end{aligned} \tag{A.6}$$

After each expansion performance, the entire system was evacuated by a turbo molecular pump. Since all valves are operated automatically, a measurement script was implemented for this study to measure a sequence of more than 100 expansion performances, with a total measurement time of about 20 h. The value of V_{inlet} is determined as the mean value of all measurements. Assuming a normal distribution of measured data, the statistical error of the mean value was determined as quotient of the standard deviation of all measured values and the square root of the number of measurements, as described in Demtröder (2008). The total uncertainty ΔV_{inlet} was determined by Gaussian error propagation based on the just described statistical error and the systematical error stated above. A new determination of V_{inlet} was done after any change of the installation. The resulting volume contents used in this study are given in Tab. A.2.

Table A.2: Resulting volume contents of V_{inlet}.

date	sample no.	V_{inlet} [ml]
11/2013 – 10/2014	7611 – 9049	34.074 ± 0.288
12/2014 – 03/2015	9218 – 9593	33.616 ± 0.287
05/2015 – today	9786 – today	33.912 ± 0.287

A.5 Evaluation of NG data from gas sample analysis

After opening a copper tube containing the sampled gas, the mixing ratio of water vapor within the inlet volume V_{inlet} depends on the amount of water, meaning its mass m_{w} within the originally closed copper tube, which can be associated with the amount of moles of water ν and the molar mass $\text{M}_{\text{w}} = 18\,\text{u}$:

$$\nu = m_{\text{w}}/\text{M}_{\text{w}} \tag{A.7}$$

The equation of state of ideal gases leads to

$$\frac{\nu}{V_{\text{sam}}} = \frac{m_{\text{w}}/\text{M}_{\text{w}}}{V_{\text{sam}}}\frac{p}{R \cdot T_{\text{sam}}} = \frac{h_{\text{sam}} \cdot e_{\text{s}}\left(T_{\text{sam}}\right)}{R \cdot T_{\text{sam}}} \tag{A.8}$$

with the saturation water vapor pressure e_{s} (see eq. (2.21)) and the relative humidity h_{sam} of the sample gas within the copper tube. The volume within the copper tube V_{sam} can be determined by an empirical formula from Wieser (2006)

$$V_{\text{sam}}\left(L\right)\,[\text{cm}^3] = B \cdot L\,[\text{cm}] + A \tag{A.9}$$

with the parameters $A = (0.12284 \pm 0.00336)\,\text{cm}^3$ and $B = (0.135830 \pm 0.000635)\,\text{cm}^2$. The temperature T_{sam} of the gas during sampling determines its water content and is, thus, a crucial parameter for the calculation of h_{inlet}. With the definition of the specific gas constant of water $R_{\text{w}} = R/\text{M}_{\text{w}} = 461.52\,\text{J}\,\text{kg}^{-1}\,\text{K}^{-1}$ the mass of water within a copper tube can be determined as follows:

$$m_{\text{w}} = \frac{h_{\text{sam}} \cdot e_{\text{s}}\left(T_{\text{sam}}\right) \cdot V_{\text{sam}}}{R_{\text{w}} \cdot T_{\text{sam}}} \tag{A.10}$$

Finally, the relative humidity h_{inlet} within the inlet volume is determined analogously to eq. (A.8) by

$$h_{\text{inlet}} = \frac{m_{\text{w}}\left(T_{\text{sam}}\right) \cdot R_{\text{w}} \cdot T_{\text{lab}}}{V_{\text{inlet}} \cdot e_{\text{s}}\left(T_{\text{lab}}\right)} \tag{A.11}$$

with the laboratory temperature T_{lab}.

The error of the molar sample gas amount in eq. (3.3) is determined as follows:

$$\begin{aligned}
\Delta\nu \quad = & \Bigg[\left(\frac{\Delta p_{\text{inlet}} \cdot \left[V_{\text{inlet}} - m_{\text{Cu}}/\rho_{\text{Cu}}\right]}{R \cdot T_{\text{lab}}}\right)^2 + \left(\frac{\Delta p_{\text{water}} \cdot \left[V_{\text{inlet}} - m_{\text{Cu}}/\rho_{\text{Cu}}\right]}{R \cdot T_{\text{lab}}}\right)^2 \\
& + \left(\frac{\left[p_{\text{inlet}} - p_{\text{water}}\right] \cdot \Delta V_{\text{inlet}}}{R \cdot T_{\text{lab}}}\right)^2 + \left(\frac{\left[p_{\text{inlet}} - p_{\text{water}}\right] \cdot \Delta m_{\text{Cu}}/\rho_{\text{Cu}}}{R \cdot T_{\text{lab}}}\right)^2 \\
& + \left(\frac{\left[p_{\text{inlet}} - p_{\text{water}}\right] \cdot \left[V_{\text{inlet}} - m_{\text{Cu}}/\rho_{\text{Cu}}\right] \cdot \Delta T_{\text{lab}}}{R \cdot T_{\text{lab}}^2}\right)^2\Bigg]^{1/2}
\end{aligned} \tag{A.12}$$

where Δp_{inlet} is estimated as 0.2 % of the measured value according to the manufacturer's data of the measurement device. The weighting error Δm_{Cu} is assumed as 0.01 g and ΔT_{lab} as 0.1°C. The inlet volume error ΔV_{inlet} follows from the volume determination as described in appendix A.4.

The error value of the arising water vapor pressure within the inlet volume

$$\Delta p_{\mathrm{water}} = \sqrt{\left(\frac{\Delta h_{\mathrm{inlet}}}{100\,\%} \cdot E\left(T_{\mathrm{lab}}\right)\right)^2 + \left(\frac{h_{\mathrm{inlet}}}{100\,\%} \cdot \Delta E\left(T_{\mathrm{lab}}\right)\right)^2} \tag{A.13}$$

follows from the uncertainty of the relative humidity within the inlet volume

$$\begin{aligned}\Delta h_{\mathrm{inlet}} &= \left[\left(\frac{\Delta m_{\mathrm{w}}\left(T_{\mathrm{sam}}\right) \cdot R_{\mathrm{w}} \cdot T_{\mathrm{lab}}}{V_{\mathrm{inlet}} \cdot E\left(T_{\mathrm{lab}}\right)}\right)^2 + \left(\frac{m_{\mathrm{w}}\left(T_{\mathrm{sam}}\right) \cdot R_{\mathrm{w}} \cdot \Delta T_{\mathrm{lab}}}{V_{\mathrm{inlet}} \cdot E\left(T_{\mathrm{lab}}\right)}\right)^2\right. \\ &\quad + \left(\frac{m_{\mathrm{w}}\left(T_{\mathrm{sam}}\right) \cdot R_{\mathrm{w}} \cdot T_{\mathrm{lab}} \cdot \Delta V_{\mathrm{inlet}}}{V_{\mathrm{inlet}}^2 \cdot E\left(T_{\mathrm{lab}}\right)}\right)^2 \\ &\quad \left. + \left(\frac{m_{\mathrm{w}}\left(T_{\mathrm{sam}}\right) \cdot R_{\mathrm{w}} \cdot T_{\mathrm{lab}} \cdot \Delta E\left(T_{\mathrm{lab}}\right)}{V_{\mathrm{inlet}} \cdot E\left(T_{\mathrm{lab}}\right)^2}\right)^2\right]^{1/2} ,\end{aligned} \tag{A.14}$$

as well as the water mass uncertainty

$$\Delta m_{\mathrm{w}} = \sqrt{\left(\frac{\Delta E\left(T_{\mathrm{sam}}\right) \cdot V_{\mathrm{sam}}}{R_{\mathrm{w}} \cdot T_{\mathrm{sam}}}\right)^2 + \left(\frac{E\left(T_{\mathrm{sam}}\right) \cdot \Delta V_{\mathrm{sam}}}{R_{\mathrm{w}} \cdot T_{\mathrm{sam}}}\right)^2 + \left(\frac{E\left(T_{\mathrm{sam}}\right) \cdot V_{\mathrm{sam}} \cdot \Delta T_{\mathrm{sam}}}{R_{\mathrm{w}} \cdot T_{\mathrm{sam}}^2}\right)^2} , \tag{A.15}$$

and the errors of the copper tube volume estimation and of the saturation water vapor pressure, respectively:

$$\Delta V_{\mathrm{sam}} = \sqrt{(\Delta B \cdot L)^2 + (\Delta A)^2 + (B \cdot \Delta L)^2} \tag{A.16}$$

$$\Delta E\left(T_{\mathrm{lab}}\right) = E\left(T_{\mathrm{lab}}\right) \cdot \Delta T_{\mathrm{lab}} \cdot \left[\frac{17.62 \cdot 243.12\,\mathrm{K}}{(243.12\,\mathrm{K} + (T - 273.15\,\mathrm{K}))^2}\right] \tag{A.17}$$

The uncertainty of the length determination was estimated on the base of repeated measurements of the same copper tube as $\Delta L = 0.2\,\mathrm{mm}$. It is more difficult to determine the uncertainty of the estimated temperature T_{sam}. Its value has to be estimated individually for every sampling site and depends on local sampling conditions. For the long-term study near Mannheim, the soil temperatures were determined by fits on the continuously logged data. A mean deviation of the measured data from these fits was estimated which is higher for shallower soil depths due to stronger temperature fluctuations. This resulted in a ΔT_{sam} value of 2.5°C for 1.0 m depth, 1.0°C for 3.0 m depth, 0.75°C for 4.4 m depth and of 0.5°C for 5.5 and 6.5 m depth, respectively. When the assumed soil temperature exceeded the atmospheric temperature during sampling, the atmospheric temperature was used instead of the soil temperature (due to water condensation in the sampling tubes) with an uncertainty of 2.5°C assumed for temperature data taken from the next DWD (2016) weather station. An uncertainty of 1.5°C was estimated for the soil temperature in Brazil.

Altogether, the analytical uncertainty of the ratio $X_{\mathrm{i}}/X_{\mathrm{atm}}$ is determined by

$$\Delta\left(\frac{X_{\mathrm{i}}}{X_{\mathrm{atm}}}\right) = \frac{\Delta X_{\mathrm{i}}}{X_{\mathrm{atm}}} = \frac{1}{X_{\mathrm{atm}}} \cdot \sqrt{\left(\frac{\Delta A_{\mathrm{STP}}}{V_{\mathrm{STP}} \cdot \nu}\right)^2 + \left(\frac{A_{\mathrm{STP}} \cdot \Delta \nu}{V_{\mathrm{inlet}} \cdot \nu^2}\right)^2} \tag{A.18}$$

where the value of ΔA_{STP} follows from the data evaluation by the software *WuCEM* and the error of the literature value of dry atmospheric air X_{atm} is neglected.

A.6 Forward modeling for shallow well groundwater

The estimation procedure for parameters applied for the forward modeling approach is described in the following. All parameters are summarized in Tab. A.3.
The equilibrium component is determined based on the measured WTT, the salinity and the gas phase composition. The fractionation parameter $F_{\mathrm{CE}} = v/q$ describes the composition of the excess air component. Recorded water level data are used to estimate the parameter q: The water column height above the pumping depth of 7.8 m allows to determine $P_B = P_A + \rho(S,T) \cdot g \cdot h$, while the pressure P_A reflects the mean atmospheric pressure at the sampling site which is 1004.6 mbar according to DWD (2016). The saturation water vapor pressure follows from the recorded WTT. The resulting values of q reflect a typical range of values observed in groundwater (Aeschbach-Hertig et al., 2000). In contrast, recorded data do not allow to determine the parameter v which is thus estimated for all modeling setups. Since only a slight dissolution of entrapped air bubbles is expected in shallow groundwater, a uniform value of $v = 0.95$ was chosen for all scenarios, which is slightly higher but still in good agreement with typically observed values of gas bubble dissolution (Aeschbach-Hertig et al., 2000). Both parameters q and v result in values of F_{CE} fluctuating between 0.80 and 0.85, which corresponds to a comparatively strong fractionated excess air pattern. The parameter value of A – which was assumed to be constant during all time steps – was modified in a way to minimize the obtained χ^2 value. The degassing term contains the parameter B^d. Since degassing is correlated with the water table level – meaning that bubble formation occurs whenever the water level reaches a minimum value – the value of B^d was scaled linearly by water level data, reaching a certain maximum value for the minimum observed water level or rather approximating to zero for maximum water level. The corresponding maximum value of B^d_{max} was arbitrarily chosen as 1 cc/kg, which should be smaller than all obtained values of A since measured saturation anomalies were mostly positive.

Table A.3: Mannheim: Parameters to be determined for the forward modeling approach and data bases for corresponding estimations.

parameter	**data base**	**scenario 1**	**scenario 2**	**scenario 3**	**scenario 4**
equilibrium component					
T [°C]	WTT data	11.6	WTT	WTT	WTT
S [g/kg]	κ_{25} data	0.72	0.72	0.72	0.72
X/X_{atm} [ ]	soil air compos.	1.00	1.00	1.00	1.32
excess air component					
v [ ]	estimated	0.95	0.95	0.95	0.95
q [ ]	water level data	1.15	1.1 – 1.2	1.1 – 1.2	1.1 – 1.2
F_{CE} [ ]	$= v/q$	0.83	0.80 – 0.85	0.80 – 0.85	0.80 – 0.85
A [cc/kg]	minimizing χ^2	2	2	8	4
degassing term					
B^d [cc/kg]	estimated / water level data	0	0	0-1	0-1

A.7 Santarém: Bias of measured GWTs by heat released from submersible pumps

Recorded temperature data of up to four different devices are in good agreement at every sampled well. However, an above-ground measurement of the GWT provides the potential for a systematical bias due to heat released by the pump (due to an efficiency below 100 %, see chapter 3.1.6). The temperature increase ΔT due to heat flux Q is

$$\Delta T = \frac{Q}{M \cdot \mathrm{c}_P} = \frac{P - E}{M \cdot \mathrm{c}_P} = \frac{P - Mgh}{M \cdot \mathrm{c}_P} = \frac{Mgh \cdot (1/\eta - 1)}{M \cdot \mathrm{c}_P} = \frac{gh \cdot (1 - \eta)}{\mathrm{c}_P \cdot \eta} \tag{A.19}$$

with the absorbed power P of the pump, the mass flow of water M, the potential energy E for pumping the water over a height distance h, the heat capacity of water c_P and the gravitational constant g (Meschede, 2015). For a specific efficiency η, the known pumping depth at each sampled well allows to estimate the potential temperature increase due to heating by the pump, assuming that all released heat warms the pumped water. Assuming an efficiency[1] of $\eta = 30\,\%$, the resulting heating of pumped water ranges from 0.02°C to 0.55°C, depending on the pumping depth. In contrast, an efficiency of $\eta = 50\,\%$ would result in a heating by less than 0.3°C, even for deepest sampled wells. It has to be noted that this estimation does not consider that the released heat is also warming subsurface soil material and non-pumped groundwater inside the well. To summarize, it cannot be certainly stated to which extent measured GWTs in Santarém are biased by heat released by the pump. However, a corresponding influence is neglected in this study, for two reasons: First, all above estimated parameter values have to be seen as a rather unrealistic upper limit of potential heating. Second, about the half of all sampled wells exhibit pumping depths of less than 20 m, for which even the maximum potential heating is comparable to the measurement uncertainty of applied devices.

---

[1] The efficiencies of the installed pumps in Santarém are likely to be higher than that of the used pump at the long-term study site in Germany, since the ratio of tube volume to tube surface (and, thus, the friction along the tube wall) decreases, given tube radii of several cm at all sampled wells near Santarém.

A.8 Gas-specific parameters for gas transport modeling

Table A.4: Gas-specific parameters for gas transport modeling. Binary diffusion coefficients are calculated according to Fuller and Giddings (1965). Thermal diffusion factors are taken from Grew and Ibbs (1952). Parameter values are given for a temperature of 298 K.

gas species	diffusivity D [cm^2/s]	thermal diff. factor α [ ]
He	0.68133	−0.38
Ne	0.30427	−0.17
N_2	0.19794	−0.071
air	0.19215	0
O_2	0.19962	0.05
Ar	0.19027	0.07
CO_2	0.15733	0.019
Kr	0.14635	0.1
Xe	0.12583	0.1

Appendix B

Measurement results and further data

B.1 Comparison argon data: MM5400 and Omnistar

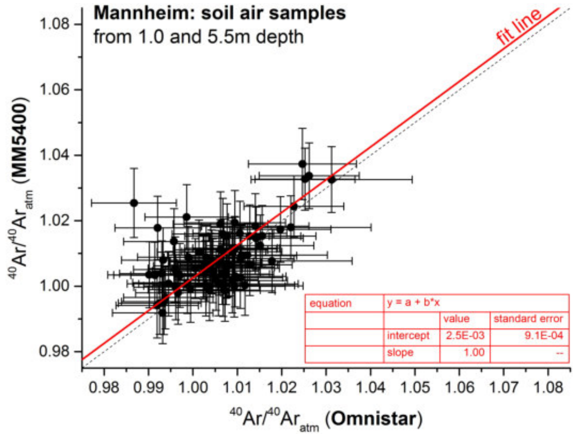

Figure B.1: Mannheim: Comparison of ^{40}Ar data measured by the *MM5400* mass spectrometer and the *Omnistar* device. The red line describes a linear fit with slope 1.

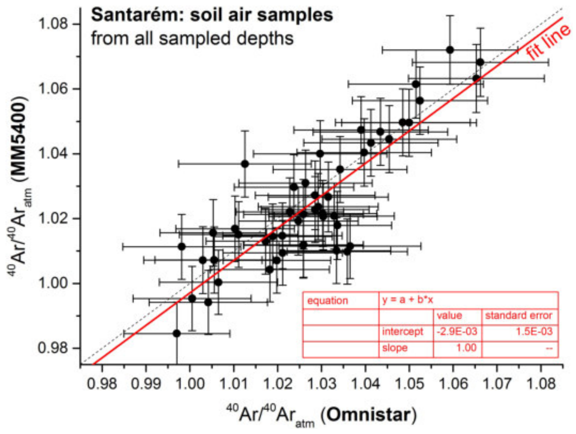

Figure B.2: Santarém: Comparison of ^{40}Ar data measured by the *MM5400* mass spectrometer and the *Omnistar* device. The red line describes a linear fit with slope 1.

B.2 Mannheim: Concentrations of Ne and Xe in shallow well groundwater

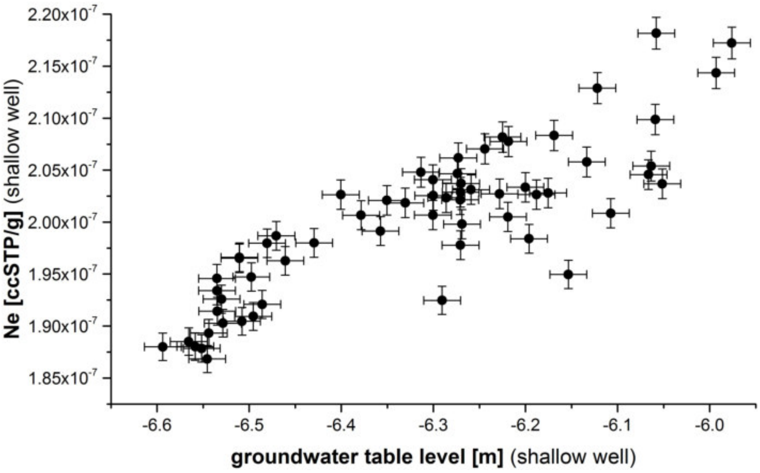

Figure B.3: Mannheim: Correlation between Ne concentrations and the groundwater table level below Earth surface (shallow well). The Spearman correlation coefficient was determined as 0.792, reflecting a significant correlation at the 0.05 level.

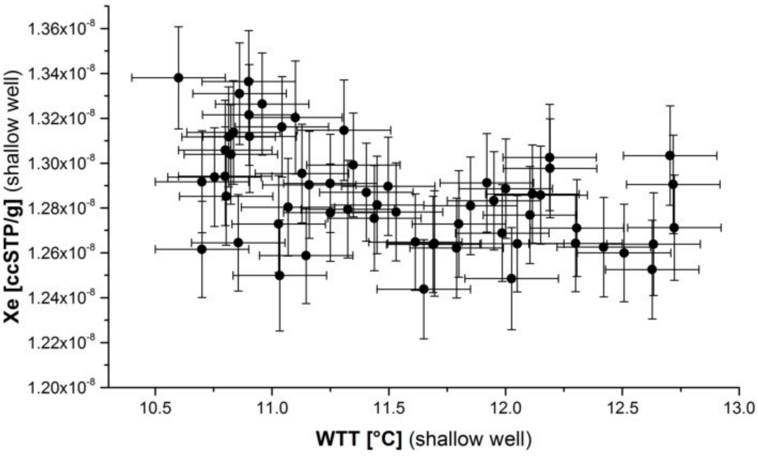

Figure B.4: Mannheim: Correlation between Xe concentrations and the WTT (shallow well). The Spearman correlation coefficient was determined as −0.446, reflecting a significant anti-correlation at the 0.05 level.

B.3 Mannheim: Additional time series of soil air composition

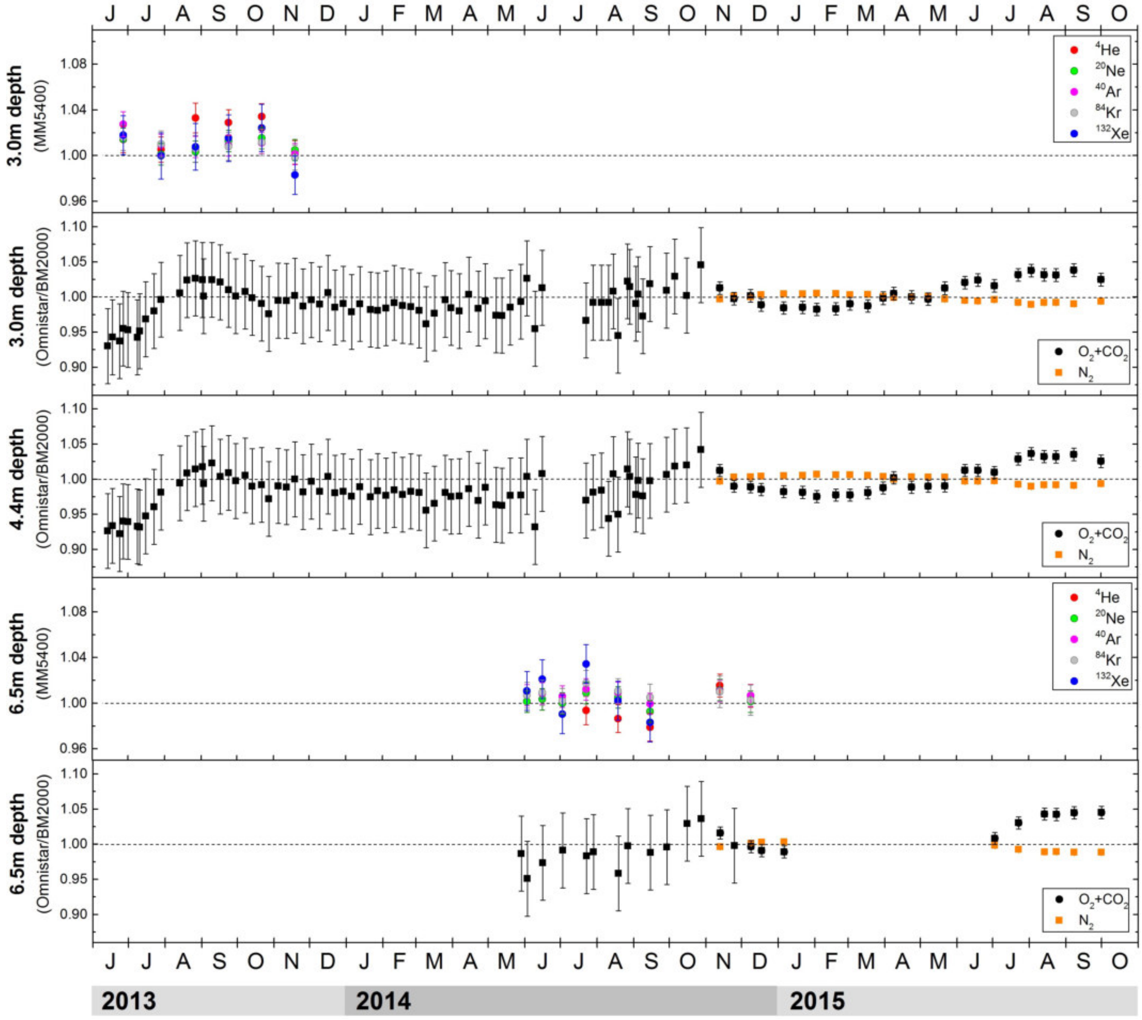

Figure B.5: Mannheim: Time series of soil air composition (O_2+CO_2 and NGs) at 3 m, 4.4 m and 6.5 m depth, respectively. Data were measured by the *MM5400* sector field mass spectrometer, by the *Omnistar* quadrupole mass spectrometer and by the *Geotech BM2000* gas analyzer, respectively. No data were available at 6.5 m depth until June 2014 as well as between February and July 2015, since the groundwater table level was less than 6.5 m below Earth surface during these periods.

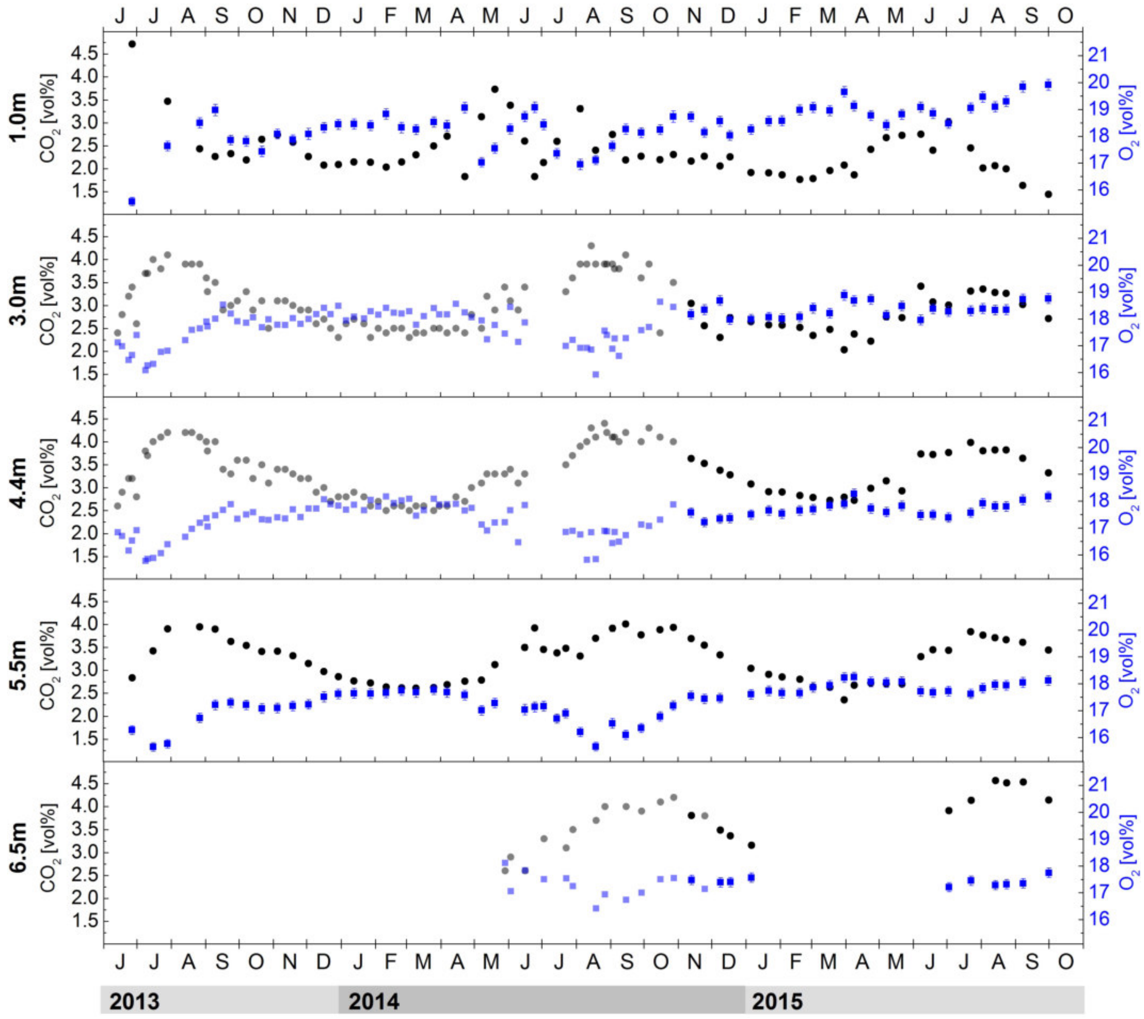

Figure B.6: Mannheim: Time series of soil air composition (O_2 and CO_2) at all sampled depths, respectively. Data were measured by means of the *Omnistar* quadrupole mass spectrometer (filled symbols) and by the *Geotech BM2000* gas analyzer (transparent filled symbols). Uncertainties (not depicted in the graph) of the *Geotech BM2000* measurements are 0.5 vol% for CO_2 and 1.0 vol% for O_2.

B.4 Mannheim: Time series of ^{220}Rn activities

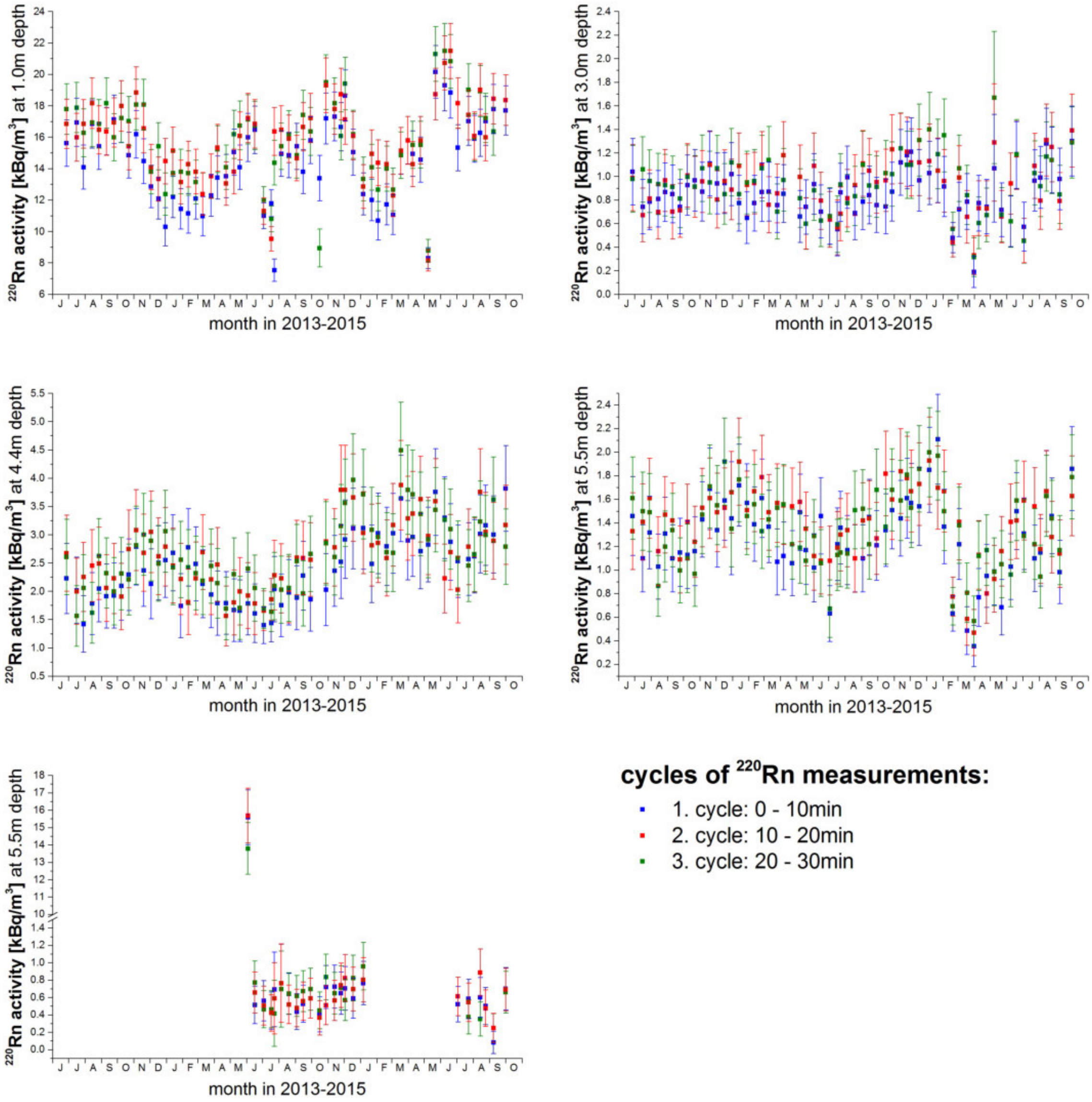

Figure B.7: Mannheim: Time series of ^{220}Rn activities in soil air. Three measurement cycles of each 10 min duration were carried out subsequently. At nearly all sampling dates, the resulting activities agree within their uncertainties, respectively. Long-term fluctuations result probably from varying soil moisture contents and, thus, varying degrees of soil aeration. The strong drop at 1.0 m depth in June/July 2014 and May 2015 resulted from a leakage in the sampling tube. No data were available at 6.5 m depth until June 2014 as well as between February and July 2015, since the groundwater table level was less than 6.5 m below Earth surface during these periods.

B.5 Mannheim: Three isotope plot

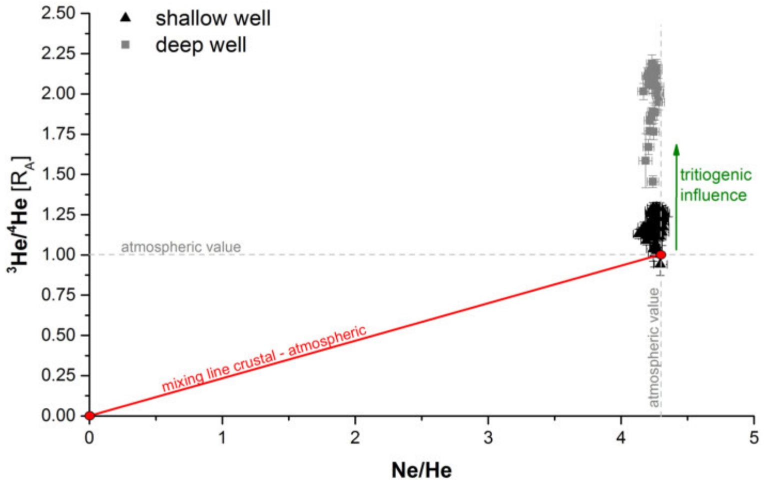

Figure B.8: Mannheim: Three isotope plot investigating the influence of different geochemical reservoirs on dissolved He contents in local groundwater. Samples show an enhanced ratio of ^{3}He/^{4}He due to tritiogenic ^{3}He production, while there is no signature of radiogenic helium.

B.6 Mannheim: Atmospheric air pressure

Figure B.9 shows a long-term record of the atmospheric air pressure near the sampling site of this study. A mean fit results in an average value of (1005.0 ± 0.1) mbar during the last 35 years. By means of the known height difference between the pressure measurement device (98.1 m a.s.l.) and the mean local water table level (94.47 m a.s.l.), the barometric formula (with a scale height of 8 300 m) results in an average air pressure of 1004.6 mbar at the groundwater water table level, corresponding to 0.991 atm.

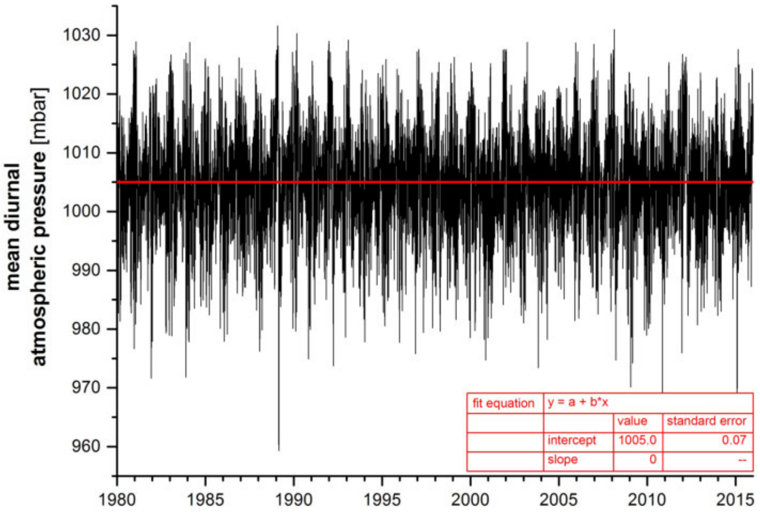

Figure B.9: Mannheim: Long-term record of atmospheric air pressure (DWD, 2016).

B.7 Mannheim: Soil air composition data

Table B.1: Mannheim: Soil air composition at 1.0 m depth.

1.0 m depth		Measurements by *Omnistar*										Measurements by *MM5400* mass spectrometer															
		N_2	ΔN_2	CO_2	ΔCO_2	^{40}Ar	$\Delta^{40}Ar$	O_2	ΔO_2	O_2+CO_2	ΔO_2+CO_2	^{3}He	$\Delta^{3}He$	^{4}He	$\Delta^{4}He$	^{20}Ne	$\Delta^{20}Ne$	^{22}Ne	$\Delta^{22}Ne$	^{36}Ar	$\Delta^{36}Ar$	^{40}Ar	$\Delta^{40}Ar$	^{84}Kr	$\Delta^{84}Kr$	^{132}Xe	$\Delta^{132}Xe$
		all data is given in units of vol%										partial pressures are normalized to their values in dry atmospheric air, respectively															
F1	2013-06-18																										
F2	2013-06-27	78.77	0.19	4.71	0.05	0.940	0.011	15.57	0.16	20.29	0.17			1.025	0.012	1.020	0.010	1.020	0.010	1.012	0.013	1.016	0.011	1.001	0.011	0.998	0.017
F3	2013-07-16																										
F4	2013-07-29	77.96	0.19	3.47	0.04	0.931	0.010	17.63	0.18	21.11	0.18	0.982	0.037	1.018	0.012	1.013	0.010	1.016	0.010	1.000	0.016	1.003	0.010	1.008	0.012	0.982	0.020
F5	2013-08-14																										
F6	2013-08-27	78.13	0.19	2.43	0.03	0.936	0.011	18.50	0.19	20.93	0.19	1.066	0.039	1.020	0.011	1.007	0.010	1.007	0.010	1.011	0.015	1.006	0.010	1.002	0.012	0.980	0.020
F7	2013-09-10	77.82	0.19	2.27	0.05	0.937	0.010	18.97	0.21	21.24	0.22																
F8	2013-09-24	78.86	0.19	2.33	0.03	0.946	0.011	17.86	0.18	20.19	0.18	0.822	0.088	1.014	0.011	1.008	0.009	1.009	0.010	1.020	0.011	1.015	0.010	1.015	0.011	1.009	0.017
F9	2013-10-08	79.04	0.19	2.19	0.05	0.950	0.011	17.81	0.19	20.01	0.20																
F10	2013-10-22	78.97	0.19	2.64	0.06	0.947	0.010	17.44	0.20	20.08	0.21	1.029	0.105	1.007	0.010	1.003	0.009	1.003	0.009	1.026	0.011	1.015	0.010	1.007	0.011	1.015	0.017
F11	2013-11-05	78.24	0.19	2.74	0.04	0.937	0.010	18.08	0.18	20.82	0.19																
F12	2013-11-19	78.62	0.19	2.58	0.03	0.941	0.011	17.86	0.18	20.44	0.18	0.923	0.037	1.001	0.012	0.996	0.009	0.995	0.009	1.014	0.023	0.999	0.009	1.005	0.011	0.981	0.017
F13	2013-12-03	78.70	0.19	2.26	0.05	0.945	0.010	18.09	0.20	20.35	0.21																
F14	2013-12-17	78.66	0.19	2.08	0.03	0.943	0.011	18.32	0.19	20.40	0.19	0.906	0.030	1.004	0.013	1.001	0.009	1.002	0.009	1.012	0.023	1.003	0.009	1.009	0.012	1.008	0.017
F15	2013-12-30	78.53	0.19	2.09	0.03	0.942	0.010	18.44	0.19	20.53	0.19																
F16	2014-01-13	78.46	0.20	2.15	0.03	0.940	0.017	18.45	0.19	20.60	0.19	1.098	0.114	1.005	0.010	0.997	0.009	0.997	0.009	1.004	0.011	1.000	0.009	0.986	0.011	1.002	0.017
F17	2014-01-28	78.51	0.19	2.14	0.03	0.942	0.010	18.40	0.19	20.54	0.19																
F18	2014-02-11	78.20	0.19	2.04	0.03	0.937	0.011	18.83	0.19	20.87	0.19	0.922	0.091	1.004	0.010	0.997	0.009	0.997	0.009	1.021	0.011	0.999	0.009	0.996	0.011	1.016	0.017
F19	2014-02-25	78.58	0.19	2.15	0.05	0.945	0.011	18.32	0.19	20.47	0.20																
F20	2014-03-10	78.51	0.19	2.30	0.03	0.943	0.011	18.25	0.19	20.55	0.19	0.959	0.036	0.991	0.012	0.997	0.010	0.999	0.010	1.017	0.025	1.000	0.009	1.003	0.011	1.020	0.017
F21	2014-03-26	78.04	0.18	2.50	0.04	0.935	0.010	18.53	0.19	21.03	0.19																
F22	2014-04-07	77.97	0.20	2.71	0.04	0.933	0.012	18.39	0.20	21.10	0.21	1.225	0.252	1.014	0.012	0.999	0.009	0.999	0.009	1.002	0.011	1.001	0.009	0.993	0.010	0.986	0.017
F23	2014-04-23	78.17	0.19	1.83	0.05	0.939	0.011	19.06	0.20	20.89	0.21																
F24	2014-05-08	78.89	0.20	3.13	0.04	0.945	0.017	17.03	0.18	20.17	0.18	0.949	0.095	0.999	0.010	1.000	0.009	0.999	0.009	1.023	0.011	1.009	0.010	1.008	0.011	1.000	0.017
F25	2014-05-20	77.78	0.19	3.73	0.05	0.937	0.017	17.55	0.18	21.29	0.19																
F26	2014-06-03	77.42	0.18	3.38	0.04	0.928	0.011	18.27	0.19	21.65	0.19	1.007	0.099	0.995	0.010	0.995	0.009	0.996	0.009	1.006	0.011	0.992	0.009	0.982	0.011	0.974	0.017
F27	2014-06-16	77.73	0.18	2.60	0.04	0.934	0.010	18.73	0.19	21.33	0.19																
F28	2014-06-25	78.16	0.19	1.83	0.02	0.938	0.011	19.08	0.19	20.90	0.19																
F29	2014-07-03	78.48	0.20	2.13	0.03	0.951	0.017	18.44	0.19	20.57	0.19	1.063	0.105	1.011	0.011	1.004	0.009	1.004	0.010	1.002	0.012	1.008	0.010	1.003	0.011	0.992	0.017
F30	2014-07-15	79.10	0.19	2.59	0.04	0.949	0.010	17.36	0.18	19.95	0.18																
F31	2014-07-23											1.004	0.017	1.051	0.011	1.047	0.010	1.047	0.010	1.065	0.016	1.052	0.011	1.022	0.015	1.075	0.028
F32	2014-08-05	78.80	0.19	3.31	0.06	0.945	0.010	16.95	0.19	20.26	0.20																
F33	2014-08-19	79.53	0.19	2.40	0.03	0.952	0.011	17.11	0.17	19.52	0.18	1.007	0.033	1.024	0.013	1.022	0.010	1.023	0.010	1.040	0.026	1.017	0.010	1.023	0.012	1.020	0.017
F34	2014-09-03	78.68	0.19	2.74	0.04	0.943	0.010	17.63	0.18	20.37	0.18																
F35	2014-09-15	78.61	0.20	2.19	0.03	0.939	0.017	18.26	0.19	20.46	0.19	0.954	0.038	0.997	0.013	1.001	0.010	1.002	0.010	0.988	0.024	1.001	0.010	1.003	0.012	1.015	0.017
F36	2014-09-29	78.66	0.19	2.27	0.04	0.944	0.010	18.13	0.18	20.40	0.19																
F37	2014-10-16	78.62	0.19	2.20	0.03	0.943	0.011	18.24	0.18	20.44	0.19	1.009	0.017	1.022	0.010	1.015	0.010	1.015	0.010	1.029	0.020	1.019	0.010	1.003	0.014	1.033	0.025
F38	2014-10-28	78.02	0.19	2.31	0.05	0.936	0.010	18.73	0.21	21.04	0.22																
F39	2014-11-13	78.17	0.18	2.16	0.02	0.933	0.011	18.73	0.19	20.89	0.19	0.968	0.020	1.014	0.010	1.011	0.009	1.010	0.009	1.012	0.019	1.009	0.009	1.014	0.014	1.005	0.024
F40	2014-11-25	78.64	0.18	2.27	0.02	0.946	0.009	18.14	0.18	20.41	0.18																
F41	2014-12-09	78.44	0.18	2.06	0.02	0.946	0.009	18.56	0.19	20.62	0.19	0.983	0.015	1.007	0.010	1.005	0.009	1.005	0.009	1.001	0.018	1.007	0.009	1.014	0.015	0.946	0.023
F42	2014-12-18	78.77	0.19	2.26	0.02	0.946	0.010	18.03	0.18	20.28	0.19																
F43	2015-01-06	78.89	0.19	1.92	0.02	0.943	0.009	18.25	0.18	20.17	0.18	1.023	0.016	1.008	0.010	1.001	0.009	1.001	0.009	1.026	0.017	1.012	0.009	1.016	0.013	1.013	0.024
F44	2015-01-22	78.59	0.18	1.91	0.02	0.940	0.009	18.56	0.19	20.47	0.19																
F45	2015-02-03	78.62	0.18	1.87	0.02	0.941	0.009	18.57	0.19	20.44	0.19	0.980	0.020	1.010	0.010	1.004	0.010	1.005	0.010	1.025	0.019	1.015	0.010	0.993	0.013	0.996	0.018
F46	2015-02-19	78.32	0.18	1.77	0.02	0.940	0.009	18.98	0.19	20.74	0.19																
F47	2015-03-03	78.20	0.18	1.78	0.02	0.940	0.009	19.08	0.19	20.86	0.19	0.999	0.020	1.009	0.010	1.004	0.010	1.005	0.010	1.007	0.020	1.007	0.010	0.994	0.014	1.016	0.018
F48	2015-03-18	78.13	0.18	1.96	0.02	0.937	0.009	18.95	0.19	20.91	0.19																
F49	2015-03-31	77.33	0.18	2.08	0.02	0.929	0.009	19.65	0.20	21.73	0.20	0.999	0.020	1.005	0.010	1.001	0.010	1.001	0.010	0.980	0.020	1.001	0.010	0.981	0.013	1.007	0.017
F50	2015-04-09	78.07	0.18	1.86	0.02	0.932	0.009	19.12	0.19	20.99	0.19																
F51	2015-04-24	77.88	0.18	2.42	0.02	0.930	0.009	18.77	0.19	21.19	0.19	1.011	0.020	1.013	0.010	0.998	0.010	0.997	0.010	1.021	0.021	1.005	0.010	1.009	0.013	1.011	0.018
F52	2015-05-08	77.97	0.18	2.68	0.03	0.933	0.009	18.42	0.18	21.10	0.19																
F53	2015-05-22	77.53	0.18	2.73	0.03	0.926	0.009	18.81	0.19	21.54	0.19	0.996	0.021	1.015	0.010	1.008	0.010	1.007	0.010	1.002	0.022	1.003	0.010	1.019	0.015	0.982	0.017
F54	2015-06-08	77.24	0.18	2.75	0.03	0.925	0.009	19.08	0.19	21.83	0.20	0.993	0.020	1.011	0.010	1.005	0.010	1.005	0.010	1.020	0.022	1.003	0.010	0.996	0.014	0.974	0.019
F55	2015-06-19	77.81	0.18	2.40	0.02	0.932	0.009	18.85	0.19	21.25	0.19	0.995	0.020	1.006	0.011	1.008	0.010	1.008	0.010					1.025	0.014	1.015	0.020
F56	2015-07-03	77.58	0.18	3.01	0.03	0.928	0.009	18.48	0.19	21.49	0.19	1.003	0.020	1.005	0.009	1.014	0.010	1.013	0.010	1.005	0.021	1.008	0.010	1.010	0.014	1.037	0.017
F57	2015-07-23	77.57	0.18	2.45	0.02	0.922	0.009	19.05	0.19	21.50	0.19	1.017	0.021	1.015	0.010	1.003	0.010	1.003	0.010	1.032	0.023	1.025	0.011	1.009	0.016	1.007	0.019
F58	2015-08-03	77.50	0.27	2.02	0.02	0.928	0.009	19.46	0.20	21.48	0.20	1.026	0.021	1.022	0.010	1.002	0.010	1.001	0.010					1.027	0.015	0.987	0.017
F59	2015-08-14	77.90	0.18	2.07	0.02	0.934	0.009	19.09	0.19	21.16	0.19																
F60	2015-08-24	77.77	0.19	2.00	0.02	0.933	0.009	19.30	0.20	21.30	0.20	1.009	0.022	1.003	0.010	1.007	0.011	1.007	0.011	0.996	0.017	0.999	0.010	1.035	0.019	1.028	0.021
F61	2015-09-08	77.59	0.19	1.64	0.02	0.928	0.009	19.84	0.20	21.48	0.20	0.979	0.026	1.006	0.010	0.998	0.010	0.999	0.010	0.983	0.017	0.995	0.010	0.978	0.014	0.999	0.017
F62	2015-10-01	77.71	0.18	1.44	0.01	0.930	0.009	19.91	0.20	21.35	0.20	0.989	0.026	1.007	0.010	1.000	0.010	1.000	0.010	0.997	0.017	1.000	0.010	1.001	0.014	1.014	0.018

Table B.2: Mannheim: Soil air composition at 3.0 m depth.

3.0 m depth		Measurements by *Omnistar*										Measurements by *MM5400* mass spectrometer															
		N_2	ΔN_2	CO_2	ΔCO_2	^{40}Ar	$\Delta^{40}Ar$	O_2	ΔO_2	O_2+CO_2	ΔO_2+CO_2	^{3}He	$\Delta^{3}He$	^{4}He	$\Delta^{4}He$	^{20}Ne	$\Delta^{20}Ne$	^{22}Ne	$\Delta^{22}Ne$	^{36}Ar	$\Delta^{36}Ar$	^{40}Ar	$\Delta^{40}Ar$	^{84}Kr	$\Delta^{84}Kr$	^{132}Xe	$\Delta^{132}Xe$
		all data is given in units of vol%										partial pressures are normalized to their values in dry atmospheric air, respectively															
F1	2013-06-18																										
F2	2013-06-27													1.014	0.012	1.014	0.010	1.015	0.010	1.025	0.013	1.028	0.011	1.016	0.011	1.018	0.017
F3	2013-07-16																										
F4	2013-07-29											0.968	0.036	1.005	0.011	1.001	0.009	1.003	0.009	1.013	0.014	1.009	0.009	1.010	0.012	1.000	0.020
F5	2013-08-14																										
F6	2013-08-27											0.996	0.037	1.033	0.013	1.003	0.009	1.004	0.009	0.983	0.014	1.008	0.009	1.006	0.012	1.008	0.020
F7	2013-09-10																										
F8	2013-09-24											1.127	0.042	1.029	0.011	1.013	0.009	1.016	0.010	1.024	0.015	1.009	0.009	1.008	0.012	1.015	0.020
F9	2013-10-08																										
F10	2013-10-22											1.025	0.038	1.034	0.011	1.015	0.010	1.014	0.010	0.998	0.014	1.011	0.009	1.012	0.012	1.024	0.021
F11	2013-11-05																										
F12	2013-11-19											0.999	0.100	1.003	0.010	1.005	0.009	1.004	0.009	1.009	0.011	1.001	0.009	0.998	0.011	0.983	0.017
F13	2013-12-03																										
F14	2013-12-17																										
F15	2013-12-30																										
F16	2014-01-13																										
F17	2014-01-28																										
F18	2014-02-11																										
F19	2014-02-25																										
F20	2014-03-10																										
F21	2014-03-26																										
F22	2014-04-07																										
F23	2014-04-23																										
F24	2014-05-08																										
F25	2014-05-20																										
F26	2014-06-03																										
F27	2014-06-16																										
F28	2014-07-03																										
F29	2014-07-15																										
F30	2014-07-23																										
F31	2014-08-05																										
F32	2014-08-19																										
F33	2014-09-03																										
F34	2014-09-15																										
F35	2014-09-29																										
F36	2014-10-06																										
F37	2014-10-16																										
F38	2014-10-28																										
F39	2014-11-13	77.86	0.18	3.05	0.03	0.926	0.011	18.17	0.18	21.22	0.18																
F40	2014-11-25	78.16	0.18	2.56	0.03	0.940	0.009	18.34	0.18	20.90	0.19																
F41	2014-12-09	78.08	0.18	2.30	0.02	0.942	0.009	18.68	0.19	20.98	0.19																
F42	2014-12-18	78.34	0.19	2.74	0.03	0.938	0.010	17.98	0.18	20.72	0.19																
F43	2015-01-06	78.44	0.18	2.64	0.03	0.939	0.009	17.98	0.18	20.63	0.18																
F44	2015-01-22	78.42	0.18	2.58	0.03	0.938	0.009	18.06	0.18	20.64	0.18																
F45	2015-02-03	78.48	0.18	2.57	0.03	0.939	0.009	18.01	0.18	20.58	0.18																
F46	2015-02-19	78.47	0.18	2.52	0.03	0.938	0.009	18.07	0.18	20.60	0.18																
F47	2015-03-03	78.32	0.18	2.34	0.02	0.941	0.009	18.40	0.19	20.74	0.19																
F48	2015-03-18	78.37	0.18	2.48	0.03	0.937	0.009	18.21	0.18	20.69	0.18																
F49	2015-03-31	78.15	0.18	2.03	0.02	0.935	0.009	18.88	0.19	20.92	0.19																
F50	2015-04-09	78.01	0.18	2.38	0.02	0.935	0.009	18.67	0.19	21.05	0.19																
F51	2015-04-24	78.12	0.18	2.22	0.02	0.933	0.009	18.73	0.19	20.95	0.19																
F52	2015-05-08	78.18	0.18	2.75	0.03	0.936	0.009	18.14	0.18	20.89	0.18																
F53	2015-05-22	77.85	0.18	2.74	0.03	0.932	0.009	18.48	0.19	21.21	0.19																
F54	2015-06-08	77.69	0.19	3.42	0.04	0.930	0.009	17.96	0.18	21.38	0.19																
F55	2015-06-19	77.62	0.18	3.08	0.03	0.927	0.009	18.38	0.18	21.45	0.19																
F56	2015-07-03	77.79	0.18	3.01	0.03	0.932	0.009	18.28	0.18	21.28	0.19																
F57	2015-07-23	77.46	0.18	3.31	0.03	0.926	0.009	18.30	0.18	21.61	0.19																
F58	2015-08-03	77.25	0.27	3.35	0.03	0.925	0.009	18.38	0.19	21.74	0.19																
F59	2015-08-14	77.46	0.18	3.28	0.03	0.929	0.009	18.33	0.18	21.61	0.19																
F60	2015-08-24	77.47	0.19	3.26	0.03	0.929	0.009	18.34	0.19	21.60	0.19																
F61	2015-09-08	77.32	0.18	3.02	0.03	0.928	0.009	18.73	0.19	21.75	0.19																
F62	2015-10-01	77.60	0.18	2.71	0.03	0.926	0.009	18.76	0.19	21.47	0.19																

Table B.3: Mannheim: Soil air composition at 4.4 m depth.

4.4 m depth		Measurements by *Omnistar*										Measurements by *MM5400* mass spectrometer															
		N_2	ΔN_2	CO_2	ΔCO_2	^{40}Ar	$\Delta^{40}Ar$	O_2	ΔO_2	O_2+CO_2	ΔO_2+CO_2	^{3}He	$\Delta^{3}He$	^{4}He	$\Delta^{4}He$	^{20}Ne	$\Delta^{20}Ne$	^{22}Ne	$\Delta^{22}Ne$	^{36}Ar	$\Delta^{36}Ar$	^{40}Ar	$\Delta^{40}Ar$	^{84}Kr	$\Delta^{84}Kr$	^{132}Xe	$\Delta^{132}Xe$
		all data is given in units of vol%										partial pressures are normalized to their values in dry atmospheric air, respectively															
F1	2013-06-18																										
F2	2013-06-27																										
F3	2013-07-16																										
F4	2013-07-29																										
F5	2013-08-14																										
F6	2013-08-27																										
F7	2013-09-10																										
F8	2013-09-24																										
F9	2013-10-08																										
F10	2013-10-22																										
F11	2013-11-05																										
F12	2013-11-19																										
F13	2013-12-03																										
F14	2013-12-17																										
F15	2013-12-30																										
F16	2014-01-13																										
F17	2014-01-28																										
F18	2014-02-11																										
F19	2014-02-25																										
F20	2014-03-10																										
F21	2014-03-26																										
F22	2014-04-07																										
F23	2014-04-23																										
F24	2014-05-08																										
F25	2014-05-20																										
F26	2014-06-03																										
F27	2014-06-16																										
F28	2014-07-03																										
F29	2014-07-15																										
F30	2014-07-23																										
F31	2014-08-05																										
F32	2014-08-19																										
F33	2014-09-03																										
F34	2014-09-15																										
F35	2014-09-29																										
F36	2014-10-06																										
F37	2014-10-16																										
F38	2014-10-28																										
F39	2014-11-13	77.86	0.18	3.64	0.04	0.928	0.011	17.57	0.18	21.21	0.18																
F40	2014-11-25	78.32	0.18	3.53	0.04	0.939	0.009	17.22	0.17	20.74	0.18																
F41	2014-12-09	78.34	0.18	3.38	0.04	0.946	0.009	17.34	0.17	20.72	0.18																
F42	2014-12-18	78.42	0.19	3.28	0.04	0.939	0.010	17.37	0.18	20.65	0.18																
F43	2015-01-06	78.48	0.18	3.08	0.03	0.939	0.009	17.50	0.18	20.58	0.18																
F44	2015-01-22	78.50	0.18	2.91	0.03	0.939	0.009	17.65	0.18	20.56	0.18																
F45	2015-02-03	78.63	0.18	2.90	0.03	0.939	0.009	17.53	0.18	20.43	0.18																
F46	2015-02-19	78.58	0.18	2.83	0.03	0.938	0.009	17.65	0.18	20.48	0.18																
F47	2015-03-03	78.58	0.18	2.79	0.03	0.942	0.009	17.69	0.18	20.48	0.18																
F48	2015-03-18	78.51	0.19	2.72	0.03	0.937	0.009	17.83	0.18	20.55	0.18																
F49	2015-03-31	78.37	0.18	2.79	0.03	0.938	0.009	17.90	0.18	20.69	0.18																
F50	2015-04-09	78.07	0.18	2.73	0.03	0.930	0.009	18.27	0.18	20.99	0.19																
F51	2015-04-24	78.35	0.18	2.99	0.03	0.938	0.009	17.72	0.18	20.71	0.18																
F52	2015-05-08	78.32	0.18	3.15	0.03	0.939	0.009	17.59	0.18	20.74	0.18																
F53	2015-05-22	78.31	0.19	2.93	0.03	0.937	0.009	17.82	0.18	20.75	0.18																
F54	2015-06-08	77.86	0.19	3.73	0.04	0.930	0.009	17.48	0.18	21.21	0.18																
F55	2015-06-19	77.86	0.18	3.72	0.04	0.932	0.009	17.49	0.18	21.21	0.18																
F56	2015-07-03	77.91	0.18	3.77	0.04	0.932	0.009	17.39	0.18	21.15	0.18																
F57	2015-07-23	77.52	0.18	3.98	0.04	0.927	0.009	17.57	0.18	21.55	0.18																
F58	2015-08-03	77.28	0.27	3.80	0.04	0.924	0.009	17.91	0.18	21.71	0.19																
F59	2015-08-14	77.45	0.18	3.82	0.04	0.928	0.009	17.80	0.18	21.62	0.18																
F60	2015-08-24	77.45	0.19	3.82	0.04	0.931	0.009	17.80	0.18	21.62	0.19																
F61	2015-09-08	77.38	0.19	3.64	0.04	0.928	0.009	18.05	0.18	21.69	0.19																
F62	2015-10-01	77.58	0.18	3.32	0.03	0.928	0.009	18.17	0.18	21.49	0.19																

Table B.4: Mannheim: Soil air composition at 5.5 m depth.

5.5 m depth		Measurements by *Omnistar*										Measurements by *MM5400* mass spectrometer															
		N_2	ΔN_2	CO_2	ΔCO_2	^{40}Ar	$\Delta^{40}Ar$	O_2	ΔO_2	$O_2 + CO_2$	$\Delta O_2 + CO_2$	^{3}He	$\Delta^{3}He$	^{4}He	$\Delta^{4}He$	^{20}Ne	$\Delta^{20}Ne$	^{22}Ne	$\Delta^{22}Ne$	^{36}Ar	$\Delta^{36}Ar$	^{40}Ar	$\Delta^{40}Ar$	^{84}Kr	$\Delta^{84}Kr$	^{132}Xe	$\Delta^{132}Xe$
		all data is given in units of vol%										partial pressures are normalized to their values in dry atmospheric air, respectively															
F1	2013-06-18													1.026	0.012	1.027	0.010	1.027	0.010	1.030	0.013	1.033	0.011	1.030	0.011	1.022	0.017
F2	2013-06-27	79.94	0.19	2.83	0.05	0.957	0.011	16.27	0.17	19.11	0.18			1.022	0.012	1.024	0.010	1.025	0.010	1.038	0.013	1.037	0.011	1.038	0.012	1.039	0.017
F3	2013-07-16	79.97	0.20	3.42	0.04	0.958	0.011	15.65	0.16	19.07	0.16	1.043	0.040	1.018	0.011	1.026	0.010	1.026	0.010	1.041	0.014	1.033	0.009	1.038	0.012	1.049	0.021
F4	2013-07-29	79.38	0.19	3.90	0.04	0.955	0.011	15.76	0.16	19.67	0.17	0.980	0.053	1.012	0.011	1.012	0.009	1.012	0.010	1.025	0.015	1.024	0.009	1.022	0.012	1.018	0.021
F5	2013-08-14											1.046	0.040	1.015	0.011	1.010	0.009	1.011	0.010	1.025	0.015	1.024	0.009	1.028	0.012	1.041	0.022
F6	2013-08-27	78.39	0.19	3.95	0.04	0.940	0.010	16.73	0.18	20.67	0.18	1.128	0.042	1.010	0.011	1.004	0.009	1.005	0.009	1.015	0.014	1.011	0.009	1.013	0.012	1.002	0.021
F7	2013-09-10	77.96	0.19	3.90	0.04	0.935	0.010	17.21	0.18	21.10	0.19	0.986	0.036	1.011	0.011	1.002	0.009	1.003	0.009	1.002	0.014	1.005	0.009	1.015	0.011	1.009	0.020
F8	2013-09-24	78.14	0.19	3.63	0.05	0.937	0.011	17.29	0.18	20.92	0.19	0.989	0.017	1.004	0.011	1.001	0.010	1.001	0.010	0.995	0.019	1.005	0.009	1.005	0.015	1.032	0.017
F9	2013-10-08	78.31	0.19	3.54	0.05	0.937	0.011	17.21	0.18	20.75	0.19	0.931	0.093	0.985	0.010	0.991	0.009	0.992	0.009	1.003	0.010	1.000	0.009	0.979	0.011	0.981	0.017
F10	2013-10-22	78.57	0.19	3.41	0.05	0.948	0.011	17.07	0.18	20.48	0.18	1.019	0.017	1.007	0.011	1.009	0.010	1.009	0.010	1.013	0.019	1.012	0.009	1.016	0.015	1.018	0.018
F11	2013-11-05	78.55	0.19	3.41	0.05	0.941	0.011	17.10	0.18	20.51	0.18	1.000	0.037	1.041	0.011	1.005	0.009	1.007	0.009	1.003	0.014	1.005	0.009	1.008	0.011	1.002	0.021
F12	2013-11-19	78.57	0.19	3.32	0.04	0.941	0.010	17.17	0.18	20.49	0.19	1.120	0.042	0.978	0.012	1.002	0.009	1.001	0.009	1.004	0.022	1.004	0.009	0.999	0.011	1.021	0.017
F13	2013-12-03	78.68	0.19	3.15	0.04	0.942	0.010	17.23	0.18	20.37	0.18	1.024	0.020	1.019	0.010	1.006	0.009	1.006	0.009	1.007	0.013	1.011	0.009	1.010	0.013	1.021	0.017
F14	2013-12-17	78.57	0.21	2.98	0.04	0.942	0.012	17.51	0.19	20.49	0.20	1.012	0.020	1.012	0.009	1.016	0.010	1.017	0.010	0.986	0.019	1.002	0.010	1.015	0.013	1.035	0.017
F15	2013-12-30	78.58	0.19	2.86	0.04	0.942	0.010	17.62	0.18	20.48	0.18	1.010	0.020	1.021	0.010	1.014	0.010	1.014	0.010	0.998	0.019	1.007	0.010	1.029	0.014	0.995	0.021
F16	2014-01-13	78.65	0.19	2.77	0.03	0.940	0.010	17.64	0.19	20.41	0.19	1.687	0.067	1.015	0.013	1.005	0.009	1.005	0.009	1.010	0.022	1.004	0.009	1.006	0.011	0.998	0.017
F17	2014-01-28	78.71	0.19	2.72	0.04	0.943	0.010	17.63	0.18	20.35	0.18																
F18	2014-02-11	78.76	0.19	2.64	0.03	0.945	0.010	17.66	0.18	20.29	0.18	0.910	0.038	1.015	0.013	1.009	0.009	1.011	0.009	0.995	0.022	1.000	0.009	0.996	0.011	1.006	0.017
F19	2014-02-25	78.69	0.19	2.62	0.04	0.943	0.010	17.75	0.18	20.36	0.19																
F20	2014-03-10	78.77	0.19	2.61	0.03	0.942	0.010	17.68	0.19	20.29	0.19	1.034	0.037	1.005	0.013	1.012	0.010	1.010	0.010	1.012	0.025	1.012	0.009	1.009	0.012	1.018	0.017
F21	2014-03-26	78.65	0.19	2.62	0.04	0.945	0.010	17.78	0.18	20.40	0.19																
F22	2014-04-07	78.69	0.19	2.69	0.03	0.941	0.010	17.68	0.19	20.37	0.19	1.004	0.033	0.991	0.012	1.001	0.009	1.000	0.009	0.980	0.025	1.006	0.009	1.015	0.011	1.017	0.017
F23	2014-04-23	78.72	0.19	2.76	0.04	0.946	0.010	17.57	0.18	20.33	0.18																
F24	2014-05-08	79.26	0.19	2.79	0.05	0.949	0.011	17.01	0.18	19.79	0.18	0.965	0.033	0.993	0.012	1.012	0.010	1.009	0.010	1.011	0.024	1.015	0.009	1.022	0.011	1.012	0.017
F25	2014-05-20	78.66	0.19	3.12	0.05	0.944	0.011	17.28	0.18	20.40	0.19	0.998	0.017	0.993	0.011	1.000	0.010	1.000	0.010	1.000	0.021	1.008	0.009	1.016	0.014	1.030	0.017
F26	2014-06-03									–	–	0.967	0.036	0.984	0.012	0.996	0.009	0.997	0.009	1.021	0.024	1.006	0.009	1.015	0.011	1.012	0.017
F27	2014-06-16	78.53	0.19	3.50	0.07	0.943	0.010	17.04	0.19	20.53	0.21																
F28	2014-06-25	78.00	0.20	3.92	0.05	0.939	0.012	17.13	0.19	21.06	0.20																
F29	2014-07-03	78.44	0.20	3.45	0.05	0.944	0.012	17.16	0.19	20.62	0.19	0.999	0.017	0.989	0.011	0.998	0.010	0.999	0.010	1.009	0.020	1.009	0.009	1.024	0.015	1.043	0.017
F30	2014-07-15	78.97	0.19	3.38	0.05	0.949	0.010	16.70	0.17	20.08	0.18																
F31	2014-07-23	78.69	0.19	3.48	0.04	0.942	0.010	16.89	0.17	20.37	0.18	0.993	0.018	0.988	0.010	1.001	0.010	1.003	0.010	0.988	0.013	1.006	0.009	1.021	0.014	1.044	0.018
F32	2014-08-05	79.53	0.20	3.31	0.04	0.963	0.017	16.20	0.17	19.50	0.17	1.021	0.020	1.019	0.010	1.021	0.010	1.022	0.010	1.019	0.021	1.033	0.010	1.048	0.014	1.058	0.019
F33	2014-08-19	79.69	0.20	3.70	0.04	0.958	0.011	15.66	0.16	19.36	0.16	1.013	0.020	1.031	0.010	1.016	0.010	1.016	0.010	1.025	0.021	1.034	0.010	1.047	0.014	1.057	0.022
F34	2014-09-03	78.62	0.19	3.91	0.07	0.944	0.010	16.53	0.19	20.44	0.20	0.992	0.019	1.012	0.009	1.012	0.010	1.014	0.010	1.007	0.021	1.016	0.010	1.028	0.014	1.024	0.018
F35	2014-09-15	78.95	0.19	4.01	0.06	0.947	0.011	16.09	0.17	20.10	0.18	1.006	0.020	1.018	0.010	1.019	0.010	1.019	0.010	0.994	0.023	1.018	0.010	1.046	0.015	1.026	0.017
F36	2014-09-29	78.93	0.20	3.77	0.05	0.955	0.017	16.35	0.17	20.12	0.18	1.017	0.019	1.015	0.010	1.017	0.011	1.018	0.011	1.013	0.019	1.018	0.010	1.039	0.016	1.059	0.020
F37	2014-10-16	78.40	0.19	3.89	0.04	0.940	0.010	16.78	0.18	20.67	0.18	1.009	0.020	1.013	0.010	1.009	0.010	1.010	0.010	1.015	0.020	1.019	0.010	1.021	0.014	1.019	0.017
F38	2014-10-28	77.94	0.19	3.93	0.05	0.943	0.017	17.18	0.18	21.12	0.18																
F39	2014-11-13	77.83	0.18	3.69	0.04	0.930	0.011	17.55	0.18	21.24	0.18	1.002	0.020	1.008	0.009	1.005	0.010	1.005	0.010	1.004	0.020	1.014	0.010	1.007	0.014	1.039	0.019
F40	2014-11-25	78.08	0.18	3.55	0.04	0.939	0.009	17.44	0.17	20.98	0.18																
F41	2014-12-09	78.26	0.18	3.33	0.04	0.944	0.009	17.46	0.18	20.80	0.18	1.032	0.016	1.023	0.010	1.004	0.009	1.004	0.009	1.018	0.020	1.003	0.009	1.020	0.014	0.991	0.024
F42	2014-12-18																										
F43	2015-01-06	78.41	0.18	3.05	0.03	0.939	0.009	17.61	0.18	20.65	0.18	0.997	0.015	1.006	0.010	0.999	0.009	0.999	0.009	0.998	0.017	1.002	0.009	0.996	0.015	0.996	0.023
F44	2015-01-22	78.42	0.18	2.91	0.03	0.937	0.009	17.73	0.18	20.64	0.18																
F45	2015-02-03	78.56	0.18	2.85	0.03	0.936	0.009	17.65	0.18	20.50	0.18	1.014	0.020	1.021	0.010	1.002	0.010	1.002	0.010	1.010	0.019	1.006	0.010	0.997	0.014	1.018	0.017
F46	2015-02-19	78.60	0.18	2.81	0.03	0.940	0.009	17.66	0.18	20.46	0.18																
F47	2015-03-03	78.56	0.18	2.64	0.03	0.941	0.009	17.86	0.18	20.50	0.18	1.017	0.020	1.019	0.010	1.008	0.010	1.007	0.010	1.012	0.021	1.011	0.010	1.004	0.014	1.015	0.018
F48	2015-03-18	78.49	0.19	2.63	0.03	0.938	0.009	17.94	0.18	20.57	0.18																
F49	2015-03-31	78.48	0.18	2.36	0.02	0.943	0.009	18.23	0.18	20.58	0.18	1.057	0.022	1.021	0.010	1.020	0.010	1.020	0.010	1.002	0.021	1.011	0.010	1.028	0.014	1.025	0.017
F50	2015-04-09	78.14	0.18	2.67	0.03	0.938	0.009	18.25	0.18	20.92	0.19	1.009	0.020	1.019	0.010	1.005	0.010	1.005	0.010	0.999	0.021	1.007	0.010	1.011	0.013	1.021	0.017
F51	2015-04-24	78.27	0.18	2.73	0.03	0.935	0.009	18.07	0.18	20.79	0.18	1.024	0.020	1.015	0.010	1.016	0.010	1.017	0.010	0.981	0.021	1.010	0.010	1.023	0.014	1.021	0.017
F52	2015-05-08	78.31	0.18	2.70	0.03	0.938	0.009	18.05	0.18	20.75	0.18	0.995	0.020	1.010	0.009	1.008	0.010	1.008	0.010	0.980	0.022	1.005	0.010	1.019	0.014	1.023	0.019
F53	2015-05-22	78.28	0.19	2.70	0.03	0.938	0.009	18.08	0.18	20.78	0.18	0.994	0.018	0.997	0.009	1.002	0.011	1.004	0.011	0.991	0.019	1.008	0.010	1.014	0.016	1.023	0.018
F54	2015-06-08	78.05	0.19	3.30	0.03	0.937	0.009	17.71	0.18	21.01	0.18	0.993	0.023	1.002	0.009	1.005	0.010	1.006	0.010	1.016	0.019	1.009	0.010	1.020	0.014	1.008	0.020
F55	2015-06-19	77.95	0.18	3.44	0.03	0.938	0.009	17.67	0.18	21.11	0.18	1.011	0.020	1.004	0.009	1.007	0.010	1.007	0.010	1.024	0.021	1.006	0.010	1.027	0.014	1.016	0.017
F56	2015-07-03	77.91	0.18	3.44	0.03	0.933	0.009	17.72	0.18	21.16	0.18	0.995	0.020	1.012	0.009	1.000	0.010	1.000	0.010	1.008	0.022	1.021	0.010	1.023	0.013	1.006	0.019
F57	2015-07-23	77.61	0.18	3.84	0.04	0.927	0.009	17.62	0.18	21.46	0.18	1.010	0.019	1.002	0.010	1.004	0.011	1.005	0.011	1.012	0.018	1.018	0.010	1.022	0.016	1.034	0.018
F58	2015-08-03	77.39	0.27	3.77	0.04	0.927	0.009	17.83	0.18	21.60	0.18	0.995	0.026	0.987	0.009	0.994	0.009	0.995	0.009	1.007	0.018	0.995	0.010	0.998	0.014	1.019	0.019
F59	2015-08-14	77.41	0.18	3.71	0.04	0.926	0.009	17.95	0.18	21.66	0.18	0.978	0.017	0.996	0.010	1.000	0.009	1.001	0.009	1.005	0.012	0.994	0.010	1.006	0.016	0.995	0.021
F60	2015-08-24	77.47	0.19	3.67	0.04	0.927	0.009	17.94	0.18	21.60	0.19	0.989	0.016	1.005	0.010	1.007	0.009	1.008	0.009	1.009	0.011	1.004	0.010	1.013	0.015	0.997	0.023
F61	2015-09-08	77.41	0.19	3.61	0.04	0.931	0.009	18.05	0.18	21.66	0.19	0.977	0.017	0.996	0.010	0.996	0.010	0.997	0.010	1.002	0.014	0.998	0.010	0.980	0.017	1.018	0.019
F62	2015-10-01	77.52	0.18	3.44	0.03	0.928	0.009	18.12	0.18	21.55	0.19	0.995	0.017	1.000	0.010	0.997	0.010	0.998	0.010	0.996	0.014	0.997	0.010	1.003	0.016	1.000	0.019

Table B.5: Mannheim: Soil air composition at 6.5 m depth.

6.5 m depth		Measurements by *Omnistar*										Measurements by *MM5400* mass spectrometer															
		N_2	ΔN_2	CO_2	ΔCO_2	^{40}Ar	$\Delta^{40}Ar$	O_2	ΔO_2	O_2+CO_2	ΔO_2+CO_2	^{3}He	$\Delta^{3}He$	^{4}He	$\Delta^{4}He$	^{20}Ne	$\Delta^{20}Ne$	^{22}Ne	$\Delta^{22}Ne$	^{36}Ar	$\Delta^{36}Ar$	^{40}Ar	$\Delta^{40}Ar$	^{84}Kr	$\Delta^{84}Kr$	^{132}Xe	$\Delta^{132}Xe$
		all data is given in units of vol%										partial pressures are normalized to their values in dry atmospheric air, respectively															
F1	2013-06-18																										
F2	2013-06-27																										
F3	2013-07-16																										
F4	2013-07-29																										
F5	2013-08-14																										
F6	2013-08-27																										
F7	2013-09-10																										
F8	2013-09-24																										
F9	2013-10-08																										
F10	2013-10-22																										
F11	2013-11-05																										
F12	2013-11-19																										
F13	2013-12-03																										
F14	2013-12-17																										
F15	2013-12-30																										
F16	2014-01-13																										
F17	2014-01-28																										
F18	2014-02-11																										
F19	2014-02-25																										
F20	2014-03-10																										
F21	2014-03-26																										
F22	2014-04-07																										
F23	2014-04-23																										
F24	2014-05-08																										
F25	2014-05-20																										
F26	2014-06-03											1.007	0.033			1.001	0.009	1.002	0.009	1.012	0.024	1.007	0.009	1.007	0.011	1.011	0.017
F27	2014-06-16											1.056	0.043			1.003	0.009	1.003	0.009	1.008	0.024	1.009	0.009	1.009	0.011	1.021	0.017
F28	2014-07-03																										
F29	2014-07-15											1.178	0.049			1.000	0.009	1.001	0.009	1.004	0.024	1.006	0.009	1.002	0.011	0.990	0.017
F30	2014-07-23																										
F31	2014-08-05											1.027	0.039	0.994	0.012	1.009	0.010	1.007	0.010	1.017	0.026	1.012	0.009	1.018	0.011	1.034	0.017
F32	2014-08-19																										
F33	2014-09-03											0.998	0.035	0.987	0.012	1.005	0.009	1.005	0.009	1.011	0.025	1.009	0.009	1.011	0.011	1.002	0.017
F34	2014-09-15																										
F35	2014-09-29											1.101	0.048	0.979	0.012	0.993	0.009	0.993	0.009	1.009	0.025	0.999	0.009	1.005	0.012	0.983	0.017
F36	2014-10-06																										
F37	2014-10-16																										
F38	2014-10-28																										
F39	2014-11-13	77.79	0.18	3.81	0.04	0.927	0.011	17.48	0.18	21.28	0.18	1.019	0.016	1.016	0.010	1.012	0.009	1.010	0.009	1.020	0.019	1.011	0.009	1.010	0.014		
F40	2014-11-25																										
F41	2014-12-09	78.18	0.18	3.49	0.04	0.943	0.009	17.39	0.17	20.88	0.18	0.997	0.015	1.007	0.010	1.001	0.009	1.001	0.009	1.012	0.018	1.007	0.009	1.003	0.013		
F42	2014-12-18	78.30	0.19	3.36	0.04	0.944	0.010	17.40	0.18	20.76	0.18																
F43	2015-01-06	78.34	0.18	3.16	0.03	0.937	0.009	17.56	0.18	20.72	0.18																
F44	2015-01-22																										
F45	2015-02-03																										
F46	2015-02-19																										
F47	2015-03-03																										
F48	2015-03-18																										
F49	2015-03-31																										
F50	2015-04-09																										
F51	2015-04-24																										
F52	2015-05-08																										
F53	2015-05-22																										
F54	2015-06-08																										
F55	2015-06-19																										
F56	2015-07-03	77.94	0.18	3.91	0.04	0.935	0.009	17.21	0.17	21.12	0.18																
F57	2015-07-23	77.49	0.18	4.14	0.04	0.924	0.009	17.45	0.17	21.59	0.18																
F58	2015-08-03																										
F59	2015-08-14	77.23	0.18	4.56	0.05	0.925	0.009	17.28	0.17	21.85	0.18																
F60	2015-08-24	77.24	0.19	4.52	0.05	0.925	0.009	17.32	0.18	21.84	0.18																
F61	2015-09-08	77.18	0.18	4.53	0.05	0.926	0.009	17.35	0.18	21.88	0.18																
F62	2015-10-01	77.18	0.18	4.15	0.04	0.923	0.009	17.75	0.18	21.89	0.18																

B.8 Mannheim: NG concentrations in groundwater

Table B.6: Mannheim (shallow well): NG concentrations in groundwater. All data are given in units of ccSTP per g of water.

ID	sampl. date	He [ccSTP/g]	ΔHe [ccSTP/g]	Ne [ccSTP/g]	ΔNe [ccSTP/g]	Ar [ccSTP/g]	ΔAr [ccSTP/g]	Kr [ccSTP/g]	ΔKr [ccSTP/g]	Xe [ccSTP/g]	ΔXe [ccSTP/g]
F1	2013-06-18	5.144E-08	4.850E-10	2.182E-07	1.527E-09	3.957E-04	2.770E-06	9.422E-08	9.422E-10	1.306E-08	2.220E-10
F2	2013-06-27	5.099E-08	3.570E-10	2.172E-07	1.521E-09	3.996E-04	2.797E-06	9.350E-08	9.350E-10	1.338E-08	2.275E-10
F3	2013-07-16	4.992E-08	4.725E-10	2.144E-07	1.501E-09	3.994E-04	2.796E-06	9.359E-08	9.359E-10	1.262E-08	2.145E-10
F4	2013-07-29	4.938E-08	4.069E-10	2.099E-07	1.469E-09	3.910E-04	2.737E-06	9.252E-08	9.557E-10	1.292E-08	2.277E-10
F5	2013-08-14	4.990E-08	3.493E-10	2.129E-07	1.490E-09	3.900E-04	2.730E-06	9.255E-08	9.255E-10	1.336E-08	2.272E-10
F6	2013-08-27	4.895E-08	3.427E-10	2.083E-07	1.458E-09	3.832E-04	2.682E-06	9.047E-08	9.047E-10	1.320E-08	2.516E-10
F7	2013-09-10	4.849E-08	3.394E-10	2.082E-07	1.457E-09	3.820E-04	2.674E-06	8.915E-08	8.915E-10	1.278E-08	2.173E-10
F8	2013-09-24	4.805E-08	4.461E-10	2.070E-07	1.449E-09	3.786E-04	2.650E-06	9.042E-08	9.042E-10	1.281E-08	2.178E-10
F9	2013-10-08	4.850E-08	3.395E-10	2.062E-07	1.443E-09	3.788E-04	2.652E-06	8.942E-08	8.942E-10	1.244E-08	2.205E-10
F10	2013-10-22	4.931E-08	3.452E-10	2.037E-07	1.426E-09	3.753E-04	2.627E-06	8.764E-08	8.849E-10	1.273E-08	2.377E-10
F11	2013-11-05	4.731E-08	3.311E-10	1.998E-07	1.399E-09	3.719E-04	2.603E-06	8.891E-08	8.985E-10	1.283E-08	2.193E-10
F12	2013-11-19	4.727E-08	3.902E-10	2.022E-07	1.415E-09	3.742E-04	2.619E-06	8.855E-08	9.135E-10	1.264E-08	2.149E-10
F13	2013-12-03	4.880E-08	3.416E-10	2.047E-07	1.433E-09	3.802E-04	2.661E-06	8.947E-08	8.947E-10	1.286E-08	2.186E-10
F14	2013-12-17	4.853E-08	3.397E-10	2.024E-07	1.416E-09	3.810E-04	2.667E-06	8.960E-08	8.960E-10	1.303E-08	2.367E-10
F15	2013-12-30	4.750E-08	3.325E-10	2.026E-07	1.418E-09	3.782E-04	2.647E-06	8.814E-08	8.814E-10	1.277E-08	2.171E-10
F16	2014-01-13	4.766E-08	3.336E-10	2.031E-07	1.422E-09	3.772E-04	2.640E-06	8.827E-08	8.827E-10	1.289E-08	2.214E-10
F17	2014-01-28	4.768E-08	3.337E-10	2.005E-07	1.404E-09	3.739E-04	2.617E-06	8.925E-08	8.925E-10	1.281E-08	2.178E-10
F18	2014-02-11	4.671E-08	3.270E-10	1.984E-07	1.389E-09	3.749E-04	2.624E-06	8.850E-08	9.489E-10	1.264E-08	2.353E-10
F19	2014-02-25	4.745E-08	3.322E-10	2.026E-07	1.419E-09	3.802E-04	2.661E-06	9.077E-08	9.077E-10	1.290E-08	2.192E-10
F20	2014-03-10	4.783E-08	3.348E-10	2.034E-07	1.423E-09	3.821E-04	2.675E-06	9.082E-08	9.572E-10	1.299E-08	2.311E-10
F21	2014-03-26	4.780E-08	3.346E-10	2.027E-07	1.419E-09	3.835E-04	2.684E-06	9.043E-08	9.043E-10	1.295E-08	2.202E-10
F22	2014-04-07	4.671E-08	3.270E-10	1.978E-07	1.384E-09	3.716E-04	2.601E-06	8.883E-08	8.883E-10	1.250E-08	2.476E-10
F23	2014-04-23	4.711E-08	3.298E-10	2.019E-07	1.413E-09	3.809E-04	2.666E-06	8.947E-08	8.947E-10	1.312E-08	2.505E-10
F24	2014-05-08	4.709E-08	3.297E-10	2.007E-07	1.405E-09	3.823E-04	2.676E-06	8.983E-08	9.148E-10	1.314E-08	2.311E-10
F25	2014-05-20	4.730E-08	3.311E-10	2.041E-07	1.429E-09	3.829E-04	2.681E-06	8.923E-08	8.923E-10	1.285E-08	2.185E-10
F26	2014-06-03	4.737E-08	3.316E-10	2.021E-07	1.415E-09	3.813E-04	2.669E-06	8.886E-08	8.886E-10	1.312E-08	2.230E-10
F27	2014-06-16	4.799E-08	3.359E-10	2.026E-07	1.419E-09	3.828E-04	2.680E-06	9.004E-08	9.004E-10	1.331E-08	2.263E-10
F29	2014-07-03	4.703E-08	3.292E-10	1.987E-07	1.391E-09	3.782E-04	2.647E-06	8.965E-08	8.965E-10	1.326E-08	2.271E-10
F30	2014-07-15	4.643E-08	3.250E-10	1.980E-07	1.386E-09	3.763E-04	2.634E-06	9.056E-08	9.796E-10	1.280E-08	2.180E-10
F31	2014-07-23	4.563E-08	3.194E-10	1.966E-07	1.376E-09	3.761E-04	2.632E-06	8.936E-08	9.130E-10	1.290E-08	2.390E-10
F32	2014-08-05	4.546E-08	3.182E-10	1.947E-07	1.363E-09	3.737E-04	2.616E-06	8.819E-08	8.819E-10	1.279E-08	2.176E-10
F33	2014-08-19	4.549E-08	3.184E-10	1.965E-07	1.376E-09	3.741E-04	2.619E-06	8.942E-08	8.942E-10	1.278E-08	2.186E-10
F34	2014-09-03	4.541E-08	3.179E-10	1.926E-07	1.348E-09	3.705E-04	2.594E-06	8.803E-08	9.703E-10	1.262E-08	2.226E-10
F35	2014-09-15	4.560E-08	3.192E-10	1.946E-07	1.362E-09	3.734E-04	2.614E-06	8.828E-08	8.828E-10	1.269E-08	2.157E-10
F36	2014-09-29	4.572E-08	3.200E-10	1.934E-07	1.354E-09	3.719E-04	2.603E-06	8.812E-08	8.812E-10	1.298E-08	2.206E-10
F36b	2014-10-06	4.470E-08	3.129E-10	1.914E-07	1.340E-09	3.654E-04	2.558E-06	8.735E-08	8.735E-10	1.271E-08	2.161E-10
F37	2014-10-16	4.407E-08	3.085E-10	1.903E-07	1.332E-09	3.670E-04	2.569E-06	8.712E-08	8.712E-10	1.263E-08	2.217E-10
F38	2014-10-28										
F39	2014-11-13	4.375E-08	3.062E-10	1.868E-07	1.308E-09	3.641E-04	2.549E-06	8.698E-08	8.748E-10	1.253E-08	2.203E-10
F40	2014-11-25	4.448E-08	3.114E-10	1.878E-07	1.315E-09	3.675E-04	2.573E-06	8.753E-08	8.753E-10	1.303E-08	2.216E-10
F41	2014-12-09	4.378E-08	3.065E-10	1.880E-07	1.316E-09	3.645E-04	2.552E-06	8.647E-08	9.493E-10	1.271E-08	2.344E-10
F42	2014-12-18	4.420E-08	3.094E-10	1.885E-07	1.320E-09	3.669E-04	2.568E-06	8.760E-08	8.760E-10	1.291E-08	2.194E-10
F43	2015-01-06	4.507E-08	3.155E-10	1.909E-07	1.337E-09	3.661E-04	2.563E-06	8.587E-08	8.609E-10	1.264E-08	2.291E-10
F44	2015-01-22	4.594E-08	3.216E-10	1.925E-07	1.347E-09	3.667E-04	2.567E-06	8.680E-08	8.680E-10	1.260E-08	2.174E-10
F45	2015-02-03	4.653E-08	3.257E-10	1.950E-07	1.365E-09	3.683E-04	2.578E-06	8.782E-08	9.247E-10	1.264E-08	2.149E-10
F46	2015-02-19	4.859E-08	3.401E-10	2.054E-07	1.438E-09	3.843E-04	2.690E-06	9.021E-08	9.105E-10	1.286E-08	2.187E-10
F47	2015-03-03	4.808E-08	3.366E-10	2.037E-07	1.426E-09	3.813E-04	2.669E-06	8.975E-08	9.018E-10	1.291E-08	2.195E-10
F48	2015-03-18	4.816E-08	3.371E-10	2.046E-07	1.432E-09	3.838E-04	2.687E-06	8.940E-08	8.940E-10	1.265E-08	2.150E-10
F49	2015-03-31	4.775E-08	3.342E-10	2.009E-07	1.406E-09	3.799E-04	2.659E-06	8.942E-08	8.942E-10	1.287E-08	2.188E-10
F50	2015-04-09	4.852E-08	3.397E-10	2.058E-07	1.441E-09	3.851E-04	2.696E-06	9.277E-08	1.011E-09	1.291E-08	2.195E-10
F51	2015-04-24	4.747E-08	3.323E-10	2.028E-07	1.420E-09	3.827E-04	2.679E-06	8.971E-08	8.971E-10	1.316E-08	2.237E-10
F52	2015-05-08	4.855E-08	3.398E-10	2.078E-07	1.454E-09	3.922E-04	2.745E-06	9.322E-08	9.322E-10	1.322E-08	2.247E-10
F53	2015-05-22	4.706E-08	3.294E-10	2.029E-07	1.420E-09	3.838E-04	2.687E-06	9.096E-08	9.096E-10	1.294E-08	2.200E-10
F54	2015-06-08	4.923E-08	3.446E-10	2.048E-07	1.434E-09	3.856E-04	2.699E-06	9.089E-08	9.319E-10	1.294E-08	2.200E-10
F55	2015-06-19	4.706E-08	3.294E-10	1.991E-07	1.394E-09	3.811E-04	2.668E-06	9.005E-08	9.063E-10	1.304E-08	2.217E-10
F56	2015-07-03	4.650E-08	3.255E-10	2.007E-07	1.405E-09	3.803E-04	2.662E-06	9.014E-08	9.014E-10	1.264E-08	2.150E-10
F57	2015-07-23	4.588E-08	3.212E-10	1.980E-07	1.386E-09	3.790E-04	2.653E-06	8.811E-08	8.811E-10	1.273E-08	2.164E-10
F58	2015-08-03	4.552E-08	3.186E-10	1.963E-07	1.374E-09	3.789E-04	2.652E-06	8.861E-08	8.861E-10	1.259E-08	2.140E-10
F59	2015-08-14	4.464E-08	3.125E-10	1.921E-07	1.345E-09	3.719E-04	2.603E-06	8.913E-08	1.026E-09	1.315E-08	2.235E-10
F60	2015-08-24	4.450E-08	3.115E-10	1.905E-07	1.333E-09	3.686E-04	2.580E-06	8.740E-08	9.501E-10	1.275E-08	2.348E-10
F61	2015-09-08	4.432E-08	3.103E-10	1.893E-07	1.325E-09	3.698E-04	2.589E-06	8.781E-08	9.181E-10	1.264E-08	2.148E-10
F62	2015-10-01	4.363E-08	3.054E-10	1.880E-07	1.316E-09	3.664E-04	2.565E-06	8.971E-08	1.019E-09	1.248E-08	2.272E-10

Table B.7: Mannheim (deep well): NG concentrations in groundwater. All data are given in units of ccSTP per g of water.

ID	sampl. date	He [ccSTP/g]	ΔHe [ccSTP/g]	Ne [ccSTP/g]	ΔNe [ccSTP/g]	Ar [ccSTP/g]	ΔAr [ccSTP/g]	Kr [ccSTP/g]	ΔKr [ccSTP/g]	Xe [ccSTP/g]	ΔXe [ccSTP/g]
F0	2013-03-20	5.212E-08	3.649E-10	2.213E-07	1.549E-09	3.975E-04	2.783E-06	9.043E-08	9.844E-10	1.333E-08	2.339E-10
F2	2013-06-27	5.245E-08	3.671E-10	2.226E-07	1.558E-09	3.988E-04	2.792E-06	9.341E-08	9.341E-10	1.346E-08	2.289E-10
F4	2013-07-29	5.224E-08	3.657E-10	2.210E-07	1.547E-09	3.990E-04	2.793E-06	9.278E-08	9.278E-10	1.338E-08	2.275E-10
F6	2013-08-27	5.286E-08	3.700E-10	2.229E-07	1.560E-09	3.987E-04	2.791E-06	9.367E-08	9.367E-10	1.358E-08	2.309E-10
F8	2013-09-24	5.263E-08	3.684E-10	2.232E-07	1.563E-09	4.010E-04	2.807E-06	9.342E-08	9.342E-10	1.336E-08	2.271E-10
F10	2013-10-22	5.746E-08	5.437E-10	2.404E-07	1.683E-09	4.114E-04	2.880E-06	9.508E-08	9.508E-10	1.285E-08	2.184E-10
F12	2013-11-19	5.179E-08	3.625E-10	2.178E-07	1.525E-09	3.970E-04	2.779E-06	9.286E-08	9.286E-10	1.326E-08	2.254E-10
F14	2013-12-17	5.283E-08	3.698E-10	2.227E-07	1.559E-09	3.989E-04	2.792E-06	9.329E-08	9.329E-10	1.327E-08	2.256E-10
F16	2014-01-13	5.295E-08	3.707E-10	2.240E-07	1.568E-09	4.010E-04	2.807E-06	9.223E-08	9.223E-10	1.315E-08	2.236E-10
F18	2014-02-11	5.256E-08	3.679E-10	2.228E-07	1.560E-09	3.987E-04	2.791E-06	9.193E-08	9.193E-10	1.309E-08	2.284E-10
F20	2014-03-10	5.315E-08	3.721E-10	2.245E-07	1.571E-09	3.989E-04	2.792E-06	9.255E-08	9.255E-10	1.313E-08	2.324E-10
F22	2014-04-07	5.360E-08	3.752E-10	2.275E-07	1.593E-09	4.026E-04	2.818E-06	9.308E-08	9.308E-10	1.338E-08	2.274E-10
F24	2014-05-08	5.494E-08	3.846E-10	2.325E-07	1.628E-09	4.041E-04	2.828E-06	9.265E-08	9.265E-10	1.319E-08	2.242E-10
F26	2014-06-03	5.291E-08	3.704E-10	2.237E-07	1.566E-09	3.975E-04	2.782E-06	9.362E-08	9.362E-10	1.342E-08	2.374E-10
F29	2014-07-03	5.264E-08	3.685E-10	2.228E-07	1.560E-09	4.013E-04	2.809E-06	9.455E-08	9.455E-10	1.366E-08	2.322E-10
F31	2014-07-23	5.165E-08	3.616E-10	2.203E-07	1.542E-09	3.974E-04	2.782E-06	9.313E-08	9.386E-10	1.334E-08	2.417E-10
F33	2014-08-19	5.413E-08	3.789E-10	2.277E-07	1.594E-09	4.025E-04	2.817E-06	9.285E-08	9.285E-10	1.325E-08	2.253E-10
F35	2014-09-15	5.220E-08	3.654E-10	2.191E-07	1.534E-09	3.991E-04	2.794E-06	9.203E-08	9.203E-10	1.346E-08	2.287E-10
F37	2014-10-16	5.215E-08	3.651E-10	2.216E-07	1.552E-09	3.982E-04	2.788E-06	9.215E-08	9.215E-10	1.292E-08	2.207E-10
F39	2014-11-13	5.327E-08	3.729E-10	2.257E-07	1.580E-09	3.994E-04	2.796E-06	9.427E-08	9.427E-10	1.386E-08	2.357E-10
F41	2014-12-03	5.191E-08	3.634E-10	2.208E-07	1.546E-09	3.972E-04	2.781E-06	9.239E-08	9.239E-10	1.357E-08	2.393E-10
F43	2015-01-06	5.196E-08	3.637E-10	2.215E-07	1.551E-09	3.975E-04	2.782E-06	9.243E-08	9.397E-10	1.320E-08	2.557E-10
F45	2015-02-03	5.242E-08	3.670E-10	2.206E-07	1.544E-09	3.964E-04	2.775E-06	9.230E-08	9.230E-10	1.323E-08	2.502E-10
F47	2015-03-03	5.225E-08	3.657E-10	2.224E-07	1.557E-09	3.995E-04	2.797E-06	9.243E-08	9.243E-10	1.321E-08	2.248E-10
F49	2015-03-31	5.227E-08	3.659E-10	2.213E-07	1.549E-09	3.990E-04	2.793E-06	9.254E-08	9.254E-10	1.316E-08	2.237E-10
F51	2015-04-24	5.295E-08	3.706E-10	2.234E-07	1.564E-09	3.948E-04	2.763E-06	9.379E-08	9.379E-10	1.359E-08	2.310E-10
F53	2015-05-22	5.119E-08	3.583E-10	2.190E-07	1.533E-09	3.959E-04	2.771E-06	9.135E-08	9.135E-10	1.310E-08	2.227E-10
F55	2015-06-19	5.267E-08	3.687E-10	2.195E-07	1.536E-09	3.996E-04	2.797E-06	9.242E-08	9.242E-10	1.330E-08	2.261E-10
F57	2015-07-23	5.196E-08	3.638E-10	2.221E-07	1.554E-09	3.985E-04	2.790E-06	9.101E-08	9.101E-10	1.298E-08	2.207E-10
F59	2015-08-14	5.188E-08	3.631E-10	2.222E-07	1.556E-09	3.962E-04	2.774E-06	9.202E-08	9.202E-10	1.326E-08	2.356E-10
F61	2015-09-08	5.191E-08	3.633E-10	2.208E-07	1.545E-09	3.946E-04	2.762E-06	9.234E-08	1.003E-09	1.343E-08	2.324E-10
F62	2015-10-01	5.195E-08	3.637E-10	2.223E-07	1.556E-09	3.963E-04	2.774E-06	9.363E-08	9.363E-10	1.303E-08	2.214E-10

B.9 Mannheim: Results of excess air model fits (shallow well)

Table B.8: Mannheim (shallow well): UA model fit results. The degassing period denotes samples between July 2014 and January 2015 (F31-F44) as well as from August 2015 on (F58-F62) and was determined based on negative values of *A* in this UA model fit.

UA model		$X/X_{atm} = 1.000$						$X/X_{atm} = 1.032$					
included NGs		He, Ne, Ar, Kr, Xe						He, Ne, Ar, Kr, Xe					
DoF		3						3					
start values		$A = 0.01$ ccSTP/g, $T = 10$°C						$A = 0.01$ ccSTP/g, $T = 10$°C					
fixed parameters		$p = 0.991 \cdot 1.000$ atm, $S = 0.72$ g/kg						$p = 0.991 \cdot 1.032$ atm, $S = 0.72$ g/kg					
ID	sampl. date	χ^2	Prob [%]	A [ccSTP/g]	ΔA [ccSTP/g]	T [°C]	ΔT [°C]	χ^2	Prob [%]	A [ccSTP/g]	ΔA [ccSTP/g]	T [°C]	ΔT [°C]
F1	2013-06-18	5.2	16.0	1.0E-03	6.7E-05	9.3	0.2	4.7	19.4	7.6E-04	6.7E-05	10.3	0.2
F2	2013-06-27	0.8	84.0	9.3E-04	5.7E-05	9.0	0.2	0.4	94.6	6.8E-04	5.7E-05	10.0	0.2
F3	2013-07-16	17.5	0.1	7.8E-04	6.6E-05	9.2	0.2	14.2	0.3	5.2E-04	6.6E-05	10.3	0.2
F4	2013-07-29	4.0	26.4	6.1E-04	6.1E-05	9.6	0.2	3.3	35.4	3.6E-04	6.1E-05	10.6	0.2
F5	2013-08-14	1.4	70.9	7.3E-04	5.6E-05	9.5	0.2	2.4	49.1	4.8E-04	5.6E-05	10.5	0.2
F6	2013-08-27	1.9	59.0	5.6E-04	5.5E-05	10.1	0.2	3.1	37.4	3.2E-04	5.5E-05	11.2	0.2
F7	2013-09-10	0.1	98.7	5.3E-04	5.4E-05	10.4	0.2	0.1	98.9	2.9E-04	5.4E-05	11.5	0.2
F8	2013-09-24	3.0	38.6	4.5E-04	6.3E-05	10.4	0.2	4.0	26.2	2.0E-04	6.3E-05	11.4	0.2
F9	2013-10-08	3.0	38.8	5.1E-04	5.4E-05	10.7	0.2	2.7	44.7	2.6E-04	5.4E-05	11.8	0.2
F10	2013-10-22	11.1	1.1	5.7E-04	5.4E-05	11.2	0.2	11.9	0.8	3.2E-04	5.5E-05	12.3	0.2
F11	2013-11-05	7.5	5.9	2.3E-04	5.3E-05	10.9	0.2	9.3	2.5	-1.5E-05	5.3E-05	11.9	0.2
F12	2013-11-19	1.1	77.7	2.8E-04	5.8E-05	10.9	0.2	1.8	60.5	3.2E-05	5.8E-05	11.9	0.2
F13	2013-12-03	5.1	16.7	4.9E-04	5.4E-05	10.5	0.2	5.7	12.6	2.5E-04	5.4E-05	11.6	0.2
F14	2013-12-17	9.8	2.0	4.0E-04	5.4E-05	10.4	0.2	10.6	1.4	1.5E-04	5.4E-05	11.4	0.2
F15	2013-12-30	0.8	85.6	3.1E-04	5.3E-05	10.7	0.2	1.0	79.5	6.4E-05	5.3E-05	11.7	0.2
F16	2014-01-13	1.3	72.4	3.4E-04	5.3E-05	10.7	0.2	2.2	52.9	9.3E-05	5.3E-05	11.7	0.2
F17	2014-01-28	7.9	4.7	2.9E-04	5.3E-05	10.8	0.2	9.4	2.4	3.8E-05	5.3E-05	11.8	0.2
F18	2014-02-11	2.6	45.0	1.3E-04	5.2E-05	10.8	0.2	3.0	39.4	-1.1E-04	5.2E-05	11.8	0.2
F19	2014-02-25	2.9	41.0	2.7E-04	5.3E-05	10.1	0.2	3.6	31.2	2.2E-05	5.3E-05	11.2	0.2
F20	2014-03-10	2.8	42.2	3.2E-04	5.4E-05	10.0	0.2	3.4	32.9	7.6E-05	5.4E-05	11.1	0.2
F21	2014-03-26	3.0	38.7	3.1E-04	5.3E-05	10.0	0.2	3.2	36.5	6.1E-05	5.3E-05	11.1	0.2
F22	2014-04-07	6.1	10.7	1.3E-04	5.2E-05	10.9	0.2	6.8	7.7	-1.2E-04	5.2E-05	12.0	0.2
F23	2014-04-23	1.2	75.6	2.2E-04	5.3E-05	10.2	0.2	1.9	58.9	-3.1E-05	5.3E-05	11.2	0.2
F24	2014-05-08	2.6	46.4	1.8E-04	5.3E-05	10.0	0.2	3.2	36.4	-6.7E-05	5.3E-05	11.1	0.2
F25	2014-05-20	0.5	92.6	2.9E-04	5.3E-05	10.2	0.2	0.1	98.8	4.6E-05	5.3E-05	11.2	0.2
F26	2014-06-03	2.5	47.6	2.6E-04	5.3E-05	10.2	0.2	3.2	35.9	1.0E-05	5.3E-05	11.3	0.2
F27	2014-06-16	6.2	10.3	3.2E-04	5.3E-05	10.0	0.2	7.5	5.7	7.5E-05	5.3E-05	11.0	0.2
F29	2014-07-03	8.6	3.5	1.4E-04	5.2E-05	10.2	0.2	10.4	1.5	-1.1E-04	5.2E-05	11.2	0.2
F30	2014-07-15	5.6	13.6	6.1E-05	5.2E-05	10.3	0.2	6.4	9.4	-1.9E-04	5.2E-05	11.4	0.2
F31	2014-07-23	1.2	76.3	-5.9E-05	5.1E-05	10.3	0.2	1.9	58.8	-3.1E-04	5.1E-05	11.4	0.2
F32	2014-08-05	1.9	59.1	-9.8E-05	5.1E-05	10.6	0.2	2.6	45.6	-3.5E-04	5.1E-05	11.7	0.2
F33	2014-08-19	1.8	61.8	-7.1E-05	5.1E-05	10.4	0.2	2.6	44.9	-3.2E-04	5.1E-05	11.5	0.2
F34	2014-09-03	5.7	12.7	-1.3E-04	5.1E-05	10.9	0.2	6.4	9.3	-3.8E-04	5.1E-05	12.0	0.2
F35	2014-09-15	2.8	43.0	-8.0E-05	5.1E-05	10.7	0.2	3.3	35.4	-3.3E-04	5.1E-05	11.8	0.2
F36	2014-09-29	8.8	3.2	-9.7E-05	5.1E-05	10.7	0.2	10.5	1.5	-3.4E-04	5.1E-05	11.8	0.2
F36b	2014-10-06	5.5	14.0	-2.3E-04	5.0E-05	11.1	0.2	7.4	6.1	-4.8E-04	5.0E-05	12.2	0.2
F37	2014-10-16	1.6	66.5	-3.3E-04	5.0E-05	11.0	0.2	2.6	45.5	-5.8E-04	5.0E-05	12.1	0.2
F38	2014-10-28												
F39	2014-11-13	6.0	11.1	-4.3E-04	4.9E-05	11.2	0.2	7.2	6.6	-6.8E-04	4.9E-05	12.3	0.2
F40	2014-11-25	15.6	0.1	-3.5E-04	5.0E-05	10.8	0.2	17.9	0.0	-6.0E-04	5.0E-05	11.9	0.2
F41	2014-12-09	4.3	23.1	-4.0E-04	5.0E-05	11.2	0.2	5.8	12.4	-6.5E-04	5.0E-05	12.3	0.2
F42	2014-12-18	8.8	3.2	-3.7E-04	5.0E-05	10.9	0.2	10.8	1.3	-6.1E-04	5.0E-05	11.9	0.2
F43	2015-01-06	6.4	9.5	-1.8E-04	5.0E-05	11.4	0.2	7.5	5.8	-4.2E-04	5.0E-05	12.5	0.2
F44	2015-01-22	11.0	1.2	-4.9E-05	5.1E-05	11.4	0.2	12.4	0.6	-3.0E-04	5.1E-05	12.5	0.2
F45	2015-02-03	11.0	1.1	6.1E-05	5.2E-05	11.2	0.2	12.6	0.6	-1.9E-04	5.2E-05	12.3	0.2
F46	2015-02-19	3.0	39.9	4.7E-04	5.4E-05	10.2	0.2	2.8	42.0	2.2E-04	5.4E-05	11.2	0.2
F47	2015-03-03	2.4	49.0	3.8E-04	5.4E-05	10.3	0.2	2.9	41.1	1.3E-04	5.4E-05	11.3	0.2
F48	2015-03-18	3.0	38.9	4.2E-04	5.4E-05	10.3	0.2	2.1	56.0	1.7E-04	5.4E-05	11.4	0.2
F49	2015-03-31	5.8	12.2	2.8E-04	5.3E-05	10.4	0.2	6.2	10.1	3.6E-05	5.3E-05	11.4	0.2
F50	2015-04-09	7.4	6.1	4.4E-04	5.4E-05	9.8	0.2	7.6	5.5	1.9E-04	5.4E-05	10.8	0.2
F51	2015-04-24	1.7	64.8	2.7E-04	5.3E-05	10.0	0.2	2.4	49.2	2.4E-05	5.3E-05	11.1	0.2
F52	2015-05-08	2.3	52.0	4.5E-04	5.4E-05	9.2	0.2	2.1	55.6	2.0E-04	5.4E-05	10.2	0.2
F53	2015-05-22	0.9	83.4	2.1E-04	5.3E-05	9.8	0.2	0.8	84.2	-3.5E-05	5.3E-05	10.9	0.2
F54	2015-06-08	10.8	1.3	5.2E-04	5.4E-05	10.1	0.2	10.8	1.3	2.7E-04	5.5E-05	11.1	0.2
F55	2015-06-19	5.2	15.7	1.5E-04	5.3E-05	10.1	0.2	5.8	11.9	-1.0E-04	5.3E-05	11.1	0.2
F56	2015-07-03	2.2	52.3	1.3E-04	5.2E-05	10.2	0.2	1.7	63.1	-1.2E-04	5.2E-05	11.2	0.2
F57	2015-07-23	1.1	77.0	1.5E-05	5.2E-05	10.4	0.2	0.6	89.5	-2.3E-04	5.2E-05	11.5	0.2
F58	2015-08-03	2.2	53.7	-6.7E-05	5.1E-05	10.4	0.2	1.2	75.7	-3.1E-04	5.1E-05	11.4	0.2
F59	2015-08-14	6.1	10.7	-2.7E-04	5.0E-05	10.4	0.2	8.2	4.2	-5.2E-04	5.1E-05	11.4	0.2
F60	2015-08-24	3.9	27.6	-2.8E-04	5.0E-05	10.9	0.2	5.0	17.2	-5.3E-04	5.0E-05	12.0	0.2
F61	2015-09-08	4.6	20.6	-3.3E-04	5.0E-05	10.8	0.2	5.2	15.9	-5.8E-04	5.0E-05	11.9	0.2
F62	2015-10-01	9.8	2.0	-4.5E-04	4.9E-05	10.8	0.2	10.9	1.3	-7.0E-04	5.0E-05	11.9	0.2

Table B.9: Mannheim (shallow well): CE model fit results. Degassing period: samples between July 2014 and January 2015 (F31-F44) and from August 2015 on (F58-F62). Based on Monte Carlo (MC) simulations, unphysical outcomes were omitted (Jung and Aeschbach, 2016). All parameter values were taken as obtained fit result, while their uncertainties were determined by MC simulations. For degassed samples (start value $F_{CE} = 3$), clusters reflecting values of $A > 0.5$ cc/g as well as $F_{CE} = 30$ were omitted. For remaining samples (start value $F_{CE} = 0$), clusters reflecting values of $A > 0.5$ cc/g were omitted. By this way, at least more than 50 % (mostly more than 90 %) of all MC simulations were still involved.

CE model		$X/X_{atm} = 1.000$								$X/X_{atm} = 1.032$								fit for given WTT			
included NGs		He, Ne, Ar, Kr, Xe								He, Ne, Ar, Kr, Xe								He, Ne, Ar, Kr, Xe			
DoF		2								2								2			
start values		$A = 0.01$ ccSTP/g, $T = 10$°C, $F_{CE} = 0$ ($F_{CE} = 3$ during degassing period)								$A = 0.01$ ccSTP/g, $T = 10$°C, $F_{CE} = 0$ ($F_{CE} = 3$ during degassing period)								$p* = 0.991$ atm, $A = 0.01$ ccSTP/g, $F_{CE} = 0$ ($F_{CE} = 3$ during deg. per.)			
fixed parameters		$p = 0.991 \cdot 1.000$ atm, $S = 0.72$ g/kg								$p = 0.991 \cdot 1.032$ atm, $S = 0.72$ g/kg								$S = 0.72$ g/kg, T = WTT			
ID	sampl. date	χ^2	Prob [%]	A [ccSTP/g]	ΔA [ccSTP/g]	F_{CE}	ΔF_{CE}	T [°C]	ΔT [°C]	χ^2	Prob [%]	A [ccSTP/g]	ΔA [ccSTP/g]	F_{CE}	ΔF_{CE}	T [°C]	ΔT [°C]	χ^2	Prob [%]	$p*$	$\Delta p*$
F1	2013-06-18	5.2	7.6	1.0E-03	6.7E-05	0.000	0.000	9.3	0.2	4.7	9.5	7.6E-04	6.7E-05	0.000	0.000	10.3	0.2	4.7	9.8	1.04	0.01
F2	2013-06-27	0.8	65.8	1.3E-03	5.6E-03	0.246	2.922	9.0	0.4	0.4	83.1	6.8E-04	5.7E-05	0.000	0.000	10.0	0.2	0.3	86.5	1.04	0.01
F3	2013-07-16	6.4	4.2	2.1E-01	7.8E-02	0.909	0.007	11.5	0.4	7.1	2.9	2.0E-01	7.0E-02	0.937	0.007	11.8	0.4	3.5	17.4	0.01	8.59
F4	2013-07-29	4.0	13.7	6.1E-04	6.1E-05	0.000	0.000	9.6	0.2	3.3	19.6	3.6E-04	6.1E-05	0.000	0.000	10.6	0.2	3.2	20.1	1.03	0.01
F5	2013-08-14	1.4	50.0	7.3E-04	5.6E-05	0.000	0.000	9.5	0.2	2.4	29.9	4.8E-04	5.6E-05	0.000	0.000	10.5	0.2	2.9	23.9	1.03	0.01
F6	2013-08-27	1.9	38.4	5.6E-04	5.5E-05	0.000	0.000	10.1	0.2	3.1	21.0	3.2E-04	5.5E-05	0.000	0.000	11.2	0.2	3.0	22.0	1.02	0.01
F7	2013-09-10	0.0	99.6	4.6E-03	1.4E-02	0.835	0.341	10.6	0.5	0.1	94.3	1.3E-03	1.9E-02	0.761	3.061	11.5	0.4	0.1	96.9	1.01	0.01
F8	2013-09-24	3.0	21.9	4.5E-04	6.3E-05	0.000	0.000	10.4	0.2	4.0	13.5	2.0E-04	6.3E-05	0.000	0.001	11.4	0.2	4.0	13.5	1.02	0.01
F9	2013-10-08	3.0	22.1	5.1E-04	5.4E-05	0.000	0.000	10.7	0.2	2.7	26.4	2.6E-04	5.4E-05	0.000	0.000	11.8	0.2	2.7	26.1	1.02	0.01
F10	2013-10-22	11.1	0.4	5.7E-04	5.5E-05	0.000	0.000	11.2	0.2	11.9	0.3	3.2E-04	5.5E-05	0.000	0.000	12.3	0.2	11.5	0.3	1.01	0.01
F11	2013-11-05	7.5	2.4	2.3E-04	5.3E-05	0.000	0.000	10.9	0.2	9.4	0.9	6.7E-11	3.4E-08	0.310	0.006	12.0	0.2	9.3	0.9	1.02	0.01
F12	2013-11-19	1.1	57.7	2.8E-04	5.8E-05	0.000	0.000	10.9	0.2	1.8	39.7	3.2E-05	4.1E-05	0.000	0.007	11.9	0.2	2.0	37.6	1.03	0.01
F13	2013-12-03	5.1	7.9	4.9E-04	5.4E-05	0.000	0.000	10.5	0.2	5.7	5.7	2.5E-04	5.4E-05	0.000	0.000	11.6	0.2	6.2	4.5	1.04	0.01
F14	2013-12-17	9.8	0.7	4.0E-04	5.4E-05	0.000	0.000	10.4	0.2	10.6	0.5	1.5E-04	5.3E-05	0.000	0.000	11.4	0.2	11.4	0.3	1.04	0.01
F15	2013-12-30	0.8	67.9	3.1E-04	5.3E-05	0.000	0.000	10.7	0.2	1.0	59.9	6.4E-05	4.4E-05	0.000	0.004	11.7	0.2	1.3	53.5	1.03	0.01
F16	2014-01-13	1.3	51.7	3.4E-04	5.3E-05	0.000	0.000	10.7	0.2	2.2	33.0	9.3E-05	4.9E-05	0.000	0.002	11.7	0.2	2.5	29.0	1.03	0.01
F17	2014-01-28	7.9	1.9	2.9E-04	5.3E-05	0.000	0.000	10.8	0.2	9.4	0.9	3.8E-05	3.9E-05	0.000	0.006	11.8	0.2	9.5	0.9	1.02	0.01
F18	2014-02-11	2.6	26.7	1.3E-04	5.1E-05	0.000	0.001	10.8	0.2	8.1	1.8	1.7E-10	2.2E-08	0.297	0.011	12.2	0.3	3.7	15.7	1.01	0.01
F19	2014-02-25	2.9	23.7	2.7E-04	5.3E-05	0.000	0.000	10.1	0.2	3.6	16.8	2.2E-05	3.6E-05	0.001	0.004	11.2	0.2	4.1	12.8	1.03	0.01
F20	2014-03-10	2.8	24.6	3.2E-04	5.3E-05	0.000	0.000	10.0	0.2	3.4	17.9	7.6E-05	4.6E-05	0.000	0.003	11.1	0.2	3.6	16.2	1.03	0.01
F21	2014-03-26	3.0	22.0	3.1E-04	5.3E-05	0.000	0.000	10.0	0.2	3.2	20.4	6.1E-05	4.3E-05	0.000	0.003	11.1	0.2	3.2	20.2	1.02	0.01
F22	2014-04-07	6.1	4.8	1.3E-04	5.1E-05	0.000	0.001	10.9	0.2	12.3	0.2	7.9E-10	4.9E-09	0.304	0.009	12.4	0.2	6.1	4.7	0.99	0.01
F23	2014-04-23	1.2	55.2	2.2E-04	5.3E-05	0.000	0.000	10.2	0.2	2.3	31.9	3.1E-10	8.4E-07	0.290	0.014	11.3	0.2	1.7	43.4	1.01	0.01
F24	2014-05-08	2.6	27.7	1.8E-04	5.3E-05	0.000	0.000	10.0	0.2	4.9	8.4	8.3E-11	1.9E-07	0.296	0.011	11.3	0.2	3.0	22.0	1.02	0.01
F25	2014-05-20	0.1	96.4	3.0E-02	1.0E-01	0.958	0.030	10.6	0.8	0.1	95.5	4.2E-02	9.9E-01	0.994	0.024	11.3	1.0	0.1	96.8	1.00	0.03
F26	2014-06-03	2.5	28.7	2.6E-04	5.3E-05	0.000	0.000	10.2	0.2	3.2	20.0	1.0E-05	3.4E-05	0.000	0.007	11.3	0.2	2.8	24.2	1.01	0.01
F27	2014-06-16	6.2	4.5	3.2E-04	5.4E-05	0.000	0.000	10.0	0.2	7.5	2.3	7.5E-05	4.6E-05	0.000	0.004	11.0	0.2	7.2	2.7	1.02	0.01
F29	2014-07-03	8.6	1.3	1.4E-04	5.1E-05	0.000	0.000	10.2	0.2	8.6	1.3	9.0E-02	3.1E-02	1.017	0.011	10.9	0.3	10.0	0.7	1.01	0.01
F30	2014-07-15	5.6	6.2	6.1E-05	4.3E-05	0.000	0.003	10.3	0.2	4.8	8.9	5.5E-02	3.3E-02	1.026	0.023	11.0	0.3	7.7	2.1	1.01	0.01
F31	2014-07-23	0.9	64.6	7.0E-02	5.6E-02	1.009	0.070	10.2	0.3	0.4	80.9	6.3E-02	7.5E-02	1.042	0.055	10.8	0.4	0.2	90.5	1.05	0.08
F32	2014-08-05	1.5	48.0	4.9E-02	5.5E-02	1.014	0.042	10.4	0.3	0.9	62.8	4.2E-02	6.6E-02	1.050	0.061	11.1	0.4	0.8	68.5	1.04	0.06
F33	2014-08-19	1.4	48.5	7.0E-02	5.2E-02	1.010	0.062	10.3	0.3	1.0	59.5	6.3E-02	5.6E-02	1.044	0.052	10.9	0.4	0.8	66.8	1.06	0.06
F34	2014-09-03	4.8	9.2	3.8E-02	3.1E-02	1.020	0.025	10.7	0.3	3.7	15.5	3.5E-02	3.2E-02	1.057	0.037	11.4	0.4	3.0	21.8	1.06	0.06
F35	2014-09-15	2.4	30.0	3.4E-02	4.3E-02	1.012	0.048	10.6	0.3	1.7	43.1	3.1E-02	4.9E-02	1.050	0.059	11.3	0.4	1.1	57.6	1.06	0.04
F36	2014-09-29	7.5	2.3	7.5E-02	3.2E-02	1.015	0.016	10.4	0.3	6.1	4.8	7.2E-02	3.6E-02	1.048	0.014	11.0	0.3	3.0	22.0	1.18	0.21
F36b	2014-10-06	2.8	24.6	8.5E-02	4.9E-02	1.033	0.020	10.6	0.3	1.9	39.6	8.4E-02	5.3E-02	1.066	0.024	11.1	0.4	0.3	85.5	1.13	0.11
F37	2014-10-16	0.2	88.3	4.3E-02	7.5E-02	1.049	0.052	10.5	0.4	0.1	97.2	3.7E-02	8.4E-02	1.087	0.068	11.2	0.6	0.0	98.9	1.07	0.04
F38	2014-10-28																				
F39	2014-11-13	2.9	23.0	3.2E-02	3.4E-02	1.067	0.044	10.6	0.4	2.1	34.4	3.1E-02	3.6E-02	1.107	0.051	11.4	0.5	1.0	59.9	1.09	0.04
F40	2014-11-25	10.1	0.7	6.9E-02	2.7E-02	1.051	0.303	10.0	0.3	8.5	1.4	6.6E-02	3.0E-02	1.086	0.012	10.6	0.4	4.1	12.9	1.19	0.09
F41	2014-12-09	1.3	51.2	6.3E-02	6.6E-02	1.058	0.046	10.4	0.4	0.9	64.9	5.7E-02	7.4E-02	1.094	0.055	11.0	0.6	0.4	83.7	1.10	0.05
F42	2014-12-18	4.3	11.6	6.9E-02	3.7E-02	1.053	0.017	10.1	0.3	3.2	19.8	6.6E-02	6.2E-02	1.088	0.018	10.6	0.5	0.9	62.3	1.15	0.07
F43	2015-01-06	4.9	8.6	6.0E-02	4.6E-02	1.026	0.028	11.0	0.3	4.0	13.6	5.5E-02	5.2E-02	1.060	0.037	11.7	0.4	2.8	25.1	1.10	0.09
F44	2015-01-22	12.0	0.2	8.7E-11	6.1E-08	0.298	0.006	11.5	0.2	8.6	1.4	5.8E-02	2.4E-02	1.042	0.010	11.8	0.3	6.0	4.9	1.17	0.30
F45	2015-02-03	11.0	0.4	6.1E-05	4.2E-05	0.000	0.003	11.2	0.2	9.8	0.7	6.7E-02	2.1E-02	1.027	0.008	11.8	0.3	16.6	0.0	1.01	0.01
F46	2015-02-19	3.0	22.9	4.7E-04	5.4E-05	0.000	0.000	10.2	0.2	2.8	24.4	2.2E-04	5.4E-05	0.000	0.000	11.2	0.2	3.0	22.1	1.05	0.01
F47	2015-03-03	2.4	29.9	3.8E-04	5.3E-05	0.000	0.000	10.3	0.2	2.9	23.7	1.3E-04	5.2E-05	0.000	0.001	11.3	0.2	3.3	19.4	1.04	0.01
F48	2015-03-18	3.0	22.1	4.2E-04	5.4E-05	0.000	0.000	10.3	0.2	2.1	35.7	1.7E-04	5.4E-05	0.000	0.000	11.4	0.2	1.9	38.6	1.03	0.01
F49	2015-03-31	5.8	5.5	2.8E-04	5.3E-05	0.000	0.000	10.4	0.2	6.2	4.4	3.6E-05	3.9E-05	0.000	0.006	11.4	0.2	6.2	4.5	1.02	0.01
F50	2015-04-09	7.4	2.5	4.4E-04	5.4E-05	0.000	0.000	9.8	0.2	7.6	2.2	1.9E-04	5.4E-05	0.000	0.000	10.8	0.2	7.8	2.0	1.04	0.01
F51	2015-04-24	1.7	43.8	2.7E-04	5.3E-05	0.000	0.000	10.0	0.2	2.4	30.0	2.4E-05	3.6E-05	0.000	0.006	11.1	0.2	2.4	30.7	1.02	0.01
F52	2015-05-08	2.3	32.2	4.5E-04	5.4E-05	0.000	0.000	9.2	0.2	2.1	35.3	2.0E-04	5.4E-05	0.000	0.001	10.2	0.2	2.2	33.4	1.04	0.01
F53	2015-05-22	0.9	64.9	2.1E-04	5.3E-05	0.000	0.000	9.8	0.2	3.6	16.1	1.0E-10	2.6E-05	0.178	0.010	10.6	0.2	0.8	65.6	1.02	0.01
F54	2015-06-08	10.8	0.5	5.2E-04	5.5E-05	0.000	0.000	10.1	0.2	10.8	0.4	2.7E-04	5.4E-05	0.000	0.000	11.1	0.2	10.8	0.5	1.01	0.01
F55	2015-06-19	5.2	7.4	1.5E-04	5.2E-05	0.000	0.001	10.1	0.2	5.0	8.2	5.4E-02	3.6E-02	1.015	0.022	10.9	0.3	5.7	5.8	1.01	0.01
F56	2015-07-03	1.8	39.9	3.2E-01	8.9E-02	0.984	0.009	10.6	0.3	1.7	42.5	4.0E-03	4.8E-02	1.044	0.077	11.2	0.3	2.0	36.6	1.01	0.01
F57	2015-07-23	1.1	59.0	1.4E-01	6.1E-02	0.997	7.568	10.5	0.2	0.6	73.8	8.3E-06	8.8E-02	29.958	0.119	11.5	0.3	0.8	67.6	1.01	0.01
F58	2015-08-03	2.2	33.7	2.3E-06	4.0E-02	29.946	0.145	10.4	0.3	1.2	55.4	1.4E-04	4.5E-02	3.310	0.163	11.4	0.3	1.4	49.6	1.02	0.01
F59	2015-08-14	2.8	25.3	9.5E-02	4.8E-02	1.039	0.020	9.6	0.3	1.8	40.5	9.5E-02	6.0E-02	1.072	0.024	10.1	0.4	0.2	89.8	1.15	0.14
F60	2015-08-24	2.0	37.4	5.1E-02	5.4E-02	1.041	0.042	10.4	0.4	1.3	51.4	4.6E-02	6.1E-02	1.077	0.053	11.1	0.5	1.0	61.9	1.06	0.06
F61	2015-09-08	3.0	22.2	2.1E-02	3.3E-02	1.056	0.060	10.5	0.3	2.2	33.1	2.1E-02	3.5E-02	1.099	0.072	11.3	0.4	1.8	41.1	1.05	0.03
F62	2015-10-01	7.1	2.8	2.9E-02	2.5E-02	1.072	0.051	10.2	0.4	6.4	4.1	2.7E-02	2.5E-02	1.112	0.062	10.9	0.5	5.5	6.3	1.08	0.04

Table B.10: Mannheim (shallow well): PR model fit results.

PR model		X/X_{atm} = 1.000								X/X_{atm} = 1.000								X/X_{atm} = 1.032							
included NGs		He, Ne, Ar, Kr, Xe								Ne, Ar, Kr, Xe								He, Ne, Ar, Kr, Xe							
DoF		2								1								2							
start values		$A = 0.01$ ccSTP/g, $T = 10$°C, $F_{PR} = 0$								$A = 0.01$ ccSTP/g, $T = 10$°C, $F_{PR} = 0$								$A = 0.01$ ccSTP/g, $T = 10$°C, $F_{PR} = 0$							
fixed parameters		$p = 0.991 \cdot 1.000$ atm, $S = 0.72$ g/kg, $\beta = 1$								$p = 0.991 \cdot 1.000$ atm, $S = 0.72$ g/kg, $\beta = 1$								$p = 0.991 \cdot 1.032$ atm, $S = 0.72$ g/kg, $\beta = 1$							
ID	sampl. date	χ^2	Prob [%]	A [ccSTP/g]	ΔA [ccSTP/g]	F_{PR}	ΔF_{PR}	T [°C]	ΔT [°C]	χ^2	Prob [%]	A [ccSTP/g]	ΔA [ccSTP/g]	F_{PR}	ΔF_{PR}	T [°C]	ΔT [°C]	χ^2	Prob [%]	A [ccSTP/g]	ΔA [ccSTP/g]	F_{PR}	ΔF_{PR}	T [°C]	ΔT [°C]
F1	2013-06-18	5.0	8.3	9.2E-04	2.0E-04	-0.06	0.14	9.2	0.2	1.8	17.5	4.9E-02	2.9E-02	3.59	0.48	13.4	1.8	4.4	11.0	6.5E-04	1.9E-04	-0.10	0.19	10.3	0.2
F2	2013-06-27	0.7	69.3	8.7E-04	1.9E-04	-0.04	0.13	9.0	0.2	0.0	91.3	4.7E-03	7.8E-03	1.59	1.55	9.7	1.1	0.2	91.1	6.0E-04	1.9E-04	-0.08	0.18	10.0	0.2
F3	2013-07-16	17.0	0.0	9.3E-04	2.5E-04	0.13	0.17	9.3	0.2	3.1	8.0	5.4E-02	3.1E-02	3.77	0.44	13.6	1.8	13.8	0.1	6.7E-04	2.6E-04	0.16	0.26	10.3	0.3
F4	2013-07-29	3.3	19.4	4.6E-04	1.7E-04	-0.18	0.21	9.5	0.2	0.0	94.2	3.5E-02	2.9E-02	3.74	0.64	12.3	1.7	2.4	30.2	2.1E-04	1.4E-04	-0.34	0.38	10.5	0.2
F5	2013-08-14	1.0	60.2	6.2E-04	1.8E-04	-0.10	0.17	9.4	0.2	0.2	67.8	1.8E-06	2.9E-05	-5.93	16.57	9.0	0.3	1.9	38.2	3.6E-04	1.7E-04	-0.18	0.26	10.4	0.2
F6	2013-08-27	1.1	57.7	4.1E-04	1.6E-04	-0.19	0.22	10.0	0.2	0.1	73.9	6.6E-12	1.1E-08	-18.10	1710.32	9.7	0.3	2.2	33.6	1.7E-04	1.3E-04	-0.38	0.43	11.0	0.2
F7	2013-09-10	0.0	98.1	6.0E-04	2.1E-04	0.07	0.21	10.5	0.2	0.0	96.7	1.1E-03	3.6E-03	0.70	3.01	10.6	0.8	0.1	96.6	3.3E-04	2.2E-04	0.09	0.40	11.5	0.3
F8	2013-09-24	3.0	22.3	4.9E-04	2.2E-04	0.06	0.29	10.4	0.2	3.4	6.4	4.5E-02	3.1E-02	4.10	0.50	13.6	1.7	4.0	13.6	2.3E-04	2.3E-04	0.07	0.65	11.4	0.3
F9	2013-10-08	2.7	26.3	4.1E-04	1.7E-04	-0.14	0.24	10.7	0.2	0.1	75.8	3.8E-02	3.0E-02	3.94	0.59	13.6	1.7	23.0	0.0	-5.3E-02	3.5E-02	6.81	2.43	10.3	1.0
F10	2013-10-22	0.3	87.4	1.6E-04	8.5E-05	-0.76	0.29	10.9	0.2	0.2	66.8	1.4E-05	1.9E-04	-3.17	13.34	10.7	0.4	34.0	0.0	-8.1E-02	2.2E-02	5.26	0.30	8.3	0.9
F11	2013-11-05	24.5	0.0	-3.4E-02	2.3E-02	5.21	0.67	9.0	0.9	2.7	10.2	4.4E-12	2.1E-08	-17.04	4749.93	10.6	0.3	4.8	9.2	-7.0E-03	1.5E-02	3.37	1.73	11.1	1.0
F12	2013-11-19	0.8	66.1	2.0E-04	1.5E-04	-0.23	0.46	10.8	0.2	1.2	27.8	2.1E-02	2.8E-02	4.01	1.00	12.3	1.5	2.1	35.0	-8.6E-04	1.8E-02	3.55	17.04	11.8	1.1
F13	2013-12-03	0.1	95.5	1.9E-04	1.0E-04	-0.57	0.30	10.3	0.2	0.1	79.9	4.6E-05	4.4E-04	-1.98	9.43	10.2	0.4	21.0	0.0	-5.4E-02	2.4E-02	5.36	0.49	9.0	0.9
F14	2013-12-17	0.1	95.5	6.3E-05	6.0E-05	-1.09	0.50	10.1	0.2	0.1	81.0	1.8E-06	7.0E-05	-4.61	38.34	10.0	0.4	11.4	0.3	-4.8E-02	2.2E-02	4.83	0.37	8.6	0.9
F15	2013-12-30	0.2	90.5	1.9E-04	1.4E-04	-0.29	0.41	10.6	0.2	0.2	66.4	3.7E-04	2.6E-03	0.33	6.93	10.6	0.7	1.3	52.7	-2.4E-02	2.4E-02	5.17	0.92	10.5	1.0
F16	2014-01-13	0.6	74.4	2.1E-04	1.4E-04	-0.30	0.37	10.6	0.2	8.9	0.3	-5.2E-02	5.2E-02	7.36	4.44	9.5	1.1	3.9	14.6	-2.6E-02	2.4E-02	5.13	0.83	10.4	1.0
F17	2014-01-28	32.6	0.0	-4.7E-02	2.3E-02	5.38	0.56	8.4	0.9	1.7	19.5	4.7E-12	1.9E-08	-17.15	4117.74	10.5	0.3	6.2	4.6	-1.1E-02	1.8E-02	3.80	1.35	10.7	1.0
F18	2014-02-11	7.4	2.4	-3.1E-02	2.5E-02	5.31	0.81	9.2	1.0	0.0	97.5	1.4E-02	3.2E-02	4.92	1.42	11.3	1.4	0.3	84.9	-1.0E-03	1.3E-03	1.46	1.09	11.5	0.3
F19	2014-02-25	1.7	43.2	1.2E-04	1.1E-04	-0.50	0.52	10.0	0.2	0.5	48.2	3.9E-02	3.2E-02	4.55	0.53	12.3	1.5	3.2	20.6	-2.2E-03	1.4E-02	3.28	5.20	10.8	0.9
F20	2014-03-10	0.7	70.9	1.3E-04	1.0E-04	-0.57	0.45	9.9	0.2	0.6	44.9	2.4E-02	3.0E-02	4.15	0.89	11.5	1.5	4.7	9.5	-1.0E-02	2.3E-02	4.42	1.65	10.3	1.0
F21	2014-03-26	27.3	0.0	-7.4E-02	2.4E-02	5.93	0.66	7.4	0.9	0.0	89.7	8.2E-03	2.3E-02	3.42	2.31	10.6	1.5	3.0	22.2	-1.6E-02	2.2E-02	4.57	1.01	10.0	1.0
F22	2014-04-07	11.7	0.3	-1.1E-02	2.3E-02	4.68	1.55	10.1	1.0	0.0	88.7	5.2E-02	3.5E-02	5.43	0.57	12.9	1.5	2.9	23.1	-1.4E-03	1.8E-03	1.66	1.10	11.6	0.4
F23	2014-04-23	12.2	0.2	-5.8E-02	2.4E-02	5.75	0.71	7.9	0.9	3.1	7.7	-2.9E-02	4.4E-02	7.09	7.10	9.4	1.3	0.7	69.7	-5.7E-03	1.7E-02	3.64	2.41	10.7	1.0
F24	2014-05-08	8.9	1.2	-5.4E-02	2.3E-02	5.45	0.54	7.7	0.9	0.7	38.9	-1.8E-02	3.3E-02	6.72	7.63	9.4	1.3	0.3	87.1	-4.5E-03	1.1E-02	3.00	2.09	10.5	0.8
F25	2014-05-20	0.4	81.5	3.4E-04	2.1E-04	0.09	0.38	10.2	0.2	0.2	66.8	2.3E-03	9.9E-03	1.91	3.98	10.6	1.2	0.1	94.9	8.3E-05	3.0E-04	0.36	2.31	11.3	0.3
F26	2014-06-03	15.1	0.1	-7.9E-02	2.3E-02	5.73	0.49	7.3	0.9	3.5	6.0	-4.6E-02	3.3E-02	6.76	3.05	9.0	1.2	0.7	70.1	-2.4E-02	2.2E-02	4.64	0.70	9.9	1.0
F27	2014-06-16	29.1	0.0	-8.3E-02	2.2E-02	5.50	0.37	6.5	0.8	4.5	3.4	-2.8E-02	3.3E-02	6.76	5.05	9.0	1.2	4.1	12.6	-3.4E-02	2.2E-02	4.64	0.48	8.9	0.9
F29	2014-07-03	9.5	0.9	-4.0E-02	2.1E-02	4.82	0.42	7.8	0.9	1.9	17.1	-5.8E-03	2.5E-02	4.06	3.17	9.6	1.3	2.0	36.3	-7.2E-03	1.0E-02	2.95	1.25	10.3	0.8
F30	2014-07-15	6.3	4.2	-3.7E-03	1.8E-02	3.71	3.81	9.8	1.0	2.8	9.3	-2.1E-04	6.2E-03	1.36	27.91	10.1	1.0	3.2	19.9	-8.4E-04	6.4E-04	0.98	0.58	11.1	0.3
F31	2014-07-23	0.4	81.6	-5.4E-04	1.3E-03	1.46	2.01	10.2	0.3	0.4	53.6	-1.2E-03	1.3E-02	2.24	9.73	10.1	1.4	1.1	58.7	-5.2E-04	2.8E-04	0.33	0.34	11.3	0.3
F32	2014-08-05	0.0	97.6	-7.9E-04	1.1E-03	1.37	1.18	10.4	0.3	0.0	93.2	-2.7E-03	1.5E-02	2.51	4.91	10.2	1.4	0.5	76.6	-6.9E-04	3.1E-04	0.44	0.29	11.5	0.3
F33	2014-08-19	1.4	48.9	-2.7E-04	5.4E-04	0.86	1.46	10.3	0.3	1.4	23.8	-7.2E-04	8.9E-03	1.80	11.48	10.3	1.1	2.2	33.4	-4.6E-04	2.4E-04	0.23	0.33	11.4	0.3
F34	2014-09-03	0.4	83.0	-1.6E-03	1.7E-03	1.65	0.93	10.5	0.4	0.4	54.9	-1.0E-03	5.7E-03	1.24	5.22	10.6	1.0	0.7	70.9	-1.0E-03	4.0E-04	0.65	0.27	11.7	0.3
F35	2014-09-15	0.2	92.6	-1.3E-03	2.4E-03	1.87	1.62	10.4	0.4	0.1	74.2	-4.0E-04	3.6E-03	0.73	8.72	10.5	0.8	0.3	86.2	-7.7E-04	3.6E-04	0.55	0.31	11.5	0.3
F36	2014-09-29	0.6	73.7	-7.0E-03	1.1E-02	3.00	1.29	9.7	0.8	0.5	47.2	-1.0E-02	2.1E-02	3.32	1.64	9.5	1.4	2.4	30.5	-1.3E-03	5.3E-04	0.85	0.30	11.4	0.3
F36b	2014-10-06	2.7	25.8	-7.3E-04	4.4E-04	0.73	0.43	10.9	0.3	1.8	18.2	-6.1E-03	1.6E-02	2.70	2.37	10.3	1.4	4.4	10.9	-8.7E-04	2.9E-04	0.38	0.21	12.0	0.3
F37	2014-10-16	0.6	72.5	-5.4E-04	2.6E-04	0.30	0.30	10.9	0.3	0.2	63.8	-3.9E-03	1.2E-02	2.17	2.80	10.4	1.3	1.5	46.2	-7.9E-04	2.3E-04	0.19	0.18	12.0	0.3
F38	2014-10-28																								
F39	2014-11-13	0.9	63.3	-9.8E-04	3.3E-04	0.52	0.22	10.9	0.3	0.6	42.9	-3.1E-03	7.7E-03	1.61	2.31	10.6	1.1	1.8	41.1	-1.2E-03	2.7E-04	0.35	0.15	12.0	0.3
F40	2014-11-25	2.7	26.1	-1.7E-03	6.4E-04	1.01	0.29	10.3	0.3	0.6	45.3	-1.7E-02	1.9E-02	3.10	0.96	8.9	1.3	4.6	10.2	-1.6E-03	3.8E-04	0.62	0.17	11.4	0.3
F41	2014-12-09	1.6	45.7	-7.9E-04	2.9E-04	0.42	0.24	11.0	0.3	0.2	63.4	-1.1E-02	1.9E-02	2.86	1.48	9.8	1.5	2.8	24.1	-1.0E-03	2.5E-04	0.28	0.16	12.1	0.3
F42	2014-12-18	2.3	31.8	-1.1E-03	4.2E-04	0.69	0.27	10.5	0.3	0.7	39.7	-1.1E-02	1.7E-02	2.80	1.38	9.5	1.4	4.0	13.7	-1.2E-03	3.0E-04	0.44	0.16	11.6	0.3
F43	2015-01-06	0.9	63.0	-1.3E-03	1.0E-03	1.32	0.64	11.0	0.3	0.0	86.5	-1.7E-02	2.2E-02	3.58	1.03	9.8	1.4	1.8	40.0	-1.1E-03	3.7E-04	0.58	0.24	12.2	0.3
F44	2015-01-22	0.9	62.9	-1.2E-02	1.5E-02	3.49	1.02	10.0	0.9	0.4	53.7	-4.9E-03	1.7E-02	2.75	3.03	10.5	1.4	1.2	53.5	-1.7E-03	8.2E-04	1.16	0.38	11.9	0.3
F45	2015-02-03	7.0	3.0	-1.9E-02	2.0E-02	4.15	0.80	9.6	1.0	1.6	21.2	-2.2E-03	1.5E-02	2.55	6.33	10.7	1.4	2.1	34.8	-2.7E-03	2.3E-03	1.81	0.74	11.6	0.4
F46	2015-02-19	0.6	75.5	2.4E-04	1.2E-04	-0.41	0.29	10.0	0.2	0.0	92.5	7.6E-03	1.9E-02	2.85	2.16	10.9	1.5	14.9	0.1	-5.3E-02	2.5E-02	5.69	0.72	9.1	0.9
F47	2015-03-03	0.0	97.6	1.6E-04	1.1E-04	-0.51	0.37	10.1	0.2	0.0	82.7	1.1E-04	1.0E-03	-0.87	8.81	10.1	0.5	6.9	3.2	-3.0E-02	2.4E-02	5.13	0.73	9.8	1.0
F48	2015-03-18	2.2	33.7	2.7E-04	1.4E-04	-0.27	0.30	10.2	0.2	0.5	46.8	1.1E-02	2.2E-02	3.15	1.68	11.4	1.6	7.9	1.9	-5.3E-02	2.7E-02	6.18	1.26	9.7	1.0
F49	2015-03-31	25.3	0.0	-7.0E-02	2.3E-02	5.56	0.46	7.4	0.9	0.0	87.7	4.9E-04	6.0E-03	1.32	11.72	10.3	1.0	2.6	27.1	-2.0E-02	2.1E-02	4.28	0.78	10.0	1.0
F50	2015-04-09	4.9	8.6	2.1E-04	1.2E-04	-0.44	0.31	9.6	0.2	0.1	69.9	7.0E-02	3.7E-02	4.59	0.34	13.6	1.7	20.0	0.0	-1.0E-02	2.8E-02	5.60	3.37	10.1	1.0
F51	2015-04-24	0.5	76.6	1.2E-04	1.1E-04	-0.48	0.51	9.9	0.2	4.2	3.9	-4.1E-02	4.3E-02	7.14	4.72	9.0	1.2	0.9	63.1	-1.8E-02	2.2E-02	4.59	0.91	9.9	1.0
F52	2015-05-08	1.5	46.2	3.1E-04	1.5E-04	-0.23	0.28	9.1	0.2	0.1	74.9	2.6E-02	2.7E-02	3.81	0.79	11.1	1.5	1.2	55.2	7.2E-05	1.0E-04	-0.61	0.76	10.1	0.2
F53	2015-05-22	13.7	0.1	-5.2E-02	3.3E-02	6.80	2.35	8.5	0.9	0.0	90.4	2.1E-02	2.8E-02	4.13	0.97	11.2	1.4	0.7	70.7	-1.8E-04	7.4E-04	1.07	3.18	10.8	0.3
F54	2015-06-08	0.8	67.2	1.3E-04	8.0E-05	-0.82	0.33	9.7	0.2	0.0	92.8	1.3E-02	2.4E-02	3.45	1.50	11.0	1.5	27.6	0.0	-6.4E-02	2.3E-02	5.30	0.39	8.1	0.9
F55	2015-06-19	8.9	1.2	-4.1E-02	2.2E-02	5.08	0.50	8.0	0.9	0.0	86.3	-1.2E-04	1.7E-02	2.71	120.14	9.9	1.4	0.1	95.4	-3.2E-03	5.3E-03	2.37	1.46	10.5	0.6
F56	2015-07-03	2.2	32.7	1.0E-04	1.7E-04	-0.11	0.92	10.2	0.2	0.4	51.7	3.0E-02	3.1E-02	4.59	0.67	11.9	1.4	1.7	43.0	-1.6E-04	2.4E-04	0.18	0.88	11.2	0.3
F57	2015-07-23	0.3	85.5	-2.5E-02	2.6E-02	6.05	2.27	9.7	1.0	1.1	30.2	9.0E-05	1.6E-02	2.66	159.90	10.4	1.4	0.5	76.7	-2.9E-04	2.2E-04	0.13	0.46	11.5	0.3
F58	2015-08-03	2.0	36.6	-1.7E-04	3.7E-04	0.57	1.50	10.3	0.3	1.5	22.8	-4.5E-12	2.2E-08	-17.00	4796.67	10.4	0.3	0.9	63.4	-4.2E-04	2.3E-04	0.18	0.34	11.4	0.3
F59	2015-08-14	3.1	20.7	-7.5E-04	3.9E-04	0.64	0.36	10.1	0.3	1.6	21.2	-1.0E-02	2.0E-02	3.02	1.69	9.2	1.4	5.0	8.1	-9.3E-04	2.8E-04	0.36	0.19	11.2	0.3
F60	2015-08-24	0.6	73.7	-7.8E-04	3.9E-04	0.64	0.35	10.7	0.3	0.1	73.4	-6.3E-03	1.7E-02	2.59	2.32	10.0	1.5	1.5	46.7	-9.5E-04	2.8E-04	0.37	0.19	11.8	0.3
F61	2015-09-08	0.1	93.1	-8.9E-04	3.8E-04	0.62	0.29	10.6	0.3	0.1	70.5	-9.4E-04	3.4E-03	0.68	3.50	10.5	0.8	0.4	81.5	-1.1E-03	2.9E-04	0.39	0.17	11.6	0.3
F62	2015-10-01	7.1	2.8	-8.1E-04	2.8E-04	0.37	0.22	10.6	0.3	7.0	0.8	-1.7E-03	4.9E-03	1.05	2.80	10.4	0.9	7.9	1.9	-1.1E-03	2.4E-04	0.26	0.14	11.6	0.3

Table B.11: Mannheim (shallow well): OD model fit results. The degassing period denotes samples between July 2014 and January 2015 (F31-F44) as well as from August 2015 on (F58-F62).

OD model									
included NGs		He, Ne, Ar, Kr, Xe							
DoF		180							
start values		A = 0.01 ccSTP/g, T = 10°C, P_{OD} = 1							
fixed parameters		p = 0.991 atm, S = 0.72 g/kg							
ID	sampl. date	χ^2	Prob [%]	A [ccSTP/g]	ΔA [ccSTP/g]	P_{OD}	ΔP_{OD}	T [°C]	ΔT [°C]
F1	2013-06-18	277.1	0.0	0.0013	0.0001	0.97	0.01	8.2	0.4
F2	2013-06-27	277.1	0.0	0.0012	0.0001	0.97	0.01	7.9	0.4
F3	2013-07-16	277.1	0.0	0.0010	0.0001	0.97	0.01	8.2	0.4
F4	2013-07-29	277.1	0.0	0.0009	0.0001	0.97	0.01	8.5	0.4
F5	2013-08-14	277.1	0.0	0.0010	0.0001	0.97	0.01	8.4	0.4
F6	2013-08-27	277.1	0.0	0.0008	0.0001	0.97	0.01	9.0	0.4
F7	2013-09-10	277.1	0.0	0.0008	0.0001	0.97	0.01	9.3	0.4
F8	2013-09-24	277.1	0.0	0.0007	0.0001	0.97	0.01	9.3	0.4
F9	2013-10-08	277.1	0.0	0.0008	0.0001	0.97	0.01	9.6	0.4
F10	2013-10-22	277.1	0.0	0.0008	0.0001	0.97	0.01	10.1	0.4
F11	2013-11-05	277.1	0.0	0.0005	0.0001	0.97	0.01	9.7	0.4
F12	2013-11-19	277.1	0.0	0.0005	0.0001	0.97	0.01	9.7	0.4
F13	2013-12-03	277.1	0.0	0.0008	0.0001	0.97	0.01	9.4	0.4
F14	2013-12-17	277.1	0.0	0.0007	0.0001	0.97	0.01	9.2	0.4
F15	2013-12-30	277.1	0.0	0.0006	0.0001	0.97	0.01	9.6	0.4
F16	2014-01-13	277.1	0.0	0.0006	0.0001	0.97	0.01	9.6	0.4
F17	2014-01-28	277.1	0.0	0.0005	0.0001	0.97	0.01	9.6	0.4
F18	2014-02-11	277.1	0.0	0.0004	0.0001	0.97	0.01	9.6	0.4
F19	2014-02-25	277.1	0.0	0.0005	0.0001	0.97	0.01	9.0	0.4
F20	2014-03-10	277.1	0.0	0.0006	0.0001	0.97	0.01	8.9	0.4
F21	2014-03-26	277.1	0.0	0.0006	0.0001	0.97	0.01	8.9	0.4
F22	2014-04-07	277.1	0.0	0.0004	0.0001	0.97	0.01	9.8	0.4
F23	2014-04-23	277.1	0.0	0.0005	0.0001	0.97	0.01	9.0	0.4
F24	2014-05-08	277.1	0.0	0.0004	0.0001	0.97	0.01	8.9	0.4
F25	2014-05-20	277.1	0.0	0.0006	0.0001	0.97	0.01	9.1	0.4
F26	2014-06-03	277.1	0.0	0.0005	0.0001	0.97	0.01	9.1	0.4
F27	2014-06-16	277.1	0.0	0.0006	0.0001	0.97	0.01	8.9	0.4
F29	2014-07-03	277.1	0.0	0.0004	0.0001	0.97	0.01	9.1	0.4
F30	2014-07-15	277.1	0.0	0.0003	0.0001	0.97	0.01	9.2	0.4
F31	2014-07-23	277.1	0.0	0.0002	0.0001	0.97	0.01	9.2	0.4
F32	2014-08-05	277.1	0.0	0.0002	0.0001	0.97	0.01	9.5	0.4
F33	2014-08-19	277.1	0.0	0.0002	0.0001	0.97	0.01	9.3	0.4
F34	2014-09-03	277.1	0.0	0.0001	0.0001	0.97	0.01	9.8	0.4
F35	2014-09-15	277.1	0.0	0.0002	0.0001	0.97	0.01	9.6	0.4
F36	2014-09-29	277.1	0.0	0.0002	0.0001	0.97	0.01	9.6	0.4
F36b	2014-10-06	277.1	0.0	0.0000	0.0001	0.97	0.01	10.0	0.4
F37	2014-10-16	277.1	0.0	-0.0001	0.0001	0.97	0.01	9.9	0.4
F38	2014-10-28								
F39	2014-11-13	277.1	0.0	-0.0002	0.0001	0.97	0.01	10.1	0.4
F40	2014-11-25	277.1	0.0	-0.0001	0.0001	0.97	0.01	9.7	0.4
F41	2014-12-09	277.1	0.0	-0.0001	0.0001	0.97	0.01	10.1	0.4
F42	2014-12-18	277.1	0.0	-0.0001	0.0001	0.97	0.01	9.8	0.4
F43	2015-01-06	277.1	0.0	0.0001	0.0001	0.97	0.01	10.3	0.4
F44	2015-01-22	277.1	0.0	0.0002	0.0001	0.97	0.01	10.3	0.4
F45	2015-02-03	277.1	0.0	0.0003	0.0001	0.97	0.01	10.1	0.4
F46	2015-02-19	277.1	0.0	0.0007	0.0001	0.97	0.01	9.1	0.4
F47	2015-03-03	277.1	0.0	0.0006	0.0001	0.97	0.01	9.2	0.4
F48	2015-03-18	277.1	0.0	0.0007	0.0001	0.97	0.01	9.2	0.4
F49	2015-03-31	277.1	0.0	0.0005	0.0001	0.97	0.01	9.3	0.4
F50	2015-04-09	277.1	0.0	0.0007	0.0001	0.97	0.01	8.7	0.4
F51	2015-04-24	277.1	0.0	0.0005	0.0001	0.97	0.01	8.9	0.4
F52	2015-05-08	277.1	0.0	0.0007	0.0001	0.97	0.01	8.1	0.4
F53	2015-05-22	277.1	0.0	0.0005	0.0001	0.97	0.01	8.7	0.4
F54	2015-06-08	277.1	0.0	0.0008	0.0001	0.97	0.01	8.9	0.4
F55	2015-06-19	277.1	0.0	0.0004	0.0001	0.97	0.01	9.0	0.4
F56	2015-07-03	277.1	0.0	0.0004	0.0001	0.97	0.01	9.1	0.4
F57	2015-07-23	277.1	0.0	0.0003	0.0001	0.97	0.01	9.3	0.4
F58	2015-08-03	277.1	0.0	0.0002	0.0001	0.97	0.01	9.3	0.4
F59	2015-08-14	277.1	0.0	0.0000	0.0001	0.97	0.01	9.2	0.4
F60	2015-08-24	277.1	0.0	0.0000	0.0001	0.97	0.01	9.8	0.4
F61	2015-09-08	277.1	0.0	-0.0001	0.0001	0.97	0.01	9.7	0.4
F62	2015-10-01	277.1	0.0	-0.0002	0.0001	0.97	0.01	9.7	0.4

Table B.12: Mannheim (shallow well): GR model fit results.

GR model		including He data										not including He data									
included NGs		He, Ne, Ar, Kr, Xe										Ne, Ar, Kr, Xe									
DoF		179										118									
start values		$A = 0.01$ ccSTP/g, $T = 10°C$, $F_{GR} = 1$,$P_{GR} = 1$										$A = 0.01$ ccSTP/g, $T = 10°C$, $F_{GR} = 1$,$P_{GR} = 1$									
fixed parameters		$p = 0.991$ atm, $S = 0.72$ g/kg, $\beta = 2/3$										$p = 0.991$ atm, $S = 0.72$ g/kg, $\beta = 2/3$									
ID	sampl. date	χ^2	Prob [%]	A [ccSTP/g]	ΔA [ccSTP/g]	P_{GR}	ΔP_{GR}	F_{GR}	ΔF_{GR}	T [°C]	ΔT [°C]	χ^2	Prob [%]	A [ccSTP/g]	ΔA [ccSTP/g]	P_{GR}	ΔP_{GR}	F_{GR}	ΔF_{GR}	T [°C]	ΔT [°C]
F1	2013-06-18	268.1	0.0	0.001	0.000	1.06	0.01	0.93	0.11	11.4	0.3	73.3	100.0	-0.049	0.018	1.46	0.16	6.10	0.35	19.0	2.8
F2	2013-06-27	268.1	0.0	0.001	0.000	1.06	0.01	0.93	0.11	11.1	0.3	73.3	100.0	-0.050	0.017	1.46	0.16	6.10	0.35	18.6	2.8
F3	2013-07-16	268.1	0.0	0.001	0.000	1.06	0.01	0.93	0.11	11.3	0.3	73.3	100.0	-0.051	0.017	1.46	0.16	6.10	0.35	18.9	2.8
F4	2013-07-29	268.1	0.0	0.000	0.000	1.06	0.01	0.93	0.11	11.6	0.3	73.3	100.0	-0.056	0.017	1.46	0.16	6.10	0.35	18.8	2.8
F5	2013-08-14	268.1	0.0	0.000	0.000	1.06	0.01	0.93	0.11	11.5	0.3	73.3	100.0	-0.054	0.017	1.46	0.16	6.10	0.35	18.8	2.8
F6	2013-08-27	268.1	0.0	0.000	0.000	1.06	0.01	0.93	0.11	12.1	0.3	73.3	100.0	-0.058	0.017	1.46	0.16	6.10	0.35	19.2	2.8
F7	2013-09-10	268.1	0.0	0.000	0.000	1.06	0.01	0.93	0.11	12.5	0.3	73.3	100.0	-0.057	0.017	1.46	0.16	6.10	0.35	19.7	2.8
F8	2013-09-24	268.1	0.0	0.000	0.000	1.06	0.01	0.93	0.11	12.4	0.3	73.3	100.0	-0.059	0.017	1.46	0.16	6.10	0.35	19.5	2.8
F9	2013-10-08	268.1	0.0	0.000	0.000	1.06	0.01	0.93	0.11	12.8	0.3	73.3	100.0	-0.058	0.017	1.46	0.16	6.10	0.35	19.9	2.8
F10	2013-10-22	268.1	0.0	0.000	0.000	1.06	0.01	0.93	0.11	13.2	0.3	73.3	100.0	-0.061	0.016	1.46	0.16	6.10	0.35	19.9	2.8
F11	2013-11-05	268.1	0.0	0.000	0.000	1.06	0.01	0.93	0.11	12.8	0.3	73.3	100.0	-0.066	0.016	1.46	0.16	6.10	0.35	19.4	2.8
F12	2013-11-19	268.1	0.0	0.000	0.000	1.06	0.01	0.93	0.11	12.8	0.3	73.3	100.0	-0.063	0.016	1.46	0.16	6.10	0.35	19.7	2.8
F13	2013-12-03	268.1	0.0	0.000	0.000	1.06	0.01	0.93	0.11	12.5	0.3	73.3	100.0	-0.061	0.016	1.46	0.16	6.10	0.35	19.3	2.8
F14	2013-12-17	268.1	0.0	0.000	0.000	1.06	0.01	0.93	0.11	12.3	0.3	73.3	100.0	-0.063	0.016	1.46	0.16	6.10	0.35	18.9	2.8
F15	2013-12-30	268.1	0.0	0.000	0.000	1.06	0.01	0.93	0.11	12.6	0.3	73.3	100.0	-0.062	0.016	1.46	0.16	6.10	0.35	19.5	2.8
F16	2014-01-13	268.1	0.0	0.000	0.000	1.06	0.01	0.93	0.11	12.7	0.3	73.3	100.0	-0.062	0.016	1.46	0.16	6.10	0.35	19.6	2.8
F17	2014-01-28	268.1	0.0	0.000	0.000	1.06	0.01	0.93	0.11	12.7	0.3	73.3	100.0	-0.065	0.016	1.46	0.16	6.10	0.35	19.3	2.8
F18	2014-02-11	268.1	0.0	-0.001	0.000	1.06	0.01	0.93	0.11	12.7	0.3	73.3	100.0	-0.067	0.016	1.46	0.16	6.10	0.35	19.3	2.8
F19	2014-02-25	268.1	0.0	0.000	0.000	1.06	0.01	0.93	0.11	12.1	0.3	73.3	100.0	-0.063	0.016	1.46	0.16	6.10	0.35	18.9	2.8
F20	2014-03-10	268.1	0.0	0.000	0.000	1.06	0.01	0.93	0.11	12.0	0.3	73.3	100.0	-0.063	0.016	1.46	0.16	6.10	0.35	18.8	2.8
F21	2014-03-26	268.1	0.0	0.000	0.000	1.06	0.01	0.93	0.11	11.9	0.3	73.3	100.0	-0.063	0.016	1.46	0.16	6.10	0.35	18.7	2.8
F22	2014-04-07	268.1	0.0	-0.001	0.000	1.06	0.01	0.93	0.11	12.8	0.3	73.3	100.0	-0.067	0.016	1.46	0.16	6.10	0.35	19.4	2.8
F23	2014-04-23	268.1	0.0	0.000	0.000	1.06	0.01	0.93	0.11	12.1	0.3	73.3	100.0	-0.064	0.016	1.46	0.16	6.10	0.35	18.9	2.8
F24	2014-05-08	268.1	0.0	-0.001	0.000	1.06	0.01	0.93	0.11	11.9	0.3	73.3	100.0	-0.065	0.016	1.46	0.16	6.10	0.35	18.6	2.8
F25	2014-05-20	268.1	0.0	0.000	0.000	1.06	0.01	0.93	0.11	12.2	0.3	73.3	100.0	-0.061	0.016	1.46	0.16	6.10	0.35	19.2	2.8
F26	2014-06-03	268.1	0.0	0.000	0.000	1.06	0.01	0.93	0.11	12.2	0.3	73.3	100.0	-0.064	0.016	1.46	0.16	6.10	0.35	19.0	2.8
F27	2014-06-16	268.1	0.0	0.000	0.000	1.06	0.01	0.93	0.11	11.9	0.3	73.3	100.0	-0.064	0.016	1.46	0.16	6.10	0.35	18.6	2.8
F29	2014-07-03	268.1	0.0	-0.001	0.000	1.06	0.01	0.93	0.11	12.1	0.3	73.3	100.0	-0.068	0.015	1.46	0.16	6.10	0.35	18.5	2.8
F30	2014-07-15	268.1	0.0	-0.001	0.000	1.06	0.01	0.93	0.11	12.2	0.3	73.3	100.0	-0.068	0.015	1.46	0.16	6.10	0.35	18.7	2.8
F31	2014-07-23	268.1	0.0	-0.001	0.000	1.06	0.01	0.93	0.11	12.1	0.3	73.3	100.0	-0.069	0.015	1.46	0.16	6.10	0.35	18.7	2.8
F32	2014-08-05	268.1	0.0	-0.001	0.000	1.06	0.01	0.93	0.11	12.4	0.3	73.3	100.0	-0.071	0.015	1.46	0.16	6.10	0.35	18.9	2.8
F33	2014-08-19	268.1	0.0	-0.001	0.000	1.06	0.01	0.93	0.11	12.3	0.3	73.3	100.0	-0.069	0.015	1.46	0.16	6.10	0.35	18.8	2.8
F34	2014-09-03	268.1	0.0	-0.001	0.000	1.06	0.01	0.93	0.11	12.7	0.3	73.3	100.0	-0.073	0.015	1.46	0.16	6.10	0.35	19.0	2.8
F35	2014-09-15	268.1	0.0	-0.001	0.000	1.06	0.01	0.93	0.11	12.5	0.3	73.3	100.0	-0.071	0.015	1.46	0.16	6.10	0.35	18.9	2.8
F36	2014-09-29	268.1	0.0	-0.001	0.000	1.06	0.01	0.93	0.11	12.5	0.3	73.3	100.0	-0.072	0.015	1.46	0.16	6.10	0.35	18.8	2.8
F36b	2014-10-06	268.1	0.0	-0.001	0.000	1.06	0.01	0.93	0.11	12.9	0.3	73.3	100.0	-0.074	0.015	1.46	0.16	6.10	0.35	19.2	2.9
F37	2014-10-16	268.1	0.0	-0.001	0.000	1.06	0.01	0.93	0.11	12.8	0.3	73.3	100.0	-0.075	0.015	1.46	0.16	6.10	0.35	19.1	2.9
F38	2014-10-28																				
F39	2014-11-13	268.1	0.0	-0.002	0.000	1.06	0.01	0.93	0.11	12.9	0.3	73.3	100.0	-0.078	0.014	1.46	0.16	6.10	0.35	18.9	2.9
F40	2014-11-25	268.1	0.0	-0.002	0.000	1.06	0.01	0.93	0.11	12.6	0.3	73.3	100.0	-0.078	0.014	1.46	0.16	6.10	0.35	18.5	2.9
F41	2014-12-09	268.1	0.0	-0.002	0.000	1.06	0.01	0.93	0.11	12.9	0.3	73.3	100.0	-0.077	0.015	1.46	0.16	6.10	0.35	19.0	2.9
F42	2014-12-18	268.1	0.0	-0.002	0.000	1.06	0.01	0.93	0.11	12.6	0.3	73.3	100.0	-0.077	0.014	1.46	0.16	6.10	0.35	18.6	2.9
F43	2015-01-06	268.1	0.0	-0.001	0.000	1.06	0.01	0.93	0.11	13.2	0.3	73.3	100.0	-0.074	0.015	1.46	0.16	6.10	0.35	19.4	2.9
F44	2015-01-22	268.1	0.0	-0.001	0.000	1.06	0.01	0.93	0.11	13.2	0.3	73.3	100.0	-0.072	0.015	1.46	0.16	6.10	0.35	19.4	2.8
F45	2015-02-03	268.1	0.0	-0.001	0.000	1.06	0.01	0.93	0.11	13.1	0.3	73.3	100.0	-0.070	0.015	1.46	0.16	6.10	0.35	19.4	2.8
F46	2015-02-19	268.1	0.0	0.000	0.000	1.06	0.01	0.93	0.11	12.1	0.3	73.3	100.0	-0.060	0.016	1.46	0.16	6.10	0.35	19.1	2.8
F47	2015-03-03	268.1	0.0	0.000	0.000	1.06	0.01	0.93	0.11	12.2	0.3	73.3	100.0	-0.062	0.016	1.46	0.16	6.10	0.35	19.1	2.8
F48	2015-03-18	268.1	0.0	0.000	0.000	1.06	0.01	0.93	0.11	12.3	0.3	73.3	100.0	-0.060	0.016	1.46	0.16	6.10	0.35	19.3	2.8
F49	2015-03-31	268.1	0.0	0.000	0.000	1.06	0.01	0.93	0.11	12.3	0.3	73.3	100.0	-0.065	0.016	1.46	0.16	6.10	0.35	19.0	2.8
F50	2015-04-09	268.1	0.0	0.000	0.000	1.06	0.01	0.93	0.11	11.7	0.3	73.3	100.0	-0.061	0.016	1.46	0.16	6.10	0.35	18.6	2.8
F51	2015-04-24	268.1	0.0	0.000	0.000	1.06	0.01	0.93	0.11	12.0	0.3	73.3	100.0	-0.063	0.016	1.46	0.16	6.10	0.35	18.8	2.8
F52	2015-05-08	268.1	0.0	0.000	0.000	1.06	0.01	0.93	0.11	11.1	0.3	73.3	100.0	-0.059	0.016	1.46	0.16	6.10	0.35	18.2	2.8
F53	2015-05-22	268.1	0.0	0.000	0.000	1.06	0.01	0.93	0.11	11.7	0.3	73.3	100.0	-0.063	0.016	1.46	0.16	6.10	0.35	18.7	2.8
F54	2015-06-08	268.1	0.0	0.000	0.000	1.06	0.01	0.93	0.11	12.0	0.3	73.3	100.0	-0.061	0.016	1.46	0.16	6.10	0.35	18.8	2.8
F55	2015-06-19	268.1	0.0	-0.001	0.000	1.06	0.01	0.93	0.11	11.9	0.3	73.3	100.0	-0.067	0.016	1.46	0.16	6.10	0.35	18.5	2.8
F56	2015-07-03	268.1	0.0	-0.001	0.000	1.06	0.01	0.93	0.11	12.1	0.3	73.3	100.0	-0.065	0.016	1.46	0.16	6.10	0.35	18.9	2.8
F57	2015-07-23	268.1	0.0	-0.001	0.000	1.06	0.01	0.93	0.11	12.3	0.3	73.3	100.0	-0.067	0.016	1.46	0.16	6.10	0.35	19.0	2.8
F58	2015-08-03	268.1	0.0	-0.001	0.000	1.06	0.01	0.93	0.11	12.2	0.3	73.3	100.0	-0.069	0.015	1.46	0.16	6.10	0.35	18.9	2.8
F59	2015-08-14	268.1	0.0	-0.001	0.000	1.06	0.01	0.93	0.11	12.1	0.3	73.3	100.0	-0.074	0.015	1.46	0.16	6.10	0.35	18.3	2.9
F60	2015-08-24	268.1	0.0	-0.001	0.000	1.06	0.01	0.93	0.11	12.7	0.3	73.3	100.0	-0.075	0.015	1.46	0.16	6.10	0.35	18.9	2.9
F61	2015-09-08	268.1	0.0	-0.002	0.000	1.06	0.01	0.93	0.11	12.5	0.3	73.3	100.0	-0.076	0.015	1.46	0.16	6.10	0.35	18.7	2.9
F62	2015-10-01	268.1	0.0	-0.002	0.000	1.06	0.01	0.93	0.11	12.5	0.3	73.3	100.0	-0.078	0.014	1.46	0.16	6.10	0.35	18.5	2.9

B.10 Mannheim: Results of excess air model fits (deep well)

Table B.13: Mannheim (deep well): UA model fit results.

UA model		X/X_{atm} = 1.000					
included NGs		He, Ne, Ar, Kr, Xe					
DoF		3					
start values		A = 0.01 ccSTP/g, T = 10°C					
fixed parameters		p = 0.991 · 1.000 atm, S = 0.72 g/kg					
ID	sampl. date	χ^2	Prob [%]	A [ccSTP/g]	ΔA [ccSTP/g]	T [°C]	ΔT [°C]
F0	2013-03-20	3.6	31.4	0.001	0.000	9.7	0.2
F2	2013-06-27	0.1	99.3	0.001	0.000	9.2	0.2
F4	2013-07-29	0.5	91.8	0.001	0.000	9.3	0.2
F6	2013-08-27	1.1	78.4	0.001	0.000	9.2	0.2
F8	2013-09-24	0.5	92.3	0.001	0.000	9.2	0.2
F10	2013-10-22	11.9	0.8	0.002	0.000	9.3	0.2
F12	2013-11-19	2.2	54.0	0.001	0.000	9.4	0.2
F14	2013-12-17	1.0	80.8	0.001	0.000	9.3	0.2
F16	2014-01-13	2.2	53.7	0.001	0.000	9.5	0.2
F18	2014-02-11	1.6	65.9	0.001	0.000	9.6	0.2
F20	2014-03-10	0.9	82.6	0.001	0.000	9.5	0.2
F22	2014-04-07	0.6	89.1	0.001	0.000	9.2	0.2
F24	2014-05-08	2.0	56.4	0.002	0.000	9.5	0.2
F26	2014-06-03	0.8	83.8	0.001	0.000	9.3	0.2
F29	2014-07-03	0.7	87.3	0.001	0.000	8.9	0.2
F31	2014-07-23	0.2	98.2	0.001	0.000	9.3	0.2
F33	2014-08-19	1.1	77.2	0.002	0.000	9.4	0.2
F35	2014-09-15	3.1	37.7	0.001	0.000	9.3	0.2
F37	2014-10-16	3.5	31.9	0.001	0.000	9.6	0.2
F39	2014-11-13	2.9	40.2	0.001	0.000	9.0	0.2
F41	2014-12-03	0.7	86.7	0.001	0.000	9.3	0.2
F43	2015-01-06	0.5	91.0	0.001	0.000	9.4	0.2
F45	2015-02-03	0.9	81.6	0.001	0.000	9.6	0.2
F47	2015-03-03	1.2	75.5	0.001	0.000	9.4	0.2
F49	2015-03-31	1.4	70.1	0.001	0.000	9.4	0.2
F51	2015-04-24	3.8	28.5	0.001	0.000	9.4	0.2
F53	2015-05-22	1.7	64.8	0.001	0.000	9.6	0.2
F55	2015-06-19	4.8	18.9	0.001	0.000	9.4	0.2
F57	2015-07-23	4.7	19.2	0.001	0.000	9.7	0.2
F59	2015-08-14	0.9	83.0	0.001	0.000	9.5	0.2
F61	2015-09-08	0.4	93.5	0.001	0.000	9.5	0.2
F62	2015-10-01	3.9	27.0	0.001	0.000	9.4	0.2

Table B.14: Mannheim (deep well): CE model fit results.

CE model		X/X_{atm} = 1.000								fit for given WTT			
included NGs		He, Ne, Ar, Kr, Xe								He, Ne, Ar, Kr, Xe			
DoF		2								2			
start values		A = 0.01 ccSTP/g, T = 10°C, F_{CE} = 0								$p*$ = 0.991 atm, A = 0.01 ccSTP/g, F_{CE} = 0			
fixed parameters		p = 0.991 · 1.000 atm, S = 0.72 g/kg								S = 0.72 g/kg, T = WTT			
ID	sampl. date	χ^2	Prob [%]	A [ccSTP/g]	ΔA [ccSTP/g]	F_{CE}	ΔF_{CE}	T [°C]	ΔT [°C]	χ^2	Prob [%]	$p*$	$\Delta p*$
F0	2013-03-20	3.0	21.9	5.9E-03	7.5E-03	0.706	0.225	10.0	0.5	3.0	22.1	1.01	0.02
F2	2013-06-27	0.1	95.7	1.2E-03	5.8E-05	0.000	0.000	9.2	0.2	0.5	76.7	1.03	0.01
F4	2013-07-29	0.5	77.7	1.2E-03	5.8E-05	0.000	0.000	9.3	0.2	0.4	81.8	1.03	0.01
F6	2013-08-27	1.1	58.6	1.3E-03	5.9E-05	0.000	0.000	9.2	0.2	2.1	34.4	1.03	0.01
F8	2013-09-24	0.4	80.6	2.4E-03	4.8E-03	0.415	0.945	9.2	0.4	0.1	95.9	1.03	0.01
F10	2013-10-22	7.1	2.9	1.6E-02	7.9E-03	0.697	0.054	10.5	0.6	6.9	3.1	1.00	0.02
F12	2013-11-19	2.2	33.9	1.1E-03	5.7E-05	0.000	0.000	9.4	0.2	2.0	37.4	1.02	0.01
F14	2013-12-17	1.0	61.6	1.3E-03	5.9E-05	0.000	0.000	9.3	0.2	0.8	67.1	1.02	0.01
F16	2014-01-13	1.3	53.3	8.3E-03	7.9E-03	0.733	0.132	9.9	0.5	0.9	63.4	1.01	0.02
F18	2014-02-11	0.8	68.2	7.8E-03	8.1E-03	0.734	0.147	10.0	0.5	0.5	76.4	1.01	0.02
F20	2014-03-10	0.8	67.9	3.1E-03	4.9E-03	0.488	0.597	9.7	0.4	0.4	82.4	1.02	0.01
F22	2014-04-07	0.1	95.1	4.9E-03	5.5E-03	0.603	0.290	9.5	0.4	0.0	97.7	1.02	0.01
F24	2014-05-08	0.1	93.2	8.3E-03	6.1E-03	0.663	0.128	10.0	0.5	0.1	96.7	1.01	0.02
F26	2014-06-03	0.8	65.4	1.3E-03	5.9E-05	0.000	0.000	9.3	0.2	1.5	46.4	1.02	0.01
F29	2014-07-03	0.7	70.5	1.2E-03	5.8E-05	0.000	0.000	8.9	0.2	1.8	41.1	1.04	0.01
F31	2014-07-23	0.2	92.6	1.8E-03	5.2E-03	0.346	1.619	9.3	0.4	0.2	89.1	1.03	0.01
F33	2014-08-19	1.0	60.6	3.1E-03	4.3E-03	0.435	0.579	9.5	0.4	0.5	79.2	1.02	0.01
F35	2014-09-15	3.1	21.3	1.1E-03	5.8E-05	0.000	0.000	9.3	0.2	3.0	22.1	1.02	0.01
F37	2014-10-16	1.4	50.4	1.6E-02	1.4E-02	0.818	0.053	10.4	0.6	1.3	51.9	1.00	0.02
F39	2014-11-13	2.9	23.1	1.4E-03	5.9E-05	0.000	0.000	9.0	0.2	5.4	6.8	1.03	0.01
F41	2014-12-03	0.7	69.5	1.1E-03	5.8E-05	0.000	0.000	9.3	0.2	1.4	50.2	1.02	0.01
F43	2015-01-06	0.1	94.3	5.1E-03	7.3E-03	0.687	0.284	9.7	0.5	0.0	98.4	1.02	0.02
F45	2015-02-03	0.9	62.6	1.2E-03	5.8E-05	0.000	0.000	9.6	0.2	0.9	64.7	1.02	0.01
F47	2015-03-03	0.3	85.0	7.6E-03	8.3E-03	0.742	0.152	9.8	0.5	0.1	93.6	1.02	0.02
F49	2015-03-31	1.2	54.1	4.1E-03	6.2E-03	0.627	0.389	9.6	0.4	0.6	72.6	1.02	0.01
F51	2015-04-24	3.8	15.0	1.3E-03	5.9E-05	0.000	0.000	9.4	0.2	5.5	6.4	1.02	0.01
F53	2015-05-22	0.1	93.3	1.2E-02	1.3E-02	0.820	0.082	10.2	0.6	0.1	94.7	1.00	0.02
F55	2015-06-19	4.8	9.2	1.2E-03	5.8E-05	0.000	0.000	9.4	0.2	4.3	11.6	1.02	0.01
F57	2015-07-23	0.3	87.1	2.3E-02	1.9E-02	0.836	0.036	10.8	0.7	0.3	84.8	0.98	0.03
F59	2015-08-14	0.2	91.9	5.7E-03	7.5E-03	0.706	0.234	9.8	0.5	0.4	83.8	1.01	0.02
F61	2015-09-08	0.4	80.8	1.1E-03	5.8E-05	0.000	0.000	9.5	0.2	1.1	58.9	1.02	0.01
F62	2015-10-01	3.3	19.0	5.5E-03	7.2E-03	0.699	0.243	9.7	0.5	3.2	20.4	1.02	0.02

Table B.15: Mannheim (deep well): PR model fit results.

PR model									
included NGs		He, Ne, Ar, Kr, Xe							
DoF		2							
start values		A = 0.01 ccSTP/g, T = 10°C, F_{PR} = 0							
fixed parameters		p = 0.991 atm, S = 0.72 g/kg, β = 1							
ID	sampl. date	χ^2	Prob [%]	A [ccSTP/g]	ΔA [ccSTP/g]	F_{PR}	ΔF_{PR}	T [°C]	ΔT [°C]
F0	2013-03-20	3.5	17.3	0.001	0.000	0.02	0.10	9.7	0.3
F2	2013-06-27	0.1	97.3	0.001	0.000	-0.02	0.10	9.2	0.2
F4	2013-07-29	0.3	87.6	0.001	0.000	-0.05	0.11	9.2	0.2
F6	2013-08-27	0.3	84.3	0.001	0.000	-0.08	0.10	9.1	0.2
F8	2013-09-24	0.5	78.8	0.001	0.000	-0.01	0.10	9.1	0.2
F10	2013-10-22	11.6	0.3	0.002	0.000	0.04	0.07	9.3	0.3
F12	2013-11-19	0.6	73.8	0.001	0.000	-0.15	0.12	9.2	0.2
F14	2013-12-17	0.6	74.4	0.001	0.000	-0.06	0.10	9.3	0.2
F16	2014-01-13	2.2	33.9	0.001	0.000	0.01	0.09	9.5	0.2
F18	2014-02-11	1.6	46.0	0.001	0.000	0.02	0.10	9.6	0.2
F20	2014-03-10	0.9	64.0	0.001	0.000	-0.01	0.09	9.5	0.2
F22	2014-04-07	0.4	80.8	0.002	0.000	0.04	0.08	9.3	0.2
F24	2014-05-08	1.3	52.2	0.002	0.000	0.06	0.07	9.6	0.3
F26	2014-06-03	0.6	72.6	0.001	0.000	-0.04	0.10	9.3	0.2
F29	2014-07-03	0.3	87.8	0.001	0.000	-0.07	0.10	8.8	0.2
F31	2014-07-23	0.2	92.4	0.001	0.000	0.01	0.11	9.3	0.2
F33	2014-08-19	1.1	58.2	0.002	0.000	-0.02	0.08	9.4	0.2
F35	2014-09-15	1.5	47.3	0.001	0.000	-0.14	0.11	9.2	0.2
F37	2014-10-16	3.3	19.0	0.001	0.000	0.04	0.10	9.7	0.2
F39	2014-11-13	2.7	25.5	0.001	0.000	-0.04	0.09	8.9	0.2
F41	2014-12-03	0.7	69.8	0.001	0.000	-0.01	0.11	9.3	0.2
F43	2015-01-06	0.4	83.3	0.001	0.000	0.04	0.10	9.5	0.3
F45	2015-02-03	0.2	90.4	0.001	0.000	-0.09	0.11	9.5	0.2
F47	2015-03-03	1.0	59.9	0.001	0.000	0.04	0.10	9.4	0.2
F49	2015-03-31	1.4	50.0	0.001	0.000	-0.02	0.10	9.4	0.2
F51	2015-04-24	3.1	21.4	0.001	0.000	-0.08	0.10	9.3	0.2
F53	2015-05-22	1.2	55.9	0.001	0.000	0.08	0.12	9.7	0.2
F55	2015-06-19	1.5	46.6	0.001	0.000	-0.19	0.11	9.2	0.2
F57	2015-07-23	3.6	16.9	0.001	0.000	0.11	0.10	9.8	0.3
F59	2015-08-14	0.0	98.0	0.001	0.000	0.10	0.10	9.6	0.3
F61	2015-09-08	0.4	81.0	0.001	0.000	-0.01	0.11	9.5	0.3
F62	2015-10-01	3.4	18.7	0.001	0.000	0.08	0.10	9.5	0.2

Table B.16: Mannheim (deep well): OD model fit results.

OD model									
included NGs		He, Ne, Ar, Kr, Xe							
DoF		95							
start values		A = 0.01 ccSTP/g, T = 10°C, P_{OD} = 1							
fixed parameters		p = 0.991 atm, S = 0.72 g/kg							
ID	sampl. date	χ^2	Prob [%]	A [ccSTP/g]	ΔA [ccSTP/g]	P_{OD}	ΔP_{OD}	T [°C]	ΔT [°C]
F0	2013-03-20	57.4	99.9	0.001	0.000	1.04	0.01	10.8	0.5
F2	2013-06-27	57.4	99.9	0.001	0.000	1.04	0.01	10.3	0.5
F4	2013-07-29	57.4	99.9	0.001	0.000	1.04	0.01	10.4	0.5
F6	2013-08-27	57.4	99.9	0.001	0.000	1.04	0.01	10.3	0.5
F8	2013-09-24	57.4	99.9	0.001	0.000	1.04	0.01	10.3	0.5
F10	2013-10-22	57.4	99.9	0.002	0.000	1.04	0.01	10.4	0.5
F12	2013-11-19	57.4	99.9	0.001	0.000	1.04	0.01	10.5	0.5
F14	2013-12-17	57.4	99.9	0.001	0.000	1.04	0.01	10.5	0.5
F16	2014-01-13	57.4	99.9	0.001	0.000	1.04	0.01	10.6	0.5
F18	2014-02-11	57.4	99.9	0.001	0.000	1.04	0.01	10.7	0.5
F20	2014-03-10	57.4	99.9	0.001	0.000	1.04	0.01	10.7	0.5
F22	2014-04-07	57.4	99.9	0.001	0.000	1.04	0.01	10.4	0.5
F24	2014-05-08	57.4	99.9	0.001	0.000	1.04	0.01	10.6	0.5
F26	2014-06-03	57.4	99.9	0.001	0.000	1.04	0.01	10.5	0.5
F29	2014-07-03	57.4	99.9	0.001	0.000	1.04	0.01	10.0	0.5
F31	2014-07-23	57.4	99.9	0.001	0.000	1.04	0.01	10.4	0.5
F33	2014-08-19	57.4	99.9	0.001	0.000	1.04	0.01	10.6	0.5
F35	2014-09-15	57.4	99.9	0.001	0.000	1.04	0.01	10.5	0.5
F37	2014-10-16	57.4	99.9	0.001	0.000	1.04	0.01	10.8	0.5
F39	2014-11-13	57.4	99.9	0.001	0.000	1.04	0.01	10.1	0.5
F41	2014-12-03	57.4	99.9	0.001	0.000	1.04	0.01	10.5	0.5
F43	2015-01-06	57.4	99.9	0.001	0.000	1.04	0.01	10.6	0.5
F45	2015-02-03	57.4	99.9	0.001	0.000	1.04	0.01	10.7	0.5
F47	2015-03-03	57.4	99.9	0.001	0.000	1.04	0.01	10.5	0.5
F49	2015-03-31	57.4	99.9	0.001	0.000	1.04	0.01	10.6	0.5
F51	2015-04-24	57.4	99.9	0.001	0.000	1.04	0.01	10.5	0.5
F53	2015-05-22	57.4	99.9	0.001	0.000	1.04	0.01	10.8	0.5
F55	2015-06-19	57.4	99.9	0.001	0.000	1.04	0.01	10.5	0.5
F57	2015-07-23	57.4	99.9	0.001	0.000	1.04	0.01	10.9	0.5
F59	2015-08-14	57.4	99.9	0.001	0.000	1.04	0.01	10.7	0.5
F61	2015-09-08	57.4	99.9	0.001	0.000	1.04	0.01	10.7	0.5
F62	2015-10-01	57.4	99.9	0.001	0.000	1.04	0.01	10.6	0.5

Table B.17: Mannheim (deep well): GR model fit results.

GR model		including He data										not including He data									
included NGs		He, Ne, Ar, Kr, Xe										Ne, Ar, Kr, Xe									
DoF		179										118									
start values		A = 0.01 ccSTP/g, T = 10°C, F_{GR} = 1, P_{GR} = 1										A = 0.01 ccSTP/g, T = 10°C, F_{GR} = 1, P_{GR} = 1									
fixed parameters		p = 0.991 atm, S = 0.72 g/kg, β = 2/3										p = 0.991 atm, S = 0.72 g/kg, β = 2/3									
ID	sampl. date	χ^2	Prob [%]	A [ccSTP/g]	ΔA [ccSTP/g]	P_{GR}	ΔP_{GR}	F_{GR}	ΔF_{GR}	T [°C]	ΔT [°C]	χ^2	Prob [%]	A [ccSTP/g]	ΔA [ccSTP/g]	P_{GR}	ΔP_{GR}	F_{GR}	ΔF_{GR}	T [°C]	ΔT [°C]
F0	2013-03-20	56.3	99.9	0.001	0.000	1.04	0.01	-0.07	0.07	10.9	0.5	40.1	98.6	0.006	0.007	0.97	0.08	2.98	1.70	9.2	1.9
F2	2013-06-27	56.3	99.9	0.001	0.000	1.04	0.01	-0.07	0.07	10.4	0.5	40.1	98.6	0.006	0.007	0.97	0.08	2.98	1.70	8.6	1.9
F4	2013-07-29	56.3	99.9	0.001	0.000	1.04	0.01	-0.07	0.07	10.5	0.5	40.1	98.6	0.006	0.007	0.97	0.08	2.98	1.70	8.7	1.9
F6	2013-08-27	56.3	99.9	0.001	0.000	1.04	0.01	-0.07	0.07	10.4	0.5	40.1	98.6	0.006	0.007	0.97	0.08	2.98	1.70	8.6	1.9
F8	2013-09-24	56.3	99.9	0.001	0.000	1.04	0.01	-0.07	0.07	10.4	0.5	40.1	98.6	0.006	0.007	0.97	0.08	2.98	1.70	8.6	1.9
F10	2013-10-22	56.3	99.9	0.002	0.000	1.04	0.01	-0.07	0.07	10.5	0.5	40.1	98.6	0.010	0.010	0.97	0.08	2.98	1.70	9.2	1.6
F12	2013-11-19	56.3	99.9	0.001	0.000	1.04	0.01	-0.07	0.07	10.6	0.5	40.1	98.6	0.005	0.006	0.97	0.08	2.98	1.70	8.7	1.9
F14	2013-12-17	56.3	99.9	0.001	0.000	1.04	0.01	-0.07	0.07	10.6	0.5	40.1	98.6	0.006	0.007	0.97	0.08	2.98	1.70	8.8	1.9
F16	2014-01-13	56.3	99.9	0.001	0.000	1.04	0.01	-0.07	0.07	10.7	0.5	40.1	98.6	0.006	0.007	0.97	0.08	2.98	1.70	9.0	1.8
F18	2014-02-11	56.3	99.9	0.001	0.000	1.04	0.01	-0.07	0.07	10.8	0.5	40.1	98.6	0.006	0.007	0.97	0.08	2.98	1.70	9.1	1.9
F20	2014-03-10	56.3	99.9	0.001	0.000	1.04	0.01	-0.07	0.07	10.8	0.5	40.1	98.6	0.006	0.007	0.97	0.08	2.98	1.70	9.1	1.8
F22	2014-04-07	56.3	99.9	0.001	0.000	1.04	0.01	-0.07	0.07	10.4	0.5	40.1	98.6	0.007	0.008	0.97	0.08	2.98	1.70	8.9	1.8
F24	2014-05-08	56.3	99.9	0.001	0.000	1.04	0.01	-0.07	0.07	10.7	0.5	40.1	98.6	0.008	0.009	0.97	0.08	2.98	1.70	9.3	1.7
F26	2014-06-03	56.3	99.9	0.001	0.000	1.04	0.01	-0.07	0.07	10.5	0.5	40.1	98.6	0.006	0.007	0.97	0.08	2.98	1.70	8.8	1.9
F29	2014-07-03	56.3	99.9	0.001	0.000	1.04	0.01	-0.07	0.07	10.1	0.5	40.1	98.6	0.006	0.007	0.97	0.08	2.98	1.70	8.3	1.9
F31	2014-07-23	56.3	99.9	0.001	0.000	1.04	0.01	-0.07	0.07	10.5	0.5	40.1	98.6	0.005	0.006	0.97	0.08	2.98	1.70	8.7	1.9
F33	2014-08-19	56.3	99.9	0.001	0.000	1.04	0.01	-0.07	0.07	10.6	0.5	40.1	98.6	0.007	0.008	0.97	0.08	2.98	1.70	9.0	1.8
F35	2014-09-15	56.3	99.9	0.001	0.000	1.04	0.01	-0.07	0.07	10.6	0.5	40.1	98.6	0.005	0.006	0.97	0.08	2.98	1.70	8.7	1.9
F37	2014-10-16	56.3	99.9	0.001	0.000	1.04	0.01	-0.07	0.07	10.8	0.5	40.1	98.6	0.006	0.007	0.97	0.08	2.98	1.70	9.1	1.9
F39	2014-11-13	56.3	99.9	0.001	0.000	1.04	0.01	-0.07	0.07	10.2	0.5	40.1	98.6	0.006	0.007	0.97	0.08	2.98	1.70	8.5	1.8
F41	2014-12-03	56.3	99.9	0.001	0.000	1.04	0.01	-0.07	0.07	10.5	0.5	40.1	98.6	0.005	0.007	0.97	0.08	2.98	1.70	8.7	1.9
F43	2015-01-06	56.3	99.9	0.001	0.000	1.04	0.01	-0.07	0.07	10.7	0.5	40.1	98.6	0.006	0.007	0.97	0.08	2.98	1.70	8.9	1.9
F45	2015-02-03	56.3	99.9	0.001	0.000	1.04	0.01	-0.07	0.07	10.8	0.5	40.1	98.6	0.006	0.007	0.97	0.08	2.98	1.70	8.9	1.9
F47	2015-03-03	56.3	99.9	0.001	0.000	1.04	0.01	-0.07	0.07	10.6	0.5	40.1	98.6	0.006	0.007	0.97	0.08	2.98	1.70	8.9	1.9
F49	2015-03-31	56.3	99.9	0.001	0.000	1.04	0.01	-0.07	0.07	10.6	0.5	40.1	98.6	0.006	0.007	0.97	0.08	2.98	1.70	8.9	1.9
F51	2015-04-24	56.3	99.9	0.001	0.000	1.04	0.01	-0.07	0.07	10.6	0.5	40.1	98.6	0.006	0.007	0.97	0.08	2.98	1.70	8.8	1.9
F53	2015-05-22	56.3	99.9	0.001	0.000	1.04	0.01	-0.07	0.07	10.9	0.5	40.1	98.6	0.005	0.006	0.97	0.08	2.98	1.70	9.1	1.9
F55	2015-06-19	56.3	99.9	0.001	0.000	1.04	0.01	-0.07	0.07	10.6	0.5	40.1	98.6	0.005	0.006	0.97	0.08	2.98	1.70	8.7	1.9
F57	2015-07-23	56.3	99.9	0.001	0.000	1.04	0.01	-0.07	0.07	10.9	0.5	40.1	98.6	0.006	0.007	0.97	0.08	2.98	1.70	9.3	1.9
F59	2015-08-14	56.3	99.9	0.001	0.000	1.04	0.01	-0.07	0.07	10.8	0.5	40.1	98.6	0.006	0.007	0.97	0.08	2.98	1.70	9.1	1.9
F61	2015-09-08	56.3	99.9	0.001	0.000	1.04	0.01	-0.07	0.07	10.7	0.5	40.1	98.6	0.006	0.007	0.97	0.08	2.98	1.70	8.9	1.9
F62	2015-10-01	56.3	99.9	0.001	0.000	1.04	0.01	-0.07	0.07	10.6	0.5	40.1	98.6	0.006	0.007	0.97	0.08	2.98	1.70	9.0	1.9

B.11 Mannheim: Fit cluster of CE model fit (shallow well)

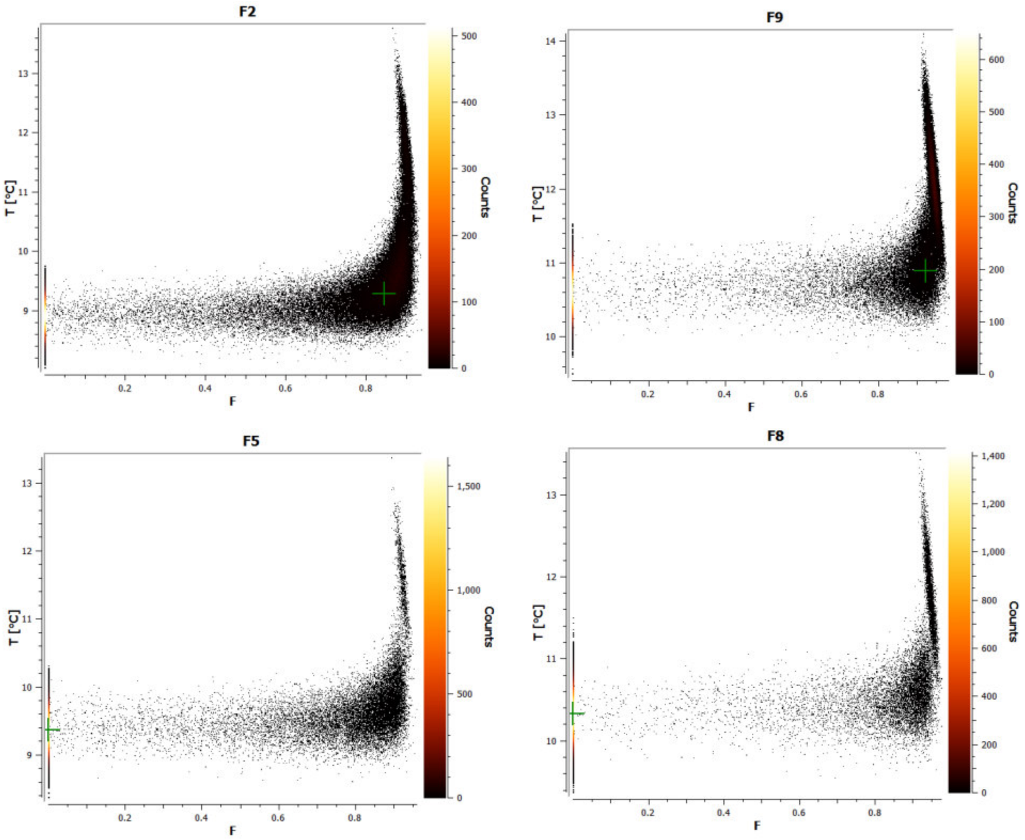

Figure B.10: Mannheim: Monte Carlo (MC) simulations of a CE model fit procedure. For most samples, MC simulations (in total 100 000) result in two clusters, reflecting different values of F_{CE}, respectively. Fit outcomes are exemplarily shown for four samples: Samples F2 and F9 result in a value of F_{CE} near 1, while samples F5 and F8 result in values of $F_{\mathrm{CE}} \approx 0$.

B.12 Mannheim: Physicochemical parameters of groundwater and stable isotope data

Table B.18: Mannheim (shallow well): Physicochemical parameters of groundwater. Data of stable isotopes of water are given relative to the VSMOW standard.

sampl. date	WTT [°C]	ΔWTT [°C]	pH	ΔpH	κ_{25} [mS/cm]	$\Delta\kappa_{25}$ [mS/cm]	ORP [mV]	ΔORP [mV]	O_2 sat. [%]	ΔO_2 sat. [%]	$\delta^{18}O$ [‰]	$\Delta\delta^{18}O$ [‰]	δ^2H [‰]	$\Delta\delta^2H$ [‰]
2013-06-18	10.8	0.2	7.67	0.02	0.923	0.005			70.8	0.5	-7.64	0.06	-54.04	0.41
2013-06-27	10.6	0.2	7.10	0.02	0.868	0.004			71.4	0.5				
2013-07-16	10.7	0.2	7.15	0.02	0.879	0.004			64.4	0.5	-7.85	0.03	-55.29	0.37
2013-07-29	10.7	0.2	7.20	0.02	0.797	0.004								
2013-08-14	10.9	0.2	7.03	0.02	0.908	0.005			78.5	0.5	-7.80	0.03	-54.82	0.20
2013-08-27	11.1	0.2							72.9					
2013-09-10	11.3	0.2							66.9					
2013-09-24	11.5	0.2							70.9		-7.83	0.07	-54.81	0.33
2013-10-08	11.7	0.2							70.4		-7.78	0.11	-54.39	0.67
2013-10-22	11.8	0.2							68.2					
2013-11-05	12.0	0.2							66.1					
2013-11-19	12.1	0.2							66.9		-7.81	0.08	-54.51	0.35
2013-12-03	12.2	0.2												
2013-12-17	12.2	0.2							67.4		-7.67	0.05	-53.82	0.19
2013-12-30	12.1	0.2							67.9					
2014-01-13	12.0	0.2							67.4		-7.75	0.08	-54.28	0.27
2014-01-28	11.8	0.2							72.1					
2014-02-11	11.7	0.2	7.11	0.02	0.946	0.005	256	2	64.0	0.3	-7.74	0.04	-54.15	0.28
2014-02-25	11.5	0.2	7.24	0.02	0.957	0.005			73.1	0.4				
2014-03-10	11.3	0.2	7.13	0.02	0.927	0.005	278	2	63.4	0.3	-7.77	0.06	-54.12	0.15
2014-03-26	11.1													
2014-04-07	11.0	0.2	7.06	0.02	0.901	0.005	233	1	62.4	0.3	-7.60	0.06	-53.82	0.22
2014-04-23	10.9													
2014-05-08	10.8	0.2	6.98	0.02	0.909	0.005	220	2	62.6	0.3	-7.82	0.03	-54.39	0.10
2014-05-20	10.8	0.2	7.06	0.02	0.895	0.004	255	2	68.4	0.3				
2014-06-03	10.8	0.2	7.09	0.03	0.898	0.004	238	1	62.0	0.3	-7.82	0.16	-54.42	0.71
2014-06-16	10.9	0.2	7.13	0.02	0.794	0.004			61.0	0.3				
2014-07-03	11.0	0.2	7.07	0.02	0.912	0.005	242	3			-7.80	0.09	-54.39	0.57
2014-07-15	11.1	0.2	6.93	0.02	0.913	0.005	145	2	58.1	0.3				
2014-07-23	11.2	0.2	6.90	0.02					60.0	0.5	-7.80	0.03	-54.45	0.24
2014-08-05	11.3	0.2	7.07	0.01	0.913	0.005	228	2	61.6	0.3				
2014-08-19	11.5	0.2	6.82	0.02	0.917	0.005	213	1	60.2	0.5	-7.75	0.05	-54.13	0.16
2014-09-03	11.8	0.2	6.95	0.02	0.903	0.005	227	1	61.2	0.3				
2014-09-15	12.0	0.2	7.02	0.02	0.894	0.004	231	1	59.9	0.3	-7.83	0.05	-55.15	0.52
2014-09-29	12.2	0.2	7.11	0.02	0.945	0.005	220	1	58.2	0.5				
2014-10-06	12.3													
2014-10-16	12.4	0.2	7.09	0.01	0.949	0.005					-7.91	0.08	-55.22	0.23
2014-10-28	12.5	0.2												
2014-11-13	12.6	0.2	7.09	0.01	0.966	0.005	283	1	55.0	0.5	-7.87	0.04	-54.81	0.31
2014-11-25	12.7	0.2	7.05	0.01	0.941	0.005	228	1	55.0	0.3				
2014-12-09	12.7	0.2	7.01	0.01	0.940	0.005	250	5	55.1	0.3	-7.79	0.24	-54.80	0.84
2014-12-18	12.7	0.2	6.98	0.01	0.921	0.005	235	1	60.2	0.3				
2015-01-06	12.6	0.2	7.03	0.02			240	1	57.2	0.3	-7.90	0.05	-55.05	0.34
2015-01-22	12.5	0.2	6.99	0.01	0.949	0.005	230	2	61.1	0.3				
2015-02-03	12.3	0.2	6.96	0.01	0.947	0.005	257	5	64.0	0.3	-7.82	0.06	-54.64	0.14
2015-02-19	12.1	0.2	7.00	0.01	0.932	0.005	278	5	64.1	0.3				
2015-03-03	11.9	0.2	7.04	0.01	0.934	0.005	235	2	68.3	0.3	-7.77	0.06	-54.72	0.24
2015-03-18	11.6	0.2	7.08	0.01	0.934	0.005	229	2	68.6	0.3				
2015-03-31	11.4	0.2	7.02	0.01	0.914	0.005	198	4	67.0	0.3	-7.80	0.05	-54.64	0.18
2015-04-09	11.2	0.2	7.10	0.01	0.911	0.005	240	2	68.2	0.3				
2015-04-24	11.0	0.2	7.13	0.01	0.928	0.005	264	5	66.8	0.3	-7.75	0.03	-54.84	0.23
2015-05-08	10.9	0.2	7.05	0.01	0.900	0.005	308	3	63.3	0.3				
2015-05-22	10.8	0.2	7.16	0.02	0.902	0.005	286	5	65.5	0.3	-7.82	0.00	-54.92	0.23
2015-06-08	10.8	0.2	7.09	0.02	0.900	0.005	239	5	64.1	0.3				
2015-06-19	10.8	0.2	6.94	0.01	0.902	0.005	317	5	61.1	0.3	-7.79	0.01	-54.89	0.15
2015-07-03	10.9	0.2	7.05	0.01	0.907	0.005	265	5	59.3	0.3				
2015-07-23	11.0	0.2	7.00	0.02	0.909	0.005	315	5	58.4	0.3	-8.05	0.02	-55.73	0.25
2015-08-03	11.1	0.2	7.05	0.01	0.910	0.005	274	2	57.5	0.3				
2015-08-14	11.3	0.2	7.07	0.01	0.902	0.005	290	5	56.8	0.3	-8.04	0.04	-55.73	0.21
2015-08-24	11.4	0.2	7.07	0.01	0.902	0.005	290	5	56.8	0.3				
2015-09-08	11.7	0.2	7.13	0.01	0.912	0.005	280	5	55.0	0.5	-8.13	0.07	-56.44	0.30
2015-10-01	12.0	0.2	6.99	0.01	0.900	0.005	229	2	54.7	0.3	-8.05	0.03	-55.60	0.05

Table B.19: Mannheim (deep well): Physicochemical parameters of groundwater. Data of stable isotopes of water are given relative to the VSMOW standard.

sampl. date	GWT [°C]	ΔGWT [°C]	pH	ΔpH	κ_{25} [mS/cm]	$\Delta\kappa_{25}$ [mS/cm]	ORP [mV]	ΔORP [mV]	O_2 sat. [%]	ΔO_2 sat. [%]	$\delta^{18}O$ [‰]	$\Delta\delta^{18}O$ [‰]	δ^2H [‰]	$\Delta\delta^2H$ [‰]
2013-06-27	11.5	0.2	7.1	0.05	0.906	0.005			18.3	0.5	-8.00	0.04	-55.43	0.35
2013-07-29	11.9	0.2	7.1	0.1	0.920	0.005					-7.81	0.01	-54.28	0.19
2013-08-27											-7.86	0.13	-54.93	0.70
2013-09-24											-8.26	0.09	-57.25	0.44
2013-10-22											-8.23	0.05	-57.62	0.47
2013-11-19											-8.11	0.01	-56.55	0.03
2013-12-17											-8.07	0.05	-56.05	0.26
2014-01-13											-7.98	0.04	-55.68	0.09
2014-02-11	11.3	0.2	7.21	0.02	0.976	0.005	244	2	18.3	0.2	-7.98	0.06	-55.55	0.43
2014-03-10	11.5	0.2	7.22	0.05	0.942	0.005	260	3	17.6	0.5	-7.97	0.03	-55.33	0.15
2014-04-07	11.7	0.2	7.13	0.02	0.925	0.005	230	1	16.8	0.2	-8.04	0.02	-55.38	0.11
2014-05-08	11.5	0.2	7.26	0.02	0.937	0.005	251	2	15.2	0.2	-8.01	0.06	-55.37	0.23
2014-06-03	12.2	0.2	7.1	0.02	0.915	0.005	230	2	18.0	0.3	-8.04	0.03	-55.58	0.01
2014-07-03	12.5	0.2	7.05	0.01	0.934	0.005	225	3	16.8	0.3	-8.06	0.00	-55.41	0.09
2014-07-23	12.1	0.2	7.02	0.02					15.3	0.3	-8.03	0.04	-55.23	0.24
2014-08-19	11.6	0.2	7.06	0.01	0.936	0.005	195	1	16.3	0.2	-7.98	0.03	-55.10	0.03
2014-09-15	11.5	0.2	6.96	0.02	0.913	0.005	214	1	16.8	0.2	-8.00	0.04	-55.16	0.37
2014-10-16	11.7	0.2	7.15	0.02	0.962	0.005	275	5			-7.91	0.02	-54.95	0.07
2014-11-13	11.5	0.2	7.14	0.02	0.981	0.005	230	1	16.6	0.2	-8.14	0.11	-56.20	0.76
2014-12-03	11.1	0.2	7.19	0.01	0.958	0.005	230	1	16.3	0.1	-8.12	0.06	-56.67	0.50
2015-01-06	11.0	0.2	7.08	0.01			224	1	17.2	0.1	-8.04	0.02	-56.08	0.12
2015-02-03	11.2	0.2	6.99	0.01	0.965	0.005	226	5	15.7	0.1	-7.93	0.15	-55.50	0.54
2015-03-03	11.4	0.2	7.06	0.01	0.959	0.005	191	3	17.9	0.2	-8.03	0.00	-55.55	0.05
2015-03-31	11.7	0.2	7.06	0.01	0.950	0.005	208	2	16.5	0.2	-8.05	0.04	-55.63	0.32
2015-04-24	12.1	0.2	7.09	0.01	0.967	0.005	253	1	18.2	0.2	-8.03	0.03	-55.61	0.30
2015-05-22	11.9	0.2	7.1	0.02	0.949	0.005	294	1	18.3	0.2	-8.09	0.04	-55.83	0.16
2015-06-19	11.6	0.2	7.01	0.02	0.936	0.005	265	4	18.1	0.1	-8.09	0.06	-55.70	0.38
2015-07-23	11.9	0.2	7.17	0.01	0.934	0.005	259	5	17.5	0.3	-7.99	0.00	-55.28	0.50
2015-08-14	11.9	0.2	7.11	0.01	0.926	0.005	298	1	16.2	0.1	-8.02	0.02	-55.28	0.09
2015-09-08	11.9	0.2	7.15	0.01	0.937	0.005	306	5	21.0	0.5	-7.98	0.05	-55.15	0.39
2015-10-01	11.7	0.2	7.15	0.01	0.917	0.005	312	2	15.1	0.1	-8.05	0.02	-55.56	0.01

B.13 Mannheim: Tritium concentrations in groundwater and dating

Table B.20: Mannheim (shallow well): Measured tritium concentrations and ^{3}He/^{4}He ratios as well as determined ^{3}H–^{3}He ages. Tritium concentrations were estimated as (6.87 ± 0.94) TU (which is the mean tritium concentration of all measured samples from the shallow well) for samples marked by an asterisk.

ID	sampl. date	^{3}H [TU]	Δ^3H [TU]	^{3}He/^{4}He	Δ^3He/^{4}He	^{3}H–^{3}He age [a]	Δ^3H–^{3}He age [a]
F1	2013-06-18	3.87	0.88				
F2	2013-06-27	7.71	0.99	1.48E-06	3.70E-08	4.5	1.6
F3*	2013-07-16	6.87	0.94				
F4	2013-07-29	6.15	0.99				
F5*	2013-08-14	6.87	0.94	1.44E-06	3.61E-08	3.6	1.7
F6	2013-08-27	7.92	0.97	1.45E-06	3.61E-08	2.6	1.5
F7*	2013-09-10	6.87	0.94	1.54E-06	3.86E-08	7.0	1.6
F8	2013-09-24	7.96	0.91	1.58E-06	1.13E-07	6.5	3.4
F9*	2013-10-08	6.87	0.94	1.58E-06	3.95E-08	8.0	1.6
F10	2013-10-22	7.30	0.90	1.57E-06	3.91E-08	8.4	1.5
F11*	2013-11-05	6.87	0.94	1.59E-06	3.98E-08	8.7	1.6
F12	2013-11-19	7.70	0.98	1.58E-06	7.90E-08	7.8	2.4
F13*	2013-12-03	6.87	0.94	1.56E-06	4.10E-08	7.8	1.7
F14	2013-12-17	9.01	0.93	1.62E-06	4.06E-08	8.9	1.2
F15*	2013-12-30	6.87	0.94	1.44E-06	3.76E-08	3.9	1.7
F16	2014-01-13	6.14	0.97	1.61E-06	4.02E-08	9.9	1.8
F17*	2014-01-28	6.87	0.94	1.53E-06	4.12E-08	7.9	1.7
F18	2014-02-11	8.32	0.92	1.61E-06	4.03E-08	7.9	1.3
F19*	2014-02-25	6.87	0.94	1.54E-06	4.02E-08	7.6	1.6
F20	2014-03-10	6.01	0.90	1.66E-06	4.14E-08	11.9	1.8
F21*	2014-03-26	6.87	0.94	1.63E-06	4.08E-08	10.0	1.6
F22	2014-04-07	7.98	0.91	1.63E-06	4.08E-08	9.0	1.4
F23*	2014-04-23	6.87	0.94	1.60E-06	3.99E-08	8.7	1.6
F24	2014-05-08	4.41	0.87	1.67E-06	4.18E-08	15.4	2.5
F25*	2014-05-20	6.87	0.94	1.71E-06	4.28E-08	11.5	1.7
F26	2014-06-03	7.38	1.02	1.71E-06	4.28E-08	11.5	1.6
F27*	2014-06-16	6.87	0.94	1.67E-06	4.19E-08	11.5	1.7
F29	2014-07-03	6.16	0.90	1.74E-06	4.36E-08	14.3	1.8
F30*	2014-07-15	6.87	0.94	1.74E-06	4.36E-08	12.8	1.7
F31	2014-07-23	5.70	0.92	1.70E-06	4.26E-08	13.0	2.0
F32*	2014-08-05	6.87	0.94	1.74E-06	4.36E-08	13.1	2.3
F33	2014-08-19	7.09	0.94	1.75E-06	4.36E-08	11.9	1.6
F34*	2014-09-03	6.87	0.94	1.79E-06	4.47E-08	14.5	2.2
F35*	2014-09-15	6.87	0.94	1.76E-06	4.40E-08	12.6	1.7
F36*	2014-09-29	6.87	0.94	1.74E-06	4.35E-08	12.0	1.7
F36b	2014-10-06						
F37*	2014-10-16	6.87	0.94	1.62E-06	4.06E-08	9.3	1.6
F38*	2014-10-28						
F39*	2014-11-13	6.87	0.94	1.75E-06	4.38E-08	13.0	1.7
F40*	2014-11-25	6.87	0.94	1.77E-06	4.41E-08	14.1	1.8
F41*	2014-12-09	6.87	0.94	1.79E-06	4.47E-08	13.6	1.7
F42*	2014-12-18	6.87	0.94	1.79E-06	4.48E-08	14.1	1.8
F43*	2015-01-06	6.87	0.94	1.69E-06	4.23E-08	12.4	2.1
F44*	2015-01-22	6.87	0.94	1.62E-06	4.04E-08	9.6	1.6
F45*	2015-02-03	6.87	0.94	1.51E-06	3.77E-08	7.1	1.5
F46*	2015-02-19	6.87	0.94	1.57E-06	3.93E-08	8.9	1.6
F47*	2015-03-03	6.87	0.94	1.57E-06	3.92E-08	8.6	1.6
F48*	2015-03-18	6.87	0.94	1.65E-06	4.12E-08	10.9	1.6
F49*	2015-03-31	6.87	0.94	1.55E-06	3.87E-08	8.4	1.6
F50*	2015-04-09	6.87	0.94	1.65E-06	4.12E-08	11.1	1.7
F51*	2015-04-24	6.87	0.94	1.62E-06	4.06E-08	10.1	1.6
F52*	2015-05-08	6.87	0.94	1.60E-06	4.01E-08	9.5	1.6
F53*	2015-05-22	6.87	0.94	1.67E-06	4.17E-08	11.0	1.6
F54*	2015-06-08	6.87	0.94	1.58E-06	3.96E-08	10.1	1.6
F55*	2015-06-19	6.87	0.94	1.70E-06	4.24E-08	12.3	1.6
F56*	2015-07-03	6.87	0.94	1.72E-06	4.29E-08	12.1	1.7
F57*	2015-07-23	6.87	0.94	1.70E-06	4.24E-08	11.5	1.6
F58*	2015-08-03	6.87	0.94	1.71E-06	4.27E-08	11.0	3.7
F59*	2015-08-14	6.87	0.94	1.76E-06	4.40E-08	13.2	1.7
F60*	2015-08-24	6.87	0.94	1.70E-06	4.26E-08	11.9	1.7
F61*	2015-09-08	6.87	0.94	1.70E-06	4.25E-08	12.0	1.7
F62*	2015-10-01	6.87	0.94	1.77E-06	4.41E-08	13.2	1.7

Table B.21: Mannheim (deep well): Measured tritium concentrations and ^{3}He/^{4}He ratios as well as determined ^{3}H−^{3}He ages. Tritium concentrations were estimated as (7.26 ± 0.97) TU (which is the mean tritium concentration of all measured samples from the deep well) for samples marked with an asterisk.

ID	sampl. date	^{3}H [TU]	Δ^3H [TU]	^{3}He/^{4}He	Δ^3He/^{4}He	^{3}H−^{3}He age [a]	Δ^3H−^{3}He age [a]
F0*	2013-03-20	7.26	0.97	2.99E-06	7.47E-08	30.6	2.1
F2	2013-06-27	7.52	0.97	2.44E-06	6.89E-08	24.6	1.9
F4	2013-07-29	7.49	1.14	2.58E-06	7.15E-08	26.3	2.3
F6	2013-08-27	8.50	1.05	2.45E-06	7.12E-08	23.3	1.8
F8	2013-09-24	9.06	1.01	2.62E-06	7.58E-08	24.3	1.7
F10	2013-10-22	9.76	1.06	2.19E-06	2.33E-07	19.2	3.6
F12	2013-11-19	10.16	0.92	2.31E-06	6.53E-08	19.4	1.4
F14	2013-12-17	9.09	0.97	2.54E-06	7.35E-08	23.6	1.6
F16	2014-01-13	5.18	0.89	2.93E-06	7.34E-08	35.6	2.8
F18	2014-02-11	5.55	0.84	2.01E-06	5.04E-08	21.9	2.2
F20*	2014-03-10	7.26	0.97	2.95E-06	7.37E-08	30.7	2.1
F22	2014-04-07	5.47	0.90	2.97E-06	7.41E-08	35.2	2.6
F24	2014-05-08	5.96	1.03	3.03E-06	7.57E-08	34.8	2.7
F26*	2014-06-03	7.26	0.97	2.93E-06	7.31E-08	30.5	2.1
F29	2014-07-03	5.31	0.88	2.96E-06	7.40E-08	35.4	2.7
F31	2014-07-23	6.60	0.95	2.99E-06	7.48E-08	32.1	2.3
F33	2014-08-19	6.01	0.98	2.90E-06	7.25E-08	33.5	2.6
F35*	2014-09-15	7.26	0.97	2.92E-06	7.30E-08	30.4	2.1
F37*	2014-10-16	7.26	0.97	2.91E-06	7.27E-08	30.1	2.1
F39*	2014-11-13	7.26	0.97	2.84E-06	7.10E-08	29.8	2.1
F41*	2014-12-03	7.26	0.97	2.93E-06	7.33E-08	30.3	2.1
F43*	2015-01-06	7.26	0.97	2.97E-06	7.43E-08	30.6	2.1
F45	2015-02-03	5.88	0.91	2.85E-06	7.12E-08	32.9	2.4
F47*	2015-03-03	7.26	0.97	2.84E-06	7.10E-08	29.5	2.1
F49*	2015-03-31	7.26	0.97	2.89E-06	7.24E-08	30.1	2.1
F51*	2015-04-24	7.26	0.97	2.95E-06	7.38E-08	30.9	2.1
F53	2015-05-22	6.74	0.88	2.83E-06	7.08E-08	30.2	2.0
F55*	2015-06-19	7.26	0.97	2.79E-06	6.97E-08	29.4	2.1
F57*	2015-07-23	7.26	0.97	2.78E-06	6.94E-08	28.7	2.0
F59*	2015-08-14	7.26	0.97	2.70E-06	6.74E-08	27.8	2.0
F61*	2015-09-08	7.26	0.97	2.61E-06	6.52E-08	27.0	2.0
F62*	2015-10-01	7.26	0.97	2.76E-06	6.89E-08	28.5	2.0

B.14 Santarém: Tritium concentrations in local precipitation of the Amazon region

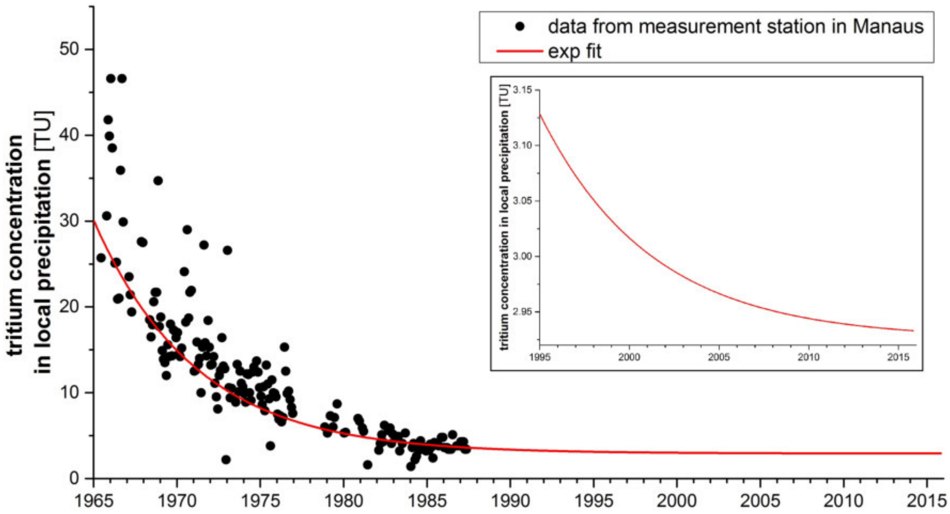

Figure B.11: Santarém: Tritium concentrations in local precipitation in Manaus (GNIP station 8233100, 3.12 ° S, 60.02 ° W), data provided by GNIP (2016). An exponential fit was carried out to determine current values of tritium in local precipitation. The time period of interest for this study is given as enlarged view.

B.15 Santarém: Overview of soil temperatures in Santarém and in the the Amazon region

Table B.22: Santarém: Overview of soil temperatures in Santarém and in the Amazon region.

vegetation	deforested		forested		depth
season	rainy	dry	rainy	dry	
Santarém:					
this study	26.7°C	31.2°C	25.3°C	27.1°C	10 cm
Miller et al. (2009)			25.5°C	24.8°C	50 cm
Amazon region:					
Zanchi et al. (2009)			26.5°C	24.0°C	15 cm
Alvalá et al. (2002)	26.5°C	24.5°C	25.0 °C	23.2°C	10 – 40 cm
Medina et al. (1980)			27.0°C	22.0°C	0 cm
Meir et al. (1996)			22.9°C	22.9°C	unknown
Davidson et al. (2000)	31.0°C	23.0°C	24.0 °C	22.0°C	10 cm
Sotta et al. (2004)			25.6°C		5 cm

B.16 Santarém: Meteorological data

Table B.23: Santarém: Meteorological stations referred to in this study. Hourly data records are available between 1998-2006 (Fitzjarrald et al., 2009).

station	coordinates	height [m a.s.l.]	river distance [m]
VilaFranca	−2.3486 °N, −55.0289 °E	16	60
Sudam	−2.5442 °N, −54.0908 °E	20	17 740
Mojuí	−2.7667 °N, −54.5792 °E	129	21 770
km117	−3.3502 °N, −54.9240 °E	167	30 900
Jamaraqua	−2.8064 °N, −55.0364 °E	15	50
Guarana	−2.6769 °N, −54.3247 °E	158	12 610
Embrapa	−2.3894 °N, −54.3286 °E	8	170
INMET	−2.5027 °N, −54.7204 °E	137	7 140
km83 (FLONA)	−3.0170 °N, −54.9707 °E	187	14 080
Belterra	−2.6431 °N, −54.9436 °E	159	4 500

Table B.24: Santarém: Mean annual values from data records of meteorological stations referred in this study (Fitzjarrald et al., 2009). MAAT denotes the mean annual atmospheric temperature, while RH denotes the relative humidity.

station	river distance [km]	height [m a.s.l.]	MAAT [°C]	RH [%]	wind speed [m/s]	insolation [W/m^2]	air pressure [mbar]
VilaFranca	56	16	28.8	79.0	0.9	275.2	1008.7
Sudam	17740	20	26.3	88.5	0.6	198.3	1007.3
Mojuí	21770	129	25.1	84.5	1.3	209.3	996.1
km117	30900	167	25.8	89.5	1.3	192.8	993.5
Jamaraqua	46	15	26.9	79.9	1.6	221.3	1010.7
Guarana	12606	158	25.6	85.3	0.9	199.1	996.2
Embrapa	168	8	27.8	82.0	2.4	247.4	1013.8
INMET	7140	137	27.7	77.7	-	-	-
km83 (FLONA)	14080	187	24.6	-	-	188.3	993.3
Belterra	4496	159	25.9	87.8	1.9	192.0	992.7

B.17 Santarém: Atmospheric air pressure

Figure B.12(a) shows mean monthly air pressures, determined based on long-term records at two different stations near Santarém. The ambient air pressure depends on the height of surface above sea level. For small height differences, the barometric height formula can be approximated as a linear function, resulting in a slope of 12 mbar/100 m for a scale height of 8 300 m, which is in good agreement with the pressure difference obtained from data shown in Fig. B.12(a). Based on a fit curve (see red line in Fig. B.12(b)), ambient air pressures can be determined for all sampled wells of this study, given their surface heights. Regarding the time series of average monthly water table levels in Rio Tapajós (see Fig. B.13), the atmospheric air pressure is close to its mean annual value during the period of strongest water table increase.

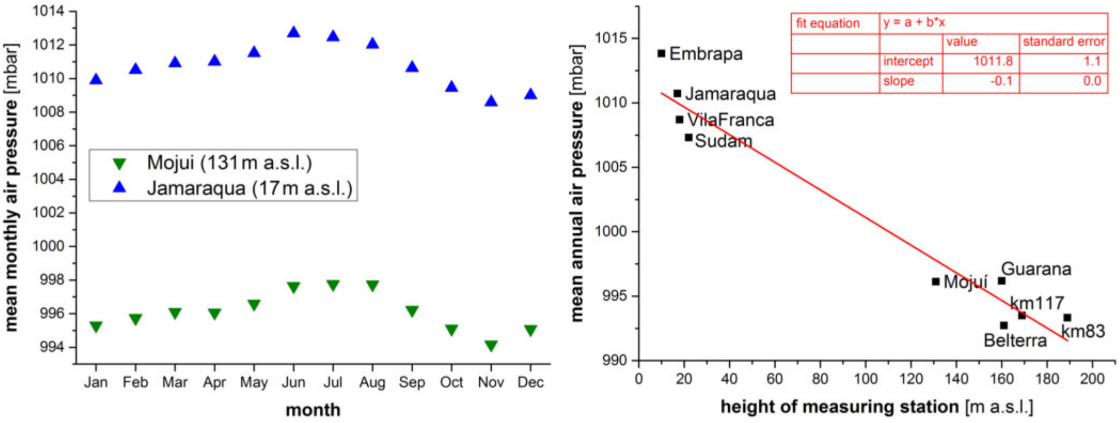

(a) Atmospheric air pressure, recorded by Fitzjarrald et al. (2009) in Jamaraqua and Mojuí.

(b) Correlation of air pressure and height of measurement station. The red line depicts a linear fit.

Figure B.12: Santarém: Atmospheric air pressure records at two different sites as well as height dependence of the air pressure in the sampling area (data source described in appendix B.16). All surface heights of meteorological stations were enhanced by 2 m which is the measurement height of the pressure record devices, respectively.

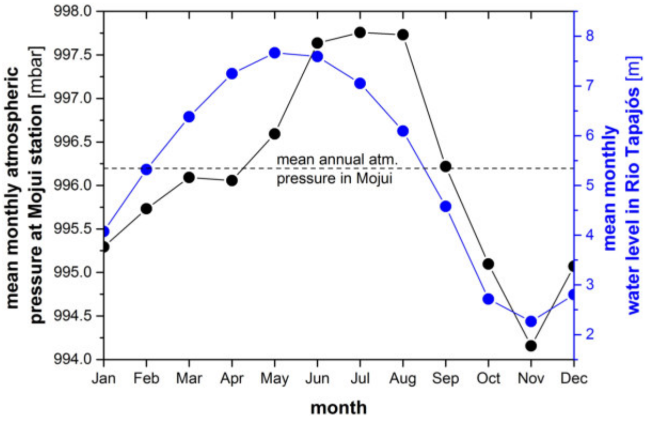

Figure B.13: Santarém: Average monthly values of atmospheric air pressure at Mojui station (Fitzjarrald et al., 2009) and water table levels in Rio Tapajós (Marinha do Brasil, 2016).

B.18 Santarém: Three isotope plot

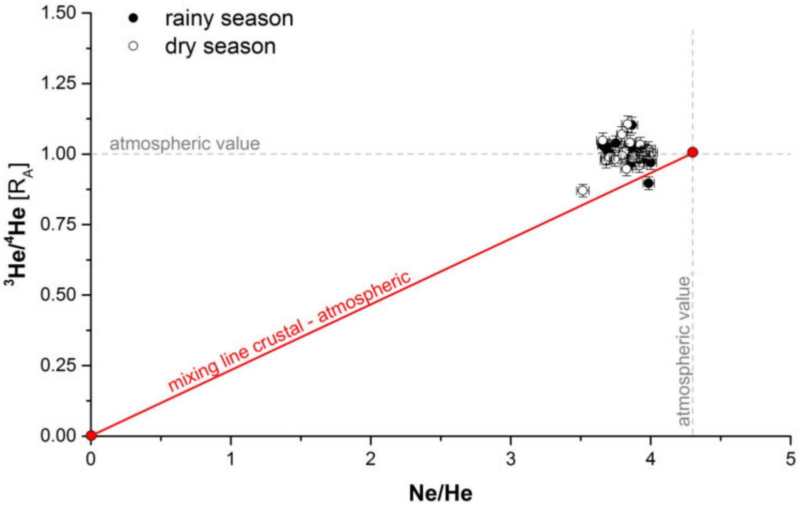

Figure B.14: Santarém: Three isotope plot indicating the influence of different geochemical reservoirs on He contents in local groundwater. Samples show an enhanced ratio of ^{3}He/^{4}He due to tritiogenic ^{3}He production.

B.19 Santarém: Assumptions about equilibration conditions during recharge

Table B.25: Santarém: Assumptions about equilibration conditions during recharge, applied for excess air model fits. The recharge temperature is estimated as the GWT during rainy season. The three wells marked by an asterisk are probably affected by geothermal heat. In-situ measurements indicated GWTs of (30.1 ± 0.4)°C (Santarém), (31.4 ± 0.2)°C (Cosanpa) and (30.2 ± 0.1)°C (Barrudada), while GWTs given for these three wells in this table are based on GWTs measured at the surrounding wells, respectively.

ID	height of site [m a.s.l.]	atmospheric air pressure [atm]	recharge temp. [°C]	Δ recharge temp. [°C]
Pajuçara	38	0.997	28.3	0.1
Santarém*	14	1.000	28.6	0.1
PontaDePedras	20	0.999	28.9	0.1
AlterDoChão2	16	1.000	28.5	0.3
Cosanpa*	86	0.991	28.4	0.4
AlterDoChão1	20	0.999	28.3	0.3
Barrudada*	42	0.997	28.0	0.4
FonteCairé	32	0.998	27.6	0.2
Mararu	37	0.997	27.8	0.3
ZooFit	41	0.997	27.9	0.1
CampoNovo	32	0.998	28.1	0.1
Peleja	48	0.996	26.2	0.3
Tipizal	145	0.985	26.1	0.2
Mapinguari	60	0.995	26.6	0.3
VilaNova	36	0.998	27.0	0.3
Jatobá	93	0.991	25.7	0.1
SantaRosa	102	0.990	26.2	0.2
Cipoal	133	0.986	26.6	0.1
Curupira	88	0.991	27.1	0.1
SãoJose	140	0.985	27.1	0.2
GrajaSãoPedro	179	0.980	25.4	0.2
Mojuí	115	0.988	25.8	0.1
Belterra	147	0.984	25.4	0.1
FLONA	87	0.991	25.8	0.1
SacradoCoraçao	88	0.991	26.2	0.1

B.20 Santarém: Soil air composition data

Table B.26: Santarém: Soil air composition during rainy season 2014 and during dry season 2015, respectively.

RAINY SEASON 2014		Measurements by *Omnistar*										Measurements by *MM5400* mass spectrometer															
location	depth [m]	N_2	ΔN_2	CO_2	ΔCO_2	^{40}Ar	$\Delta^{40}Ar$	O_2	ΔO_2	O_2+CO_2	ΔO_2+CO_2	^3He	Δ^3He	^4He	Δ^4He	^{20}Ne	$\Delta^{20}Ne$	^{22}Ne	$\Delta^{22}Ne$	^{36}Ar	$\Delta^{36}Ar$	^{40}Ar	$\Delta^{40}Ar$	^{84}Kr	$\Delta^{84}Kr$	^{132}Xe	$\Delta^{132}Xe$
		all data is given in units of vol%										partial pressures are normalized to their values in dry atmospheric air, respectively															
Mararu	1	81.26	0.21	3.19	0.05	0.977	0.014	14.58	0.16	17.76	0.17	1.020	0.043	1.051	0.014	1.048	0.011	1.044	0.010	1.051	0.026	1.050	0.010	1.050	0.012	1.067	0.017
Mararu	2	82.68	0.21	5.19	0.08	0.992	0.014	11.14	0.13	16.33	0.15	1.114	0.047	1.043	0.013	1.062	0.011	1.059	0.011	1.068	0.028	1.068	0.011	1.070	0.013	1.071	0.017
Mararu	3	81.92	0.21	2.50	0.05	0.979	0.014	14.60	0.16	17.10	0.17	1.131	0.041	1.049	0.014	1.051	0.011	1.050	0.011	1.056	0.028	1.056	0.010	1.058	0.013	1.067	0.017
AlterDoChão1	1	80.45	0.21	4.25	0.07	0.958	0.014	14.35	0.16	18.60	0.17	1.070	0.035	1.032	0.013	1.041	0.010	1.041	0.010	1.032	0.027	1.040	0.010	1.047	0.013	1.039	0.017
AlterDoChão1	2	81.23	0.21	4.61	0.07	0.971	0.014	13.18	0.15	17.80	0.16	1.021	0.032	1.043	0.013	1.045	0.010	1.043	0.010	1.053	0.027	1.047	0.010	1.036	0.012	1.052	0.017
FLONA	1											1.108	0.037	1.010	0.013	1.031	0.010	1.036	0.010	1.030	0.028	1.030	0.010	1.029	0.012	1.029	0.017
FLONA	2	80.08	0.21	5.87	0.08	0.955	0.014	13.10	0.15	18.97	0.17	1.030	0.037	1.020	0.013	1.035	0.010	1.034	0.010	1.034	0.026	1.031	0.010	1.032	0.012	1.045	0.017
Peleja	2	80.31	0.21	5.46	0.08	0.962	0.014	13.27	0.15	18.73	0.17	1.053	0.039	1.051	0.012	1.037	0.010	1.037	0.010	1.045	0.025	1.035	0.010	1.036	0.013	1.011	0.017
Mapinguari	1	80.78	0.21	5.23	0.08	0.973	0.014	13.02	0.15	18.25	0.17	1.121	0.042	1.045	0.014	1.046	0.010	1.046	0.010	1.033	0.028	1.045	0.010	1.038	0.012	1.080	0.018
Mapinguari	2															1.038	0.010	1.037	0.010	1.043	0.028	1.046	0.010	1.033	0.013	1.019	0.017
Mapinguari	3	80.81	0.21	7.27	0.10	0.967	0.014	10.95	0.13	18.22	0.16	1.071	0.039	1.060	0.012	1.044	0.010	1.044	0.010	1.033	0.026	1.047	0.010	1.035	0.013	1.035	0.017
Mapinguari	4											1.099	0.046	1.043	0.014	1.055	0.011	1.053	0.011	1.027	0.027	1.051	0.010	1.044	0.012	1.045	0.017
ZooFit	2	81.39	0.21	8.27	0.11	0.975	0.014	9.36	0.11	17.63	0.16	1.043	0.040	1.040	0.013	1.048	0.010	1.048	0.010	1.017	0.026	1.050	0.010	1.050	0.012	1.045	0.017
VilaNova	5	82.52	0.21	6.42	0.09	0.991	0.014	10.07	0.12	16.49	0.15	1.091	0.044	1.057	0.014	1.056	0.011	1.057	0.011	1.074	0.027	1.063	0.011	1.064	0.012	1.064	0.017
Tipizal	1	82.20	0.21	2.86	0.05	0.985	0.014	13.95	0.16	16.81	0.16	1.137	0.046	1.047	0.014	1.064	0.011	1.064	0.011	1.059	0.028	1.072	0.011	1.065	0.012	1.080	0.017
Curupira	2	79.26	0.21	4.49	0.07	0.942	0.014	15.30	0.17	19.80	0.18	1.003	0.039	1.014	0.013	1.021	0.010	1.019	0.010	1.041	0.026	1.037	0.010	1.034	0.012	1.027	0.017
CampoNovo	1											1.062	0.039	1.051	0.014	1.032	0.010	1.031	0.010	1.041	0.026	1.037	0.010	1.038	0.012	1.034	0.018
CampoNovo	2	80.69	0.21	0.77	0.04	0.969	0.014	17.57	0.19	18.34	0.20	1.099	0.033	1.024	0.013	1.045	0.010	1.044	0.010	1.038	0.027	1.043	0.010	1.045	0.012	1.073	0.017
SãoJose	1	81.66	0.21	3.88	0.06	0.978	0.014	13.48	0.15	17.36	0.16					1.058	0.011	1.060	0.011	1.070	0.029	1.061	0.010	1.065	0.013	1.049	0.017
AlterDoChão2	3	80.79	0.21	3.10	0.05	0.967	0.014	15.15	0.17	18.24	0.18	1.000	0.099	1.042	0.011	1.037	0.010	1.037	0.010	1.052	0.012	1.040	0.010	1.034	0.012	1.025	0.017

DRY SEASON 2015		Measurements by *Omnistar*										Measurements by *MM5400*															
location	depth [m]	N_2	ΔN_2	CO_2	ΔCO_2	^{40}Ar	$\Delta^{40}Ar$	O_2	ΔO_2	O_2+CO_2	ΔO_2+CO_2	^3He	Δ^3He	^4He	Δ^4He	^{20}Ne	$\Delta^{20}Ne$	^{22}Ne	$\Delta^{22}Ne$	^{36}Ar	$\Delta^{36}Ar$	^{40}Ar	$\Delta^{40}Ar$	^{84}Kr	$\Delta^{84}Kr$	^{132}Xe	$\Delta^{132}Xe$
		all data is given in units of vol%										partial pressures are normalized to their values in dry atmospheric air, respectively															
AlterDoChão1	1	78.14	0.19	1.10	0.05	0.936	0.013	19.83	0.21	20.92	0.22	1.001	0.020	0.995	0.014	0.995	0.010	0.995	0.010	1.001	0.012	1.000	0.010	0.996	0.014	1.011	0.024
AlterDoChão1	2	80.12	0.20	0.47	0.05	0.957	0.013	18.45	0.20	18.93	0.20	1.024	0.026	1.040	0.011	1.039	0.011	1.039	0.010	1.004	0.018	1.027	0.011	1.029	0.015	1.032	0.018
VilaNova	1	79.16	0.19	1.25	0.03	0.951	0.011	18.64	0.19	19.89	0.19	1.004	0.026	1.031	0.010	1.028	0.010	1.028	0.010	0.997	0.018	1.022	0.011	1.011	0.015	1.013	0.018
VilaNova	2	80.25	0.19	2.21	0.04	0.961	0.011	16.58	0.17	18.79	0.18	0.997	0.017	1.023	0.011	1.014	0.012	1.015	0.012	1.005	0.016	1.010	0.010	0.993	0.018	0.989	0.018
AlterDoChão2	1	78.79	0.19	0.96	0.05	0.948	0.013	19.30	0.20	20.26	0.21	1.026	0.020	1.018	0.014	1.007	0.010	1.006	0.010	1.016	0.012	1.014	0.010	1.009	0.016	0.984	0.032
AlterDoChão2	2	78.74	0.19	1.46	0.05	0.95	0.013	18.85	0.20	20.31	0.21	1.005	0.020	1.012	0.014	1.001	0.010	1.000	0.010	1.007	0.011	1.009	0.010	1.005	0.016	0.981	0.023
ZooFit	1	78.96	0.19	1.09	0.05	0.95	0.013	19.00	0.20	20.09	0.21	1.007	0.019	1.031	0.013	1.029	0.011	1.029	0.012	1.005	0.014	1.015	0.010	1.057	0.020	1.059	0.020
CampoNovo	1	79.00	0.19	0.11	0.05	0.954	0.013	19.94	0.21	20.05	0.22	1.017	0.020	1.014	0.014	1.004	0.010	1.003	0.010	1.020	0.012	1.012	0.010	1.000	0.015	1.016	0.026
CampoNovo	2	78.63	0.19	0.62	0.05	0.94	0.013	19.81	0.21	20.43	0.22	1.006	0.020	1.032	0.013	1.028	0.011	1.028	0.011	1.020	0.014	1.017	0.010	1.056	0.020	1.069	0.020
Mararu	1	78.64	0.19	1.45	0.05	0.964	0.013	18.95	0.20	20.40	0.21	1.029	0.019	1.018	0.012	1.012	0.011	1.012	0.011	1.001	0.014	1.010	0.010	1.042	0.019	1.045	0.020
Mararu	2	78.50	0.19	3.55	0.07	0.947	0.013	16.99	0.18	20.55	0.20	1.016	0.020	1.008	0.014	1.002	0.010	1.002	0.010	0.997	0.012	1.004	0.010	0.994	0.015	1.003	0.023
Peleja	1	78.68	0.19	3.48	0.07	0.935	0.013	16.90	0.18	20.38	0.19	1.033	0.023	1.037	0.011	1.030	0.011	1.030	0.011	1.011	0.017	1.007	0.010	1.027	0.019	1.029	0.019
Peleja	2	79.25	0.19	5.07	0.09	0.941	0.013	14.73	0.16	19.81	0.18	1.042	0.019	1.034	0.013	1.021	0.011	1.021	0.011	1.011	0.014	1.015	0.010	1.029	0.019	1.029	0.020
Mapinguari	1	79.48	0.19	1.68	0.03	0.959	0.011	17.89	0.18	19.57	0.19	1.049	0.020	1.036	0.013	1.034	0.011	1.035	0.012	1.017	0.015	1.021	0.010	1.043	0.019	1.047	0.020
Mapinguari	2	79.68	0.19	2.25	0.04	0.957	0.011	17.12	0.18	19.37	0.18	1.021	0.020	1.030	0.014	1.022	0.010	1.021	0.011	1.046	0.013	1.023	0.010	1.004	0.016	1.009	0.024
FLONA	1	77.23	0.18	3.85	0.05	0.927	0.011	17.99	0.19	21.85	0.19	0.999	0.019	0.985	0.014	0.983	0.010	0.983	0.010	0.995	0.012	0.985	0.010	0.971	0.013	0.995	0.024
FLONA	2	77.93	0.18	5.10	0.06	0.935	0.011	16.03	0.17	21.13	0.18	1.004	0.025	1.035	0.010	1.025	0.010	1.024	0.010	1.006	0.019	1.016	0.010	1.016	0.014	1.007	0.018
Curupira	1	77.96	0.19	1.58	0.05	0.934	0.013	19.53	0.21	21.10	0.21	0.993	0.019	1.001	0.012	1.001	0.011	1.000	0.011	0.996	0.014	0.994	0.010	1.027	0.019	1.033	0.021
Curupira	2	79.06	0.19	4.29	0.08	0.946	0.013	15.71	0.17	20.00	0.19	1.030	0.020	1.035	0.013	1.026	0.011	1.024	0.011	1.009	0.014	1.013	0.010	1.050	0.019	1.040	0.019
Tipizal	1	79.61	0.20	3.50	0.07	0.961	0.013	15.93	0.17	19.43	0.19	1.030	0.020	1.032	0.013	1.026	0.011	1.026	0.011	1.021	0.014	1.021	0.010	1.048	0.019	1.052	0.023
Tipizal	2	78.84	0.19	5.66	0.10	0.954	0.013	14.55	0.16	20.20	0.19	1.018	0.020	1.025	0.012	1.020	0.011	1.020	0.011	1.015	0.014	1.012	0.010	1.049	0.019	1.041	0.021
SãoJose	1	79.07	0.19	0.99	0.05	0.953	0.013	18.99	0.20	19.98	0.21	0.997	0.026	1.033	0.011	1.025	0.010	1.025	0.010	1.026	0.018	1.019	0.010	1.008	0.016	0.983	0.017
SãoJose	2	77.46	0.19	2.70	0.06	0.931	0.013	18.91	0.20	21.61	0.21	0.992	0.021	0.998	0.014	0.990	0.010	0.990	0.010	0.975	0.012	0.995	0.010	1.010	0.016	0.994	0.029
SantaRosa	4	78.64	0.19	0.50	0.03	0.949	0.011	19.91	0.20	20.41	0.21	1.024	0.020	1.009	0.012	1.011	0.011	1.011	0.011	1.016	0.015	1.007	0.010	1.043	0.019	1.071	0.021
Barrudada	5	80.28	0.20	2.63	0.06	0.96	0.013	16.13	0.17	18.76	0.18	1.023	0.018	1.020	0.011	1.030	0.012	1.031	0.012	1.035	0.020	1.027	0.011				
Barrudada	1	77.87	0.19	4.29	0.08	0.929	0.013	16.91	0.18	21.20	0.20	1.025	0.020	1.027	0.014	1.016	0.010	1.014	0.010	1.019	0.012	1.011	0.010	1.009	0.016	1.017	0.035
Barrudada	2	79.29	0.19	0.27	0.05	0.952	0.013	19.49	0.21	19.76	0.21	0.995	0.025	1.032	0.010	1.016	0.010	1.017	0.010	1.035	0.018	1.030	0.010	1.040	0.015	1.023	0.019
Belterra	1	79.35	0.19	1.80	0.03	0.958	0.011	17.89	0.18	19.69	0.19	1.041	0.020	1.029	0.013	1.017	0.011	1.017	0.011	1.024	0.015	1.022	0.010	1.024	0.020	1.048	0.021
Belterra	2	79.76	0.19	1.48	0.03	0.962	0.011	17.80	0.18	19.28	0.19	1.013	0.027	1.030	0.011	1.026	0.010	1.025	0.010	1.011	0.018	1.018	0.011	1.018	0.015	1.027	0.018
Pajuçara	1	79.69	0.20	0.03	0.05	0.954	0.013	19.32	0.20	19.35	0.21	1.051	0.018	1.047	0.012	1.038	0.012	1.038	0.012	1.002	0.021	1.021	0.011	1.032	0.016	1.039	0.018
Pajuçara	2	80.28	0.20	0.26	0.05	0.957	0.013	18.50	0.20	18.76	0.20	1.051	0.020	1.038	0.013	1.033	0.011	1.033	0.012	1.015	0.015	1.024	0.010	1.027	0.019	1.024	0.020
FLONA_B	1	78.01	0.19	2.77	0.06	0.933	0.013	18.29	0.19	21.06	0.20	0.977	0.025	1.016	0.010	1.006	0.010	1.007	0.010	1.000	0.018	1.007	0.010	1.003	0.014	1.007	0.019

B.21 Santarém: Determining factors of soil air composition

The sampling of the topmost meter of soil material at the most of the sampling sites provides an insight into local soil structure. Based on soil material observations, the estimation of a typical grain size diameter of topmost soils allows to investigate a correlation between soil air composition and soil structure. It has to be noted that structures of the sampled soil cores (meaning only the topmost meter) may be not representative for deeper layers.

To investigate an impact of local above-ground vegetation on soil air composition, it was tried to quantify the type of local vegetation at each sampling site. For this purpose, a value between 0 (no local vegetation) and 1 (rain forest) was allocated, based on local observations. Even though such a "vegetation index" has to be seen rather as a rough estimation, its relative variations should allow for reliable conclusions.

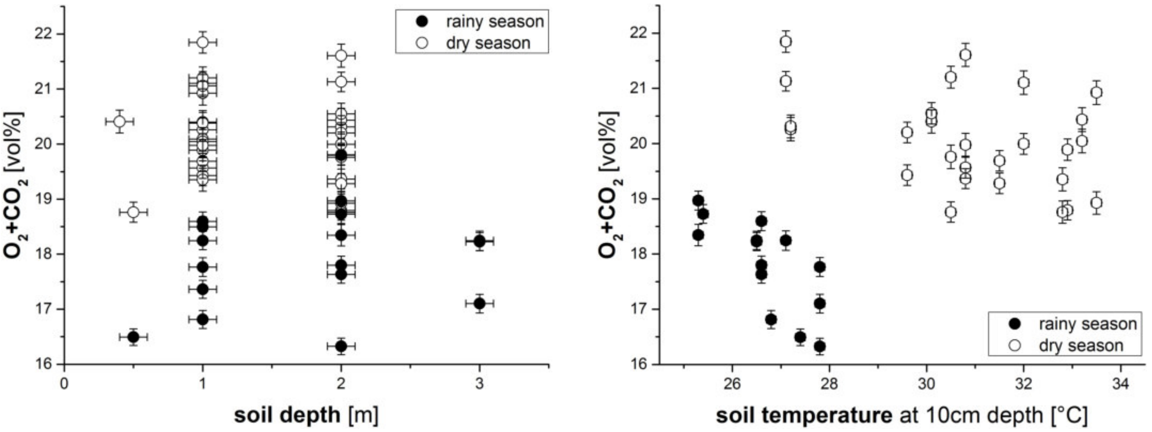

(a) Soil depth: The depth uncertainty is estimated as 0.1 m according to the design of sampling tubes.

(b) Soil temperature: According to manufacturer's data, the temperature uncertainty accounts for 0.1°C.

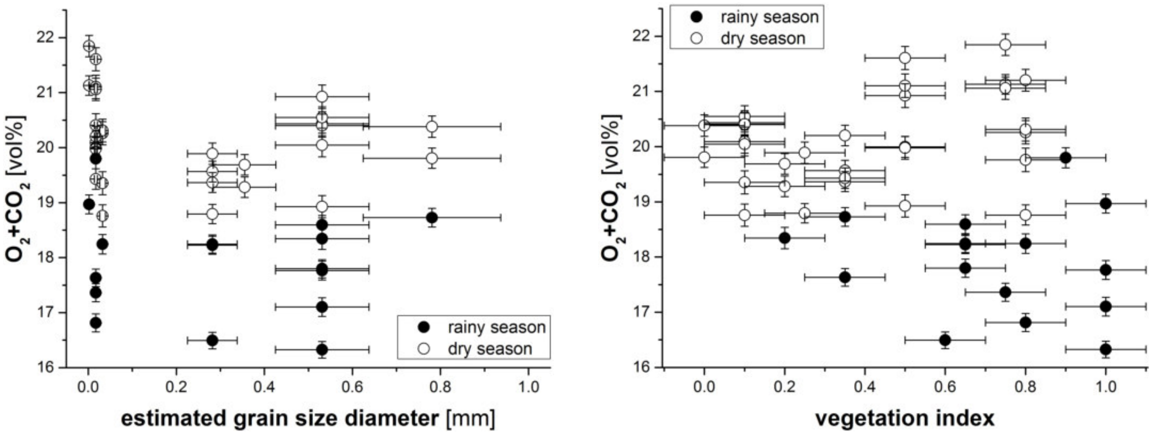

(c) Grain size of soil particles: The relative uncertainty of grain size was estimated as 20 %.

(d) Above-ground vegetation: The uncertainty of vegetation index was estimated as 0.1.

Figure B.15: Santarém: Correlation of different parameters and O_2+CO_2 sum values in soil air, distinguished according to rainy season (filled symbols) and dry season (open symbols).

B.22 Santarém: NG concentrations in groundwater

Table B.27: Santarém: NG concentrations in groundwater. All data are given in units of ccSTP per g of water.

ID	He [ccSTP/g]	ΔHe [ccSTP/g]	Ne [ccSTP/g]	ΔNe [ccSTP/g]	Ar [ccSTP/g]	ΔAr [ccSTP/g]	Kr [ccSTP/g]	ΔKr [ccSTP/g]	Xe [ccSTP/g]	ΔXe [ccSTP/g]
rainy season (2014)										
Santarém	6.292E-08	4.778E-10	2.432E-07	1.703E-09	3.137E-04	2.196E-06	6.293E-08	6.512E-10	7.914E-09	1.426E-10
AlterDoChão2	6.192E-08	4.335E-10	2.401E-07	1.681E-09	3.165E-04	2.216E-06	6.381E-08	6.857E-10	8.036E-09	1.429E-10
AlterDoChão1	5.759E-08	4.032E-10	2.264E-07	1.585E-09	3.047E-04	2.133E-06	6.219E-08	6.976E-10	7.981E-09	1.427E-10
FonteCairé	1.393E-07	9.751E-10	5.095E-07	3.566E-09	5.056E-04	3.539E-06	9.035E-08	9.515E-10	1.041E-08	1.779E-10
Mararu	5.197E-08	3.638E-10	2.046E-07	1.432E-09	2.959E-04	2.071E-06	6.266E-08	6.266E-10	8.070E-09	1.457E-10
ZooFit	6.218E-08	4.353E-10	2.409E-07	1.686E-09	3.214E-04	2.250E-06	6.538E-08	6.539E-10	8.432E-09	1.505E-10
CampoNovo	5.989E-08	4.193E-10	2.361E-07	1.653E-09	3.353E-04	2.347E-06	6.975E-08	7.202E-10	8.867E-09	1.671E-10
Peleja	7.907E-08	5.535E-10	3.037E-07	2.126E-09	3.683E-04	2.578E-06	7.301E-08	7.353E-10	9.138E-09	1.653E-10
Tipizal	6.832E-08	4.782E-10	2.645E-07	1.851E-09	3.307E-04	2.315E-06	6.702E-08	6.702E-10	8.617E-09	1.534E-10
Mapinguari	1.033E-07	8.316E-10	3.811E-07	2.668E-09	3.977E-04	2.784E-06	7.581E-08	7.581E-10	9.072E-09	1.674E-10
VilaNova	5.210E-08	3.647E-10	2.005E-07	1.403E-09	2.940E-04	2.058E-06	6.172E-08	6.577E-10	8.140E-09	1.454E-10
SantaRosa	5.494E-08	4.233E-10	2.197E-07	1.538E-09	3.045E-04	2.131E-06	6.276E-08	6.451E-10	8.217E-09	1.495E-10
Curupira	5.267E-08	3.687E-10	2.099E-07	1.469E-09	3.012E-04	2.108E-06	6.341E-08	7.064E-10	8.242E-09	1.498E-10
SãoJose	1.016E-07	7.115E-10	3.760E-07	2.632E-09	3.930E-04	2.751E-06	7.345E-08	7.363E-10	8.943E-09	1.616E-10
FLONA	5.084E-08	3.840E-10	2.013E-07	1.409E-09	2.944E-04	2.061E-06	6.254E-08	6.350E-10	8.155E-09	1.396E-10
dry season (2015)										
Pajuçara	7.268E-08	5.953E-10	2.799E-07	1.960E-09	3.524E-04	2.467E-06	6.898E-08	6.898E-10	8.434E-09	1.434E-10
Santarém	6.753E-08	4.727E-10	2.563E-07	1.794E-09	3.188E-04	2.231E-06	6.367E-08	7.051E-10	8.164E-09	1.666E-10
PontaDePedras	6.781E-08	5.694E-10	2.640E-07	1.848E-09	3.406E-04	2.384E-06	6.821E-08	7.091E-10	8.473E-09	1.579E-10
AlterDoChão2	6.016E-08	4.211E-10	2.349E-07	1.644E-09	3.111E-04	2.178E-06	6.267E-08	6.344E-10	8.203E-09	1.821E-10
Cosanpa	7.685E-08	7.656E-10	2.701E-07	1.891E-09	3.424E-04	2.397E-06	6.872E-08	6.899E-10	8.689E-09	1.534E-10
AlterDoChão1	5.877E-08	4.114E-10	2.311E-07	1.618E-09	3.095E-04	2.167E-06	6.339E-08	6.339E-10	7.980E-09	1.744E-10
Barrudada	5.901E-08	4.907E-10	2.313E-07	2.551E-09	3.001E-04	2.101E-06	6.036E-08	6.774E-10	7.652E-09	1.386E-10
FonteCairé	6.751E-08	6.303E-10	2.590E-07	1.813E-09	3.392E-04	2.374E-06	6.940E-08	9.333E-10	8.562E-09	1.579E-10
Mararu	5.161E-08	3.922E-10	2.022E-07	1.415E-09	2.929E-04	2.050E-06	6.268E-08	6.268E-10	8.095E-09	1.639E-10
ZooFit	5.217E-08	4.071E-10	2.089E-07	1.463E-09	2.964E-04	2.075E-06	6.256E-08	6.806E-10	8.117E-09	1.577E-10
CampoNovo	5.901E-08	5.481E-10	2.344E-07	1.691E-09	3.382E-04	2.367E-06	7.144E-08	7.901E-10	9.060E-09	1.873E-10
Peleja	7.876E-08	6.451E-10	3.003E-07	2.102E-09	3.585E-04	2.510E-06	7.111E-08	7.111E-10	8.953E-09	1.522E-10
Tipizal	7.077E-08	5.997E-10	2.818E-07	2.825E-09	3.448E-04	2.414E-06	6.976E-08	8.251E-10	8.920E-09	1.971E-10
Mapinguari	1.005E-07	7.751E-10	3.701E-07	2.591E-09	4.015E-04	2.811E-06	7.612E-08	7.612E-10	9.036E-09	1.828E-10
VilaNova	4.987E-08	3.491E-10	1.957E-07	1.370E-09	2.810E-04	1.967E-06	6.004E-08	6.410E-10	8.224E-09	1.876E-10
Jatobá	6.801E-08	5.840E-10	2.603E-07	1.822E-09	3.318E-04	2.323E-06	6.802E-08	7.609E-10	8.556E-09	1.721E-10
SantaRosa	4.893E-08	4.042E-10	1.954E-07	1.368E-09	2.878E-04	2.015E-06	6.172E-08	6.227E-10	8.026E-09	1.483E-10
Cipoal	8.621E-08	7.708E-10	3.174E-07	2.222E-09	3.637E-04	2.546E-06	7.157E-08	8.423E-10	8.830E-09	1.840E-10
Curupira	4.922E-08	3.728E-10	1.947E-07	1.363E-09	2.847E-04	1.993E-06	6.168E-08	6.259E-10	8.186E-09	1.763E-10
SãoJose	1.060E-07	7.422E-10	3.926E-07	2.748E-09	4.021E-04	2.815E-06	7.454E-08	7.454E-10	8.919E-09	1.975E-10
GrajaSãoPedro	1.082E-07	1.476E-09	4.109E-07	2.876E-09	4.436E-04	3.105E-06	8.129E-08	1.686E-09	9.322E-09	1.585E-10
Mojuí	6.455E-08	5.389E-10	2.500E-07	2.113E-09	3.249E-04	2.274E-06	6.638E-08	7.145E-10	8.399E-09	1.543E-10
Belterra	1.455E-07	1.429E-09	5.320E-07	3.724E-09	5.037E-04	3.526E-06	9.332E-08	9.332E-10	1.080E-08	2.164E-10
FLONA	5.131E-08	4.207E-10	2.025E-07	1.418E-09	2.940E-04	2.058E-06	6.239E-08	6.239E-10	8.215E-09	1.397E-10
SacradoCoraçao	7.115E-08	5.987E-10	2.664E-07	1.865E-09	3.248E-04	2.274E-06	6.582E-08	7.535E-10	8.216E-09	1.736E-10

B.23 Santarém: Tritium concentrations in groundwater

Table B.28: Santarém: Measured tritium concentrations (sampled during rainy season) and ^{3}He/^{4}He ratios (sampled during dry season).

ID	^{3}H [TU]	Δ^{3}H [TU]	^{3}He/^{4}He	Δ^{3}He/^{4}He
Pajuçara			1.44E-06	3.65E-08
Santarém	1.77	0.93	1.48E-06	3.70E-08
PontaDePedras			1.38E-06	3.51E-08
AlterDoChão2	1.72	0.98	1.38E-06	3.44E-08
Cosanpa			1.20E-06	3.07E-08
AlterDoChão1	1.84	0.84	1.38E-06	3.46E-08
Barrudada			1.33E-06	3.37E-08
FonteCairé	1.40	0.97	1.53E-06	3.96E-08
Mararu	0.75	0.82	1.36E-06	3.42E-08
ZooFit	0.28	0.89	1.39E-06	3.51E-08
CampoNovo	0.89	0.90	1.39E-06	3.50E-08
Peleja	1.69	0.94	1.40E-06	3.55E-08
Tipizal	5.03	1.00	1.41E-06	3.58E-08
Mapinguari	3.09	0.83	1.37E-06	3.45E-08
VilaNova	2.09	0.84	1.43E-06	3.58E-08
Jatobá			1.31E-06	3.34E-08
SantaRosa	2.03	0.84	1.38E-06	3.50E-08
Cipoal			1.35E-06	3.46E-08
Curupira			1.39E-06	3.49E-08
SãoJose	15.93	0.88	1.37E-06	3.42E-08
GrajaSãoPedro			1.38E-06	3.80E-08
Mojuí			1.36E-06	3.46E-08
Belterra			1.45E-06	3.76E-08
FLONA			1.38E-06	3.50E-08
SacradoCoraçao			1.36E-06	3.46E-08

B.24 Santarém: Results of excess air model fits

Table B.29: Santarém: UA model fit results.

UA model	$X/X_{atm} = 1.000$						$X/X_{atm} = 1.045$					
included NGs	Ne, Ar, Kr, Xe						Ne, Ar, Kr, Xe					
DoF	3						3					
start values	A = 0.01 ccSTP/g, T = 25°C						A = 0.01 ccSTP/g, T = 25°C					
fixed parameters	individual p, S = 0 g/kg						individual p, S = 0 g/kg					
ID	χ^2	Prob [%]	A [ccSTP/g]	ΔA [ccSTP/g]	T [°C]	ΔT [°C]	χ^2	Prob [%]	A [ccSTP/g]	ΔA [ccSTP/g]	T [°C]	ΔT [°C]
Pajuçara	35.1	0.0	5.7E-03	1.2E-04	23.8	0.3	29.0	0.0	5.4E-03	1.2E-04	25.5	0.3
Santarém	2.5	28.5	4.5E-03	1.1E-04	26.7	0.4	1.5	46.6	4.1E-03	1.1E-04	28.5	0.4
PontaDePedras	17.5	0.0	4.7E-03	1.1E-04	23.7	0.3	13.3	0.1	4.4E-03	1.1E-04	25.5	0.3
AlterDoChão2	5.6	6.1	3.3E-03	9.9E-05	26.2	0.3	4.2	12.4	2.9E-03	1.0E-04	28.0	0.4
Cosanpa	9.6	0.8	5.1E-03	1.1E-04	23.4	0.3	6.6	3.6	4.8E-03	1.1E-04	25.1	0.3
AlterDoChão1	4.9	8.7	3.0E-03	9.8E-05	25.9	0.3	2.9	23.1	2.7E-03	9.8E-05	27.7	0.3
Barrudada	3.8	15.2	3.3E-03	1.5E-04	28.1	0.4	2.2	33.8	2.9E-03	1.5E-04	30.0	0.4
FonteCairé	14.3	0.1	4.4E-03	1.1E-04	23.1	0.4	10.6	0.5	4.1E-03	1.1E-04	24.8	0.4
Mararu	0.6	73.9	1.4E-03	8.6E-05	25.4	0.3	0.6	75.4	1.1E-03	8.6E-05	27.2	0.3
ZooFit	0.4	83.2	1.8E-03	8.9E-05	25.6	0.3	0.0	99.3	1.5E-03	8.9E-05	27.4	0.3
CampoNovo	11.1	0.4	2.9E-03	1.0E-04	20.6	0.3	7.9	1.9	2.5E-03	1.0E-04	22.2	0.3
Peleja	6.3	4.2	6.7E-03	1.2E-04	23.3	0.3	4.0	13.4	6.4E-03	1.2E-04	25.0	0.3
Tipizal	1.3	52.4	5.8E-03	1.6E-04	23.1	0.4	0.5	78.5	5.4E-03	1.6E-04	24.8	0.4
Mapinguari	22.1	0.0	1.1E-02	1.5E-04	22.8	0.4	18.0	0.0	1.0E-02	1.5E-04	24.5	0.4
VilaNova	5.2	7.6	1.1E-03	8.4E-05	26.9	0.3	7.4	2.5	7.8E-04	8.5E-05	28.8	0.3
Jatobá	3.3	18.9	4.6E-03	1.1E-04	23.8	0.4	1.8	40.7	4.2E-03	1.1E-04	25.5	0.4
SantaRosa	0.3	84.4	1.1E-03	8.3E-05	25.5	0.3	0.3	85.0	7.6E-04	8.3E-05	27.3	0.3
Cipoal	5.5	6.5	7.8E-03	1.3E-04	23.4	0.4	3.5	17.4	7.4E-03	1.3E-04	25.2	0.4
Curupira	2.0	37.0	1.0E-03	8.3E-05	25.7	0.3	3.7	16.0	7.0E-04	8.4E-05	27.5	0.3
SãoJose	12.3	0.2	1.2E-02	1.6E-04	24.4	0.4	9.6	0.8	1.2E-02	1.6E-04	26.1	0.4
GrajaSãoPedro												
Mojuí	4.6	10.0	4.1E-03	1.2E-04	24.3	0.3	2.6	27.0	3.7E-03	1.2E-04	26.0	0.4
Belterra												
FLONA	0.2	92.8	1.5E-03	8.6E-05	25.2	0.3	0.1	93.1	1.1E-03	8.6E-05	26.9	0.3
SacradoCoraçao	1.4	49.6	5.0E-03	1.1E-04	25.8	0.4	0.6	74.4	4.7E-03	1.1E-04	27.6	0.4

Table B.30: Santarém: OD model fit results.

OD model								
included NGs	Ne, Ar, Kr, Xe							
DoF	180							
start values	A = 0.01 ccSTP/g, T = 25°C, P_{OD} = 1							
fixed parameters	individual p, S = 0 g/kg							
ID	χ^2	Prob [%]	A [ccSTP/g]	ΔA [ccSTP/g]	P_{OD}	ΔP_{OD}	T [°C]	ΔT [°C]
Pajuçara	86.0	0.0	0.0043	0.0002	1.19	0.02	30.4	0.8
Santarém	86.0	0.0	0.0031	0.0002	1.19	0.02	33.7	0.9
PontaDePedras	86.0	0.0	0.0034	0.0002	1.19	0.02	30.4	0.9
AlterDoChão2	86.0	0.0	0.0019	0.0002	1.19	0.02	33.2	0.9
Cosanpa	86.0	0.0	0.0037	0.0002	1.19	0.02	30.0	0.8
AlterDoChão1	86.0	0.0	0.0017	0.0002	1.19	0.02	32.9	0.9
Barrudada	86.0	0.0	0.0019	0.0002	1.19	0.02	35.1	0.9
FonteCairé	86.0	0.0	0.0030	0.0002	1.19	0.02	29.8	0.9
Mararu	86.0	0.0	0.0001	0.0002	1.19	0.02	32.4	0.9
ZooFit	86.0	0.0	0.0005	0.0002	1.19	0.02	32.6	0.9
CampoNovo	86.0	0.0	0.0015	0.0002	1.19	0.02	27.1	0.8
Peleja	86.0	0.0	0.0053	0.0002	1.19	0.02	29.9	0.8
Tipizal	86.0	0.0	0.0044	0.0002	1.19	0.02	29.8	0.9
Mapinguari	86.0	0.0	0.0092	0.0002	1.19	0.02	29.4	0.9
VilaNova	86.0	0.0	-0.0002	0.0002	1.19	0.02	34.1	0.9
Jatobá	86.0	0.0	0.0032	0.0002	1.19	0.02	30.6	0.9
SantaRosa	86.0	0.0	-0.0002	0.0002	1.19	0.02	32.4	0.9
Cipoal	86.0	0.0	0.0064	0.0002	1.19	0.02	30.2	0.9
Curupira	86.0	0.0	-0.0003	0.0002	1.19	0.02	32.7	0.9
SãoJose	86.0	0.0	0.0107	0.0002	1.19	0.02	31.1	0.9
GrajaSãoPedro								
Mojuí	86.0	0.0	0.0027	0.0002	1.19	0.02	31.0	0.9
Belterra								
FLONA	86.0	0.0	0.0001	0.0002	1.19	0.02	32.0	0.9
SacradoCoraçao	86.0	0.0	0.0037	0.0002	1.19	0.02	32.7	0.9

Table B.31: Santarém: CE model fit results.

CE model	$X/X_{atm} = 1.000$								$X/X_{atm} = 1.045$								fit for given GWT			
included NGs	Ne, Ar, Kr, Xe								Ne, Ar, Kr, Xe								Ne, Ar, Kr, Xe			
DoF	2								2								2			
start values	$A = 0.01$ ccSTP/g, $T = 25$°C, $F_{CE} = 0$								$A = 0.01$ ccSTP/g, $T = 25$°C, $F_{CE} = 0$								$p* = 1$ atm, $A = 0.01$ ccSTP/g, $F_{CE} = 0$			
fixed parameters	individual p, $S = 0$ g/kg								individual p, $S = 0$ g/kg								$S = 0$ g/kg, $T =$ GWT			
ID	χ^2	Prob [%]	A [ccSTP/g]	ΔA [ccSTP/g]	F_{CE}	ΔF_{CE}	T [°C]	ΔT [°C]	χ^2	Prob [%]	A [ccSTP/g]	ΔA [ccSTP/g]	F_{CE}	ΔF_{CE}	T [°C]	ΔT [°C]	χ^2	Prob [%]	$p*$	$\Delta p*$
Pajuçara	0.0	96.8	2.6E-02	5.7E-03	0.476	0.029	28.6	1.2	0.0	98.1	2.5E-02	6.2E-03	0.499	0.032	29.9	1.2	0.0	95.9	0.99	0.04
Santarém	0.6	44.9	8.4E-03	3.2E-03	0.315	0.135	27.8	0.9	0.7	40.5	6.9E-03	3.3E-03	0.280	0.200	29.2	0.9	0.6	42.4	1.02	0.03
PontaDePedras	0.1	76.6	1.9E-02	5.2E-03	0.496	0.042	27.1	1.1	0.1	81.5	1.8E-02	5.5E-03	0.517	0.049	28.4	1.1	0.0	83.1	1.06	0.04
AlterDoChão2	1.9	17.4	1.1E-02	5.0E-03	0.512	0.102	27.8	1.0	2.0	15.3	9.1E-03	5.3E-03	0.518	0.140	29.2	1.0	1.9	16.3	1.02	0.03
Cosanpa	0.0	92.0	1.4E-02	3.6E-03	0.407	0.060	25.6	0.9	0.0	86.1	1.3E-02	3.7E-03	0.414	0.075	26.9	0.9	0.1	79.9	1.08	0.03
AlterDoChão1	0.2	69.7	1.2E-02	5.8E-03	0.565	0.083	27.8	1.1	0.1	74.6	1.1E-02	6.2E-03	0.581	0.109	29.2	1.0	0.1	71.5	1.01	0.03
Barrudada	0.2	69.2	1.0E-02	4.7E-03	0.505	0.108	29.6	1.0	0.2	63.9	8.5E-03	4.9E-03	0.506	0.152	31.1	1.0	0.1	75.3	0.94	0.03
FonteCairé	1.2	27.7	1.7E-02	5.1E-03	0.504	0.048	26.0	1.1	1.1	30.3	1.6E-02	5.4E-03	0.523	0.057	27.3	1.1	1.0	30.8	1.05	0.04
Mararu	0.6	44.9	9.1E-03	8.3E-03	0.628	0.181	26.2	0.7	0.6	45.3	1.1E-03	5.3E-02	0.000	0.357	27.2	0.7	0.7	41.4	1.05	0.02
ZooFit	0.0	84.4	8.6E-03	6.2E-03	0.569	0.174	26.4	0.7	0.0	91.1	8.4E-03	7.0E-03	0.605	0.188	28.1	0.7	0.0	90.2	1.05	0.03
CampoNovo	1.1	29.0	2.1E-02	9.6E-03	0.660	0.043	23.2	1.1	1.0	31.7	2.0E-02	1.1E-02	0.692	0.050	24.5	1.1	0.7	40.0	1.18	0.04
Peleja	0.0	90.9	1.2E-02	2.6E-03	0.267	0.066	25.0	0.8	0.0	84.5	1.1E-02	2.7E-03	0.258	0.083	26.3	0.8	0.0	85.1	1.03	0.03
Tipizal	0.0	95.8	8.7E-03	2.8E-03	0.208	0.132	24.0	0.9	0.0	89.9	7.3E-03	2.8E-03	0.164	0.188	25.3	0.9	0.0	86.8	1.05	0.03
Mapinguari	0.5	49.5	2.1E-02	2.7E-03	0.229	0.031	26.7	1.1	0.4	53.9	2.0E-02	2.8E-03	0.234	0.035	28.1	1.1	0.5	49.4	0.99	0.03
VilaNova	5.2	2.3	1.1E-03	1.1E-03	0.000	0.106	26.9	0.4	7.4	0.7	7.8E-04	6.1E-04	0.000	0.070	28.8	0.4	5.2	2.3	0.99	0.03
Jatobá	0.5	47.0	9.4E-03	3.3E-03	0.345	0.112	25.1	0.9	0.4	51.7	7.9E-03	3.4E-03	0.321	0.161	26.4	0.9	0.5	49.1	1.01	0.03
SantaRosa	0.3	58.5	1.1E-02	1.2E-02	0.695	0.176	26.2	0.6	0.3	56.8	7.6E-04	7.0E-02	0.000	0.398	27.3	0.7	0.3	61.0	1.00	0.02
Cipoal	0.2	67.5	1.3E-02	2.5E-03	0.217	0.064	25.3	1.0	0.1	72.7	1.2E-02	2.6E-03	0.208	0.079	26.7	1.0	0.1	72.4	1.03	0.03
Curupira	2.0	15.8	1.0E-03	6.2E-03	0.000	0.171	25.7	0.4	3.7	5.6	7.0E-04	1.5E-02	0.000	0.125	27.5	0.4	3.2	7.4	1.02	0.02
SãoJose	0.0	87.7	1.9E-02	2.3E-03	0.160	0.033	27.5	1.1	0.0	82.4	1.8E-02	2.4E-03	0.160	0.038	28.9	1.1	0.0	89.1	0.97	0.03
GrajaSãoPedro	1121.2	0.0	2.4E-02	4.3E-04	0.198	0.007	24.9	0.3	1476.3	0.0	2.7E-02	1.4E-03	0.230	0.012	27.6	0.8	895.0	0.0	0.99	0.03
Mojuí	0.1	72.0	1.1E-02	3.8E-03	0.430	0.093	25.8	0.9	0.1	77.7	9.1E-03	4.0E-03	0.425	0.127	27.2	0.9	0.1	72.1	0.99	0.03
Belterra	2001.2	0.0	2.3E-02	9.4E-04	0.059	0.011	20.3	0.6	2.2	13.6	2.5E-02	2.0E-03	0.082	0.022	22.6	1.0	1.8	18.2	1.13	0.04
FLONA	0.0	84.3	8.4E-03	6.9E-03	0.611	0.180	25.8	0.6	0.1	70.5	1.1E-03	2.0E-02	0.000	0.349	26.9	0.6	0.1	82.2	1.00	0.02
SacradoCoraçao	0.4	51.9	7.6E-03	2.8E-03	0.218	0.155	26.6	0.9	0.3	56.9	6.1E-03	2.8E-03	0.155	0.239	28.0	0.9	0.4	50.6	0.98	0.03

Table B.32: Santarém: PR model fit results.

PR model	X/X_{atm} = 1.000								X/X_{atm} = 1.000								X/X_{atm} = 1.045							
included NGs	He, Ne, Ar, Kr, Xe								Ne, Ar, Kr, Xe								Ne, Ar, Kr, Xe							
DoF	2								1								2							
start values	A = 0.01 ccSTP/g, T = 25°C, F_{PR} = 0								A = 0.01 ccSTP/g, T = 25°C, F_{PR} = 0								A = 0.01 ccSTP/g, T = 25°C, F_{PR} = 0							
fixed parameters	individual p, S = 0 g/kg, β = 1								individual p, S = 0 g/kg, β = 1								individual p, S = 0 g/kg, β = 1							
ID	χ^2	Prob [%]	A [ccSTP/g]	ΔA [ccSTP/g]	F_{PR}	ΔF_{PR}	T [°C]	ΔT [°C]	χ^2	Prob [%]	A [ccSTP/g]	ΔA [ccSTP/g]	F_{PR}	ΔF_{PR}	T [°C]	ΔT [°C]	χ^2	Prob [%]	A [ccSTP/g]	ΔA [ccSTP/g]	F_{PR}	ΔF_{PR}	T [°C]	ΔT [°C]
Pajuçara	32.8	0.0	6.2E-03	3.2E-04	0.07	0.04	24.1	0.4	2.4	12.3	3.0E-02	8.9E-03	1.61	0.28	31.0	2.1	2.0	15.2	2.8E-02	8.9E-03	1.59	0.30	32.1	2.1
Santarém	2.6	27.0	4.4E-03	2.7E-04	-0.02	0.04	26.6	0.4	1.0	31.6	7.5E-03	3.2E-03	0.50	0.41	28.1	1.4	1.0	32.7	5.9E-03	2.8E-03	0.34	0.46	29.3	1.3
PontaDePedras	16.0	0.0	5.2E-03	3.1E-04	0.08	0.04	24.0	0.4	0.6	42.6	2.1E-02	7.8E-03	1.45	0.34	28.9	1.9	0.5	48.7	1.9E-02	7.5E-03	1.40	0.38	30.1	1.9
AlterDoChão2	5.3	7.2	3.5E-03	2.7E-04	0.06	0.05	26.3	0.4	3.0	8.1	7.8E-03	4.5E-03	0.84	0.55	28.0	1.6	2.9	9.0	6.0E-03	4.0E-03	0.69	0.64	29.3	1.5
Cosanpa	14.2	0.1	4.0E-03	2.2E-04	-0.24	0.04	22.9	0.3	0.7	41.8	1.4E-02	4.8E-03	0.99	0.32	26.6	1.4	0.5	46.1	1.2E-02	4.5E-03	0.90	0.36	27.8	1.4
AlterDoChão1	4.3	11.8	3.4E-03	2.7E-04	0.09	0.05	26.1	0.4	0.0	85.9	1.1E-02	6.7E-03	1.28	0.55	29.0	1.9	0.0	92.8	9.0E-03	6.0E-03	1.15	0.64	30.1	1.8
Barrudada	3.0	22.9	3.8E-03	4.1E-04	0.14	0.07	28.4	0.5	0.6	43.2	8.2E-03	4.2E-03	0.90	0.50	30.2	1.5	0.5	46.3	6.2E-03	3.7E-03	0.75	0.58	31.4	1.4
FonteCairé	14.4	0.1	4.5E-03	2.9E-04	0.01	0.04	23.1	0.4	0.1	80.7	2.0E-02	7.7E-03	1.47	0.36	27.9	1.8	0.1	74.0	1.8E-02	7.4E-03	1.40	0.40	29.0	1.8
Mararu	0.6	72.5	1.3E-03	2.0E-04	-0.08	0.10	25.4	0.3	0.5	47.8	2.2E-03	2.7E-03	0.43	1.21	25.8	1.2	0.5	48.2	6.2E-04	1.2E-03	-0.53	1.91	27.0	0.9
ZooFit	0.2	89.9	2.1E-03	2.7E-04	0.15	0.09	25.8	0.4	0.0	93.4	3.3E-03	3.1E-03	0.58	0.91	26.3	1.2	0.0	91.8	1.6E-03	2.0E-03	0.08	1.25	27.5	1.1
CampoNovo	10.7	0.5	3.0E-03	2.8E-04	0.05	0.06	20.7	0.4	0.0	96.6	2.3E-02	1.4E-02	1.99	0.54	25.4	2.4	0.0	92.6	2.0E-02	1.4E-02	1.98	0.62	26.5	2.4
Peleja	6.0	5.1	6.9E-03	3.2E-04	0.03	0.03	23.4	0.4	0.4	52.6	1.3E-02	3.5E-03	0.65	0.26	25.7	1.2	0.3	55.5	1.1E-02	3.3E-03	0.55	0.28	26.9	1.2
Tipizal	0.6	73.3	6.6E-03	4.5E-04	0.14	0.04	23.5	0.5	0.1	79.3	8.7E-03	3.2E-03	0.40	0.36	24.3	1.3	0.1	80.7	7.1E-03	2.8E-03	0.26	0.39	25.5	1.3
Mapinguari	22.6	0.0	1.1E-02	3.8E-04	0.00	0.02	22.9	0.4	0.2	69.1	2.8E-02	5.7E-03	0.93	0.20	29.0	1.9	0.1	73.7	2.6E-02	5.5E-03	0.89	0.21	30.2	1.8
VilaNova	5.0	8.4	1.0E-03	1.9E-04	-0.09	0.12	26.9	0.4	1.8	18.0	1.3E-05	6.3E-05	-4.40	4.83	25.7	0.5	2.7	9.8	4.4E-12	3.1E-09	-18.94	700.59	27.7	0.4
Jatobá	3.4	18.0	4.5E-03	2.8E-04	-0.01	0.04	23.8	0.4	0.1	71.4	9.7E-03	3.9E-03	0.73	0.39	25.9	1.4	0.2	68.1	7.7E-03	3.5E-03	0.59	0.44	27.0	1.3
SantaRosa	0.3	85.5	1.2E-03	2.3E-04	0.08	0.13	25.6	0.3	0.2	61.9	1.8E-03	2.7E-03	0.49	1.44	25.8	1.1	0.2	62.7	3.4E-04	9.2E-04	-0.80	2.68	27.0	0.8
Cipoal	6.4	4.0	7.4E-03	3.2E-04	-0.05	0.03	23.3	0.4	0.0	97.4	1.5E-02	3.9E-03	0.62	0.26	26.3	1.5	0.0	99.8	1.3E-02	3.6E-03	0.53	0.28	27.4	1.5
Curupira	1.9	38.8	9.6E-04	1.9E-04	-0.07	0.13	25.7	0.4	0.0	89.7	2.7E-05	1.1E-04	-3.61	4.09	24.7	0.5	0.2	67.1	4.5E-12	3.4E-09	-18.82	759.30	26.6	0.4
SãoJose	11.8	0.3	1.2E-02	4.1E-04	0.02	0.02	24.5	0.5	0.8	37.4	2.3E-02	4.5E-03	0.64	0.19	29.0	1.8	0.7	39.5	2.1E-02	4.4E-03	0.59	0.20	30.2	1.8
GrajaSãoPedro																								
Mojuí	4.3	11.7	4.3E-03	3.2E-04	0.04	0.05	24.4	0.4	0.0	91.1	1.0E-02	4.4E-03	0.91	0.41	26.6	1.4	0.0	96.0	8.3E-03	3.9E-03	0.77	0.46	27.8	1.4
Belterra																								
FLONA	0.2	92.4	1.4E-03	2.2E-04	-0.01	0.10	25.2	0.3	0.1	79.8	2.0E-03	2.3E-03	0.32	1.09	25.4	1.0	0.1	79.1	7.2E-04	1.2E-03	-0.42	1.66	26.7	0.8
SacradoCoraçao	1.7	42.0	4.8E-03	2.7E-04	-0.06	0.04	25.7	0.4	0.2	64.9	7.8E-03	3.0E-03	0.43	0.38	27.1	1.3	0.2	63.7	6.1E-03	2.7E-03	0.26	0.42	28.3	1.3

Table B.33: Santarém: GR model fit results.

GR model	including He data										not including He data									
included NGs	He, Ne, Ar, Kr, Xe										Ne, Ar, Kr, Xe									
DoF	179										118									
start values	A = 0.01 ccSTP/g, T = 25°C, F_{GR} = 1, P_{GR} = 1										A = 0.01 ccSTP/g, T = 25°C, F_{GR} = 1, P_{GR} = 1									
fixed parameters	individual p, S = 0 g/kg, $\beta = 2/3$										individual p, S = 0 g/kg, $\beta = 2/3$									
ID	χ^2	Prob [%]	A [ccSTP/g]	ΔA [ccSTP/g]	P_{GR}	ΔP_{GR}	F_{GR}	ΔF_{GR}	T [°C]	ΔT [°C]	χ^2	Prob [%]	A [ccSTP/g]	ΔA [ccSTP/g]	P_{GR}	ΔP_{GR}	F_{GR}	ΔF_{GR}	T [°C]	ΔT [°C]
Pajuçara	164.7	0.0	0.004	0.000	1.17	0.02	0.02	0.03	29.8	0.8	47.3	33.9	0.015	0.003	0.99	0.05	1.92	0.28	25.7	1.5
Santarém	164.7	0.0	0.003	0.000	1.17	0.02	0.02	0.03	33.2	0.8	47.3	33.9	0.012	0.002	0.99	0.05	1.92	0.28	28.4	1.6
PontaDePedras	164.7	0.0	0.003	0.000	1.17	0.02	0.02	0.03	29.8	0.8	47.3	33.9	0.012	0.003	0.99	0.05	1.92	0.28	25.3	1.6
AlterDoChão2	164.7	0.0	0.002	0.000	1.17	0.02	0.02	0.03	32.4	0.8	47.3	33.9	0.009	0.002	0.99	0.05	1.92	0.28	27.3	1.7
Cosanpa	164.7	0.0	0.004	0.000	1.17	0.02	0.02	0.03	30.2	0.8	47.3	33.9	0.013	0.003	0.99	0.05	1.92	0.28	25.1	1.6
AlterDoChão1	164.7	0.0	0.002	0.000	1.17	0.02	0.02	0.03	32.1	0.8	47.3	33.9	0.008	0.002	0.99	0.05	1.92	0.28	26.9	1.7
Barrudada	164.7	0.0	0.002	0.000	1.17	0.02	0.02	0.03	34.3	0.8	47.3	33.9	0.009	0.002	0.99	0.05	1.92	0.28	29.3	1.7
FonteCairé	164.7	0.0	0.003	0.000	1.17	0.02	0.02	0.03	29.3	0.8	47.3	33.9	0.012	0.002	0.99	0.05	1.92	0.28	24.5	1.6
Mararu	164.7	0.0	0.000	0.000	1.17	0.02	0.02	0.03	31.9	0.8	47.3	33.9	0.004	0.001	0.99	0.05	1.92	0.28	25.6	1.8
ZooFit	164.7	0.0	0.000	0.000	1.17	0.02	0.02	0.03	31.8	0.8	47.3	33.9	0.005	0.002	0.99	0.05	1.92	0.28	26.0	1.8
CampoNovo	164.7	0.0	0.002	0.000	1.17	0.02	0.02	0.03	26.6	0.8	47.3	33.9	0.007	0.002	0.99	0.05	1.92	0.28	21.2	1.6
Peleja	164.7	0.0	0.005	0.000	1.17	0.02	0.02	0.03	29.4	0.8	47.3	33.9	0.017	0.003	0.99	0.05	1.92	0.28	25.5	1.5
Tipizal	164.7	0.0	0.004	0.000	1.17	0.02	0.02	0.03	28.8	0.8	47.3	33.9	0.015	0.003	0.99	0.05	1.92	0.28	25.1	1.5
Mapinguari	164.7	0.0	0.010	0.000	1.17	0.02	0.02	0.03	29.1	0.8	47.3	33.9	0.027	0.005	0.99	0.05	1.92	0.28	26.8	1.3
VilaNova	164.7	0.0	0.000	0.000	1.17	0.02	0.02	0.03	33.6	0.8	47.3	33.9	0.003	0.001	0.99	0.05	1.92	0.28	27.0	1.8
Jatobá	164.7	0.0	0.003	0.000	1.17	0.02	0.02	0.03	30.1	0.8	47.3	33.9	0.012	0.002	0.99	0.05	1.92	0.28	25.4	1.6
SantaRosa	164.7	0.0	0.000	0.000	1.17	0.02	0.02	0.03	31.8	0.8	47.3	33.9	0.003	0.001	0.99	0.05	1.92	0.28	25.6	1.8
Cipoal	164.7	0.0	0.007	0.000	1.17	0.02	0.02	0.03	30.0	0.8	47.3	33.9	0.020	0.004	0.99	0.05	1.92	0.28	26.5	1.4
Curupira	164.7	0.0	0.000	0.000	1.17	0.02	0.02	0.03	32.2	0.8	47.3	33.9	0.003	0.001	0.99	0.05	1.92	0.28	25.7	1.8
SãoJose	164.7	0.0	0.011	0.000	1.17	0.02	0.02	0.03	30.6	0.9	47.3	33.9	0.032	0.005	0.99	0.05	1.92	0.28	29.5	1.3
GrajaSãoPedro																				
Mojuí	164.7	0.0	0.003	0.000	1.17	0.02	0.02	0.03	30.5	0.8	47.3	33.9	0.011	0.002	0.99	0.05	1.92	0.28	25.6	1.6
Belterra																				
FLONA	164.7	0.0	0.000	0.000	1.17	0.02	0.02	0.03	31.5	0.8	47.3	33.9	0.004	0.001	0.99	0.05	1.92	0.28	25.3	1.7
SacradoCoraçao	164.7	0.0	0.004	0.000	1.17	0.02	0.02	0.03	32.4	0.8	47.3	33.9	0.013	0.003	0.99	0.05	1.92	0.28	27.8	1.6

B.25 Santarém: Physicochemical parameters of groundwater and stable isotope data

Table B.34: Santarém: Physicochemical parameters of groundwater. Data of stable isotopes of water are given relative to the VSMOW standard.

ID	GWT [°C]	ΔGWT [°C]	pH	ΔpH	κ_{25} [µS/cm]	$\Delta\kappa_{25}$ [µS/cm]	ORP [mV]	ΔORP [mV]	O_2 [mg/l]	ΔO_2 [mg/l]	$\delta^{18}O$ [‰]	$\Delta\delta^{18}O$ [‰]	δ^2H [‰]	$\Delta\delta^2H$ [‰]
rainy season (2014)														
Santarém	30.1	0.4	4.03	0.02	183	1			6.52	0.02	-6.11	0.05	-36.67	0.44
AlterDoChão2	28.5	0.3	3.79	0.05	220	1	343	5	2.30	0.03	-5.88	0.03	-35.36	0.15
AlterDoChão1	28.3	0.3	4.03	0.08	89	1	68	10	6.06	0.08	-6.52	0.02	-40.44	0.28
FonteCairé	27.6	0.2	4.25	0.03	73	1					-6.40	0.04	-38.46	0.27
Mararu	27.8	0.3	4.02	0.05	136	1	430	3	5.40	0.03	-4.86	0.00	-25.84	0.05
ZooFit	27.9	0.1	5.11	0.02	215	1			5.19	0.03	-6.12	0.03	-36.29	0.24
CampoNovo	28.1	0.1	4.26	0.15	92	1			3.16	0.03	-5.91	0.02	-34.76	0.17
Peleja	26.2	0.3	4.16	0.10	134	1	213	10	3.15	0.08	-5.84	0.06	-35.37	0.18
Tipizal	26.1	0.2	4.22	0.10	78	1	223	10	5.49	0.15	-5.91	0.05	-34.21	0.30
Mapinguari	26.6	0.3	4.14	0.10	143	1	411	3	3.78	0.05	-5.74	0.03	-33.66	0.06
VilaNova	27.0	0.3	5.00	0.03	178	1			1.34	0.03	-5.74	0.05	-33.36	0.32
SantaRosa	26.2	0.2	4.19	0.15	78	1	343	10	3.40	0.05	-5.73	0.02	-33.43	0.10
Curupira	27.1	0.1	4.61	0.10	148	1	142	2	0.57	0.04	-4.97	0.00	-28.77	0.03
SãoJose	27.1	0.2	2.87	0.15	141	1			5.24	0.05	-5.95	0.04	-35.05	0.02
FLONA	25.8	0.1	4.19	0.09	135	1			4.33	0.05	-5.39	0.01	-30.87	0.05
dry season (2015)														
Pajuçara	28.8	0.1	4.07	0.01	18	1	330	5	8.20	0.20	-3.94	0.05	-32.74	0.07
Santarém	30.4	0.2	3.74	0.01	77	1	360	5	7.36	0.02	-6.29	0.08	-37.95	0.33
PontaDePedras	29.4	0.1	3.71	0.02	50	1	325	10	5.52	0.02	-6.34	0.02	-37.39	0.04
AlterDoChão2	29.0	0.2	3.46	0.01	259	1	313	5	1.65	0.02	-5.73	0.02	-33.86	0.02
Cosanpa	31.9	0.2	4.84	0.01	23	1	299	5	4.73	0.05	-7.11	0.00	-43.85	0.15
AlterDoChão1	28.7	0.1	3.85	0.01	40	1	313	10	6.70	0.02	-6.19	0.04	-38.23	0.33
Barrudada	30.7	0.1	4.50	0.01	260	1	317	10	4.10	0.01	-6.38	0.05	-37.14	0.41
FonteCairé	28.8	0.2	5.24	0.02	29	1	283	10	6.73	0.05	-4.82	0.05	-35.98	0.24
Mararu	27.9	0.1	4.01	0.01	35	1	347	5	4.05	0.05	-5.57	0.04	-31.43	0.18
ZooFit	28.9	0.1	4.95	0.02	61	1	251	5	7.00	0.02	-3.64	0.01	-30.83	0.05
CampoNovo	28.5	0.1	4.01	0.01	20	1	300	5	2.72	0.02	-6.01	0.03	-35.68	0.08
Peleja	26.7	0.1	4.08	0.01	29	1	320	5	3.58	0.01	-6.08	0.02	-35.94	0.05
Tipizal	26.4	0.2	4.05	0.01	25	1	356	10	5.98	0.01	-5.90	0.01	-34.54	0.03
Mapinguari	26.9	0.1	3.83	0.01	34	1	302	5	1.91	0.05	-5.87	0.03	-34.22	0.05
VilaNova	28.7	0.1	4.72	0.01	27	1	70	5	0.49	0.02	-5.99	0.02	-35.25	0.10
Jatobá	26.2	0.0	3.97	0.03	27	1	334	5	1.70	0.01	-6.12	0.03	-35.67	0.02
SantaRosa	26.4	0.1	4.05	0.03	26	1	355	5	3.77	0.01	-5.66	0.01	-33.13	0.06
Cipoal	27.1	0.1	3.99	0.05	27	1	332	5	4.48	0.01	-6.20	0.01	-36.49	0.05
Curupira	27.5	0.1	4.41	0.01	70	1	126	10	0.17	0.01	-4.56	0.04	-26.22	0.04
SãoJose	27.2	0.1	3.94	0.01	30	1	318	10	5.35	0.50	-5.86	0.02	-34.67	0.06
GrajaSãoPedro	25.9	0.2	4.05	0.03	24	1	346	5	5.78	0.10	-3.93	0.01	-29.67	0.01
Mojuí	26.3	0.1	4.04	0.02	27	1	331	10	5.05	0.20	-5.64	0.01	-33.30	0.17
Belterra	25.9	0.1	4.12	0.01	19	1	283	10	8.00	0.40	-5.96	0.05	-35.37	0.23
FLONA	26.1	0.3	3.92	0.01	25	1	294	5	2.76	0.01	-5.34	0.01	-30.94	0.09
SacradoCoraçao	26.7	0.1	3.79	0.01	33	1	350	5	5.70	0.50	-5.75	0.02	-33.81	0.08

B.26 CE model outcomes for a stepwise adding of excess air

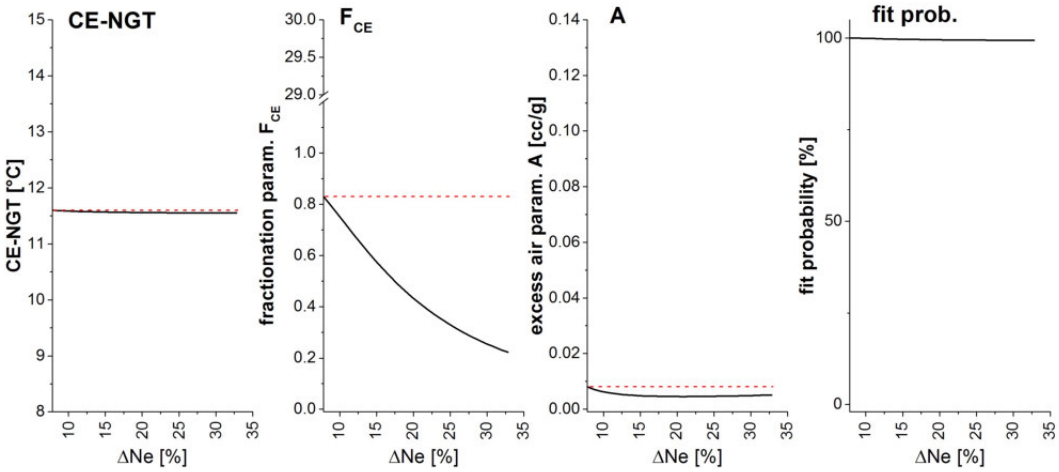

(a) Small amount of excess air: synthetic samples created for $T = 11.6°C$, $F = 0.83$ and $A = 8\,cc/kg$.

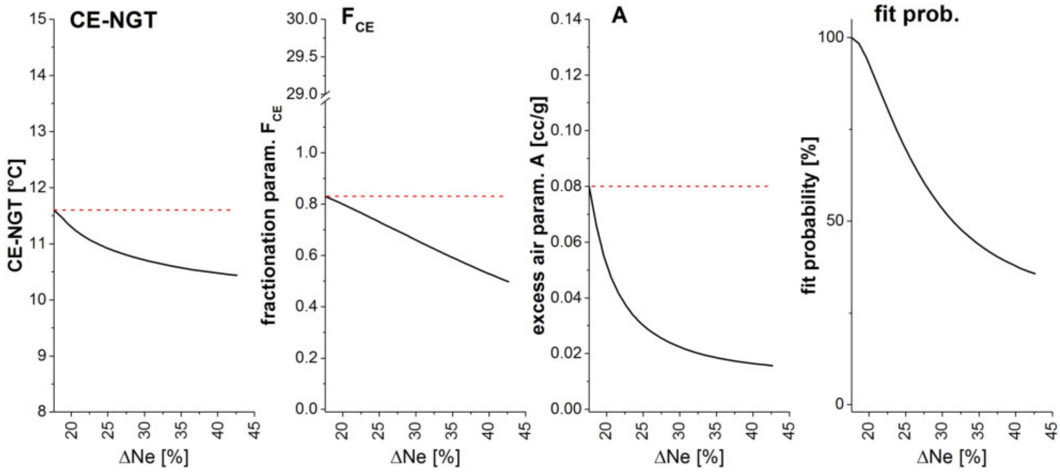

(b) Large amount of excess air: synthetic samples created for $T = 11.6°C$, $F = 0.83$ and $A = 80\,cc/kg$.

Figure B.16: Mannheim: Illustration of CE model fit outcomes from *PANGA* for synthetic NG data. An initial synthetic sample was created for given recharge conditions (see labeling below graphs) according to the CE model setup. A stepwise increasing amount of unfractionated excess air was subsequently added to this sample, in steps of each ΔNe = 1 %. Thus, the CE model setup provides no exact description of the resulting NG pattern, resulting in bias fit outcomes as depicted.

List of Tables

2.1 Mixing ratios of the eight most abundant gases in dry atmospheric air 20
2.2 Fractions of isotopes of different NG species in homogeneously mixed dry atmospheric air 32
2.3 Half-lives of natural Rn isotopes 37
2.4 Stable isotopes and molar fractions of oxygen and hydrogen 40

3.1 *Omnistar*: Composition of reference gases 57
3.2 *Omnistar*: Average reproducibility of measurements 60
3.3 *MM5400*: Single sample uncertainties and standard deviations of reference samples . 69

5.1 Mannheim: Sum values of O_2+CO_2 and mixing ratios of N_2/NGs in soil air 95
5.2 Mannheim: Overview of applied excess air model fits and obtained parameter values for shallow well samples 114
5.3 Mannheim: Overview of applied excess air model fits and obtained parameter values for deep well samples 116
5.4 Mannheim: Obtained χ^2 values of different forward modeling scenarios 134

6.1 Santarém: Sum values of O_2+CO_2 and mixing ratios of N_2/NGs in soil air 140
6.2 Santarém: Overview of the applied excess air model fits and parameter values 151

A.1 Parameter values for the temperature dependency of the solubility of non-polar gases 177
A.2 Resulting volume contents of V_{inlet} 180
A.3 Mannheim: Parameters of the forward modeling approach 183
A.4 Gas-specific parameters for gas transport modeling 185

B.1 Mannheim: Soil air composition at 1.0 m depth 193
B.2 Mannheim: Soil air composition at 3.0 m depth 194
B.3 Mannheim: Soil air composition at 4.4 m depth 195
B.4 Mannheim: Soil air composition at 5.5 m depth 196
B.5 Mannheim: Soil air composition at 6.5 m depth 197
B.6 Mannheim (shallow well): NG concentrations in groundwater 198
B.7 Mannheim (deep well): NG concentrations in groundwater 199
B.8 Mannheim (shallow well): UA model fit results 200

B.9 Mannheim (shallow well): CE model fit results 201
B.10 Mannheim (shallow well): PR model fit results 202
B.11 Mannheim (shallow well): OD model fit results 203
B.12 Mannheim (shallow well): GR model fit results 204
B.13 Mannheim (deep well): UA model fit results 205
B.14 Mannheim (deep well): CE model fit results 205
B.15 Mannheim (deep well): PR model fit results 206
B.16 Mannheim (deep well): OD model fit results 206
B.17 Mannheim (deep well): GR model fit results 207
B.18 Mannheim (shallow well): Physicochemical parameters of groundwater and stable isotopes of water 209
B.19 Mannheim (deep well): Physicochemical parameters of groundwater and stable isotopes of water 210
B.20 Mannheim (shallow well): Determined ^{3}H–^{3}He ages 211
B.21 Mannheim (deep well): Determined ^{3}H–^{3}He ages 212
B.22 Santarém: Overview of soil temperatures in Santarém and in the Amazon region . . . 213
B.23 Santarém: Meteorological stations referred to in this study 214
B.24 Santarém: Mean annual values from data records of meteorological stations 214
B.25 Santarém: Assumptions about equilibration conditions during recharge 217
B.26 Santarém: Soil air composition during rainy and dry season 218
B.27 Santarém: NG concentrations in groundwater 220
B.28 Santarém: Measured tritium concentrations and ^{3}He/^{4}He ratios 221
B.29 Santarém: UA model fit results 222
B.30 Santarém: OD model fit results 222
B.31 Santarém: CE model fit results 223
B.32 Santarém: PR model fit results 224
B.33 Santarém: GR model fit results 225
B.34 Santarém: Physicochemical parameters of groundwater and stable isotopes of water . 226

List of Figures

1.1 Summary of expected subsurface gas dynamics determining short-term fluctuations of NG concentrations in soil air and groundwater 2

2.1 Typical soil water characteristics for a loamy soil as well as for a sandy soil 9
2.2 Overview of different subsurface zones, defined according to their water content . . . 10
2.3 Schematic illustration of interactions between atmosphere and biosphere in the carbon cycle 13
2.4 Illustration of aerobic and anaerobic regions in a small-scale soil structure 14
2.5 Schematic illustration of the nitrogen cycle interactions between atmosphere and biosphere 15
2.6 Simulated soil respiration rate in a certain soil depth for varying soil temperature and soil moisture contents 18
2.7 Seasonal variations of soil respiration for different climate conditions on the northern hemisphere 18
2.8 Contents of O_2 and CO_2 in a silty clay soil 18
2.9 Diurnal and annual fluctuations of soil temperature 28
2.10 Empirical Ostwald solubilities for NGs as well as for O_2 and N_2 30
2.11 Different components of dissolved NGs in groundwater 33
2.12 Three isotope plot 36
2.13 Tritium concentrations in precipitation in Stuttgart from 1961 to 2012 39
2.14 Schematic illustration of isotope fractionation during the formation of precipitation . 43

3.1 Sampling procedure for soil air 46
3.2 Principle of the TDR method and exemplary data evaluation 47
3.3 In-situ measurement of volumetric soil moisture 49
3.4 Groundwater sampling during field campaign in Brazil 51
3.5 *Omnistar*: Setup of the device 53
3.6 *Omnistar*: Operating principle of ion separation by quadrupole mass spectrometry . . 54
3.7 *Omnistar*: Illustration of the evaluation procedure 58
3.8 *Omnistar*: Time series of N_2, O_2, CO_2 and ^{40}Ar from calibration measurements . . . 59
3.9 *Omnistar*: Effect of long storage durations 61
3.10 *MM5400*: Determination of NG mixing ratios in gas samples 64

3.11 *MM5400*: Time series of measured reference samples 68
3.12 Overview of excess air models applied in this study 72
3.13 Theoretically expected correlation between O_2+CO_2 and NG mixing ratios 75
3.14 Architecture of the implemented soil gas transport model 81

4.1 Installation of the long-term sampling site near Mannheim 84
4.2 Setup of the long-term sampling site near Mannheim 85
4.3 Contour lines of the topmost groundwater aquifer in the Rhine-Neckar region 86
4.4 Climate data from a measurement site in Mannheim Vogelstang 87
4.5 Long-term records of meteorological conditions in the sampling area near Mannheim 87
4.6 Climate conditions in South America 88
4.7 Climatic conditions in the study area near Santarém 89
4.8 Water level fluctuations of the Amazon river in the sampling area near Santarém . . . 89
4.9 Long-term records of meteorological conditions and river water table fluctuations of Rio Tapajós in the sampling area near Santarém 90
4.10 Topography of the sampling area around the city of Santarém 91
4.11 Schematic cross section of groundwater flow conditions near Santarém 91

5.1 Mannheim: O_2+CO_2 time series in soil air at different depths 94
5.2 Mannheim: Time series of soil air composition near Mannheim at 1.0 m and 5.5 m depth 94
5.3 Mannheim: Correlation of O_2+CO_2 concentrations with mixing ratios of N_2, ^{20}Ne and ^{132}Xe in soil air 96
5.4 Mannheim: Measured activities of ^{222}Rn at all sampled depths 97
5.5 Mannheim: Time series of volumetric soil moisture contents 98
5.6 Mannheim: Time series of soil temperature 99
5.7 Mannheim: Measured time series of physical parameters at the shallow well 101
5.8 Mannheim: Measured time series of NGs and stable isotopes at the shallow well . . . 103
5.9 Mannheim: Measured time series at the deep well 105
5.10 Mannheim: Measured contents of stable isotopes of water at both sampled wells . . . 106
5.11 Mannheim: Xe-Ne plots illustrating dissolved NG contents of samples from both investigated wells 107
5.12 Mannheim: NGTs determined by excess air model fits for shallow well samples . . . 109
5.13 Mannheim: NGTs determined by excess air model fits for shallow well samples, allowing for variations of gas phase NG composition with respect to atmosphere . . . 112
5.14 Mannheim: NGTs determined by means of excess air model fits for deep well samples 115
5.15 Mannheim: Correlation between soil air mixing ratios of O_2+CO_2 and volumetric soil moisture contents 117
5.16 Mannheim: Correlation between soil air mixing ratios of O_2+CO_2 and soil temperatures 117
5.17 Mannheim: Modeled soil air content of O_2+CO_2 119
5.18 Mannheim: Modeled soil air composition 120

5.19 Mannheim: Modeled data, showing relative contributions of different transport processes . . . 121
5.20 Mannheim: Comparison of modeled and measured soil air composition . . . 122
5.21 Mannheim: Fractionation plots showing modeled and measured NG mixing ratios in soil air . . . 122
5.22 Mannheim: Groundwater table level at a well in Heddesheim . . . 124
5.23 Mannheim: Monthly groundwater level changes and annual distribution of monthly water table increases . . . 126
5.24 Mannheim: Stable isotopes of water: $\delta^{18}O$ and $\delta^{2}H$ . . . 127
5.25 Mannheim: Evaluation of dissolved NG contents in groundwater from different wells in the Rhine-Neckar region around the sampling site near Mannheim . . . 129
5.26 Mannheim: Measured and forward modeled saturation anomalies . . . 133
5.27 Mannheim: NGT determination by CE model fits for forward modeled data . . . 135
5.28 Mannheim: Illustration of dissolved NG contents in synthetic groundwater samples for varying degrees of degassing . . . 136

6.1 Santarém: Correlation between O_2+CO_2 contents in soil air and mixing ratios of N_2, ^{20}Ne and ^{132}Xe . . . 140
6.2 Santarém: Physical parameter analysis for the unsaturated zone . . . 142
6.3 Santarém: Typical isotopic composition of precipitation . . . 143
6.4 Santarém: Map of the sampling region, illustrating the spatial distribution of $\delta^{18}O$ . . 143
6.5 Santarém: Measured GWT data . . . 144
6.6 Santarém: Physicochemical parameters in groundwater . . . 145
6.7 Santarém: Dissolved NG contents in sampled groundwater . . . 146
6.8 Santarém: Estimated recharge time of sampled groundwater . . . 147
6.9 Santarém: Xe-Ne plot containing NG data from all sampled wells during rainy and dry season . . . 149
6.10 Santarém: Estimated NGTs from excess air model fits . . . 150
6.11 Santarém: Measured concentrations of helium as well as modeled helium concentrations by PR model fits with and without an inclusion of helium data . . . 150
6.12 Santarém: Estimated NGTs from different excess air model fits assuming enhanced NG mixing ratios in soil air with respect to dry atmospheric air . . . 152
6.13 Santarém: Measured concentrations of helium as well as modeled helium concentrations by GR model fits with and without an inclusion of helium data . . . 153
6.14 Santarém: Correlation of soil air composition and volumetric soil moisture contents . 154
6.15 Santarém: Comparison of measured soil air data and model outcomes . . . 156
6.16 Santarém: Fractionation plots showing modeled and measured NG mixing ratios in soil air . . . 157
6.17 Santarém: CE model parameters describing the formation of excess air . . . 159
6.18 Santarém: Mean annual values of meteorological parameters . . . 160

6.19 Santarém: NG mixing ratios in soil air, estimated for given recharge temperatures by a CE model fit . . . 162
6.20 Santarém: Correlation of p^* with ^{40}Ar mixing ratios in soil air . . . 163

7.1 Dependence of soil air composition on soil temperature and volumetric soil moisture 166
7.2 Measured soil air composition in the tropics and mid-latitudes . . . 166
7.3 Summary of subsurface gas dynamics determining short-term fluctuations of NG concentrations in soil air and groundwater . . . 173

A.1 Calibration curves for the three used *ECH2O* FDR sensors . . . 178
A.2 Exemplary determination of gas mixing ratios for samples from copper tubes analyzed by the *Omnistar* device . . . 179

B.1 Mannheim: Comparison of ^{40}Ar data measured by the *MM5400* mass spectrometer and the *Omnistar* device . . . 187
B.2 Santarém: Comparison of ^{40}Ar data measured by the MM5400 mass spectrometer and the *Omnistar* device . . . 187
B.3 Mannheim: Correlation between Ne concentrations and the groundwater table level (shallow well) . . . 188
B.4 Mannheim: Correlation between Xe concentrations and the WTT (shallow well) . . . 188
B.5 Mannheim: Time series of soil air composition (O_2+CO_2 and NGs) . . . 189
B.6 Mannheim: Time series of soil air composition (O_2 and CO_2) . . . 190
B.7 Mannheim: Time series of ^{220}Rn activities in soil air . . . 191
B.8 Mannheim: Three isotope plot . . . 192
B.9 Mannheim: Long-term record of atmospheric air pressure . . . 192
B.10 Mannheim: Monte Carlo simulations of a CE model fit procedure . . . 208
B.11 Santarém: Tritium concentrations in local precipitation in Manaus . . . 213
B.12 Santarém: Atmospheric air pressure records at two different sites and height dependence of the air pressure in the sampling area . . . 215
B.13 Santarém: Average monthly values of atmospheric air pressure at Mojui station and river water level . . . 215
B.14 Santarém: Three isotope plot . . . 216
B.15 Santarém: Correlation of different parameters and O_2+CO_2 sum values in soil air . . 219
B.16 Mannheim: Illustration of CE model fit outcomes for synthetic NG data . . . 227

Bibliography

[ABAS 2010] ABAS, Associação Brasileira de Águas Subterrâneas: Alter do Chão: O maior aquífero do mundo. In: *Revista Água e Meio Ambiente Subterrâneo* Ano 3, 16 (2010)

[Aeschbach-Hertig 1994] Aeschbach-Hertig, W: *Helium und Tritium als Tracer für physikalische Prozesse in Seen*, ETH Zürich, Dissertation, 1994

[Aeschbach-Hertig et al. 2002a] Aeschbach-Hertig, W ; Beyerle, U ; Holocher, J ; Peeters, F ; Kipfer, R: Excess air in groundwater as a potential indicator of past environmental changes. In: IAEA (Hrsg.): *Study of Environmental Change Using Isotope Techniques* Bd. 13/P. Vienna : IAEA, 2002, p. 174–183

[Aeschbach-Hertig et al. 2008] Aeschbach-Hertig, W ; El-Gamal, H ; Wieser, M ; Palcsu, L: Modeling excess air and degassing in groundwater by equilibrium partitioning with a gas phase. In: *Water Resources Research* 44 (2008), No. 8

[Aeschbach-Hertig et al. 1999a] Aeschbach-Hertig, W ; Hofer, M ; Kipfer, R ; Imboden, DM ; Wieler, R: Accumulation of mantle gases in a permanently stratified volcanic Lake (Lac Pavin, France). In: *Geochimica et Cosmochimica Acta* 63 (1999), No. 19, p. 3357–3372

[Aeschbach-Hertig et al. 1996] Aeschbach-Hertig, W ; Kipfer, R ; Hofer, M ; Wieler, R ; Signer, P et al.: Quantification of gas fluxes from the subcontinental mantle: The example of Laacher See, a maar lake in Germany. In: *Geochimica et cosmochimica acta* 60 (1996), No. 1, p. 31–41

[Aeschbach-Hertig et al. 1999b] Aeschbach-Hertig, W ; Peeters, F ; Beyerle, U ; Kipfer, R: Interpretation of dissolved atmospheric noble gases in natural waters. In: *Water Resources Research* 35 (1999), No. 9, p. 2779–2792

[Aeschbach-Hertig et al. 2000] Aeschbach-Hertig, W ; Peeters, F ; Beyerle, U ; Kipfer, R: Palaeotemperature reconstruction from noble gases in ground water taking into account equilibration with entrapped air. In: *Nature* 405 (2000), No. 6790, p. 1040–1044

[Aeschbach-Hertig and Solomon 2013] Aeschbach-Hertig, W ; Solomon, DK: Noble gas thermometry in groundwater hydrology. In: *The noble gases as geochemical tracers*. Springer, 2013, p. 81–122

[Aeschbach-Hertig et al. 2002b] Aeschbach-Hertig, W ; Stute, M ; Clark, JF ; Reuter, RF ; Schlosser, P: A paleotemperature record derived from dissolved noble gases in groundwater of the Aquia Aquifer (Maryland, USA). In: *Geochimica et Cosmochimica Acta* 66 (2002), No. 5, p. 797–817

[Akça et al. 2005] AKÇA, E ; ALBA, SAG ; BIALOUSZ, S ; BERGER, B ; BIELEK, P ; BLUM, W ; BREUNING-MADSEN, H ; BUIVYDAITE, VV ; CANGIR, C et al.: Soil Atlas of Europe. In: *Publications Office of the European Union, L-2995 Luxembourg* (2005), p. 128

[Alvalá et al. 2002] ALVALÁ, RCS ; GIELOW, R ; DA ROCHA, HR ; FREITAS, HC ; LOPES, JM ; MANZI, AO ; VON RANDOW, C ; DIAS, MAF S. ; CABRAL, OMR ; WATERLOO, MJ: Intradiurnal and seasonal variability of soil temperature, heat flux, soil moisture content, and thermal properties under forest and pasture in Rondônia. In: *Journal of Geophysical Research: Atmospheres* 107 (2002), No. D20

[Amos et al. 2005] AMOS, RT ; MAYER, KU ; BEKINS, BA ; DELIN, GN ; WILLIAMS, RL: Use of dissolved and vapor-phase gases to investigate methanogenic degradation of petroleum hydrocarbon contamination in the subsurface. In: *Water Resources Research* 41 (2005), No. 2

[ANA 2016] ANA, Agencia Nacional de Águas: Sistema de Informacoes Hidrológicas. (2016). – URL `http://hidroweb.ana.gov.br/default.asp`. – accessed on 2016/03/04

[Andrews and Lee 1979] ANDREWS, JN ; LEE, DJ: Inert gases in groundwater from the Bunter Sandstone of England as indicators of age and palaeoclimatic trends. In: *Journal of Hydrology* 41 (1979), No. 3, p. 233–252

[Arrhenius 1889] ARRHENIUS, S: On the reaction velocity of the inversion of cane sugar by acids. In: *Journal of Physical Chemistry* 4 (1889), p. 226

[Audi et al. 2003] AUDI, G ; BERSILLON, O ; BLACHOT, J ; WAPSTRA, AH: The NUBASE evaluation of nuclear and decay properties. In: *Nuclear Physics A* 729 (2003), No. 1, p. 3–128

[Auer et al. 1996] AUER, LH ; ROSENBERG, ND ; BIRDSELL, KH ; WHITNEY, EM: The effects of barometric pumping on contaminant transport. In: *Journal of Contaminant Hydrology* 24 (1996), No. 2, p. 145–166

[Baertschi 1976] BAERTSCHI, P: Absolute ^{18}O content of standard mean ocean water. In: *Earth and Planetary Science Letters* 31 (1976), No. 3, p. 341–344

[Ballentine and Burnard 2002] BALLENTINE, CJ ; BURNARD, PG: Production, release and transport of noble gases in the continental crust. In: *Reviews in mineralogy and geochemistry* 47 (2002), No. 1, p. 481–538

[Ballentine and Hall 1999] BALLENTINE, CJ ; HALL, CM: Determining paleotemperature and other variables by using an error-weighted, nonlinear inversion of noble gas concentrations in water. In: *Geochimica et Cosmochimica Acta* 63 (1999), No. 16, p. 2315–2336

[Bartlett et al. 2004] BARTLETT, Marshall G. ; CHAPMAN, David S. ; HARRIS, Robert N.: Snow and the ground temperature record of climate change. In: *Journal of Geophysical Research: Earth Surface* 109 (2004), No. F4

[Beck 2014] Beck, B: *Lokalisierung von aktiven geologischen Störungszonen im Oberrheingraben durch Messung von ^{3}He/^{4}He-Verhältnissen in der Bodenluft*, Institut für Umweltphysik, Universität Heidelberg, Diploma, 2014

[Bender 2003] Bender, K: Grundwasserströmungsmodell für den Grossraum Rhein-Neckar. In: *Grundwasser - Zeitschrift der Fachsektion Hydrogeologie* 8/1 (2003), p. 41–49

[Benson and Krause Jr 1976] Benson, BB ; Krause Jr, D: Empirical laws for dilute aqueous solutions of nonpolar gases. In: *The Journal of Chemical Physics* 64 (1976), No. 2, p. 689–709

[Benson and Krause Jr 1980] Benson, BB ; Krause Jr, D: Isotopic fractionation of helium during solution: A probe for the liquid state. In: *Journal of Solution Chemistry* 9 (1980), No. 12, p. 895–909

[Berglund and Wieser 2011] Berglund, M ; Wieser, ME: Isotopic compositions of the elements 2009 (IUPAC Technical Report). In: *Pure and Applied Chemistry* 83 (2011), No. 2, p. 397–410

[Bertolo et al. 2006] Bertolo, R ; Hirata, R ; Sracek, O: Geochemistry and geochemical modeling of unsaturated zone in a tropical region in Urânia, São Paulo state, Brazil. In: *Journal of Hydrology* 329 (2006), No. 1, p. 49–62

[Beyerle et al. 2000] Beyerle, U ; Aeschbach-Hertig, W ; Imboden, DM ; Baur, H ; Graf, T ; Kipfer, R: A mass spectrometric system for the analysis of noble gases and tritium from water samples. In: *Environmental Science & Technology* 34 (2000), No. 10, p. 2042–2050

[Beyerle et al. 2003] Beyerle, U ; Rueedi, J ; Leuenberger, M ; Aeschbach-Hertig, W ; Peeters, F ; Kipfer, R ; Dodo, A: Evidence for periods of wetter and cooler climate in the Sahel between 6 and 40 kyr BP derived from groundwater. In: *Geophysical Research Letters* 30 (2003), No. 4

[Bischof 1837] Bischof, G: Die Wärmelehre des Innern unseres Erdkörpers. In: *Ein Inbegriff aller mit der Wärme in Beziehung stehender Erscheinungen in und auf der Erde / nach physikalischen, chemischen und geologischen Untersuchungen* (1837)

[Blicher-Mathiesen et al. 1998] Blicher-Mathiesen, G ; McCarty, GW ; Nielsen, LP: Denitrification and degassing in groundwater estimated from dissolved dinitrogen and argon. In: *Journal of Hydrology* 208 (1998), No. 1, p. 16–24

[Blume et al. 2009] Blume, H-P ; Brümmer, GW ; Horn, R ; Kandeler, E ; Kögel-Knabner, I ; Kretzschmar, R ; Stahr, K ; Wilke, B-M: *Scheffer/Schachtschabel: Lehrbuch der Bodenkunde*. Springer-Verlag, 2009

[Brennwald et al. 2003] Brennwald, MS ; Hofer, M ; Peeters, F ; Aeschbach-Hertig, W ; Strassmann, K ; Kipfer, R ; Imboden, DM: Analysis of dissolved noble gases in the porewater of lacustrine sediments. In: *Limnology and Oceanography/Methods* 1 (2003), p. 51–62

[Brusseau 1994] Brusseau, ML: Transport of reactive contaminants in heterogeneous porous media. In: *Reviews of Geophysics* 32 (1994), No. 3, p. 285–313

[Brutsaert and Jirka 1984] BRUTSAERT, W ; JIRKA, GH: *Gas transfer at water surfaces*. Reidel Publishing, Dordrecht, 1984

[Bührer and Ambühl 1975] BÜHRER, H ; AMBÜHL, H: Die Einleitung von gereinigtem Abwasser in Seen. In: *Schweizerische Zeitschrift für Hydrologie* 37 (1975), No. 2, p. 347–369

[Bunnell and Tait 1974] BUNNELL, FL ; TAIT, DEN: Mathematical simulation models of decomposition processes. In: *Soil organisms and decomposition in tundra* (1974), p. 207–225

[Burnard 2013] BURNARD, P: *The Noble Gases as Geochemical Tracers*. Springer, 2013

[Carbon Cycle Group Heidelberg 2014] CARBON CYCLE GROUP HEIDELBERG: Measurements by the Carbon Cycle Group, Institut für Umweltphysik, Universität Heidelberg, personal communication. (2014)

[Castro et al. 2007] CASTRO, MC ; HALL, CM ; PATRIARCHE, D ; GOBLET, P ; ELLIS, BR: A new noble gas paleoclimate record in Texas - Basic assumptions revisited. In: *Earth and Planetary Science Letters* 257 (2007), No. 1, p. 170–187

[Castro et al. 2000] CASTRO, MC ; STUTE, M ; SCHLOSSER, P: Comparison of ^{4}He ages and ^{14}C ages in simple aquifer systems: implications for groundwater flow and chronologies. In: *Applied Geochemistry* 15 (2000), No. 8, p. 1137–1167

[Cey et al. 2009] CEY, BD ; HUDSON, GB ; MORAN, JE ; SCANLON, BR: Evaluation of noble gas recharge temperatures in a shallow unconfined aquifer. In: *Ground Water* 47 (2009), No. 5, p. 646–659

[Cey 2009] CEY, Bradley D.: On the accuracy of noble gas recharge temperatures as a paleoclimate proxy. In: *Journal of Geophysical Research: Atmospheres* 114 (2009), No. D4

[Chapman and Dootson 1917] CHAPMAN, S ; DOOTSON, FW: XXII. A note on thermal diffusion. In: *The London, Edinburgh, and Dublin Philosophical Magazine and Journal of Science* 33 (1917), No. 195, p. 248–253

[Chow et al. 2011] CHOW, TT ; LONG, H ; MOK, HY ; LI, KW: Estimation of soil temperature profile in Hong Kong from climatic variables. In: *Energy and Buildings* 43 (2011), No. 12, p. 3568–3575

[Clark and Fritz 1997] CLARK, ID ; FRITZ, P: *Environmental isotopes in hydrogeology*. CRC press, 1997

[Clements and Wilkening 1974] CLEMENTS, WE ; WILKENING, MH: Atmospheric pressure effects on 222Rn transport across the Earth-air interface. In: *Journal of Geophysical Research* 79 (1974), No. 33, p. 5025–5029

[Clever 1979] CLEVER, HL: *Krypton, Xenon and Radon-Gas Solubilities*. 2. Pergamon Press, Tarrytown, N.Y., 1979

[Cook and Solomon 1997] Cook, PG ; Solomon, DK: Recent advances in dating young groundwater: chlorofluorocarbons, $^3H^3He$ and ^{85}Kr. In: *Journal of hydrology* 191 (1997), No. 1, p. 245–265

[Craig 1961] Craig, H: Isotopic variations in meteoric waters. In: *Science* 133 (1961), No. 3465, p. 1702–1703

[Craig and Gordon 1965] Craig, H ; Gordon, LI: Deuterium and oxygen 18 variations in the ocean and the marine atmosphere. (1965)

[Craig et al. 1988] Craig, H ; Horibe, Y ; Sowers, T: Gravitational separation of gases and isotopes in polar ice caps. In: *Science* 242 (1988), No. 4886, p. 1675–1678

[Cunningham and Williams 1980] Cunningham, RE ; Williams, RJJ: *Diffusion in gases and porous media*. Bd. 1. Springer, 1980

[Dalton 1826] Dalton, J: On the constitution of the atmosphere. In: *Philosophical Transactions of the Royal Society of London* 116 (1826), No. 1/3, p. 174–188

[Daniels 2004] Daniels, DJ: *Ground penetrating radar*. Bd. 1. Iet, 2004

[Dansgaard 1964] Dansgaard, W: Stable isotopes in precipitation. In: *Tellus* 16 (1964), No. 4, p. 436–468

[Darcy 1856] Darcy, H: *Les fontaines publiques de la ville de Dijon: exposition et application...* Victor Dalmont, 1856

[Davidson et al. 2000] Davidson, Eric A. ; Verchot, Louis V. ; Cattânio, J H. ; Ackerman, Ilse L. ; Carvalho, JEM: Effects of soil water content on soil respiration in forests and cattle pastures of eastern Amazonia. In: *Biogeochemistry* 48 (2000), No. 1, p. 53–69

[De Groot and Mazur 2013] De Groot, SR ; Mazur, P: *Non-equilibrium thermodynamics*. Courier Corporation, 2013

[de Wit et al. 1980] de Wit, JC ; Straaten, CM ; Mook, WG: Determination of the Absolute Hydrogen Isotopic Ratio of V-SMOW and SLAP. In: *Geostandards Newsletter* 4 (1980), No. 1, p. 33–36

[Demtröder 2008] Demtröder, W: *Experimentalphysik 1: Mechanik und Wärme*. Springer, 2008

[Dörr and Münnich 1990] Dörr, H ; Münnich, KO: ^{222}Rn flux and soil air concentration profiles in West-Germany. Soil ^{222}Rn as tracer for gas transport in the unsaturated soil zone. In: *Tellus B* 42 (1990), No. 1, p. 20–28

[DWD 2016] DWD: WebWerdis. (2016). – URL `https://werdis.dwd.de/werdis/start_js_JSP.do`. – accessed on 2016/04/30

[Elberling et al. 1998] Elberling, B ; Larsen, F ; Christensen, S ; Postma, D: Gas transport in a confined unsaturated zone during atmospheric pressure cycles. In: *Water Resources Research* 34 (1998), No. 11, p. 2855–2862

[Elderfield et al. 2006] ELDERFIELD, H ; HOLLAND, HD ; TUREKIAN, KK: *The oceans and marine geochemistry*. Bd. 6. Elsevier, 2006

[van Elsas et al. 2006] ELSAS, JD van ; TREVORS, JT ; JANSSON, JK ; NANNIPIERI, P: *Modern soil microbiology*. CRC Press, 2006

[Engelhardt 2015] ENGELHARDT, Lara: *Bestimmung von Bodenparametern im Raum Heddesheim im Kontext der Untersuchung von Transportprozessen in der ungesättigten Bodenzone*, Institut für Umweltphysik, Universität Heidelberg, Staatsexamen, 2015

[Faybishenko 1995] FAYBISHENKO, BA: Hydraulic Behavior of Quasi-Saturated Soils in the Presence of Entrapped Air: Laboratory Experiments. In: *Water Resources Research* 31 (1995), No. 10, p. 2421–2435

[Fayer and Hillel 1986] FAYER, MJ ; HILLEL, D: Air encapsulation: I. Measurement in a field soil. In: *Soil Science Society of America Journal* 50 (1986), No. 3, p. 568–572

[Fick 1855] FICK, A: Über Diffusion. In: *Poggendorff's Annalen der Physik* 94 (1855), p. 59–86

[Fitzjarrald et al. 2009] FITZJARRALD, DR ; SAKAI, RK ; DE MORAES, OLL: LBA-ECO CD-03 Mesoscale Meteorological Data, Santarem Region, Para, Brazil: 1998-2006. Data set from Oak Ridge National Laboratory Distributed Active Archive Center. In: *Oak Ridge, Tennessee, U.S.A.* (2009). – URL `http://daac.ornl.gov`

[Flühler and Roth 2004] FLÜHLER, H ; ROTH, K: Physik der ungesättigten Zone. In: *Skript zur Vorlesung Bodenphysik and der ETH Zürich, Version* (2004)

[Fortuin and Willemsen 2005] FORTUIN, NPM ; WILLEMSEN, A: Exsolution of nitrogen and argon by methanogenesis in Dutch ground water. In: *Journal of Hydrology* 301 (2005), No. 1

[Freundt et al. 2013] FREUNDT, F ; SCHNEIDER, T ; AESCHBACH-HERTIG, W: Response of noble gas partial pressures in soil air to oxygen depletion. In: *Chemical Geology* 339 (2013), p. 283–290

[Friedrich 2007] FRIEDRICH, R: *Grundwassercharakterisierung mit Umwelttracern: Erkundung des Grundwassers der Odenwald-Region sowie Implementierung eines neuen Edelgas-Massenspektrometersystems*, Institut für Umweltphysik, Universität Heidelberg, Dissertation, 2007

[Fuller and Giddings 1965] FULLER, EN ; GIDDINGS, JC: A comparison of methods for predicting gaseous diffusion coefficients. In: *Journal of Chromatographic Science* 3 (1965), No. 7, p. 222–227

[Gardi et al. 2015] GARDI, C ; ANGELINI, M ; BARCELÓ, S ; COMERMA, J ; CRUZ GAISTARDO, C ; ENCINA ROJAS, A ; JONES, A ; KRASILNIKOV, P ; MENDONÇA SANTOS BREFIN, ML ; MONTANARELLA, L ; MUÑIZ UGARTE, O ; SCHAD, P ; VARA RODRÍGUEZ, MI ; VARGAS, R. ; RAVINA DA SILVA, M (eds): Soil Atlas of Latin America and the Caribbean, European Commission. In: *Publications Office of the European Union, L-2995 Luxembourg* (2015), p. 176

[Gat 1980] GAT, JR: The isotopes of hydrogen and oxygen in precipitation. In: *Handbook of environmental isotope geochemistry. Vol. 1.* 1980

[Gerardi 2007] GERARDI, M.: Oxidation-reduction potential and wastewater treatment. In: *Interstate Water Report, New England Interstate Water Pollut. Control Comm., Lowell, Mass* (2007). – URL `http://www.neiwpcc.org/iwr/reductionpotential.asp`. – accessed on 2016/02/12

[Gerhards 2008] GERHARDS, H: *Ground penetrating radar as a quantitative tool with applications in soil hydrology*, Institut für Umweltphysik, Universität Heidelberg, Dissertation, 2008

[Gisi 1997] GISI, U: *Bodenökologie*. Georg Thieme Verlag, 1997

[GNIP 2016] GNIP: IAEA/WMO, Global Network of Isotopes in Precipitation (GNIP). (2016). – URL `http://www.iaea.org/water`. – accessed on 02/03/2016

[Google Earth 2016] GOOGLE EARTH: Google Inc.: v.7.1.5.1557. (2016)

[Graham 2002] GRAHAM, DW: Noble gas isotope geochemistry of mid-ocean ridge and ocean island basalts: Characterization of mantle source reservoirs. In: *Reviews in Mineralogy and Geochemistry* 47 (2002), No. 1, p. 247–317

[Greenwood et al. 1988] GREENWOOD, NN ; EARNSHAW, A ; HÜCKMANN, K: *Chemie der Elemente*. Bd. 1. VcH Weinheim, 1988

[Grew and Ibbs 1952] GREW, KE ; IBBS, TL: *Thermal diffusion in gases*. University Press, 1952

[Grothe 1992] GROTHE, J: *Datenerfassung und Datenauswertung am Heidelberger Low-Level-Tritium-Meßsystem*, Institut für Umweltphysik, Universität Heidelberg, Diploma, 1992

[Hall et al. 2005] HALL, CM ; CASTRO, MC ; LOHMANN, KC ; MA, L: Noble gases and stable isotopes in a shallow aquifer in southern Michigan: Implications for noble gas paleotemperature reconstructions for cool climates. In: *Geophysical Research Letters* 32 (2005), No. 18

[Hall et al. 2006] HALL, CM ; CASTRO, MC ; LOHMANN, KC ; MA, L: Reply to comment by Klump et al. on "Noble gases and stable isotopes in a shallow aquifer in southern Michigan: Implications for noble gas paleotemperature reconstructions for cool climates". In: *Geophysical Research Letters* 33 (2006), No. 24

[Hall et al. 2012] HALL, CM ; CASTRO, MC ; LOHMANN, KC ; SUN, T: Testing the noble gas paleothermometer with a yearlong study of groundwater noble gases in an instrumented monitoring well. In: *Water Resources Research* 48 (2012), No. 4

[Heaton and Vogel 1981] HEATON, THE ; VOGEL, JC: “Excess air” in groundwater. In: *Journal of Hydrology* 50 (1981), p. 201–216

[Hofer and Imboden 1998] HOFER, Markus ; IMBODEN, Dieter M.: Simultaneous determination of CFC-11, CFC-12, N2, and Ar in water. In: *Analytical Chemistry* 70 (1998), No. 4, p. 724–729

[Holocher et al. 2002] HOLOCHER, J ; PEETERS, F ; AESCHBACH-HERTIG, W ; HOFER, M ; BRENNWALD, M ; KINZELBACH, W ; KIPFER, R: Experimental investigations on the formation of excess air in quasi-saturated porous media. In: *Geochimica et Cosmochimica Acta* 66 (2002), No. 23, p. 4103–4117

[Holocher et al. 2003] Holocher, J ; Peeters, F ; Aeschbach-Hertig, W ; Kinzelbach, W ; Kipfer, R: Kinetic model of gas bubble dissolution in groundwater and its implications for the dissolved gas composition. In: *Environmental Science & Technology* 37 (2003), No. 7, p. 1337–1343

[Horstmann 2016] Horstmann, E: *Development of a mobile membrane inlet system for the analysis of dissolved gas concentrations*, Institut für Umweltphysik, Universität Heidelberg, Master, 2016

[IAEA 1977] IAEA: Consultants' meeting on stable isotope standards and intercalibration in Hydrolgy and in Geochemistry, Internal report. (1977), p. 35

[Ibbs et al. 1928] Ibbs, TL ; Grew, KE ; Hirst, AA: Thermal diffusion at low temperatures. In: *Proceedings of the Physical Society* 41 (1928), No. 1, p. 456

[INMET 2016] INMET, Instituto Nacional de Meteorologia: Dados Meteorológicos. (2016). – URL `http://www.inmet.gov.br`. – accessed on 2016/06/02

[Jacox et al. 2016] Jacox, MG ; Hazen, EL ; Zaba, KD ; Rudnick, DL ; Edwards, CA ; Moore, AM ; Bograd, SJ: Impacts of the 2015-2016 El Niño on the California Current System: Early assessment and comparison to past events. In: *Geophysical Research Letters* (2016)

[Jenner 2014] Jenner, F: *Untersuchung kurzzeitiger SF_6- und FCKW-Variationen in der Bodenluft im Kontext der Datierung jungen Grundwassers*, Institut für Umweltphysik, Universität Heidelberg, Bachelor, 2014

[Jenner 2016] Jenner, F: *unpublished data*, Institut für Umweltphysik, Universität Heidelberg, Master, 2016

[Jones et al. 2014] Jones, KL ; Lindsay, MBJ ; Kipfer, R ; Mayer, KU: Atmospheric noble gases as tracers of biogenic gas dynamics in a shallow unconfined aquifer. In: *Geochimica et Cosmochimica Acta* 128 (2014), p. 144–157

[Jung and Aeschbach 2016] Jung, M ; Aeschbach, W: A new software tool for the analysis of noble gas data sets from (ground)water. In: *Environmental Modelling & Software* submitted paper (2016)

[Jung et al. 2013] Jung, M ; Wieser, M ; Oehsen, A von ; Aeschbach-Hertig, W: Properties of the closed-system equilibration model for dissolved noble gases in groundwater. In: *Chemical Geology* 339 (2013), p. 291–300

[Kaatze 1989] Kaatze, U: Complex permittivity of water as a function of frequency and temperature. In: *Journal of Chemical and Engineering Data* 34 (1989), No. 4, p. 371–374

[Karstens et al. 2015] Karstens, U ; Schwingshackl, C ; Schmithüsen, D ; Levin, I: A process-based ^{222}radon flux map for Europe and its comparison to long-term observations. In: *Atmospheric Chemistry and Physics* 15 (2015), No. 22, p. 12845–12865

[Kaudse 2014] Kaudse, T: *Noble gases in groundwater of the Azraq Oasis, Jordan, and along the central Dead Sea Transform-Two case studies*, Institut für Umweltphysik, Universität Heidelberg, Dissertation, 2014

[Kipfer et al. 2002] Kipfer, R ; Aeschbach-Hertig, W ; Peeters, F ; Stute, M: *Noble gases in lakes and ground waters*. Mineral Soc America, 2002. – 615–700 S

[Kirkham and Powers 1972] Kirkham, D ; Powers, WL: *Advanced soil physics*. Wiley, 1972

[Klenk and Jaumann 2015] Klenk, P ; Jaumann, S: *Electromagnetic Methods in Applied Geophysics*. Heidelberg, 2015 (Practical Course Environmental Physics)

[Klinkenberg 1941] Klinkenberg, LJ: American Petroleum Institute. In: *Drilling and Productions Practices* (1941), p. 200–213

[Kluge et al. 2007] Kluge, T ; Ilmberger, J ; Von Rohden, C ; Aeschbach-Hertig, W: Tracing and quantifying groundwater inflow into lakes using radon-222. In: *Hydrology and Earth System Sciences Discussions Discussions* 4 (2007), No. 3, p. 1519–1548

[Klump et al. 2008] Klump, S ; Cirpka, OA ; Surbeck, H ; Kipfer, R: Experimental and numerical studies on excess-air formation in quasi-saturated porous media. In: *Water resources research* 44 (2008), No. 5

[Klump et al. 2006] Klump, S ; Kipfer, R ; Cirpka, OA ; Harvey, CF ; Brennwald, MS ; Ashfaque, KN ; Badruzzaman, ABM ; Hug, SJ ; Imboden, DM: Groundwater dynamics and arsenic mobilization in Bangladesh assessed using noble gases and tritium. In: *Environmental Science & Technology* 40 (2006), No. 1, p. 243–250

[Klump et al. 2007] Klump, S ; Tomonaga, Y ; Kienzler, P ; Kinzelbach, W ; Baumann, T ; Imboden, DM ; Kipfer, R: Field experiments yield new insights into gas exchange and excess air formation in natural porous media. In: *Geochimica et Cosmochimica Acta* 71 (2007), No. 6, p. 1385–1397

[Kulongoski et al. 2009] Kulongoski, JT ; Hilton, DR ; Izbicki, JA ; Belitz, K: Evidence for prolonged El Nino-like conditions in the Pacific during the Late Pleistocene: a 43ka noble gas record from California groundwaters. In: *Quaternary Science Reviews* 28 (2009), No. 23, p. 2465–2473

[Landau and Lifschitz 1991] Landau, LD ; Lifschitz, EM: *Lehrbuch der theoretischen Physik VI - Hydrodynamik*. 5. Akademie-Verlag, Berlin, 1991

[Lange and Dean 1979] Lange, NA ; Dean, JA: *Lange's Handbook of Chemistry*. McGraw-Hill, 1979

[Le Quéré et al. 2015] Le Quéré, C ; Moriarty, R ; Andrew, RM ; Canadell, JG ; Sitch, S ; Korsbakken, JI ; Friedlingstein, P ; Peters, GP ; Andres, RJ ; Boden, TA et al.: Global Carbon Budget 2015. In: *Earth System Science Data* 7 (2015), p. 349–396

[Leinfelder 2014] Leinfelder, D: *Cavity Ring-Down Spectroscopy for stable water isotope analysis – An instrument characterisation study*, Institut für Unweltphysik, Universität Heidelberg, Master, 2014

[Libby 1946] Libby, WF: Atmospheric helium three and radiocarbon from cosmic radiation. In: *Physical Review* 69 (1946), No. 11-12, p. 671

[Lippmann et al. 2005] Lippmann, J ; Erzinger, J ; Zimmer, M ; Schloemer, S ; Eichinger, L ; Faber, E: On the geochemistry of gases and noble gas isotopes (including ^{222}Rn) in deep crustal fluids: the 4000 m KTB-pilot hole fluid production test 2002-03. In: *Geofluids* 5 (2005), No. 1, p. 52–66

[Lippmann et al. 2003] Lippmann, J ; Stute, M ; Torgersen, T ; Moser, DP ; Hall, JA ; Lin, L ; Borcsik, M ; Bellamy, RES ; Onstott, TC: Dating ultra-deep mine waters with noble gases and 36 Cl, Witwatersrand Basin, South Africa. In: *Geochimica et Cosmochimica Acta* 67 (2003), No. 23, p. 4597–4619

[Lu et al. 2014] Lu, Z-T ; Schlosser, P ; Smethie, WM ; Sturchio, NC ; Fischer, TP ; Kennedy, BM ; Purtschert, R ; Severinghaus, JP ; Solomon, DK ; Tanhua, T et al.: Tracer applications of noble gas radionuclides in the geosciences. In: *Earth-Science Reviews* 138 (2014), p. 196–214

[LUBW 1999] LUBW: *Hydrogeologische Kartierung und Grundwasserbewirtschaftung Rhein-Neckar-Raum, Fortschreibung 1983-1998.* Stuttgart, Wiesbaden, Mainz : Ministerium für Umwelt und Verkehr Baden-Württemberg; Hessisches Ministerium für Umwelt, Landwirtschaft und Forsten; Ministerium für Umwelt und Forsten Rheinland-Pfalz, 1999

[LUBW 2016] LUBW, Landesanstalt für Umwelt Messungen und Naturschutz Baden-Württemberg: Daten- und Kartendienst der LUBW. (2016). – URL `http://udo.lubw.baden-wuerttemberg.de/public`. – accessed on 04/30/2016

[Lucas and Unterweger 2000] Lucas, LL ; Unterweger, MP: Comprehensive review and critical evaluation of the half-life of Tritium. In: *Journal of research-National institute of standards and technology* 105 (2000), No. 4, p. 541–550

[Ma et al. 2004] Ma, L ; Castro, MC ; Hall, CM: A late Pleistocene-Holocene noble gas paleotemperature record in southern Michigan. In: *Geophysical research letters* 31 (2004), No. 23

[Ma et al. 2005] Ma, L ; Castro, MC ; Hall, CM ; Walter, LM: Cross-formational flow and salinity sources inferred from a combined study of helium concentrations, isotopic ratios, and major elements in the Marshall aquifer, southern Michigan. In: *Geochemistry, Geophysics, Geosystems* 6 (2005), No. 10

[Mächler et al. 2012] Mächler, L ; Brennwald, MS ; Kipfer, R: Membrane inlet mass spectrometer for the quasi-continuous on-site analysis of dissolved gases in groundwater. In: *Environmental science & technology* 46 (2012), No. 15, p. 8288–8296

[Maiss et al. 1994] Maiss, M ; Ilmberger, J ; Münnich, KO: Vertical mixing in Ueberlingersee (Lake Constance) traced by SF_6 and heat. In: *Aquatic sciences* 56 (1994), No. 4, p. 329–347

[Mamyrin and Tolstikhin 1984] Mamyrin, BA ; Tolstikhin, IN: Helium isotopes in nature. (1984)

[Marinha do Brasil 2016] MARINHA DO BRASIL, Capitania Fluvial de S.: Serviço de Documentação da Marinha - Revista Marítima Brasileira. (2016)

[Massmann and Farrier 1992] MASSMANN, J ; FARRIER, DF: Effects of atmospheric pressures on gas transport in the vadose zone. In: *Water resources research* 28 (1992), No. 3, p. 777–791

[Mayer et al. 2002] MAYER, KU ; FRIND, EO ; BLOWES, DW: Multicomponent reactive transport modeling in variably saturated porous media using a generalized formulation for kinetically controlled reactions. In: *Water Resources Research* 38 (2002), No. 9

[Mayer 2012] MAYER, S: *Analyzing short-term fluctuations of noble gas concentrations in soil air and groundwater*, Institut für Unweltphysik, Universität Heidelberg, Master, 2012

[Mazor 1972] MAZOR, E: Paleotemperatures and other hydrological parameters deduced from noble gases dissolved in groundwaters; Jordan Rift Valley, Israel. In: *Geochimica et Cosmochimica Acta* 36 (1972), No. 12, p. 1321–1336

[Medina et al. 1980] MEDINA, E ; KLINGE, H ; JORDAN, C ; HERRERA, R: Soil respiration in Amazonian rain forests in the Rio-Negro-Basin. In: *Flora* 170 (1980), No. 3, p. 240–250

[Meibom et al. 2005] MEIBOM, A ; SLEEP, NH ; ZAHNLE, K ; ANDERSON, DL: Models for noble gases in mantle geochemistry: Some observations and alternatives. In: *Geological Society of America Special Papers* 388 (2005), p. 347–363

[Meir et al. 1996] MEIR, P ; GRACE, J ; LLOYD, J ; MIRANDA, AC: Soil respiration in a rainforest in Amazonia, and in Cerrado in Central Brazil. In: *Amazonian deforestation and climate* 1 (1996)

[Mercury et al. 2004] MERCURY, L ; PINTI, DL ; ZEYEN, H: The effect of the negative pressure of capillary water on atmospheric noble gas solubility in ground water and palaeotemperature reconstruction. In: *Earth and Planetary Science Letters* 223 (2004), No. 1, p. 147–161

[Meschede 2015] MESCHEDE, D: *Gerthsen Physik*. Springer-Verlag, 2015

[Michel et al. 2015] MICHEL, RL ; AGGARWAL, P ; ARAGUAS-ARAGUAS, L ; KURTTAS, T ; NEWMAN, BD ; VITVAR, T: A simplified approach to analysing historical and recent tritium data in surface waters. In: *Hydrological Processes* 29 (2015), No. 4, p. 572–578

[Miller et al. 2009] MILLER, S ; GOULDEN, ML ; ROCHA, HR da: LBA−ECO CD−04 Meteorological and Flux Data, km 83 Tower Site, Tapajós National Forest. Dataset from Oak Ridge National Laboratory Distributed Active Archive Center. (2009). – URL `http://daac.ornl.gov`. – accessed on 2016/06/02

[Millington and Quirk 1961] MILLINGTON, RJ ; QUIRK, JP: Permeability of porous solids. In: *Transactions of the Faraday Society* 57 (1961), p. 1200–1207

[Molins and Mayer 2007] MOLINS, S ; MAYER, KU: Coupling between geochemical reactions and multicomponent gas and solute transport in unsaturated media: A reactive transport modeling study. In: *Water Resources Research* 43 (2007), No. 5

[Mook 2000] Mook, WG: *Environmental Isotopes in the hydrological cycle. Principles and applications.*. Bd. 39. IAEA Publish, 2000

[Muñoz-Carpena et al. 2004] Muñoz-Carpena, R ; Shukla, S ; Morgan, K: Field devices for monitoring soil water content. In: *University of Florida Cooperative Extension Service, Institute of Food and Agricultural Sciences, EDIS* (2004)

[Nazaroff 1992] Nazaroff, WW: Radon transport from soil to air. In: *Reviews of Geophysics* 30 (1992), No. 2, p. 137–160

[Nazaroff and Sextro 1989] Nazaroff, WW ; Sextro, RG: Technique for measuring the indoor radon-222 source potential of soil. In: *Environmental science & technology* 23 (1989), No. 4, p. 451–458

[Oana 1957] Oana, S: Bestimmung von Argon in besonderem Hinblick auf gelöste Gase in natürlichen Gewässern. In: *The Journal of earth sciences, Nagoya University* 5 (1957), p. 103–105

[Oliveira 1996] Oliveira, JR: Potencialidades Hidrogeológicas da Área Urbana de Santarém, com Proposta Técnica para Projeto de Poços Tubulares Profundos para Captação de Água Subterrânea. In: *Relatório Técnico. Companhia de Pesquisa de Recursos Minerais (CPRM), Programa de Integração Mineral em Municípios da Amazônia - Primaz. Belém, Pará.* (1996)

[Ottow 2011] Ottow, JCG: *Mikrobiologie von Böden: Biodiversität, Ökophysiologie und Metagenomik*. Springer-Verlag, 2011

[Ozima and Podosek 2002] Ozima, Minoru ; Podosek, Frank A.: *Noble gas geochemistry*. Cambridge University Press, 2002

[Paldus and Kachanov 2005] Paldus, BA ; Kachanov, AA: An historical overview of cavity-enhanced methods. In: *Canadian Journal of Physics* 83 (2005), No. 10, p. 975–999

[Paul and Clark 1996] Paul, EA ; Clark, FE: *Soil microbiology and biochemistry*. 2. Michigan, Colorado : Academic Press, 1996

[Peeters et al. 2003] Peeters, F ; Beyerle, U ; Aeschbach-Hertig, W ; Holocher, J ; Brennwald, MS ; Kipfer, R: Improving noble gas based paleoclimate reconstruction and groundwater dating using 20 Ne/22 Ne ratios. In: *Geochimica et Cosmochimica Acta* 67 (2003), No. 4, p. 587–600

[Peixóto and Oort 1983] Peixóto, JP ; Oort, AH: The atmospheric branch of the hydrological cycle and climate. (1983), p. 5–65

[Pfeiffer Vacuum 2010] Pfeiffer Vacuum: OmniStar^{TM} Gasanalysesystem GSD320 Betriebsanleitung. In: *BG 5953 BD* 2010-9 (2010)

[Platten 2006] Platten, JK: The Soret effect: a review of recent experimental results. In: *Journal of applied mechanics* 73 (2006), No. 1, p. 5–15

[Poling et al. 2000] Poling, BE ; Prausnitz, JM ; O'Connell, JP: *The properties of gases and liquids*. Mcgraw-Hill Professional, 2000. – 768 S

[Popovičová and Brusseau 1997] Popovičová, J ; Brusseau, ML: Dispersion and transport of gas-phase contaminants in dry porous media: effect of heterogeneity and gas velocity. In: *Journal of contaminant Hydrology* 28 (1997), No. 1, p. 157–169

[Porcelli et al. 2002] Porcelli, D ; Ballentine, CJ ; Wieler, R: *Noble gases in geochemistry and cosmochemistry*. Mineral Soc America, 2002

[Powell et al. 1988] Powell, WG ; Chapman, DS ; Balling, N ; Beck, AE: Continental heat-flow density. In: *Handbook of terrestrial heat-flow density determination*. Springer, 1988, p. 167–222

[Prandtl et al. 2013] Prandtl, L ; Oswatitsch, K ; Wieghardt, K: *Führer durch die Strömungslehre*. Springer-Verlag, 2013

[Radiochemical Institute Karlsruhe 1996] Radiochemical Institute Karlsruhe: Karlsruher Nuklidkarte. 6 (1996)

[Raich and Schlesinger 1992] Raich, JW ; Schlesinger, WH: The global carbon dioxide flux in soil respiration and its relationship to vegetation and climate. In: *Tellus B* 44 (1992), No. 2, p. 81–99

[Ramanathan 1977] Ramanathan, KR: Isotope techniques in groundwater hydrology. In: *Proceedings of the first national symposium on application of isotope techniques in hydrology and hydraulics [held at] Poona, November 24-27, 1974*, 1977

[Ratkowsky et al. 1982] Ratkowsky, DA ; Olley, J ; McMeekin, TA ; Ball, A: Relationship between temperature and growth rate of bacterial cultures. In: *Journal of Bacteriology* 149 (1982), No. 1

[Rau 1999] Rau, I: *Multitracerstudie zum Langzeitspeicherverhalten von heterogenporösen Medien: am Beispiel des Karstgrundwasserleiters der südlichen Fränkischen Alb*, Fakultät für Geowissenschaften, Universität München, Dissertation, 1999

[Ritterbusch et al. 2014] Ritterbusch, F ; Ebser, S ; Welte, J ; Reichel, T ; Kersting, A ; Purtschert, R ; Aeschbach-Hertig, W ; Oberthaler, MK: Groundwater dating with Atom Trap Trace Analysis of ^{39}Ar. In: *Geophysical Research Letters* 41 (2014), No. 19, p. 6758–6764

[Robinson et al. 2003] Robinson, DA ; Jones, SB ; Wraith, JM ; Or, D ; Friedman, SP: A review of advances in dielectric and electrical conductivity measurement in soils using time domain reflectometry. In: *Vadose Zone Journal* 2 (2003), No. 4, p. 444–475

[Roedel and Wagner 2010] Roedel, W ; Wagner, T: *Physik unserer Umwelt: Die Atmosphäre*. Springer-Verlag, 2010

[Roth et al. 1990] Roth, K ; Schulin, R ; Fühler, H ; Attinger, W: Calibration of time domain reflectometry for water content measurement using a composite dielectric approach. In: *Water Resources Research* 26 (1990), No. 10, p. 2267–2273

[Rozanski et al. 1991] ROZANSKI, K ; GONFIANTINI, R ; ARAGUAS-ARAGUAS, L: Tritium in the global atmosphere: Distribution patterns and recent trends. In: *Journal of Physics G: Nuclear and Particle Physics* 17 (1991), No. S, p. S523

[Sakaki et al. 2008] SAKAKI, T ; LIMSUWAT, A ; SMITS, KM ; ILLANGASEKARE, TH: Empirical two-point α-mixing model for calibrating the ECH2O EC-5 soil moisture sensor in sands. In: *Water resources research* 44 (2008), No. 4

[Scanlon et al. 2002] SCANLON, BR ; NICOT, JP ; MASSMANN, JW: *Soil Physics Companion, chap. Soil gas movement in unsaturated systems*. CRC press, 2002

[Schell et al. 1970] SCHELL, WR ; SAUZAY, G ; PAYNE, BR: Tritium injection and concentration distribution in the atmosphere. In: *Journal of Geophysical Research* 75 (1970), No. 12, p. 2251–2266

[Schlosser et al. 1989] SCHLOSSER, P ; STUTE, M ; SONNTAG, C ; MÜNNICH, KO: Tritiogenic ^{3}He in shallow groundwater. In: *Earth and Planetary Science Letters* 94 (1989), No. 3, p. 245–256

[Schlosser and Winckler 2002] SCHLOSSER, P ; WINCKLER, G: Noble gases in ocean waters and sediments. In: *Reviews in mineralogy and geochemistry* 47 (2002), No. 1, p. 701–730

[Schmidt et al. 2009] SCHMIDT, A ; STRINGER, CE ; HAFERKORN, U ; SCHUBERT, M: Quantification of groundwater discharge into lakes using radon-222 as naturally occurring tracer. In: *Environmental Geology* 56 (2009), No. 5, p. 855–863

[Schneider 2009] SCHNEIDER, T: *Einfluss von Sauerstoffzehrung auf Edelgaspartialdrücke in Bodenluft*, Institut für Umweltphysik, Universität Heidelberg, Diploma, 2009

[Schneider 2014] SCHNEIDER, T: *Eine Paläoklimastudie an einem Grundwasseraquifersystem in der Nordchinesischen Ebene*, Institut für Umweltphysik, Universität Heidelberg, Dissertation, 2014

[Sclater et al. 1980] SCLATER, JG ; JAUPART, C ; GALSON, D: The heat flow through oceanic and continental crust and the heat loss of the Earth. In: *Reviews of Geophysics* 18 (1980), No. 1, p. 269–311

[Severinghaus et al. 1996] SEVERINGHAUS, JP ; BENDER, ML ; KEELING, RF ; BROECKER, WS: Fractionation of soil gases by diffusion of water vapor, gravitational settling, and thermal diffusion. In: *Geochimica et Cosmochimica Acta* 60 (1996), No. 6, p. 1005–1018

[Solomon et al. 2010] SOLOMON, DK ; GENEREUX, DP ; PLUMMER, LN ; BUSENBERG, E: Testing mixing models of old and young groundwater in a tropical lowland rain forest with environmental tracers. In: *Water resources research* 46 (2010), No. 4

[Sonntag 1990] SONNTAG, D: Important new values of the physical constants of 1986, vapor pressure formulations based on the ITS-90, and psychrometer formulate. In: *Meteorologische Zeitschrift* 70 (1990), No. 5, p. 340–344

[Sotta et al. 2004] Sotta, ED ; Meir, P ; Malhi, Y ; Nobre, AD ; Hodnett, M ; Grace, J: Soil CO2 efflux in a tropical forest in the central Amazon. In: *Global Change Biology* 10 (2004), No. 5, p. 601–617

[Stanley et al. 2009] Stanley, RHR ; Baschek, B ; Lott, DE ; Jenkins, WJ: A new automated method for measuring noble gases and their isotopic ratios in water samples. In: *Geochemistry, Geophysics, Geosystems* 10 (2009), No. 5

[Stute 1989] Stute, M: *Edelgase im Grundwasser: Bestimmung von Paläotemperaturen und Untersuchung der Dynamik von Grundwasserfließsystemen*, Institut für Umweltphysik, Universität Heidelberg, Dissertation, 1989

[Stute et al. 1995] Stute, M ; Forster, M ; Frischkorn, H ; Serejo, A ; Clark, JF ; Schlosser, P ; Broecker, WS ; Bonani, G: Cooling of tropical Brazil (5°C) during the last glacial maximum. In: *Science* 269 (1995), No. 5222, p. 379–383

[Stute and Schlosser 1993] Stute, M ; Schlosser, P: Principles and applications of the noble gas paleothermometer. In: *Climate change in continental isotopic records* (1993), p. 89–100

[Stute and Sonntag 1992] Stute, M ; Sonntag, C: *Palaeotemperatures derived from noble gases dissolved in groundwater and in relation to soil temperature*. 1992

[Stute and Talma 1998] Stute, M ; Talma, AS: Glacial temperatures and moisture transport regimes reconstructed from noble gases and δ 18 O, Stampriet aquifer, Namibia. In: *Isotope techniques in the study of environmental change*. 1998

[Stute et al. 2007] Stute, M ; Zheng, Y ; Schlosser, P ; Horneman, A ; Dhar, RK ; Datta, Saugata ; Hoque, MA ; Seddique, AA ; Shamsudduha, M ; Ahmed, KM et al.: Hydrological control of As concentrations in Bangladesh groundwater. In: *Water Resources Research* 43 (2007), No. 9

[Stute and Schlosser 2000] Stute, Martin ; Schlosser, Peter: Atmospheric noble gases. In: *Environmental tracers in subsurface hydrology*. Springer, 2000, p. 349–377

[Sültenfuß et al. 2009] Sültenfuss, J ; Roether, W ; Rhein, M: The Bremen mass spectrometric facility for the measurement of helium isotopes, neon, and tritium in water. In: *Isotopes in environmental and health studies* 45 (2009), No. 2, p. 83–95

[Sun et al. 2010] Sun, T ; Hall, CM ; Castro, MC: Statistical properties of groundwater noble gas paleoclimate models: Are they robust and unbiased estimators? In: *Geochemistry, Geophysics, Geosystems* 11 (2010), No. 2

[Sun et al. 2008] Sun, T ; Hall, CM ; Castro, MC ; Lohmann, KC ; Goblet, P: Excess air in the noble gas groundwater paleothermometer: A new model based on diffusion in the gas phase. In: *Geophysical Research Letters* 35 (2008), No. 19

[Tancredi 1996] Tancredi, NSH: Recursos Hídricos Subterrâneos de Santarém: Fundamentos para uso e proteção. In: *Tese de Doutorado, Centro de Geociências, Universidade Federal do Pará, Belém, Pará* (1996), p. 167

[Tanikawa and Shimamoto 2006] Tanikawa, W ; Shimamoto, T: Klinkenberg effect for gas permeability and its comparison to water permeability for porous sedimentary rocks. In: *Hydrology and Earth System Sciences Discussions* 3 (2006), No. 4, p. 1315–1338

[Tans and Keeling 2015] Tans, P ; Keeling, R: In: *Water Resources Research* (2015). – URL `www.esrl.noaa.gov/gmd/ccgg/trends`. – accessed on 2016/04/24

[Tapajós et al. 2016] Tapajós, R ; Dias, D F. ; Machado, CJF: Fluxo Hídrico Subterrâneo no Sistema Aquífero da Bacia do Igarapé Irurá - Santarém/Pará. In: *Publication in preparation* (2016)

[Täsch 1987] Täsch, M: *Einschichtung der Reuss in den Urnersee*, ETH Zürich, Diploma, 1987

[Theng et al. 1989] Theng, BKG ; Tate, KR ; Sollins, P ; Moris, N ; Nadkarni, N: *Constituents of organic matter in temperate and tropical soils*. University of Hawaii Press Honolulu, 1989

[Thorstenson and Pollock 1989] Thorstenson, DC ; Pollock, DW: Gas transport in unsaturated porous media: The adequacy of Fick's law. In: *Reviews of Geophysics* 27 (1989), No. 1, p. 61–78

[Urey 1947] Urey, HC: *The thermodynamic properties of isotopic substances*. Royal Society of Chemistry, 1947. – 562–581 S

[Vardag et al. 2015] Vardag, SN ; Gerbig, C ; Janssens-Maenhout, G ; Levin, I: Estimation of continuous anthropogenic CO_2: Model-based evaluation of CO_2, CO, $\delta^{13}C(CO_2)$ and $\delta^{14}C(CO_2)$ tracer methods. In: *Atmospheric Chemistry and Physics* 15 (2015), No. 22, p. 12705–12729

[Verwaltungsverlag 2012] Verwaltungsverlag: City map Heidelberg. (2012)

[Visser et al. 2007] Visser, A ; Broers, HP ; Bierkens, MFP: Dating degassed groundwater with $^3H/^3He$. In: *Water Resources Research* 43 (2007), No. 10

[Visser et al. 2014] Visser, A ; Fourré, E ; Barbecot, F ; Aquilina, L ; Labasque, T ; Vergnaud, V ; Esser, BK et al.: Intercomparison of tritium and noble gases analyses, $^3H/^3He$ ages and derived parameters excess air and recharge temperature. In: *Applied Geochemistry* 50 (2014), p. 130–141

[Weiss 1970] Weiss, RF: The solubility of nitrogen, oxygen and argon in water and seawater. 17 (1970), No. 4, p. 721–735

[Weiss 1971] Weiss, RF: Solubility of helium and neon in water and seawater. In: *Journal of Chemical & Engineering Data* 16 (1971), No. 2, p. 235–241

[Whiticar et al. 1986] Whiticar, MJ ; Faber, E ; Schoell, M: Biogenic methane formation in marine and freshwater environments: CO_2 reduction vs. acetate fermentation-isotope evidence. In: *Geochimica et Cosmochimica Acta* 50 (1986), No. 5, p. 693–709

[Whitman 1923] WHITMAN, WG: The two-film theory of gas absorption. In: *Chemical and Metallurgical Engineering* 29 (1923), p. 146–148

[Wieser 2006] WIESER, M: *Entwicklung und Anwendung von Diffusionssamplern zur Beprobung gelöster Edelgase in Wasser*, Institut für Unweltphysik, Universität Heidelberg, Diploma, 2006

[Wieser 2010] WIESER, M: *Imprints of climatic and environmental change in a regional aquifer system in an arid part of India using noble gases and other environmental tracers*, Institut für Unweltphysik, Universität Heidelberg, Dissertation, 2010

[Wolter 2016] WOLTER, K: NOAA/ESRL. In: *Physical Sciences Division* (2016). – URL `http://www.esrl.noaa.gov/psd/enso/mei`. – accessed on 2016/07/04

[Wood 1995] WOOD, M: *Environmental soil biology*. Springer Science & Business Media, 1995

[Yamaguchi et al. 1967] YAMAGUCHI, M ; FLOCKER, WJ ; HOWARD, FD: Soil atmosphere as influenced by temperature and moisture. In: *Soil Science Society of America Journal* 31 (1967), No. 2, p. 164–167

[Zanchi et al. 2009] ZANCHI, FB ; DA ROCHA, HR ; DE FREITAS, HC ; KRUIJT, B ; WATERLOO, MJ ; MANZI, AO: Measurements of soil respiration and simple models dependent on moisture and temperature for an Amazonian southwest tropical forest. In: *Biogeosciences Discussions* 6 (2009), No. 3, p. 6147–6177

[Zhang 2005] ZHANG, T: Influence of the seasonal snow cover on the ground thermal regime: An overview. In: *Reviews of Geophysics* 43 (2005), No. 4

Danksagungen

Auf dem Weg zu meiner Dissertation haben mich viele mir nahe stehenden Menschen begleitet, bei denen ich mich auf diesem Wege herzlich bedanken möchte.

An erster Stelle steht Prof. Dr. Werner Aeschbach. Seine motivierende Art und vielfältige Unterstützung während meines gesamten Studiums vom Bachelor bis zur Dissertation waren ein wertvoller Bestandteil meiner Studienzeit. Danke für die angenehme Arbeitsatmosphäre und die absolute Verlässlichkeit, insbesondere in stressigen Zeiten, und für die persönliche Begleitung zur ersten Messkampagne in Brasilien. Mir werden insbesondere auch die gemeinsamen Gruppenausflüge, Weihnachtsfeiern und das ein oder andere Schachspiel in guter Erinnerung bleiben.

Prof. Dr. Ingeborg Levin danke ich für die Bereitschaft der Übernahme des Zweitgutachtens meiner Dissertation.

Die wissenschafltiche Arbeit der letzten Jahre war mit vielen Reisen verbunden. Unvergessen bleiben die beiden mehrwöchigen Aufenthalte zu Messkampagnen im tropischen Santarém in Brasilien. Therese Weißbach und Florian Jenner haben mich dorthin begleitet, bei hoher Luftfeuchtigkeit, ungewohnten Lebensmitteln der besonderen Art, Papageien, Schlangen und Krokodilen sowie einem ständigen Wechsel aus tropischer Hitze und Klimaanlagen-Kälte. Vielen Dank für eure Begleitung ans Ende der Welt, die Bereitschaft all die Wochen im Provisorien-Alltag zu verbringen und zahlreiche Kisten durch Flughafen und Regenwald mit zu schleppen.
Mein besonderer Dank gilt Prof. Dr. Bernhard Peregovich von der Unsiversität in Santarém, der sich mit uns sowohl durch den unvorstellbaren brasilianischen Bürokratie-Dschungel geschlagen hat als auch uns über Wochen hinweg jeden Tag bei der Probeentnahme begleitet hat. Viele seiner Kollegen haben uns überaus gastfreundlich empfangen. Mein Dank gilt ebenso der Direktorin der Universität, Prof. Raimunda Monteiro und Prof. Carlos Machado, die uns in jeder erdenklichen Weise geholfen und einige brasilianische Traditionen näher gebracht haben. Muito obrigado!!
Weitere Dienstreisen zu Konferenzen und Probenahmen führten uns nach Wien, Paris, Zürich, Regensburg, Stuttgart, Bad Krozingen, und weit über 100 mal die nähere Umgebung von Heidelberg. In dieser Zeit war mir Florian Jenner ein treuer, zuverlässiger und wertvoller Begleiter. Vielen Dank dafür!

Mein weiterer Dank für Unterstützung gilt
- der Gemeinde Heddesheim für die Möglichkeit auf ihrem Grundstück während der vergangenen drei Jahre unsere Messstelle einrichten zu dürfen,
- Klaus Bender von der MVV Energie AG, der bei der Suche einer geeigneten Messstelle geholfen und den Kontakt nach Brasilien ermöglicht hat,
- Bjoern Schäfer für die Möglichkeit der Probenahme im Tropenhaus der Wilhelma in Stuttgart,
- Angelika Gassama für die freundliche und geduldige Unterstützung bei allen Belangen die mit dem Institutsbus zu tun hatten

– und der Deutschen Forschungsgemeinschaft für die Finanzierung dieses Projektes (Grant AE 93/11).

Für die gemeinsame Zeit am Institut für Umweltphysik danke ich ganz besonders Florian Jenner, Therese Weißbach, Sanam Vardag, Arne Kersting und Neta Tsur für die Abwechslung vom Arbeitsalltag bei unzähligen Keks-, Smoothie- und Eispausen.
Für den gemeinsamen Messbetrieb am Massenspektrometer, auch im Schichtbetrieb, danke ich vor allem Tillmann Kaudse, Florian Jenner und Therese Weißbach. Aber auch dem Rest der Crew, Florian Freundt, Benno Beck und natürlich unseren beiden Technikern Karl Reis und Stefan Schäfer. Vor allem Karl möchte ich danken für die viele Mühe, mit der er unseren Arbeitsbetrieb aufrecht erhält und dafür dass ich dank ihm nun wieder mit Licht am Fahrrad nach Hause fahren kann.
Für die zahlreichen Diskussionen meiner Messdaten danke ich Johann Ilmberger und Tillmann Kaudse, von denen ich auch schon während meiner Masterarbeit viel gelernt habe.
Auch die Gruppe der regelmäßigen Mensa-Gänger aus unserer Arbeitsgruppe soll hier natürlich nicht unerwähnt bleiben.

Für das zeitintensive Korrekturlesen meine Disseration danke ich Arne Kersting, Therese Weißbach, Tim Schneider, Sanam Vardag, Johann Ilmberger und vor allem Florian Jenner.

Für viele gemeinsame Erlebnisse und die schöne Zeit neben dem Studium möchte ich meinen Freunden danken. Ganz besonders danke ich Florian Jenner, Markus Als sowie Kathrin und Michel Kettner. Ich bin sehr dankbar für die vielen Erlebnisse und die gemeinsame Zeit mit euch, die wir zum Teil bereits schon seit der Schulzeit miteinander verbringen.

Last but not least danke ich herzlich meinen Eltern Andrea und Michael Mayer, die mich durch mein Leben begleiten, mich gefördert, unterstützt und stets ermutigt haben, meinen Weg zu gehen. In diesen Dank schließe ich meine Geschwister Thomas und Tabea, und meine Großeltern mit ein.